7-12-2014

An Ultrawideband Dual-Linear Polarization Feed for Solar Microwave Observation

Cecil Compeau Jr.

Cecil Richard Compeau, Jr.
Candidate

Electrical & Computer Engineering
Department

This dissertation is approved, and it is acceptable in quality and form for publication:

Approved by the Dissertation Committee:

Prof. Christos G. Christodoulou, Chairperson

Prof. Mark A. Gilmore, Co-Chairperson

Prof. John A. J. Matthews

Dr. Stephen M. White

Dr. Silvio E. Barbin

AN ULTRAWIDEBAND DUAL-LINEAR POLARIZATION FEED FOR SOLAR MICROWAVE OBSERVATION

by

CECIL RICHARD COMPEAU, JR.

B.S., Materials Science & Engineering, MIT, 1976
M.S., Materials Science & Engineering, MIT, 1978

DISSERTATION

Submitted in Partial Fulfillment of the
Requirements for the Degree of

Doctor of Philosophy

Engineering

The University of New Mexico
Albuquerque, New Mexico

May, 2014

ACKNOWLEDGMENTS

I would like to acknowledge the Air Force Research Laboratory for financial support of my dissertation work, both by the Student Career Experience Program assistantship and by support from contract FA9453-09-C-0309 from the Solar Disturbance Prediction Program.

I would also like to acknowledge the University of New Mexico Electrical & Computer Engineering Department for financial support via Teaching Assistantships and Research Assistantships, and the Walter E. King Fellowship.

The following individuals were instrumental and I would like to thank them wholeheartedly:

AFRL

Dr. Joel Mozer, Dr. Richard Radick, Dr. Nick Arge, Dr. Carl Henney, Dr. Stephen White, Ms. Elizabeth Luebchow, Mr. Anthony Gutierrez.

Electrodynamic

Brock Roberts, Melcoy Pablo.

MIT

Prof. Ron Latanision.

UNM

Prof. Greg Heileman, Prof. Christos Christodoulou, Prof. Mark Gilmore, Prof. Edl Schamiloglu, Prof. Luke Lester, Prof. Ramiro Jordan, Prof. John Matthews, Dr. Jerald Buchenauer, Dr. Carl Baum, Dr. Tengiz Svimonishvli, Dr. Silvio Barbin, Mr. Christopher Leach, Ms. Elmyra Grelle, Ms. Mimi Stephens.

Other

Ms. Adelaide Horn, my parents.

AN ULTRAWIDEBAND DUAL-LINEAR POLARIZATION FEED FOR SOLAR MICROWAVE OBSERVATION

Cecil Richard Compeau, Jr.
B.S., Materials Science & Engineering, MIT, 1976
M.S., Materials Science & Engineering, MIT, 1978
Doctor of Philosophy, Engineering, University of New Mexico, 2014

ABSTRACT

The study of Solar Microwave Bursts (SMB's) emanating from the sun is important from several perspectives. SMB's are well correlated to Coronal Mass Ejections (CME's) and therefore can provide insight into the physics of the sun. SMB's and CME's can interfere with microwave communication systems such as cell phones, satellites, and radar, and can adversely affect the accuracy of the Global Positioning System. Furthermore, CME's can be hazardous to individuals and equipment in earth orbit as well as causing power grid blackouts. The rapid detection of SMB's and their subsequent effect on space weather is a key element of responsibility of the United States Air Force (USAF). Identification of the source eliminates the possibility of intentional jamming or a systems failure. When such a determination is made, warnings can be issued so that measures can be taken such as using different communication frequencies or modes, or to place satellites in a safe mode. Currently the USAF operates the Radio Solar Telescope Network (RSTN) consisting of three parabolic dish antennas each at four locations to continuously observe the sun in the microwave spectrum. The 2.4m RSTN dishes have feeds that are single polarization at four discrete frequencies between 1.4 and 8.8GHz. Expanding the capability of these existing dishes with a single ultrawideband feed to cover 1-10GHz would improve observations, while adding a dual polarization capability could facilitate improved monitoring should there be future developments in spectrum usage. A feed with folded diamond-shaped elements in a damped cavity has been designed and constructed, funded under contract FA9453-09-C-0309 from the USAF Solar Disturbance Prediction Program, with a simulated bandwidth of 0.9 - 12 GHz. Subsequent characterization from 2 - 8 GHz showed good correlation between simulation

and measurement, and that the feed meets virtually all performance specifications that were tested.

Table of Contents

List of Figures

List of Tables

Chapter 1: Introduction

Civilian and military agencies rely heavily upon microwave communications in the 1-5 GHz range. Solar flares and other releases of energy in this spectrum can cause disruption in such communications, so detecting their occurrence is both desirable and necessary. Furthermore, the observation of solar microwave emission spectra and polarization state yields insight into the physics related to various solar phenomena.

> *"The electromagnetic radiation is of exceptional importance as a diagnostic tool for understanding the origin and physics of various dynamic solar phenomena."* [1]

The application of this work is directed towards USAF-related considerations and requirements towards developing an upgraded feed for full-disk solar microwave observation.

The USAF Radio Solar Telescope Network (RSTN) provides continuous solar monitoring at 8 fixed frequencies - 245, 410, 610, 1415, 2695, 4995, 8800, and 15400 MHz - from facilities located in Australia, Hawaii, Italy, and Massachusetts. These four installations monitor radio emissions from solar flares and other releases of energy from the sun. Data are fed back to the Air Force Weather Agency which notifies military and civilian personnel concerned with space, weather, power and communications when events take place that may cause disruptions to normal services. Such notifications are based upon radio flux levels thus the need for accurate and robust calibration of the telescopes.

Scientific research capabilities could be enhanced if RSTN's current single-frequency, single-polarization systems were to be replaced with broadband, dual-polarization elements. Currently the feeds for 1415MHz and beyond are single-polarization dipole or horn antennas. A broadband antenna would facilitate improved spectral measurements and a dual-polarization capability would yield polarization information, both of which provide valuable information for space weather monitoring. For possible RSTN application, 1-5GHz would be desirable as a minimum target bandwidth because this range covers both GPS and cellular frequencies, although

extending the upper frequency limit to 8.8GHz or beyond would also be desirable. Dual linear polarization is desired due to its ease of calibration.

A consideration for a feed in this application is the minimization of its *beam squint*. Beam squint is a condition where the desired lobe of the antenna is offset from the antenna's bore sight and may be induced intentionally, such as by array phasing, or unintentionally via geometric and/or phasing factors. One example of a situation where squint was problematic occurred with the Owens Valley Solar Array (OVSA), one of the facilities providing solar microwave observations to the USAF. In 2011 it was discovered that the commercially available broadband dual-linear polarization log-periodic feed used in the OVSA exhibited an undesirable amount of squint, measured to be as much as 26 arc minutes [2], comparable to the sun's angular diameter of approximately 32 arc minutes. The squint was not systematic and it varied with frequency so that the pointing error could not be calibrated out by the telescope pointing software. It was hypothesized that the squint is due to physical asymmetries in the LPDA.

For full-disk solar observations in systems such as RSTN a parabolic dish on the order of 2m diameter is used so that the beam width of the system fully covers the sun's disk. As the gain of a parabolic reflector increases with frequency, for a constant feed beam width the overall system beam width will narrow as frequency increases. In this context an excessive amount of beam squint will move the beam so that not all of the solar disk is observed, or even cause the beam to point entirely away from the sun. Thus it is desirable to minimize the beam squint of the broadband feed.

A RSTN dish requires a beam width of about 135° to fully illuminate the dish as it is a prime-focus system. Broadband horn antennas have suitable bandwidth and squint performance but with directivities that increase with frequency. A representative typical broadband antenna, the A-INFO JXTXLB-SJ-10100 1-10GHz dual-linear polarization horn has a half-power beam width (HPBW) of 105° at 1GHz but only 22° at 10GHz [3]. This is contrasted to a log-periodic dipole array (LPDA) such as the TECOM antenna used in the OVSA, which, as is the case for LPDA's, only exhibits about a 2° change in beam width over frequency [4].

A final consideration is minimizing the defocusing loss. A parabolic reflector has a unique focal point. When this focal point does not coincide with the phase center of the feed a defocusing loss occurs that increases exponentially with its displacement [5]. Because of this phenomenon, feeds that exhibit significant movement of the phase center along the axis directed towards dish center will exhibit undesirable defocusing losses. An example would be an LPDA, where the phase center travels along its longitudinal axis towards the apex as frequency increases. In comparison, planar structures would be expected to exhibit little longitudinal movement in the phase center with correspondingly low defocusing losses.

An upgraded feed for RSTN would therefore have the following qualities:

- Bandwidth of 1-5GHz (or higher)
- Beam width to satisfactorily illuminate a RSTN dish
- Reasonable variation of directivity over the frequency band
- Small amount of beam squint
- Acceptable defocusing loss

Achievement of these goals would facilitate improved solar microwave observations from the perspectives of space weather considerations and solar physics studies. Such a feed could be used for a RSTN upgrade. This dissertation describes the analysis, design, and development of a feed that could be used in a RSTN upgrade, or, form the basis of further development work.

The next chapter, *Detailed Problem Description,* gives an historical overview of solar microwave observations and an outline of solar processes related to such emissions to provide context for the accompanying antenna design requirements and specifications.

Chapter 3, *Possible Antenna Designs,* describes the antennas that were tried and covers limitations and/or difficulties encountered.

Chapter 4, *Design Solutions,* discusses the antenna that was shown to meet requirements in simulation.

Chapter 5, *Test Results,* presents measurements of the antennas and comparison with simulations.

Chapter 6, *Conclusions,* summarizes the work and discusses future opportunities for continued research in this direction.

Chapter 2: Detailed Problem Description

Historical Overview of Solar Microwave Observations

Solar microwave emissions have been discussed in the literature as far back as the 1940's. Martyn suggested by application of the concept of optical depth that for frequencies greater than 300MHz the origin of microwave radiation would be located in the chromosphere, the second major main layer of the sun's atmosphere that lies above the photosphere and below the transition region [6].

In 1947 a radio telescope comprised of a dipole with reflector at the focus of a four foot parabolic dish was used for solar observations at a wavelength of 10.7cm (2.8 GHz), and with a main lobe width of 6° to view the entire solar disk. Radio emission intensity was noted to be closely associated with sunspots, either the number of sunspots or their total area [7].

By 1950, bursts of solar emissions at 2.8 GHz were correlated with sudden ionospheric disturbances (SID), and reported by the Central Radio Propagation Laboratory [8]. This is one of the earliest examples of terrestrial radio propagation, as affected by space weather phenomenon, being routinely monitored.

A polarimeter for 9.5 GHz observations was developed in the late 1950's, using a circular waveguide with a rotating phase shifter, mounted on a 1.1m parabolic dish. The system allowed for all four Stokes parameters to be measured with minimum detectable intensities on the order of 5 Solar Flux Units (SFU). One SFU equals 10^{-22} $Wm^{-2}Hz^{-1}$. Observations showed the change in polarization from a typical bipolar sunspot at central meridian passage [9].

By 1957 the polarization and intensity of solar radio bursts had been continuously observed at 1, 2, 3.75, and 9.4GHz. The sense of polarization was seen to sometimes vary with frequency, e.g., reverse between 2 and 3.75 GHz. At the time this was interpreted to be due to the motion of the source [10].

An investigation from conducted between 1957 and 1959 at 2.8GHz seemed to support the identification of an emitting region of a post-burst increase with the X-rays responsible for the SID. When observed in microwaves, a solar flare was seen to have two parts: a single burst, then a subsequent rise in flux levels called a post-burst increase. Post-burst increases were seen to have the same characteristic lifetimes as SID's [11].

Microwave observations have also shed insight into large solar features. Observations made at 7 GHz during the 1966 total solar eclipse revealed that each hemisphere had a different polarization sense, left-handed in the northern hemisphere and right-handed in the southern. The inference was that the sun had a general solar magnetic field, poloidal in nature, with main contribution from the poles [12].

It was known that solar microwave bursts showed circular polarization. A polarimeter was developed, using a dual-polarization horn antenna at the prime focus of a parabolic dish, to measure all four Stokes parameters at 8.918 GHz and at three different bandwidths, 40 kHz, 400 kHz and 5 MHz. This was done to measure the linear component and its Faraday rotation, with the result that analysis of 68 bursts showed that most of the bursts were circularly polarized, and that no linear polarization was observed within the accuracy of the instrument. It was expected that the Faraday rotation of the burst emission had a typical value of 10^3-10^4 radians, and if the period of rotation is less than the polarimeter's integration time, no linear polarization would be observed [13].

Overview of Solar Radio Emission Mechanisms

A good overview of solar radio emission mechanisms is provided by [14] and is referenced extensively in this overview except where noted otherwise.

Solar microwave emissions can be coherent or incoherent depending upon the source mechanism. The following mechanisms produce incoherent radiation: thermal bremsstrahlung, gyroresonance emission, and gyrosynchrotron emission.

Thermal Bremsstrahlung

Bremsstrahlung emission is produced when individual electrons are accelerated by path deflection due to the Coulomb force between an electron and an ion. In the radio spectrum it is the relatively distant encounters of electrons with ions that predominates, rather than the rarer close passes and subsequent large deflections. Since this is the dominant radio emission mechanism throughout most of the corona it is discussed the greatest detail. It is used to diagnose physical conditions in the quiet sun, active regions, and the decay phase of certain flares.

Bremsstrahlung emissivity is derived by considering the energy radiated by an electron at a distance *d* and velocity *v* from an ion Z_i , multiplying by the rate of these encounters, and then integrating over all *d* and *v*. In the pre-1985 derivation only Maxwellian velocity distributions were considered. It is also common to introduce the Gaunt factor $G(T,\omega)$ that is proportional to the log of d_{max}/d_{min}. T is temperature in Kelvin and ω is angular frequency, d_{max} and d_{min} are maximum and minimum impact parameters, respectively. Since collisions at a given d yield emission at about $\omega \leq v/d$, then $d_{max} \approx v/\omega$, where v is electron velocity. However, d_{min} varies due to electron energy. For low-energy electrons, d_{min} is approximately the distance where the electron undergoes a 90° deflection, but for higher-energy electrons it is related to the de Broglie wavelength. Once the absorption coefficient is calculated, the emissivity is related to it by Kirchhoff's Law.

When a magnetic field is present, the x-mode is more strongly absorbed and emitted than the o-mode. There is also a net, weak polarization of the x-mode. The o-mode, or "ordinary" wave, has the same dispersion relationship whether in a plasma or free space and its cutoff frequency is the plasma frequency. The x-mode is the "extraordinary" wave, with a more complicated dispersion relation and the wave gyrating in the opposite sense as the electron.

Gyroresonance Emission

In a magnetized plasma, accelerations from electron gyration around field lines can be dominant over those from particle collisions. Instead of bremsstrahlung emission, gyroresonance (or cyclotron) emission and absorption is produced for non relativistic particles. It can provide a measurement of magnetic fields in solar active regions.

Since bremsstrahlung emission goes as $n^2T^{-1/2}$ and gyrosynchrotron emission goes as $nT^{\alpha}B^{\beta}$ ($\alpha,\beta>1$) then bremsstrahlung will dominate if the density is sufficiently high or if temperature or field strength is sufficiently low. In some cases, bremsstrahlung will dominate at low frequencies and gyrosynchrotron at high frequencies. Gyroresonance emission is seen at low harmonics of the electron gyrofrequency, $2.8\cdot|\mathbf{B}|$ MHz. In the range of magnetic fields found in the corona ($\leq$ 2500 G) this yields microwave emissions from 1-20 GHz that may be highly polarized [15].

Gyrosynchrotron Emission

Gyrosynchrotron radiation is produced for mildly relativistic particles (Lorentz factor γ less than 2 or 3). For completeness it should be noted that synchrotron radiation is produced by highly relativistic particles ($\gamma >> 1$). Gyrosynchrotron emission occurs at harmonics 10 to 100 times that of the gyrofrequency, however the emissions at these harmonics have broadened and overlapped to form a smoother spectrum. Harmonics 10-100 are associated with temperatures in the range of $5x10^7$-$5x10^9$ K, and the associated emissions are typically produced by non thermal electrons in flares. In general, such observations provide diagnostics of physical conditions in flaring sources.

The following mechanisms can produce coherent emissions: plasma radiation, and electron-cyclotron masers.

Plasma Radiation

Plasma emission occurs from the oscillation of electrons about ions and involves two stages. Either stage may include plasma instabilities, wave-wave and/or wave-particle interactions, and induced emission. In the first stage, Langmuir (longitudinal) waves must be produced in the plasma. In the second stage, some of this wave energy must be converted to electromagnetic (transverse) waves that can propagate through the plasma.

An accepted mechanism to produce high levels of Langmuir waves is the "two stream" instability, where fast electrons overtake slower electrons. To convert the Langmuir wave energy into electromagnetic waves requires both frequency and momentum matching. Two possible ways of achieving this conversion are scattering, and direct conversion. Scattering may occur by interactions with low frequency waves like ion-sound. Direct conversion may occur in regions with sharp density gradients, and for this process to be efficient, such variations must occur on scales of 10-100 km.

For second harmonic radiation, it is proposed that two Langmuir waves coalesce to produce a radio wave, but their wave vectors must be anti-parallel to do so. Such backward waves might be produced by the scattering of Langmuir waves off ions or low frequency waves.

Plasma radiation occurs at the plasma frequency and its second harmonic, but typically never higher. For the sun this is seen in the 100-300 MHz range for the fundamental and 2-5 GHz for the harmonic. Bursts are typically highly polarized.

Electron-Cyclotron Masers

Masers that amplify emissions near the electron-cyclotron frequency can form when both an electron population inversion is present along with a relatively strong field or a low density plasma. Such a population inversion may occur when electrons become energized within magnetic flux tubes that have converging legs with footprints in a high density atmosphere. [14] summarizes ten steps in the sequence leading to maser formation which will not be described here for purposes of brevity. In summary, electron energies are probably in the range of 10 keV - 1 MeV for maser action, and an individual pulse of maser radiation has a small bandwidth, on the order of 1%. However, with radiation occurring from many different heights along the flux tube the overall frequency range may be 2:1 or greater. Gyroresonance absorption can be very strong, and given that the amount of energy involved may be large, on the order of 10^{27}-10^{30} ergs/s for flares, this absorption may heat a large volume of plasma to ~10^{7} K to subsequently radiate in soft X-rays.

Information regarding plasma parameters and magnetic field configuration during flares may be gathered from the source location and fine structure of solar radio bursts. Figure 1 from [1] depicts some of the characteristics and associated phenomena of solar radio bursts. It should be noted that in nearly all cases, drifting bursts tend to drift from high to lower frequencies, and the stated values in the Frequency Range column are ranges of observed frequencies and not bandwidths. Also, there currently is not general agreement on the Type IV sub-types.

In an analysis of 57 type IV radio bursts with pulsations, at least 86% were accompanied by proton fluxes originating from the sun. When no protons had been recorded (14%), the corresponding flares had been in the eastern hemisphere. The pulse train duration was seen to decrease with increasing flux of > 10 MeV protons, such that the shortest series of pulsations are associated with protons with a hard spectrum. The authors show that this correlates with an MHD model of pulsations, with pulse train

duration determined by proton pitch-angle diffusion caused by Alfven waves in coronal magnetic loops [16].

TYPE	CHARACTERISTICS	DURATION	FREQUENCY RANGE	ASSOCIATED PHENOMENA
I	Short, narrow-bandwidth bursts. Usually occur in large numbers with underlying continuum.	Single burst: ~ 1 second Storm: hours - days	80 – 200 MHz	Active regions, flares, eruptive prominences.
II	Slow frequency drift bursts. Usually accompanied by a (usually stronger intensity) second harmonic.	3- 30 minutes	Fundamental: 20 – 150 MHz	Flares, proton emission, magnetohydrodynamic shockwaves.
III	Fast frequency drift bursts. Can occur singularly, in groups, or storms (often with underlying continuum). Can be accompanied by a second harmonic	Single burst: 1 - 3 seconds Group: 1 -5 minutes Storm: minutes - hours	10 kHz – 1 GHz	Active regions, flares.
IV	Stationary Type IV: Broadband continuum with fine structure	Hours - days	20 MHz – 2 GHz	Flares, proton emission.
	Moving Type IV: Broadband, slow frequency drift, smooth continuum.	30 – 2 hours	20 – 400 MHz	Eruptive prominences, magnetohydrodynamic shockwaves.
	Flare Continua: Broadband, smooth continuum.	3 – 45 minutes	25 – 200 MHz	Flares, proton emission.
V	Smooth, short-lived continuum. Follows some type III bursts. Never occur in isolation.	1-3 minutes	10 - 200 MHz	Same as type III bursts.

Figure 1: Solar radio burst classifications.
Type IV sub-bursts are controversial [17].

An active region model was presented by [18] whereby thermal cyclotron radiation was produced by hot plasma filling the magnetic tube in the corona above a group of sunspots. An observed 1.658 GHz line corresponded to the third harmonic of the electron gyrofrequency, subsequently yielding the magnetic field along the magnetic tube axis. This study demonstrated that the analysis of cyclotron lines can be a tool for diagnostics of magnetic fields and plasma in solar flares and active regions.

Thus, energy distribution in flare regions may be examined by observing the solar microwave bursts generated by different energy populations of electrons, e.g., gyrosynchrotron, synchrotron and thermal bremsstrahlung [1]. Additionally, improved temporal resolution while observing narrow-band radio emission spikes leads to a better selection of models describing associated physical processes. For example, exponential distributions tend to support an open driven plasma model [19].

In addition to providing diagnostics and warnings regarding solar events, solar microwave emissions are capable of directly interfering with various electronic systems. On 6 December 2006 a burst from an X6 solar flare made the Global Differential Global Positioning System (GPS) system unavailable for several minutes. This system generates

corrections to GPS and other satellite orbits each second. Also, the Federal Aviation Administration Wide Area Augmentation System (WAAS), which can safely guide an aircraft to within 200 feet above a runway, lost guided runway approach service for about 15 minutes. Although RSTN states its maximum observable power flux as 100,000 SFU at 1.1415 GHz, RSTN only reported 13,000 SFU's for the event when 1,000,000 was observed by the Owens Valley Solar Array and confirmed by the observed reduction in carrier-to-noise ratio for GPS receivers [20].

In summary, radio observations provide valuable insight into solar structure and phenomena. As an example, Figure 2 and Figure 3 show the active region AR6615 at microwave frequencies ranging from 5 GHz to 15 GHz. As a result, structures not apparent in white light continuum are revealed.

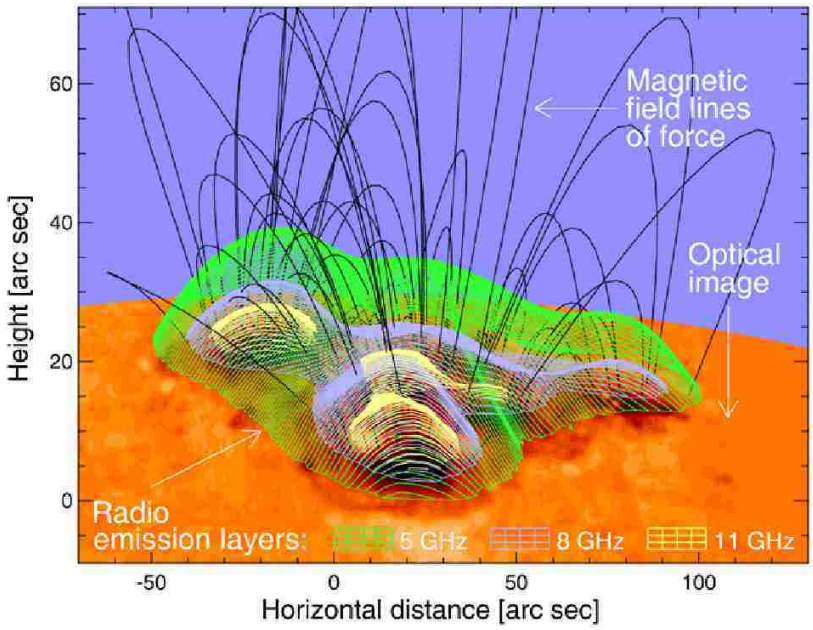

Figure 2: Active solar region AR6615 with extrapolated field lines.
Three coronal gyroresonance surfaces are shown: 5 GHz (B = 600 G), 8 GHz (B = 950 G) and 11 GHz (B = 1300 G). [21]

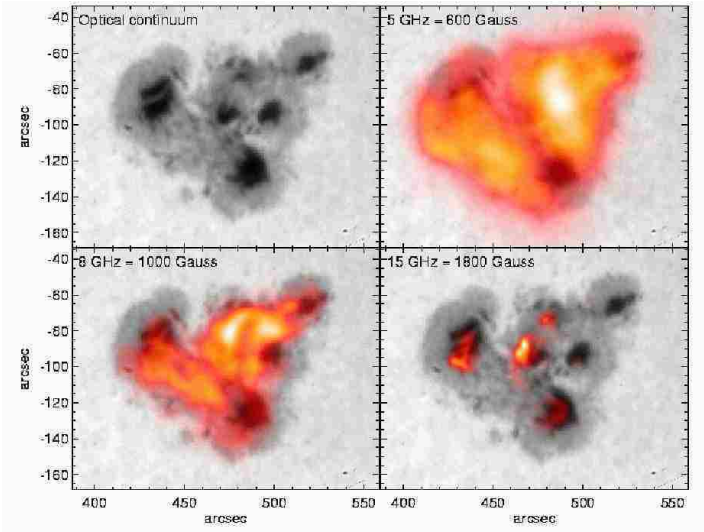

Figure 3: VLA observations of AR6615 at 5, 8.4 and 15 GHz.
The radio brightness distribution has been superimposed on the white light continuum [22].

Bandwidth

The USAF RSTN network provides continuous monitoring of full-disk solar microwave emissions from locations Australia, Hawaii, Italy, and Massachusetts as shown below in Figure 4. Monitoring is performed at 8 fixed frequencies: 245, 410, 610, 1415, 2695, 4995, 8800, and 15400 MHz.

Figure 4: Locations of USAF Radio Solar Telescope Network (RSTN).
RSTN provides continuous solar radio observation 245, 410, 610, 1415, 2695, 4995, 8800, and 15400 MHz. [23]

Each RSTN installation has three, prime-focus parabolic reflector systems as shown in Figure 5. The diameter of each dish is sized to provide full-disk solar observation over the frequency range of the feeds used with its dish. The 2.4m dish is visible in the upper left of Figure 5 and has four horn feeds to cover 1415, 2695, 4995, and 8800 MHz. The dish has a 0.375 focal length to diameter (f/D) ratio.

This dissertation is concerned with the possible feed upgrade for the 2.4m dish for two reasons. At 2.4m diameter the maximum frequency at which the full solar disk may be observed reliably is not much beyond 10GHz thereby limiting the upper frequency of an upgraded feed. Additionally, the National Solar Observatory in Sunspot, New Mexico has a 2.1m, 0.375 f/D dish and pointing system known as the Solar Radio Burst Locator (SRBL) that could be used as proof of concept for an upgraded feed.

Figure 5: RSTN installation antennas.
The 2.4m dish at left covers 1415, 2695, 4995, 8800 MHz [24].

The gain of a parabolic dish is frequency dependent and given by the formula:

$$G_{dBi} = 10\log_{10}(\eta A\frac{4\pi}{\lambda^2}) \qquad (2\text{-}1)$$

where A = Aperture Area, η = Efficiency and λ = Wavelength. For a parabolic reflector the efficiency is less than one as the feed and its support structure poses a central obstruction [25] and this will be later discussed in detail. Using this relationship the system's Half Power Beam Width (HPBW) may be calculated from the gain by considering the relationship between gain and directivity:

$$G(\theta,\varphi) = e_{cd}\, D(\theta,\varphi) \tag{2-2}$$

where $G(\theta,\varphi)$ = Gain in dBi (decibels above isotropic), and $D(\theta,\varphi)$ = efficiency. e_{cd} is the product of the conduction efficiency e_c and the dielectric efficiency e_d and is denoted as the antenna radiation efficiency, which relates the gain and directivity of an antenna. For purposes of these computations the efficiency e_{cd} is given a value of unity.

For antennas with one major lobe and negligible side lobes, and that is rotationally symmetric, an approximation for the directivity becomes:

$$D_o \approx 4\pi/\Omega_A \tag{2-3}$$

where Ω_A is the solid angle defining the flow of power for an antenna with constant radiation intensity. The beam solid angle Ω_A can be approximated as

$$\Omega_A \approx \Theta_{1r}\, \Theta_{2r} \tag{2-4}$$

Where Θ_{1r} is the half-power beam width in one plane and Θ_{2r} is the half-power beam width in the plane at a right angle. Both are in radians. If working in degrees then the directivity may be approximated as:

$$D_o = \frac{41{,}253}{\Theta_{1d}\Theta_{2d}} \tag{2-5}$$

For the 2.4m RSTN dish the HPBW vs. frequency for different values of η is shown in Table 1: Calculated HPBW vs. Frequency vs. Efficiency for 2.4m RSTN Dish. HPBW is narrower for higher efficiencies. While the efficiency of the RSTN system is unknown, the HPBW must be sufficient to cover the entire solar disk (0.54°), to include pointing and tracking uncertainties and errors, and to accommodate any beam squint in the system.

The beam width of the 2.4m RSTN dish has been reported to be 2° at 4.995GHz and 1° at 8.8GHz [23], corresponding approximately to η=0.7 at 5GHz and η=0.8 at 9GHz as shown in Table 1. Such a beam width allows for nearly half a degree of tracking and pointing error, and beam squint, at 8.8GHz.

The effect of decreasing HPBW with increasing frequency is shown in Figure 6, where it can be seen that as frequency increases, system pointing, tracking and alignment becomes more critical.

Table 1: Calculated HPBW vs. Frequency vs. Efficiency for 2.4m RSTN Dish

Frequency	Gain, dBi	HPBW, deg					
		η=0.5	η=0.6	η=0.7	η=0.8	η=0.9	η=1.0
1 GHz	25.6	11.43	10.43	9.66	9.04	8.52	8.08
2 GHz	31.6	5.71	5.22	4.83	4.52	4.26	4.04
3 GHz	35.1	3.81	3.48	3.22	3.01	2.84	2.69
4 GHz	37.6	2.86	2.61	2.41	2.26	2.13	2.02
5 GHz	39.5	2.29	2.09	1.93	1.81	1.70	1.62
6 GHz	41.1	1.90	1.74	1.61	1.51	1.42	1.35
7 GHz	42.5	1.63	1.49	1.38	1.29	1.22	1.15
8 GHz	43.6	1.43	1.30	1.21	1.13	1.06	1.01
9 GHz	44.6	1.27	1.16	1.07	1.00	0.95	0.90
10 GHz	45.6	1.14	1.04	0.97	0.90	0.85	0.81
11 GHz	46.4	1.04	0.95	0.88	0.82	0.77	0.73
12 GHz	47.1	0.95	0.87	0.80	0.75	0.71	0.67
13 GHz	47.8	0.88	0.80	0.74	0.70	0.66	0.62
14 GHz	48.5	0.82	0.75	0.69	0.65	0.61	0.58
15 GHz	49.1	0.76	0.70	0.64	0.60	0.57	0.54
16 GHz	49.6	0.71	0.65	0.60	0.56	0.53	0.51
17 GHz	50.2	0.67	0.61	0.57	0.53	0.50	0.48
18 GHz	50.7	0.63	0.58	0.54	0.50	0.47	0.45
19 GHz	51.1	0.60	0.55	0.51	0.48	0.45	0.43
20 GHz	51.6	0.57	0.52	0.48	0.45	0.43	0.40

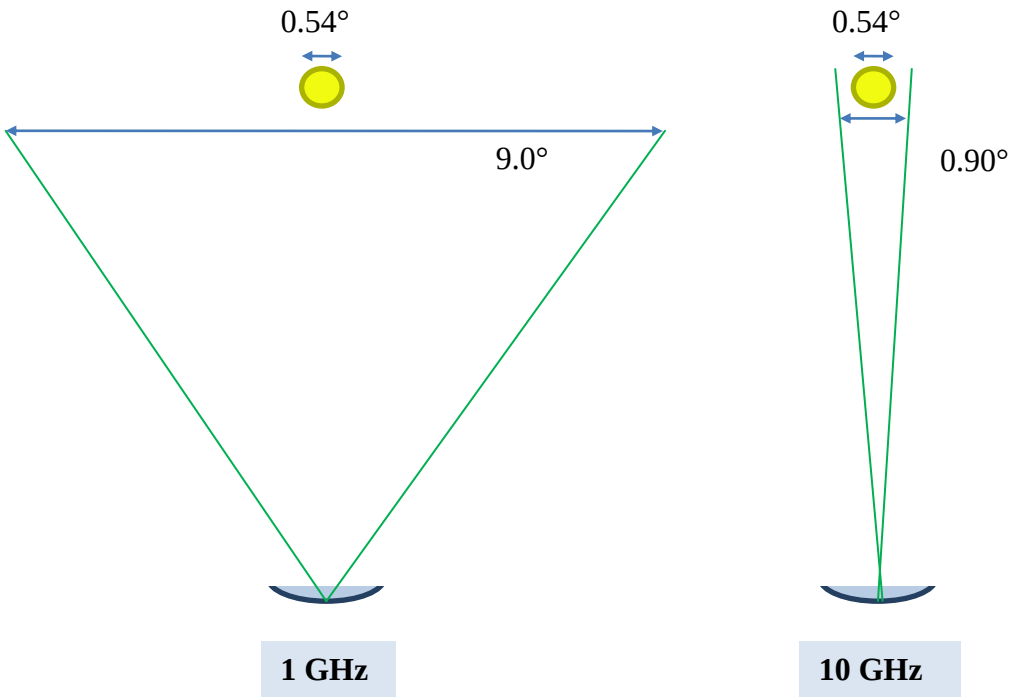

Figure 6: HPBW variation over frequency for a RSTN dish.
At 1GHz the 2.4m RSTN system adequately covers the solar disk without requiring great precision from pointing, tracking and alignment. At 10GHz this is no longer the case.

Dish Illumination

Although solar microwave observation systems receive electromagnetic signals and are not intended to transmit, the term *dish illumination* is used when referring to how a feed's radiation pattern projects onto the dish. This is from the concept of reciprocity which states that an antenna's radiation is the same whether transmitting or received assuming realistic power levels.

Feed taper, dish illumination, and the simulated illumination of the 2.4m RSTN dish is modeled and discussed in Appendix A: Dish Illumination. For the φ direction the RSTN feed taper is simulated to be approximately 6.4dB and between 14.3 and 16.7dB for the θ direction. An improved feed would more evenly illuminate a RSTN dish by increasing the feed taper in the phi direction. A minimum of 10dB of feed taper for both theta and phi directions is set as the performance target.

Polarization

A dual-polarization capability is a desired feature of an upgraded RSTN feed. As described in a previous section on solar radio emission mechanisms, polarization state gives deeper insight when interpreting microwave observations. Dual polarization is also desirable to handle future developments in spectrum usage, for example, the Global Positioning System (GPS) is currently right-hand circularly polarized (RCP) [26] but future systems may incorporate left-hand circular polarization (LCP). An upgraded feed should address all polarization states.

The simplest implementation from an observational viewpoint would be a feed with dual circular (LCP and RCP) polarization. Since solar microwave emissions are circularly polarized due to Faraday rotation [13] an observation would consist of measuring the signal amplitude received by each circularly polarized element to infer both flux and polarization state.

Circularly polarized feeds present a challenge when considering calibration. As previously stated, RSTN's foremost goal is to measure solar flux levels which then serve as triggers for appropriate action. It is simpler to construct a feed with dual-linear polarization and calibrate each polarization separately with a precise source such as a broadband horn antenna. Doing so imposes a burden on reconstructing the polarization state from the received signals and necessitates the measurement of all four Stokes parameters and subsequent calculation of the polarization state.

Stokes parameters, developed by George Gabriel Stokes in 1852, are a set of values that may be used to calculate polarization state. There are several ways in which the parameters may be expressed but for a dual-linear polarization system with **x** and **y** polarization directions, the parameters are defined to be:

$I = \langle |E_x|^2 + |E_y|^2 \rangle$

$Q = \langle |E_x|^2 - |E_y|^2 \rangle$

$U = 2\langle |E_x| \, |E_y| \cos \varphi \rangle$

$V = 2\langle |E_x| \, |E_y| \sin \varphi \rangle$

where E_x and E_y are the **x** and **y** electric field vectors, respectively, and φ is the phase difference between E_x and E_y. [27], [28]

The four parameters form a Stokes vector from which polarization state may be inferred. The parameters form a vector of the form (I, Q, U, V). Several examples of such a vector depicting common polarization states are illustrated below.

(1,0,0,0) = unpolarized

(1,0,0,-1) = LCP

(1,0,0,1) = RCP

(1,1,0,0) = **x** linear polarized

(1,-1,0,0) = **y** linear polarized

It was desirable to incorporate a dual-polarization feed that was simpler to calibrate at the expense of increased numerical computation to retrieve the polarization state, thus a dual-linear antenna was selected [29].

A dual-polarization feed with 1-10GHz bandwidth would be a contributing addition to existing solar radio observatories, which are surveyed in Table 2. Only one observatory is both broadband and dual-linear polarization: the Owens Valley Solar Array (OVSA). However, the log-periodic dipolar array (LPDA) feed used at OVSA has a known issue with *beam squint*, and furthermore must suffer some amount of *defocusing loss* due to its non-planar structure. Beam squint and defocusing loss will be discussed in the following sections.

Table 2: A Survey of Solar Radio Observatories
L: 1.15-1.73 GHz, **S**: 1.72-2.60 GHz, **C**: 3.95-6.1 GHz, **X**: 8.0-10.0 GHz

Observatory	**Feed Type**	**Band/BW (GHz)**	**Polarization**
VLA	Horns	1-2, 2-4, 4-8	Dual Linear
Green Bank	Horns	L, S, C, X	Dual Linear
Nobeyama	Horns	17, 34	Dual Circular
ETH	Log-Periodic	L, S, C	Dual Linear
K-SRBL	Log Spiral	1-18	RCP
Arecibo	Horns	L, S, C, X	Dual Linear
RSTN	Horns	1.4,2.7, 5, 8.8	Linear
Culgoora	Conical Helix	2-4, 4-8	LCP
Owens Valley	Log-Periodic	1-18	Dual Linear
Algonquin	Patch	L, 2.2-2.4, X	Dual Linear

Beam Squint

Beam squint refers to the angle at which the main lobe's maximum is offset from the bore sight (or array normal) of the antenna. Figure 7 illustrates the effect of beam squint by depicting a feed's main lobe at frequencies F_1 and F_2. At frequency F_1 the feed has a large squint. At frequency F_2 the squint is less but is still non-zero. Beam squint is undesirable in a frequency-agile system and especially when the squint varies with frequency. In a frequency-agile system relatively large blocks up spectral data, up to 500 MHz, may be down converted and digitized. The system is rapidly swept from lowest frequency to highest, pulling in such data blocks. At the Owens Valley Solar Array (OVSA) the entire sweep takes 680ms. If the beam squint varies with frequency the pointing and tracking systems will be unable to correct for the squint.

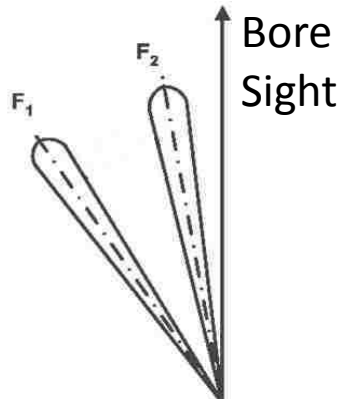

Figure 7: Illustration of Beam Squint.
A feed's main lobe deviates from its intended (bore sight) direction due to beam squint.

The Owens Valley Solar Array is one of two ultrawideband solar observatories, and uses a dual-linear polarization log-periodic feed. Log-periodic feeds can be very broadband and have the added benefit of near-constant radiation patterns when considering the main lobes full-width half-maximum (FWHM). Such a near-constant FWHM is desirable for efficiently illuminating a dish over a wide range of frequencies. Many broadband feeds, such as ridged horns, vary considerably in their FWHM over a broadband range [30]. For example, the A-INFO JXTXLB-SJ-10100 1-10GHz dual-polarization circular horn has a FWHM of 105° at 1 GHz and 22° at 10GHz [3]. This will result in the dish being grossly under-illuminated at high frequency while exaggerating the central obstruction posed by the feed.

OVSA uses the TECOM 201302 dual-linear polarized log-periodic feed that has a half-power beam width of approximately 70° over its 1-18 GHz range. In 2011 it was discovered that this feed exhibited a beam squint that was frequency dependent and not systematic. As measured on Antenna 7 relative to Antenna 5 at OVSA, the magnitude of beam squint was measured to be as great as 26 arc minutes (arcmin). Given that the sun's diameter is about 32 arcmin, this is a significant offset. Figure 8 depicts the magnitude of offset relative to the beam center as measured by OVSA [2].

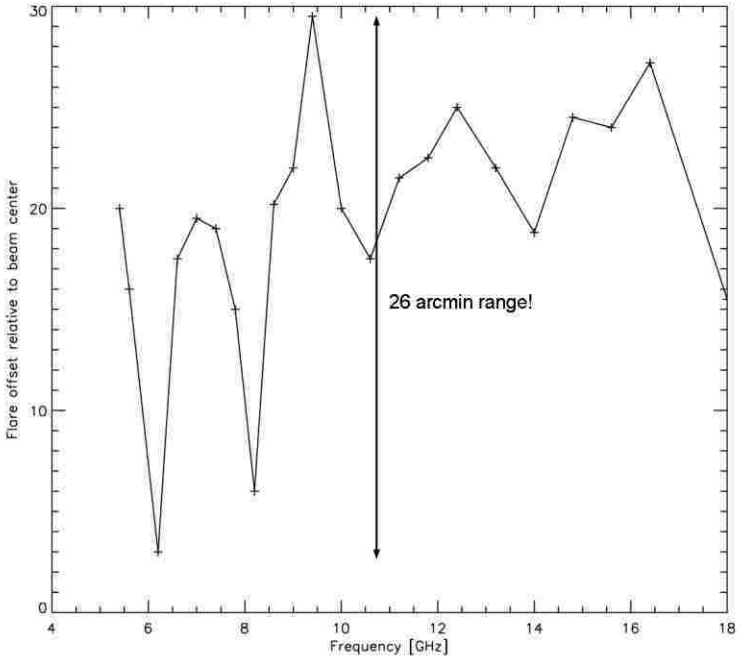

Figure 8: Magnitude of Beam Squint Induced Offset vs. Frequency at OVSA
The peak observed offset of nearly 30 arc minutes is comparable to the sun's angular diameter of 32 arc minutes. [2]

As shown in Figure 6, at 10 GHz a RSTN dish system cannot tolerate much pointing or tracking error to reliably observe the full solar disk. Thus an improved feed should minimize beam squint. This may be accomplished by developing a highly symmetric structure that can be reasonably fabricated.

A simulation study using CST Microwave Studio revealed that squint can be induced via the introduction of physical offsets. This is discussed in depth in Appendix A: Dish Illumination and Beam Squint.

Physical Size

The other ultrawideband solar observatory is the Solar Radio Burst Locator (SRBL) located in Owens Valley. There also exists a SRBL in Korea known as KSRBL, that has the same dish parameters and uses the same feed. The SRBL is unique because it uses beam squint to locate a solar radio burst.

Gordon Hurford invented the concept of SRBL in the late 1980's at the California Institute of Technology. At the time he was researching broadband spiral feeds at the Owens Valley Radio Observatory (OVRO) and intending to measure solar spectra in real

time. To do so required sampling many different frequencies at a high rate. The spectra he observed varied as a function of location of the solar source, where sources off-center from the antenna's central axis showed periodicity. These periodic dips would later be attributed to the detector geometry [31].

SRBL is unique because it can locate solar microwave bursts without mechanical scanning or interferometry, and does so very quickly. Due to the geometry of the planar log spiral antenna, the burst location may be inferred from the received spectrum. Dr. Hurford first noticed the correlation between spectral modulations and burst location, as shown in Figure 9 with measured values presented in Figure 10. These modulations are evident in both quiet-sun and burst spectra, and form the basis of SRBL's ability to locate SMB's.

A representation of the log-spiral antenna is shown in Figure 11. The traces vary in radius with angle approximately as r = (7.5cm) $e^{-n/6}$, where n is the number of turns. Radiation incident upon the traces is preferentially absorbed at radii of approximately one-quarter of a wavelength in the circularly polarized receiver. However, since the logarithmic spiral does not comprise a set of nested circles, the response at resonance is not centered and instead geometrically follows at radii

$$R \approx \frac{-dr}{dn} \approx \frac{\lambda}{4};\ \text{n = number of turns}$$

which is close to the sun's apparent diameter at 2GHz. Stated differently, SRBL's effective electrical center is offset from antenna center, and spirals around at increasing radii for increasing wavelengths. Spectra therefore contain modulations varying in phase and amplitude depending upon the location of the microwave burst.

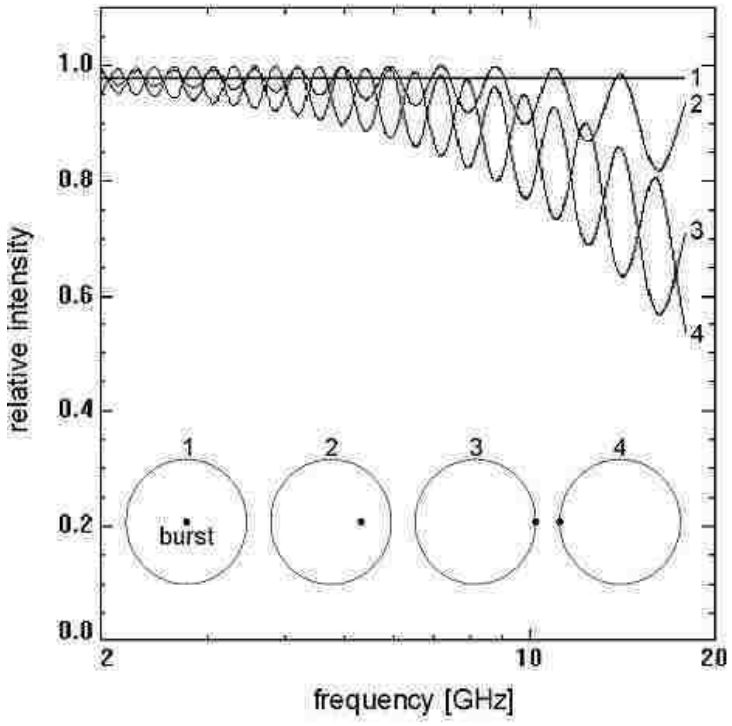

Figure 9: SRBL spectral modulation as a function of burst location

Spectral modulation by position of burst on the sun (left). Curves 1 through 4 correspond to the depicted locations on the solar disk, which are 1) antenna center, 2) halfway to the west limb of the sun, 3) at the west limb, and 4) at the east limb. [32] Page 4.

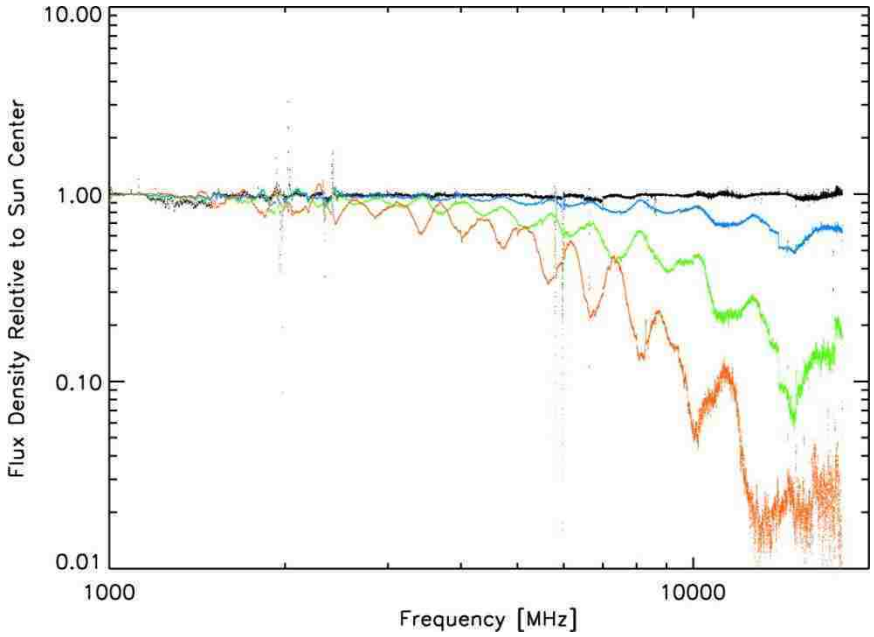

Figure 10: Measured SRBL solar amplitude spectrum.

Solar amplitude spectrum, scaled to the peak solar amplitude, for various offsets from the nominal Sun center. Colors: *black*–Sun center, *blue*–offset in elevation by -0.1°, *green*–offset in elevation by -0.5°, *red*–offset in elevation by +1.0°. The fluctuation amplitude grows with offset distance, and the phase of the fluctuation reflects the direction of the offset. This is the basis for the solar burst locating ability of the KSRBL. [33] Figure 11.

Both SRBL and KSRBL use a 2.1m, f/D=0.375 dish. These parameters are the same as a RSTN dish. The Air Force Research Laboratory (AFRL) possesses a SRBL currently located in Sunspot, NM, that is not used for solar observation although it points and tracks. This would allow for testing of the ultrawideband feed developed in the course of this research, should the AFRL be interested in doing so.

The mounting cavity for SRBL is 175mm in diameter and 100mm deep. These physical dimensions were used as guidelines for the development of the feed described in this research.

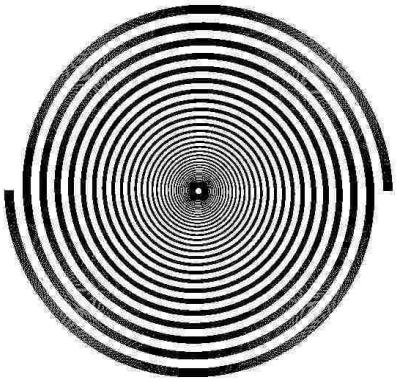

Figure 11: SRBL Log-planar spiral feed.

Figure 2: SRBL's interleaved receiving traces drawn to scale. The antenna is 7 inches wide, and is coaxial with the parabolic dish's axis of symmetry. A planar structure, its face is clad with two copper interleaved spirals, which range from 0.15cm to 7.5cm in radius. Each spiral can efficiently receive a CW or CCW polarized wave. [31]

Defocusing Loss

Defocusing loss is an important consideration because it reduces system sensitivity and may be frequency dependent, thus imposing an additional calibration and processing burden. This loss occurs when the region of the feed that is resonant at a given frequency is not located at the focal point of the dish. Feeds with three-dimensional structures (i.e., non-planar feeds) are likely to cause defocusing loss. Log-periodic feeds (as well as broadband horns) resonate at different points along their longitudinal axis due to the physics of their operation and thus some defocusing loss is to be expected [30]. Figure 12 demonstrates the concept of defocusing loss while Figure 13 plots calculated values of such losses.

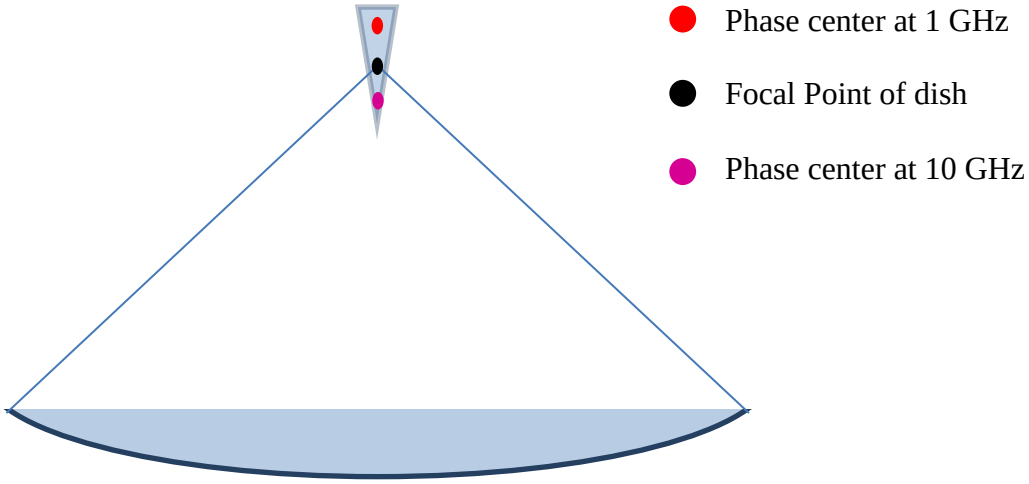

Figure 12: Defocusing Loss in a Non-Planar Feed
A non-planar feed is located about the focal point of a parabolic reflector. As the phase center (resonant plane) of the feed moves with frequency the system is no longer in perfect focus.

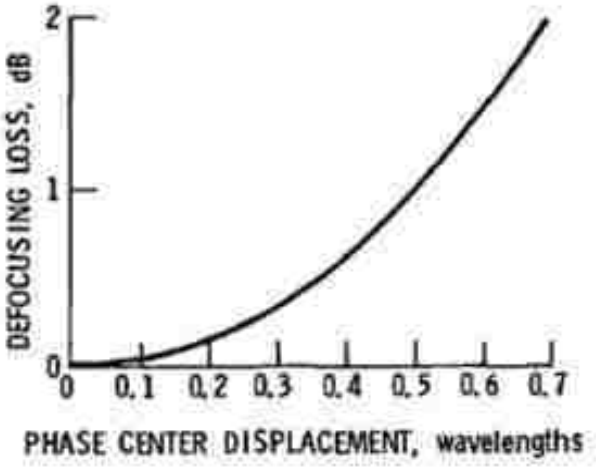

Figure 13: Defocusing Loss as a Function of Phase Center Displacement
[5] Figure X, p.]

The broadband feed used at OVSA is a TECOM 201302, 1-18GHz log periodic dipole array and is shown in Figure 14. The feed is hermetically sealed and TECOM does not revealed the number of elements within or their respective lengths and locations. According to the manufacturer's datasheet the LPDA has a maximum Voltage Standing Wave Ratio (VSWR) of 3:1, a gain of 5 dBi minimum, and the structure is 236mm in length.

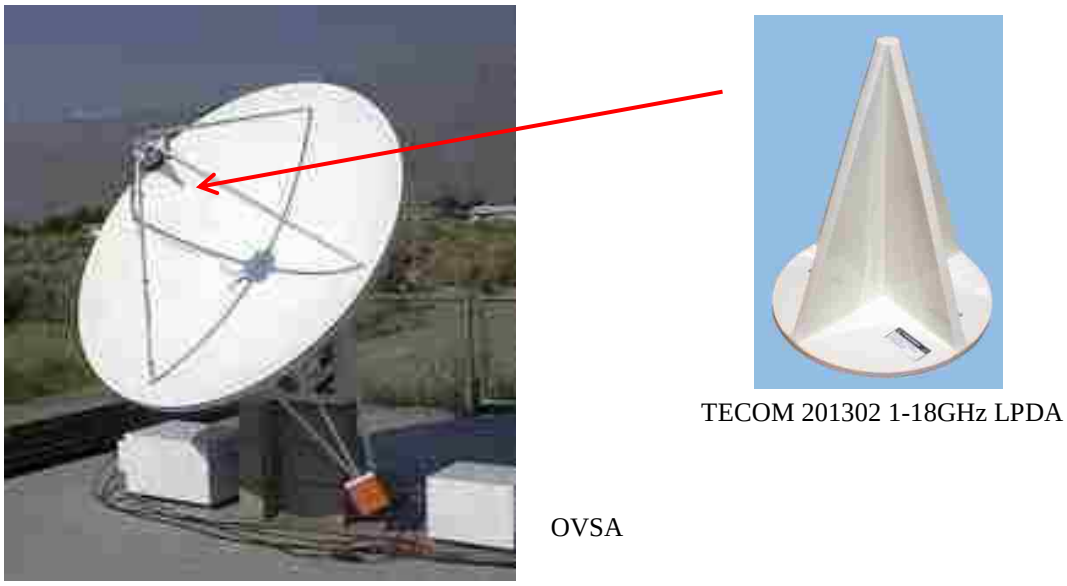

Figure 14: LPDA Feed Used in OVSA.
[34]

It is not expected that the phase center of the TECOM antenna would shift beyond the physical limits of its structure, i.e., 236mm, and less displacement would be expected over the 1-10GHz range. While the design details of the TECOM LPDA are unknown it is possible to estimate the phase center displacement by calculating the structure of an LPDA with the same bandwidth, gain, and overall length as the TECOM LPDA [35]. The results are tabulated in Table 3.

At 10 GHz a resonant half-wave dipole is on the order of 14mm in length. The output of the LPDA calculator is shown on the next page where it can be seen that Element 9 has a length of 14.3mm. This element will be nearly resonant at 10GHz and if no other elements are resonant, would define the location of the phase center. The distance from Element 1 to Element 9 is calculated to be 198.5mm. While this is only an estimate it serves to set a target for phase center displacement in an improved feed, so the displacement specification was set to be less than or equal to 198.5mm.

Table 3: Simulated Design Parameters for TECOM 201302 LPDA

**** Logarithmic Periodic Dipole Antenna ****

http://www.changpuak.ch/electronics/lpda.php

Design by www.changpuak.ch

JavaScript Version August 2010

Min. Frequency : 1000 MHz

Max. Frequency : 18000 MHz

Boomlength : 230 mm

Gain : 7 dB

Element 1 : Length : 75 mm, Diameter : 1 mm, Distance 1 : Length : 44 mm

Element 2 : Length : 61 mm, Diameter : 0.8 mm, Distance 2 : Length : 35.7 mm

Element 3 : Length : 49.6 mm, Diameter : 0.7 mm, Distance 3 : Length : 29 mm

Element 4 : Length : 40.3 mm, Diameter : 0.6 mm, Distance 4 : Length : 23.6 mm

Element 5 : Length : 32.7 mm, Diameter : 0.5 mm, Distance 5 : Length : 19.2 mm

Element 6 : Length : 26.6 mm, Diameter : 0.4 mm, Distance 6 : Length : 15.6 mm

Element 7 : Length : 21.6 mm, Diameter : 0.3 mm, Distance 7 : Length : 12.7 mm

Element 8 : Length : 17.6 mm, Diameter : 0.2 mm, Distance 8 : Length : 10.3 mm

Element 9 : Length : 14.3 mm, Diameter : 0.2 mm, Distance 9 : Length : 8.4 mm

Element 10 : Length : 11.6 mm, Diameter : 0.2 mm, Distance 10 : Length : 6.8 mm

Element 11 : Length : 9.5 mm, Diameter : 0.1 mm, Distance 11 : Length : 5.5 mm

Element 12 : Length : 7.7 mm, Diameter : 0.1 mm, Distance 12 : Length : 4.5 mm

Element 13 : Length : 6.2 mm, Diameter : 0.1 mm, Distance 13 : Length : 3.7 mm

Element 14 : Length : 5.1 mm, Diameter : 0.1 mm, Distance 14 : Length : 3 mm

Element 15 : Length : 4.1 mm, Diameter : 0.1 mm, Distance 15 : Length : 2.4 mm

Design Targets

In the previous sections the various design and performance considerations have been discussed. As a result, the antenna design for this research should have the following target specifications:

- Dual-linear polarization
- Bandwidth of at least 1-5 GHz with 1-10GHz being desirable
- VSWR ≤ 3
- Feed taper to satisfactorily illuminate a RSTN dish, of 10dB or better, along with improved taper in the phi direction.
- Phase center displacement less than 198.5mm over the 1-10GHz range
- A structure to minimize or eliminate beam squint
- Physical size to fit into a 175mm diameter by 100mm depth SRBL cavity

In the next chapter, antenna designs which were considered but not selected will be analyzed and discussed.

Chapter 3: Possible Antenna Designs

Frequency Independent Antennas

A breakthrough in antenna technology occurred in the 1950's with the development of frequency independent structures possessing geometries specified by angles. Such antennas were capable of bandwidths as great as 40:1 where previous implementations were limited to bandwidths of about 2:1. With a structure defined by angles, characteristics such as polarization, input impedance, and radiation pattern do not change as the antenna's size changes. Changing the physical size of the antenna changes its frequency range of operation but not the previously stated characteristics.

Analytical treatments of frequency independent antennas were performed by [36] and [37] performed and their work is summarized in the following.

First the assumption is made that the frequency independent antenna has a geometry described in spherical coordinates (r,θ,φ), and that both feed terminals are infinitely close to the origin. The terminals are assumed to be symmetrically located about the $\theta=0,\pi$ axis. The antenna is assumed to be perfectly conducting and surrounded by an infinite isotropic and homogeneous medium.

The antenna's surface or a surface's edge may then be described by the curve

$$r = F(\theta,\varphi) \tag{3-1}$$

where r denotes the distance along the surface or edge. A scaling factor, K, may be introduced such that if the antenna is to be scaled to a frequency K times lower than the initial frequency, the antenna's physical surface shall become K times larger. This preserves the same electrical dimensions and this new surface is described by

$$r' - K F(\theta,\varphi) \tag{3-2}$$

The two surfaces are identical and congruent if both surfaces are infinite. Rotation in φ will preserve congruence. However, translation and/or rotation in θ does not preserve congruence because of the symmetrical location of the feed terminals.

To preserve congruence an antenna may be rotated by an angle C such that

$$K F(\theta,\varphi) = F(\theta,\varphi+C) \tag{3-3}$$

This implies that the angle of rotation C is dependent upon K but not on θ or φ. If the value of K is not restricted, i.e., $0 \leq K \leq \infty$, then the surface will rotated by C in φ as

frequency changes. The radiation pattern and input impedance will be frequency independent since the structure remains congruent through the rotation.

Differentiating with respect to C,

$$\frac{d}{dC}\left[KF(\theta,\varphi)\right]=\frac{dK}{dC}F(\theta,\varphi)=\frac{\partial}{\partial C}\left[F(\theta,\varphi+C)\right] \tag{3-4}$$

$$=\frac{\partial}{\partial(\varphi+C)}\left[F(\theta,\varphi+C)\right] \tag{3-5}$$

Differentiating with respect to φ,

$$\frac{\partial}{\partial\varphi}\left[KF(\theta,\varphi)\right]=K\frac{\partial F(\theta,\varphi)}{\partial\varphi}=\frac{\partial}{\partial\varphi}\left[F(\theta,\varphi+C)\right] \tag{3-6}$$

$$=\frac{\partial}{\partial(\varphi+C)}\left[F(\theta,\varphi+C)\right] \tag{3-7}$$

Equating (3-5) and (3-7),

$$\frac{dK}{dC}F(\theta,\varphi)=K\frac{\partial F(\theta,\varphi)}{\partial\varphi} \tag{3-8}$$

This can be rewritten by substituting (3-1) as

$$\frac{1}{K}\frac{dK}{dC}=\frac{1}{r}\frac{\partial r}{\partial\varphi} \tag{3-9}$$

The left side of the equation is not dependent on φ or θ. A general solution of the surface of the antenna $r = F(\theta,\varphi)$ is

$$r=F(\theta,\varphi)=e^{a\varphi}f(\theta) \tag{3-10}$$

where

$$a=\frac{1}{K}\frac{dK}{dC} \tag{3-11}$$

and $f(\theta)$ is an arbitrary function.

Equation (3-10) must describe the surface of an antenna for it to possess frequency independent characteristics.

An equiangular plane spiral curve antenna may be defined by setting the derivative of $f(\theta)$ in (3-10)

$$\frac{df}{d\theta}=f'(\theta)=A\delta\left(\frac{\pi}{2}-\theta\right) \tag{3-12}$$

where δ is the Dirac delta function and A is a constant. (3-11) reduces to

$$r\big|_{\theta=\pi/2} = \rho = \begin{cases} Ae^{a\varphi} = \rho_o e^{a(\varphi-\varphi_o)} & \theta = \dfrac{\pi}{2} \\ 0 & elsewhere \end{cases} \tag{3-13}$$

where

$$A = \rho_o e^{-a\varphi_o} \tag{3-14}$$

Equation (3-11) can be written in wavelengths as

$$\rho_\lambda = \frac{\rho}{\lambda} = \frac{A}{\lambda} e^{a\varphi} = Ae^{a\left(\varphi - \ln \lambda/a\right)} = Ae^{a(\varphi-\varphi_1)} \tag{3-15}$$

where

$$\varphi_1 \frac{1}{a}\ln(\lambda) \tag{3-16}$$

Equation (3-13) may also be expressed as

$$\varphi = \frac{1}{a}\ln\left(\frac{\rho}{A}\right) = \tan\Psi \ln\left(\frac{\rho}{A}\right) = \tan\Psi\left(\ln\rho - \ln A\right) \tag{3-17}$$

where 1/a denotes the spiral's rate of expansion and Ψ is the angle between the tangent to the spiral and the radial distance ρ. This is denoted in Figure 15 below.

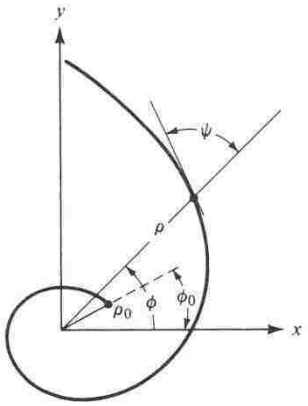

Figure 15: Geometric definition of equiangular planar spiral antenna.

[30] Fig. 11.1a, p. 615

As implied by equation (3-15), changing the wavelength is equal to changing φ_o which results in a rotation of the pattern of the infinite structure. A second spiral implemented as a solid metal surface in place of a line provides for a balanced system,

with radiating elements P and Q each of overall length L_o. The curves of the edges of arm P are defined as

$$\rho_2 = \rho_2' e^{a\varphi} \tag{3-18}$$

$$\rho_3 = \rho_3' e^{a\varphi} = \rho_2' e^{a(\varphi-\delta)} \tag{3-19}$$

where

$$\rho_3' = \rho_2' e^{-a\delta} \tag{3-20}$$

so that

$$K = \frac{\rho_3}{\rho_2} < 1 \tag{3-21}$$

The second arm Q is defined as

$$\rho_4 = \rho_4' e^{a\varphi} = \rho_2' e^{a(\varphi-\pi)} \tag{3-22}$$

where

$$\rho_4' = \rho_2' e^{-a\pi} \tag{3-23}$$

$$\rho_5 = \rho_5' e^{a\varphi} \tag{3-24}$$

$$= \rho_4' e^{a(\varphi-\delta)} = \rho_2' e^{a(\varphi-\pi-\delta)} \tag{3-25}$$

where

$$\rho_5' = \rho_4' e^{-a\delta} = \rho_2' e^{-a(\pi+\delta)} \tag{3-26}$$

This results in the equiangular metallic spiral plate antenna shown below in Figure 16. Such structures are broadband and exhibit little variation of input impedance and radiation pattern over frequency.

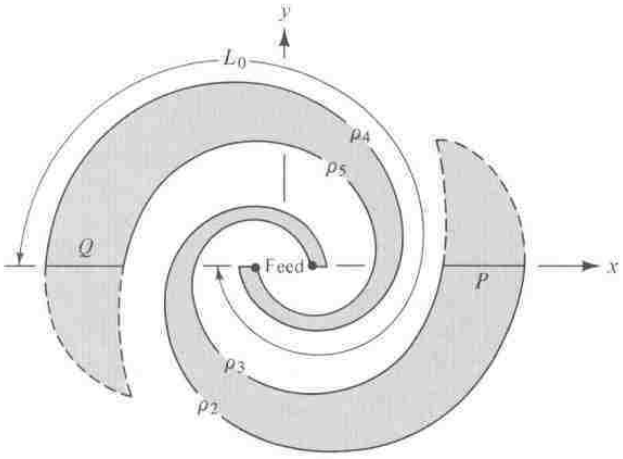

Figure 16: Spiral plate equiangular antenna.

[30] Figure 11.2, p. 617

The length of the arms dictates the polarization of the radiated wave. At low frequencies where the arm length is small compared to the wavelength, linear polarization is achieved. The wave becomes increasingly elliptically polarized as frequency increases and eventually becomes circularly polarized. While this structure is broadband in nature it does not meet the requirement of dual linear polarization.

Log-Periodic Structures

Another development was that of the log-periodic structure described by [38]. The structure cannot be specified by angles alone thus it is not completely frequency independent.

Figure 17 depicts a planar log-periodic structure with edges defined by the angle $\alpha/2$. A length parameter must be included to specify the distance from the origin to a given point on the metal surface. The shape of this structure in spherical coordinates (r,θ,φ) may be expressed as

$$\theta = \text{periodic function of } [b \ln(r)] \tag{3-27}$$

and an example would be

$$\theta = \theta_o \sin\left[b \ln\left(\frac{r}{r_o} \right) \right] \tag{3-28}$$

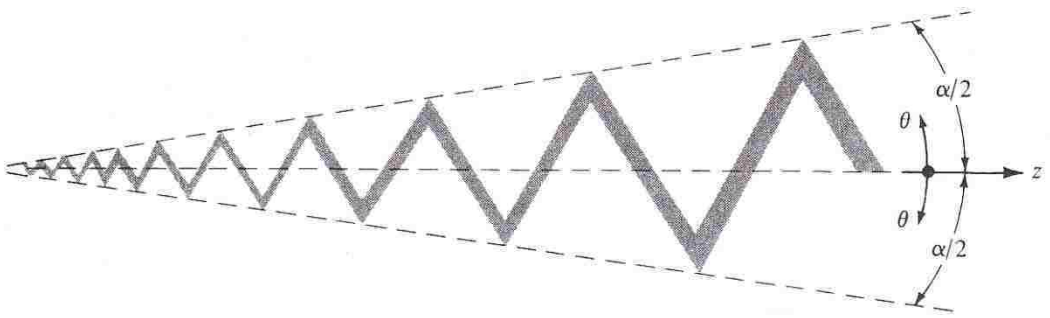

Figure 17: Metal strip log-periodic configuration.

Figure 11.5a, p. 620 [30]

When considering equation (3-28) it is apparent that values of θ repeat whenever the radial frequency completes a 2π cycle, where ln(ω) = ln(2πf) differs by 2π/b. This implies that the system's performance is determined by the logarithm of the frequency, hence the term *log-periodic*.

A log-periodic antenna based upon this configuration is shown in Figure 18, consisting of two coplanar arms. The radiation pattern is highly unidirectional towards the apex of the structure and the polarization is linear. While log-periodic structures are not completely frequency independent the amplitude and impedance variations can be small assuming proper design techniques.

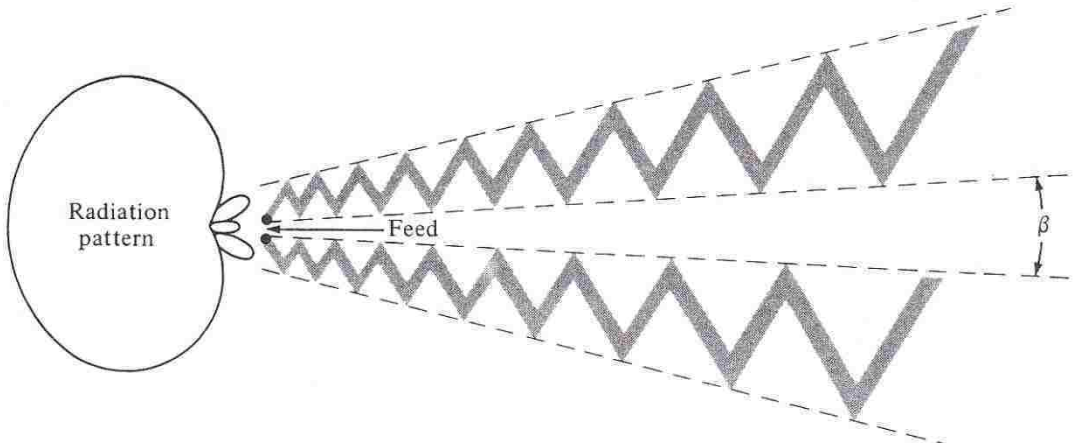

Figure 18: Log-periodic metal strip antenna.

Figure 11.5(b), p. 620 [30]

Three design principles are discussed by [38]. The first, the use of angles to describe the antenna's geometry, has been described previously. The second principle is that the input impedance of an antenna is constant with frequency provided the antenna is identical to its complement. The third principle concerns the design of a structure such that its performance repeats periodically as the logarithm of the frequency.

This second principle is derived from an extension of Babinet's principle by [39]. Assuming a metal sheet and its complementary structure with impedances Z_s and Z_c respectively, a relationship between their impedances is derived as

$$Z_s Z_c = \frac{\eta^2}{4} \tag{3-29}$$

If the sheet and its complement are equal and the structure is in free space, then

$$Z_s = Z_c = Z \tag{3-30}$$

and

$$Z^2 = \frac{\eta_o^2}{4} \tag{3-31}$$

so $Z = \eta_o/2 = 60\pi$ ohms which is not dependent upon frequency. Using this concept it is possible to design an antenna with a constant input impedance however an infinite structure would be required. However, there are no restrictions placed upon the shape of the elements provided they are identical complements. This is confirmed by dividing the plane in which the structure resides into four equal quadrants, which alternate between free space and conductor. The lines dividing the quadrants may possess any shape. The necessary condition for equal complement occurs when any dividing line is rotated 90° about the center and in doing so it becomes coincident with the adjacent dividing line.

Log periodic structures may be visualized by applying the transformation of

$$z = \ln w \tag{3-32}$$

where both z and w are complex numbers. If

$$w = \rho e^{j\theta} \tag{3-33}$$

and

$$z = x + jy \tag{3-34}$$

then by equating real and imaginary components it can be seen that

$$\rho = e^{x} \text{ or } x = ln(\rho) \text{ and} \tag{3-35}$$

$$\theta = y \tag{3-36}$$

Implementation of this transformation causes circles in the w plane to map into vertical lines in the z plane, and radial lines in the w plane to map into horizontal lines in the z plane. This is most easily seen with a bow tie antenna and is depicted in Figure 19. ρ is rotated through the angle θ and the flare angle of the bow tie is denoted as angle α. ρ is infinite for an ideal infinite structure so the transform extends from negative to positive infinity in the x-direction of the z plane. As θ is increased it passes through free space and then conductor, which will have a thickness α in the y-direction of the z plane.

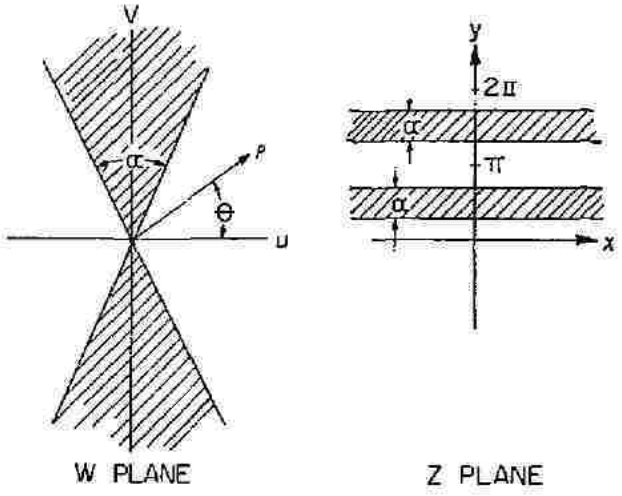

Figure 19: Transformation of bow tie antenna to z plane.

Fig. 1(a) [38]

The same transformation may be applied to the equiangular plane spiral discussed previously and is shown in Figure 20.

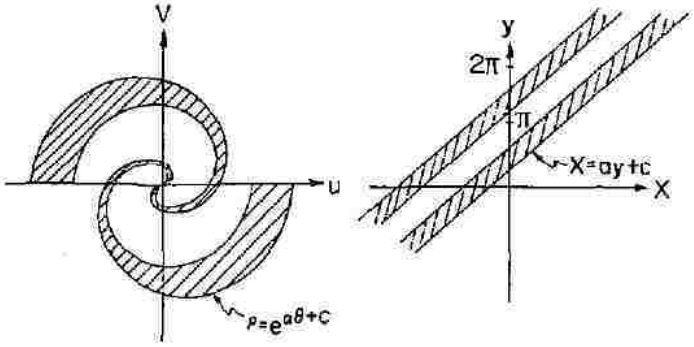

Figure 20: Transformation of equiangular planar spiral antenna to z plane.

Fig. 1(a), [38]

Other log-periodic antennas such as the tooth structure shown in Figure 21 were defined. Similar to a bow tie with slots cut from it, the outer edges are defined by the angle α and the inner-edge separation between teeth defined by the angle β. Referring to Figure 22, the geometric ratio of the log-periodic structure is defined to be

$$\tau = \frac{R_n}{R_{n+1}} \tag{3-37}$$

The width of the antenna slot is defined as

$$\chi = \frac{r_n}{R_{n+1}} \tag{3-38}$$

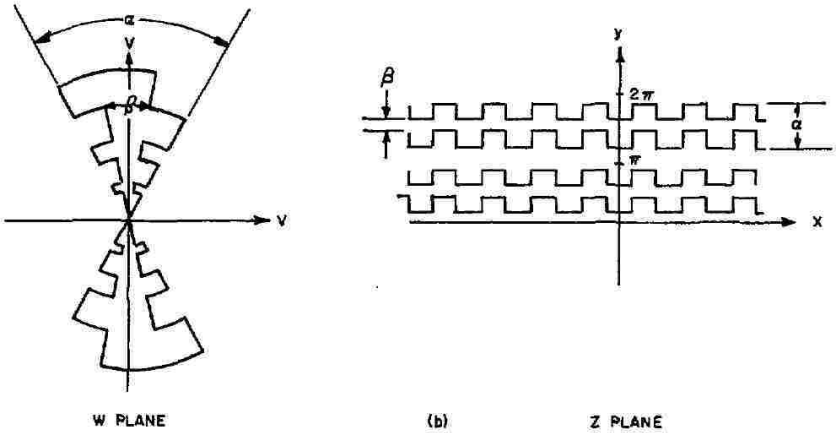

Figure 21: Transformation of log-periodic tooth structure into the z plane.

Fig. 1(a) [38]

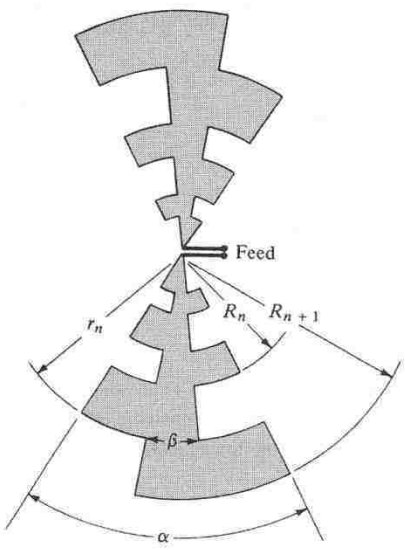

Figure 22: Geometry of log-periodic tooth structure antenna.

Figure 11.6(a), p. 621 [30]

The period of operation is defined by the geometric ratio τ. If two frequencies f_1 and f_2 differ by one period then their relationship to the geometric ratio τ is

$$\tau = \frac{f_1}{f_2}, \quad f_2 > f_1 \tag{3-39}$$

Unlike the equiangular planar spiral antenna the log-periodic tooth structure is linearly polarized. Structures of this type exist so it was not pursued further.

Log-Periodic Dipole Arrays

An extension of the concepts described so far yields the log-periodic dipole array (LPDA). LPDA's are constructed from coplanar dipoles fed by booms or a similar structure and an example is shown in Figure 23. Since the adjacent closely-spaced short dipoles are nearly 180° out of phase, they radiate little energy and interference effects are negligible. The longer and larger-spaced elements radiate, producing a phase progression so that radiation is in the direction of the shorter elements.

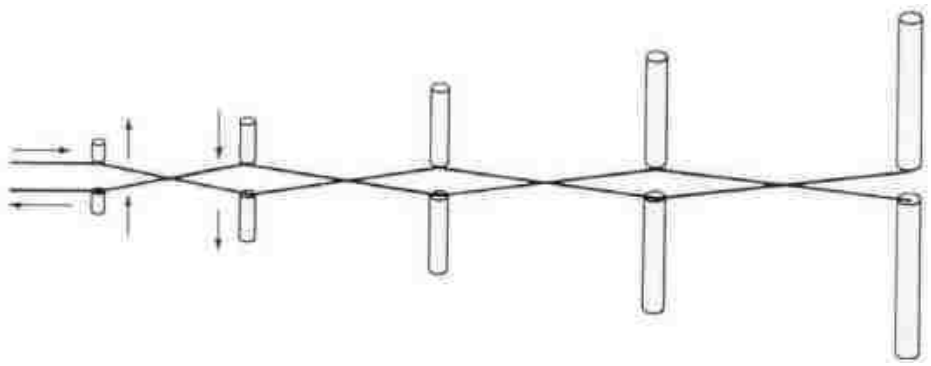

Figure 23: Log-periodic dipole array.

Figure 11.9(c), p. 624 [30]

In a log-periodic dipole array the lengths (l_n's), spacings (R_n's), diameters (d_n's), and gap spacings at dipole centers (s_n's) increase logarithmithically. The rate of logarithmic increase is specified by the inverse of the geometric ratio τ, as

$$\frac{1}{\tau} = \frac{l_{n+a}}{l_n} = \frac{R_{n+1}}{R_n} = \frac{d_{n+1}}{d_n} = \frac{s_{n+1}}{s_n} \tag{3-40}$$

The structure is also specified by a parameter known as the spacing factor σ defined as

$$\sigma = \frac{R_{n+1} - R_n}{2l_{n+1}} \tag{3-41}$$

The apex of the structure encloses an angle of 2α, where α is defined as

$$\alpha = \tan^{-1}\left[\frac{1-\tau}{4\sigma}\right] \tag{3-42}$$

The drawing shown in Figure 24 denotes these parameters.

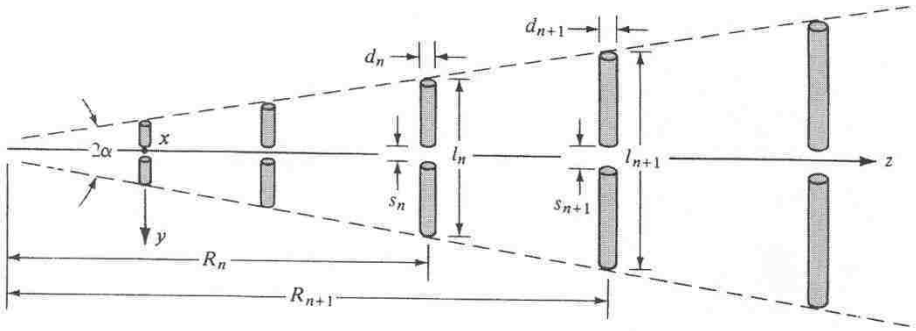

Figure 24: Spacing parameters of an LPDA.

Figure 11.9(a), p. 624 [30]

An infinite structure would be required to achieve pure log-periodic behavior. In practice the structure must be truncated at both ends thus limiting the operational bandwidth. Figure 25 depicts an 11-element LPDA that is active in approximately the middle of its operating frequency band. The region towards the apex consisting of feed line and short dipoles is inactive and the region behaves as a transmission line. At the opposite end the longer dipoles are not resonant so the region is inactive and acting as a stop.

The cutoff frequencies of such a structure may be calculated via the electrical lengths of the shortest and longest dipole elements. The lower cutoff frequency is approximately that of the longest element being $\lambda/2$. The upper cutoff frequency is where the shortest element is approximately $\lambda/2$ but only when the active region is narrow. In practice the active region extends beyond the shortest element.

The active region occurs about elements whose electrical lengths are nearly $\lambda/2$ or slightly smaller than $\lambda/2$. As the frequency increases the active region moves towards shorter elements, and the energy traveling toward the longer, inactive elements attenuates rapidly so that little is reflected from the truncated end.

This movement of the active region has an associated movement of the phase center. For this reason an LPDA is not always the best choice of feed for a broadband reflector antenna system due to the defocusing loss shown in Figure 13.

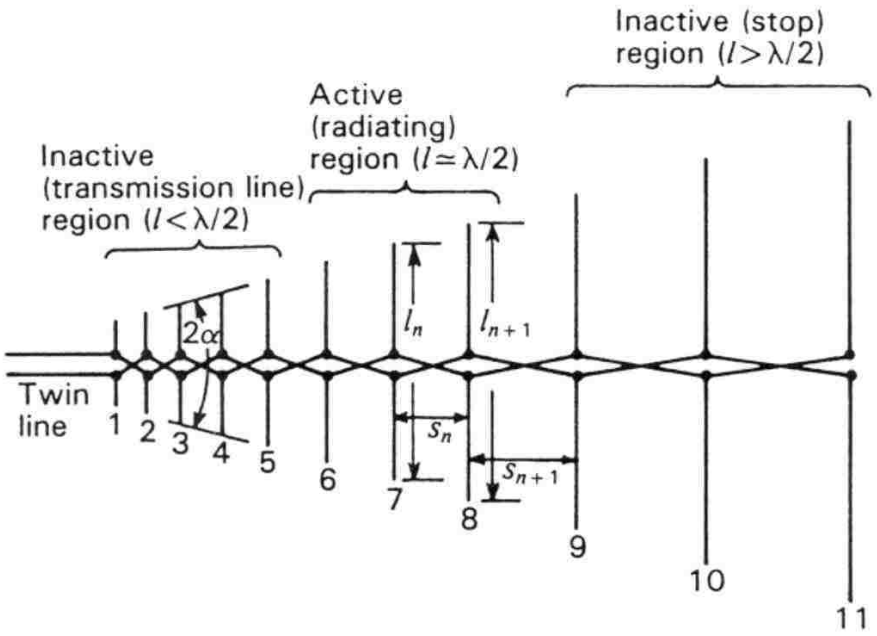

Figure 25: Central and inactive regions of an LPDA.

Page 11. [40]

Using the LPDA shown in Figure 25 as an example, when driven at a mid-band frequency the feeder-line voltages at the base of the elements is almost constant. A progressive phase change occurs for approximately each λ/4 (in free space) length of transmission line. This implies that the phase velocity in the transmission line in this region is about 0.6 of that of the free-space phase velocity as a result of shunt capacitive loading by the smaller elements. This can be seen by referring to Figure 26 where the imaginary component of dipole impedance is seen to be negative (i.e., capacitive) when the elements are shorter than about 0.47 of a wavelength, and becomes positive (i.e., inductive) when elements are longer. The lower phase velocity seen in the transmission line region is due to this shunt capacitive loading of the feed line by the shorter elements.

High current excitation occurs in elements 6, 7 and 8 in the example, Figure 25. The current and excitation of the longer elements (ninth and beyond) is small due to the efficient radiation of power in the active region, and thus the truncated larger end does not greatly affect performance. The linear increase of the current's phase in the active region from the shorter to longer elements ensures that the radiated wave travels towards the feed.

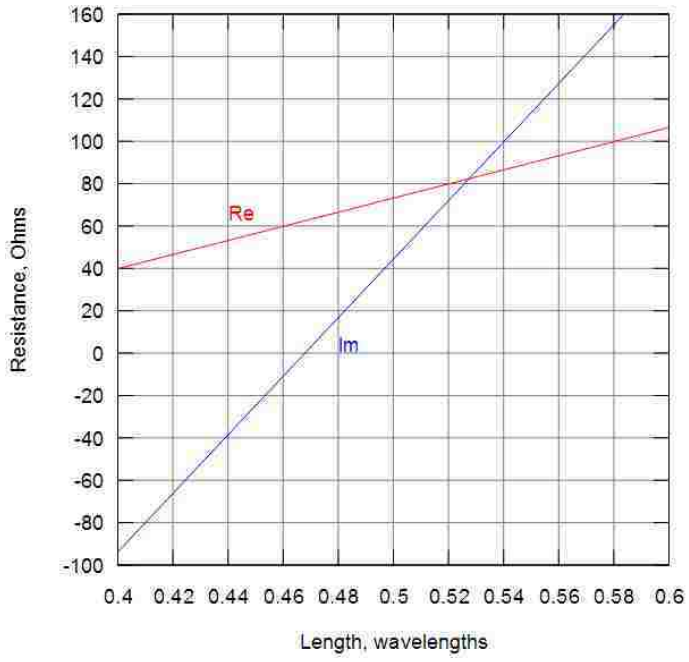

Figure 26: Impedance vs. Frequency of dipole antenna.

[41]

The input impedance of an LPDA plotted versus frequency will be repetitive, and if plotted versus log frequency it will be periodic. An example of this behavior is shown in Figure 27. Pattern, side lobe level, directivity and beam width also vary periodically.

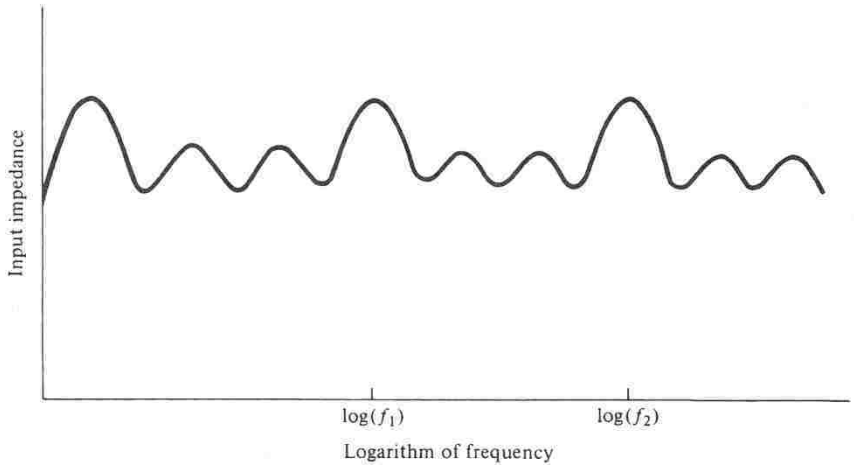

Figure 27: Typical input impedance vs. frequency of LPDA.

Figure 11.11, p. 628 [30]

If such variations are acceptable for the application then the antenna may be very broadband. The factor Δ quantifies the relative frequency span of each cycle, and is determined by the geometric ratio previously discussed, such that

$$\Delta = \ln(f_2) - \ln(f_1) = \ln\left(\frac{1}{\tau}\right) \tag{3-43}$$

Robert L. Carrel conducted an extensive analysis of LPDA design [42] and aids for the design of an LPDA. The bandwidth of the active region, B_{ar}, may be approximated as

$$B_{ar} = 1.1 + 7.7(1-\tau)^2 \cot\alpha \tag{3-44}$$

A larger bandwidth than required is typically designed, with the relationship

$$B_s = BB_{ar} = B\left[1.1 + 7.7(1-\tau)^2 \cot\alpha\right] \tag{3-45}$$

where B_s is the designed bandwidth and B is the desired bandwidth.

The total length of the LPDA structure is represented as

$$L = \frac{\lambda_{\max}}{4}\left(1 - \frac{1}{B_s}\right)\cot\alpha \tag{3-46}$$

where

$$\lambda_{\max} = 2l_{\max} = \frac{v}{f_{\min}} \tag{3-47}$$

The total number of elements N is described by

$$N = 1 + \frac{\ln(B_s)}{\ln(1/\tau)} \tag{3-48}$$

The feed line conductor spacing is calculated as follows once the input impedance, diameter of dipole elements, and diameter of feed line conductors has been specified.

$$Z_a = 120\left[\ln\left(\frac{l_n}{d_n}\right) - 2.25\right] \tag{3-49}$$

The center-to-center spacing s of the feed line rods of diameter d is

$$s = d\cosh\left(\frac{Z_o}{125}\right) \tag{3-50}$$

Carrel [42] also computed constant directivity contours versus τ and σ to be used with the above equations to aid in the design of an LPDA. These are shown in Figure 28, where

$\sigma' = \sigma / \sqrt{\tau}$ = relative mean spacing

Z_a = average characteristic impedance of the elements

R_{in} = real input impedance

Z_o = characteristic impedance of the feeder line

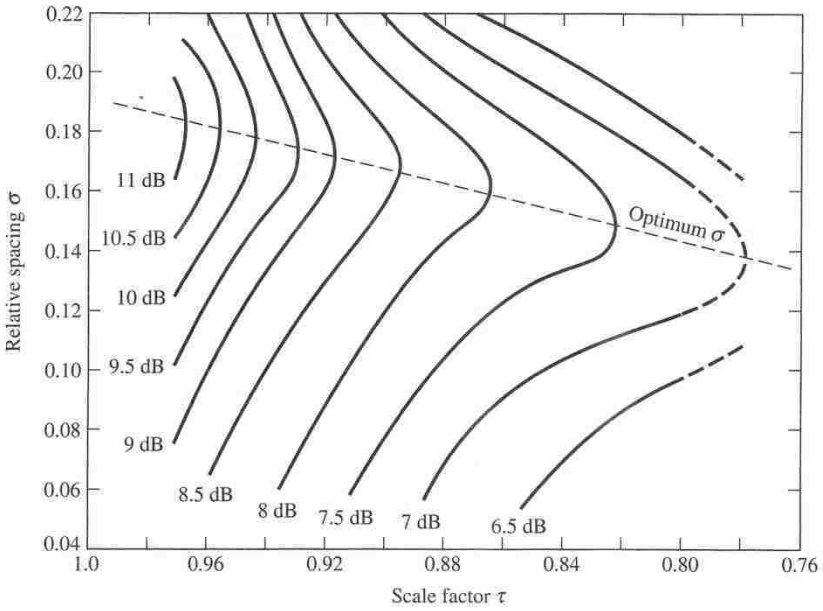

Figure 28: Carrel's constant directivity contours for LPDA design.

Figure 65, p. 118 [42]

Given the preceding equations and graph, [30] p. 633 outlines a design procedure for the LPDA as:

1. Given D_o (dB), determine α and τ from Figure 28.
2. Determine α using (3-42).
3. Determine B_{ar} using (3-44) and B_s using (3-45).
4. Find L using (3-46) and N using (3-48).
5. Determine Z_a using (3-49) and $\sigma' = \sigma / \sqrt{\tau}$.
6. Determine Z_o/R_{in} from [42].
7. Find s using (3-50).

Highly Symmetrical Log-Periodic Dipole Array

As previously discussed, the LPDA is a broadband feed with little gain variation over its frequency range. However it was discovered at OVSA that the TECOM 1-18 GHz dual-linearly polarized LPDA feed exhibited beam squint. If the beam squint could be minimized or eliminated the LPDA is a reasonable choice to feed a parabolic dish if the defocusing loss is acceptable in the system.

It is hypothesized that beam squint in an LPDA arises from asymmetries in the LPDA system, whether from physical asymmetries (such as misalignment) or phase errors from a balun. Simulations were performed on a resonant half-wave dipole in CST Microwave Studio (MWS) to explore this hypothesis. Element 7, referenced in Table 3 in the design calculations of an LPDA similar to the TECOM, is used for this simulation study. This element has a length of 21.6mm, a diameter of 0.3mm and a feed gap of 0.5mm.

The first simulation depicts the dipole with no asymmetry and the model is shown in Figure 29. As expected, the S-parameters and radiation pattern are that of a dipole and the main lobe is oriented at $\varphi=180°$ (or 0°) as expected. The S-parameters and radiation pattern are shown in Figure 30 and Figure 31, respectively.

Figure 29: Resonant Half-Wave Dipole Model.

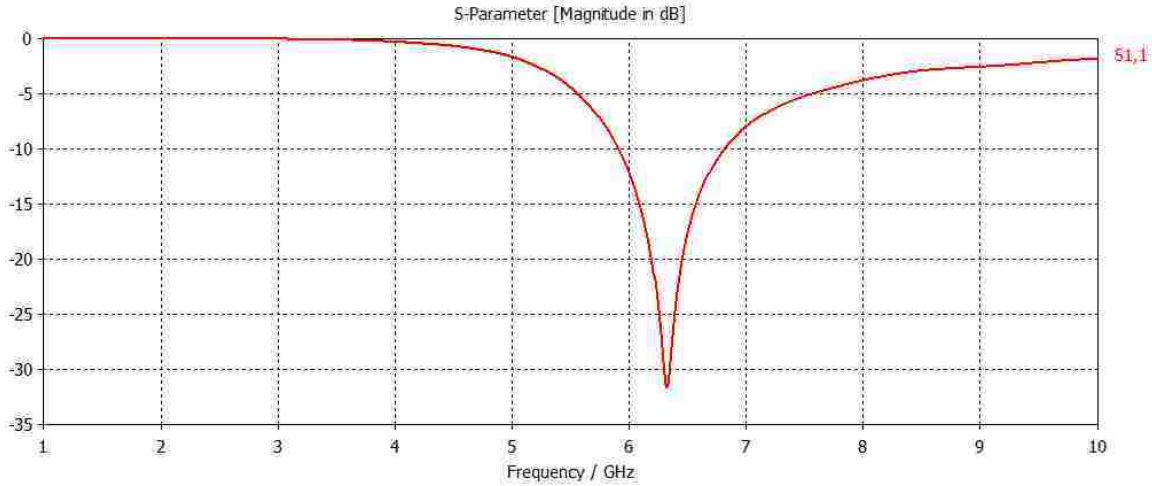

Figure 30: Simulated S-Parameters of Half-Wave Dipole.

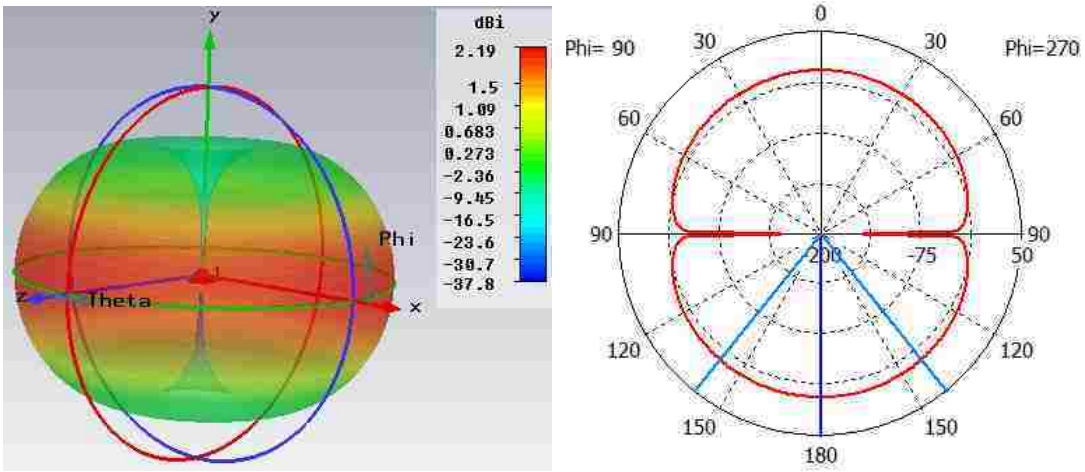

Frequency = 6.3
Main lobe magnitude = 2.2 dBi
Main lobe direction = 180.0 deg.
Angular width (3 dB) = 77.6 deg.

Figure 31: Simulated Radiation Pattern of Symmetrical Half-Wave Dipole.

This half-wave dipole is symmetrical in all ways. Both elements comprising the dipole are identical cylinders lying in the same plane. No beam squint would be expected from such a symmetrical structure.

In Figure 32 below an intentional offset has been incorporated. The element in the positive y direction has been translated in the z direction by 250µm to model a physical misalignment in an actual LPDA.

Figure 32: Half-Wave Dipole With Intentional Offset

The simulated radiation pattern is shown in Figure 33, and depicts that the main lobe direction has shifted by one degree, from 180.0° to 179.0°. This represents a one degree beam squint. In the previous chapter the squint from the TECOM feed in the OVSA was shown to have a 26 arc minute, or 0.4°, range. A subsequent MWS simulation showed that an offset of only 100µm was sufficient to produce a squint of 0.4°. Therefore, if z is the bore sight direction and one element of a half-wave dipole is translated in z, a squint will occur.

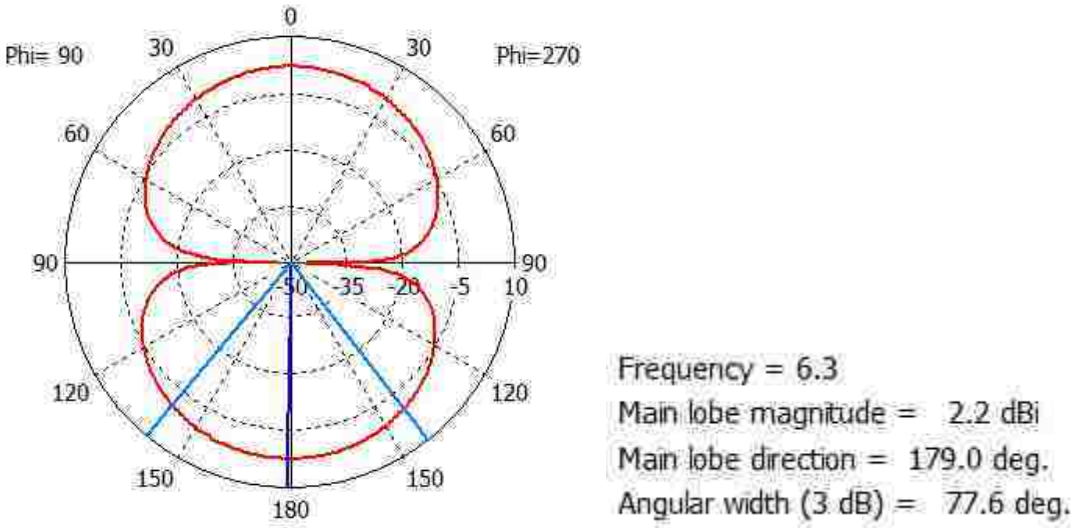

Figure 33: Simulated Radiation Pattern for Offset Dipole.

It may be possible in an LPDA that one element of a half-wave dipole is angled with respect to the plane in which the dipole was intended to be placed. This was modeled in MWS by angling one element in the positive z direction rather than translating it as was just analyzed. An angle of 5° was chosen for the first simulation, and the half-wave dipole model is shown in Figure 34.

Figure 34: Half-Wave Dipole with Intentional 5° Offset.

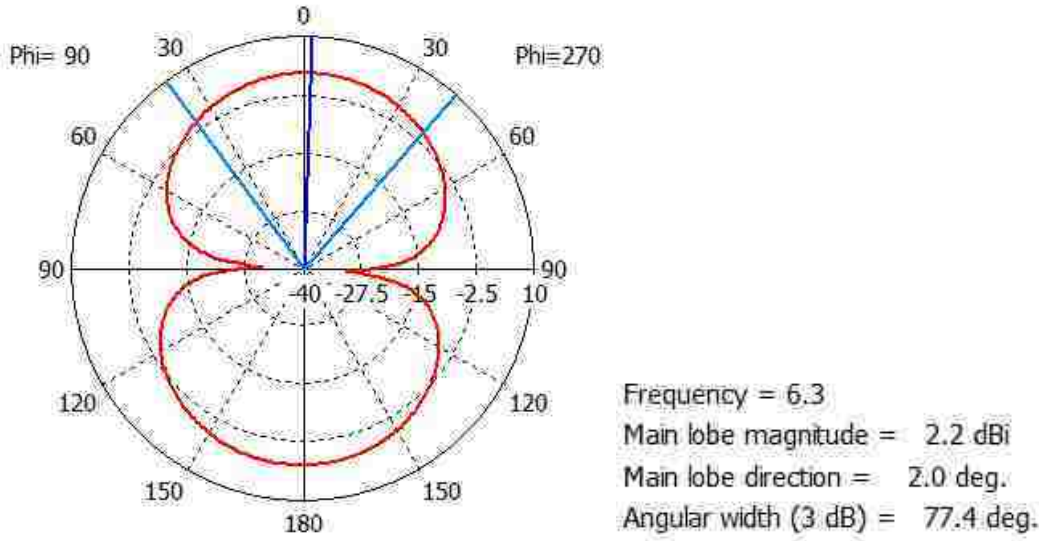

Figure 35: Simulated Radiation Pattern of Dipole With 5° Offset

The simulated radiation pattern for the dipole with an intentional 5° angle is shown in Figure 35, and it can be seen that the main lobe has shifted by 2.0°. Further simulation revealed that angling one of the dipole elements by only 1.25° was sufficient to induce a beam squint of 0.5°.

Therefore angling one of the dipole elements may also give rise to beam squint. Such angles may arise from a warped printed circuit board (PCB) in the case of a printed structure, or other form of physical misalignment such as arising from the implementation of the LPDA's boom structure.

Referring back to the OVSA's measured beam squint in Figure 8 it can be observed that the squint changes with frequency but not in a systematic fashion. The squint increases or decreases as frequency increases. It may be possible to explain this behavior by considering that dipole elements translated by as little as 100μm or angled by

as little as 1.25° are sufficient to induce the observed squint, and the likelihood that not all elements in an LPDA are translated or angled by the same amount or in the same direction.

As previously discussed, for an LPDA as frequency increases the longer elements become less resonant and the shorter elements become more resonant. Consider an LPDA with elements having asymmetries such as shown in an exaggerated fashion in Figure 36. While elements #4 and #6 have no physical asymmetries the other four elements contain an asymmetry in the form of an angle or a translation. Element #1 will induce a squint away from bore sight in the positive y direction; element #2 in the negative y direction; element #3 in the positive y direction, and element #5 in the negative y direction.

At the highest frequency it is likely the beam will squint in the positive y direction, when dipole #2 starts becoming more strongly resonant the squint will start moving in the opposite direction. This will again reverse at an even lower frequency when dipole #3 is more strongly resonant. Physical asymmetries of this form may account for the observed squint in Figure 8.

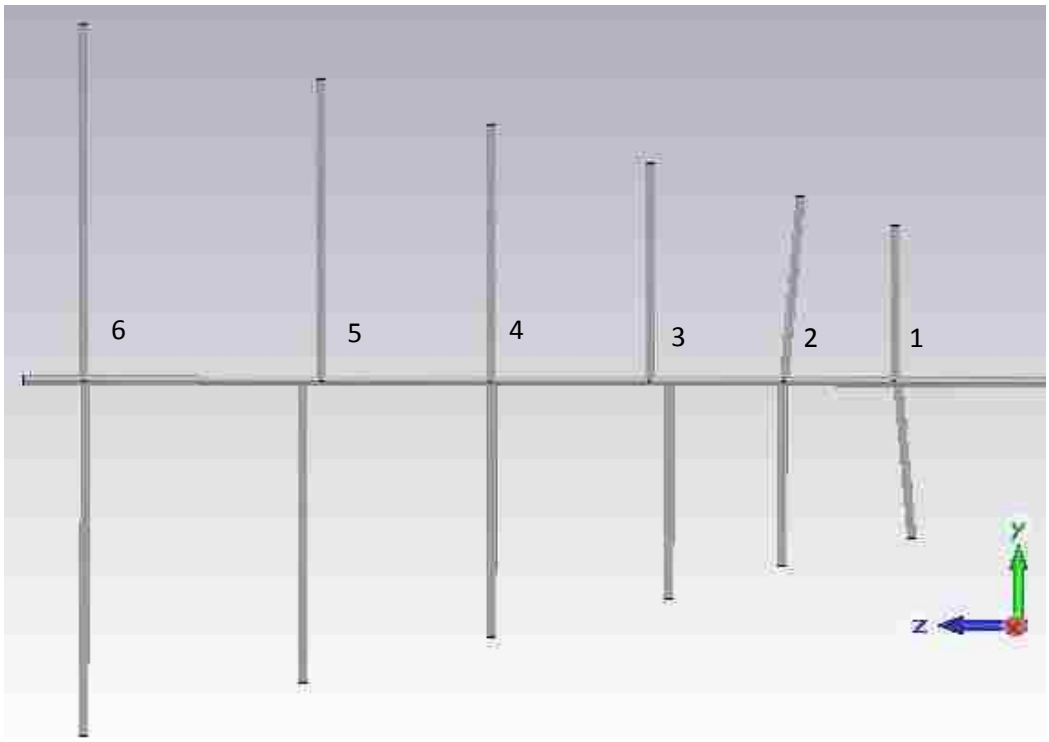

Figure 36: LPDA Model With Exaggerated Asymmetries.

This LPDA structure with exaggerated asymmetries was simulated in MWS over a range of frequencies with the result that the main lobe squinted back and forth as predicted. The results are shown in Figure 37. It would therefore seem plausible that physical asymmetries in the TECOM LPDA could, at least in part, be responsible for the beam squint seen in that feed.

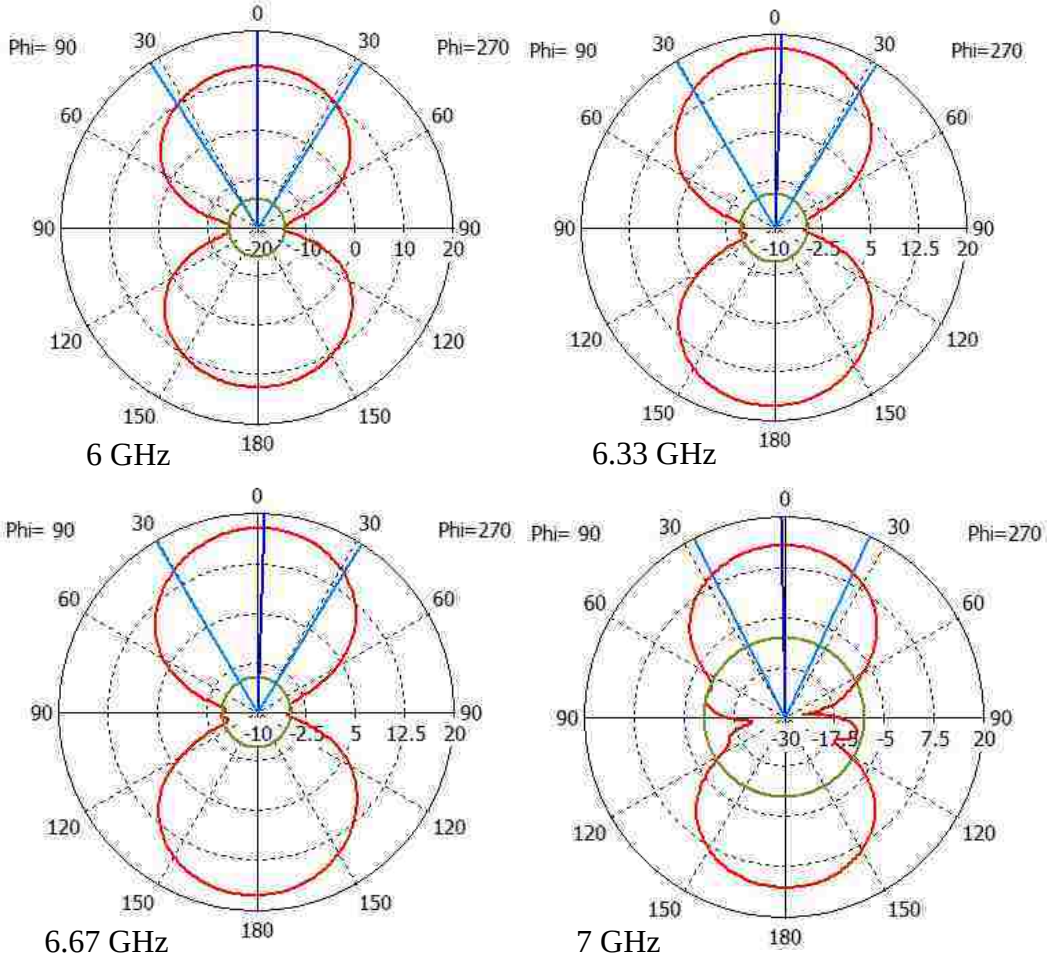

Figure 37: Simulated Beam Squint from LPDA with Physical Asymmetries.

Simulations show that displacements or offsets as little as 100µm or 1° could account for 0.5° of beam squint in an LPDA. It is possible that other asymmetries in the construction of an LPDA could also cause beam squint. One possible source of squint may be interactions between elements and the feed boom. With this in mind, it may be possible that an LPDA could be designed to have perfect symmetry, at least in theory, throughout the entire structure. This perfect symmetry is a design concept and does not

take into account asymmetries due to the fabrication process so it was not pursued further. The structure is shown in Appendix D: Perfect Symmetry Log-Periodic Dipole Array.

Chapter 4: Design Solution

In this chapter a design solution based upon bowtie radiating elements will be presented. This design was simulated in CST Microwave Studio and subsequently fabricated. Performance measurements of the antenna and comparison with simulated performance will be discussed in the next chapter.

Biconical Antenna

The biconical antenna is a simple configuration that can yield broadband performance. An infinitesimally thin bowtie antenna is the two dimensional analog of the biconical and shall be discussed before detailing the design solutions.

A biconical antenna consists of two conductive cones of infinite geometry, driven at the vertices, as illustrated in Figure 38. Such a configuration may be considered as a uniformly tapered transmission line.

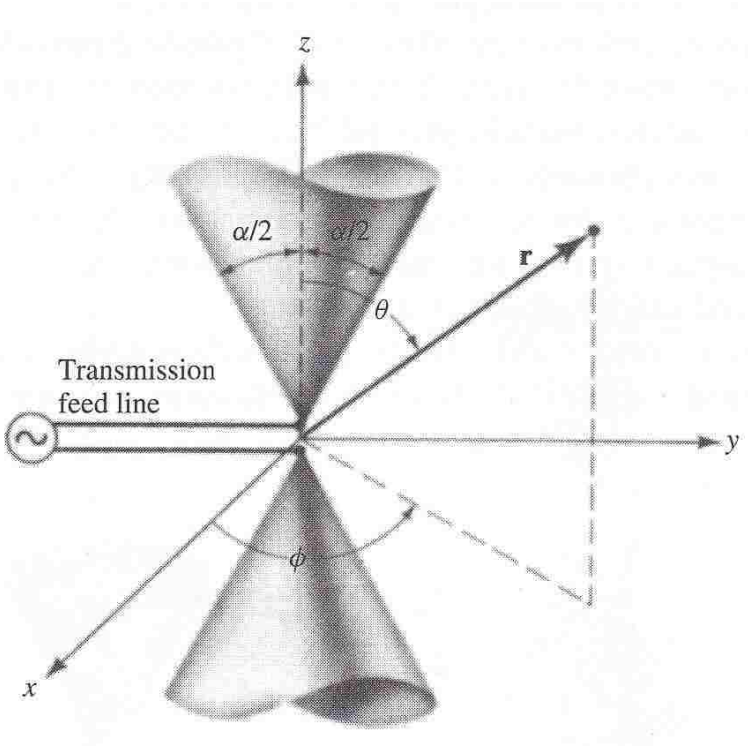

Figure 38: Biconical antenna geometry.

Figure 9.3(a), p. 500 [30]

A voltage Vi at the input terminals produces spherical waves. At any point, ($r,\theta=\theta_c,\varphi$) a voltage V between the cones and current I on the cone surface will exist as shown in Figure 39. The characteristic impedance of the transmission line can be found from these.

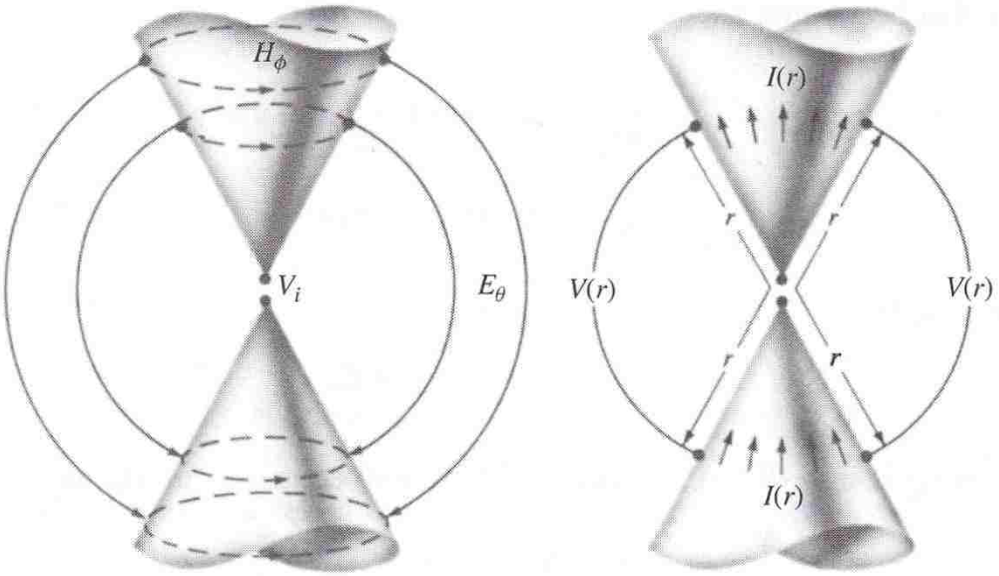

Figure 39: Voltages and currents for infinite biconical antenna.

Figure 9.4, p. 501 [30]

To perform an analysis of the radiated fields, transverse electromagnetic (TEM) mode excitation is assumed. In TEM mode, **E** and **H** are transverse to the direction of wave propagation. The analysis begins by considering the time harmonic form of Faraday's law

$$\nabla \times \overline{E} = -j\omega\mu\overline{H} \tag{4-1}$$

for spherical coordinates where it is assumed that the **E** field only has an E_θ component independent of φ due to the symmetry of the biconical geometry. In spherical coordinates and with only an E_θ component, the curl of the **E** field reduces to

$$\nabla \times \overline{E} = \hat{a}_\varphi \frac{1}{r}\frac{\partial}{\partial r}(rE_\theta) = -j\omega\mu(\hat{a}_r H_r + \hat{a}_\theta H_\theta + \hat{a}_\varphi H_\varphi) \tag{4-2}$$

As shown in Figure 39, **H** only has an H_φ component which is a constraint for TEM mode with **E** being E_θ. Equation (4-2) further simplifies to

$$\frac{1}{r}\frac{\partial}{\partial r}\left(rE_\theta\right) = -j\omega\mu H_\varphi) \tag{4-2a}$$

The time harmonic form of Ampere's law states

$$\nabla \times \overline{H} = j\omega\varepsilon\overline{E} \tag{4-3}$$

Applying this to spherical coordinates with the constraint of only E_θ and H_φ components with no dependence on φ due to the symmetry as shown in Figure 39 yields

$$\hat{a}_r \frac{1}{r^2\sin\theta}\left[\frac{\partial}{\partial\theta}\left(r\sin\theta H_\varphi\right)\right] - \hat{a}_\theta \frac{1}{r\sin\theta}\left[\frac{\partial}{\partial r}\left(r\sin\theta H_\varphi\right)\right] = j\omega\varepsilon\left(\hat{a}_\theta E_\theta\right) \tag{4-4}$$

However,

$$\frac{\partial}{\partial\theta}\left(r\sin\theta H_\varphi\right) = 0 \tag{4-4a}$$

so

$$-\frac{1}{r\sin\theta}\left[\frac{\partial}{\partial r}\left(r\sin\theta H_\varphi\right)\right] = j\omega\varepsilon E_\theta \tag{4-4b}$$

which reduces to

$$\frac{1}{r}\frac{\partial}{\partial r}\left(rH_\varphi\right) = -j\omega\varepsilon E_\theta \tag{4-5}$$

which when substituted into (4-2a) yields

$$-\frac{1}{j\omega\varepsilon r}\frac{\partial}{\partial r}\left[\frac{\partial}{\partial r}\left(rH_\varphi\right)\right] = -j\omega\mu H_\varphi \tag{4-6}$$

or

$$\frac{\partial^2}{\partial r^2}\left(rH_\varphi\right) = -\omega^2\mu\varepsilon\left(rH_\varphi\right) = -k^2\left(rH_\varphi\right) \tag{4-6a}$$

Solutions for (4-6a) must also satisfy (4-4a), so the θ variations of H_φ must have the form

$$H_\varphi = \frac{f(r)}{\sin\theta} \tag{4-7}$$

A solution that represents a wave propagating outward is if

$$f(r) = H_o\frac{e^{-jkr}}{r} \tag{4-8}$$

so that

$$H_{\varphi} = \frac{H_o}{\sin\theta}\frac{e^{-jkr}}{r} \tag{4-8a}$$

The wave propagating inward is discarded. In TEM mode the magnetic field is related to the electric field by the intrinsic impedance, expressed as

$$E_{\theta} = \eta H_{\varphi} = \eta\frac{H_o}{\sin\theta}\frac{e^{-jkr}}{r} \tag{4-9}$$

At a distance r from the origin, the voltage between two corresponding points on the cones is

$$V(r)\int_{\alpha/2}^{\pi-\alpha/2}\bar{E}\bullet d\bar{l} = \int_{\alpha/2}^{\pi-\alpha/2}\left(\hat{a}_{\theta}E_{\theta}\right)\bullet\left(\hat{a}_{\theta}rd\theta\right) = \int_{\alpha/2}^{\pi-\alpha/2}E_{\theta}rd\theta \tag{4-10}$$

By applying (4-9),

$$V(r) = \eta H_o e^{-jkr}\int_{\alpha/2}^{\pi-\alpha/2}\left(\frac{d\theta}{\sin\theta}\right) = \eta H_o e^{-jkr}\ln\left[\frac{\cot(\alpha/4)}{\tan(\alpha/4)}\right] \tag{4-10a}$$

or

$$V(r) = \eta H_o e^{-jkr}\ln\left[\cot\left(\frac{\alpha}{4}\right)\right] \tag{4-10b}$$

At a distance r from the origin, the current on the surface of the cones may be found by using (4-8a) as

$$I(r) = \int_0^{2\pi}H_{\varphi}r\sin\theta d\varphi = H_o e^{-jkr}\int_0^{2\pi}d\varphi = 2\pi H_o e^{-jkr} \tag{4-11}$$

Given the previous expressions for current (4-11) and voltage (4-10b), the characteristic impedance Z_c may be expressed as

$$Z_c = \frac{V(r)}{I(r)} = \frac{\eta H_o e^{-jkr}\ln\left[\cot\left(\frac{\alpha}{4}\right)\right]}{2\pi H_o e^{-jkr}} = \frac{\eta}{2\pi}\ln\left[\cot\left(\frac{\alpha}{4}\right)\right] \tag{4-12}$$

for two cones the characteristic impedance is twice this value,

$$Z_c = \frac{\eta}{\pi}\ln\left[\cot\left(\frac{\alpha}{4}\right)\right] \tag{4-12a}$$

This characteristic impedance is a pure resistance, and in a medium of free space may be expressed as,

$$Z_c = Z_{in} = 120 \ln\left[\cot\left(\frac{\alpha}{4}\right)\right] \tag{4-12b}$$

Expression (4-12b) permits the half-cone angle α of the biconical antenna to be chosen to be close to that of the transmission line driving the antenna. For example, if α is chosen to be 33° then $Z_c = 50\Omega$.

The antenna's radiation resistance is expressed as

$$P_{rad} = \oiint_S \overline{W}_{avg} \bullet d\overline{S} = \int_0^{2\pi} \int_{\alpha/2}^{\pi-\alpha/2} \frac{|E|^2}{2\eta} r^2 \sin\theta d\theta d\varphi = \pi\eta |H_o|^2 \int_0^{\pi-\alpha/2} \frac{d\theta}{\sin\theta} \tag{4-13}$$

which when evaluated becomes

$$P_{rad} = 2\pi\eta |H_o|^2 \ln\left[\cot\left(\frac{\alpha}{4}\right)\right] \tag{4-13a}$$

and by using (4-11) evaluated at r=0 the radiation resistance then becomes

$$R_r = \frac{2P_{rad}}{[I(0)]^2} = \frac{2\left[2\pi\eta |H_o|^2 \ln\left[\cot\left(\frac{\alpha}{4}\right)\right]\right]}{[2\pi H_o]^2} = \frac{\eta}{\pi} \ln\left[\cot\left(\frac{\alpha}{4}\right)\right] \tag{4-14}$$

For the infinite biconical antenna the characteristic impedance (4-12a) is equal to the radiation resistance (4-14).

In practice a biconical antenna will be of finite length. In addition to the TEM mode there will be higher order modes that will reflect at the length of the cone. This may be viewed as a load impedance Z_L connected from the end of one cone to the other. In this manner the finite length biconical antenna may be analyzed as a transmission line, with a characteristic impedance Z_c terminated in a load impedance Z_L. The input impedance Z_{in} of the biconical antenna's input terminals then becomes

$$Z_{in} = Z_c \frac{Z_L + jZ_c \tan(\beta l)}{Z_c + jZ_L \tan(\beta l)} \tag{4-15}$$

Z_L may be determined by calculating Z_m at a point of maximum current by assuming a sinusoidal current distribution [43]. The impedance Z_m occurs between the current maximum on one cone and the current maximum on the other, and is located at a distance of λ/4 from the open end. In this manner Z_L can be transformed over a λ/4 line. Z_{in} is then transformed over a transmission line of impedance Z_c and length l, as

$$Z_L = Z_c \frac{Z_m + jZ_c \tan(\beta x)}{Z_c + jZ_m \tan(\beta x)} \tag{4-16}$$

where

$$\beta x = \frac{\pi}{2} \tag{4-16a}$$

thus

$$Z_L = \frac{Z_c^2}{Z_m} \tag{4-16b}$$

where Z_m has the form $R_m + jX_m$. [44] provided expressions for R_m and X_m for thin biconical antennas as

$$R_m = 60Ci(2\beta l) + 30[0.577 + \ln(\beta l) - 2Ci(2\beta l) + Ci(4\beta l)]$$
$$\times \quad \cos(2\beta l) + 30[Si(4\beta l) - 2Si(2\beta l)\sin(2\beta l)] \tag{4-17a}$$

$$X_m = 60Si(2\beta l) + 30[Ci(2\beta l) - \ln(\beta l) - 0.577]\sin(2\beta l) - 30[Si(4\beta l)]\cos(2\beta l) \tag{4-17b}$$

where *Ci* and *Si* are cosine and sine integrals, respectively. Finally,

$$Z_{in} = Z_c \frac{Z_c + jZ_m \tan(\beta l)}{Z_m + jZ_c \tan(\beta l)} \tag{4-18}$$

where $Z_m = R_m + jX_m$ and Z_c is given by (4-12b).

Microwave Studio was used to simulate a biconical antenna of 150mm overall length with $\alpha = 45°$ as shown in Figure 40. The red region in the center is a discrete port used to excite the structure.

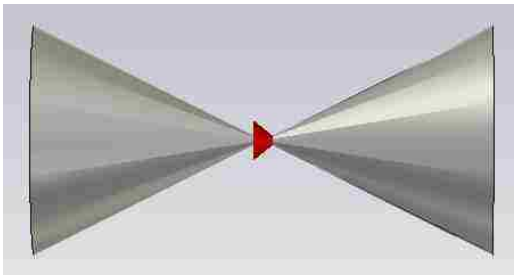

Figure 40: Biconical antenna model for simulation.

The simulated input impedance and radiation patterns are shown in Figure 41 and Figure 42, respectively. As anticipated, both input impedance and radiation patterns vary with frequency as a result of higher order modes.

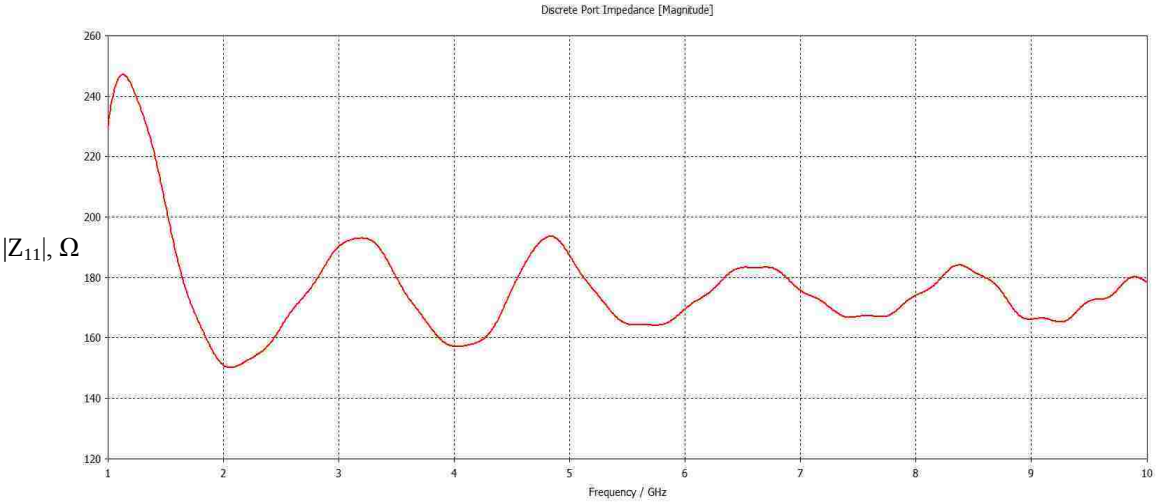

Figure 41: Input impedance of simulated biconical antenna.

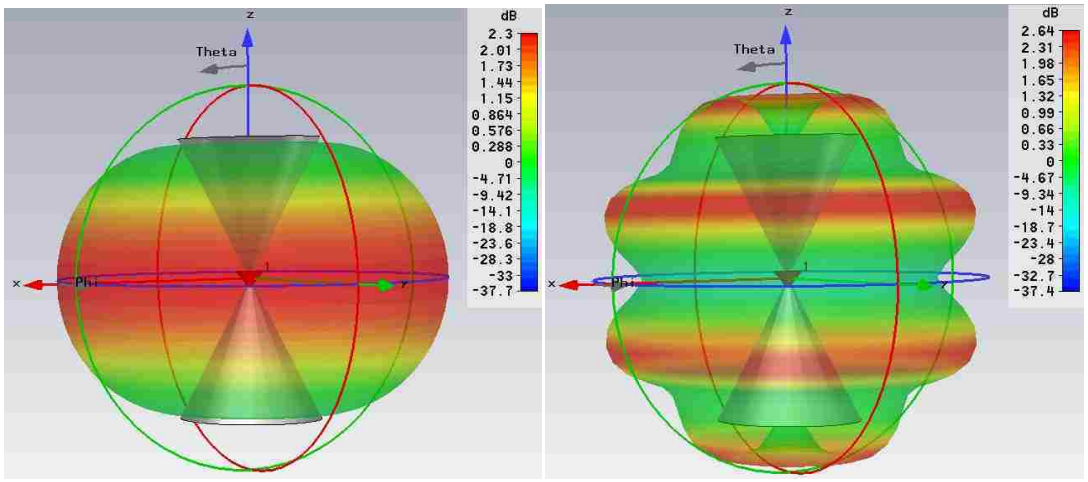

(a) 1 GHz (b) 5 GHz

Figure 42: Simulated radiation patterns of biconical antenna.

In many applications the mass of a solid biconical antenna would be disadvantageous. It was found that a wire frame approximation to a solid biconical often yielded satisfactory results with the advantage of having much less weight and wind resistance. A commercially available example is depicted in Figure 43.

Figure 43: Wire simulation biconical antenna.

[45]

Given the biconical antenna's desirable performance characteristics, approximations and variations have been developed. A structure that lends itself to PCB fabrication techniques is the bow tie antenna which in the case of an infinitesimally thin metal layer is a two-dimensional approximation of the biconical structure previously discussed. The bow tie is not as broadband as a biconical.

Transmission line theory can be applied to calculate the impedance of a bow tie antenna as [46]:

$$Z = \sqrt{\frac{2\mu_o}{\varepsilon_{eff} + \varepsilon_o}} \cdot \frac{K(k)}{K'(k)} \tag{4-19}$$

where K and K' are elliptic integrals of the first kind,

$$K(k) = \int_0^1 \frac{dx}{\sqrt{(1-x^2)(1-k^2x^2)}} \tag{4-20a}$$

$$K'(k) = K(k') \tag{4-20b}$$

$$k' = \sqrt{1-k^2} \tag{4-20c}$$

$$k = \tan^2(45° - \theta/4) \tag{4-20d}$$

where θ is the bow angle in degrees.

No reference was discovered regarding the radiation integral of a bowtie antenna, likely due to the lack of rotational symmetry in such a structure. [47] provides a rigorous analysis of the bowtie yielding a set of matrices to be solved numerically after specifying the number of modes of ***J***in both x- and y-directions. If too few modes are specified the solution will not converge, and if too many are chosen the computation time becomes long. Given that this research concerns the development of an ultrawideband antenna such an approach would require specifying a different number of current modes at

different frequencies, as there will be many more modes at 10GHz than at 1GHz. As a result three-dimensional (3D) time-domain simulation was performed.

3D Simulation

Simulations for this research were performed using Computer Simulation Technology (CST) Microwave Studio (MWS), a commercially available simulation package for 3D electromagnetic simulation. MWS has six solvers:

- Transient (Time Domain) - broadband applications
- Frequency Domain - electrically small structures and/or devices with a high Q
- Eigenmode - closed resonant structures
- Integral Equation - electrically large structures (tens to hundreds of wavelengths)
- Multilayer - planar modeling of microstrips and transmission lines
- Asymptotic - for objects many thousands of wavelengths

Since the design goal for the antenna was a 6:1 bandwidth or greater, the Transient solver was used exclusively.

Both Transient and Frequency Domain solvers in MWS use the Finite Integration Technique (FIT) for numerical analysis. FIT was first proposed by [48] as a numerical method using the integral, rather than differential, form of Maxwell's equations. FIT was shown to be the first algorithm that could calculate modes and propagation constants of waveguides possessing arbitrary shape and including lossy materials. While FIT is well-known for application to time-domain solvers it was first applied to frequency domain simulations.

In 1983 the MAFIA ("solving **MA**xwell's equations with the **F**inite **I**ntegration **A**lgorithm") Collaboration commenced as a consortium of universities, research institutes, and accelerator laboratories. Its goal was to develop a FIT-based application to solve electromagnetic problems. MAFIA was used extensively for accelerator simulation where it is too costly to prototype.

The code continued to evolve with additions and improvements such as triangular meshes, waveguide boundary conditions, stable sub gridding algorithms, and non-orthogonal grids. Modules were constructed for various electromagnetic applications, Particle-in-Cell, coupled electromagnetic-circuit problems, and more. A brief overview

of the Finite Integration Technique may be found in Appendix B: The Finite Integration Technique (FIT).

Time domain (Transient) simulations were used exclusively since they are better suited for broadband analysis and affordable hardware acceleration.

Simulation Platform

It became clear upon commencing broadband time domain simulations of proposed structures that a desktop PC with a quad-core CPU was insufficient Simulations would run for days and often would abort before producing results.

Microwave Studio supports GPU acceleration for time domain simulations via GPU (graphics processing unit) devices such as the Tesla C2075. The C2075 is a 448-core, 6GB, 1.15GHz GPU capable of 515 GFLOPS (giga floating operations per second) in double precision mode. Multiple GPU's may be used for simulation but each GPU requires a software accelerator token to be activated. Our academic license included one accelerator token.

The C2075 requires a PCIx-16 full-height slot along with commensurate power supply and cooling capability. The UNM ECE Department did not have a PC that could accommodate a C2075 so a Windows 7 based high performance PC was researched and configured. Xi Computers of San Clemente, CA, was a vendor experienced in building GPU-based workstations. The PC workstation was configured and purchased, with the following configuration:

- Asus P8Z77 workstation motherboard
- Intel i7 3770K @ 4.1GHz quad-core CPU
- 32GB 1866MHz DDR3 RAM
- Two Tesla C2075 GPU's
- 240GB solid state drive and 2TB SATA hard drive
- 1300W power supply
- CM-HAF XM high ventilation enclosure
- An additional accelerator token

Figure 44: Xi workstation internal view

In Figure 44 the two C2075 GPU's are seen to the left of center, above the 1300W power supply, while the red device is the 240 GB solid state drive. This solid state drive was chosen to reduce disk access time to further reduce simulation times.

The two GPU's effected a reduction in simulation times along with the capability to reliably simulate up to about 40 million mesh cells. Once the matrix coefficients for a given simulation were calculated and loaded into the GPU's, simulations were sped up by nearly a factor of twenty. All structures simulated ran reliably to completion with the longest simulation taking less than an hour and a half.

Diamond Feed

The feed built and tested for this research is comprised of diamond-shaped radiating elements in a damped cavity and is hereafter referred to as the diamond feed. This design solution began with an effort to extend the bandwidth of a bow tie antenna which is typically on the order of 3:1, with the goal of achieving 5:1 or better. Once the bandwidth had been improved studies were undertaken to improve the radiation patterns for the application of illuminating a RSTN dish.

The starting point was a planar bowtie structure consisting of thin copper on a dielectric substrate. The effect of several parameters on a bow tie antenna were examined in pursuit of a design solution and are discussed in the following sections. Two fundamental qualities were noted during the design process: bandwidth and radiation pattern.

Bandwidth was observed by noting the input impedance over a given frequency range. It was decided that the feed would use a balun or coupler with two 50Ω ports, effectively presenting 100Ω to a pair of elements. With a VSWR target of 3:1 in a 100Ω system the magnitude of input impedance must therefore remain less than or equal to 300Ω.

The VSWR may be derived from the impedance mismatch of the system. The reflection coefficient Γ may be expressed as

$$\Gamma = \frac{Z_L - Z_S}{Z_L + Z_S} \tag{4-21}$$

where Z_L is the load impedance and Z_S is the source impedance of 100Ω as described above.

VSWR may then be defined as

$$VSWR = \frac{1+|\Gamma|}{1-|\Gamma|} \tag{4-22}$$

To achieve a VSWR of 3, |Γ| must be 0.5 and smaller values of |Γ| will yield a lower VSWR. Substituting Z_L=100Ω and Γ=0.5 into (4-21) and (4-22) results in a source impedance Z_S of 300Ω. Thus the goal was to achieve a magnitude of impedance of 300Ω or less.

During the course of development, three-dimensional (3D) gain patterns, expressed as dBi or decibel isotropic, were examined as such patterns quickly yielded insight into the antenna's ability to illuminate a RSTN dish.

Effect of Metal Thickness

In this study a bow tie antenna constructed of PEC in free space, with a chosen flare angle of 60° and a feed gap of 2mm by 2mm, was parametrically stepped through thickness of PEC, to include common microwave substrate metal thicknesses. The overall length of the bowtie was 150mm, corresponding to half the length of a free space 1GHz wave.

Metal thicknesses in microwave substrate boards are expressed in ounces, corresponding to the weight of copper necessary to cover a square foot of board with a layer of uniform thickness. Common metal thicknesses and their metric equivalents are

½ ounce = 0.017395mm

1 ounce = 0.03479mm

2 ounce = 0.06958 ounce

The magnitude of input impedance is plotted in Figure 45, where it can be seen that the variation in metal thickness in this range does not affect input impedance. This result implies that the choice of microwave substrate metal thickness is not an important consideration.

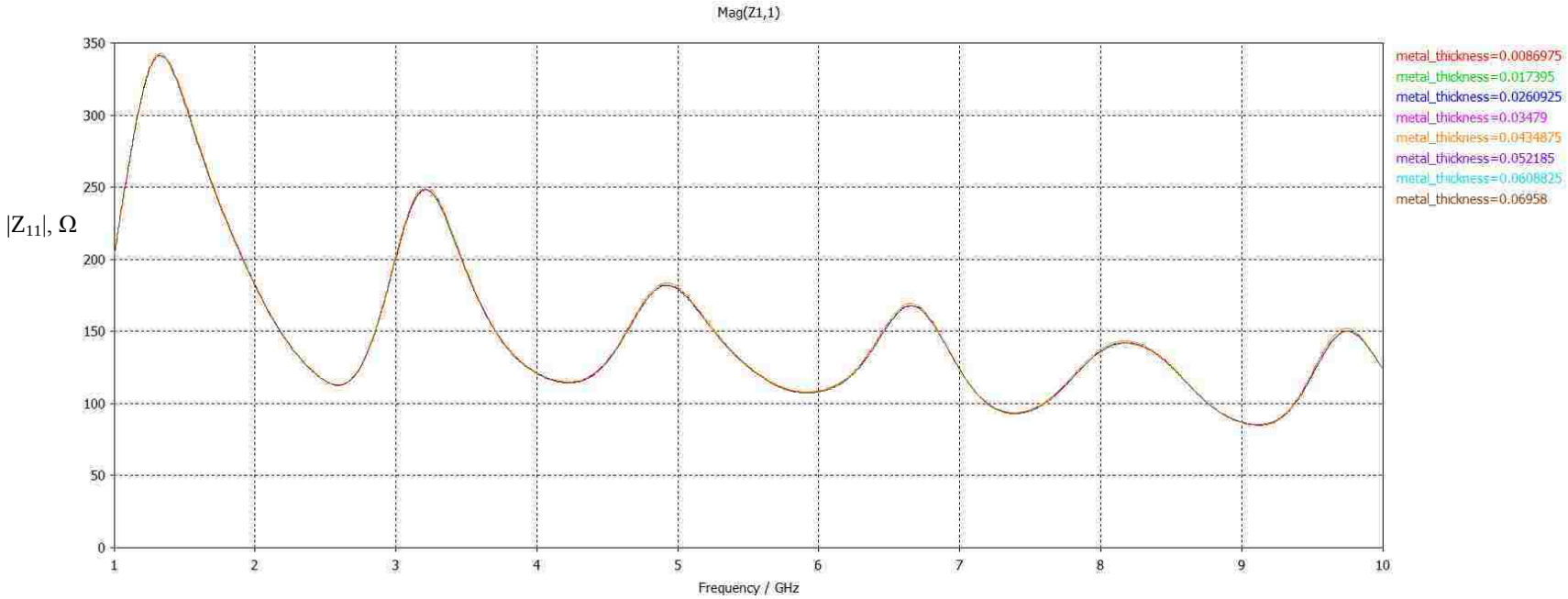

Figure 45: Effect of metal thickness on input impedance

Figure 45 above shows very little variation of magnitude of input impedance for metal thicknesses ranging from 1/4 ounce to 2 ounce. Thus it does not greatly matter which metallization is chosen, increasing flexibility of fabrication.

The effect of metal thickness on radiation pattern was also investigated although the patterns were not expected to be a function of frequency since the input impedance was not affected by metal thickness.

Far field gain simulations were performed for metal thicknesses of 0.30, 0.06, and 0.03millimeters and results are shown in Figure 46. The gain decreases very slightly as metal thickness increases. The center of the parabolic dish is in the Z-direction. It is noteworthy that at 10GHz the main lobe has split and pattern lobes are now spilling over the edge of the RSTN f/D=0.375 dish.

f = 1GHz

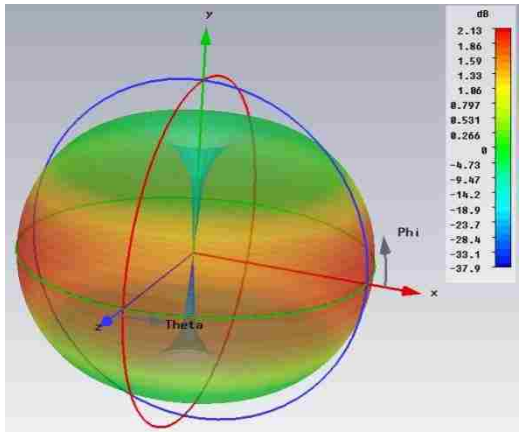

t = 0.03mm

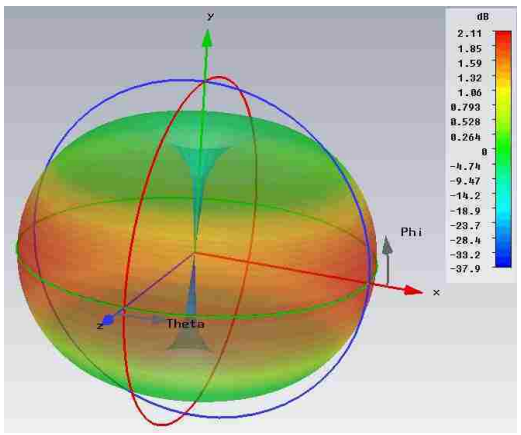

t = 0.06mm

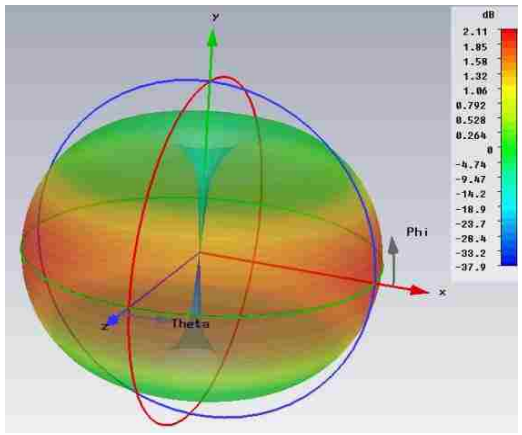

t = 0.3mm

f = 10GHz

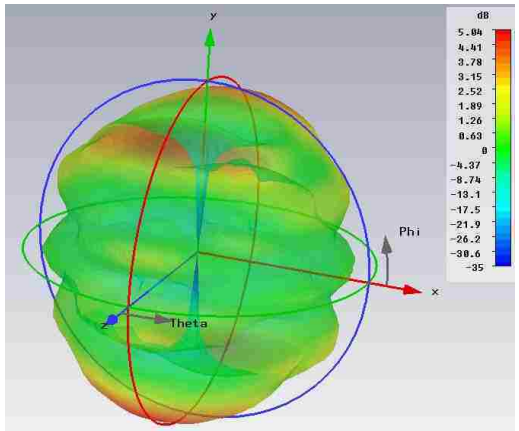

t = 0.03mm

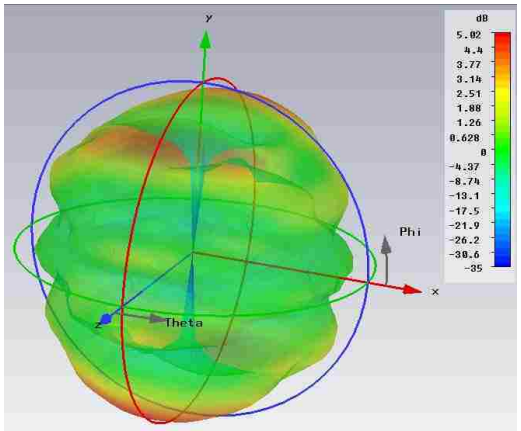

t = 0.06mm

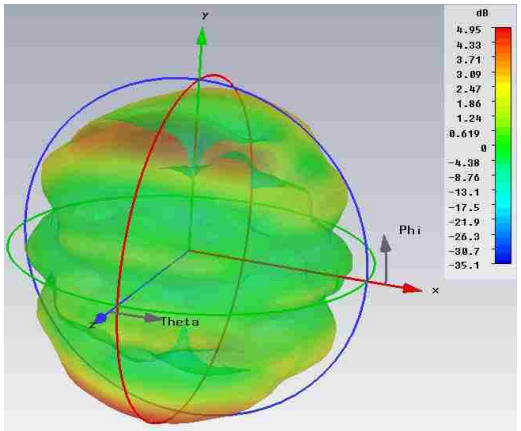

t = 0.3mm

Figure 46: Effect of metal thickness on bow tie radiation patterns

The radiating elements must reside upon a substrate unless they are thick enough to support their own weight. A simulation study of the effect of substrate thickness was performed, using ε_r=3.5 as a commonly-available microwave substrate relative permittivity. The substrate thickness was swept from 0.127mm corresponding to a very thin substrate, to the commonly-available 1.651mm thick substrate which corresponds to 0.065" thickness. The magnitude of input impedance to the bow tie was plotted against frequency in Figure 47where it can be seen that thicker substrates load the bow tie and tend to damp the impedance variations.

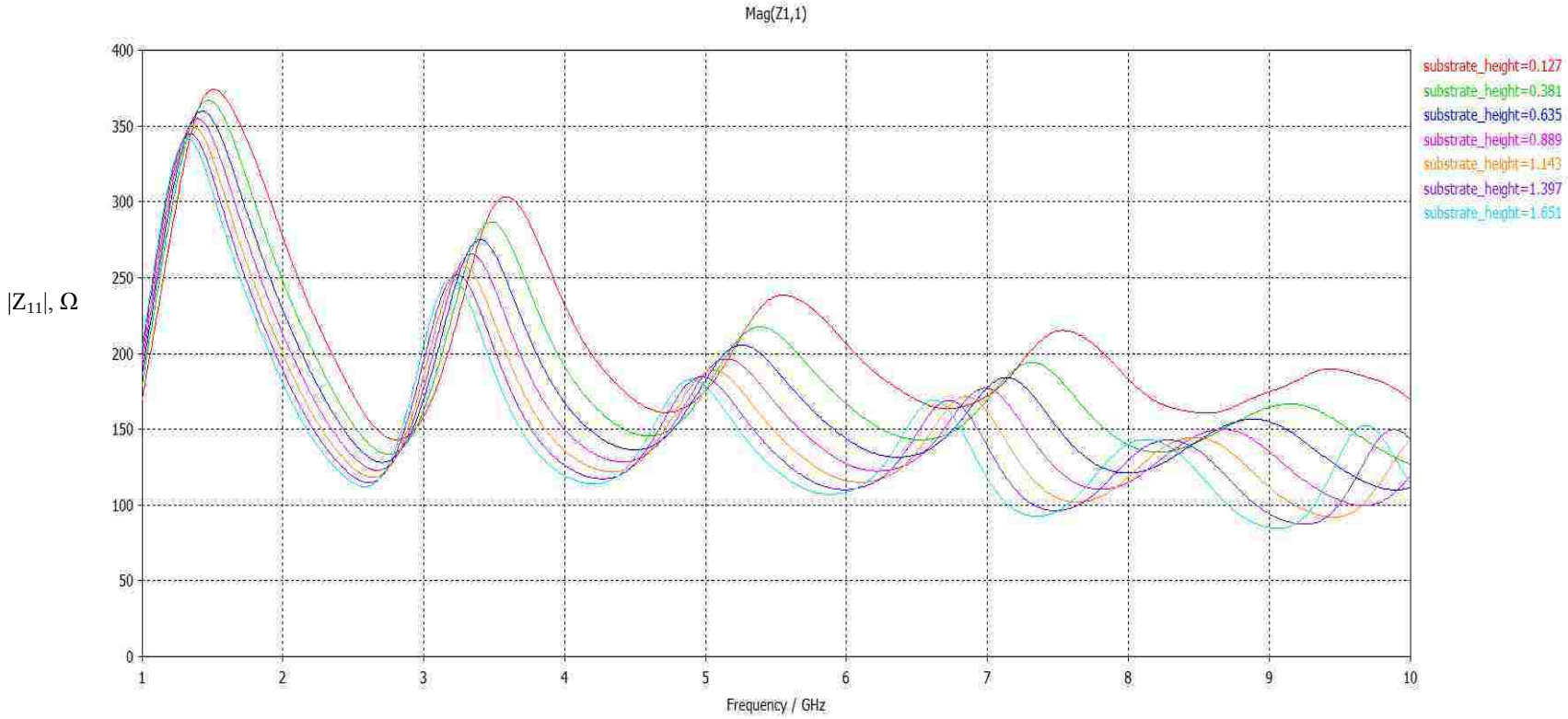

Figure 47: Magnitude of input impedance vs. substrate thickness.

Effect of Bow Tie Flare Angle

Simulations were performed to sweep the bow tie flare angle from 25° to 85°, and the magnitude of input impedance is shown in Figure 48. For these simulations a 0.762mm thick (0.030") Arlon AD320 substrate with ε_r=3.2 was used as this was an available substrate. As expected, the input impedance decreased with increasing flare angle. Wider flare angles also produced smaller variations in impedance at higher frequencies and thus are considered to be more broadband than a bow tie with a smaller flare angle.

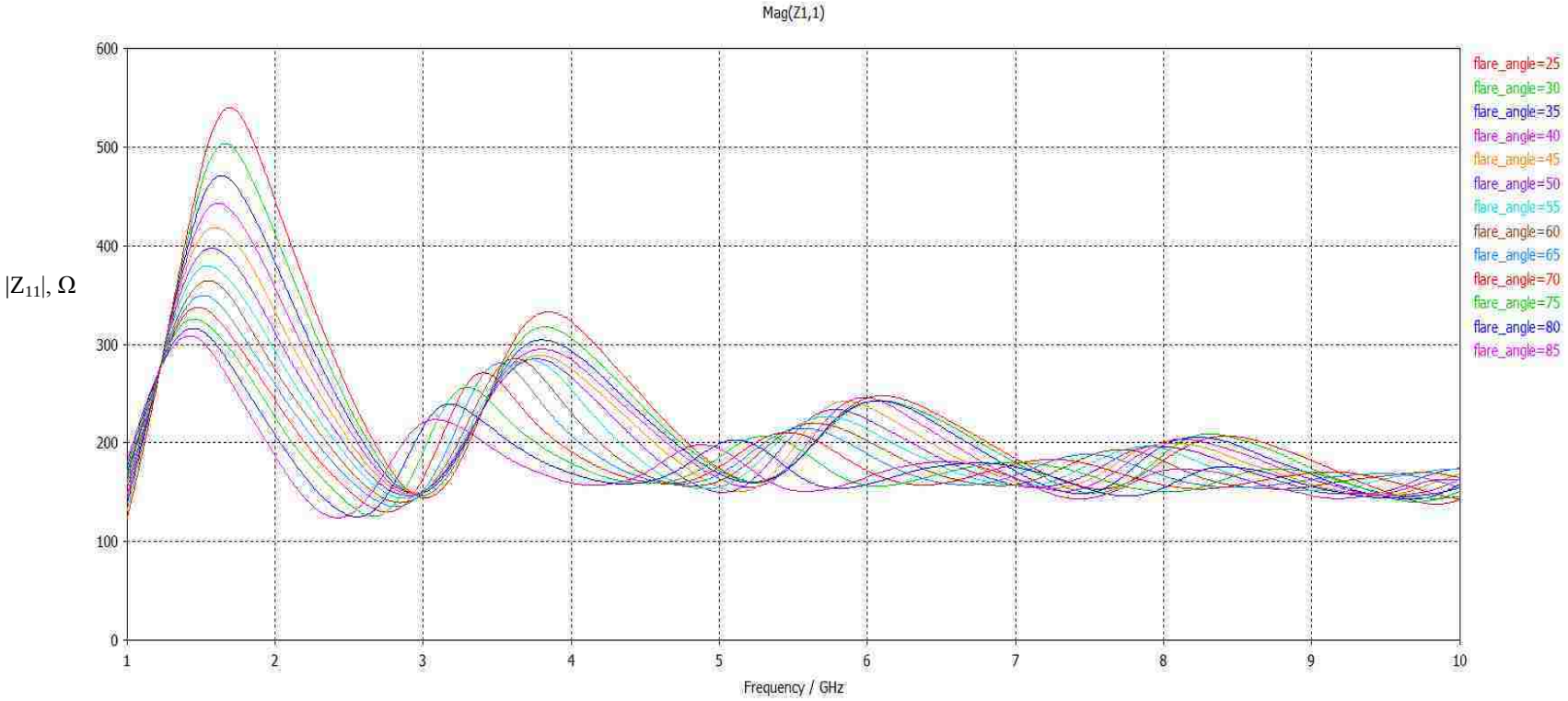

Figure 48: Effect of bow tie flare angle on magnitude of input impedance.

Far field radiation patterns for flare angles of 30, 40, 50, 60, 70 and 80° were simulated and are shown in the following Figure 49 through Figure 51. No large variation in the 3D patterns are observed due to varying flare angle in this range.

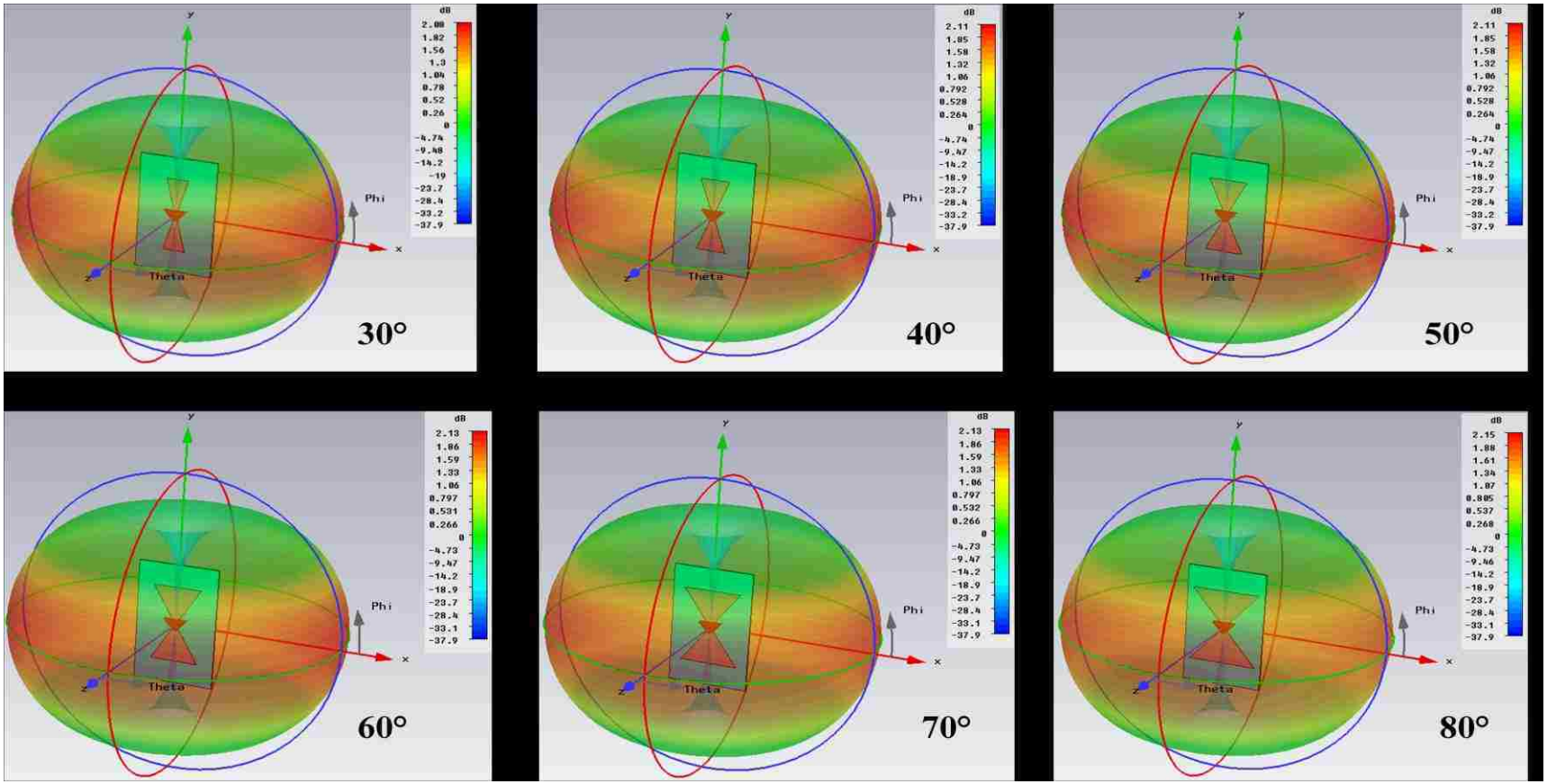

Figure 49: Effect of bow tie flare angle on radiation pattern at 1GHz.

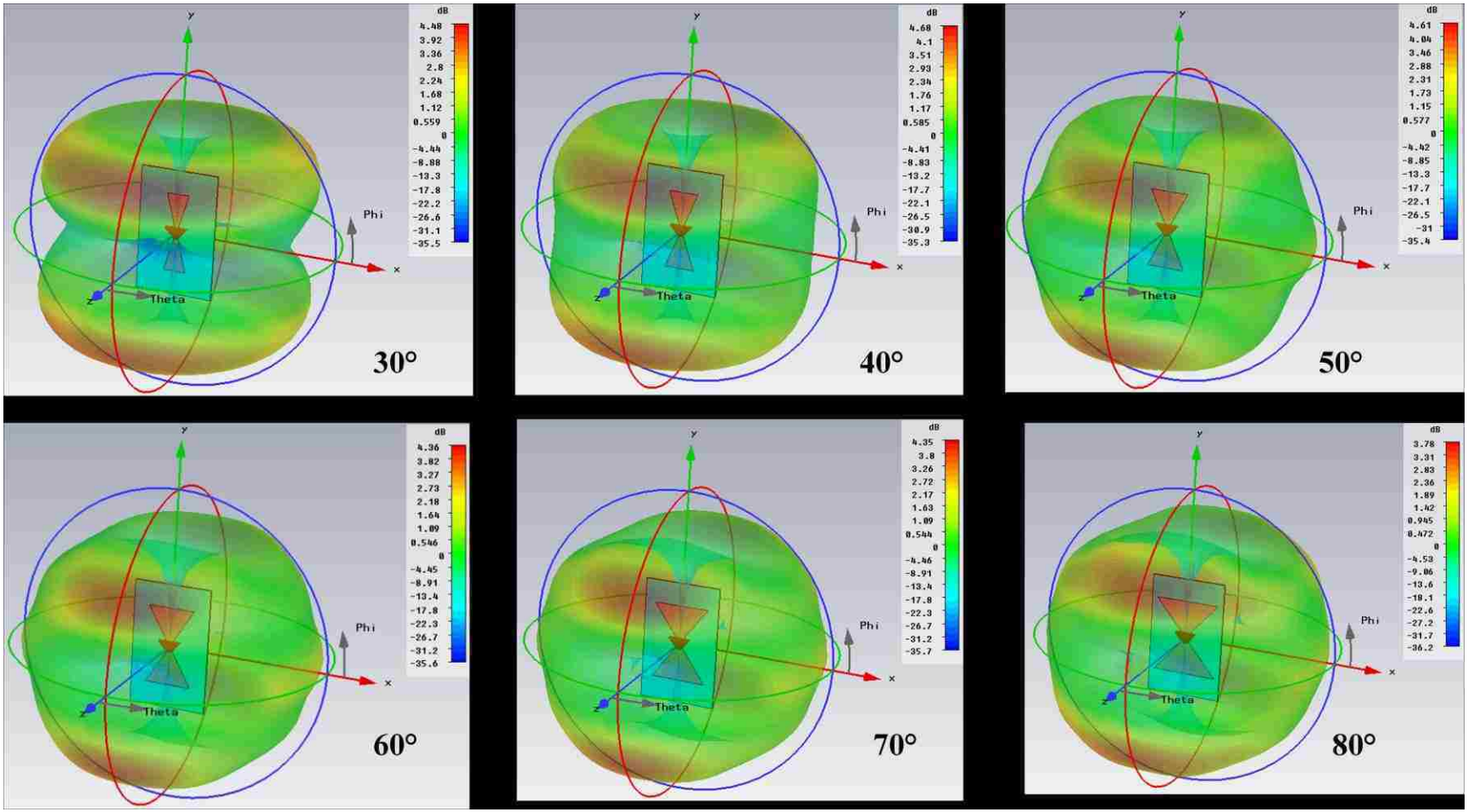

Figure 50: Effect of bow tie flare angle on radiation pattern at 5GHz.

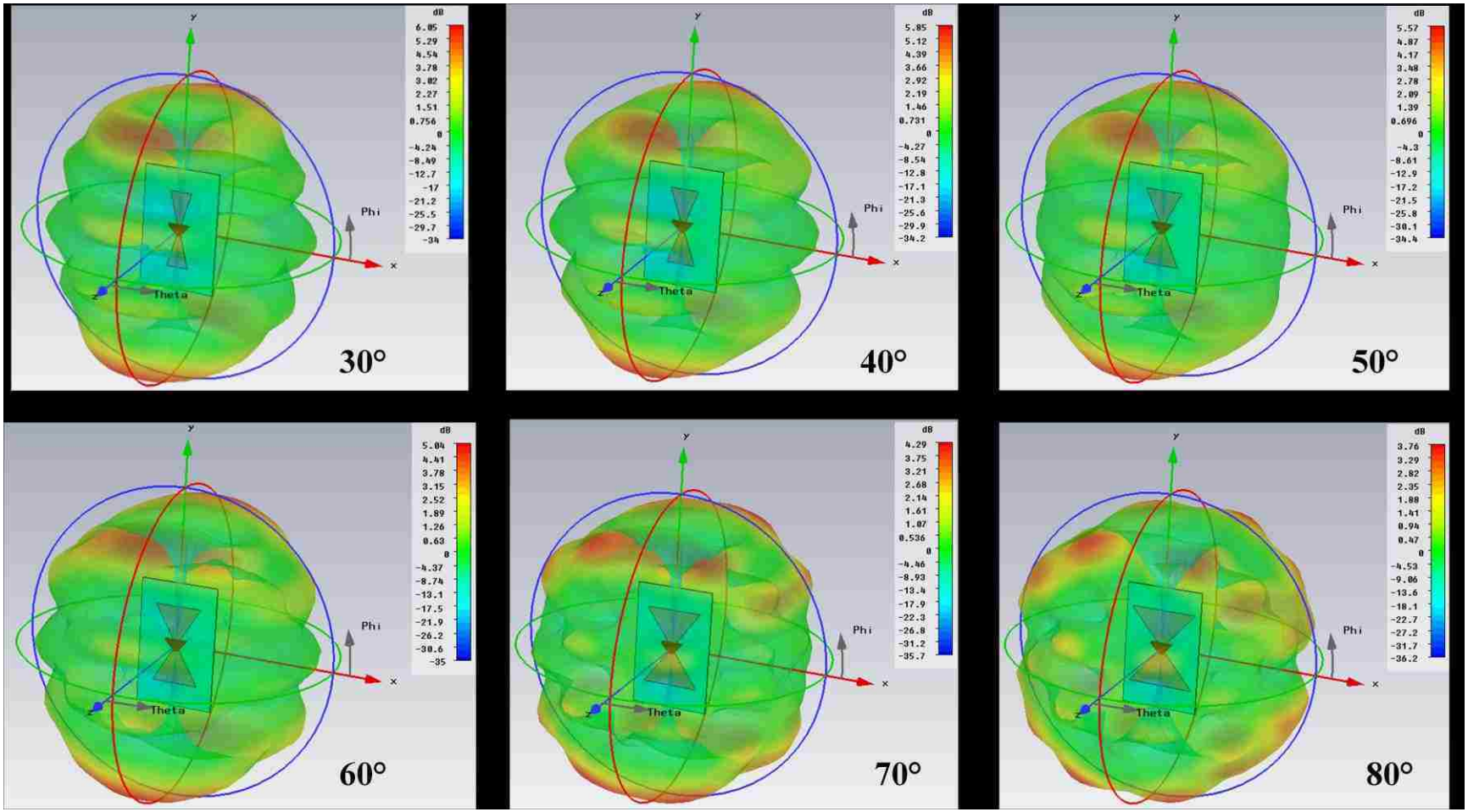

Figure 51: Effect of bow tie flare angle on radiation pattern at 10GHz.

Effect of Feed Gap Size

The bow tie must be truncated at the feed point and this is referred to as the feed gap. It was defined to be square such that the spacing between bow tie dipole elements was equal to the width at the truncation point. The feed gap is shown in Figure 52. The red triangle is a discrete port used for excitation, yellow is copper, and brown is substrate. The red line depicts the point of converge if the triangular shaped bow tie elements were not truncated at the feed point.

Magnitude of input impedance is shown for two different feed gaps, 1mm and 6mm. Larger gaps lowered overall input impedance and also reduced impedance variation with frequency, as shown in Figure 53. Feed gap size had little effect on 3D radiation patterns, as shown in Figure 54.

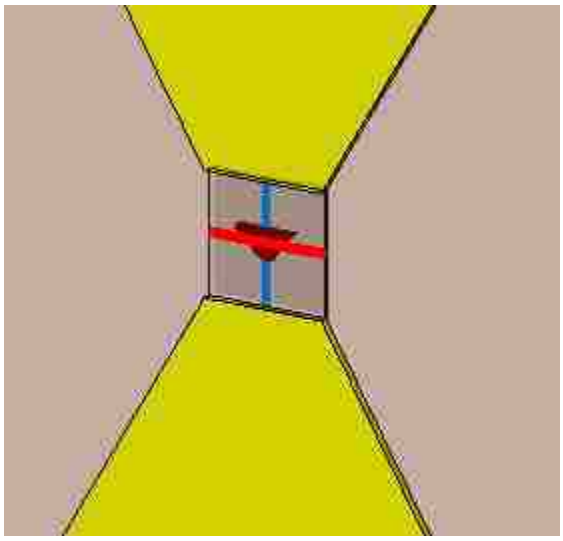

Figure 52: Bow tie feed gap.

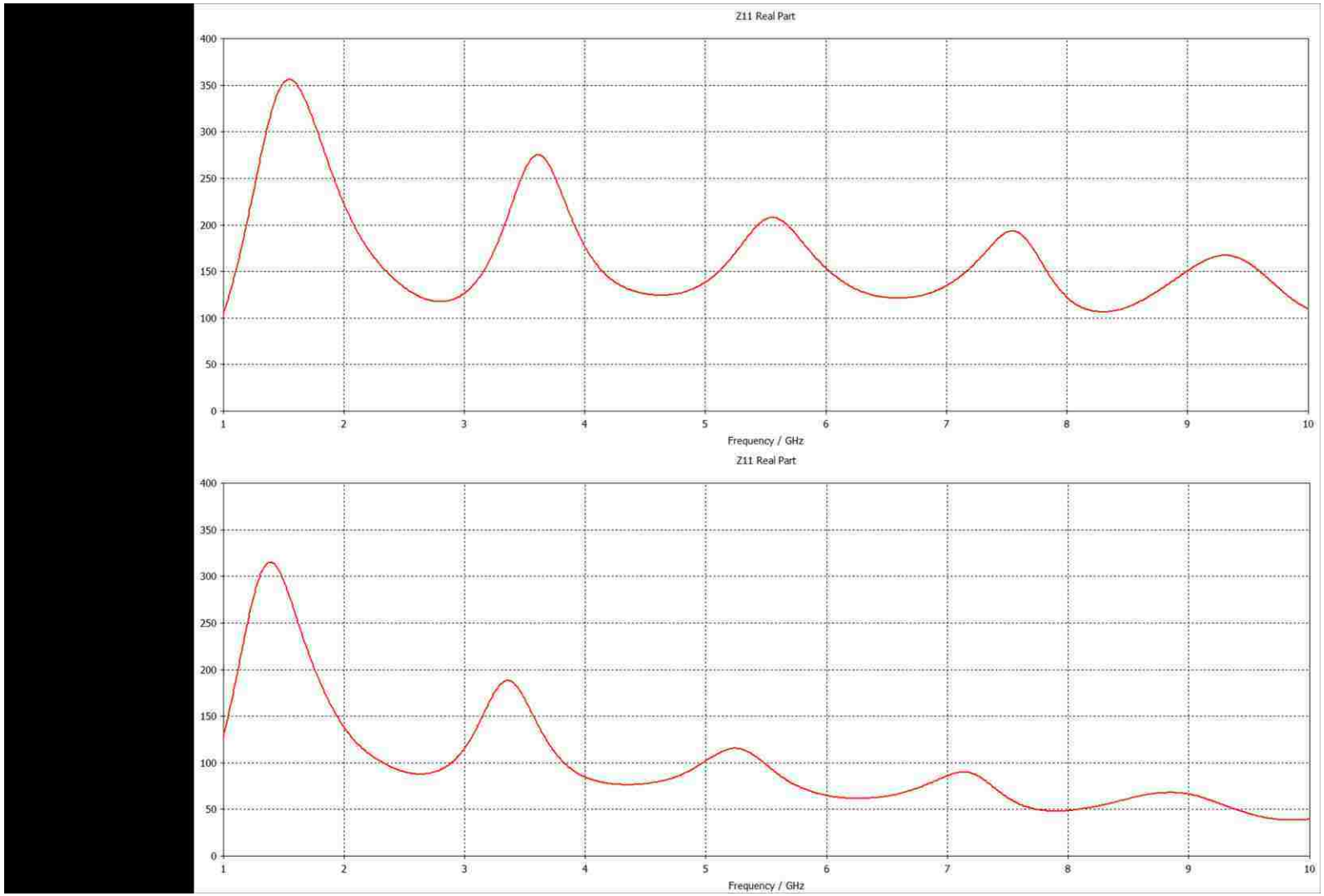

Figure 53: Effect of feed gap size on magnitude of input impedance.

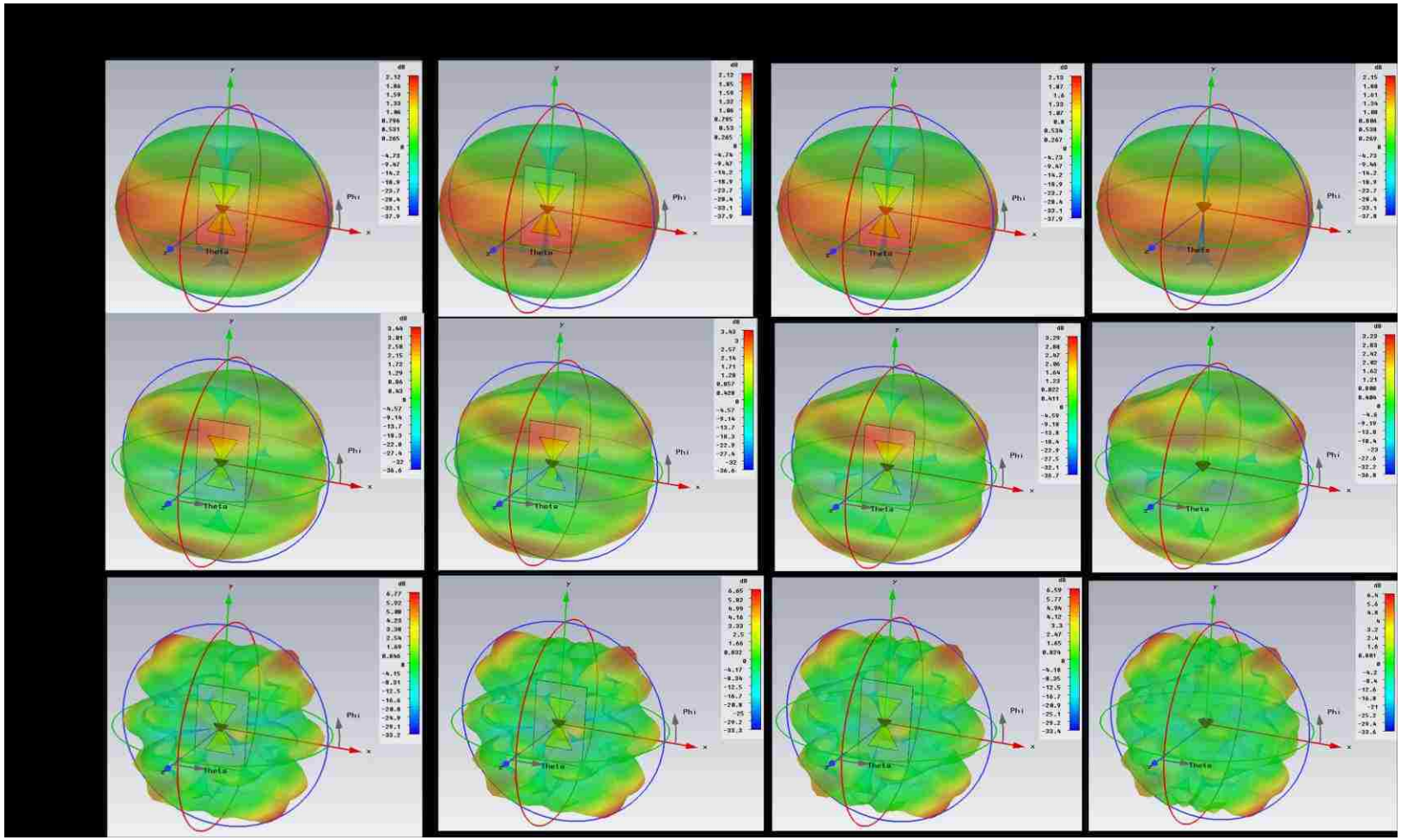

Figure 54: Effect of feed gap size on radiation pattern.

Figure 55 depicts a simulation of the radiation pattern of a bow tie antenna on substrate whose half-wave resonant frequency is 1GHz with 50° flare angle at 10GHz. The Z-axis points towards dish center. As the bow tie bandwidth is usable over a 2:1 or perhaps 3:1 range it was expected there would be issues at higher frequencies. The simulation shows there are two nulls directed at the dish while the main lobes are directed away from the dish. Such a structure as modeled cannot be used for the desired bandwidth of 6:1 (or greater) without modification.

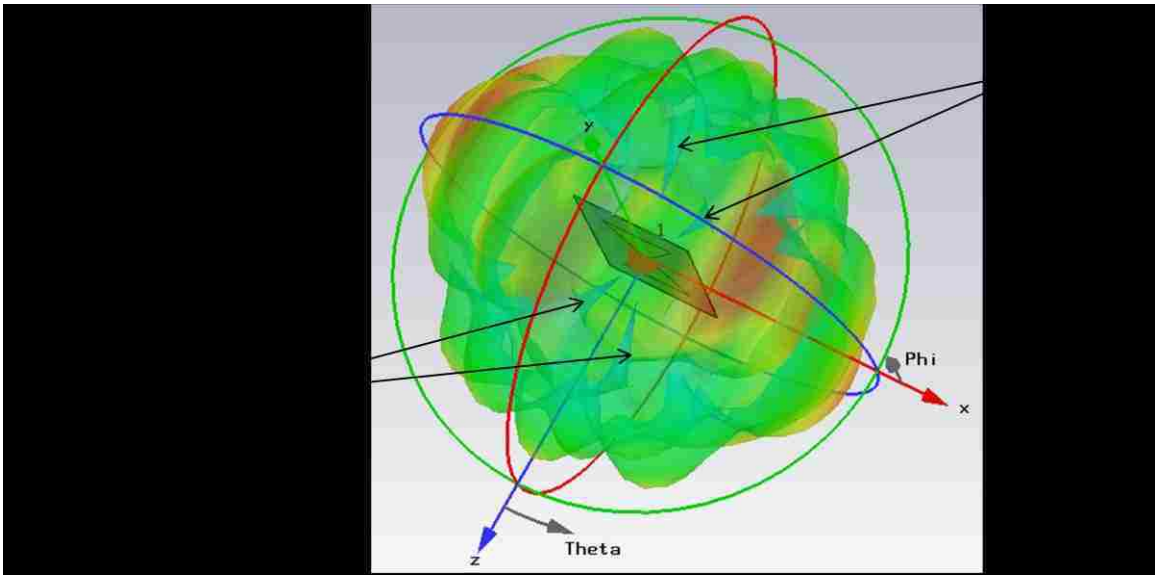

Figure 55: Undesirable nulls and lobes at high frequency.

Effect of Serrations

In an effort to lower the bow tie's impedance the effect of cutting serrations into the outer edge of the bow tie was examined. The number of serrations was varied from six down to one as shown in Figure 56 in bow ties with 30° flare angles. The depth of the serration was then parametrically stepped for each configuration and the resulting magnitude of input impedance was plotted against frequency. These plots are shown in Figure 57 through Figure 63. The parameter *cone_length* denotes the cut depth in mm.

These simulation results show that the addition of serrations does not lower the impedance of the first peak and only shows a small lowering of impedance above 4GHz. For this reason serrated elements were not further pursued.

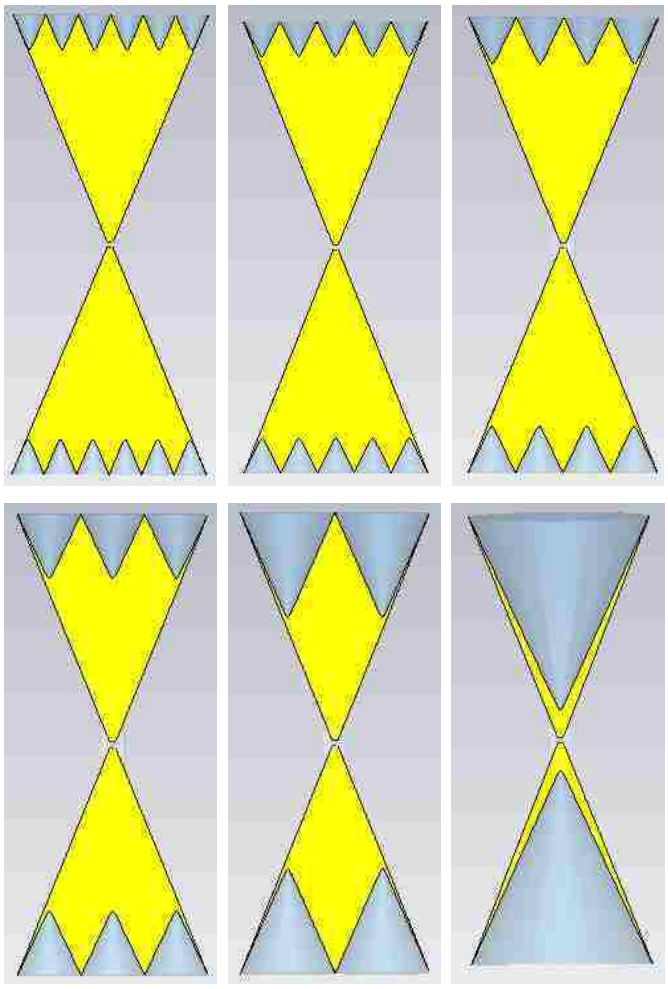

Figure 56: Serrations cut into bow-tie elements.

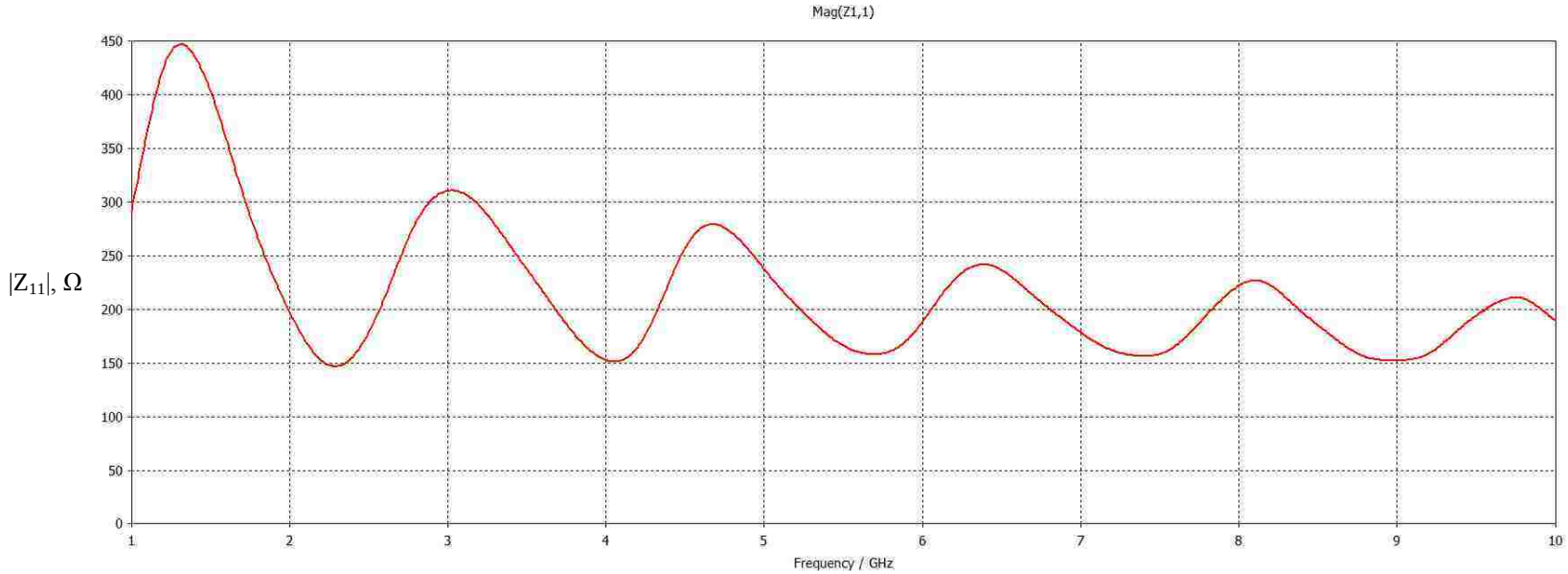

Figure 57: Impedance vs. frequency for bow-tie with no serrations.

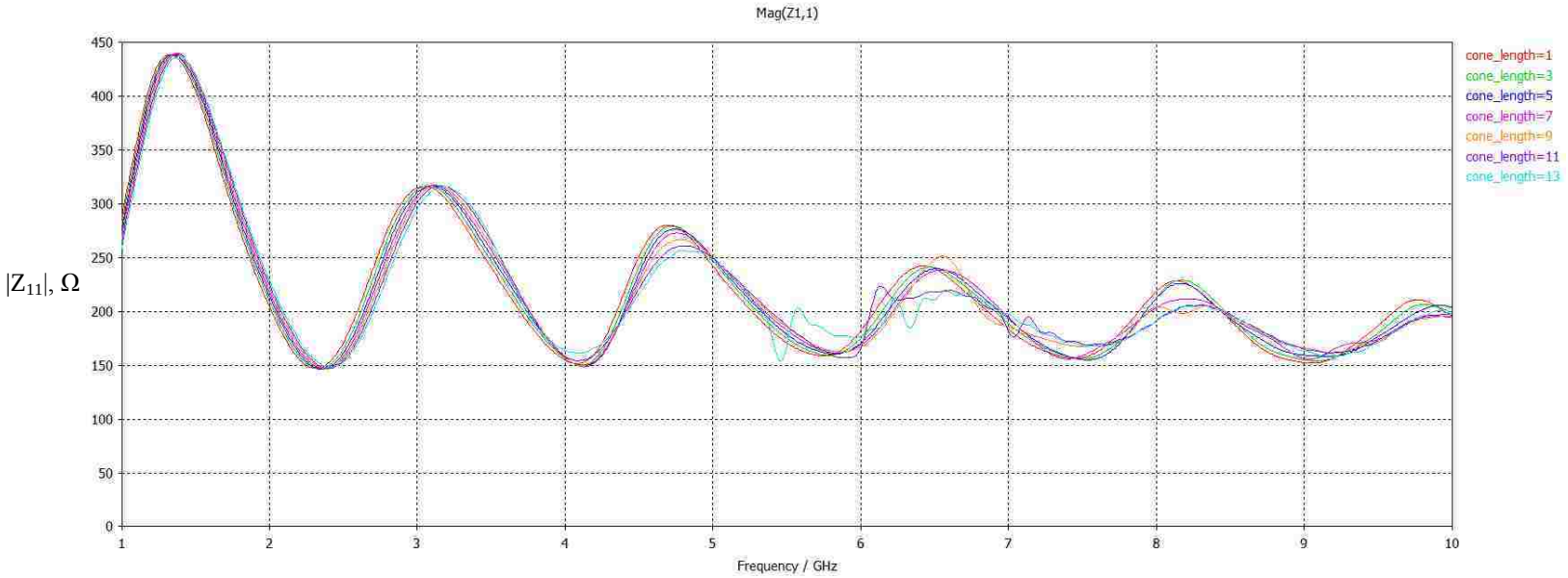

Figure 58: Impedance vs. frequency for bowtie with six serrations.

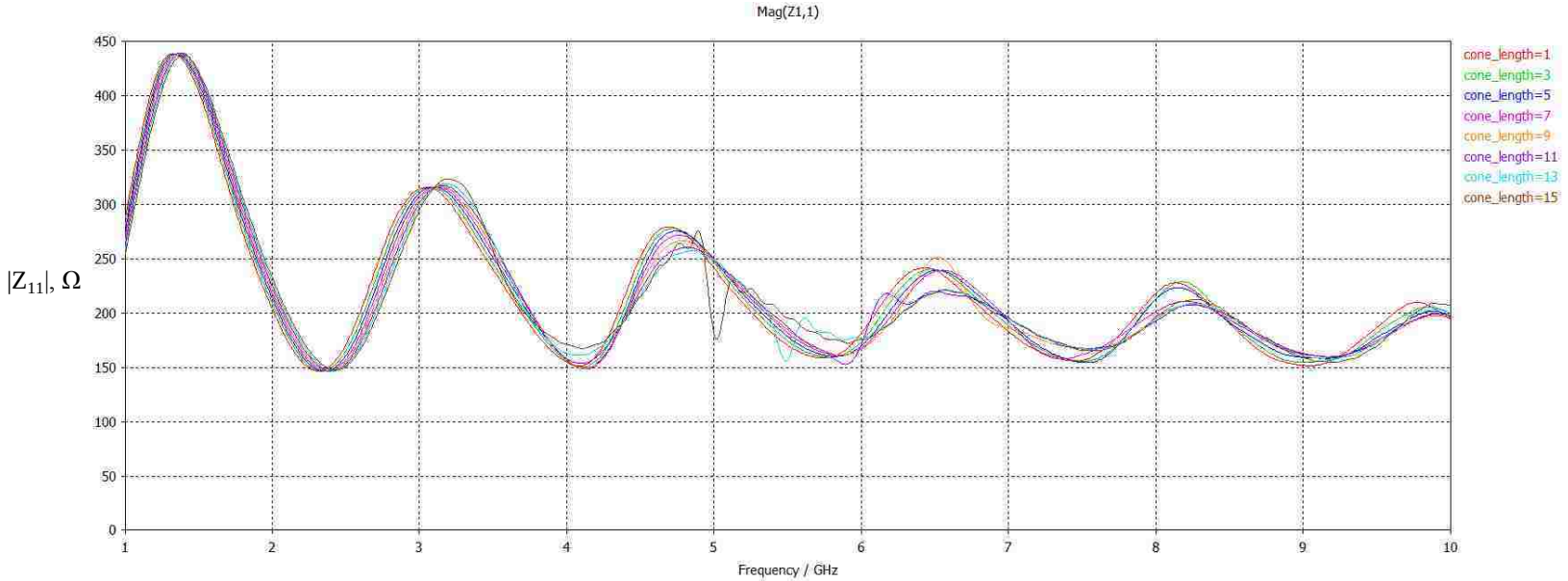

Figure 59: Impedance vs. frequency for bowtie with five serrations.

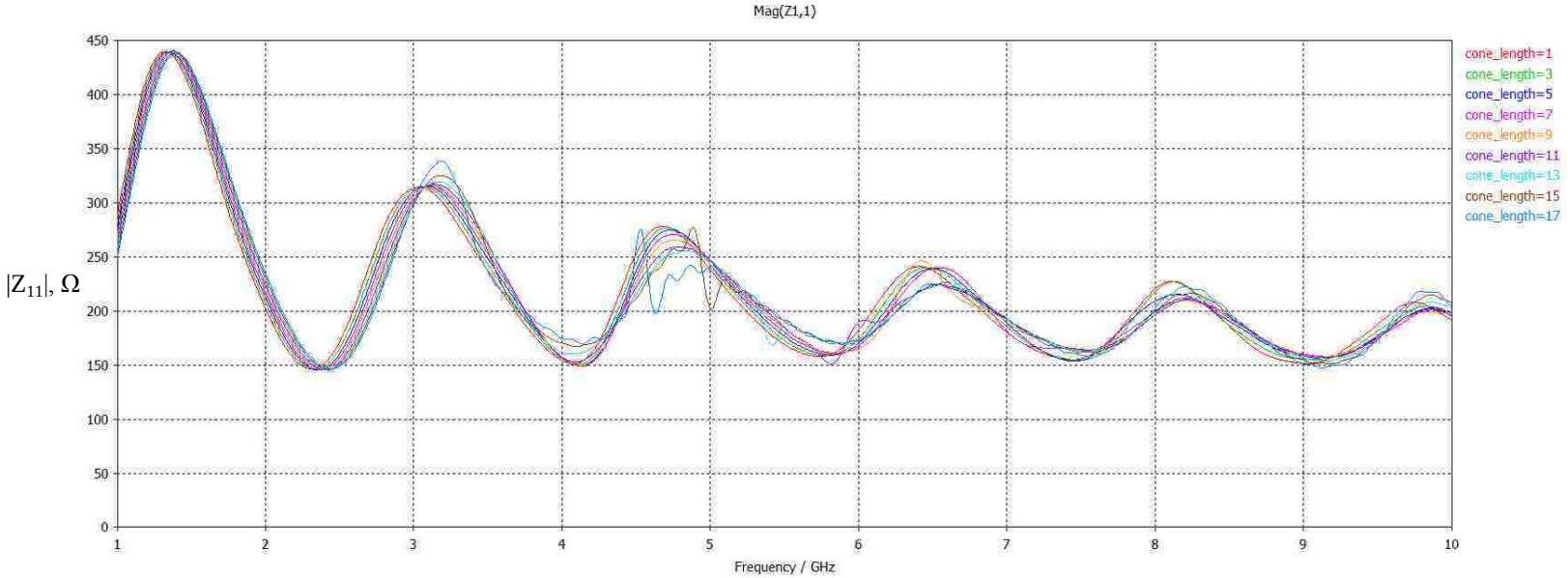

Figure 60: Impedance vs. frequency for bowtie with four serrations.

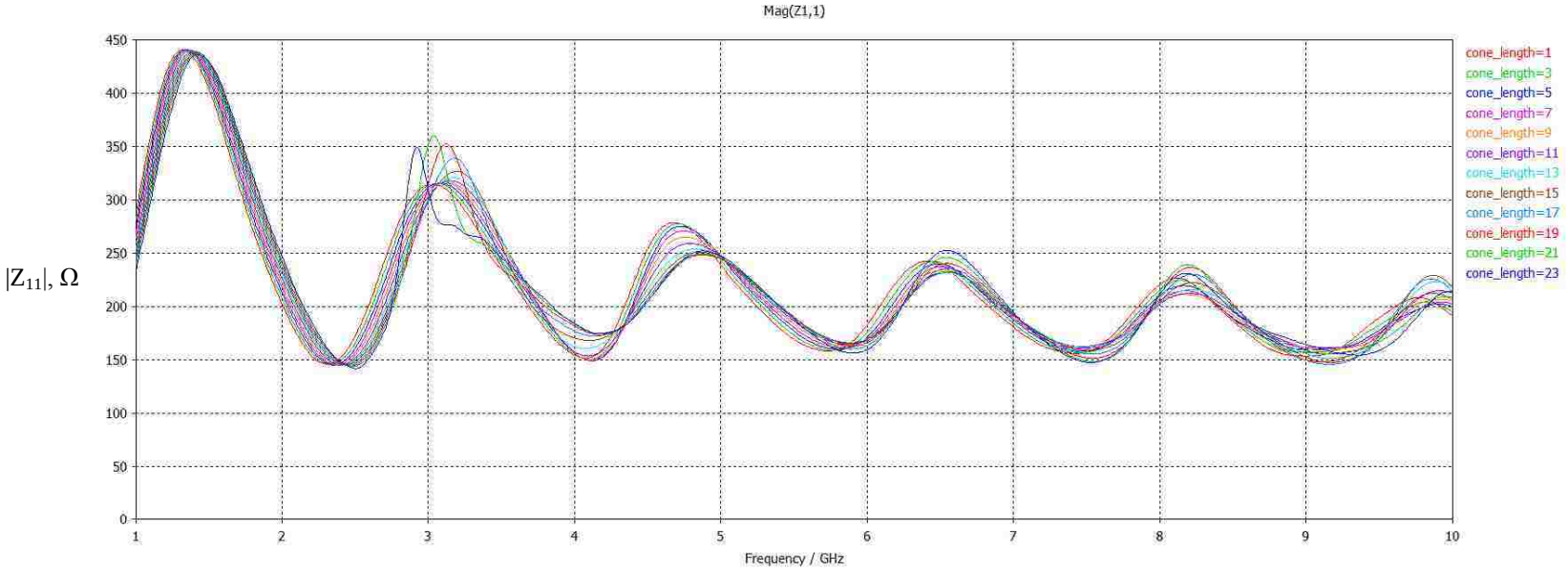

Figure 61: Impedance vs. frequency for bowtie with three serrations.

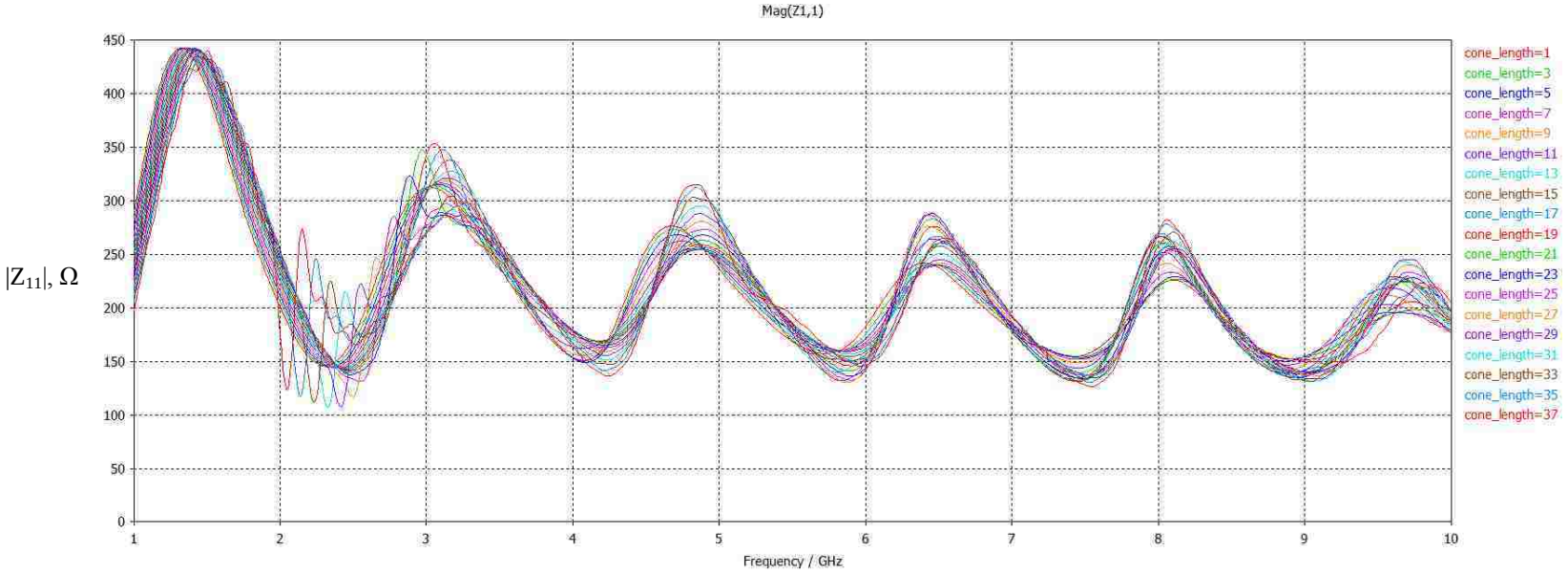

Figure 62: Impedance vs. frequency for bowtie with two serrations.

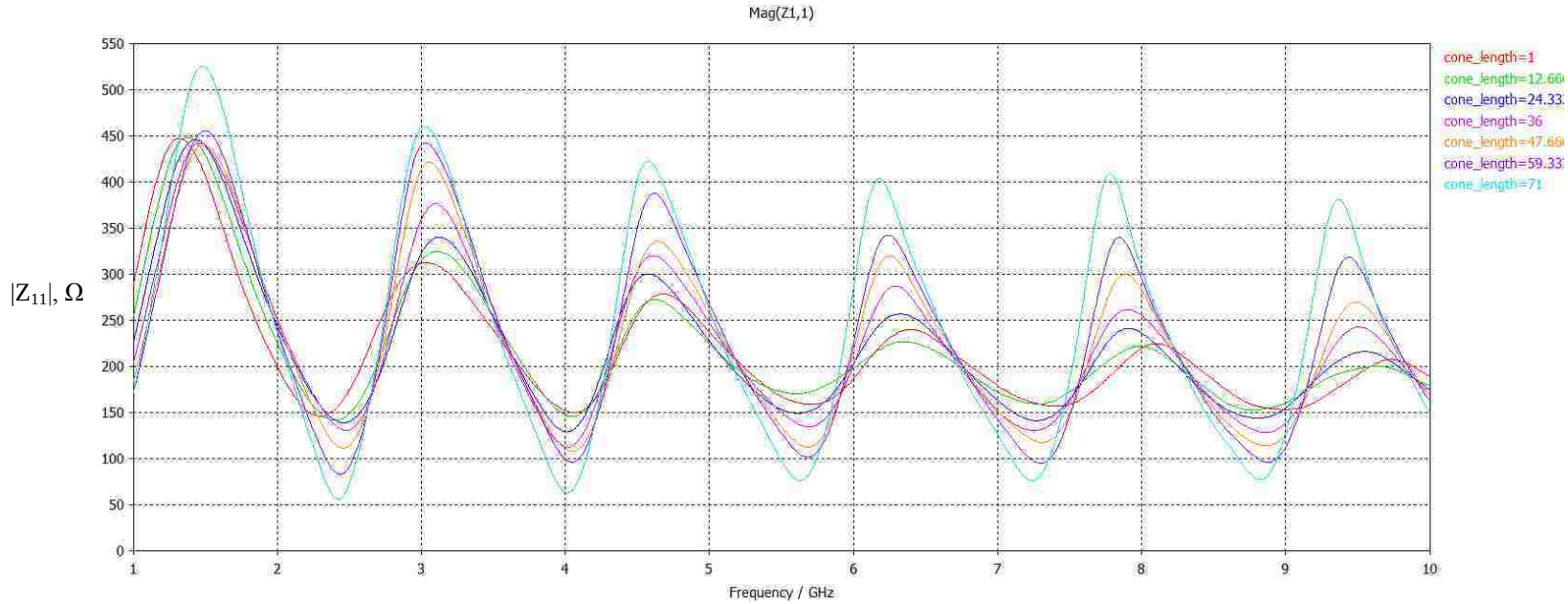

Figure 63: Impedance vs. frequency for bowtie with one serration.

Effect of Folding a Bowtie

Given that the lobes move away from the Z-axis with increasing frequency it seemed reasonable to introduce a fold angle to the bow tie structure as shown below in Figure 64. It could be expected that the radiation pattern might become more tightly constrained by such a structure.

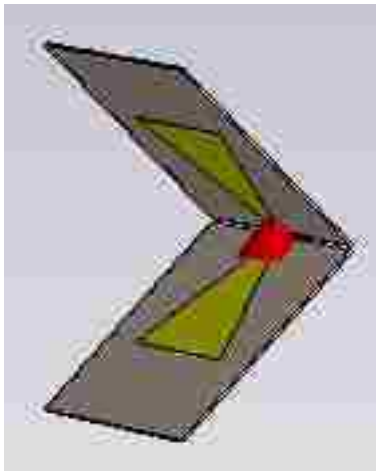

Figure 64: Folded bow tie on substrate.

The magnitude of input impedance versus frequency was simulated for four fold angles, 15°, 30°, 45° and 60°. It should be noted that a fold angle of 0° corresponds to the planar bow tie structure discussed in the previous section.

Radiation patterns were also simulated for fold angles of 0°, 20°, 40° and 60° and the results are presented in Figure 66, Figure 67 and Figure 68. As expected the main lobe moves in the direction of the fold. Whereas lobes pointed away from dish center with a planar bowtie structure, folding the bowtie has the effect of 'concentrating' the pattern.

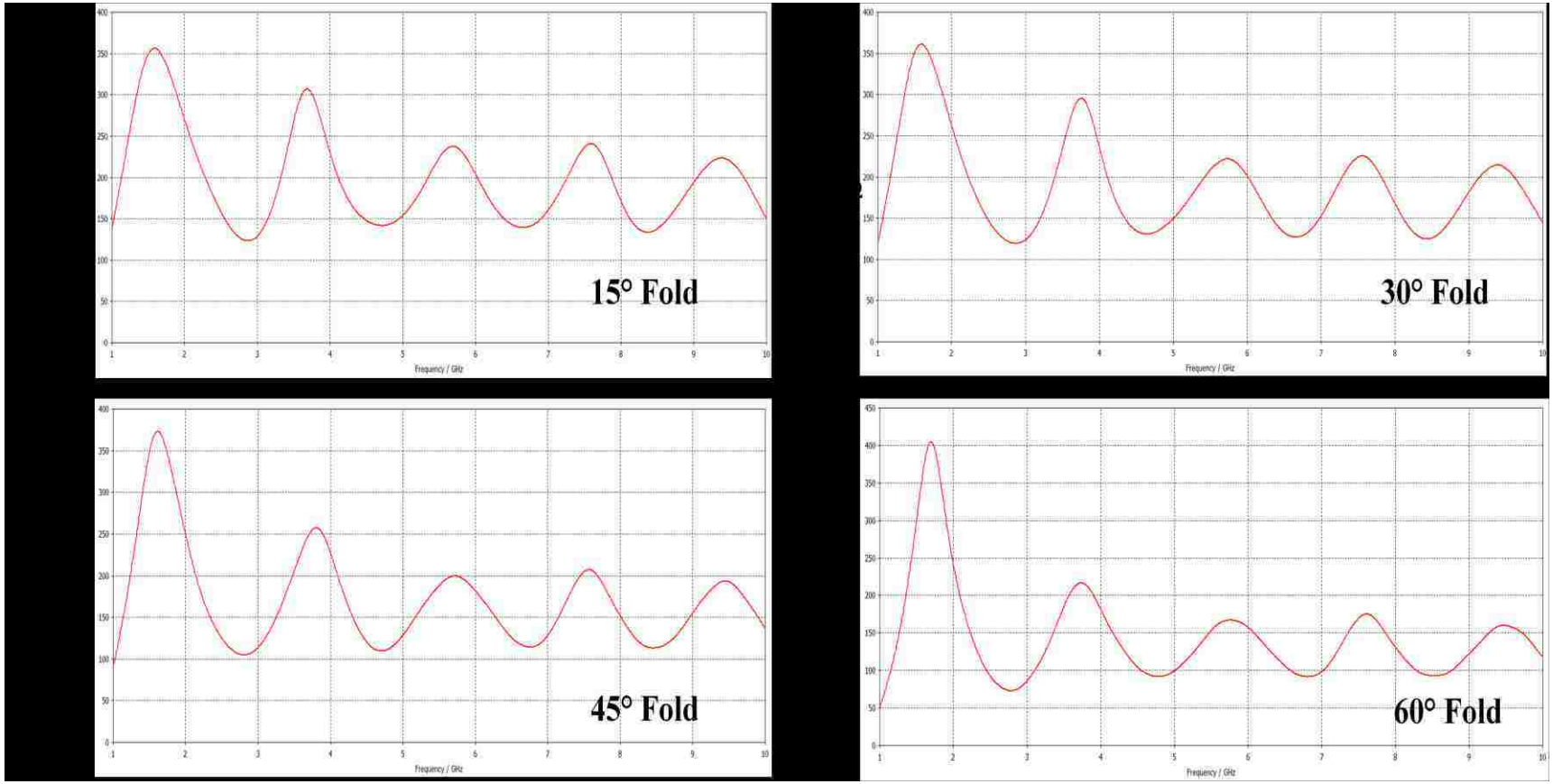

Figure 65: Magnitude of input impedance as function of fold angle.

1GHz

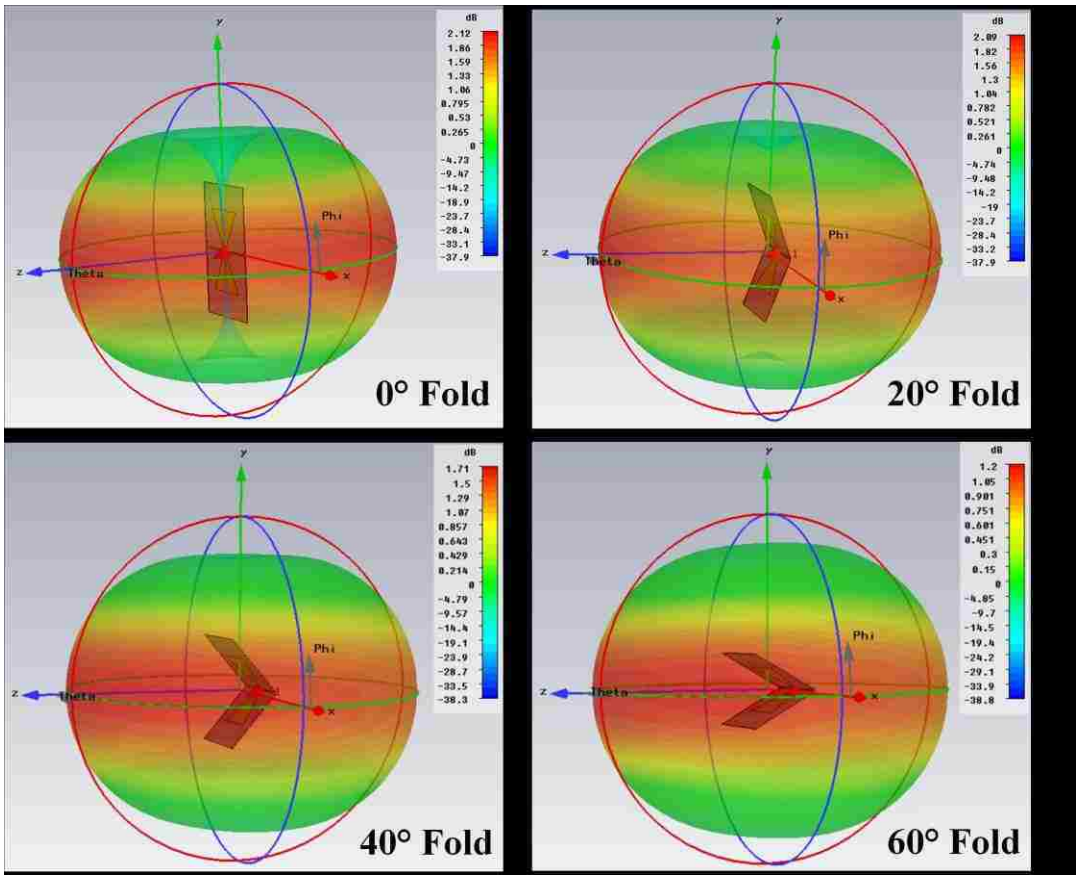

Figure 66: Effect of fold angle on radiation pattern at 1GHz.

5GHz

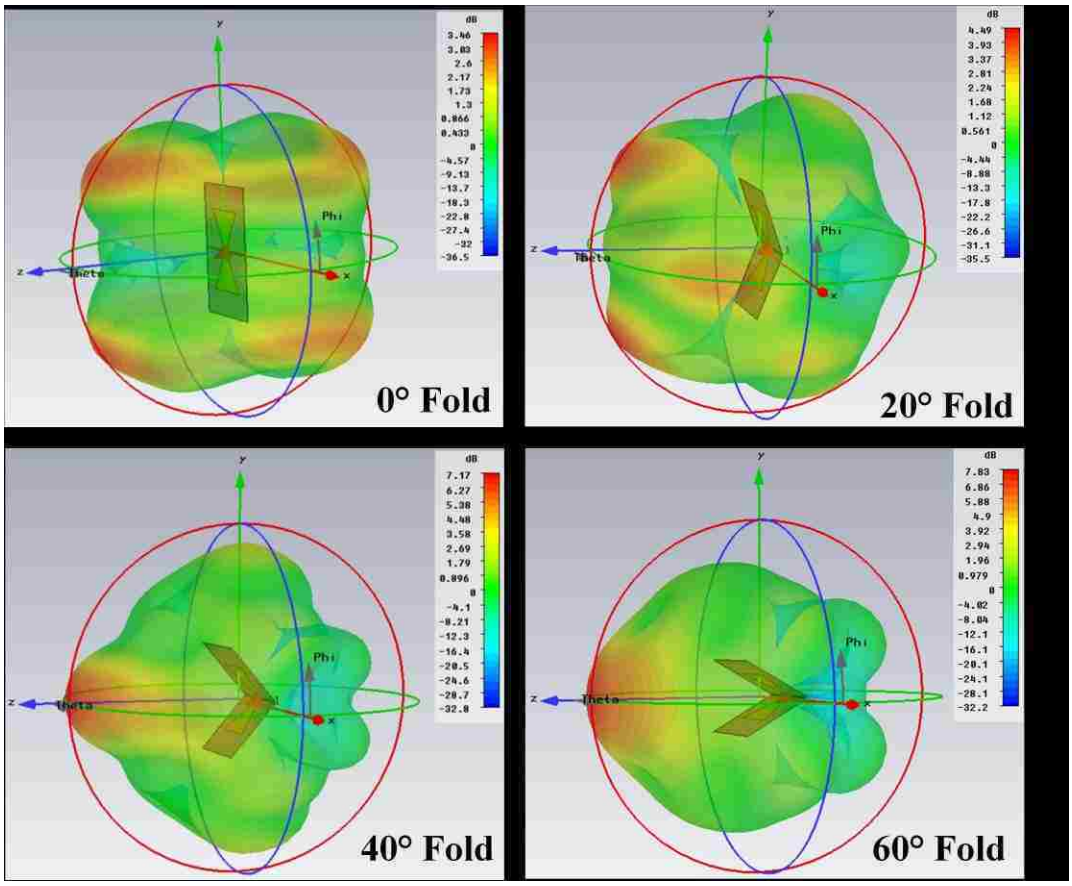

Figure 67: Effect of fold angle on radiation pattern at 5GHz.

10GHz

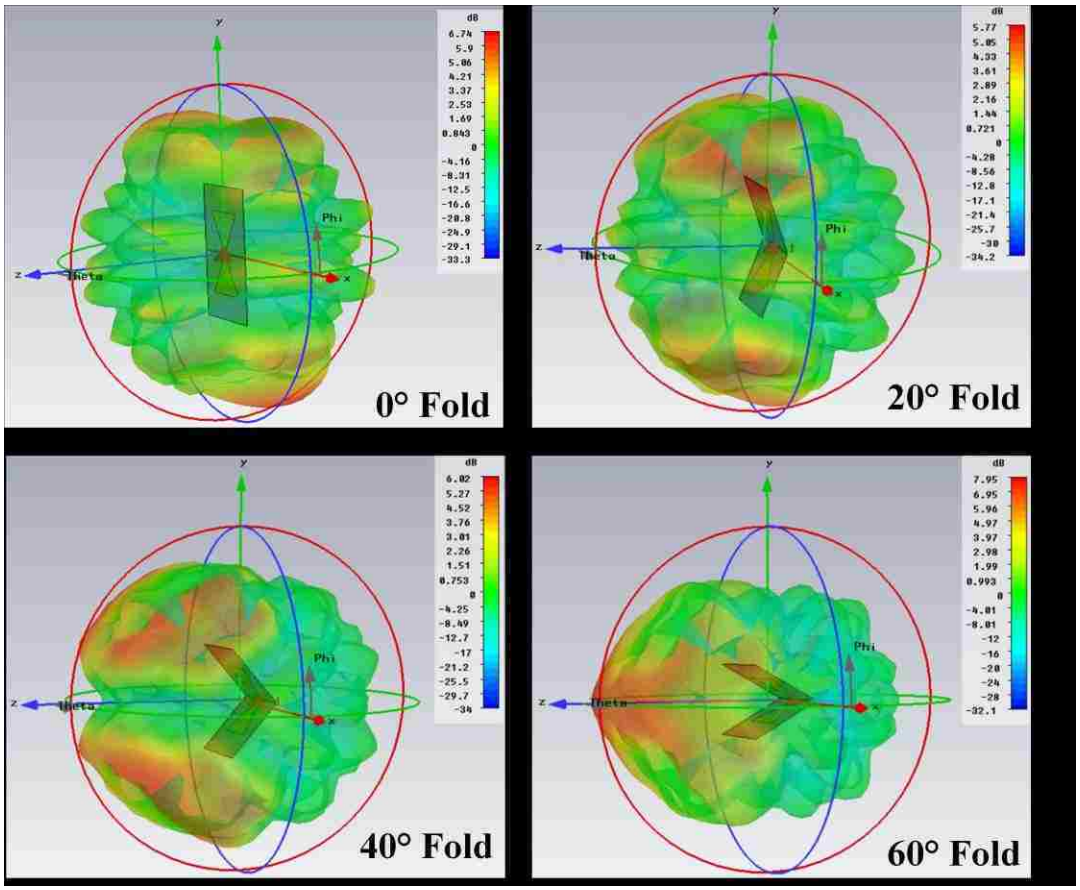

Figure 68: Effect of fold angle on radiation pattern at 10GHz.

Up to this point the bow tie structure has been on a substrate larger than the metal. The substrate was then sized to be the same as the metallization as shown in Figure 69 below. In the figure both bow tie metal regions are the same size, with 60° flare angle and 60° fold angle, 1oz copper on 0.030" Arlon 320 substrate, and where the feed gap is a 2mm square.

The trimmed structure on the left is 990,000 mesh cells whereas the untrimmed structure on the right is 21.9 million mesh cells. Due to the difference in the number of mesh cells the trimmed structure simulates in much less time.

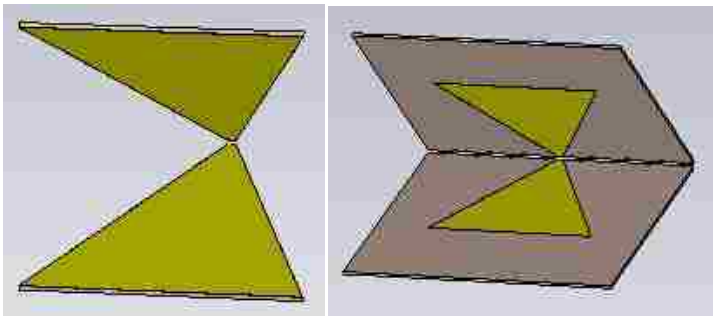

Figure 69: Trimmed bow tie on substrate.

A simulation comparison of the magnitude of input impedance was performed to compare the two structures and is shown in Figure 70, where it can be seen that the trimmed structure is higher in impedance. Radiation patterns were also simulated for the two structures and are depicted in Figure 71. The radiation patterns have fewer and less-pronounced lobes and nulls for the trimmed structure.

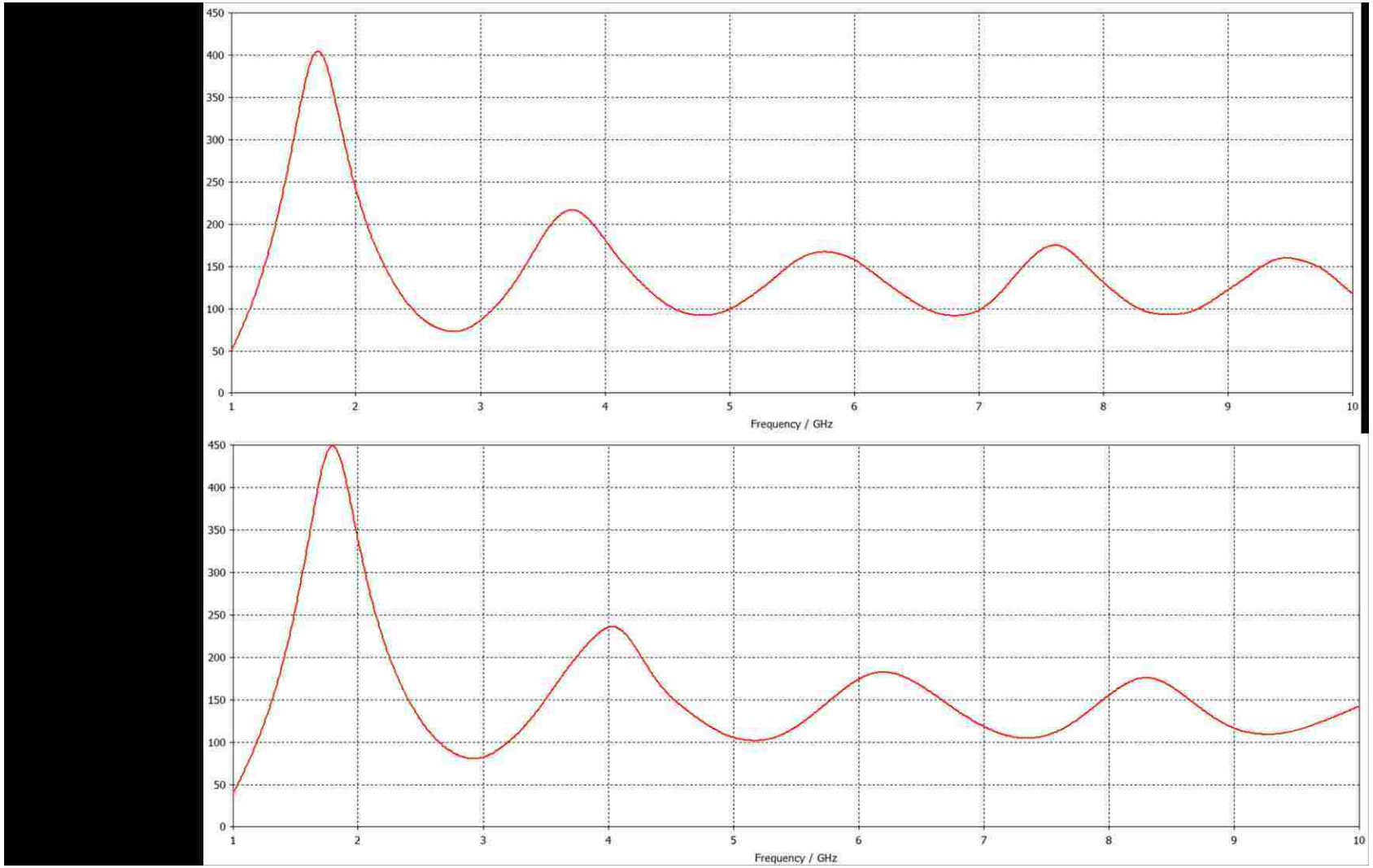

Figure 70: Effect of substrate trimming on magnitude of input impedance.

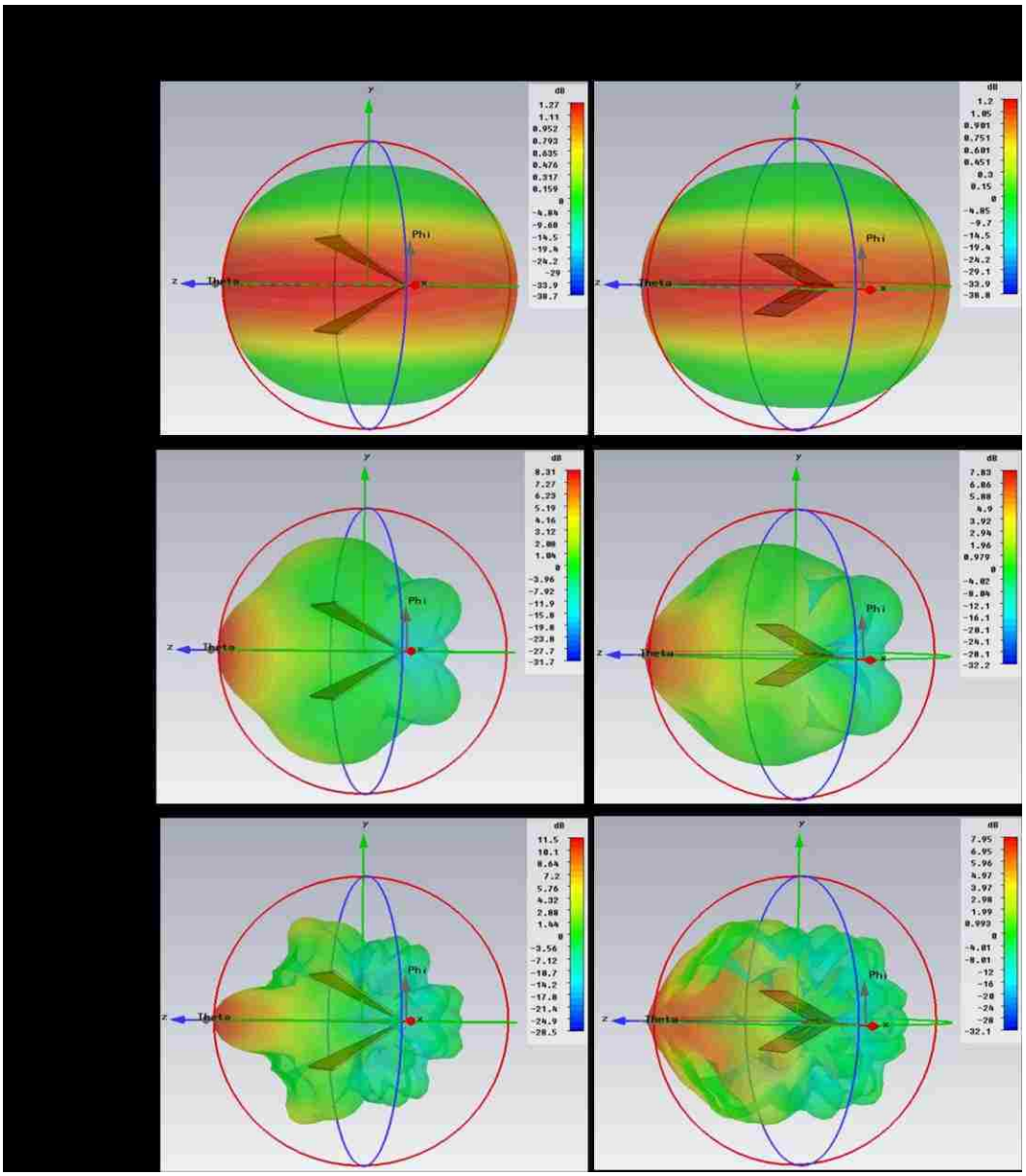

Figure 71: Effect of substrate trimming on radiation patterns.

It can be seen in Figure 71 that a folded bow tie has better radiation pattern behavior at high frequency than does a planar structure and is approaching a reasonable illumination for a RSTN dish. A folded structure will give rise to defocusing loss due to phase center displacement with frequency but will likely be less than a broadband LPDA which is a physically longer structure.

One possible method of improving impedance over frequency is by the application of a microwave-absorbent material. ECCOSORB MF-117 manufactured by Emerson & Cuming Microwave Products was selected because it is absorbent in the 1-18 GHz range, Microwave Studio had a model for the material, and it was readily available.

MF-117 is a magnetically loaded epoxide sheet material and it is described in Appendix C: ECCOSORB RF Absorbent Material.

A set of simulations were performed on a planar bow tie with a 30° flare angle to explore the effect of the MF-117. The first simulation applied a 0.040" layer of MF-117 and the results are depicted in Figure 72 where the MF-117 was shown to reduce the impedance variation above 2GHz.

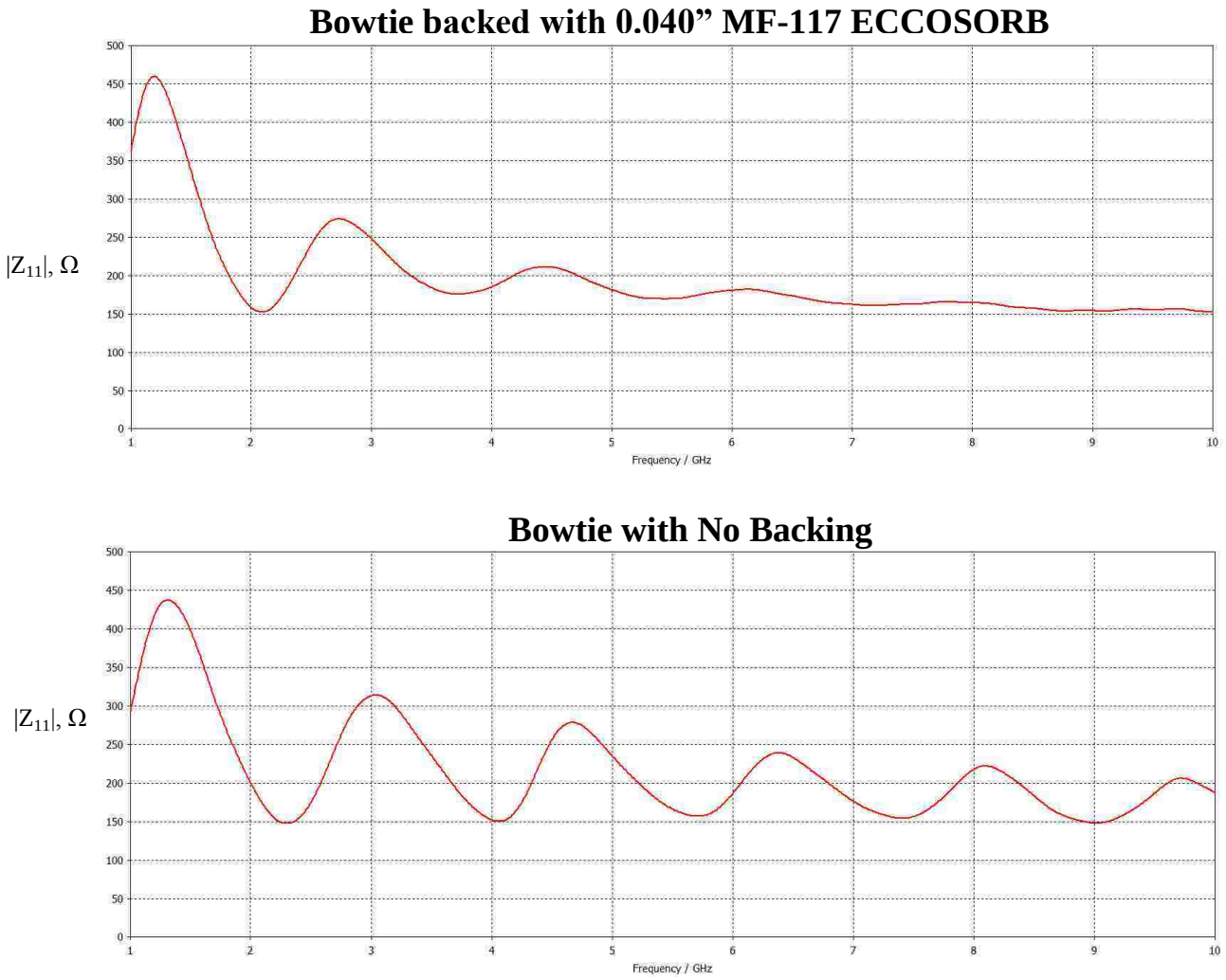

Figure 72: Effect of ECCOSORB MF-117 backing on bowtie.

ECCOSORB MF-117 is available in a variety of thicknesses from 0.125" (3.2mm) to 1.0" (25.4mm) in 0.125" (3.2mm) increments. The thickness was parametrically stepped in MWS and the magnitude of impedance was plotted against frequency for each thickness as shown in Figure 73.

As the thickness increased the variation of impedance over frequency decreased. In particular, when the thickness was 10.6mm or more the first impedance peak was reduced to less than 300Ω.

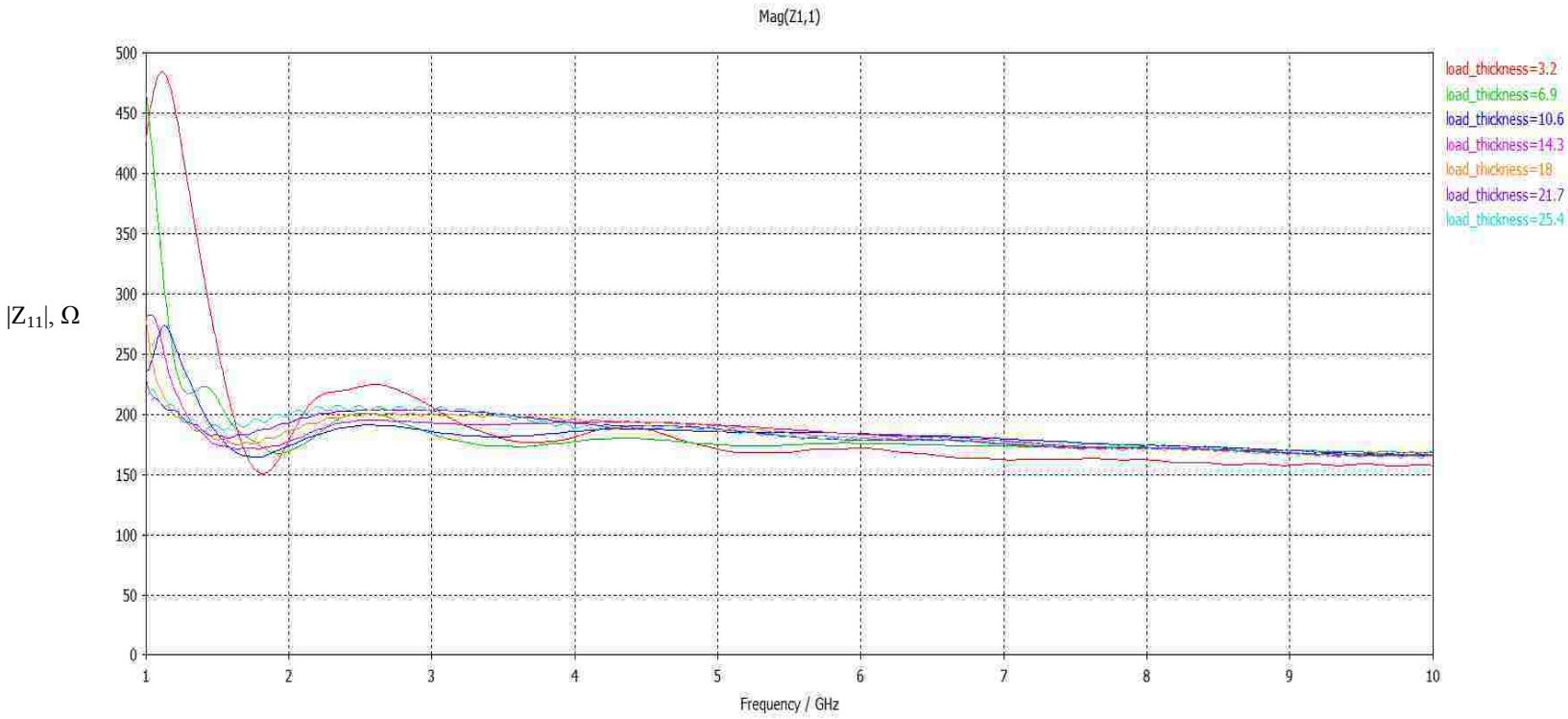

Figure 73: Effect of absorber thickness on magnitude of impedance.

Thick absorbent layers were shown in simulation to smooth out the impedance vs. frequency curve. A simulation was run using 18mm thick MF-117. The radiation pattern at 10 GHz is shown below in Figure 74. While the side lobes and nulls have been mostly eliminated, the overall gain is very low, about -0.6 dBi. This result indicates that using very thick absorbent layers will degrade the gain of the antenna.

The magnitude of impedance vs. frequency plot is shown in Figure 75 where the impedance is seen to be less than 280Ω at 1 GHz, and 200Ω or less above about 1.25 GHz. For this structure there appears to be a tradeoff between gain and impedance.

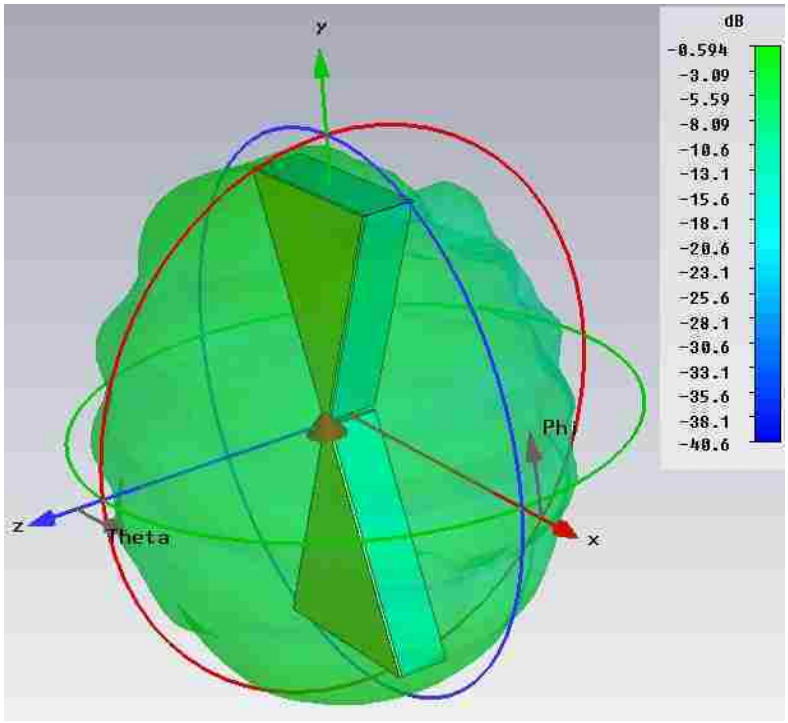

Figure 74: Radiation pattern for 18mm thick MF-117.

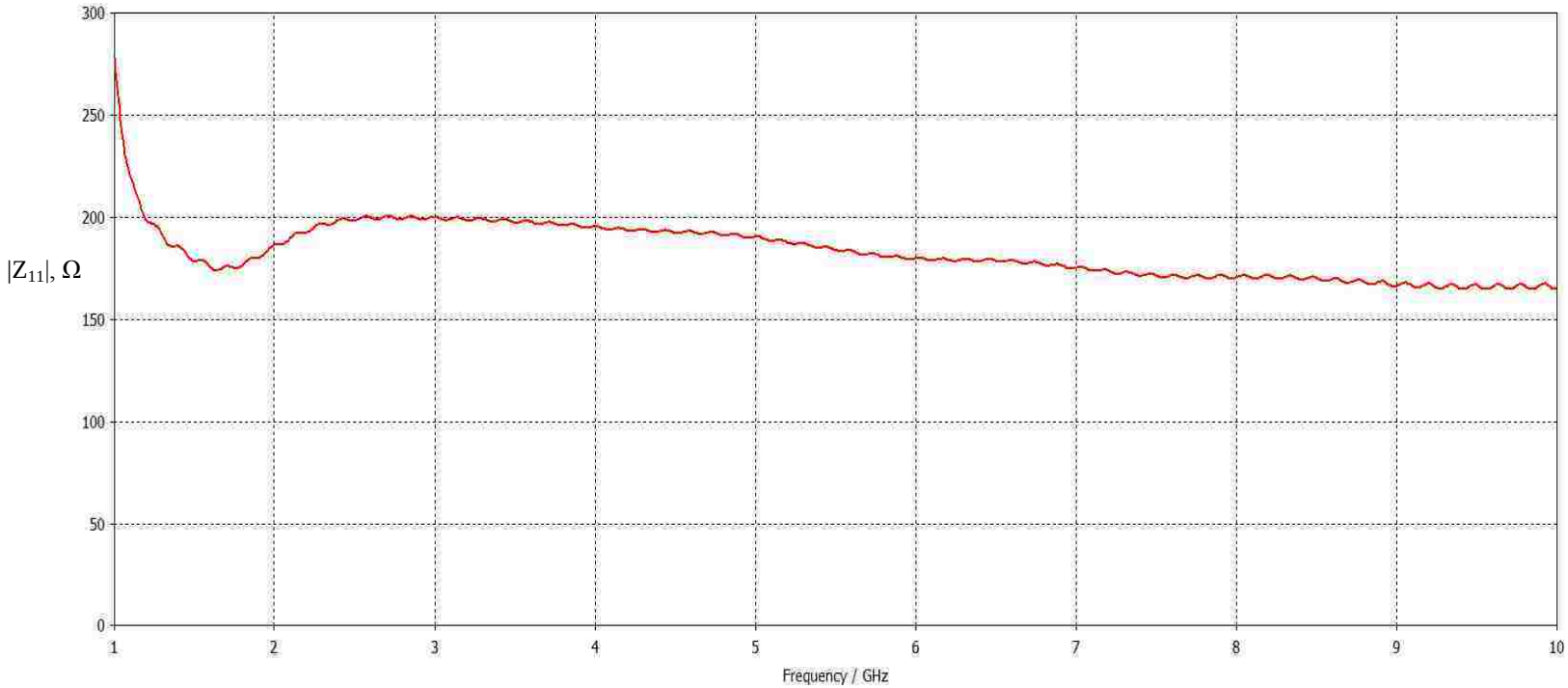

Figure 75: Magnitude of impedance plot for 18mm layer.

The flat outer edge of the bow tie may give rise to reflections producing standing waves and the formation of nulls and side lobes. This was examined in simulation by defining the width of the bow tie's tip as a variable and then parametrically stepping it through several values. This geometry is shown in Figure 76 for four tip widths. A width of zero yields a diamond-shaped radiator. Widths of 16 and 33mm define a wider tip while for this structure a tip width of 66mm was just the original bow tie structure.

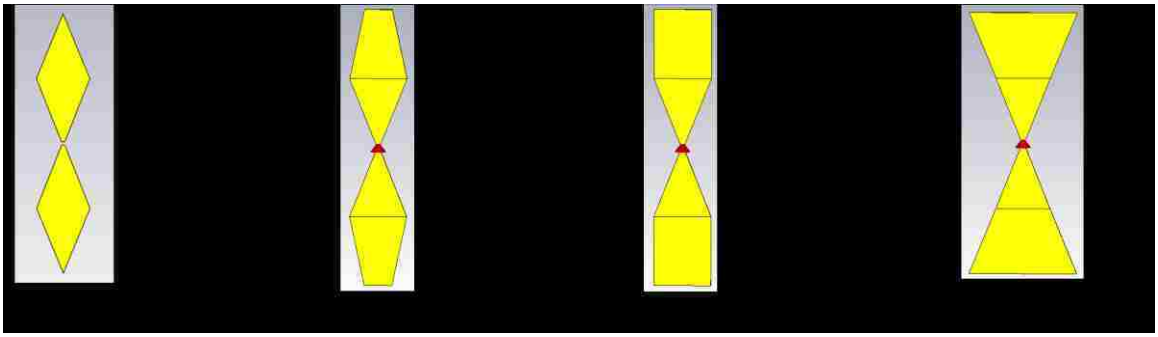

Figure 76: Bow tie tip geometry.

For simulation purposes a tip width of zero could not be defined so 100μm was used. The bow tie was held at a 30° flare angle as in previous simulations. The simulation results of magnitude of impedance vs. frequency are shown in Figure 77 where it can be seen that the 100μm wide tip has the lowest magnitude of impedance at low frequency. Compared to the bow tie this single modification reduced the magnitude of impedance of the first peak by nearly 100Ω. For this reason the diamond-shaped radiator was used for the development prototype.

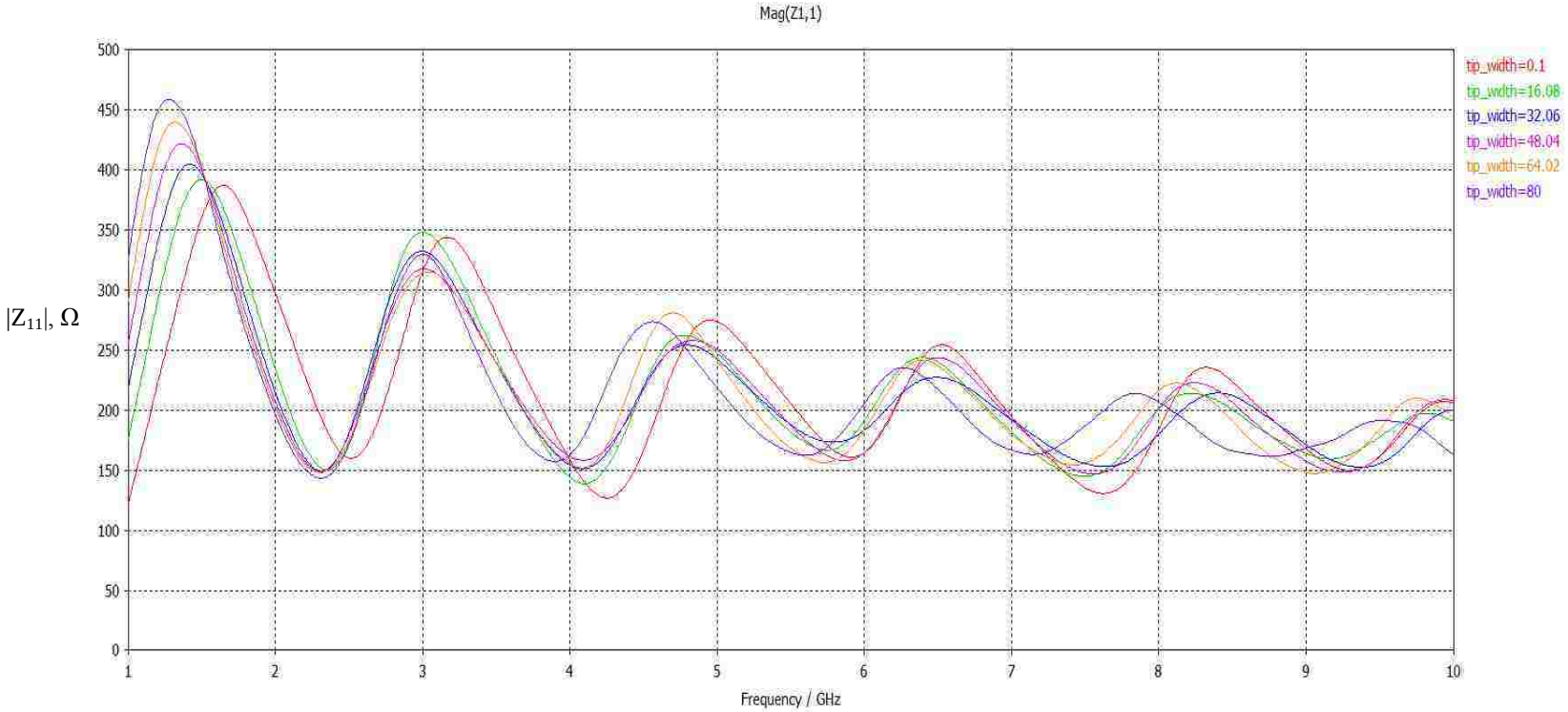

Figure 77: Magnitude of impedance for different tip geometries.

Effect of Cutouts

Having established that a diamond-shaped element had the lowest input impedance of the shapes studied in Figure 76, cutouts were simulated to determine if they would further improve input impedance. Two types of cutout were examined, cutouts in the center and cutouts on the edge, as shown in Figure 78.

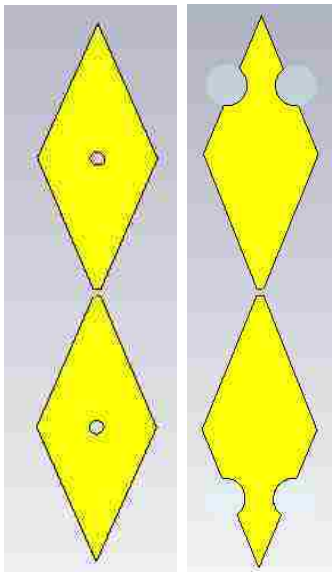

Figure 78: Cutouts in bowtie elements.

An exhaustive set of simulations was not performed as preliminary results were not encouraging. Impedance vs. frequency is plotted in Figure 79 through Figure 82.

In Figure 79, the effect of changing the size of a centered cutout on input impedance is explored. The parameter *circle_radius* denotes the radius of the cutout, and was parametrically stepped from approximately zero (0.01mm radius) to 15.0025mm radius. Of the four cutout radii simulated, none were shown to reduce the input impedance when the cutout was centered on the diamond-shaped structure.

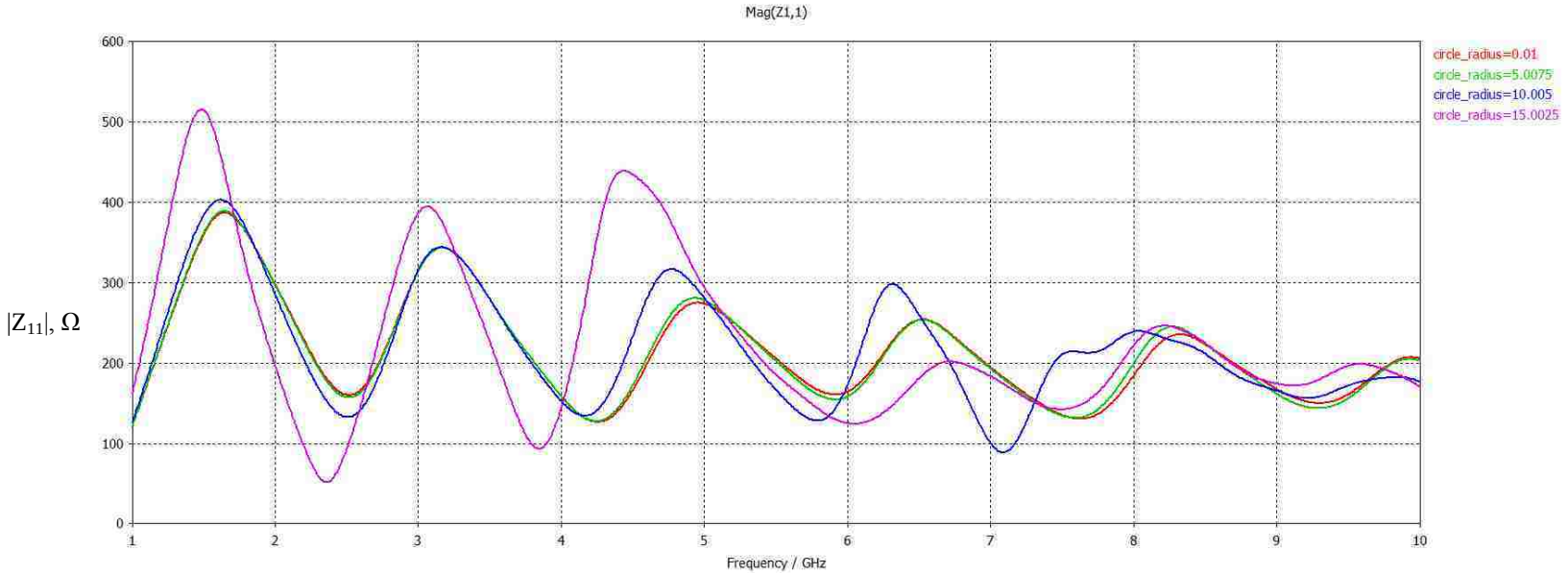

Figure 79: Impedance vs. frequency for cutouts in center.

In Figure 80, cutouts were placed 50mm away from the feed point at the center of the structure and then stepped through three sizes. As before, no cutout size greater than zero improved the input impedance.

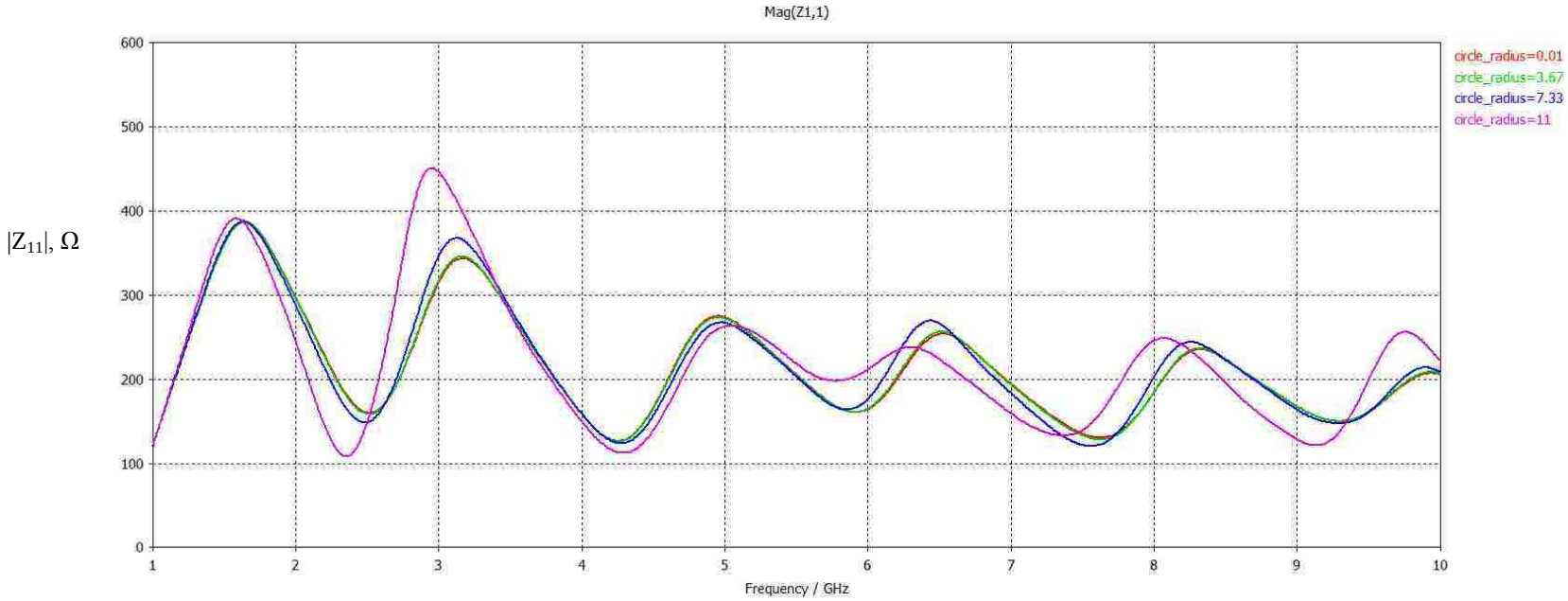

Figure 80: Impedance vs. frequency for cutouts 50mm from feed point.

In Figure 81, a cutout of constant 7mm radius was stepped through distances from the feed point ranging from 20 to 60mm, and the magnitude of input impedance was plotted. No location was found to be an improvement over the absence of a cutout.

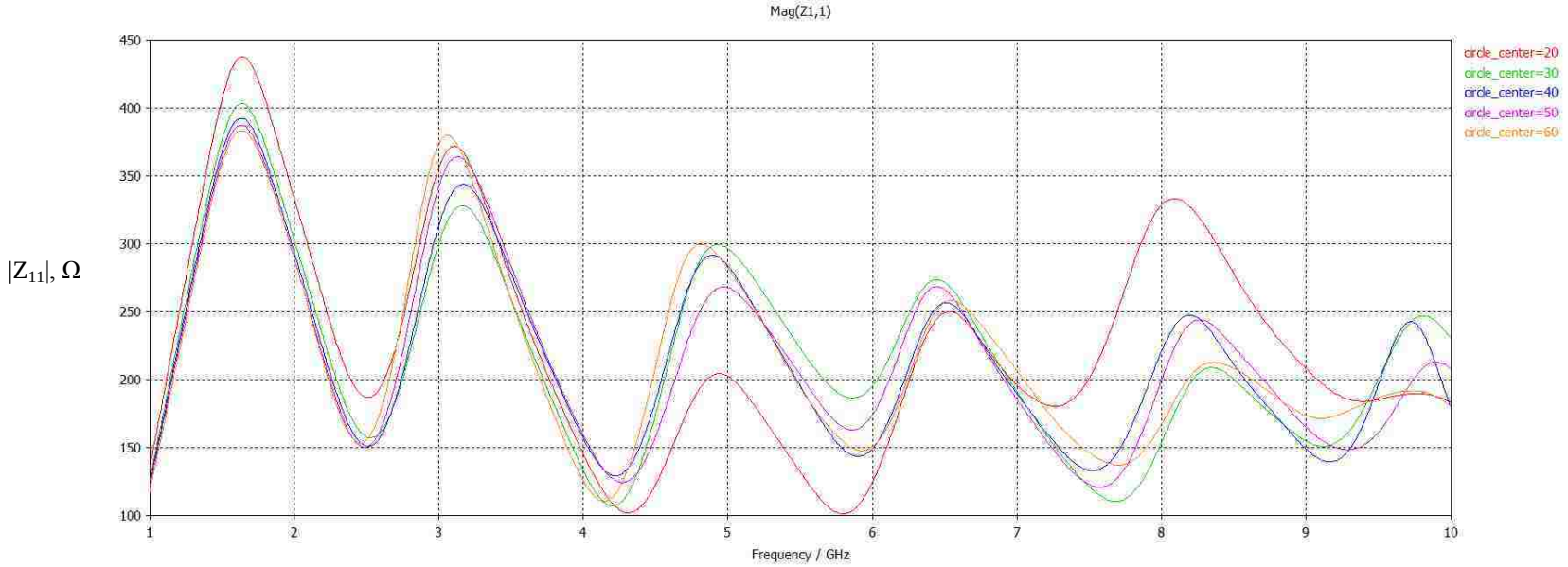

$|Z_{11}|$, Ω

Figure 81: Impedance vs. frequency for cutouts of varying location.

Finally, the effect of cutouts on the outer edges, as shown in Figure 78, was plotted in Figure 82. No cutout greater than zero radius provided any benefit across the 1-10GHz range. At this point further study of cut outs was abandoned.

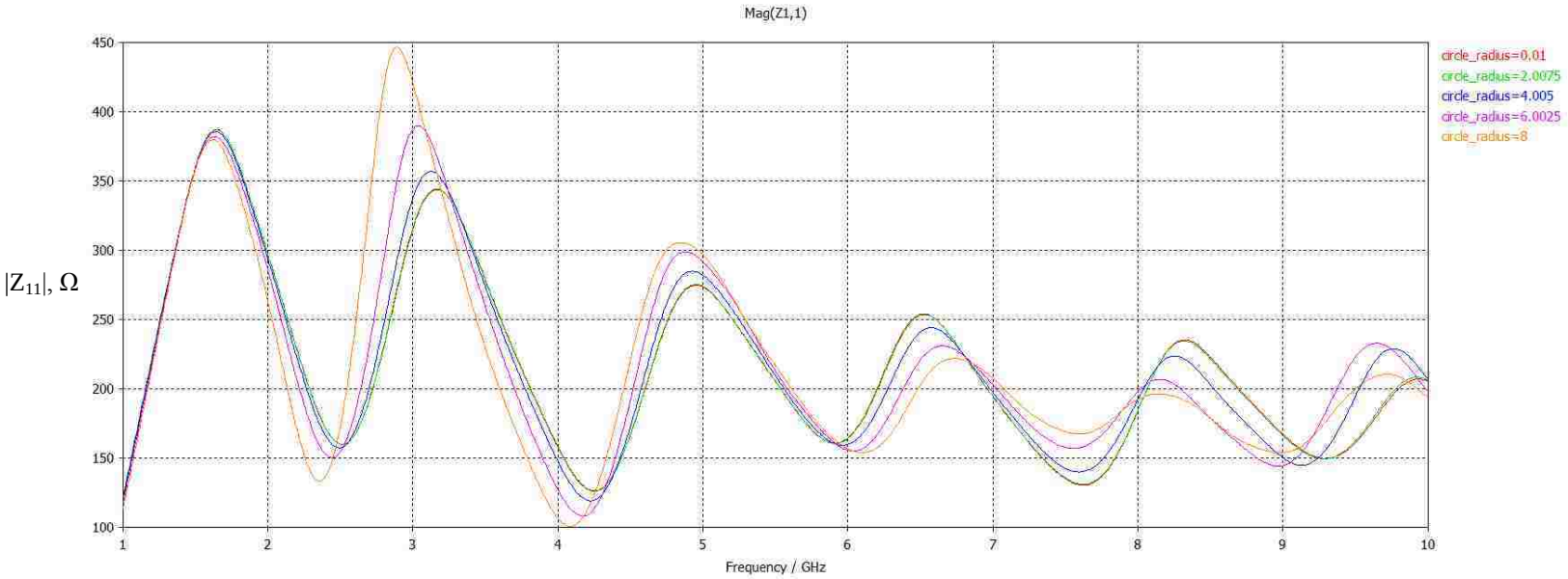

Figure 82: Impedance vs. frequency for cutouts on outer edges.

Angling, or folding, the diamond-shaped radiators was tried in an attempt to improve performance since positive effects were seen when the bowtie element was folded. A diamond-shaped element with a 50° flare and folded at 45° was selected for simulation studies. These choices are a tradeoff between bandwidth, beam width, phase center displacement, and physical layout.

It was shown that broadening a bowtie-shaped element by increasing its flare angle has the effect of improving bandwidth, as depicted in Figure 48 where flare angles from 25° to 85° were examined in simulation. It was expected that increasing the flare angle of a diamond-shaped element would also improve bandwidth. Angling the elements improves the beam width for purposes of dish illumination as shown in Figure 68 where the effect of different fold angles at 10GHz was simulated.

For minimal phase center displacement a fully planar feed would be desirable, yet such a configuration does not produce broadband radiation patterns suitable for illuminating a RSTN dish. Greater fold angles produce improved radiation patterns at the expense of allowing for phase center displacement. Additionally, physical constraints must be observed. Elements with large flare angles cannot be positioned with large fold angles because they would touch each other.

In consideration of these factors, a diamond-shaped element with a 50° flare and folded at 45° was selected as a baseline approach as it represented a reasonable tradeoff as described. Work was then directed towards making this geometry meet performance specifications. It is likely that other geometries could meet performance requirements, however, this research was directed towards finding an engineering solution and building a prototype rather than performing an exhaustive simulation study of geometries. This is left for future work.

Folded Diamond-Shaped Elements

Diamond-shaped elements with a 50° flare and 45° fold were simulated. 1 ounce copper on 0.030" thick Arlon AD320 was selected as the material. This material was chosen because a quantity was available and Microwave Studio had a model for the substrate. The simulation results are shown in Figure 83and Figure 84.

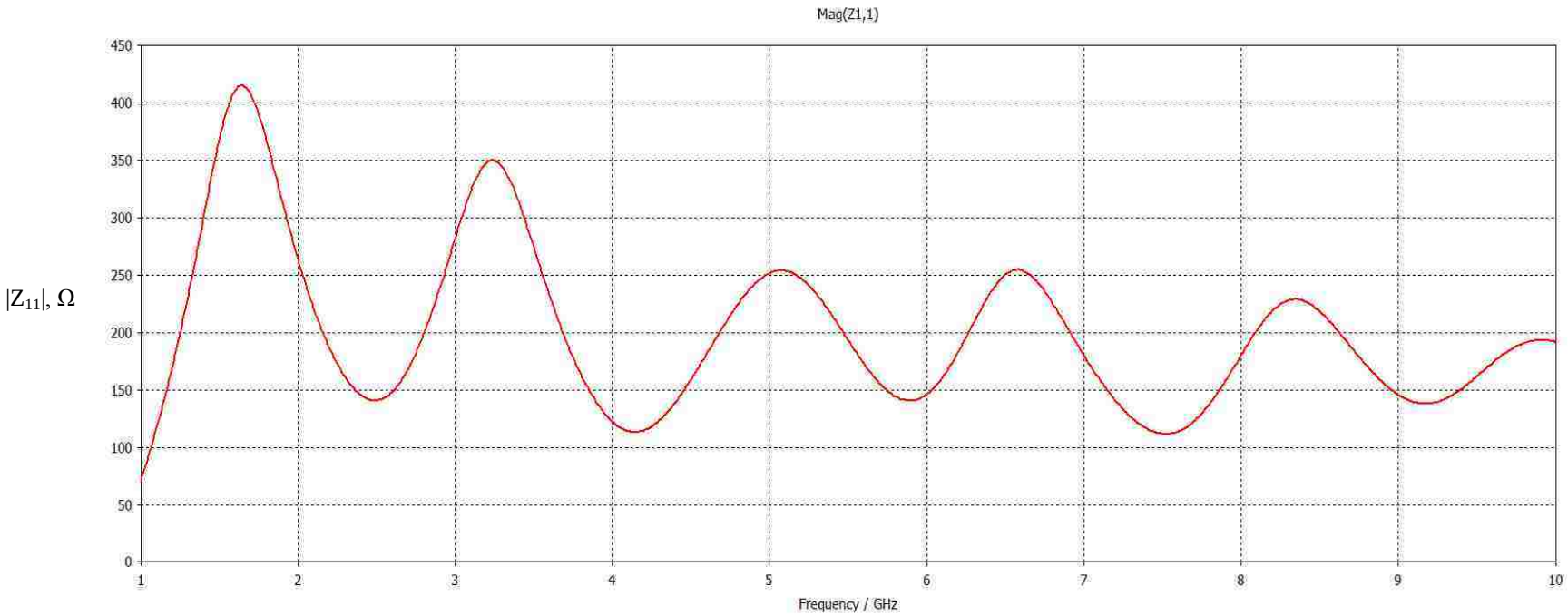

Figure 83: Input impedance of folded diamond-shaped element

It can be seen in the plot above that resonances are still present, and that the desired input impedance of 300Ω is not yet being met.

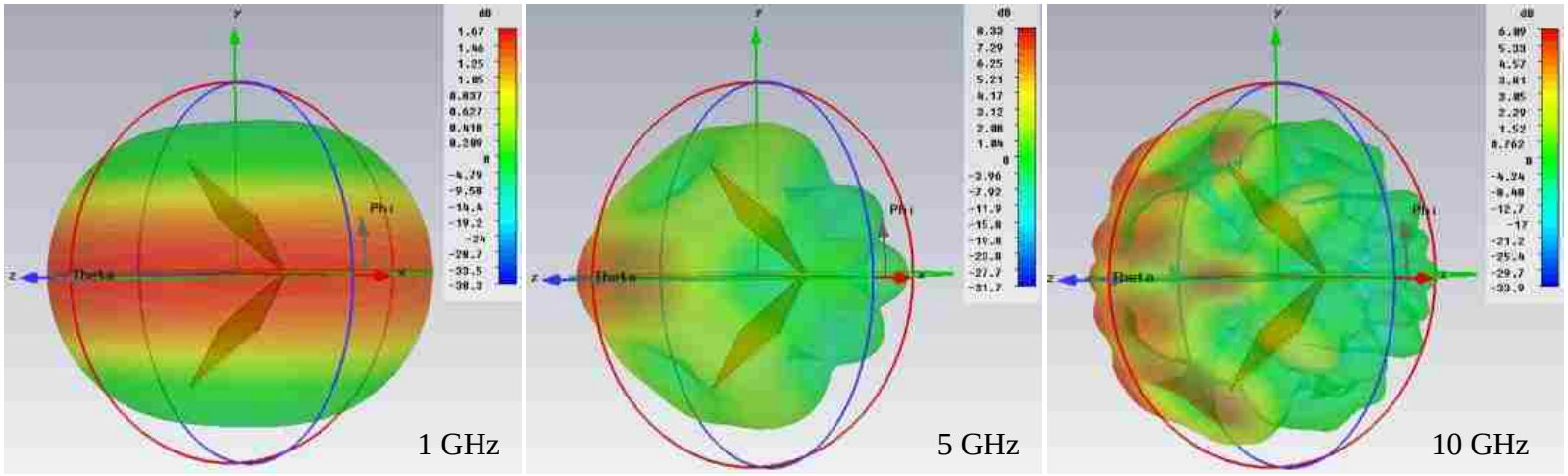

Figure 84: Radiation patterns of folded diamond-shaped element

3D patterns show that at 1GHz the folded diamond-shaped elements behave in a manner similar to a simple dipole, at 5 GHz tend to narrow the beam width directed towards dish center, and at 10 GHz produces multiple lobes directed towards the dish.

It is illustrative to effect a comparison between a folded bowtie and a folded diamond-shaped element with the same flare and fold angles, and using the same materials. This is best illustrated by comparing the 3D radiation patterns at 10 GHz as shown below in Figure 85. The Z-axis is pointing towards dish center. The bowtie element's pattern, shown at the top, has lobes (highlighted in red) that point away from dish center. In comparison, the diamond element, shown at bottom, has more lobes directed towards the dish.

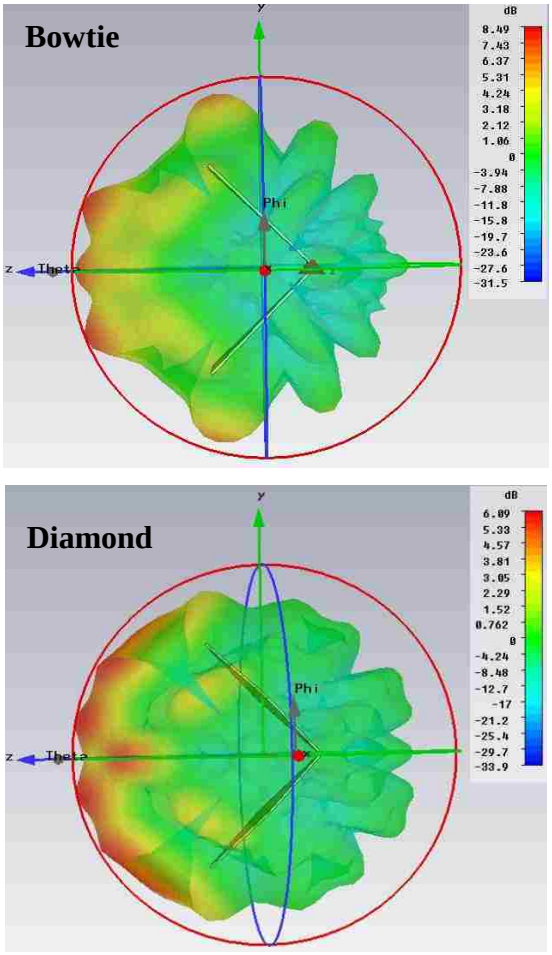

Figure 85: Bowtie vs. diamond-shaped element 3D pattern

Folding the diamond-shaped elements has a degrading effect on input impedance, raising the peak impedance values by approximately 33Ω. This is addressed with the application of an RF-absorbent backing.

Effect of Absorbent Backing

Simulations were performed to examine the effect of absorber thickness on the diamond-shaped elements. Planar elements were used for this study to reduce simulation time and because simulations had been performed on a planar bowtie. As before, ECCOSORB MF-117 was used as the absorbing material because a model was available in Microwave Studio and it is a popular material. Its characteristics are discussed in Appendix C: ECCOSORB RF Absorbent Material.

As before, the same diamond-shaped element with 50° flare and 45° fold was used. MF-117 is available in thicknesses that are a multiple of 1/8 inch, or 3.2mm. For this study, 3.2, 6.4, and 12.7 mm thicknesses were compared and the results are shown in Figure 87. As expected, thicker absorbent layers tend to flatten out the impedance vs. frequency response.

Since the absorbent material constitutes loss, simulations were performed to determine if the absorbent material needed to cover the entire element in order to be effective. This was done by parametrically sweeping the distance from the feed gap to the edge of the absorbent material, as shown below in Figure 86, where the copper diamond-shaped elements are yellow and the absorbent material is green. Simulations were performed with 12.7mm thick MF-117 material recessed from 2 to 40mm. Results are shown in Figure 88 with the expected result that greater coverage yields a flatter impedance curve.

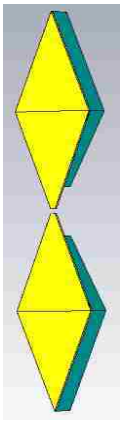

Figure 86: Recessed absorbent material

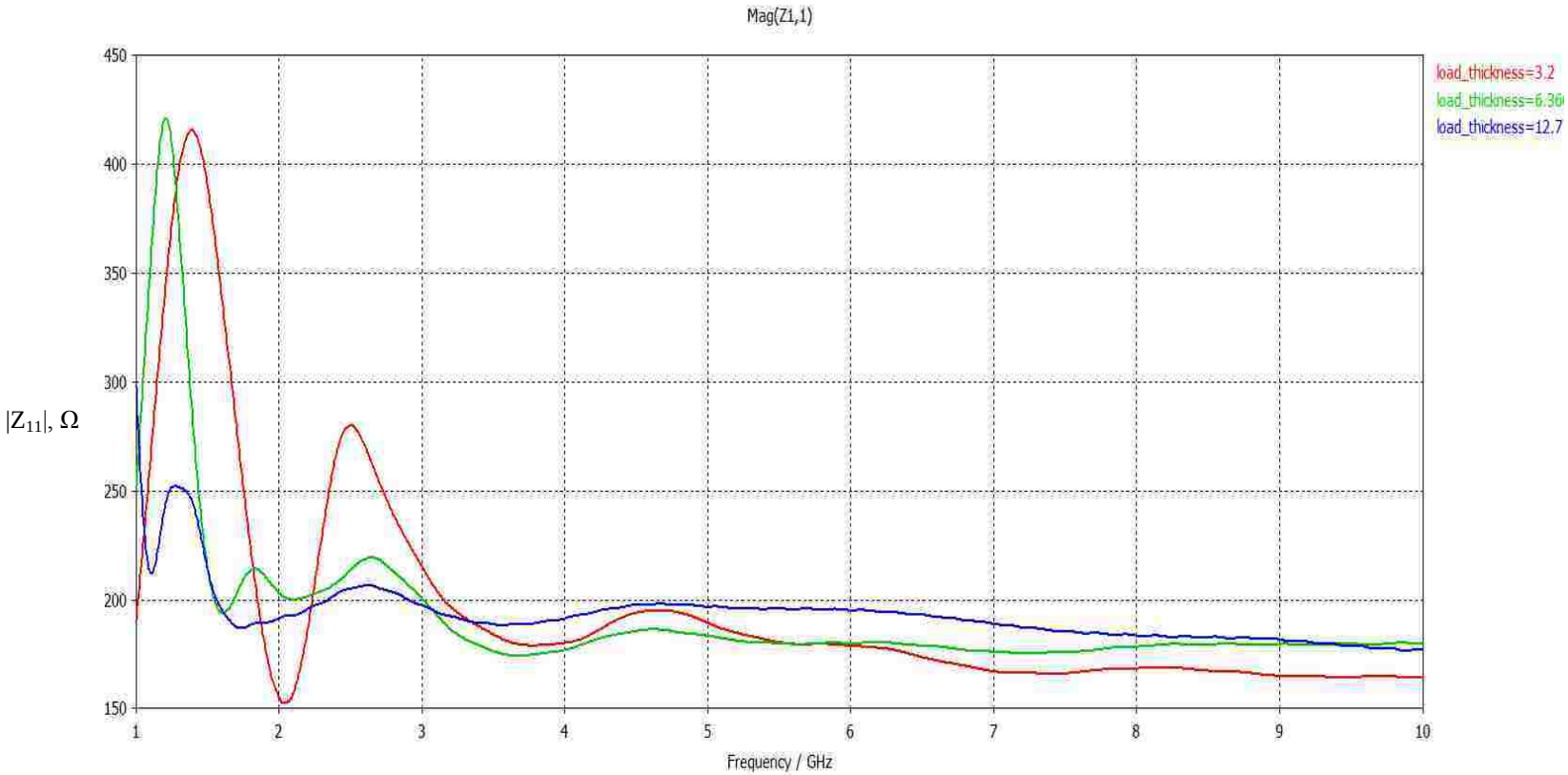

Figure 87: Input impedance vs. MF-117 thickness

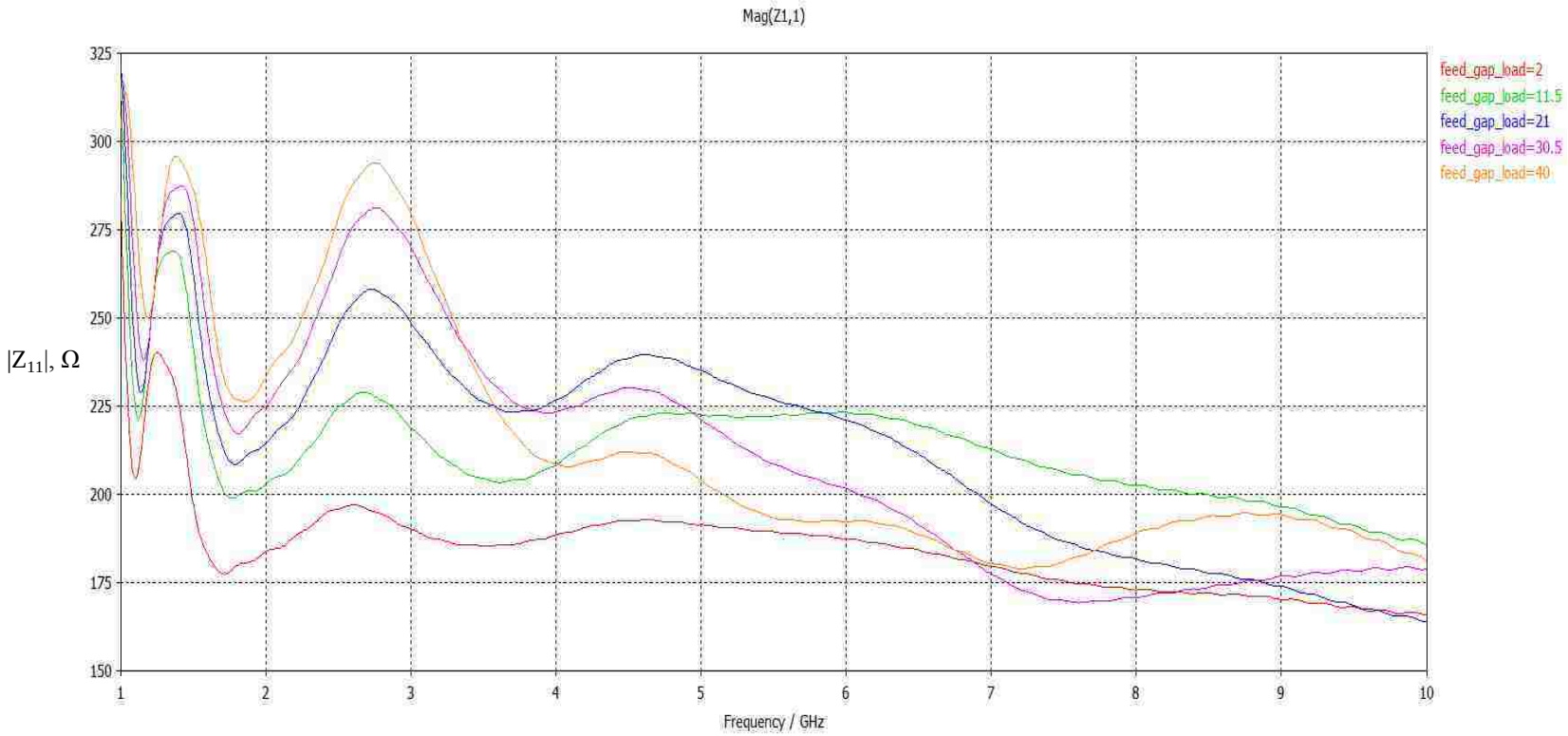

Figure 88: Effect of recessing absorbent material

A 12.7mm thick MF-117 absorbent layer covering the entire back of the diamond-shaped element, in the absence of other structure, produces a maximum impedance of 275Ω which would yield a VSWR of 2.75. 3D radiation patterns were simulated with this configuration and the results are shown in Figure 89, where it is observed that the radiation patterns are becoming more suitable for illuminating a dish in that the main lobe is reasonably uniform and directed towards dish center.

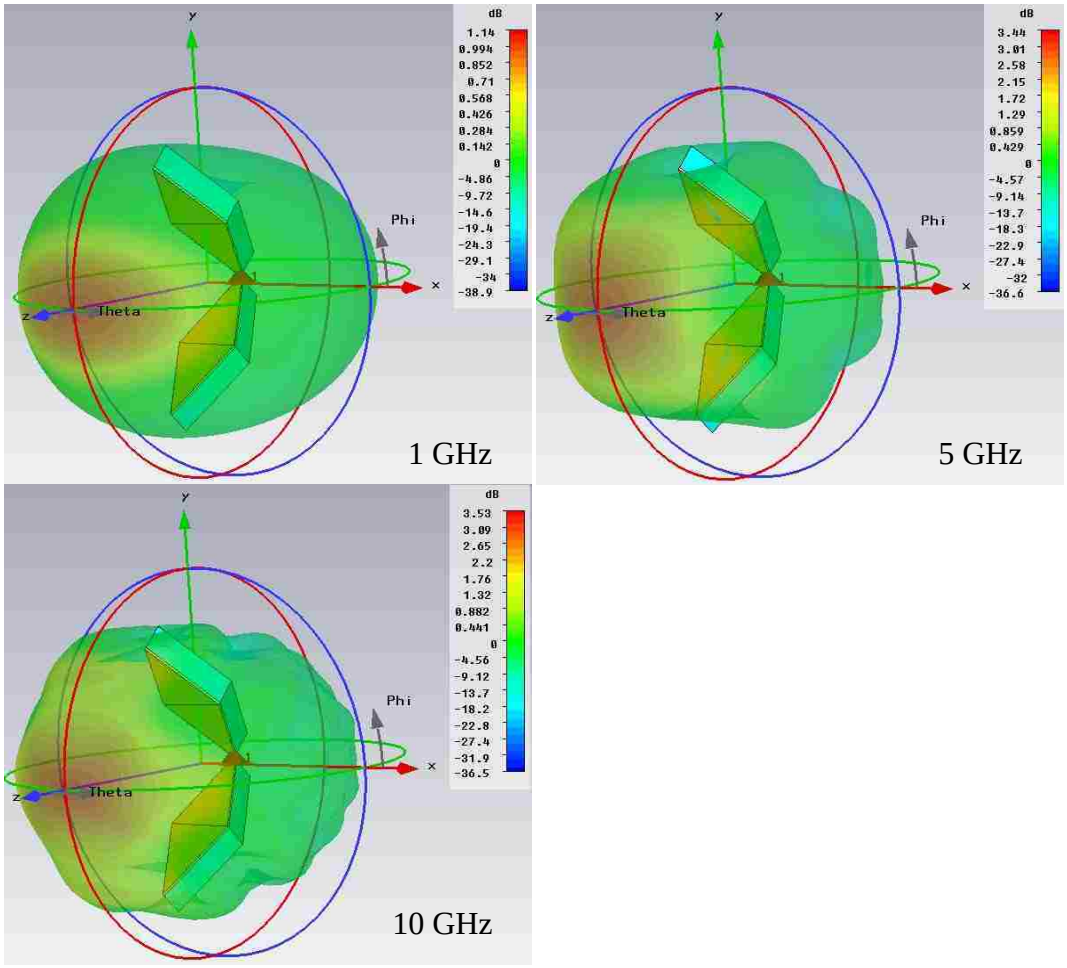

Figure 89: Radiation patterns using 12.7mm thick MF-117

Since the radiating elements will eventually need to be supported and connected electrically a support structure was investigated started with a cylindrical cavity lined with 3.2mm of MF-117. Using the diamond-shaped radiators of size and angles

previously described, a parameterized MF-117 lined can was created in Microwave Studio. The diamond-shaped elements did not have an absorbent backing for this study.

As shown in Figure 90, Can_height is the distance from the element feed points to the cavity opening and Can_Depth is the distance from the feed points to the bottom of the cavity. Can_Radius is the distance from the center of the feed gap to the inner edge of the cavity.

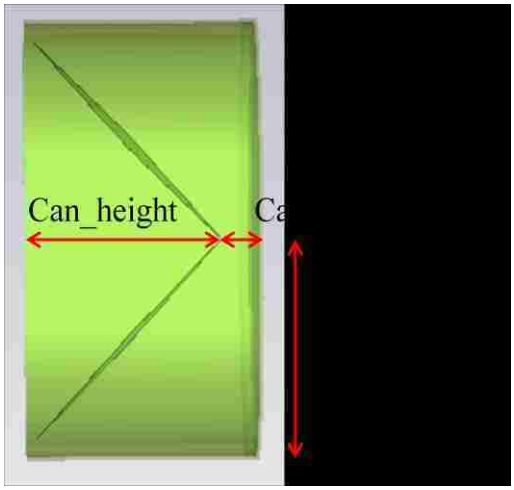

Figure 90: Parameterized lined cavity

The first parametric study conducted was the effect of changing the cavity radius from 65 to 105mm. The minimum value of approximately 65mm is the point at which the edge of the radiators overlap the inner MF-117 lining. The maximum value of 105mm was chosen as the largest size that would fit into a RSTN feed housing.

Simulations were performed holding the cavity height at 60mm and the depth at 10mm. Results are shown in Figure 91, where it is seen that a cavity radius of 85mm yields the lowest first and second peak.

In the next set of simulations the cavity radius was held at 85mm, the depth at 10mm, and the height was swept from 60 to 140mm. These results are shown in Figure 92, where the 60mm cavity height yields the best performance, and yields a feed that will easily fit into a SRBL housing.

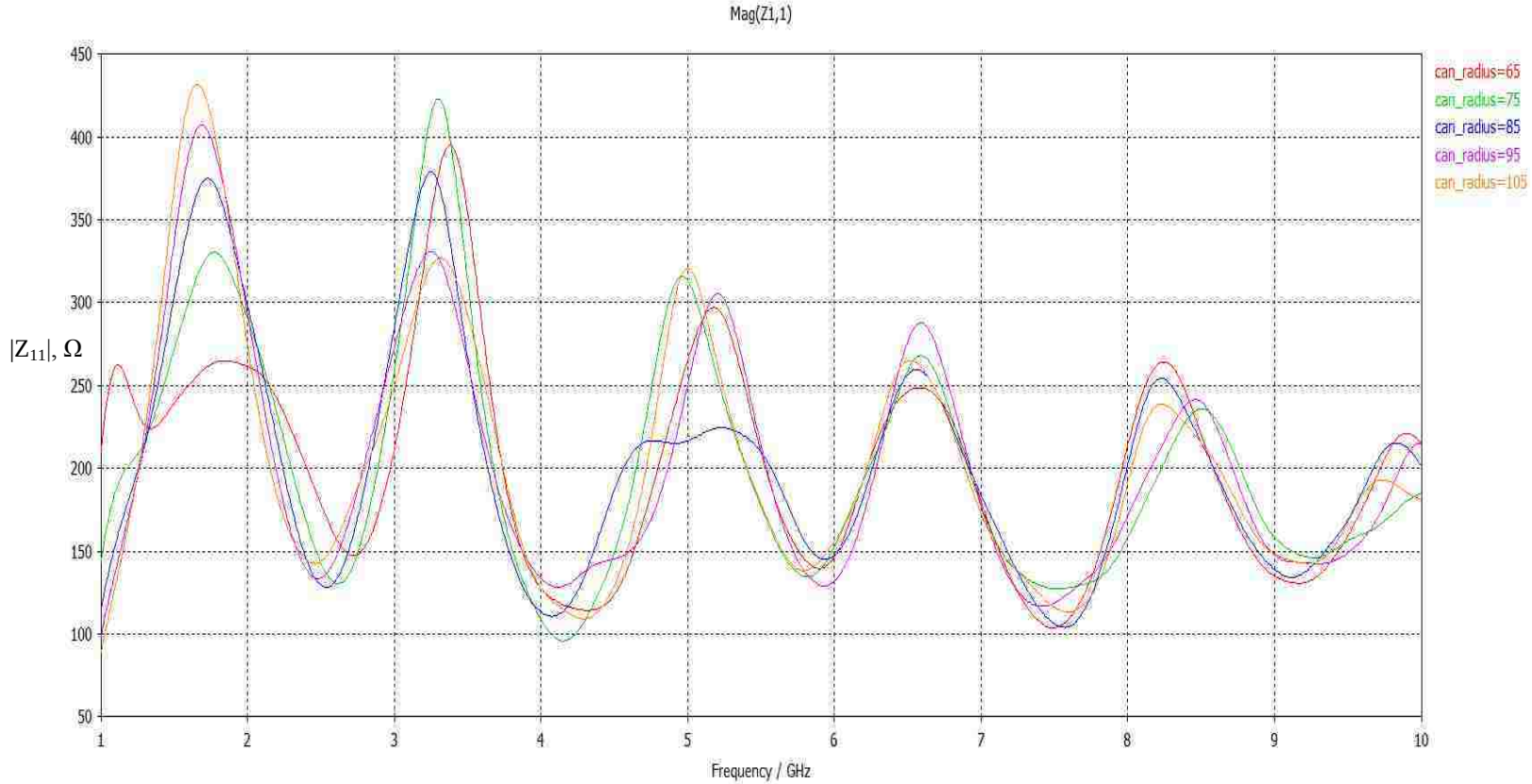

Figure 91: Effect of cavity radius

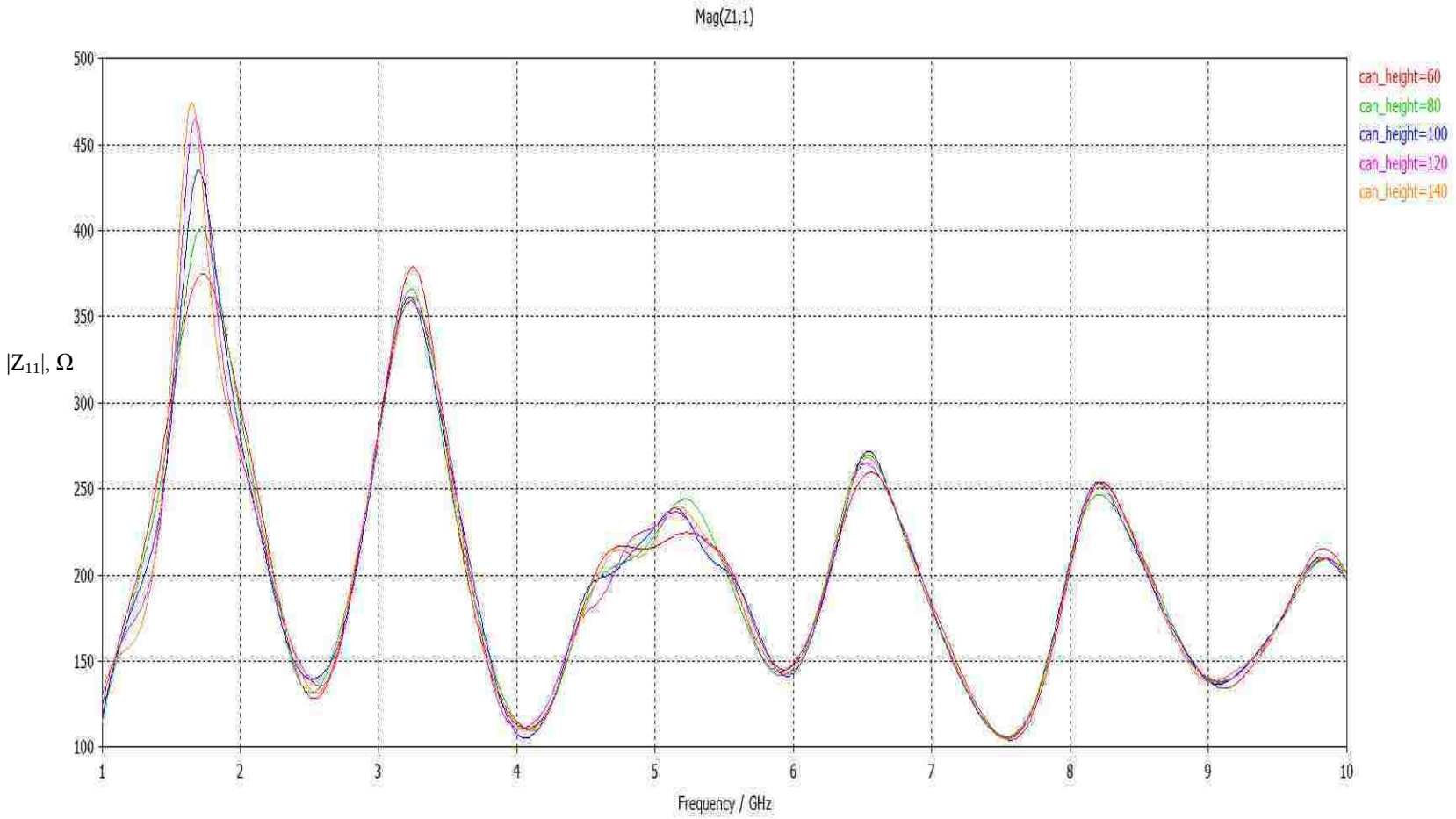

Figure 92: Effect of cavity height

The cavity depth was then parametrically swept from 10 to 50mm while holding the cavity radius at 85mm and height at 60mm. The impedance vs. frequency curve was plotted and is shown in Figure 93, where it is seen that the shallowest cavity depth of 10mm is most effective.

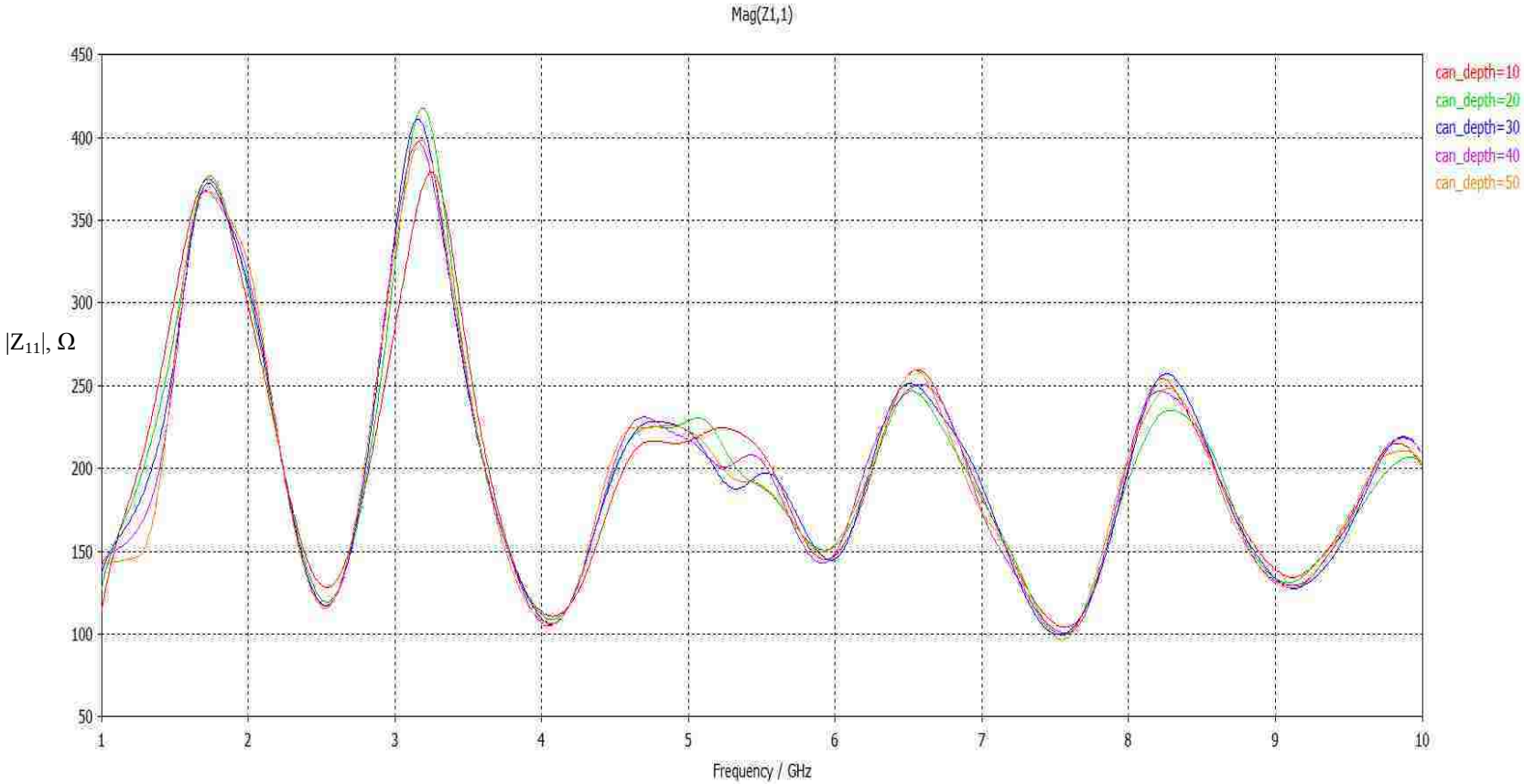

Figure 93: Effect of cavity depth

3D radiation patterns were then simulated with cavity dimensions of 85mm radius, 60mm height, and 10mm depth. The results are shown in Figure 94, where it is seen that the radiation patterns are becoming more reasonable for purposes of dish illumination. As the diamond-shaped elements did not have an absorbent backing for these simulations, it was hoped that the addition of such a backing would further improve performance.

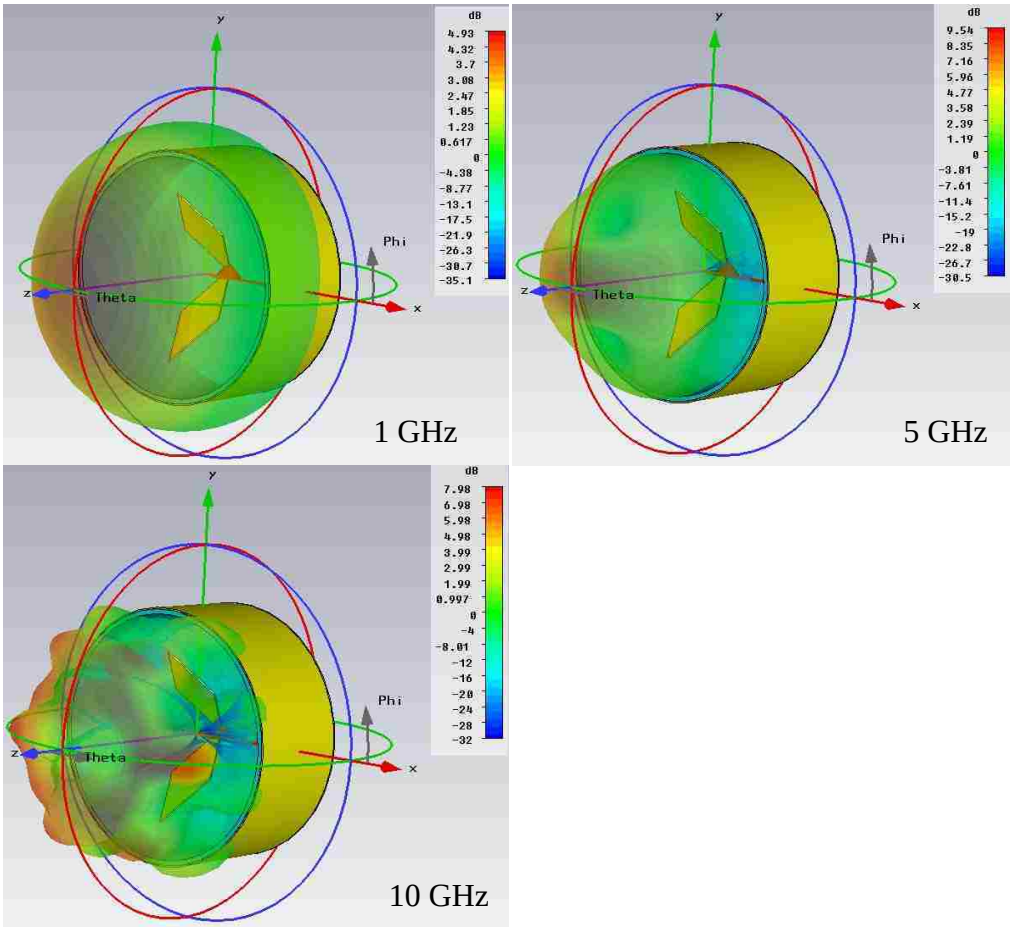

Figure 94: Radiation patterns for 85x60x10 cavity

The next step was to run simulations using the cavity configuration in the preceding section but using diamond elements with 3.2mm of absorbent backing. The results are shown in Figure 95, where it is seen that the input impedance is close to the 300Ω target.

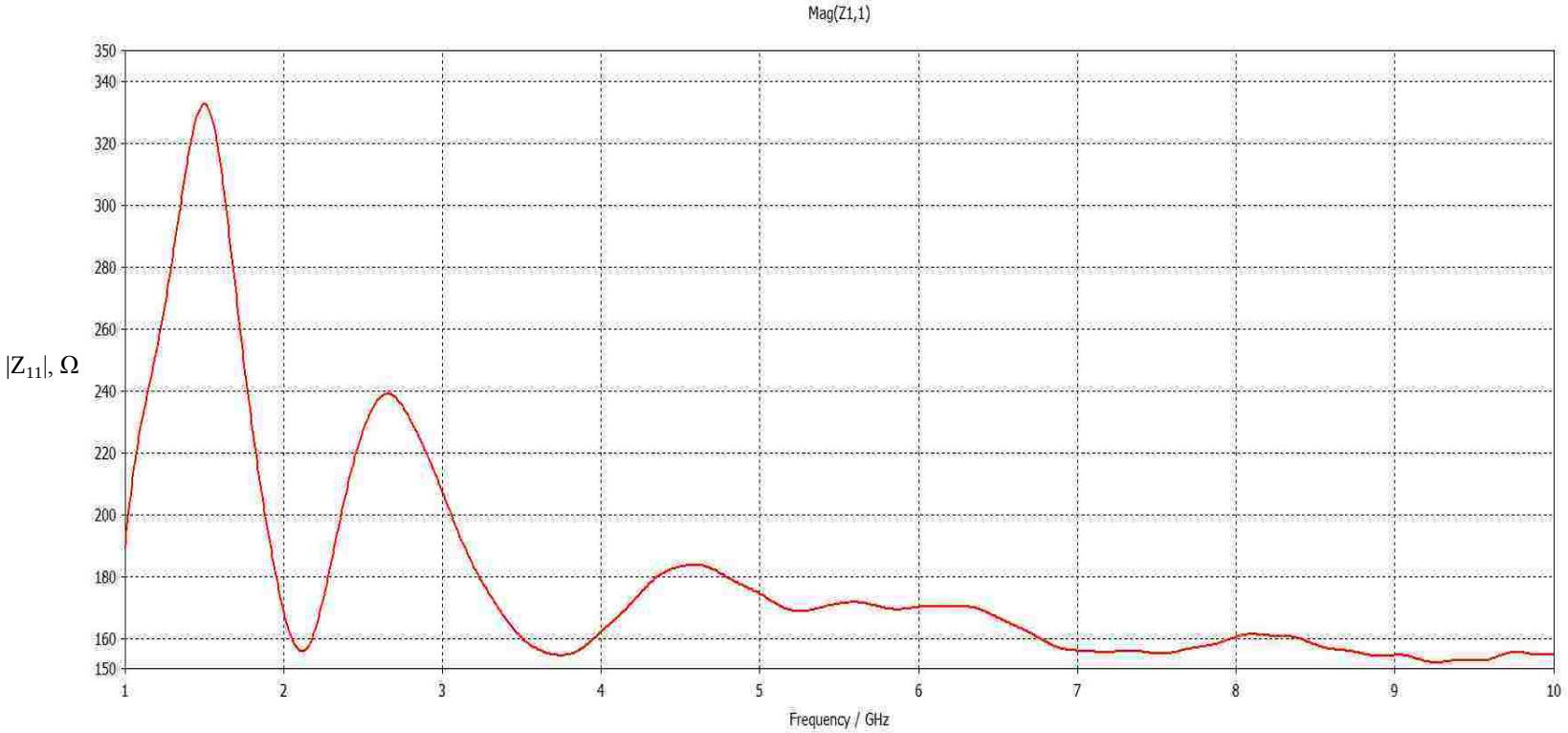

Figure 95: Damped elements in damped cavity

The corresponding radiation patterns are shown below in Figure 96. Reasonable radiation patterns were observed although the 5GHz pattern was narrow.

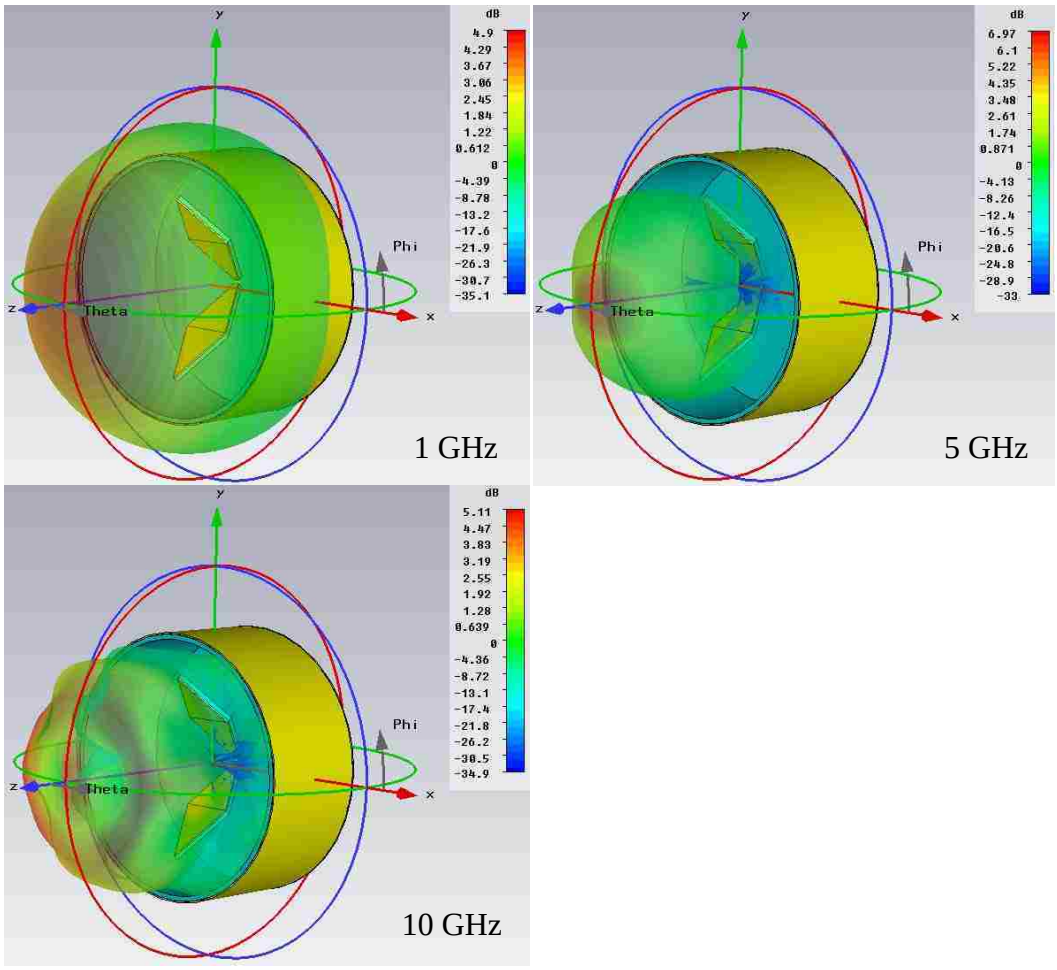

Figure 96: Radiation patterns of damped elements in damped cavity

Instead of a planar layer of damping material in the bottom of the cavity, a damper with a conical shape was studied. It was implemented as shown in Figure 97. The addition of this structure greatly increased the number of mesh cells and thus the simulation time.

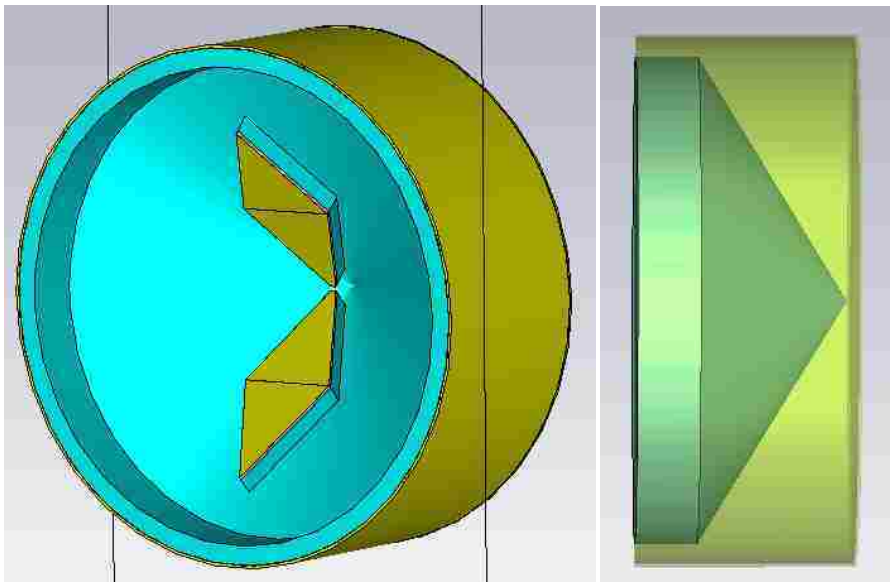

Figure 97: First attempt at conical damper

The resulting impedance vs. frequency curve is shown in Figure 98, which has an improved response, staying at or below 300Ω except in the range of 1.2-1.3 GHz. Corresponding 3D radiation patterns were plotted and are shown in Figure 99.

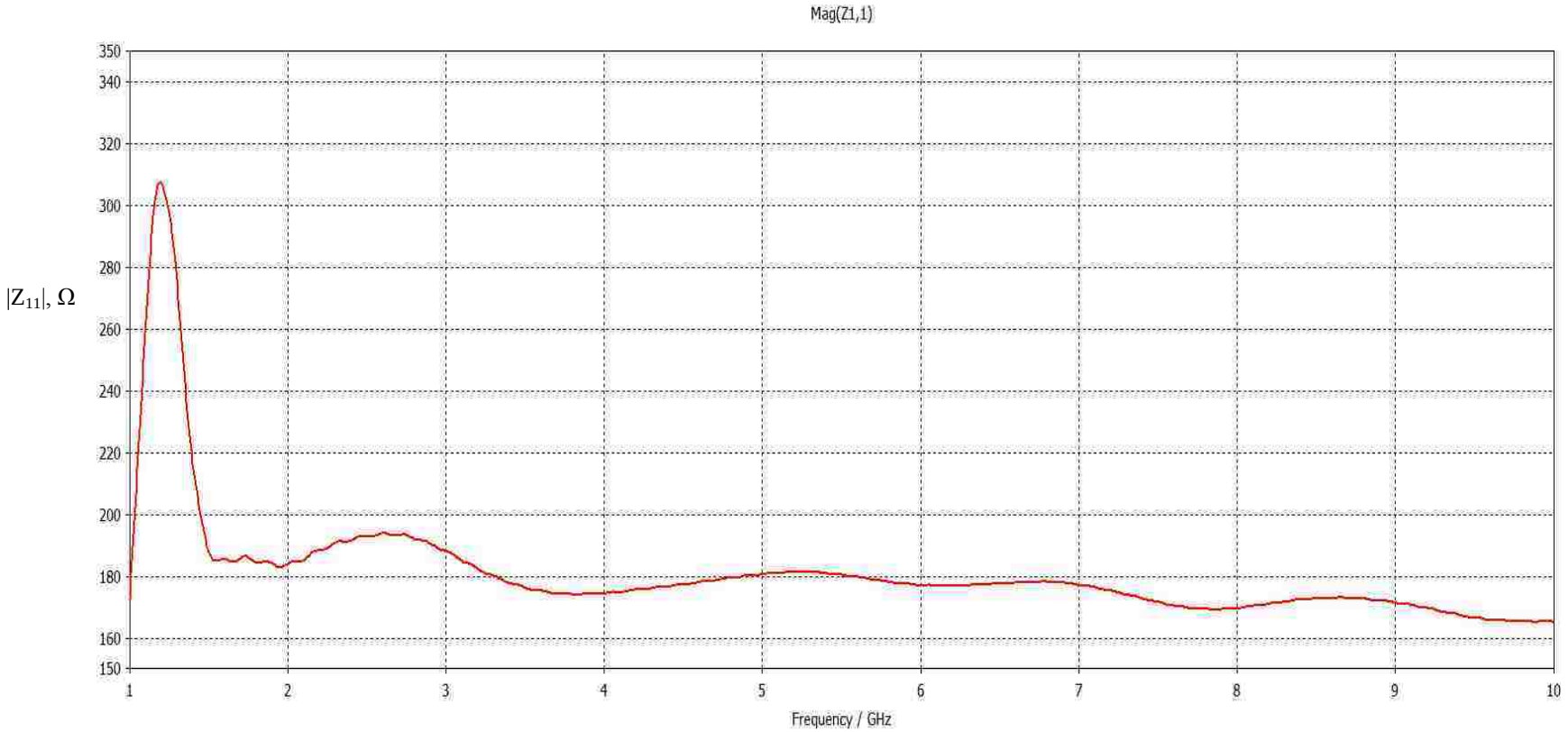

Figure 98: Impedance vs. frequency for first attempt conical damper

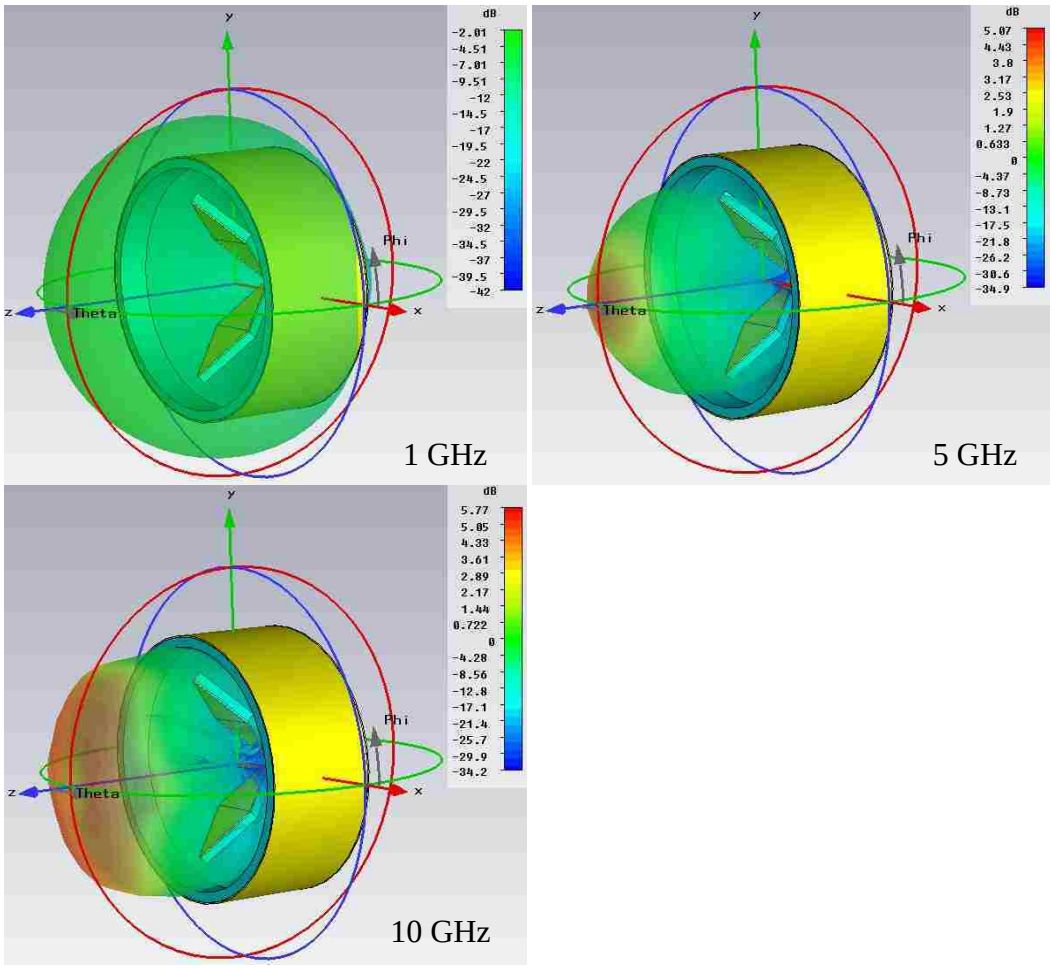

Figure 99: Radiation patterns for first attempt conical damper

While the radiation patterns at 5 and 10Ghz appear to be acceptable, the inclusion of the conical damper has heavily reduced the directivity at 1 GHz, effectively preventing the feed taper target from being achieved. In an attempt to regain some of the lost directivity the damping material was removed from the back of the diamond elements and it was re-simulated. The resulting radiation patterns are shown in Figure 100 where it is seen that the directivity is still too low at 1 GHz to effectively illuminate the dish.

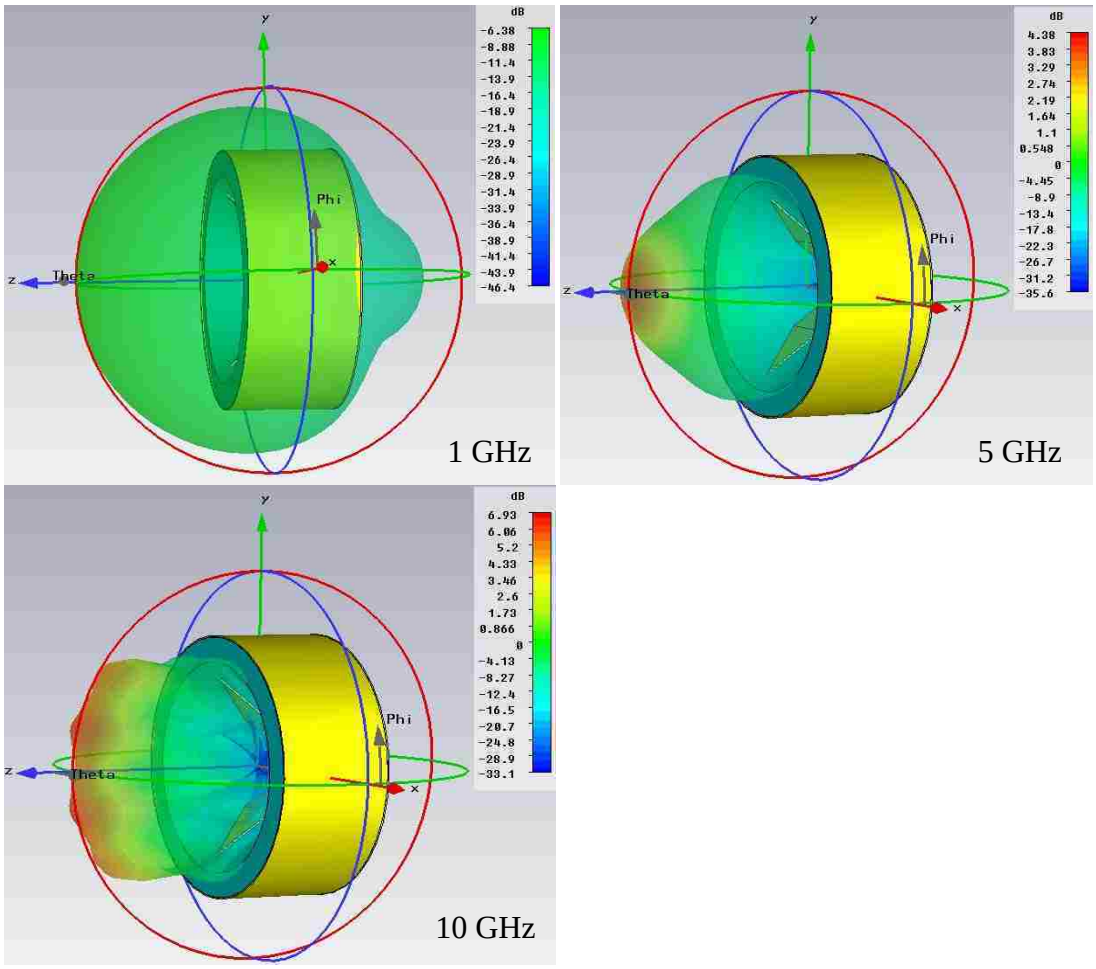

Figure 100: Radiation patterns after removing backing

It appeared that the conical damper was too absorptive, so a thinner damper was simulated. It was 3.2mm thick in the center, increasing to 6.4mm thick at the edges. The simulation results are shown in Figure 101 and Figure 102. While the input impedance is now below 300Ω over the entire frequency range, the 3D radiation patterns show poor directivity at 1 GHz.

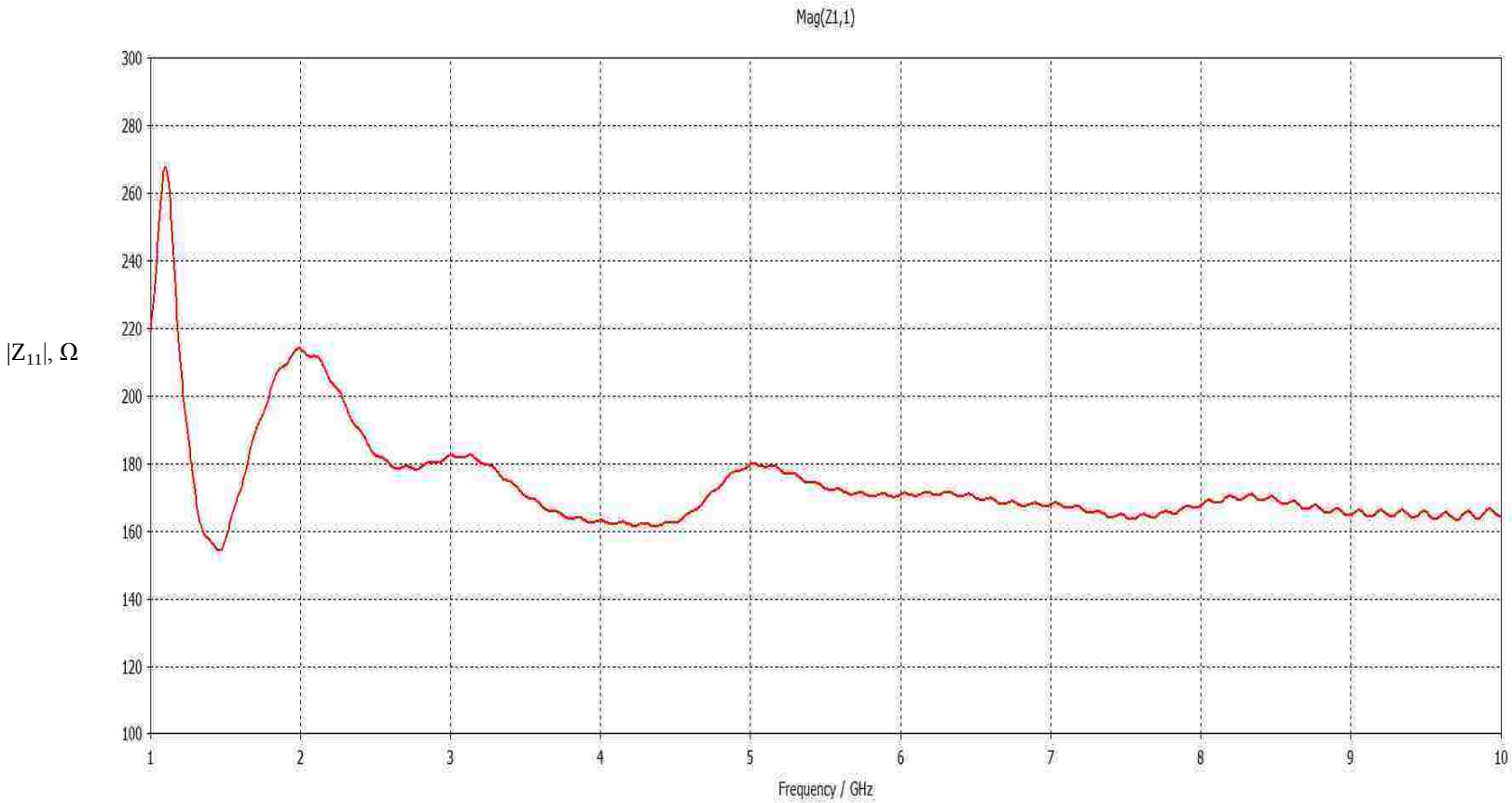

$|Z_{11}|$, Ω

Figure 101: Impedance vs. frequency for thinner conical damper

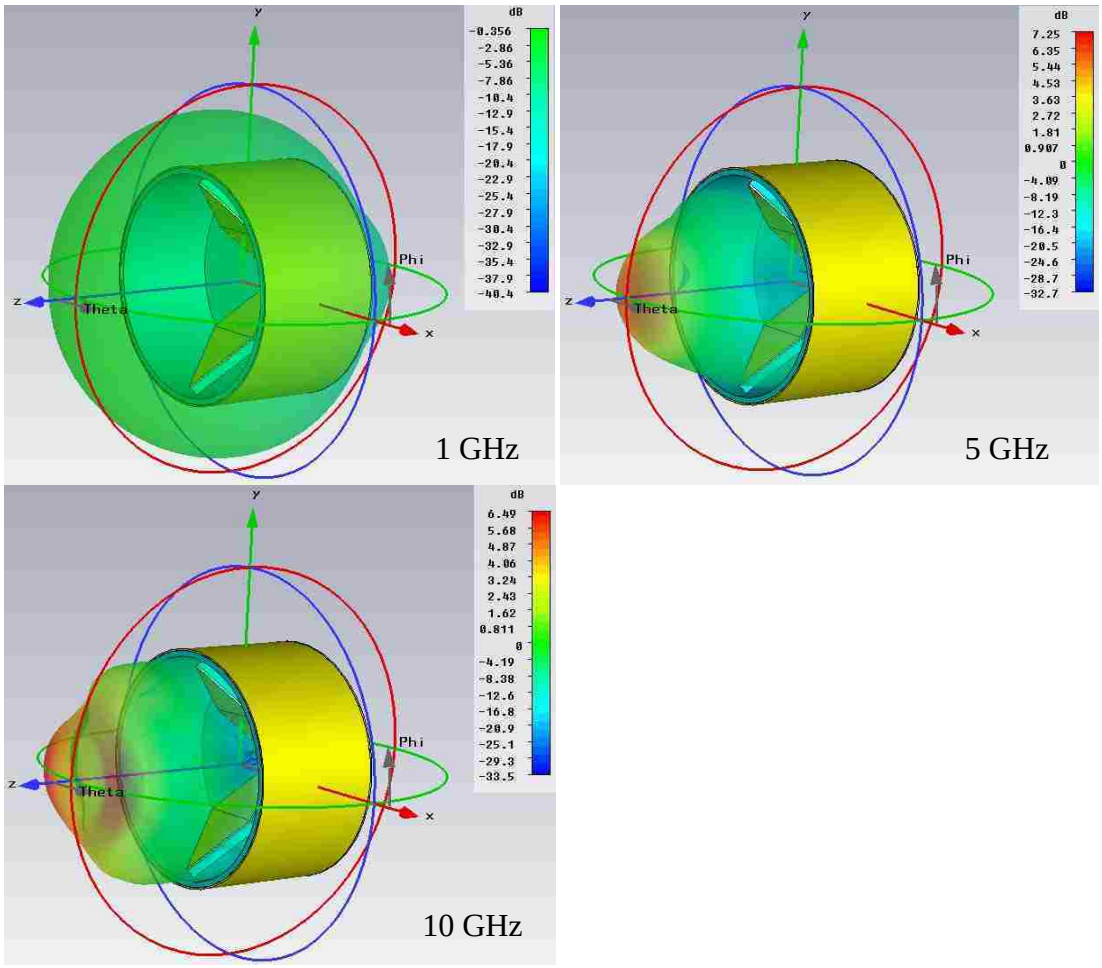

Figure 102: Radiation patterns with thinner conical damper

After this, several simulations were performed varying the height of the conical damper from 20 to 70mm.. The best response was seen with a 20mm high cone but the radiation pattern did not have sufficient taper for the RSTN application, as shown in Figure 103 where the feed taper is only 5.03 dB.

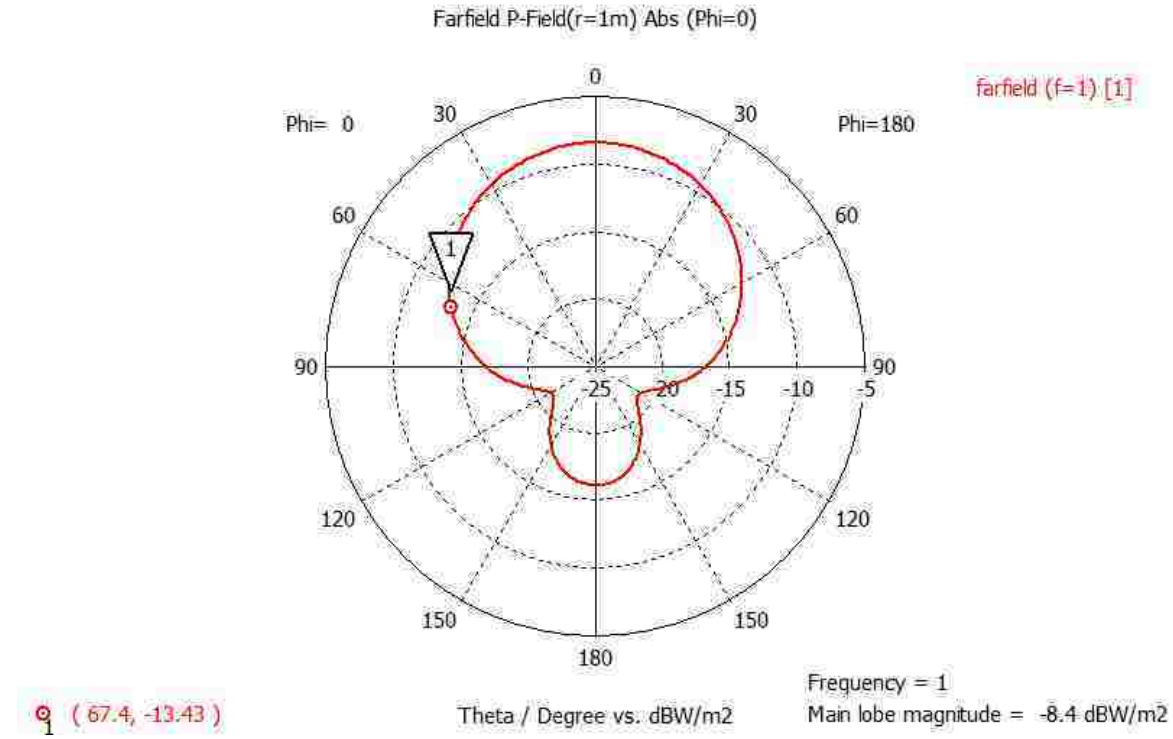

Figure 103

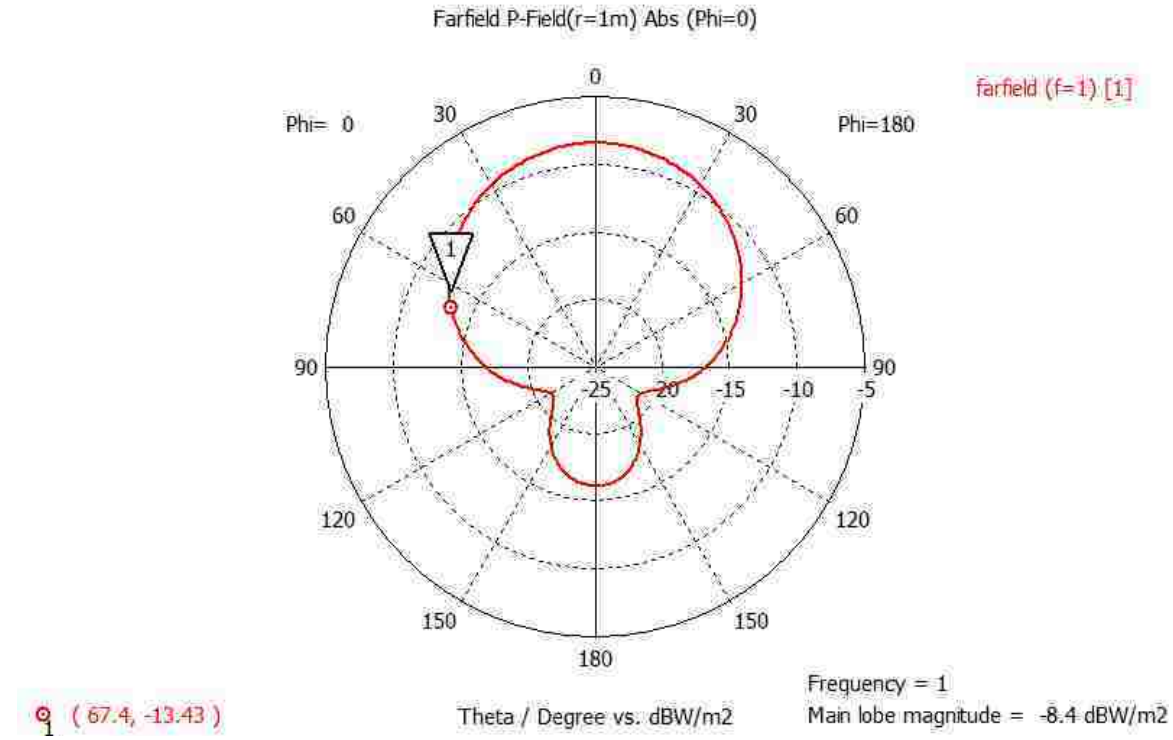

Figure 103: Power pattern with 20mm high conical damper

Simulations were again performed but with the conical damper inverted from its previous orientation such that the highest point of the absorbent material was in the center and the thinnest portion at the edges.

The first attempt used a cone height of 5mm, a cavity radius of 60mm and a cavity height of 60mm. with the result a feed taper of only 5.1dB. The cavity height was increased to 80mm but the feed taper stayed the same. Increasing the cavity height to 100mm resulted in bandwidth degradation as $S_{1,1}$ was only met above 1.6 GHz.

The last simulation in this series increased the cavity radius to 65mm and set the cavity height at 80mm, with a 5mm high conical damper. The results were promising, as seen by the impedance vs. frequency plot shown in Figure 104, and the radiation patterns shown in Figure 105.

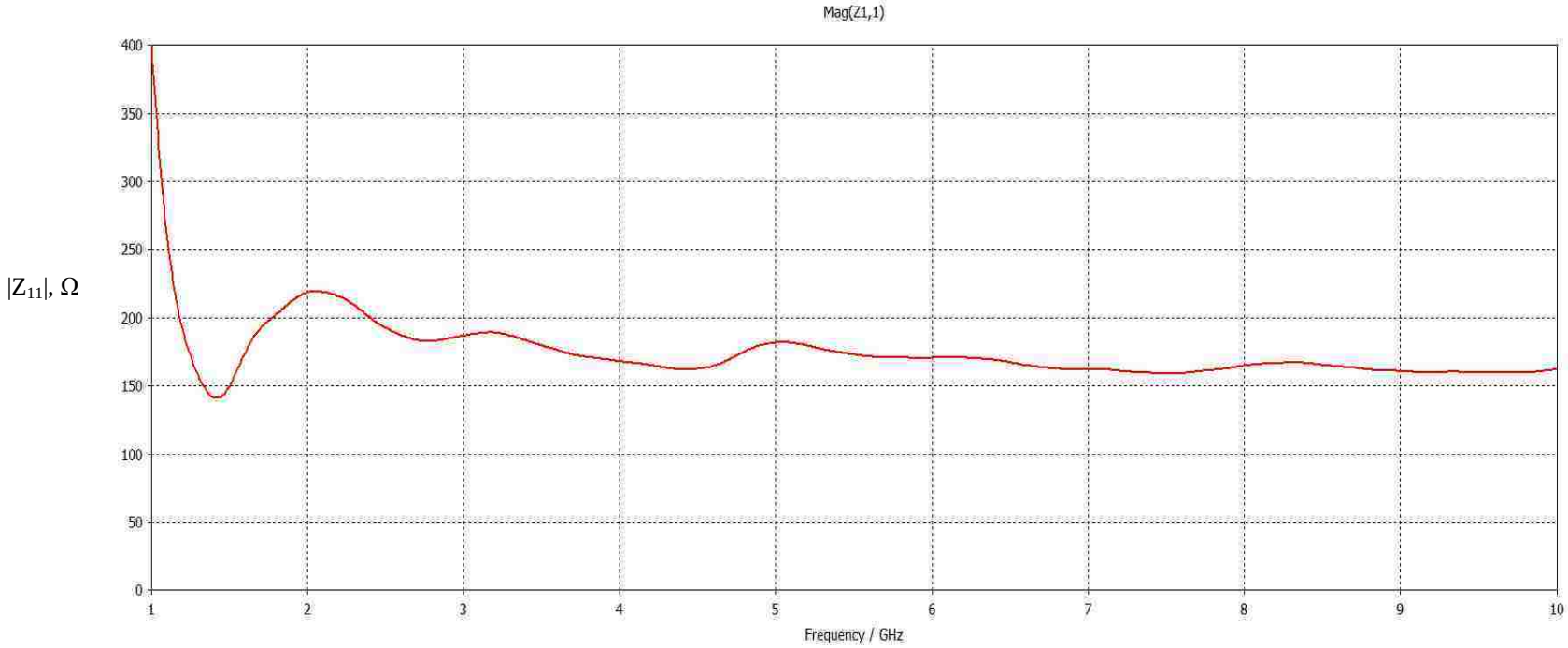

$|Z_{11}|$, Ω

Figure 104: Impedance vs. frequency for inverted conical damper

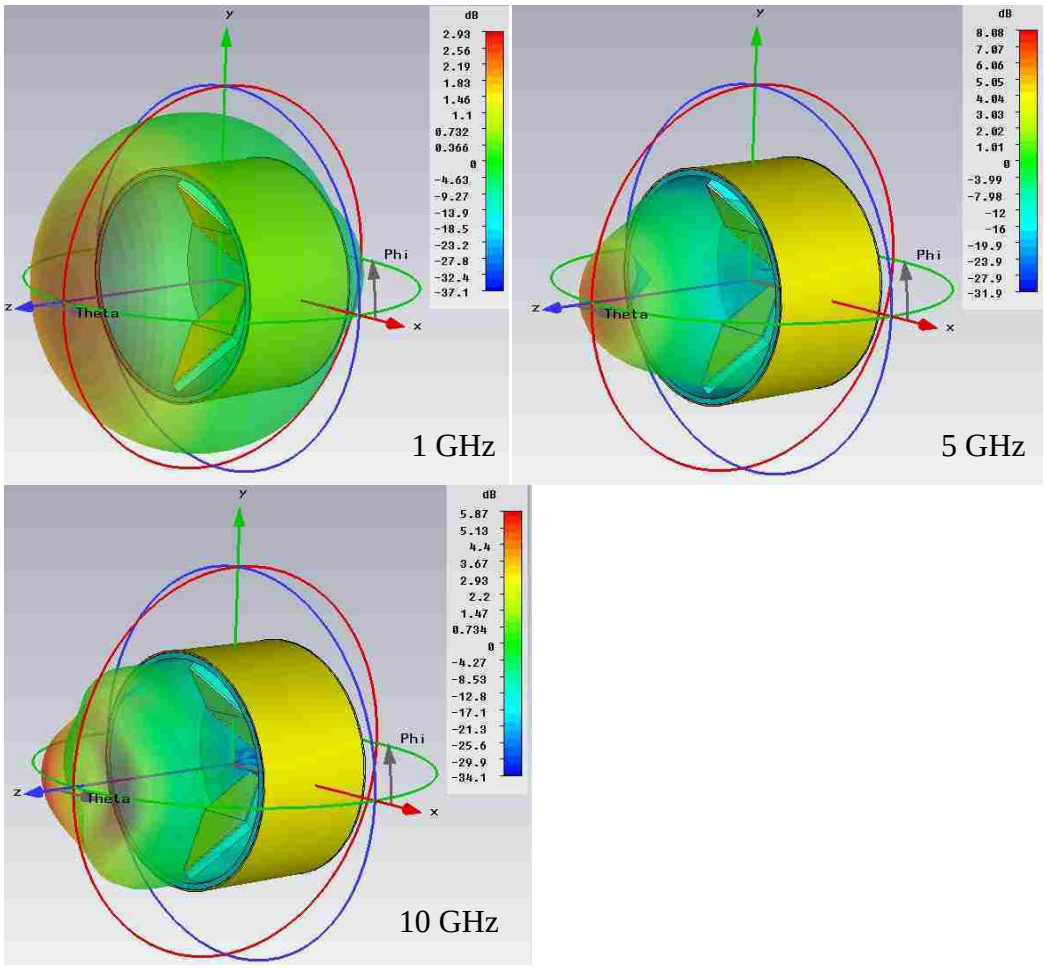

Figure 105: Radiation patterns for inverted conical damper

Beamforming

A further attempt was made to increase the directivity at low frequency by adding a lip at the aperture of the feed as shown in Figure 106. It was thought that the addition of such a ring would partially block electric field lines from wrapping around the rip of the diamond-shaped elements, thus confining the field.

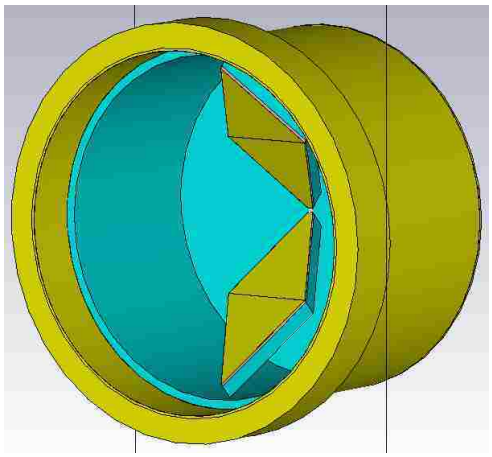

Figure 106: Diamond feed with aperture ring

The first simulation of this series defined an aperture ring that was 10mm wide and 20mm deep, with the result that the feed taper at 1GHz increased to 5.7 dB. Next, the aperture ring was increased to 35mm wide and reduced to 10mm thick, increasing the feed taper at 1GHz to 7.8 dB. It appeared that a wider ring improved the taper, so in the next simulation the aperture ring was increased to 45mm of width. This resulted in a feed taper of 9.74 dB at 1GHz, which was very close to the target of 10dB.

Next, annular rings were cut into the aperture ring, as shown in Figure 107, having a radius of 2mm. The taper at 1GHz remained relatively unchanged at 9.73 dB.

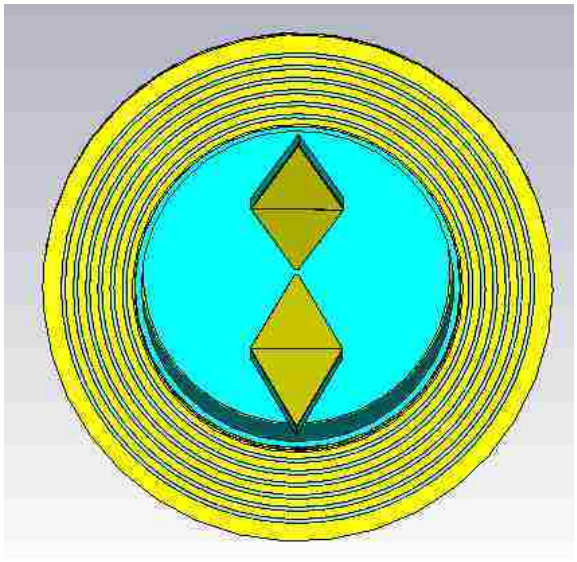

Figure 107: Annular rings

The annular rings had little effect and would require more machining to fabricate so the approach was abandoned. The last set of simulations were performed with the following physical parameters:

- 50° flare angle on the diamond-shaped radiators
- 45° fold angle for the diamond-shaped radiators
- Cavity height of 80mm
- Cavity radius of 80mm
- Cavity depth of 10mm
- 5mm high conical damper
- 9.525mm thick aperture ring (as 0.375" copper was to be used)
- 45mm wide aperture ring
- An additional 6.4mm of MF-117 on the outside of the cavity

This configuration yielded satisfactory radiation patterns although $S_{1,1}$ was not at or below -10 dB across the entire 0.9 to 12 GHz frequency range. It was decided that it was close enough and that fabrication should commence.

Detailed simulation results are shown in Appendix F: Diamond Feed Simulation Results.

A comparison of simulated power patterns is made in Figure 108. The diamond feed is shown on the left at 1.5 GHz and the simulated RSTN dipole feed at 1.4 GHz on the right. It can be seen that the diamond feed has a more symmetric power pattern at this frequency and should therefore have less spillover.

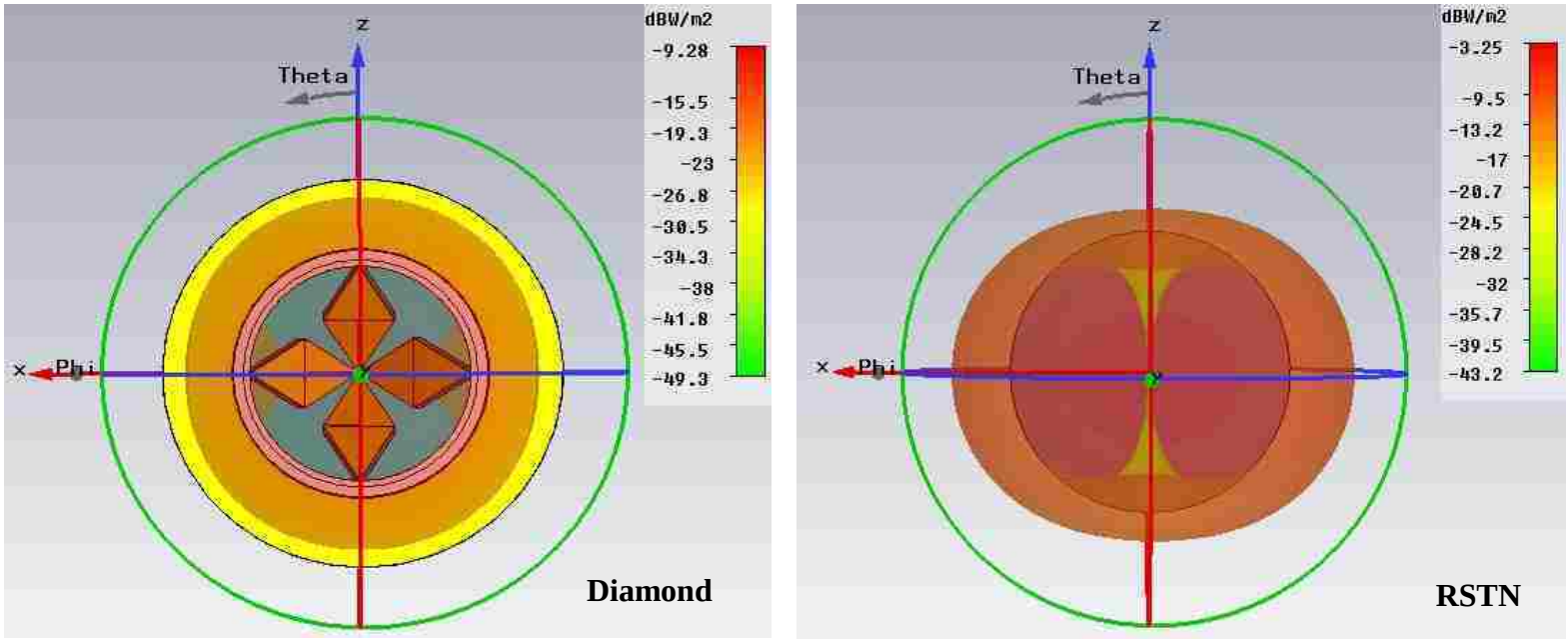

Figure 108: Comparison of end-on power patterns

Alternate Aperture Ring

The aperture ring was implemented with 0.375" copper as such material was on hand for fabrication. However, a thinner aperture ring may be effective in practice and would reduce both weight and cost, as the skin depth of copper in this frequency range is on the order of a micrometer.

A simulation was performed in which the aperture ring was reduced to 1mm in thickness which is the same as the copper cavity material. This aperture ring is shown in Figure 109. As this simulation was not performed until after the feed was fabricated, the prototype uses the thicker 9.525mm aperture ring.

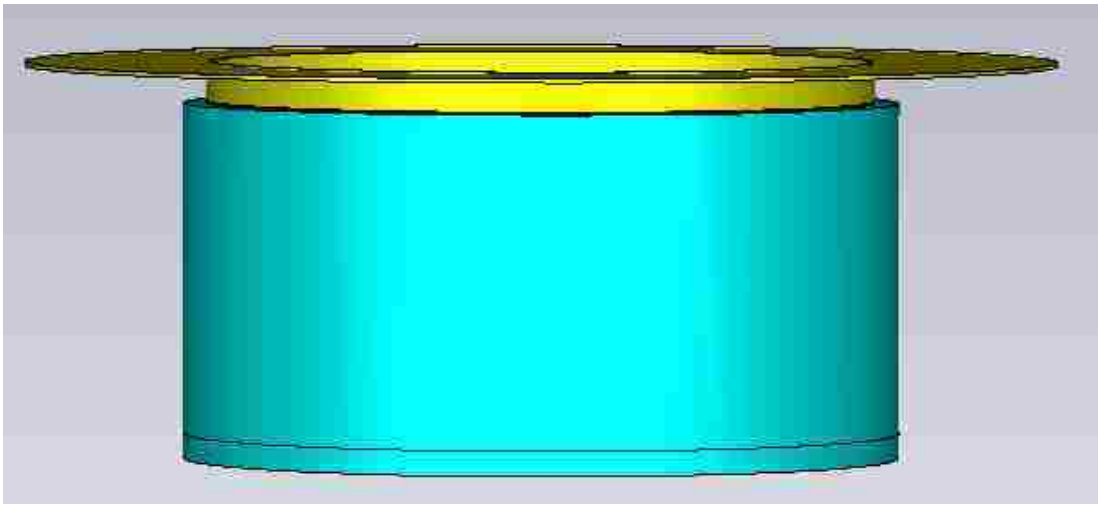

Figure 109: Aperture ring of reduced thickness

A comparison of simulated $S_{1,1}$ performance is shown in Figure 110 where it is seen that little difference exists. Figure 111 and Figure 112 compare realized gain patterns for 2 GHz and 8 GHz, respectively, for both theta and phi. Feed tapers differ by less than 0.5 dB as shown in Table 4: Feed Taper vs. Aperture Ring Thickness, suggesting that the thinner ring could be effective in practice.

Table 4: Feed Taper vs. Aperture Ring Thickness

Frequency, GHz	Taper in θ for 1mm ring, dB	Taper in θ for 9.525mm ring, dB	Taper in φ for 1mm ring, dB	Taper in φ for 9.525mm ring, dB
2	12.81	12.81	14.15	14.25
8	16.60	16.82	20.95	21.44

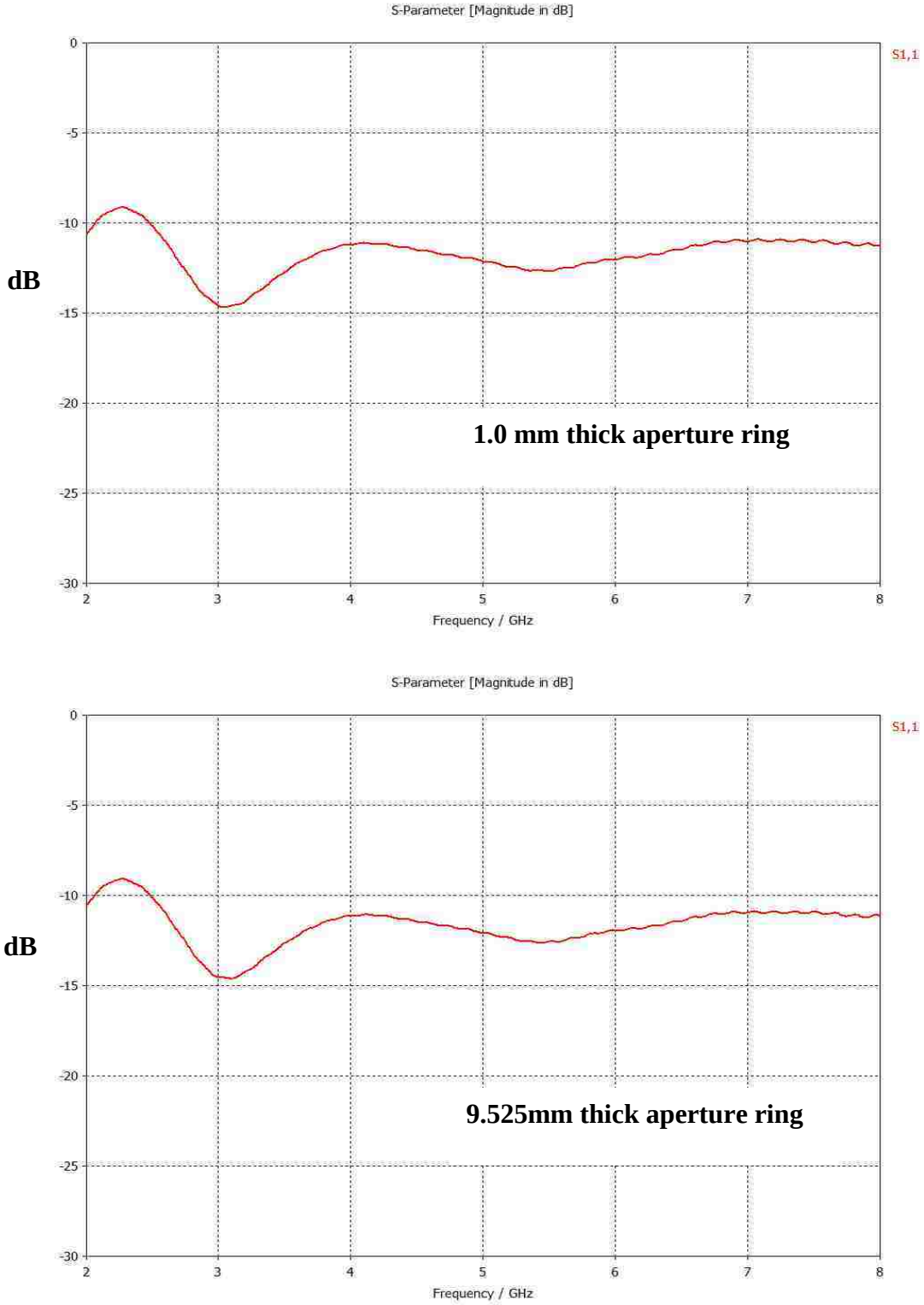

Figure 110: S1,1 comparison of 1mm vs. 9.525mm thick aperture ring

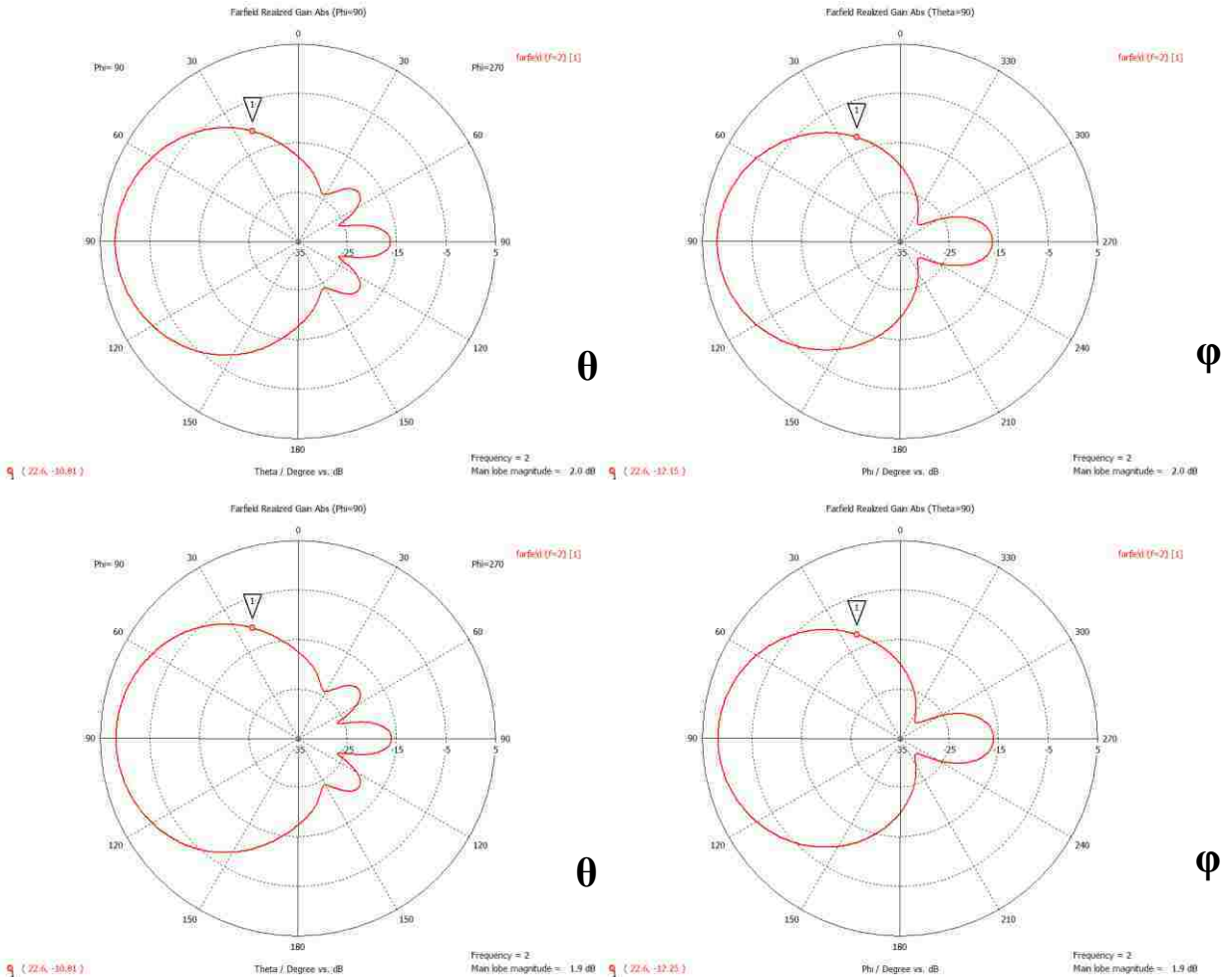

Figure 111: 2GHz realized gain comparison of 1mm vs. 9.525mm thick aperture ring

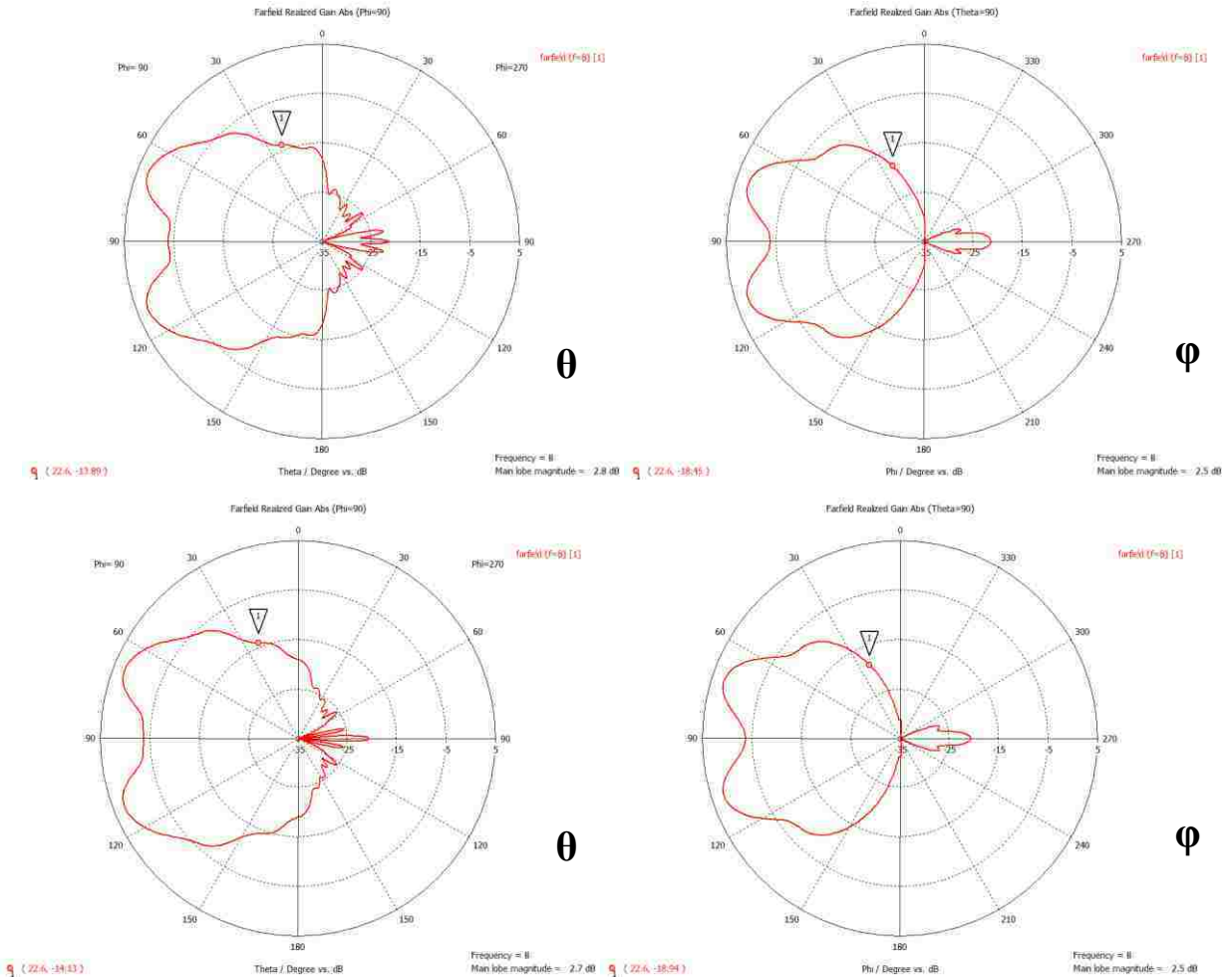

Figure 112: 8GHz realized gain comparison of 1mm vs. 9.525mm thick aperture ring

Fabrication

The diamond feed was built in collaboration with a local company, Electrodynamic, that is experienced in the fabrication of microwave devices. CNC techniques were used to construct the diamond-shaped elements to a tolerance better than 25μm. Detailed build dimensions are shown in Appendix G: Diamond Feed Build Dimensions.

Photos of the completed device are shown in Figure 113.

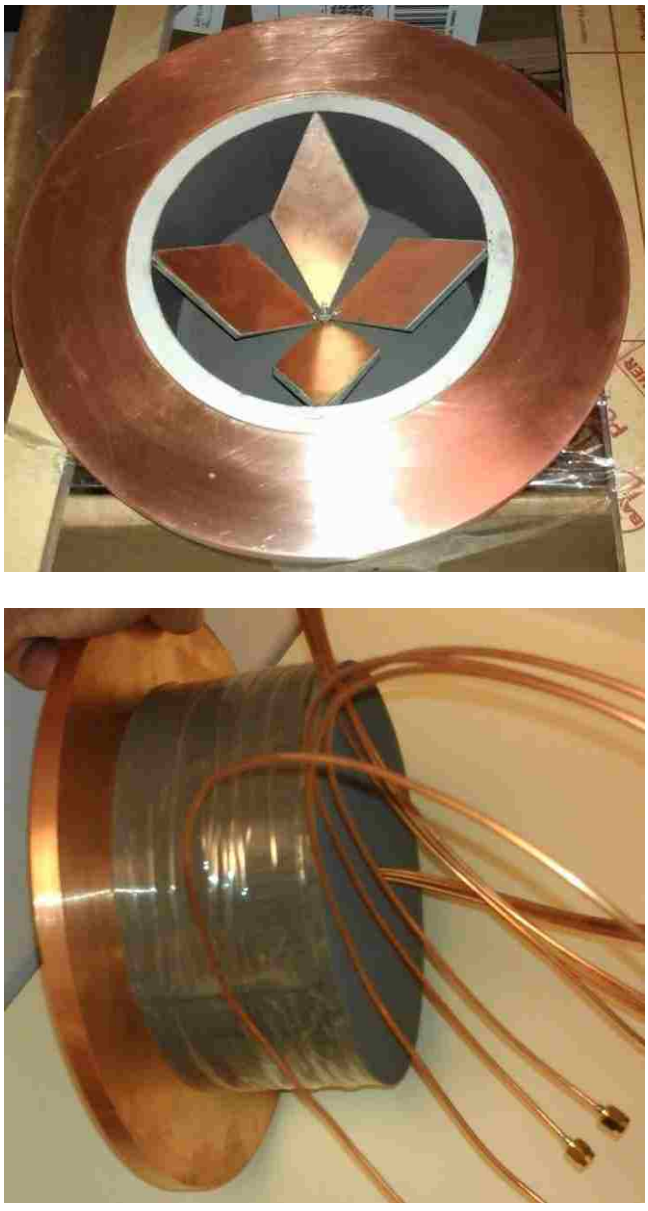

Figure 113: Diamond feed as fabricated, front and side views

Chapter 5: Test Results

Testing was performed at the Wireless Research Center of North Carolina (WRCNC) because they had the capability to perform 3D testing with 1° spatial resolution. WRCNC's test apparatus is a Satimo SG 64 spherical near-field system. A photo of the SG 64 [49] is shown in Figure 114.

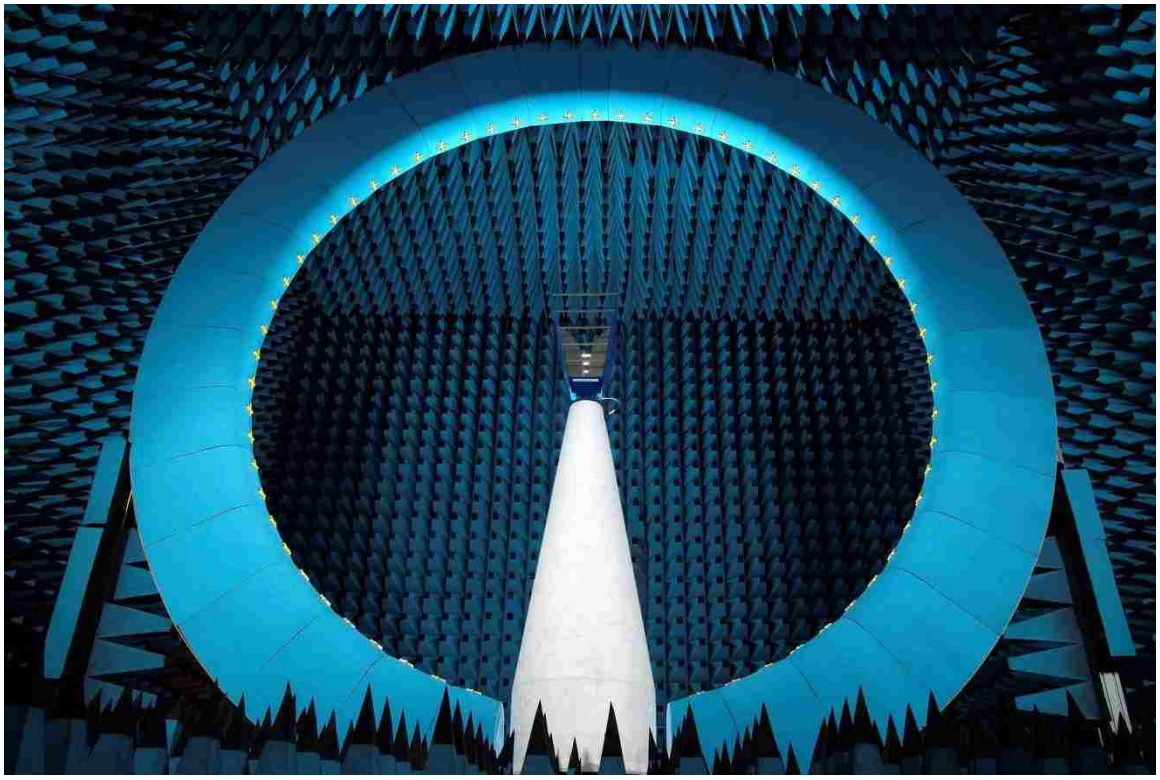

Figure 114: Satimo SG 64 spherical near-field test system

The Satimo system measures the complex field values in two orthogonal polarizations, then performs a transform to yield the far-field. This process is defined in [50] and is discussed in greater detail in [51]. The near-field is sampled at 5.29° samples in theta and phi. The measured near-field values are then fitted with spherical wave expansion, and finally transformed to far-field mathematically.

While the feed was simulated to meet requirements from 0.9 to 12 GHz it was only tested from 2 - 8 GHz due to cost constraints. A suitable broadband balun, such as the Hyperlabs HL9402, cost over $2,000 for which budget was not available.

Additionally, testing over such a wide frequency range with fine spatial resolution would have resulted in increased testing costs. To stay within budget, a relatively inexpensive 2 to 8 GHz,180° degree hybrid coupler manufactured by RF-Lambda was used. If test results were satisfactory and correlated well with simulations over the 2-8 GHz range then there would be some confidence that the feed would perform over a wider frequency range.

The RF-Lambda RFHB02G08GPI coupler has a specified amplitude unbalance of ±0.8dB and phase unbalance of ±8.0° [52]. This level of unbalance did not permit effectively testing the beam squint of the feed. A balun such as the HL9402, with a maximum of ±0.3° phase unbalance, would have been required to better characterize beam squint.

Photographs of the diamond feed in the Satimo test chamber as taken by the WRCNC test technician are shown, where Figure 115 shows the +X and +Y axis directions, and Figure 116 shows the +Y and +Z directions.

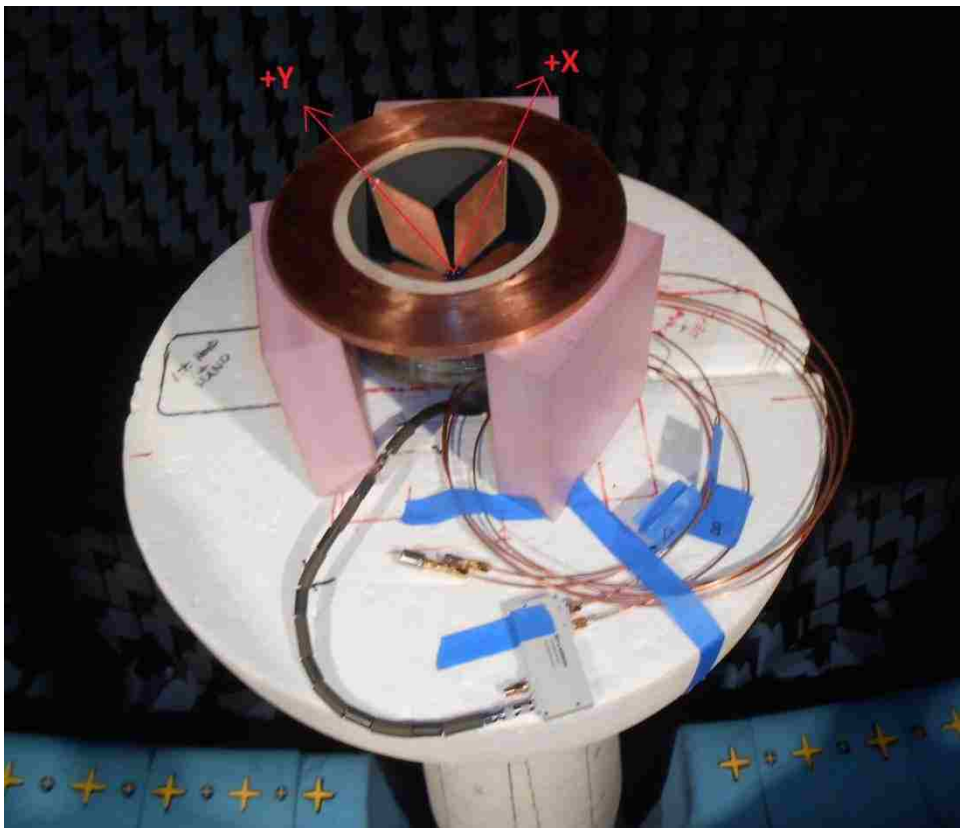

Figure 115: Diamond feed in Satimo test chamber

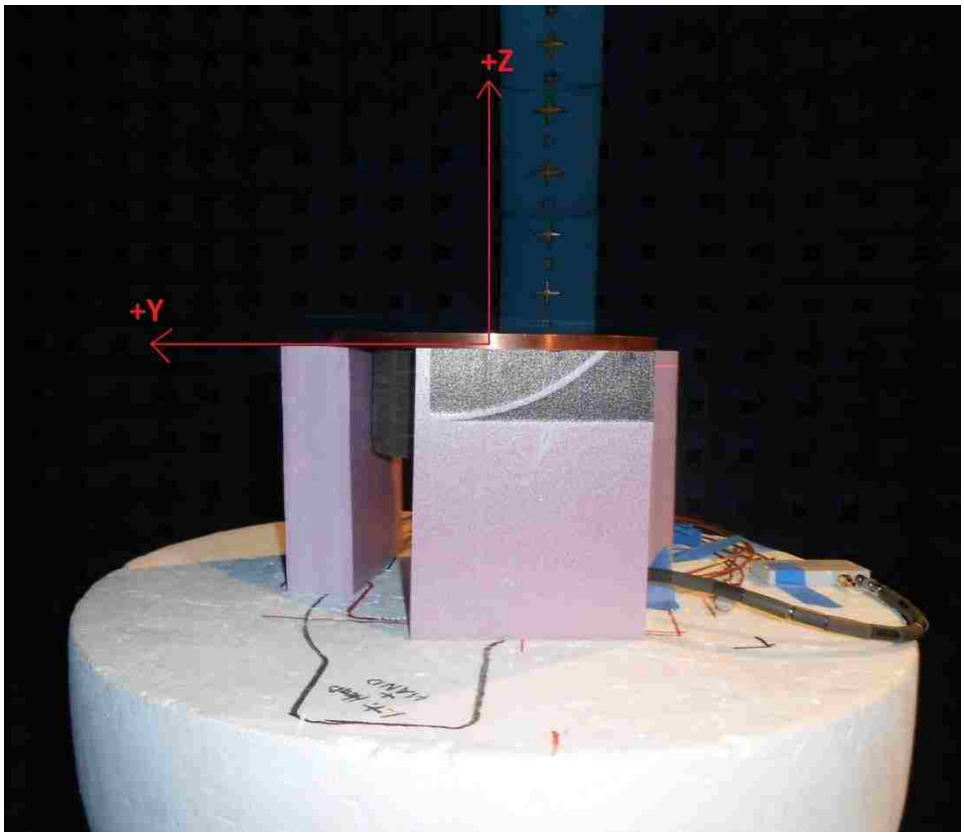

Figure 116: Diamond feed in Satimo test chamber

Only one pair of diamond-shaped radiating elements, those aligned with the X-axis, were driven for testing due to the symmetry of the feed. The 180° hybrid coupler along with 50Ω terminations on the unused coupler port and the unused diamond element pair may be seen in Figure 115.

Summary of Measured Performance

The measured performance of the diamond feed is summarized below in Table 5: Summary of Measured Performance. Each parameter will be examined in greater detail later in this chapter.

Table 5: Summary of Measured Performance

Feature / Parameter	**Target**	**Result**	**Notes**
Bandwidth	1-6 GHz	Meets 2-8 GHz	Limited by coupler
Polar Patterns	Correlation	Good correlation to simulations	
Feed Taper	10 dB	Meets all but 5 GHz (9.4 dB)	Exceeds current RSTN feed taper
Cross-Polarization	10 dB	Meets all but 3 GHz (5.4 dB)	
Phase Center Displacement	< 198.5mm	Meets (66.1mm)	Simulation results, not verified by testing
Physical Size	Fit SRBL	Meets	
Beam Squint	Minimize	1° - 2°	Degraded by coupler phase unbalance and not tested with sufficient spatial resolution
3D Realized Gain Patterns	Correlation	Good resemblance to simulations	

$S_{1,1}$

$S_{1,1}$ was characterized by WRCNC. This was done to expedite testing, and also because they are a certified test facility. Simulation in Microwave Studio and measurement at 6,001 frequency points was performed from 2 - 8 GHz and the results are shown below. At every measured frequency, $S_{1,1}$ was -10 dB or better which meets the performance target, and in general measurements followed the envelope set by simulation. Resonances of a periodic nature are seen in the test data which were not revealed in simulation, as simulations did not model the coupler, cable, or termination used.

A measured value of $S_{1,1}$ of -10 dB ($S_{1,1}$ = 0.1) or better meets the VSWR target of ≤ 3, since

$$VSWR = \frac{1 + S_{1,1}}{1 - S_{1,1}}$$

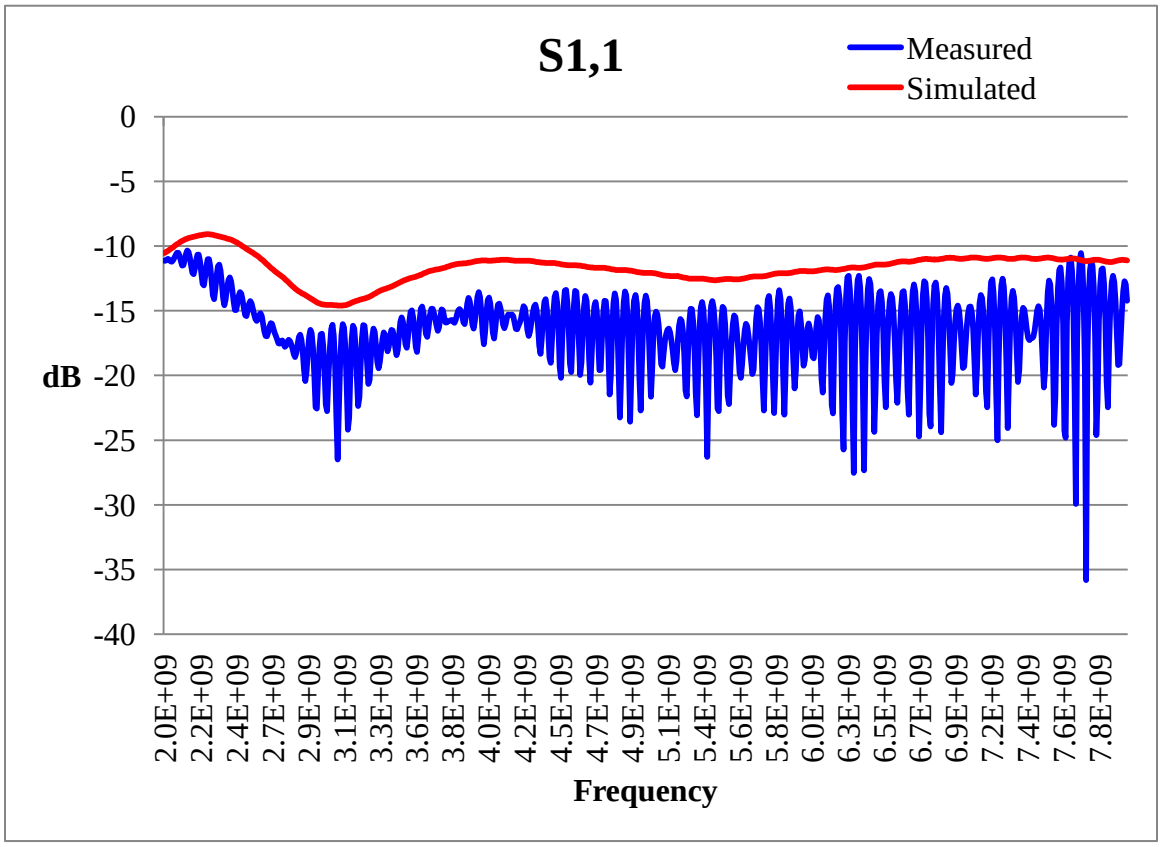

Figure 117: Measured S1,1 for diamond feed from 2-8 GHz

Polar Radiation Patterns

WRCNC performed three-dimensional realized gain pattern testing using the Satimo SG-64 spherical near-field tester. Both the SG-64 and Microwave Studio output pattern data in the form of text files which were subsequently converted to Excel format and then plotted in Matlab.

Figure 118 below shows the coordinate system used for testing. The copper-colored diamond-shaped elements represent the driven elements in the feed for one polarization. The positive X-axis is aligned with one of the elements as shown and is in the plane of the page, the Y-axis is in the plane of the page, and the positive Z-axis is coming out of the page. Two polar plots were constructed for each frequency. One plot is labeled *Theta* and depicts the polar pattern for $\varphi=0°$ when θ is swept through 360°. The other plot is labeled *Phi* and depicts the polar pattern for $\varphi=90°$ when θ is swept through 360°. Both patterns give insight into how well the RSTN dish is illuminated by measuring the feed taper.

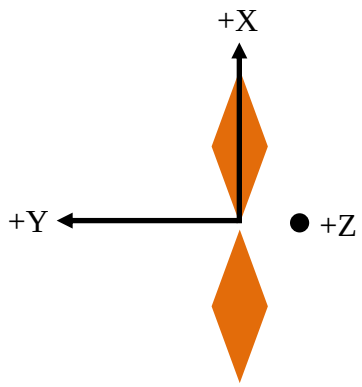

Figure 118: Coordinate system used for testing

Realized gain is the ratio of the power radiated by the antenna to the power accepted by the antenna, thus it accounts for reflection losses at the input. In this test configuration the accepted power is at the input of the 180° hybrid coupler. The coupler has a loss that is not known other than its maximum insertion loss is 1.5dB. The coaxial cable connecting the coupler to the feed has a frequency-dependent loss. Therefore the measured realized gain must be less than the simulated realized gain, as the losses of the coupler and cabling were not simulated.

The frequency-dependent loss per 100m of the coaxial cable is given by the manufacturer at nine frequencies from 400MHz to 18GHz [53]. The losses from 2 to 10 GHz were plotted versus frequency in Excel and a second-order polynomial trend line produced an excellent fit to data, yielding the following equation for the cable loss in dB per 100m as

$$Attenuation\ (dB) = -0.9785f^2 + 30.095f + 45.91$$

where f is the frequency in GHz. The plot is shown below in Figure 119.

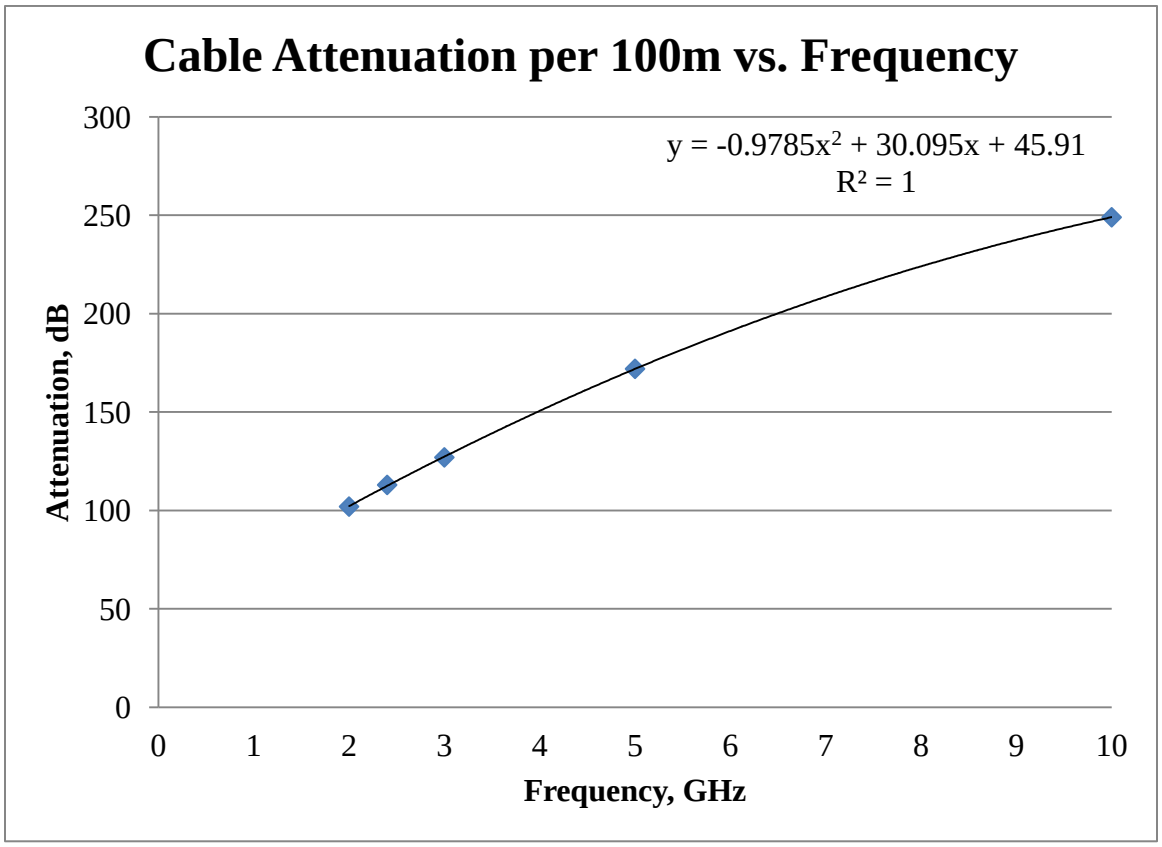

Figure 119: Derived coaxial cable attenuation

At a cable length of 2.1m the frequency-dependent cable attenuation was estimated using the fitting function. To this value was added a 1.5 dB loss factor for the coupler resulting in the correction values tabulated in Table 6: Loss Correction Factors. These corrections were added to the realized gain measurements of the feed and subsequently plotted in polar form.

Table 6: Loss Correction Factors

Frequency, GHz	Cable Loss, dB	Coupler Loss, dB	Correction Factor, dB
2	2.1	1.5	3.6
3	2.7	1.5	4.2
4	3.2	1.5	4.7
5	3.6	1.5	5.1
6	4.0	1.5	5.5
7	4.4	1.5	5.9
8	4.7	1.5	6.2

In general the polar plots show good correlation with simulation. At low frequency the corrected measured realized gain exceeds the simulated value. This may be due to either the cable or the coupler, or both, having less loss than modeled at low frequency.

The most notable difference between simulation and measurement is the shape and amplitude of the back lobes. Some of the discrepancy could be due to phase and amplitude unbalance of the coupler, and the presence of the unshielded coupler and coaxial cable beneath the base of the antenna. None of these were modeled in simulation.

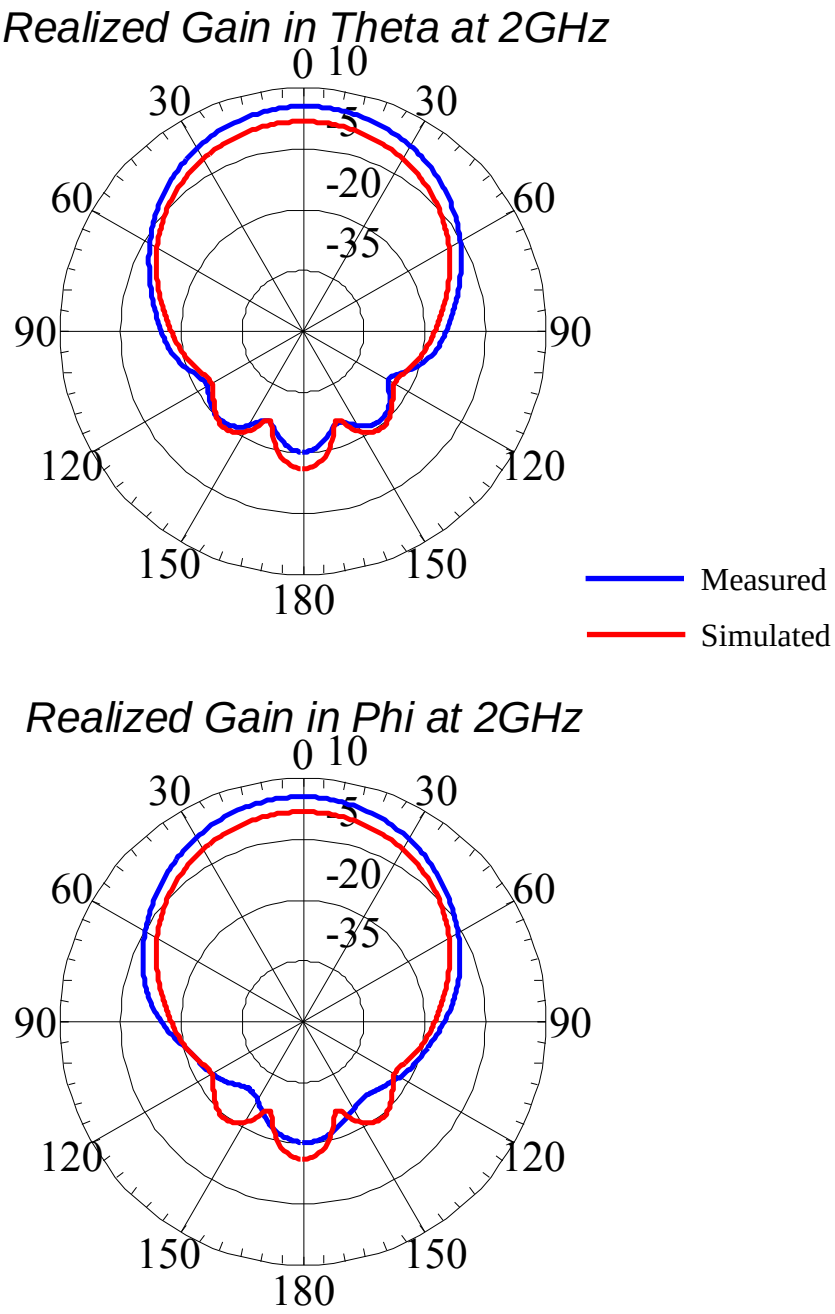

Figure 120: 2 GHz realized gains for theta and phi

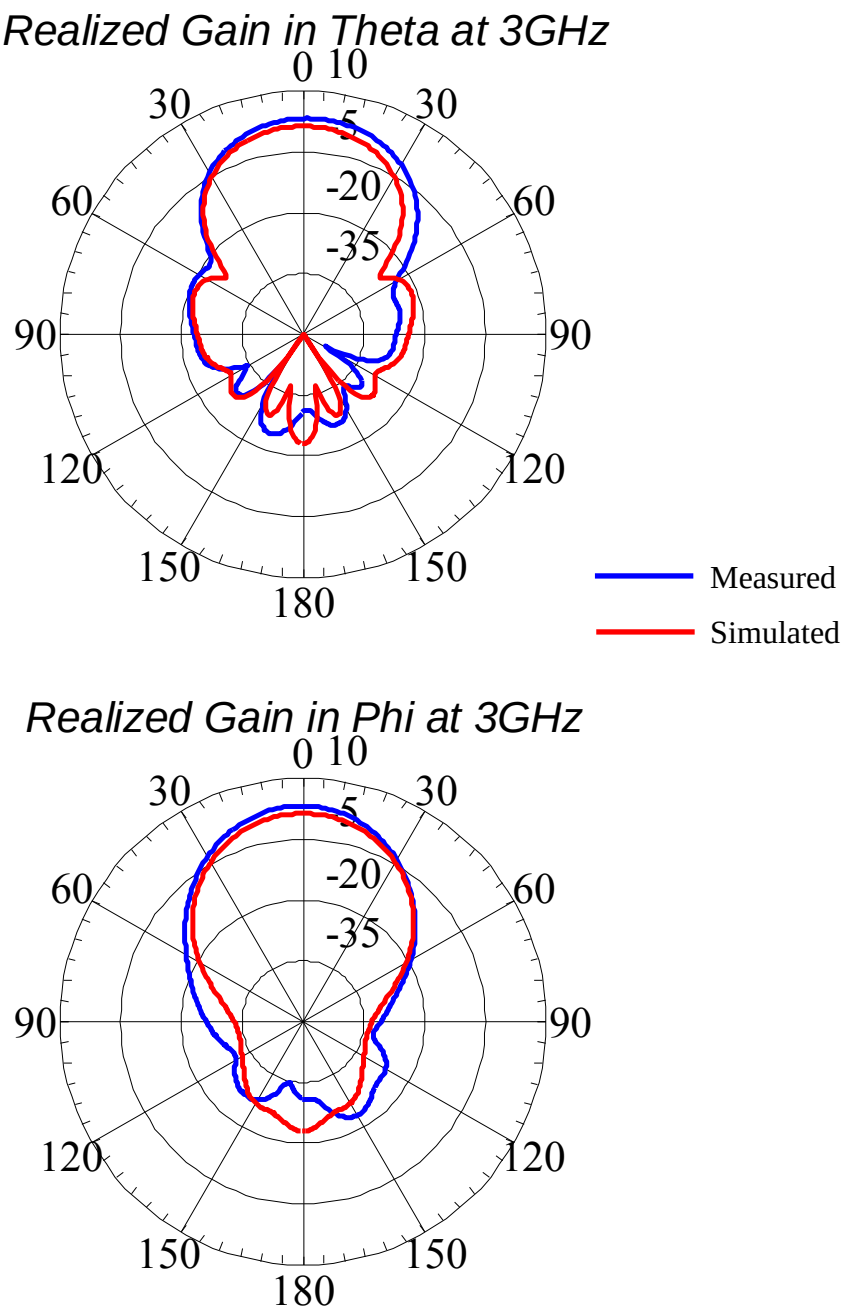

Figure 121: 3 GHz realized gains for theta and phi

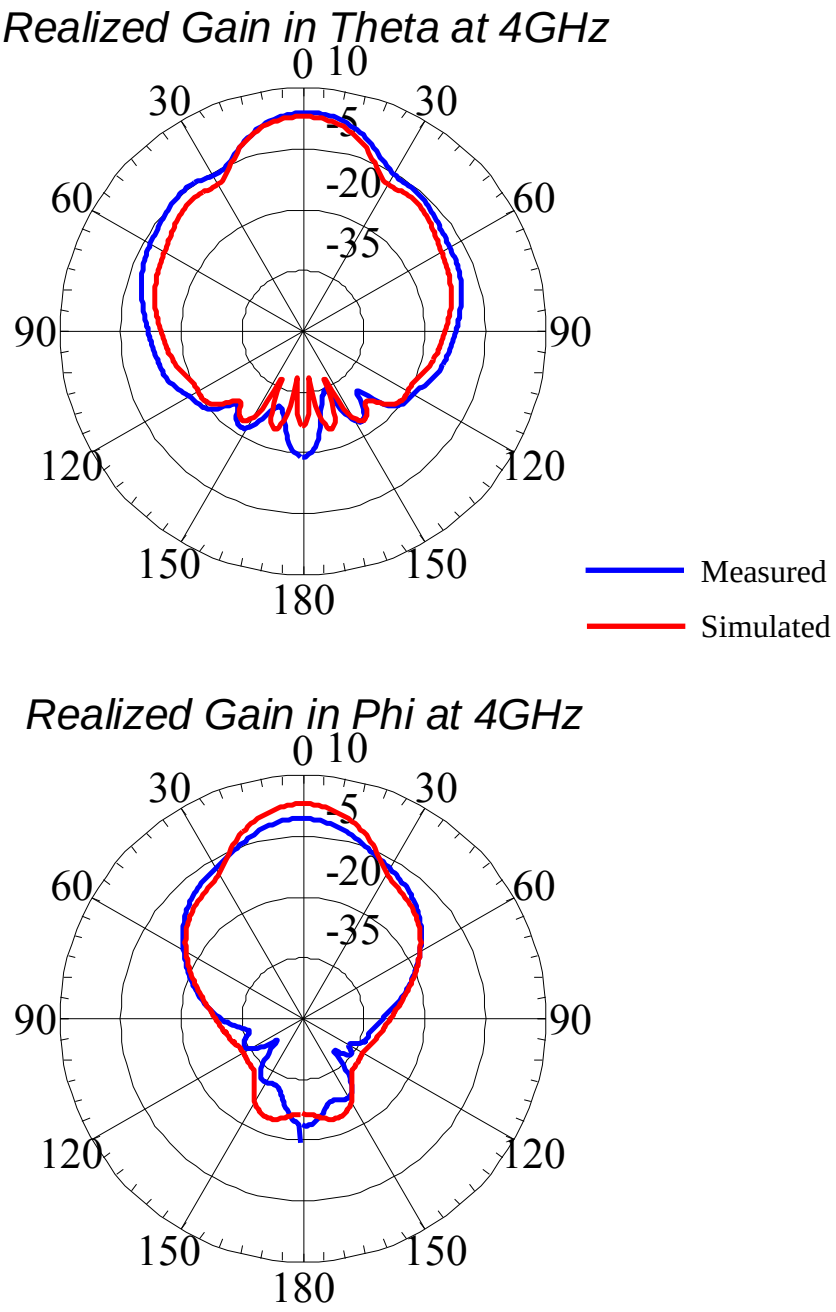

Figure 122: 4 GHz realized gains for theta and phi

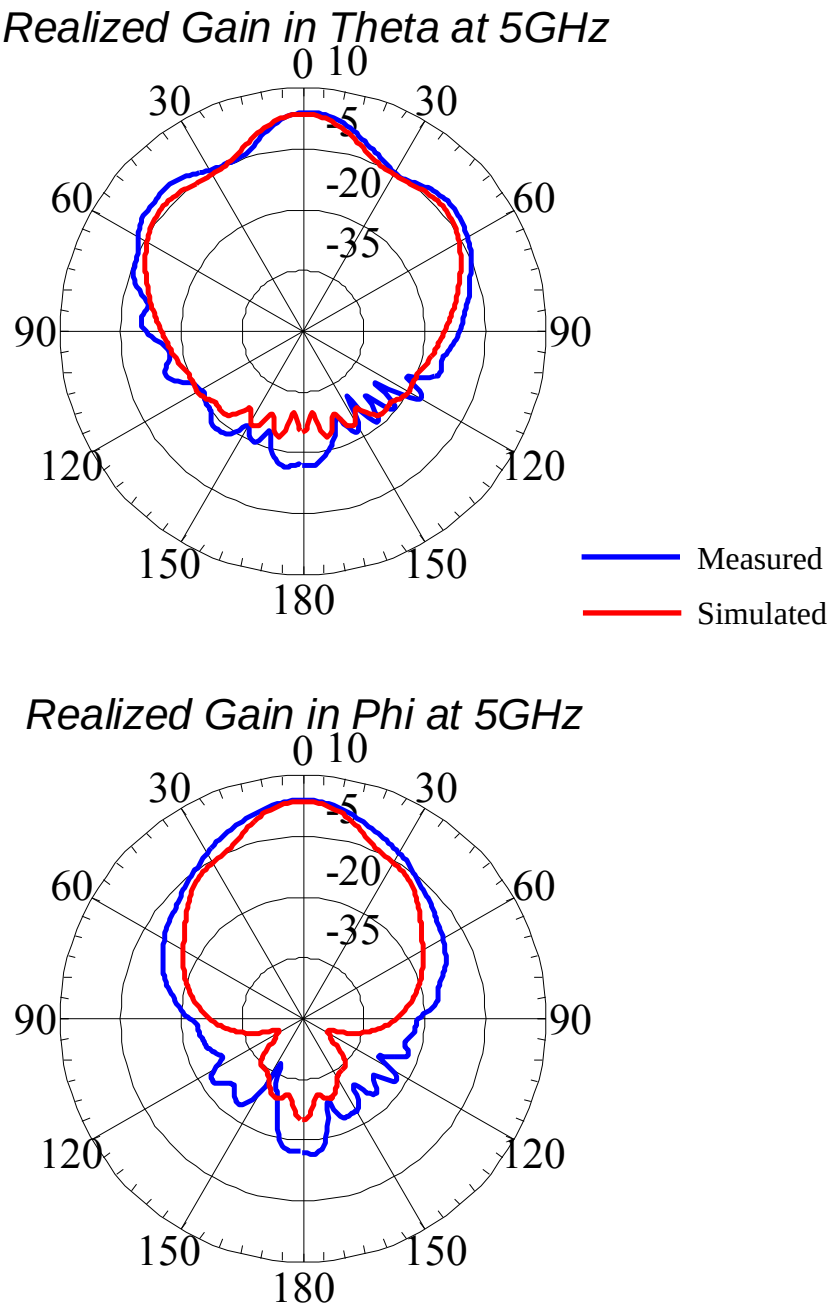

Figure 123: 5 GHz realized gains for theta and phi

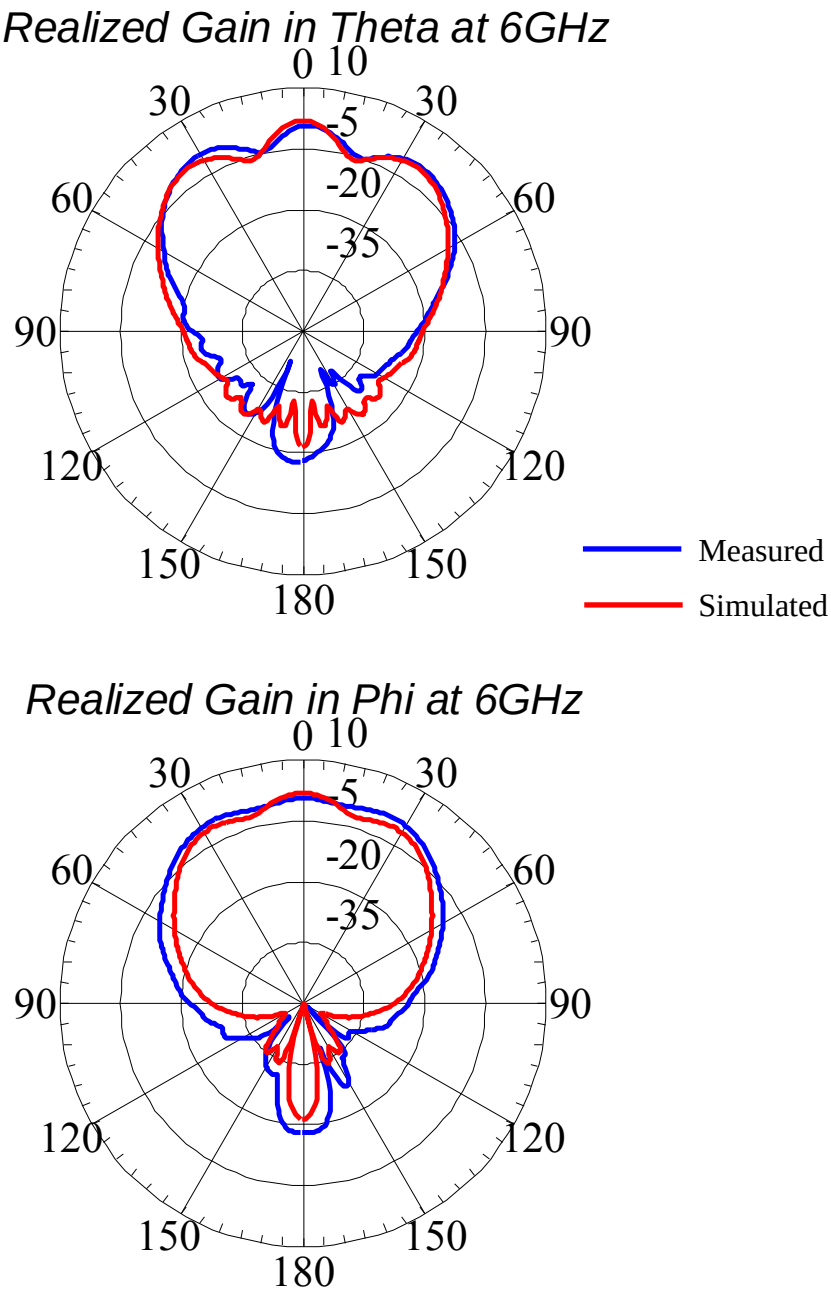

Figure 124: 6 GHz realized gains for theta and phi

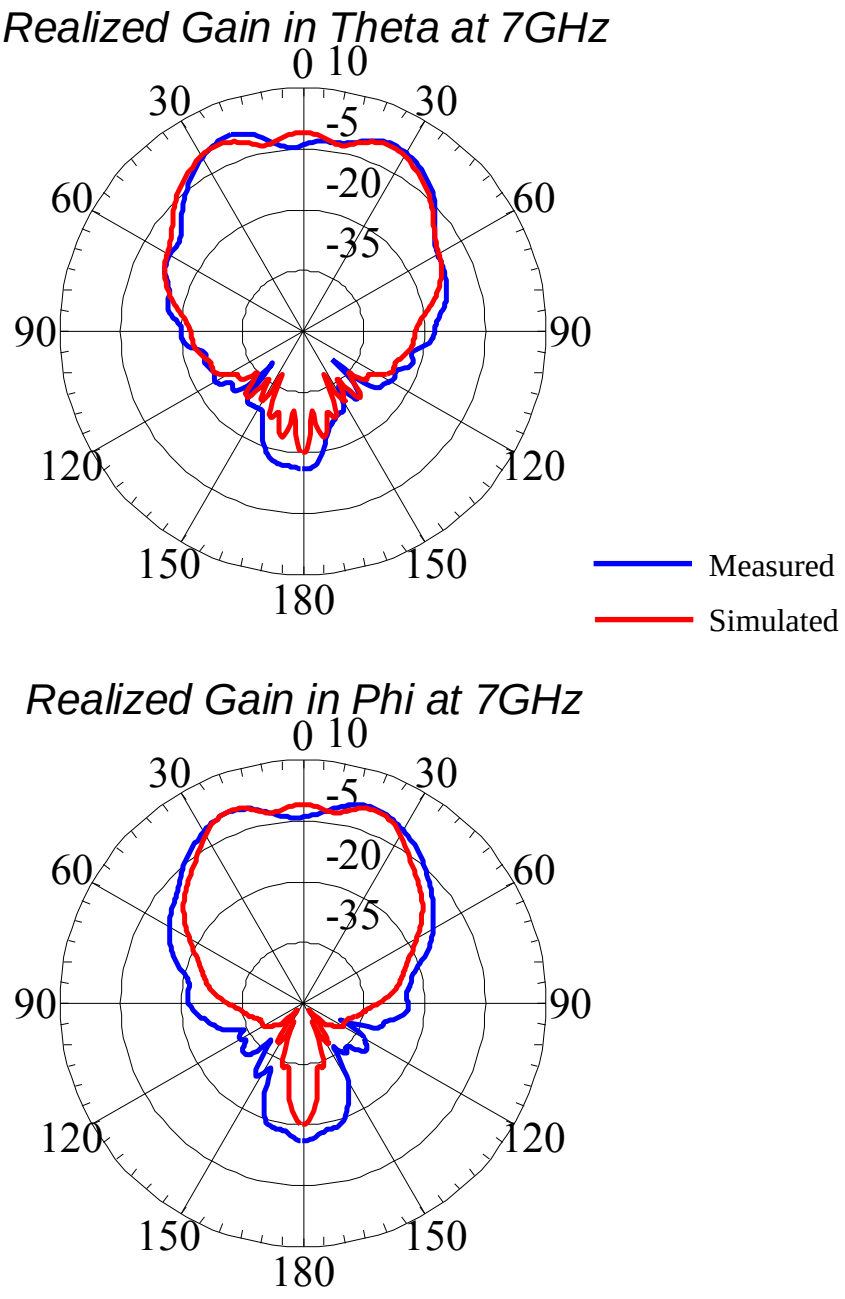

Figure 125: 7 GHz realized gains for theta and phi

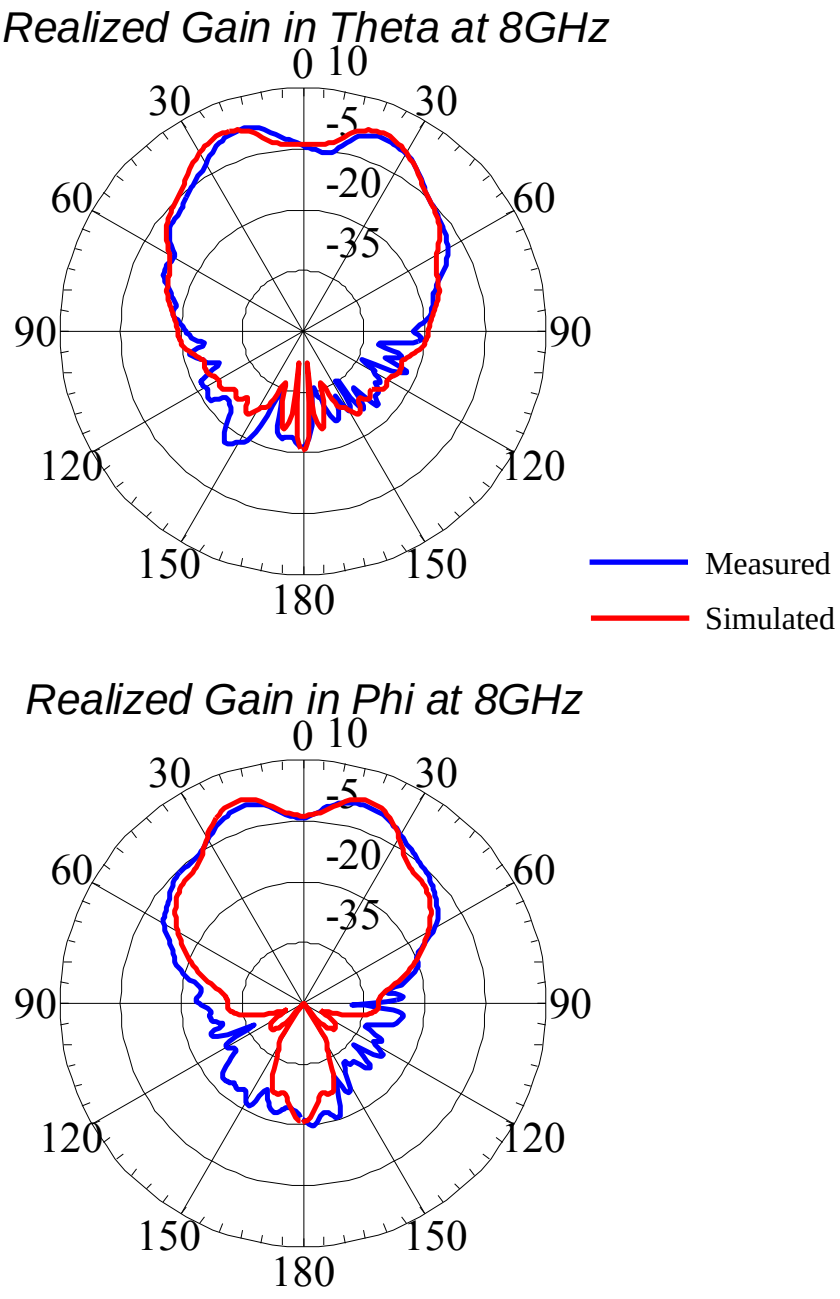

Figure 126: 8 GHz realized gains for theta and phi

Feed Taper

Feed taper is an important parameter because it determines how effectively the dish is illuminated. A low value of taper indicates much spillover, where a very high value indicates that not all of the dish is being illuminated. As previously stated, the optimum range for taper is on the order of 10-22 dB, measured as the difference between the maximum power and the power at dish edge.

The performance target for this parameter was set at 10dB or better. At that time little was known about RSTN's feed taper as it was a system implemented in the 1960's and no documentation was available. Information later became available stating that three of the RSTN frequencies, 1.415GHz, 2.695GHz, and 4.995GHz, were implemented as half-wave dipoles located a quarter-wave above a ground plane.

Feed taper values were derived from test data provided by WRCNC by subtracting the realized gain at dish edge, ±67.4°, from the maximum gain. The results are listed in Table 7: Simulated vs. Measured Feed Taper Values with the result that all measured feed taper values met exceeded the 10dB target except for 5GHz, where the taper was 9.4 dB. The taper in Phi exceeded that of the current RSTN feed therefore the diamond feed should better illuminate the RSTN dish than the current Kelvin feed.

Table 7: Simulated vs. Measured Feed Taper Values

	Simulated		Measured	
Frequency, GHz	**Theta**	**Phi**	**Theta**	**Phi**
2	12.7	14.2	14.2	12.5
3	22.8	26.4	23.4	22.8
4	14.3	22.9	11.4	18.5
5	11.5	21.7	9.4	16.5
6	14.0	18.8	14.8	12.7
7	13.6	22.7	14.3	15.9
8	16.8	21.4	14.9	15.8

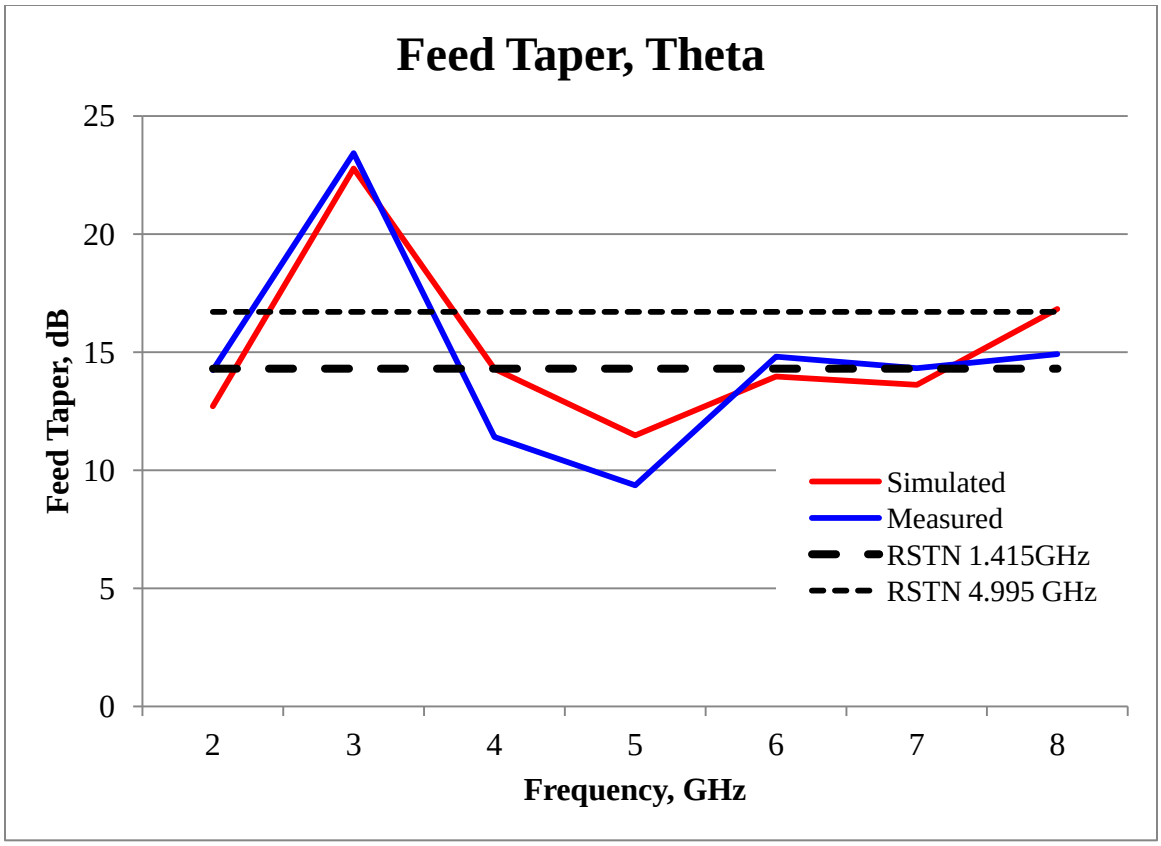

Figure 127: Feed taper for theta

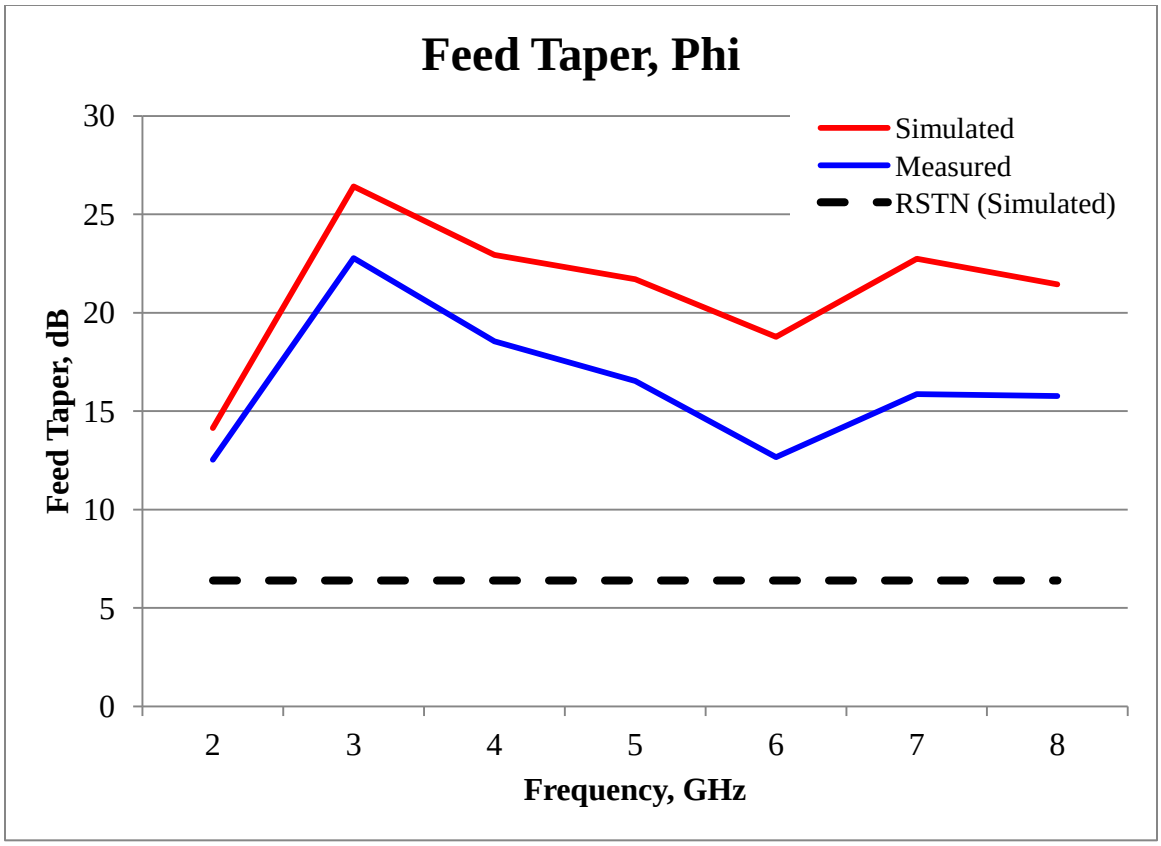

Figure 128: Feed taper for phi

Cross-Polarization

Cross-polarization is a measure of the polarization purity of an antenna as it expresses the ratio of the desired polarization to the orthogonal polarization detected by the antenna. The performance target for cross-polarization was set to be 10dB or better over the ±67.4° subtended by the dish.

As before, with the radiating elements oriented as shown in Figure 118, E(Theta) represents the co-polarization and E(Phi) the cross-polarization. An examination of the data showed that the cross-polarization target was met for all test frequencies except for 3GHz, as shown in Table 8 below and in the following polar plots.

Table 8: Co- and Cross-Polarization

Frequency, GHz	Co-Polarization, dB	Cross-Polarization, dB	Difference, dB
2	-12.3	-37.7	25.4
3	-25.5	-30.0	4.5
4	-11.9	-29.6	17.7
5	-10.3	-36.5	26.2
6	-19.5	-39.9	20.4
7	-18.9	-38.5	19.6
8	-19.2	-30.3	11.1

Further simulation studies suggests that the degradation in cross-polarization exhibited at 3 GHz may be due to misalignments, and are discussed in Chapter 6: Conclusions.

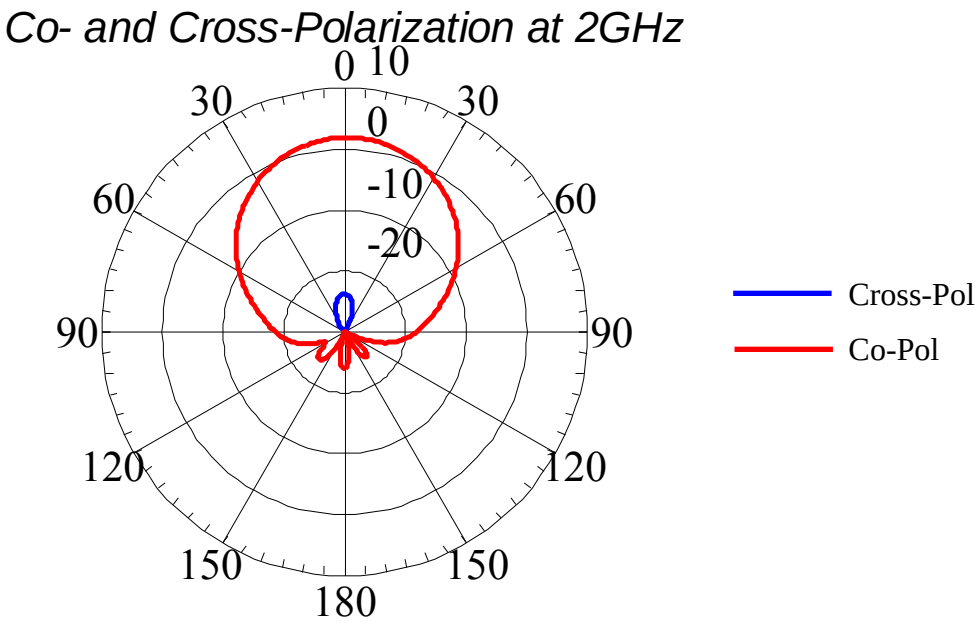

Figure 129: 2 GHz polarization plot

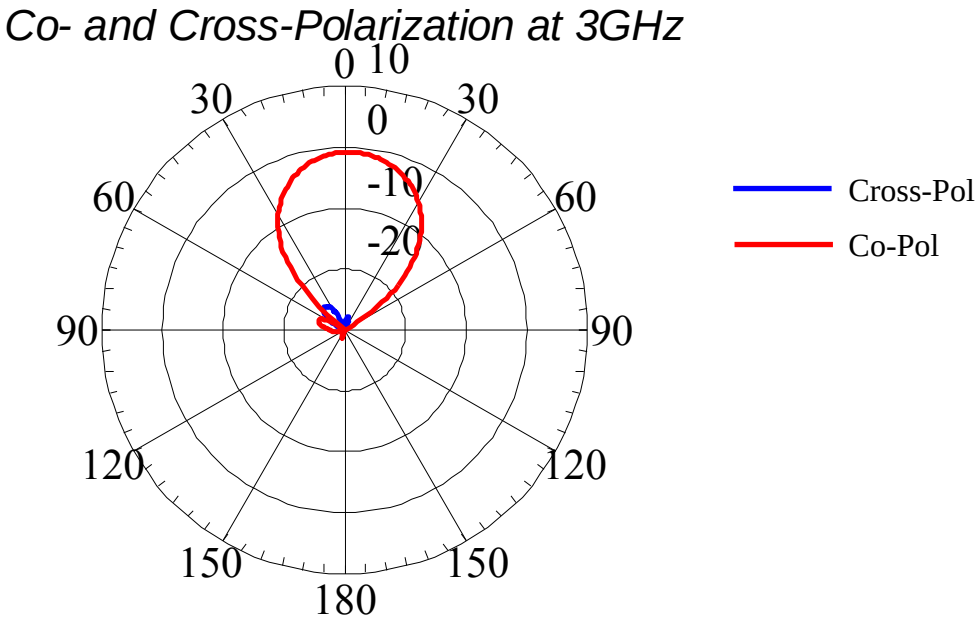

Figure 130: 3 GHz polarization plot

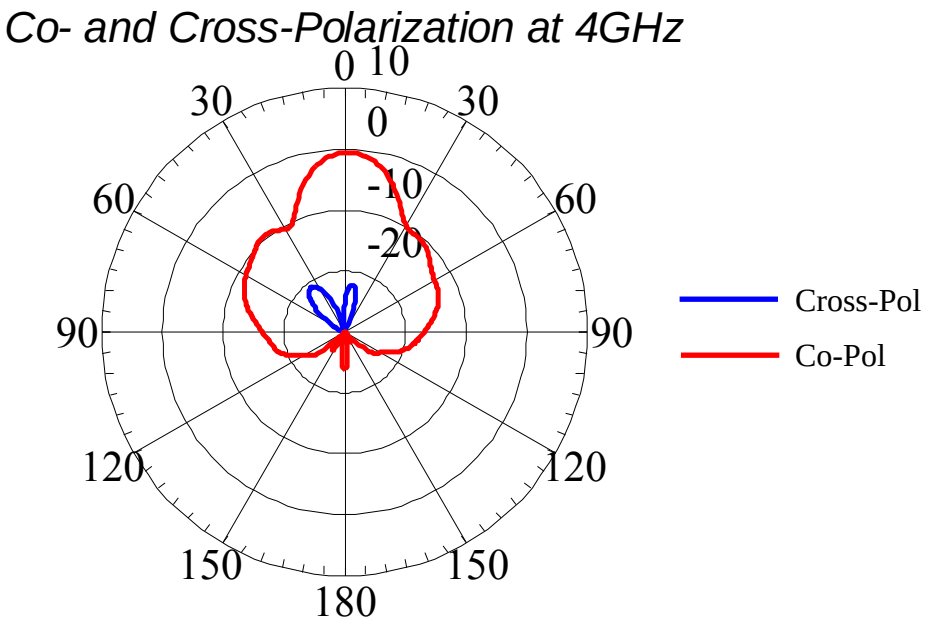

Figure 131: 4 GHz polarization plot

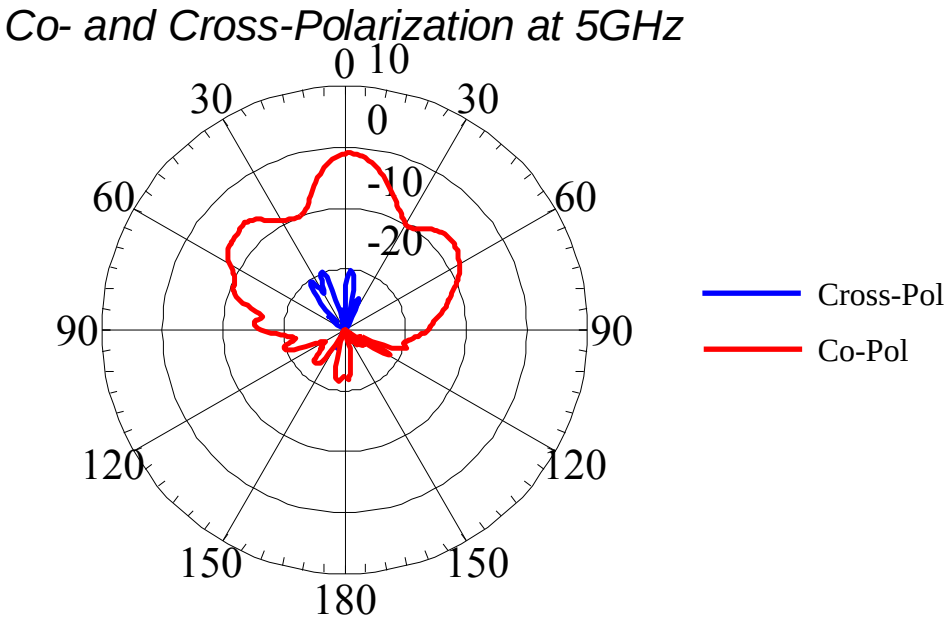

Figure 132: 5 GHz polarization plot

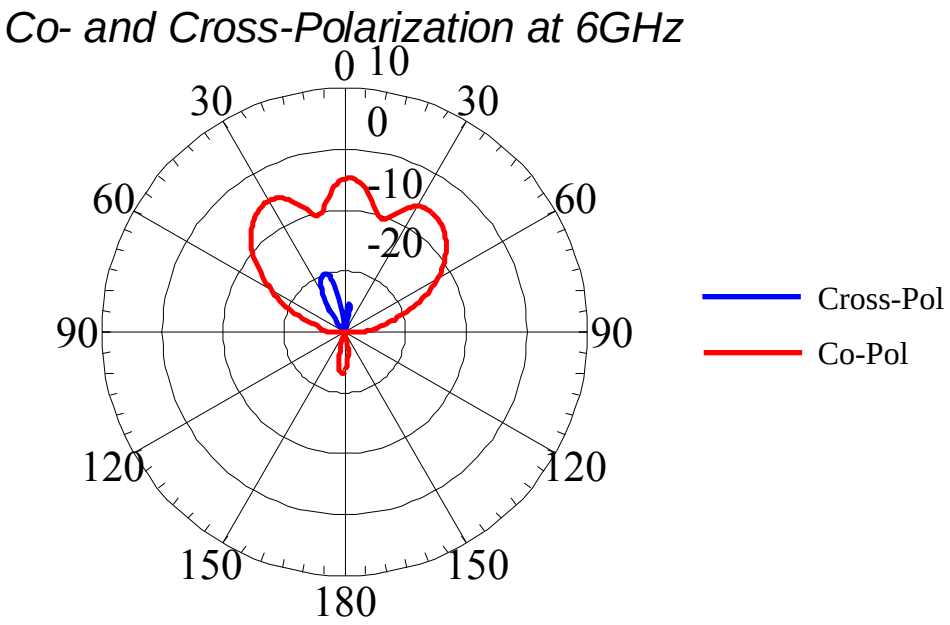

Figure 133: 6 GHz polarization plot

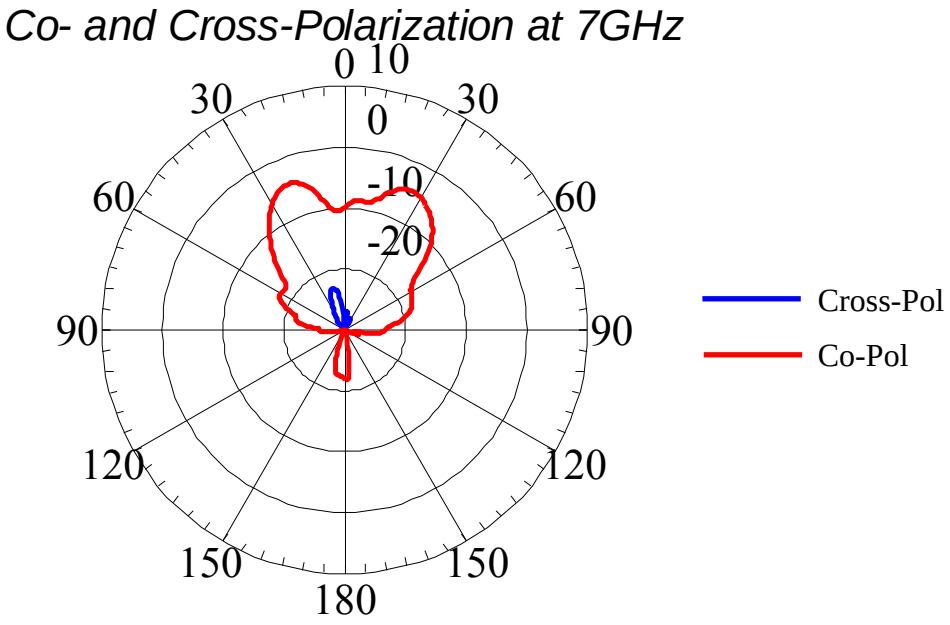

Figure 134: 7 GHz polarization plot

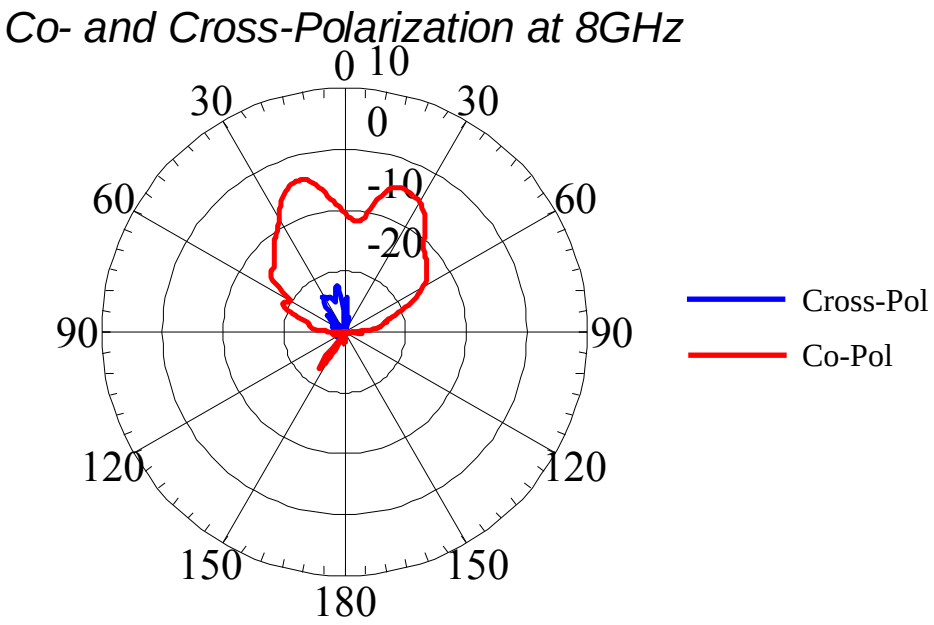

Figure 135: 8 GHz polarization plot

Phase Center Displacement

As previously discussed, large displacements of the phase center give rise to defocusing losses. Neither UNM nor WRCNC had the equipment to measure the location of the phase center so only simulation results can be presented as shown in Table 9 below. The performance target was to exceed the phase center movement of the TECOM 201302 LPDA feed used at the Owens Valley Solar Observatory. Its movement was estimated to be on the order of 198mm. The maximum movement of the phase center of the diamond feed was simulated to be 66.1mm.

Table 9: Simulated Phase Center Displacement

Frequency	Simulated Phase Center Location, mm
0.9	38.7
1	56.4
2	88.2
3	55.1
4	88.9
5	95.0
6	104.8
7	77.1
8	81.4
10	101.2
12	99.0

Physical Dimensions

The diamond feed was designed to fit into a SRBL cavity with little modification so that the feed could be used in a functional solar radio telescope, and to be of a size to cause only minor modification to the housing should it be installed in a RSTN system. These design targets were met.

Table 10 below compares the sizes of the SRBL and RSTN housings to the diamond feed and the TECOM LPDA. The diamond feed fits into the SRBL housing with minimal modification. The ring of the diamond feed is 50mm larger in diameter than the RSTN housing. This is acceptable as the RSTN housing would have been modified in any event should a new feed be installed. As a point of reference the TECOM LPDA is too large in diameter to fit into the RSTN housing.

Table 10: Physical Dimensions

System / Feed	Diameter, mm	Height, mm
SRBL	175	100
RSTN	200	> 400
Diamond Feed	160 (base) 250 (ring)	90
TECOM LPDA	203	240

Figure 136 depicts a photo of a SRBL system [54] with a scale drawing of the diamond feed in black and orange, showing how the diamond feed could mount into a SRBL system.

Figure 136: Mock up of diamond feed mounted in a SRBL system

3D Radiation Patterns

Three-dimensional (3D) radiation patterns were simulated in Microwave Studio and tested at WRCNC's test facility using the Satimo SG-64. Both simulations and measurements were performed with 1° spatial resolution.

Screenshots of measured vs. simulated 3D radiation patterns depicting realized gain are shown on the following pages. Measured patterns are at the top and simulated patterns are at the bottom. Each plot contains 131,044 data points.

Measured patterns were displayed using software provided by Satimo, MWShowOGL, whereas simulated patterns are displayed in Microwave Studio. MWShowOGL only has one color ramp and the data cannot be normalized whereas Microwave Studio has four color ramps and both normalization and display range can be set by the user. Microwave Studio patterns were therefore normalized and ranged to match MWShowOGL, and the color ramp Farfire was chosen as it most closely matches that of MWShowOGL.

In general there is good correlation between simulated and measured patterns looking down the bore sight, i.e., along the Z-axis. This is the most important correlation as it concerns how the dish is illuminated. Less correlation is seen when comparing side profiles of simulated versus measured patterns such as when looking down the Y-axis. Discrepancies are to be expected since the phase and amplitude unbalances of the coupler were not modeled, nor was the presence of the unshielded cabling and coupling in the test set up.

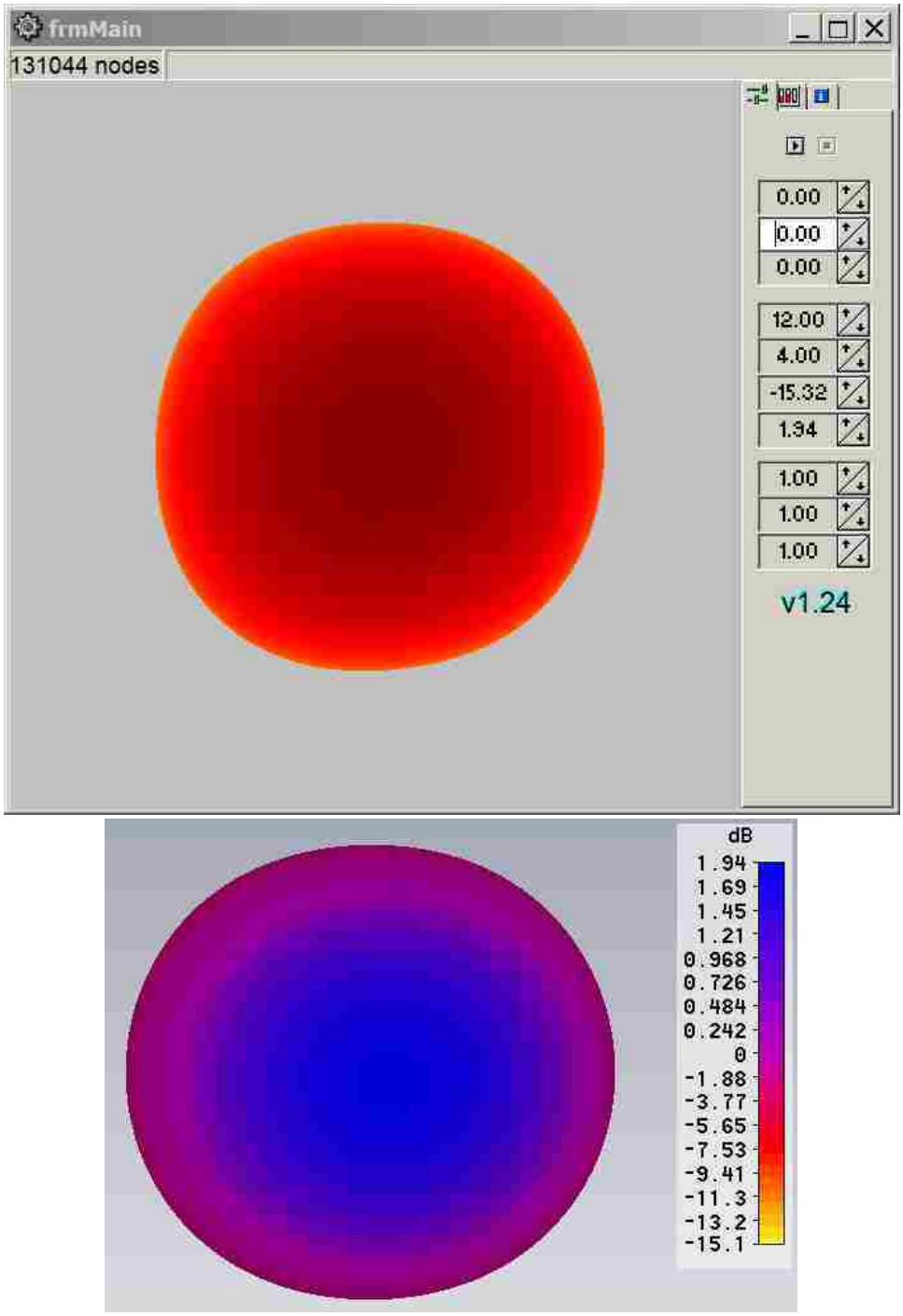

Figure 137: 2 GHz realized gain patterns, measured (top) and simulated (bottom)

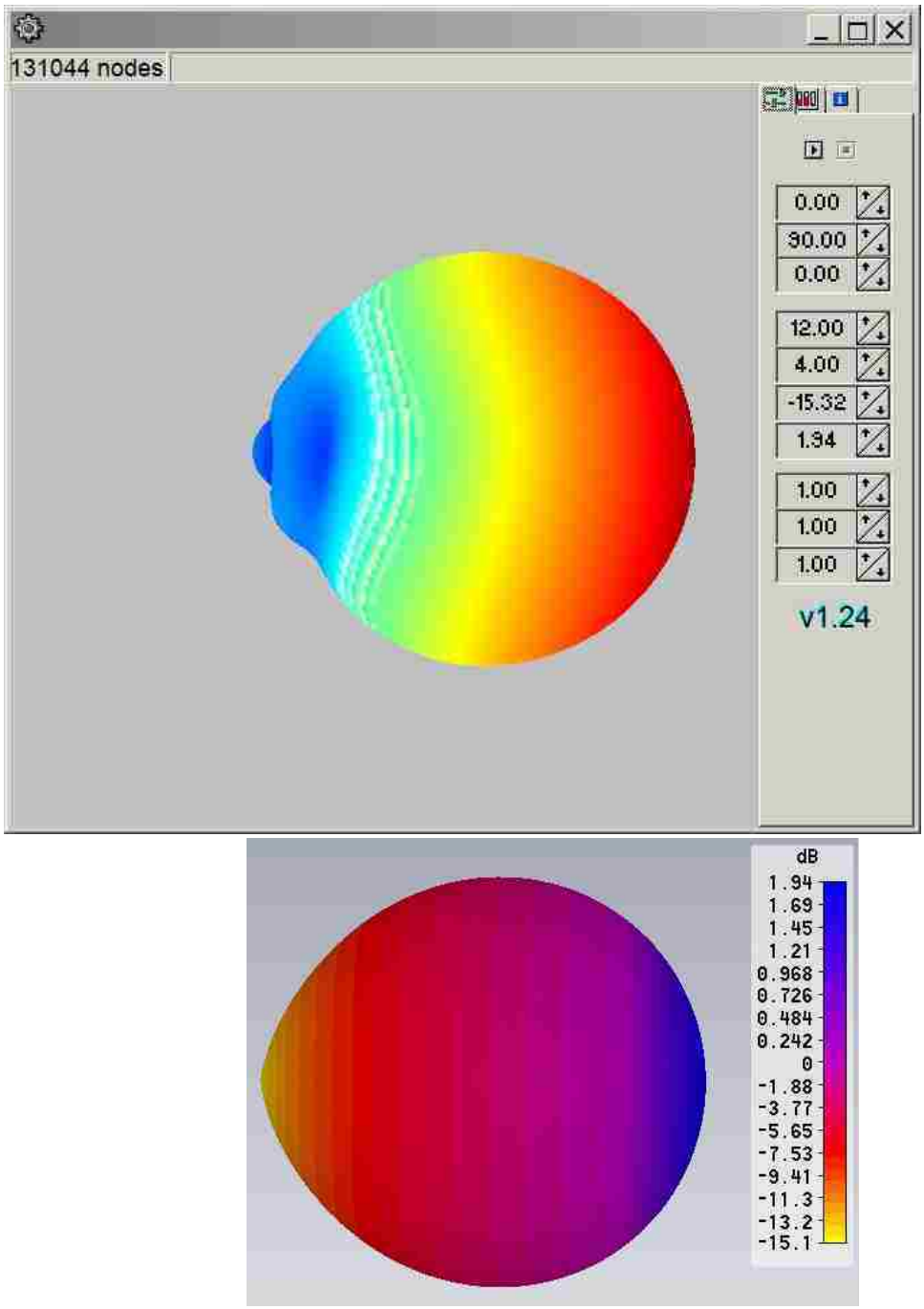

Figure 138: 2 GHz 3D realized gain, measured (top) and simulated (bottom)

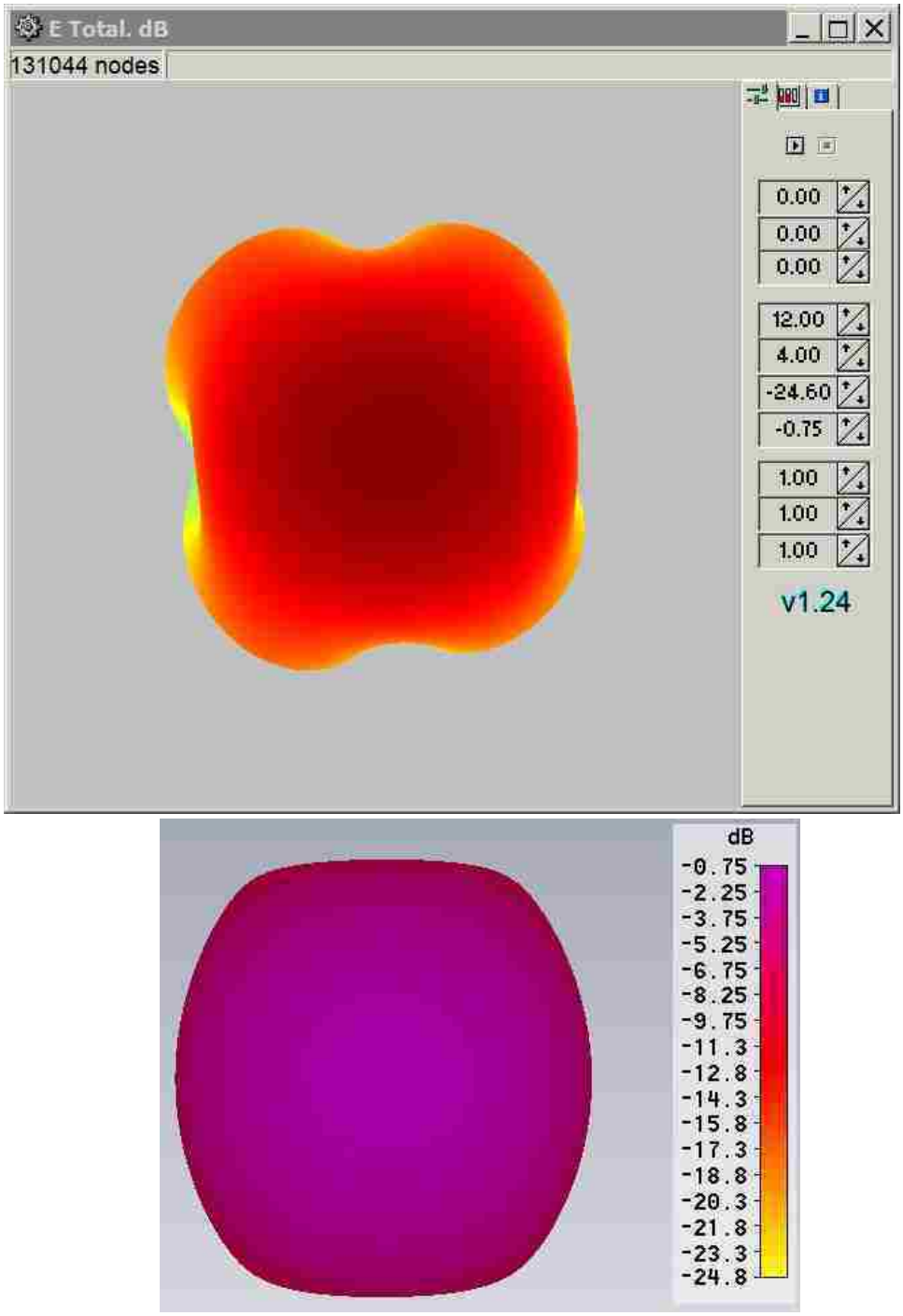

Figure 139: 3 GHz 3D realized gain, measured (top) and simulated (bottom)

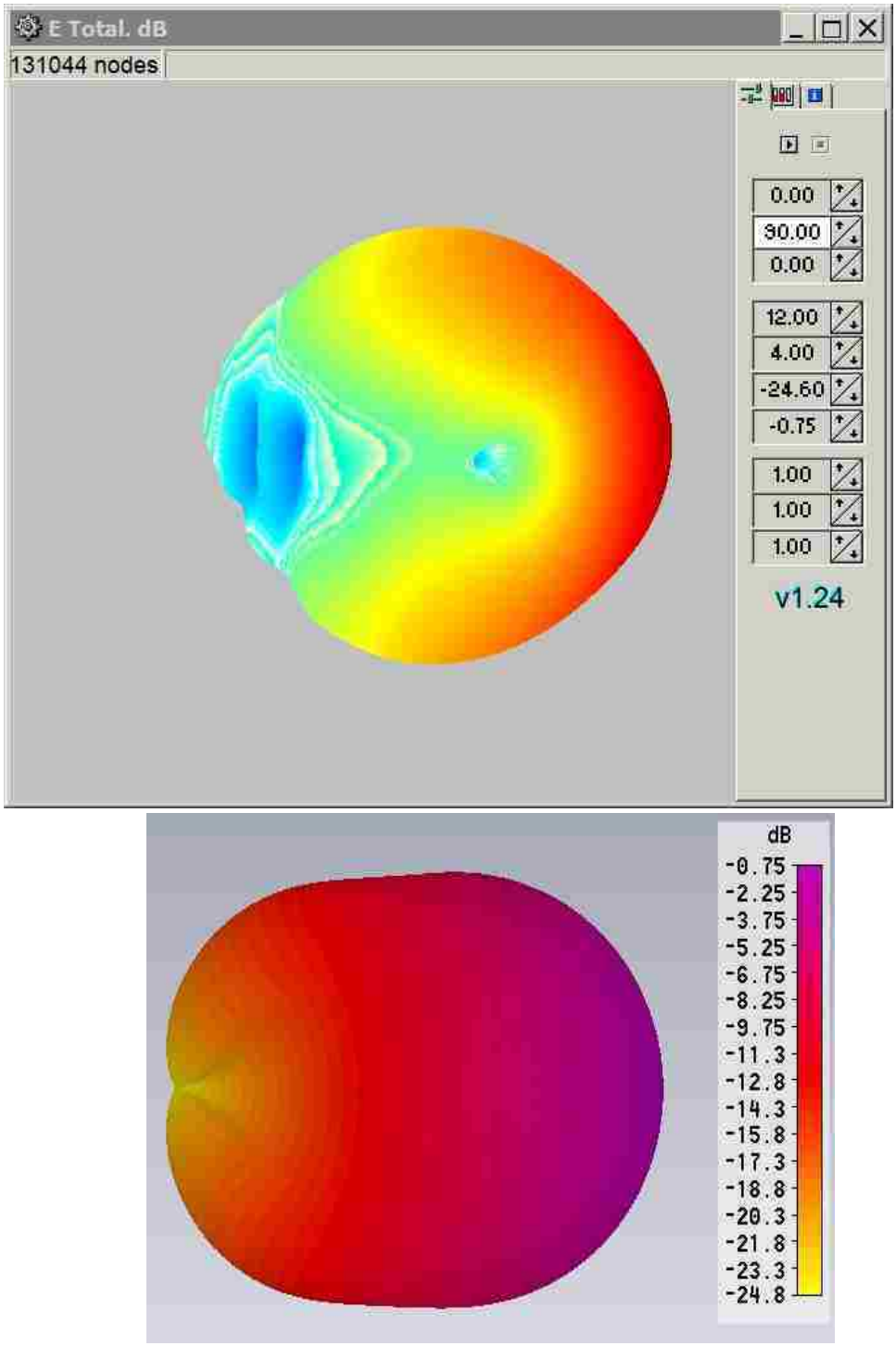

Figure 140: 3 GHz 3D realized gain, measured (top) and simulated (bottom)

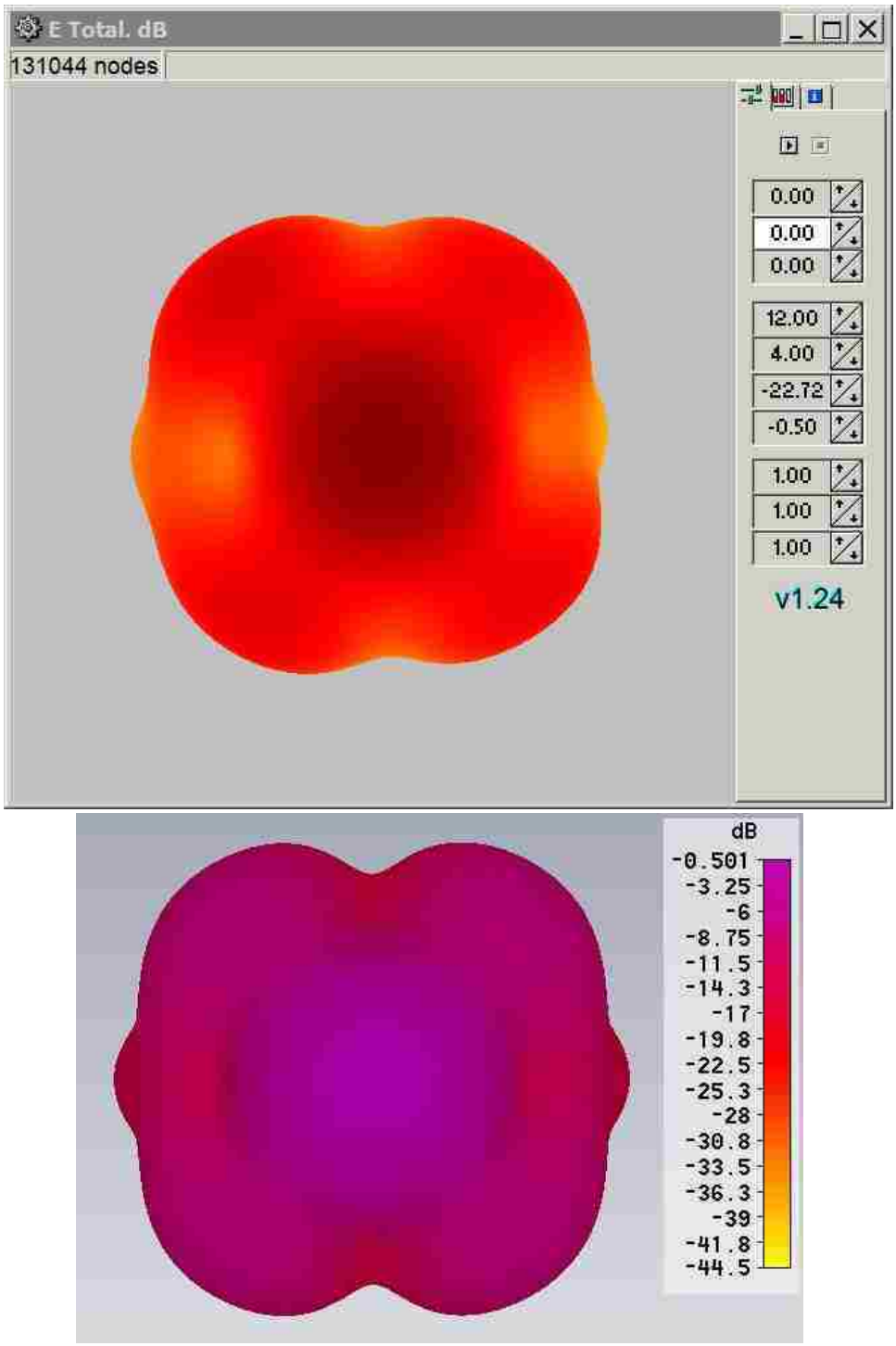

Figure 141: 4 GHz 3D realized gain, measured (top) and simulated (bottom)

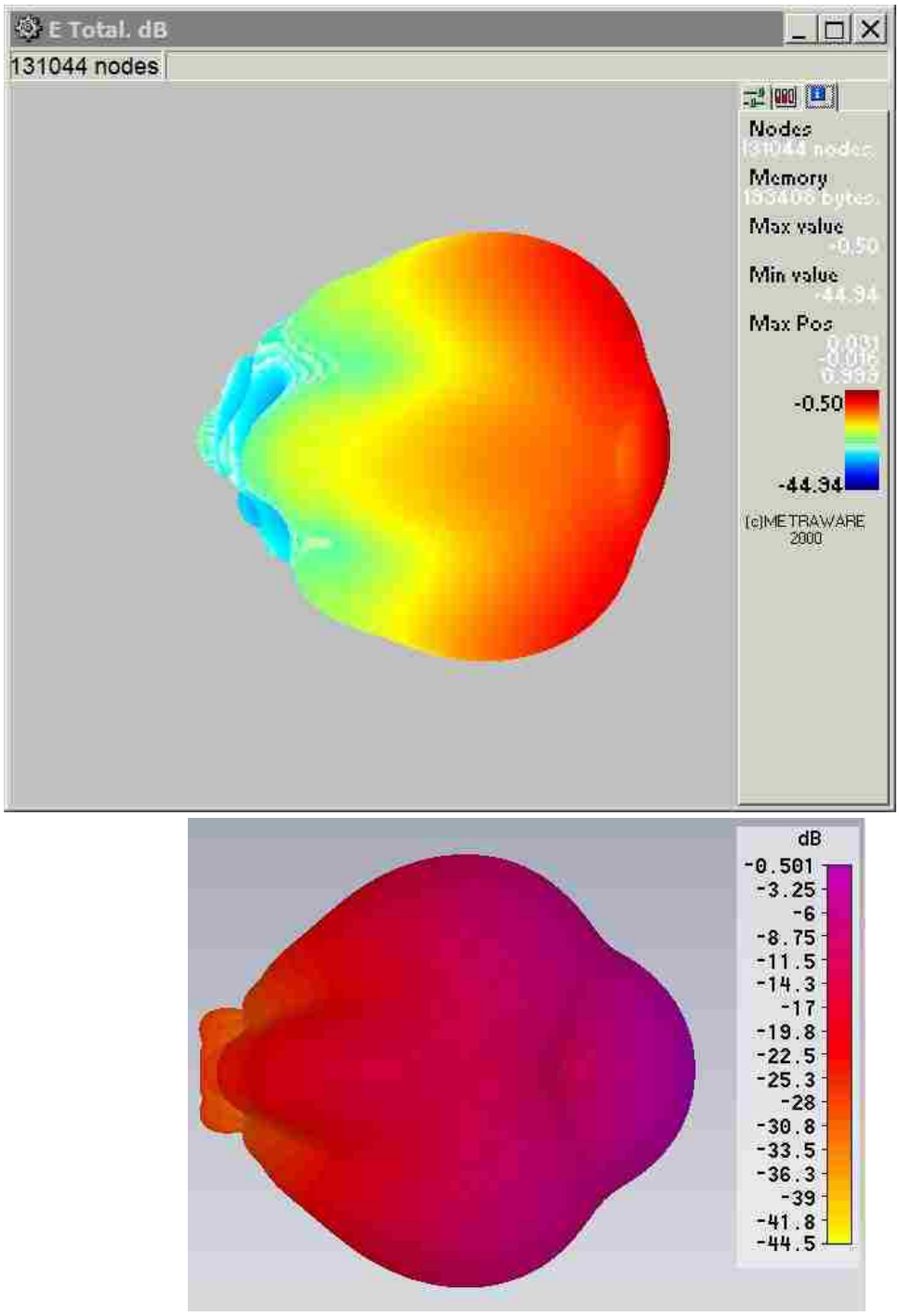

Figure 142: 4 GHz 3D realized gain, measured (top) and simulated (bottom)

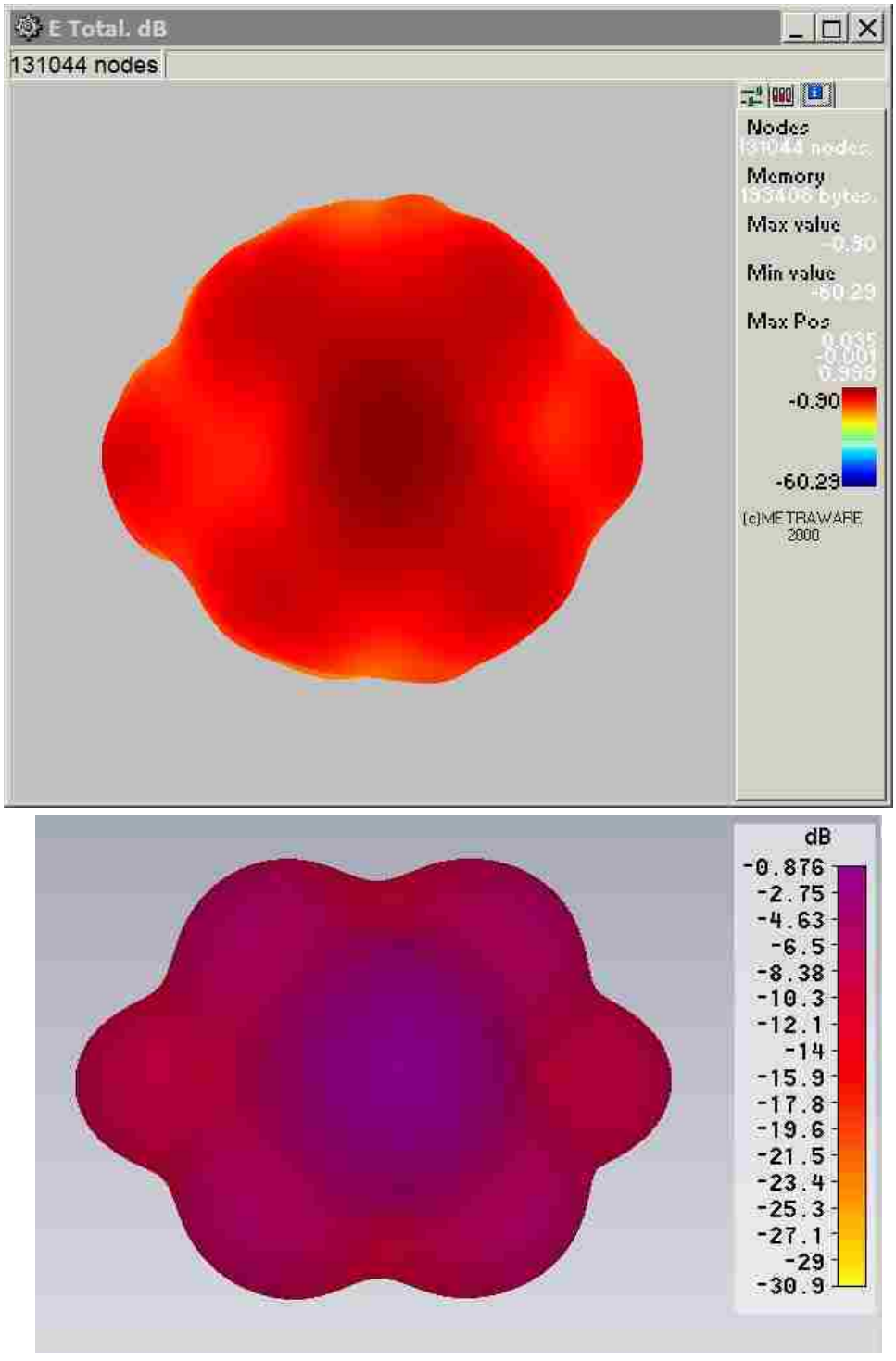

Figure 143: 5 GHz 3D realized gain, measured (top) and simulated (bottom)

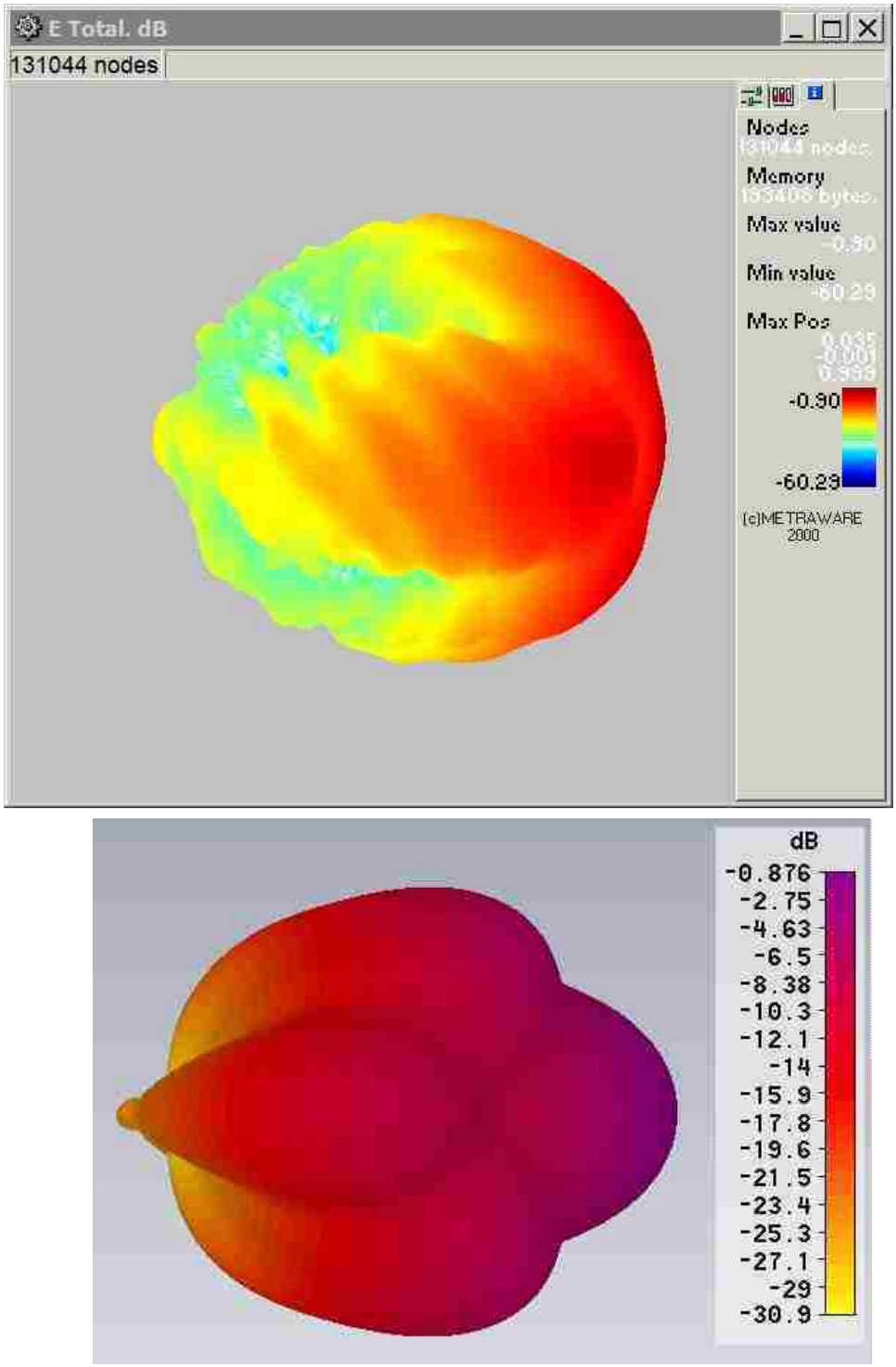

Figure 144: 5 GHz 3D realized gain, measured (top) and simulated (bottom)

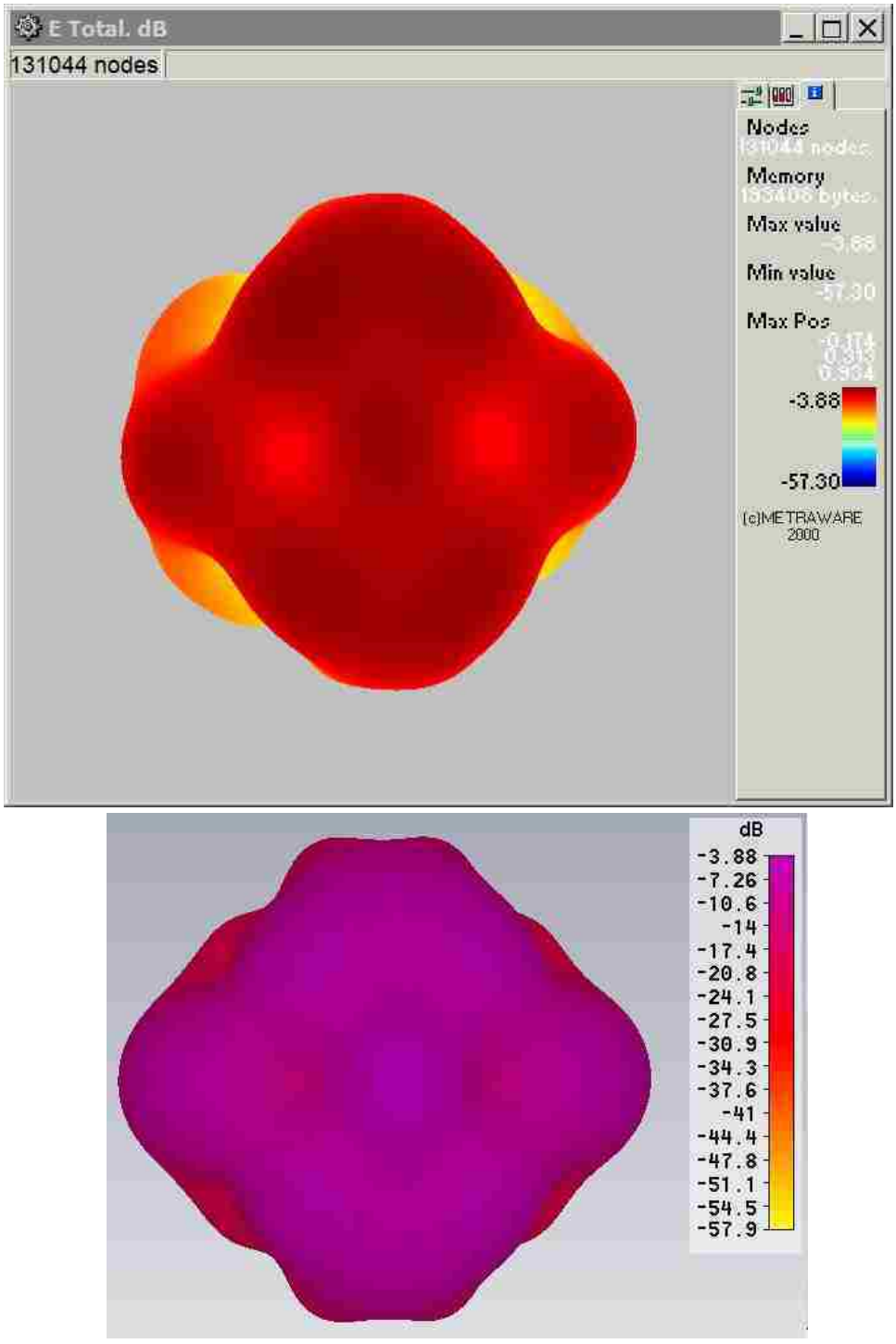

Figure 145: 6 GHz 3D realized gain, measured (top) and simulated (bottom)

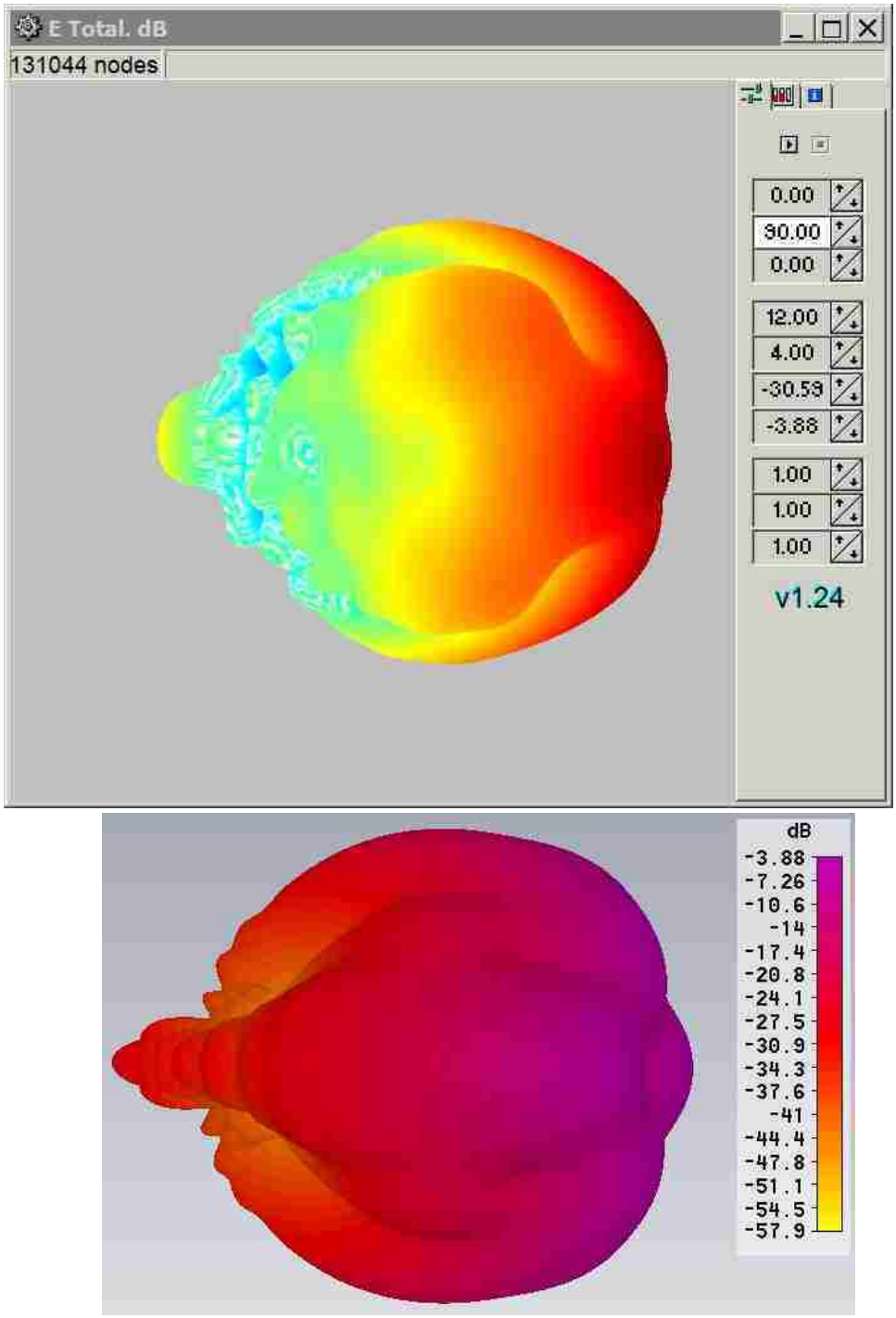

Figure 146: 6 GHz 3D realized gain, measured (top) and simulated (bottom)

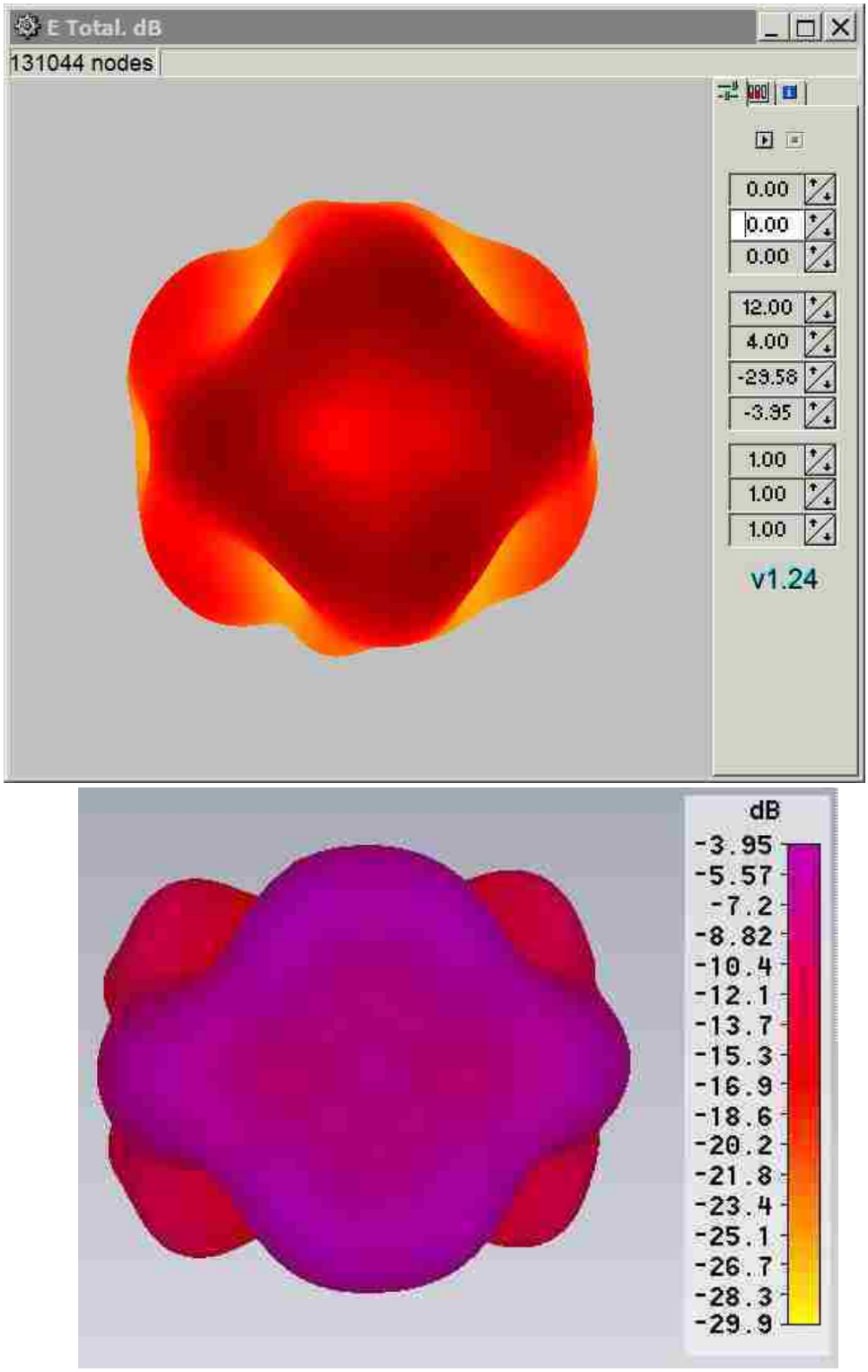

Figure 147: 7 GHz 3D realized gain, measured (top) and simulated (bottom)

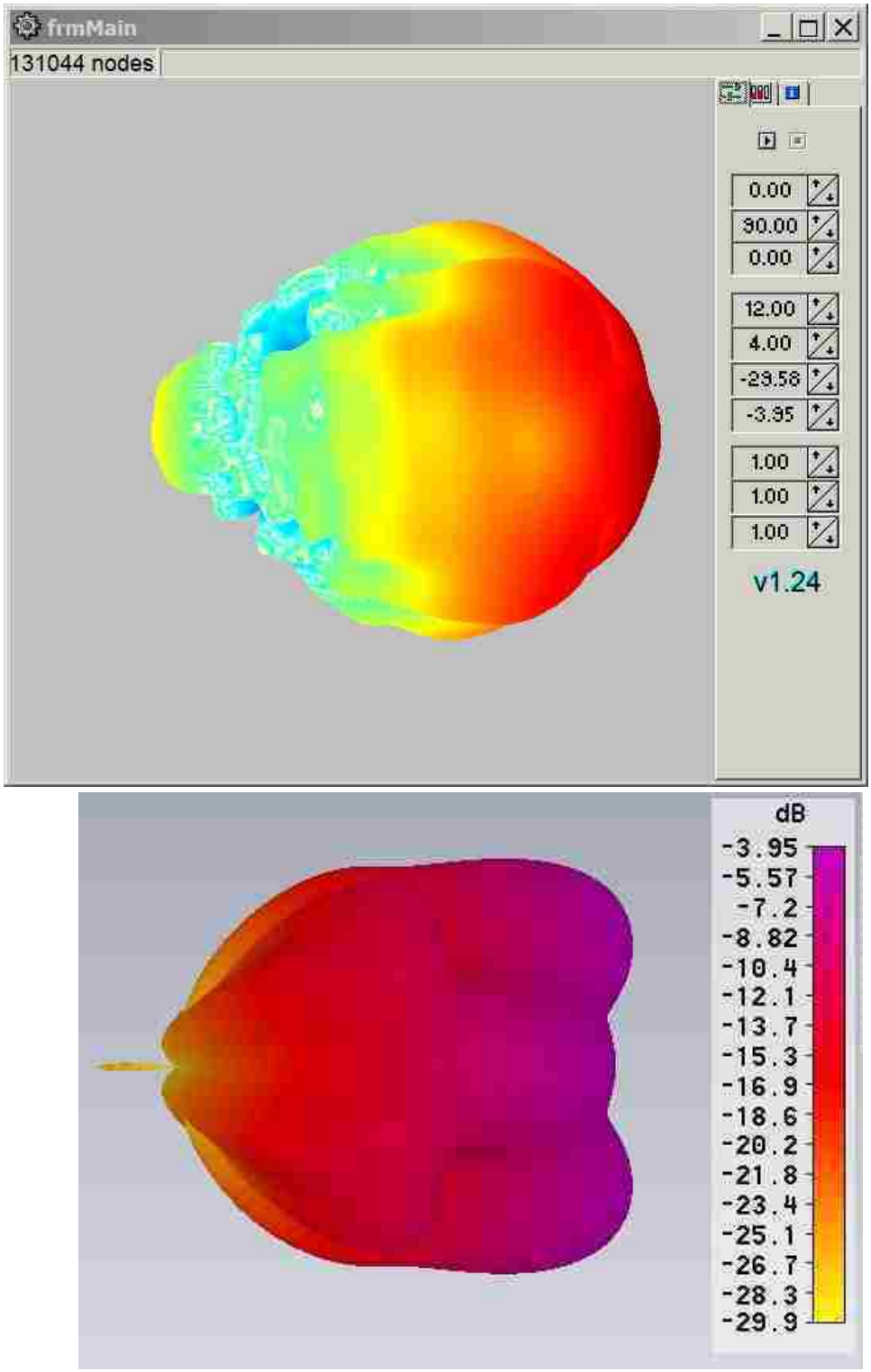

Figure 148: 7 GHz 3D realized gain, measured (top) and simulated (bottom)

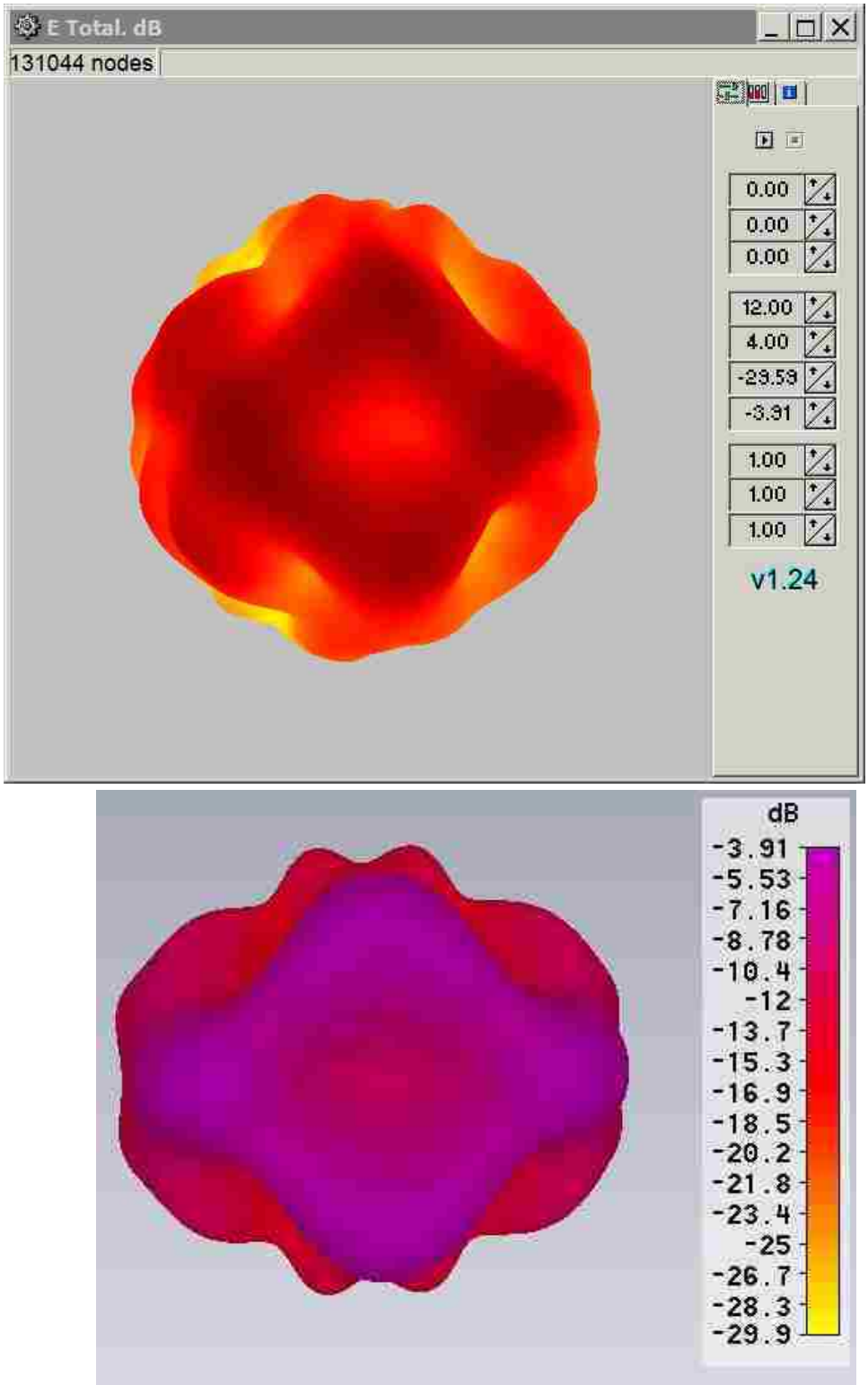

Figure 149: 8 GHz 3D realized gain, measured (top) and simulated (bottom)

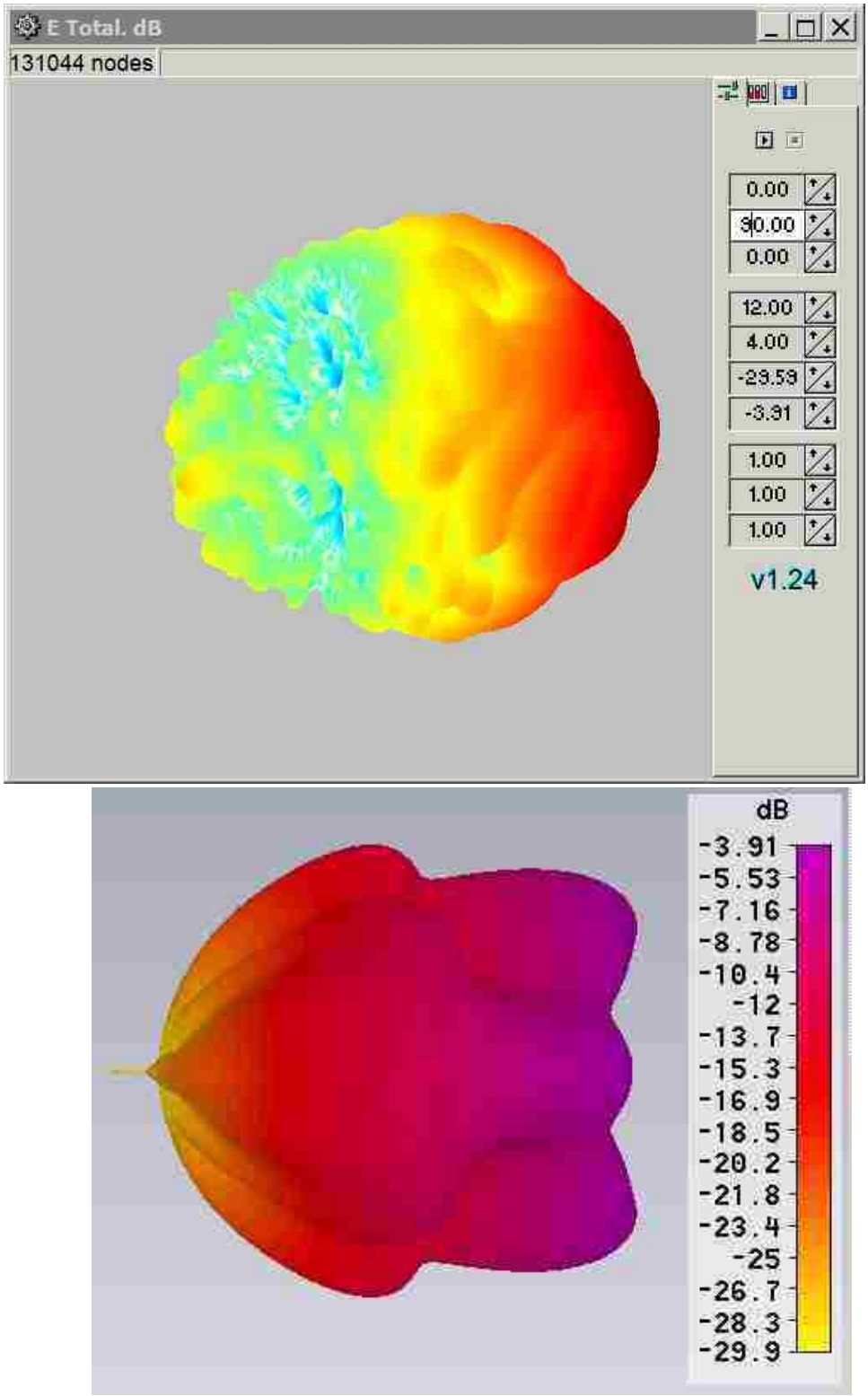

Figure 150: 8 GHz 3D realized gain, measured (top) and simulated (bottom)

Beam Squint

If the diamond feed were to be used in an imaging system such as OVSA then a minimal beam squint would be desired, and certainly less than that of the existing TECOM LPDA feed used at OVSA. Beam squint should also be minimized if used in a RSTN system because at high frequency the system beam width is not much broader than the angular width of the sun.

The actual beam squint of the TECOM LPDA or RSTN Kelvin feed is unknown since we neither had one of these feeds nor did we have the budget to perform characterization. Simulations previously presented (Figure 37) showed that small manufacturing offsets on the order of 1° or 100μm could cause 1° of beam squint in a half-wave dipole. It was also shown in simulation that in n an LPDA with many elements, each of which might have a different offset, it is possible that a frequency-dependent beam squint might develop. It was therefore a goal to develop a structure with a minimum number of elements and features so that beam squint might be minimized.

To effectively measure beam squint a high spatial resolution would have to be used when testing, which increases the test cost. A balun would have to be used that has very low phase and amplitude unbalance. While the Hyperlabs HL9402 balun [55] has ±0.2.0° phase unbalance, it was beyond our budget. The RF Lambda RFH02B08GPI 180° hybrid coupler and testing at WRCNC with 1° resolution fit our budget constraints. However, the coupler is specified to have ±8.0° of phase unbalance over the 2-8 GHz range which made it not possible to adequately characterize beam squint.

Beam squint measurements were extracted from test data and are shown in Table 11: Measured Beam Squint With Coupler. The squint ranged from 1 to 2°. If one or both of the diamond-shaped elements were misaligned then a frequency-independent squint of perhaps 1° could have resulted, and the remaining variation originating from the coupler. This is supposition and cannot be verified without higher precision testing with an appropriate balun.

Table 11: Measured Beam Squint With Coupler

Frequency	Measured Squint With Coupler
2 GHz	+1°
3 GHz	+2°
4 GHz	+1°
5 GHz	+2°
6 GHz	+2°
7 GHz	+2°
8 GHz	+2°

Chapter 6: Conclusions

A feed using diamond-shaped radiating elements in a damped cavity has been designed and fabricated, and subsequently characterized at a professional test facility. Results have shown that, of the parameters that were tested, the feed met all performance targets except for:

- Feed taper in theta at 5 GHz, by 0.6 dB
- Cross-polarization at 3 GHz, by 5.5 dB

Beam squint was not effectively tested because the cost would have been prohibitive. Phase center displacement was not measured because neither WRCNC nor UNM had the facilities to do so. These are the subject of future work.

Feed taper at 5 GHz is not a great concern as it missed the target by only 0.6dB, and is still greater than the simulated taper of the current RSTN feed. Therefore the discrepancy was not investigated further.

Simulation studies were undertaken to further explore the high cross-polarization at 3 GHz. One of the driven diamond elements was twisted on its longitudinal axis by 4° and simulated at 2 and 3 GHz. The results are shown in Figure 151 where is it seen that the simulated performance is similar to that of the measured performance of Figure 129 and Figure 130. The cross-polarization component in simulation is skewed to the left of the polar plot, meets the 10 dB target at 2 GHz, but fails at 3 GHz. Given that the diamond elements were supported at the top by glue to the Arlon ring, and at the bottom by the central conductor of the coaxial cable feed, it is possible that one or more elements were misaligned from their correct positions and a high cross-polarization was induced.

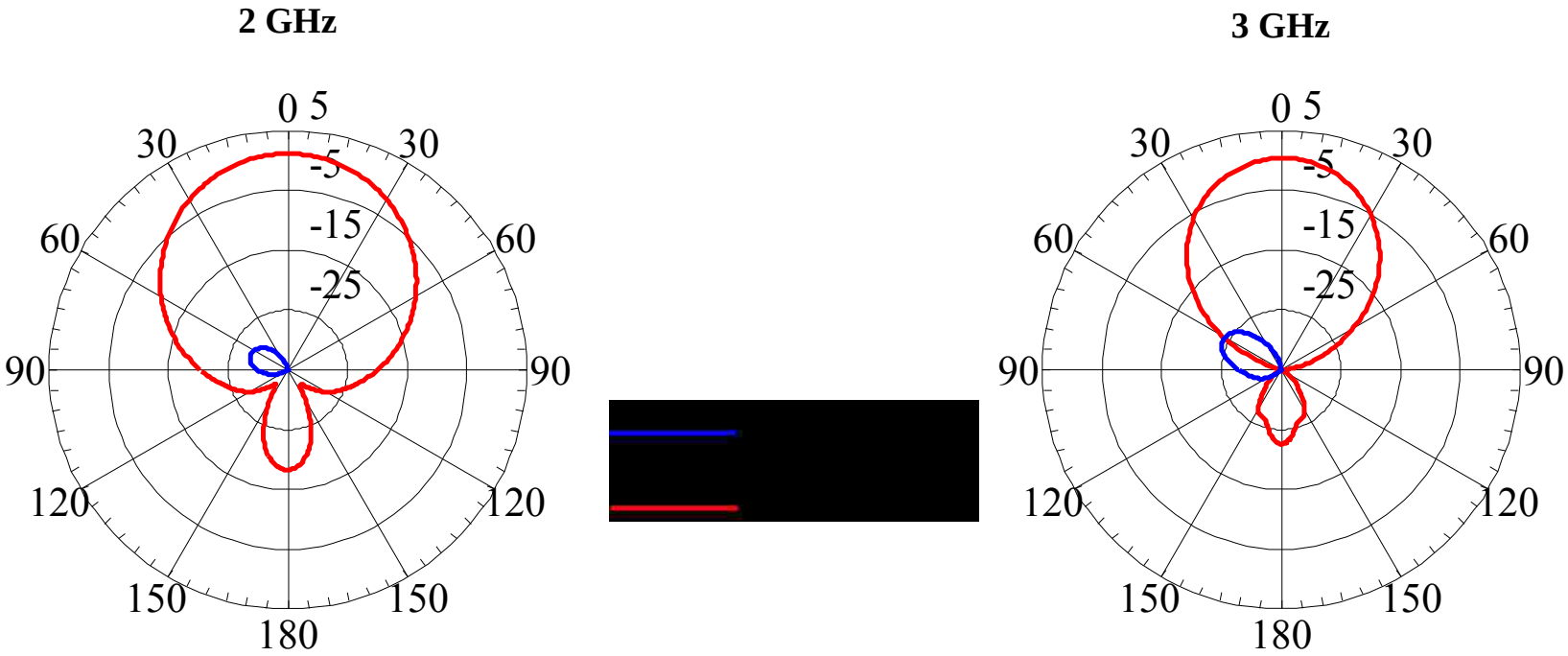

Figure 151: Simulated cross-polarization due to misalignment

Future Work

Several areas of further research and development exist that might yield an improved design and/or further insight into the behavior of the feed.

Simulation Study of Other Geometries

Element shapes other than diamond-shaped could be explored with respect to performance and it is likely there are others that are suitable. In this research no other shapes were simulated because the diamond was yielding reasonable results and the goal was to produce an engineering solution to upgrade a RSTN system.

Aperture Ring

A 0.375" thick copper aperture ring was used because Electrodynamic had this material on hand, and this thickness would have facilitated solid attachment to the SRBL feed housing. In future work, the feed could be fabricated such that the aperture ring was removable. In this manner the effect of other or modified aperture rings, or no aperture ring, could be characterized. Simulations suggest that a 1mm thick aperture ring would be effective and this could be explored.

Conical Damper

There may be more optimal solutions to damping than the conical ECCOSORB MF-117 damper used in the diamond feed. Different geometries of MF-117 or other materials might further improve performance. Other geometries were not explored in the course of this research because an engineering solution was found.

Beam Squint Characterization

Beam squint could be more effectively characterized if further funding were available. The use of a precision phase-matched balun such as the Hyperlabs HL9402 balun would help facilitate such testing by minimizing phase-induced squint. While the data sheet indicates a maximum phase unbalance of ±2.0°, Hyperlabs has produced units with as little as ±0.18° of phase unbalance at 10 GHz [56]. Effective squint characterization would also require higher spatial precision than the 1° resolution used for

this research. WRCNC is capable of 0.1° resolution but a rigid test fixture to hold the feed would have to be developed [57]. Testing costs would increase substantially. The data set produced by WRCNC for 2-8 GHz testing with 1° resolution was 898 MB of files in text format, but would be much larger at 0.1° resolution.

Wider Bandwidth Testing

Bandwidth testing was limited by the 2-8 GHz range of the RF-Lambda coupler due to budget constraints. The HL9402 balun has a specified bandwidth of 5 MHz to 20 GHz, which would allow the diamond feed to be characterized over the entire 0.9 to 12 GHz simulation range. It would not be productive to test above 12 GHz because above that frequency the gain of the dish is sufficiently high that the beam width is less than the angular width of the sun. This is why the RSTN 15.4 GHz feed is paired with a 1m dish with less gain than the 2.4m dish.

Dielectric Cover

The diamond feed was fabricated with an open face for simplicity of fabrication or repair. While the RSTN housing is sealed and pressurized, the diamond feed could be constructed with the dielectric support ring being one solid piece so that the elements were sealed inside. An improved method of supporting the elements would be required and this is discussed in the next paragraph.

Solid Support of Radiating Elements

Currently the diamond elements are supported at the base by the coaxial cable's central conductor, and at the tip by the dielectric support ring. While the diamond elements were CNC machined to a tolerance better than 25μm such an alignment tolerance could not be effected with the current support system. It may be possible to CNC machine a dielectric support structure to which the diamond elements are attached, eliminating much of the uncertainty in their location. A simulation study could be performed to explore such support structures.

Dr. Baum's Design Suggestion

Simulations of the design configuration suggested by Dr. Baum and documented in Appendix E: Dr. Carl Baum's Design Suggestion, show promise. This is a simpler, planar structure so it is reasonable to assume that it would be easier to fabricate, could have less beam squint, and less phase center displacement.

Appendices

Appendix A: Dish Illumination and Beam Squint

Dish Illumination

The term illumination taper refers to how the main lobe illuminates the dish. A perfect illumination taper would uniformly illuminate the entire surface of the dish and have a null everywhere else, yielding no spillover. This cannot be realized with a practical feed so compromises must be considered.

Figure 152 depicts a perfectly illuminated dish with no illumination loss and no signal spillover, while Figure 153 shows a uniformly illuminated dish. Uniform illumination as shown will still have some illumination loss. Neither pattern is physically realizable as drawn.

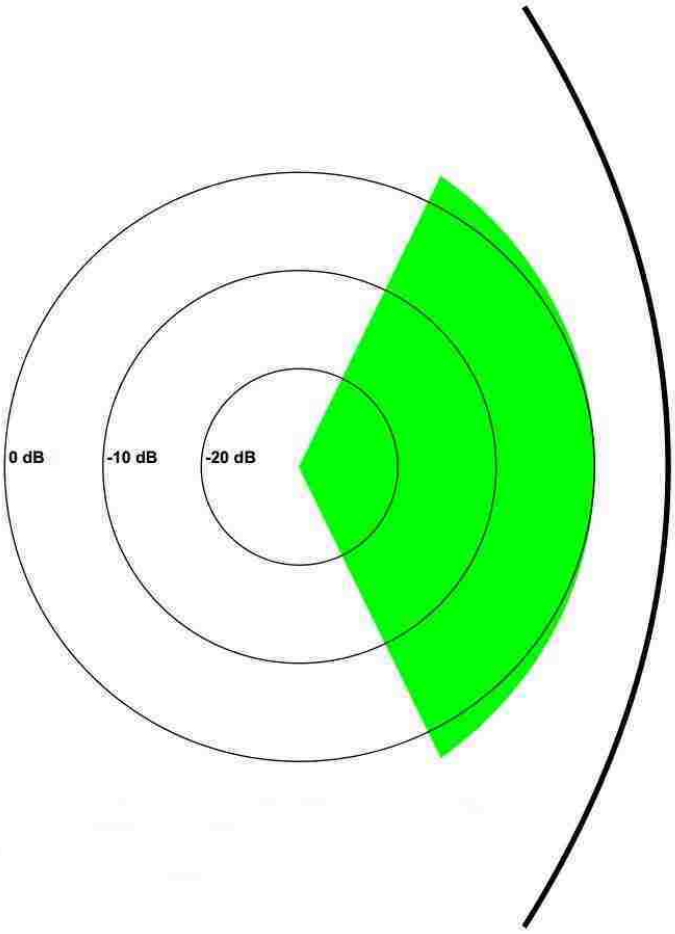

Figure 152: Perfectly Illuminated Parabolic Dish.

[58]

A perfectly illuminated parabolic dish as shown above in Figure 152 would have the same power density everywhere on its surface and zero spillover. Since the dish is parabolic in shape it is farther from the feed's phase center at the edges than in the center of the dish. Because radiated power follows an inverse square law, the feed's radiated power must increase away from dish center.

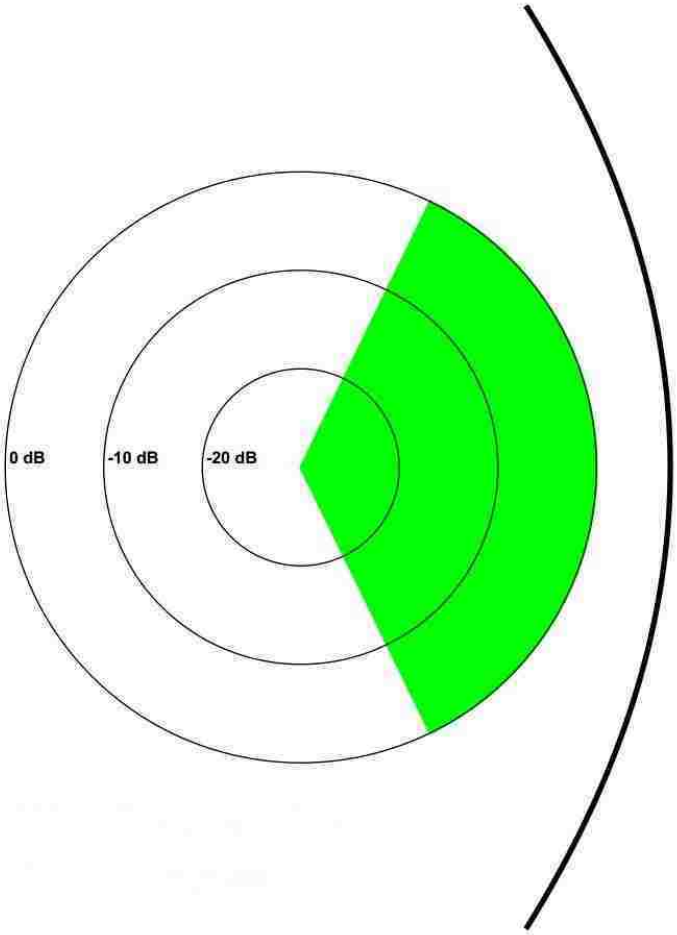

Figure 153: Uniformly Illuminated Parabolic Dish.
[58]

Figure 153 above depicts a uniformly illuminated parabolic dish, where the radiated power is constant over the angle subtended by the dish but zero elsewhere. The greatest power density will occur at dish center, and will decrease away from dish center due to the inverse-square law.

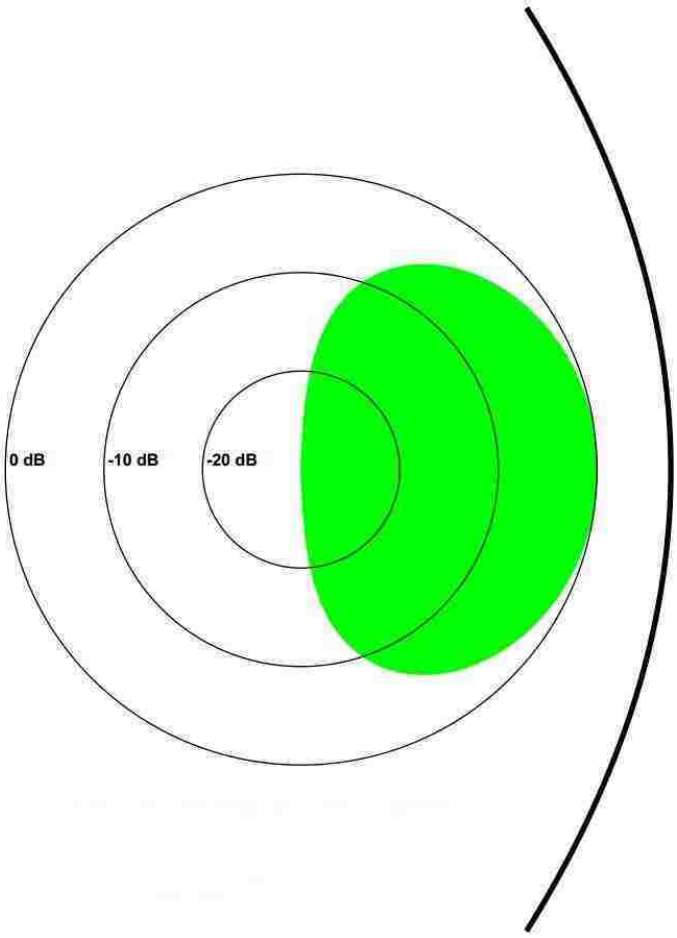

Figure 154: Typical Horn Illumination of Parabolic Dish.
[58]

In Figure 154 above, the radiation pattern of a typical horn feed is shown. In this depiction there is illumination loss away from dish center, and some radiation spills over the dish. A dish illuminated in this manner and pointed at the sun will detect three microwave emission sources: the sun, the microwave background of the sky, and terrestrial emissions such as those emitted from nearby 300°K objects or other radio sources.

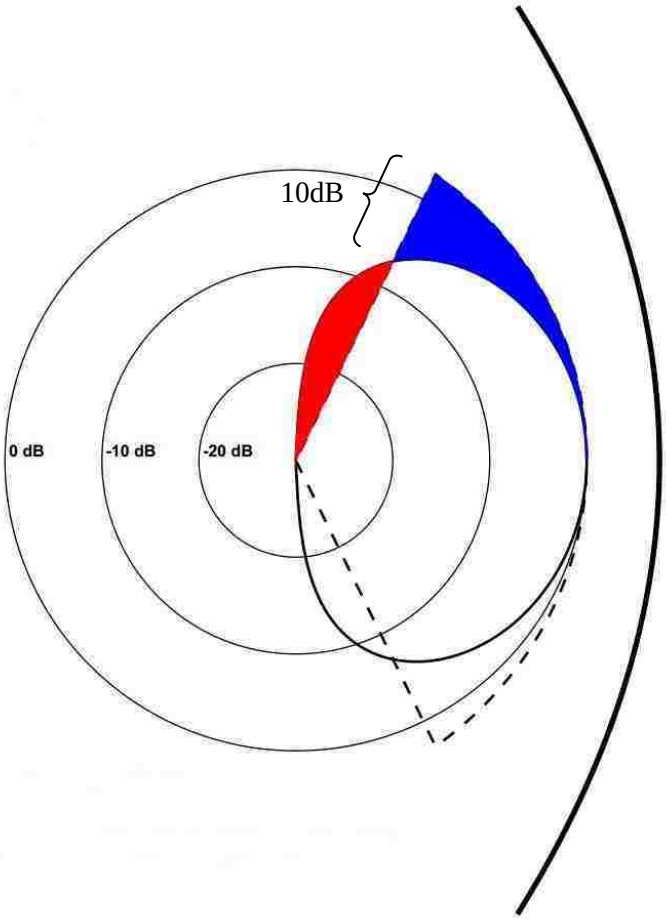

Figure 155: Typical vs. Desired Dish Illumination.
Red area indicates spillover, blue indicates under-illumination. [58]

In Figure 155 the typical dish illumination from a feed horn is compared to the ideal illumination. One figure of merit of a parabolic dish is its degree of curvature expressed as the f/D ratio, where f = focal length and D = diameter. Dishes with small f/D require broader feed patterns than dishes with higher f/D. In Figure 10 the dish is drawn with f/D = 0.4, where the RSTN and SRBL dishes are f/D = 0.375.

Figure 155 also illustrates an illumination taper of 10 dB. The difference in radiated power from ideal illumination to actual illumination is 10 dB as shown.

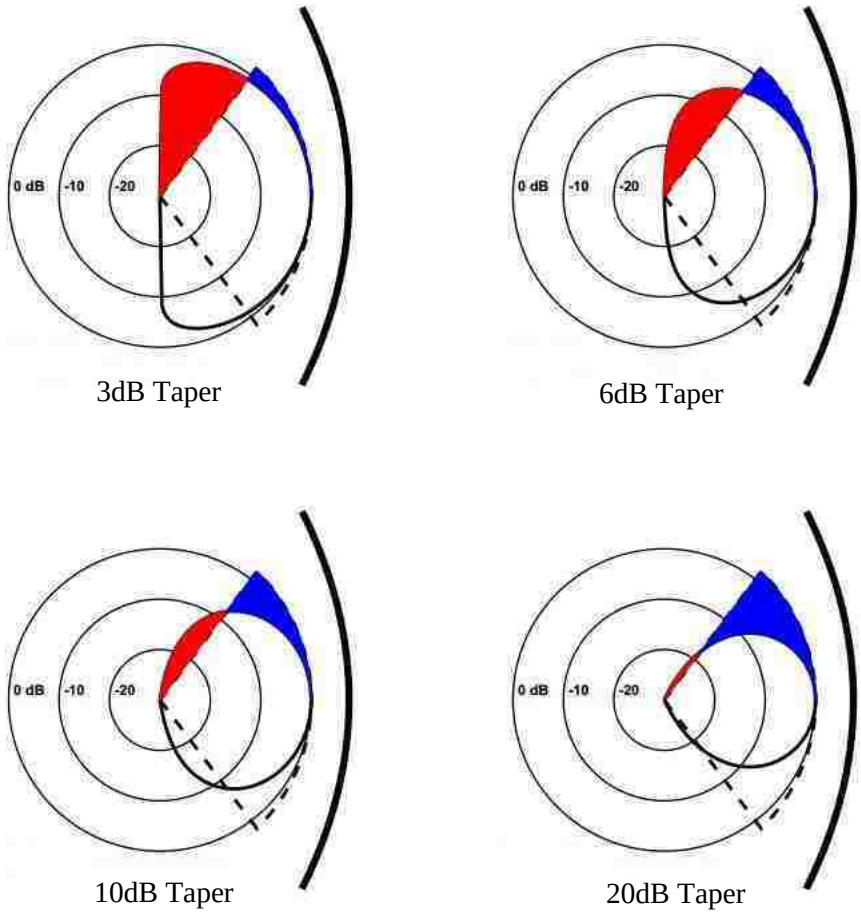

Figure 156: Dish Illumination with Various Illumination Tapers.
Red area indicates spillover, blue indicates under-illumination. [58]

Various illumination tapers are depicted above in Figure 156 for an f/D = 0.5 dish. These difference illumination tapers will produce differing amounts of spillover and illumination loss. It can be seen that a 3dB taper produces the least amount of illumination loss but the greatest amount of spillover loss, whereas the 20dB taper is just the opposite.

Illumination taper is related to directivity. A feed antenna with high directivity will have a narrow main lobe resembling the 20dB taper, whereas a feed with low directivity such as a half-wave dipole will resemble the 3dB taper pattern.

The RSTN dish is 2.4m in diameter with an f/D = 0.375. Using a prime-focus antenna calculator, the angle subtended by the dish is 134.8° as shown in Figure 157.

Antenna Diameter	cm	240
Antenna depth	cm	15.625
Focal length	cm	240
f/D ratio		.375
Feedhorn beamwidth (from relector edge to reflector edge)	Deg	134.8

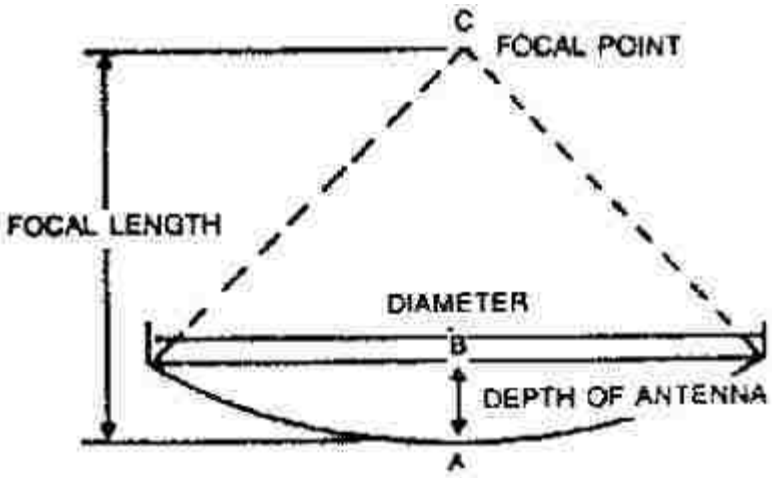

Figure 157: Beam Width to Illuminate a RSTN Dish.
[59]

This is in good agreement with calculations performed earlier by [60]. The angle subtended by a parabolic reflector for a given f/D ratio was calculated and plotted and shown in Figure 158. Thus the ideal beam width for illuminating a RSTN dish would subtend 134.8° and with an infinitely steep taper. Such a radiation pattern is not possible so other tapers must be considered.

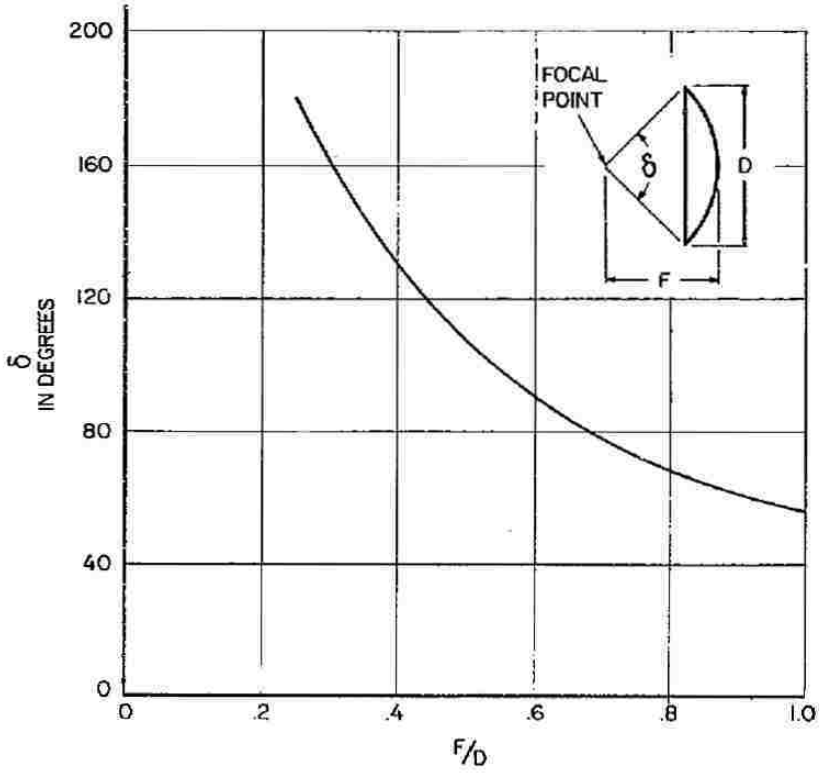

Figure 158: Plot of angle subtended by parabolic reflector vs. f/D ratio.

Figure 2, p. 129. [60]

A consideration with respect to illumination taper is the system efficiency. If all the feed's energy were directed towards the dish, a maximum aperture efficiency of 100% would result. In Figure 159, the efficiency resulting from a $\cos^n(\theta)$ shaped feed pattern illuminating a 0.5 f/D dish was plotted by [61]. It can be seen that the overall efficiency, NT, varies little with tapers in the range of 8 to 12 dB, yielding an overall efficiency of about 80% for an f/D 0.5 dish. A maximum efficiency of 81% is achieved with an 11dB edge taper for a $\cos^n(\theta)$ shaped feed pattern [62].

Several factors contribute to the overall efficiency of a parabolic reflector, such as illumination taper, spillover loss, asymmetries between E- and H-planes, focal point error, feed side lobes, blockage by the feed and support structures, and imperfections in the parabolic surface [58].

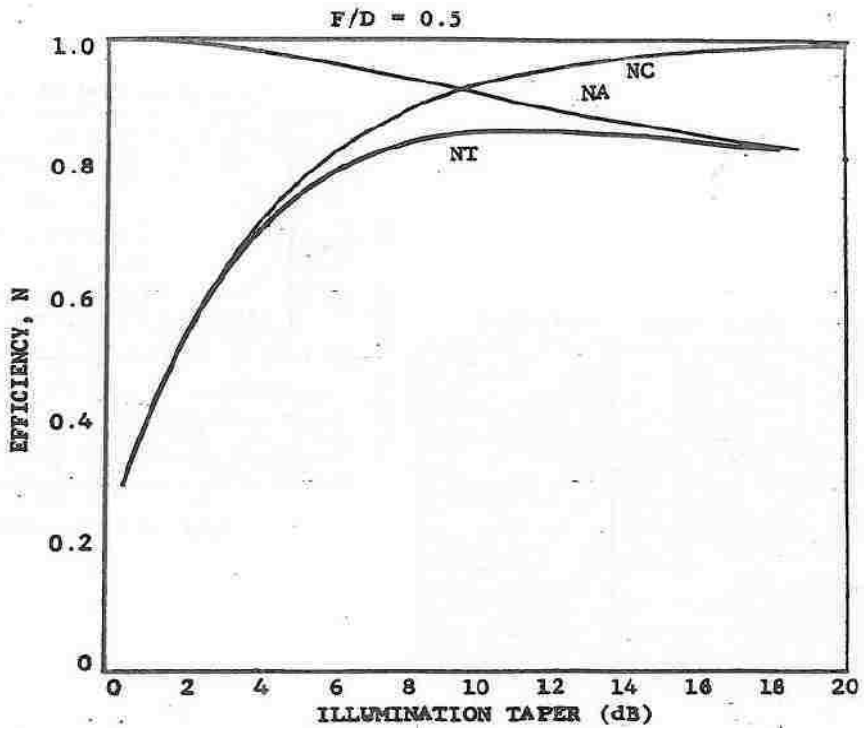

Figure 159: Efficiency vs. Illumination Taper for 0.5 f/D Parabolic Dish.

Figure 2, p. 79. [61]
The overall efficiency NT is relatively constant in the 8-12dB range of illumination taper. NA is the spillover efficiency and NC is the taper efficiency.

Additional attenuation occurs due to the inverse-square law, as previously discussed. This is depicted in Figure 160 as plotted by [61]. At 67° off-axis the space attenuation is approximately 3.2 dB. This is in reasonable agreement with [63] where a space attenuation of 3.4dB is interpolated from the table of space attenuation as a function of f/D ratio. Assuming the space attenuation at the edge of a RSTN dish is on the order of 3.2dB, the illumination taper of the feed is increased by 3.2dB at dish edge. For example, to achieve an overall illumination taper of 10dB would require the feed to contribute 6.8dB of additional attenuation at the angle corresponding to the edge of the dish.

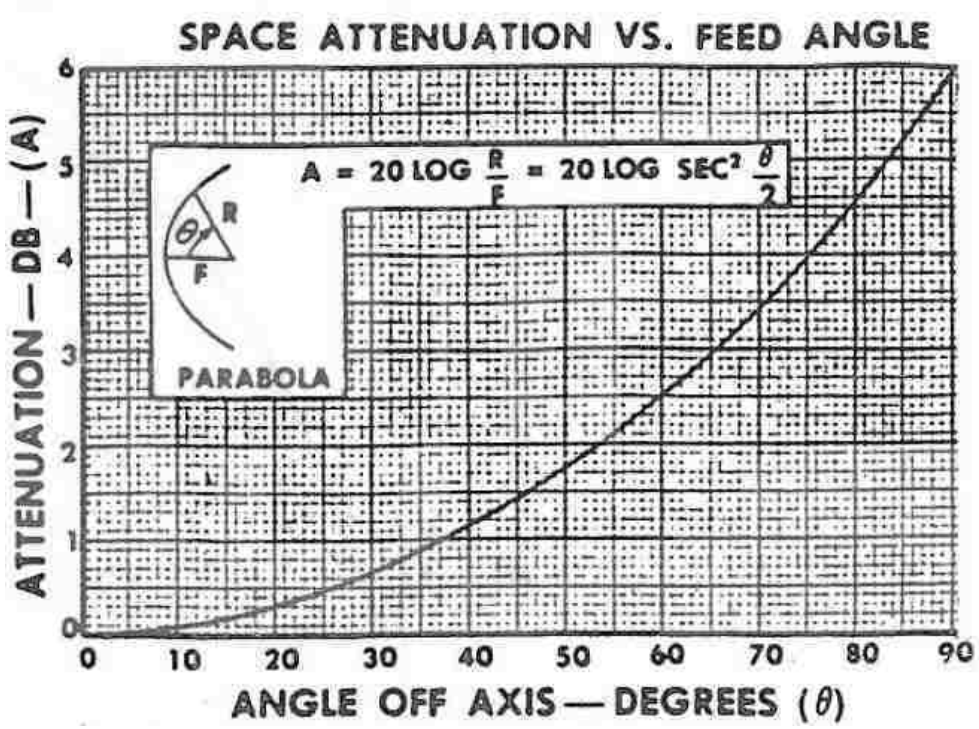

Figure 160: Space Attenuation vs. Feed Angle.

Figure 4, p. 80. Illumination is attenuated due to the inverse-square law. **[61]**

RSTN 2.4m Dish Feed

The Air Force Geophysics Laboratory developed the RSTN system in the 1970's [23] and few specifics are available regarding the feeds used for the 2.4m system.

Dr. John Kennewell [64] reported that the feed unit is a Kelvin feed, as it was manufactured by the Kelvin Manufacturing Company, 26 Conn St., Woburn, MA, 0181. Subsequent searches were unable to locate this company or obtain further information regarding their feed.

Four discrete frequencies are detected by the 2.4m RSTN dish: 1.415, 2.695, 4.995, and 8.800 GHz. The three lowest frequencies are detected by half-wave dipoles, and the 8.800 GHz signal is detected by a waveguide-fed horn. These four antennas are sealed in a housing which is kept pressurized by compressed air. The system is depicted in Figure 161, where the four feed elements are named Kelvin Feed.

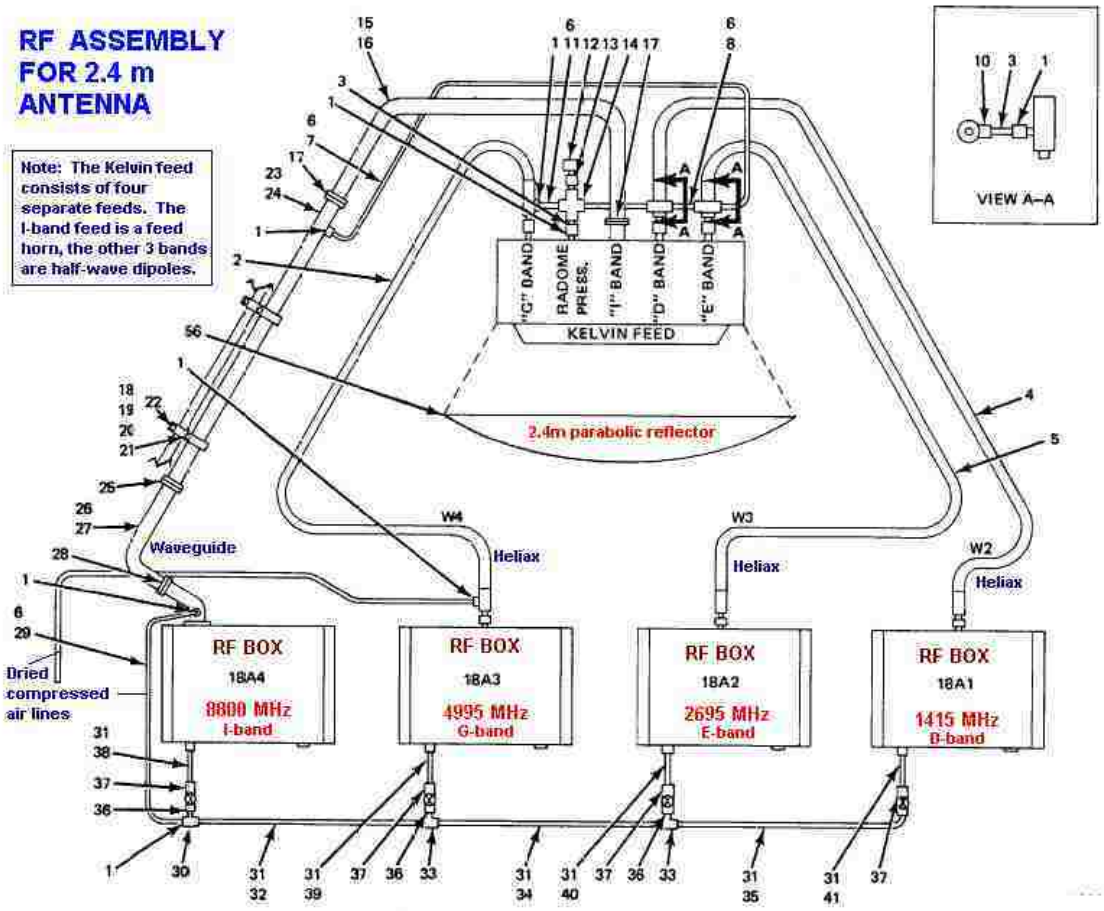

Figure 161: RF Assembly for RSTN 2.4m system
[64]

Dr. Kennewell [64] provided a sketch of the antenna arrangement within the Kelvin feed as shown in Figure 162.

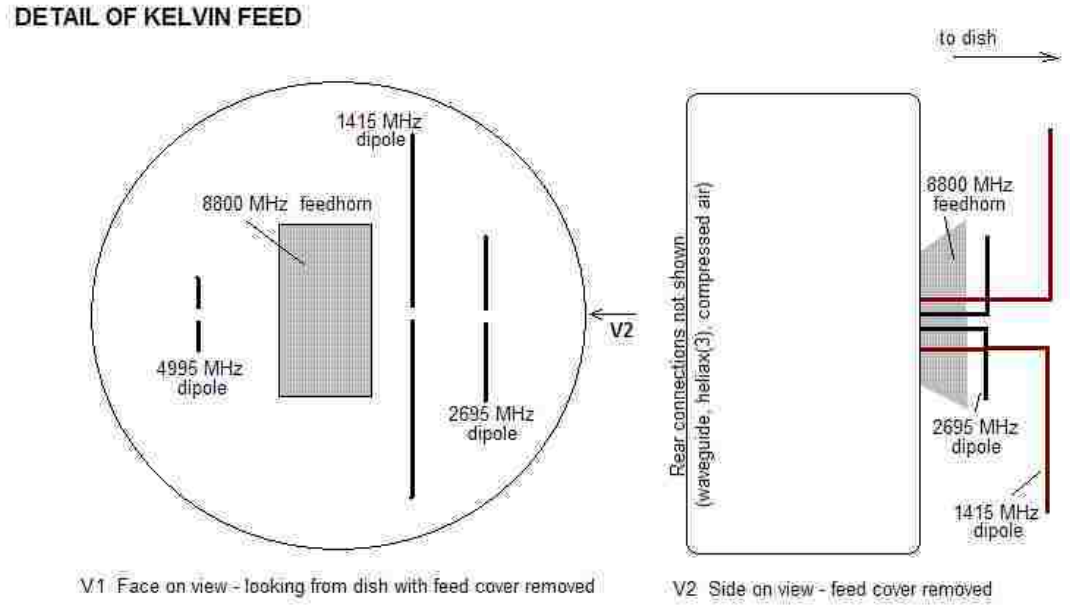

Figure 162: Sketch of Kelvin feed.
[64]

As shown in Figure 162, the four feed elements are adjacent in the feed housing. The approximate length L_D of each half-wave dipole is calculated using the corresponding free-space wavelength, as

1.415 GHz ⟶ λ_o = 21.2 cm ⟶ L_D = 10.6 cm

2.695 GHz ⟶ λ_o = 11.1 cm ⟶ L_D = 5.57 cm

4.995 GHz ⟶ λ_o = 0.060 cm ⟶ L_D = 0.030 cm

The dimensions of the feed housing are unknown but may be approximated from a photograph of the 2.4m RSTN system provided by [65]. Given that the dish is 2.4m wide, the length and width of the feed housing may be estimating. The feed housing's width is estimated to be 20.2cm. These dimensions are shown in Figure 163. The dimensions of the half-wavelength dipoles as calculated above are consistent with a feed housing on the order of 20cm in diameter.

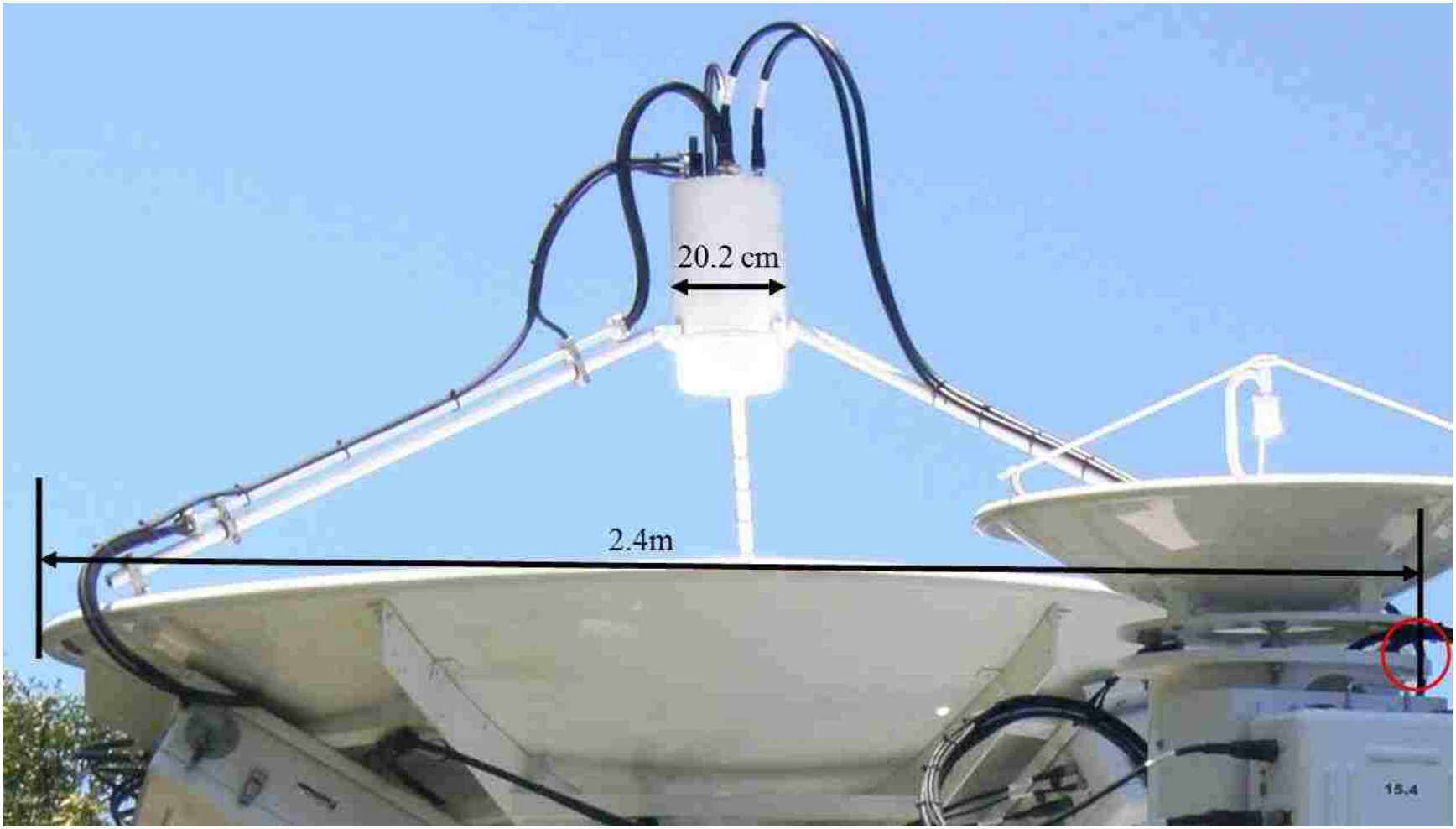

Figure 163: Calculated width of RSTN 2.4m dish feed housing.
[65]

As shown in Figure 162 the 1.415 GHz dipole is closest to the dish. [64] states that there is a ground plane within the feed housing and that the dipoles are a quarter wavelength from the ground plane.

Mounting a dipole above a ground plane induces several effects but two are considered in this application. The first is that, depending upon the spacing between the ground plane and the dipole, lobes are introduced according to the relationship [30],

$$\text{number of lobes} \approx 2\left(\frac{h}{\lambda}\right) \tag{A-1}$$

where h is the dipole height above the ground plane in wavelengths and λ is the wavelength. Given that for the dipoles the distance to the ground plane is one-quarter of a wavelength, no additional lobes are introduced.

The second relevant consideration regards directivity. If a dipole above a perfectly conducting infinite ground plane is sufficiently close to only have one lobe then the directivity is increased. This is because the radiation pattern is constrained to the half-plane in which the dipole resides. In this manner a dipole above a ground plane will not have excessive spillover, as will be discussed in the next section, Dish Illumination.

While it is possible to calculate the radiation pattern resulting from a resonant half-wavelength dipole that is one-quarter of a wavelength above an infinite ground plane, it is more straightforward and less error-prone to utilize Microwave Studio for this purpose. The 1.415 and 4.995GHz dipoles were then modeled and simulated.

A model of the lowest frequency dipole, 1.415 GHz, was captured as shown in Figure 164. This dipole was chosen because it is physically the largest of the three so the finite ground plane, with a maximum of 20.2cm diameter, would show the greatest deviation from a dipole over an infinite ground plane.

The dipole was placed 53.0 mm above a disk-shaped ground plane, corresponding to one-quarter of a free-space wavelength at 1.415 GHz, of 20cm diameter with an arbitrary thickness of 1mm. The dipole is oriented such that its longitudinal axis is in the z direction and is one-quarter of a wavelength above the ground plane in the y direction. In this manner the radiation patterns of θ and φ will give insight into how the RSTN 2.4m is illuminated by such a dipole.

The model for the 1.415 GHz RSTN dipole is shown in Figure 164. The impedance plot for the dipole confirms resonance at the proper frequency and is shown in Figure 166.

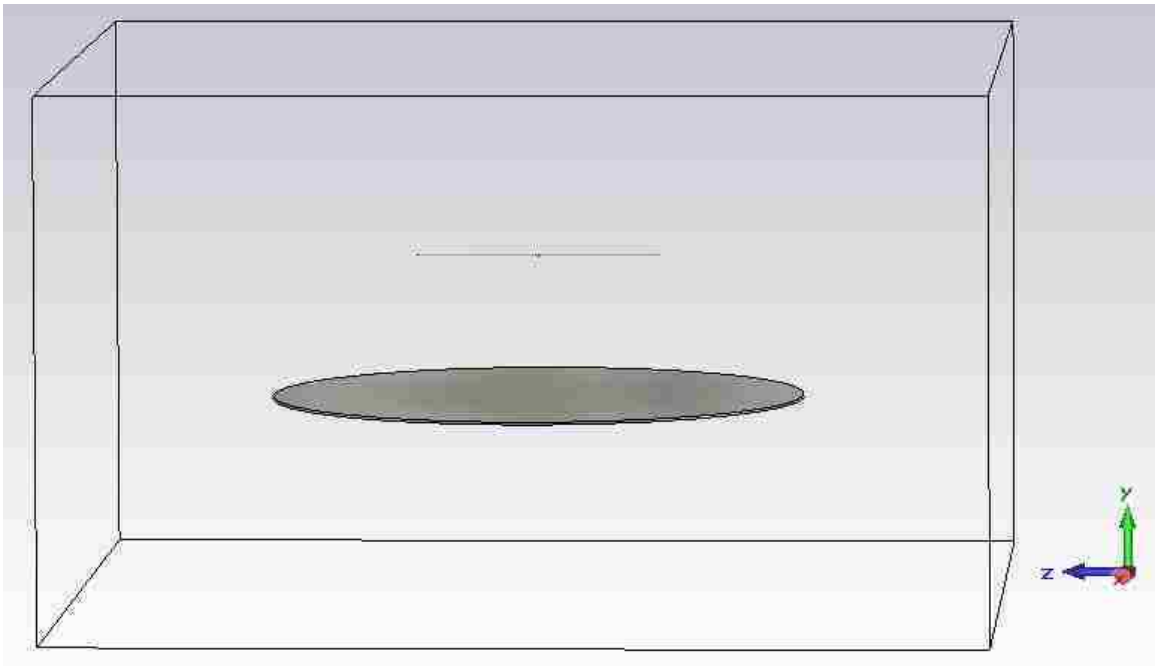

Figure 164: RSTN feed dipole model.

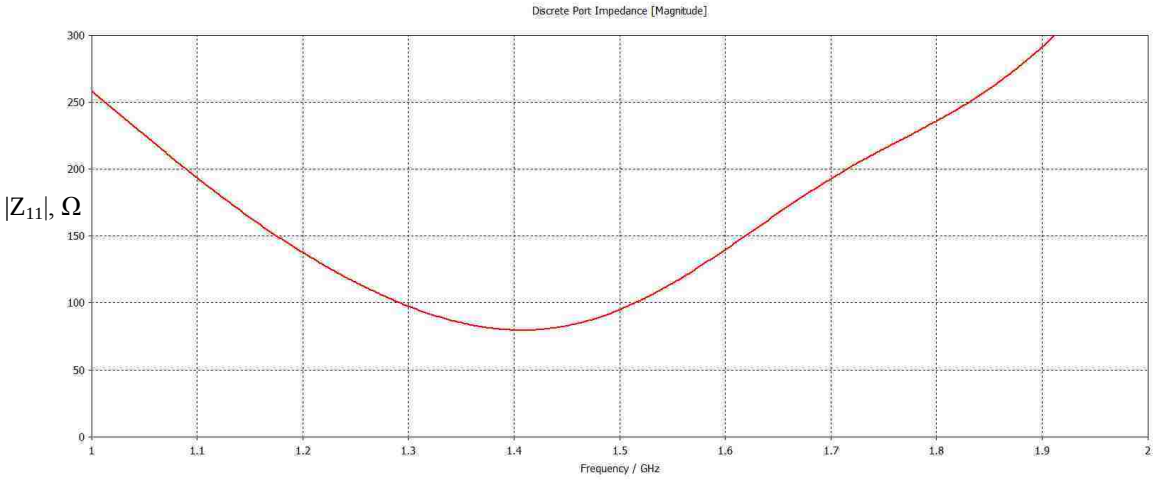

Figure 165: Impedance vs. frequency for modeled RSTN dipole.

Figure 166 depicts the simulated illumination as seen by the dish. As expected, the radiation power pattern is broader in φ than in θ.

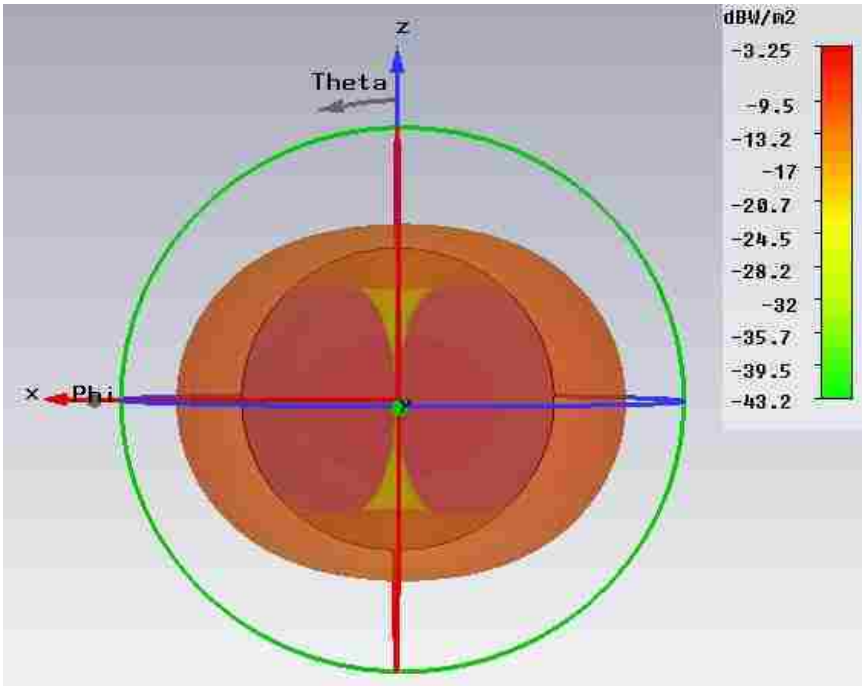

Figure 166: Dipole illumination of dish.

Figure 168and Figure 167 depict the 2D power patterns of the dipole for both φ and θ, respectively, where it is again apparent that the radiation pattern is broader in φ than in θ.

Each power plot has a blue reference circle depicting 10dB less power than the main lobe magnitude. Each plot also has a marker positioned at 22.6° corresponding to the edge of the 2.4m, f/D=0.375 RSTN dish. The power at that point is calculated by MWS and listed in red on the lower left of the plot.

For the 1.415 GHz dipole, the φ power pattern is -9.583dB from maximum at dish edge. For the θ pattern it is -17.64dB down from the maximum. Since the main lobe magnitude is -3.2 dB, this corresponds to a feed taper of 6.383dB for φ and 14.32dB for θ.

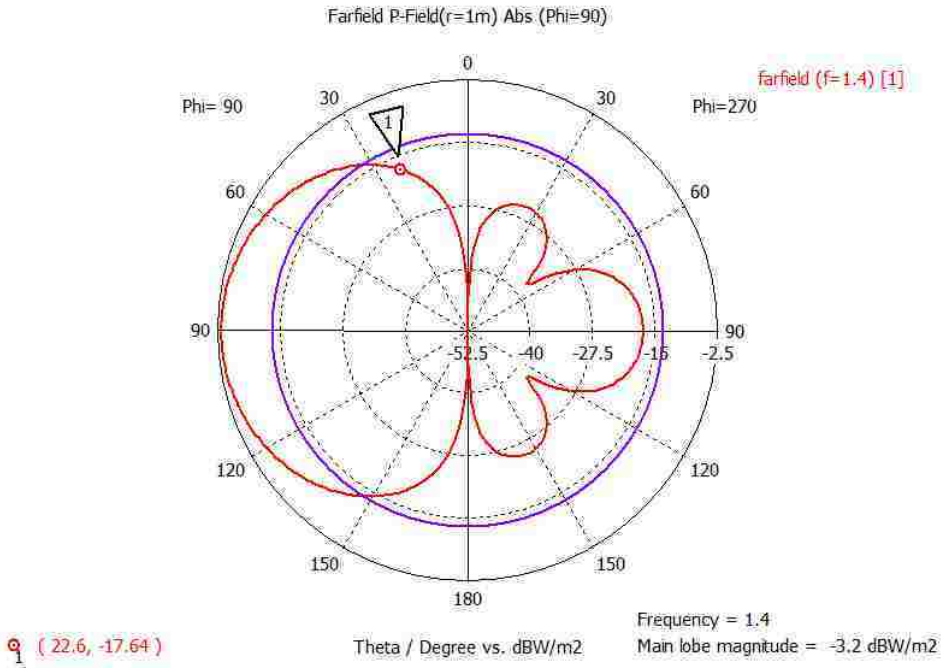

Figure 167: Power pattern of 1.415 GHz RSTN dipole in theta.

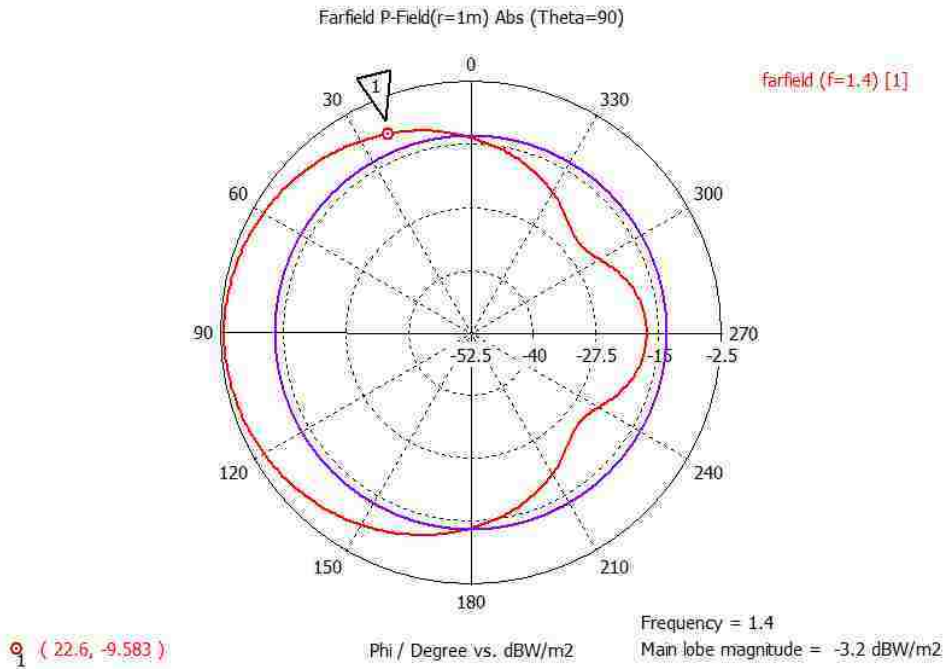

Figure 168: Power pattern of 1.415 GHz RSTN dipole in phi.

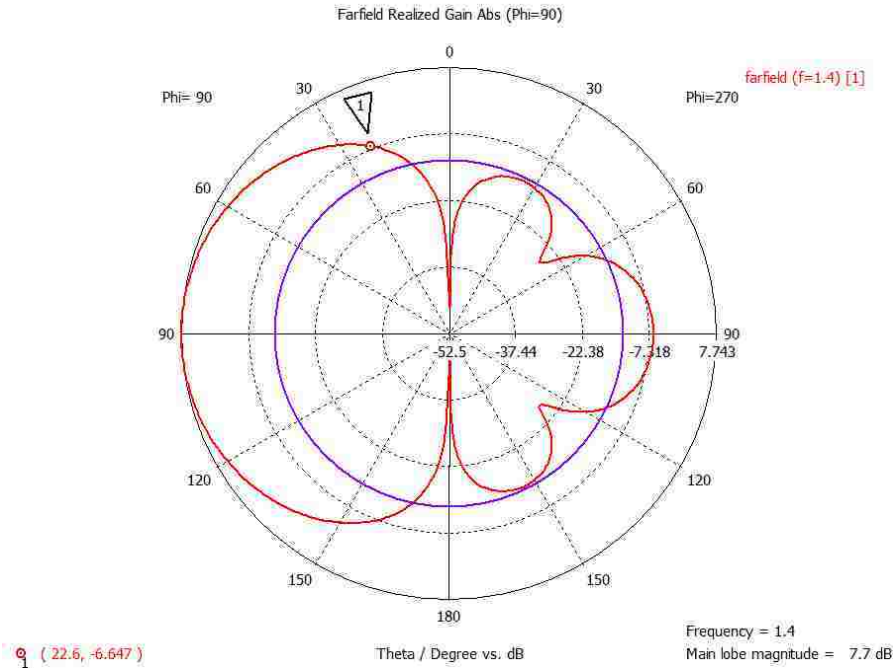

Figure 169: Realized gain pattern of 1.415 GHz RSTN dipole in theta

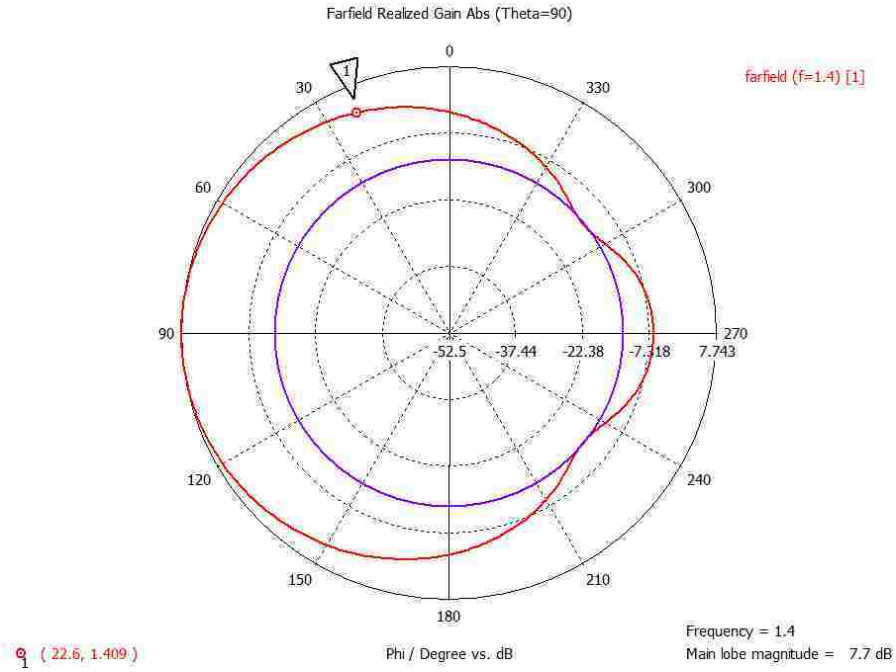

Figure 170: Realized gain pattern of 1.415 GHz RSTN dipole in phi

The antenna testing lab produces results expressed in realized gain. Plotting realized gain in Figure 169 and Figure 170, the simulated 1.415 GHz feed taper is measured to be 14.347 dB in theta and 6.291 dB in phi. These figures are very close to the power pattern values.

The same was done for the 4.995 GHz RSTN dipole. As before, resonance at the proper frequency was verified as shown in Figure 171.

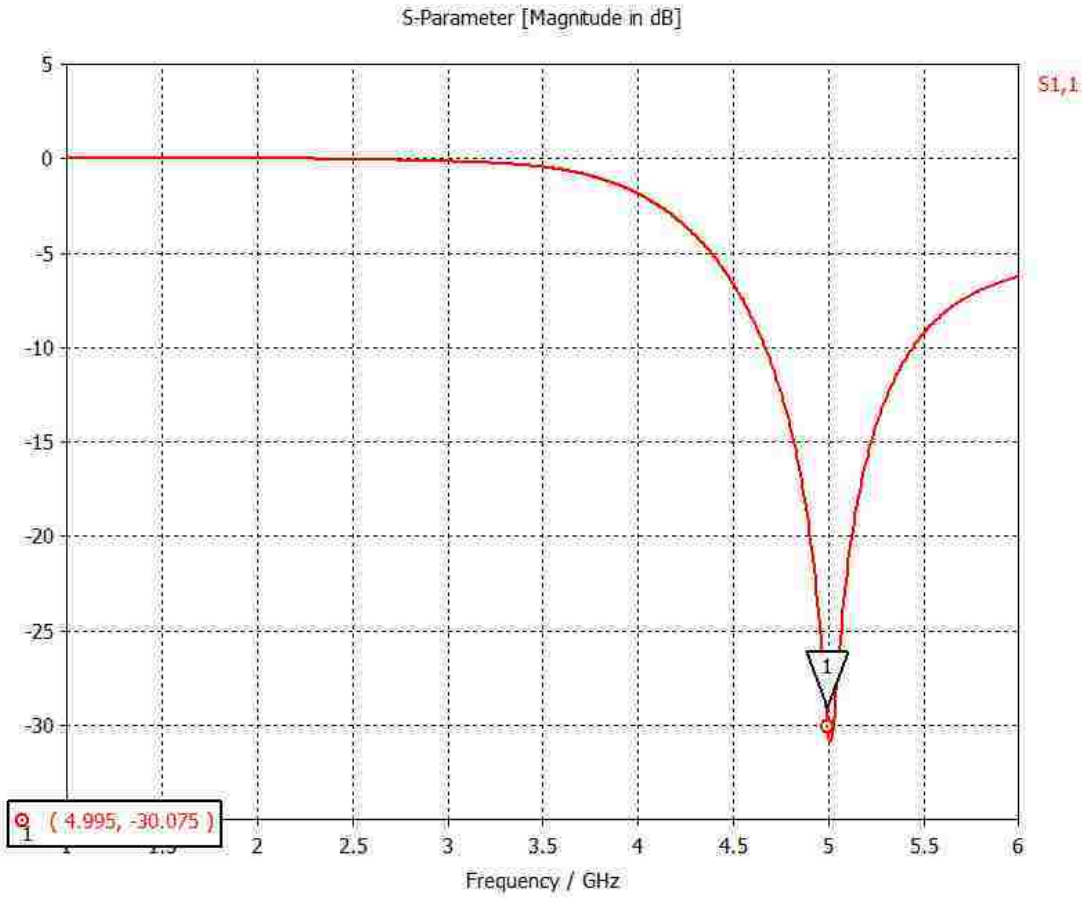

Figure 171: S1,1 of 4.995 GHz RSTN dipole

After confirming resonance, polar power patterns were for the 4.995 GHz dipole are plotted in Figure 172 and Figure 173, while the realized gain patterns are shown in Figure 174 and Figure 175. From the power patterns, the feed taper is calculated to be 16.67 dB in theta and 6.521 dB in phi. The realized gain patterns yield 16.676 dB in theta and 6.529 dB in phi. Once again the values for power and realized gain are very close. This is important so that realized gain measurements from the test lab may be used to calculate actual feed taper.

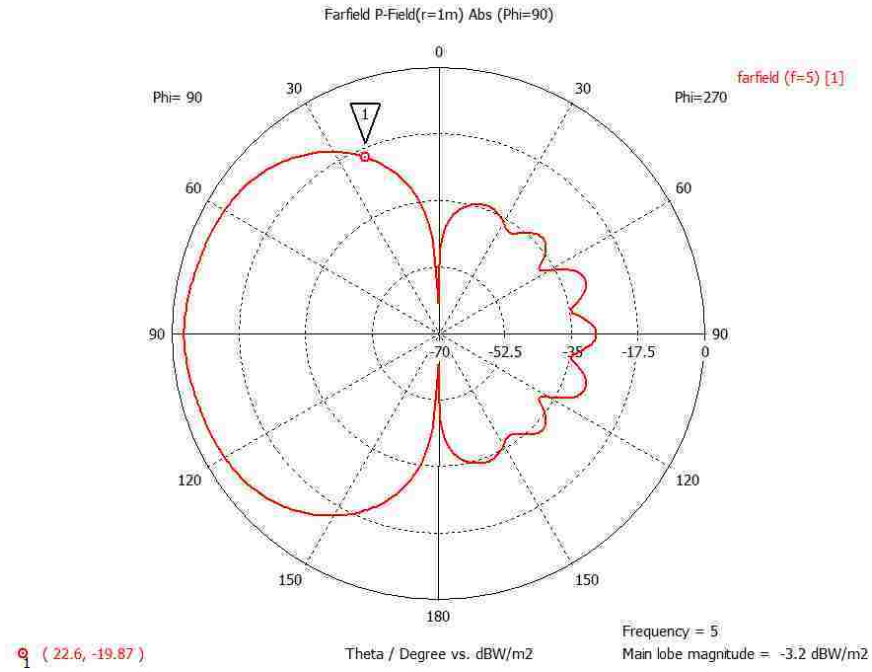

Figure 172: Power pattern of 4.995 GHz RSTN dipole in theta

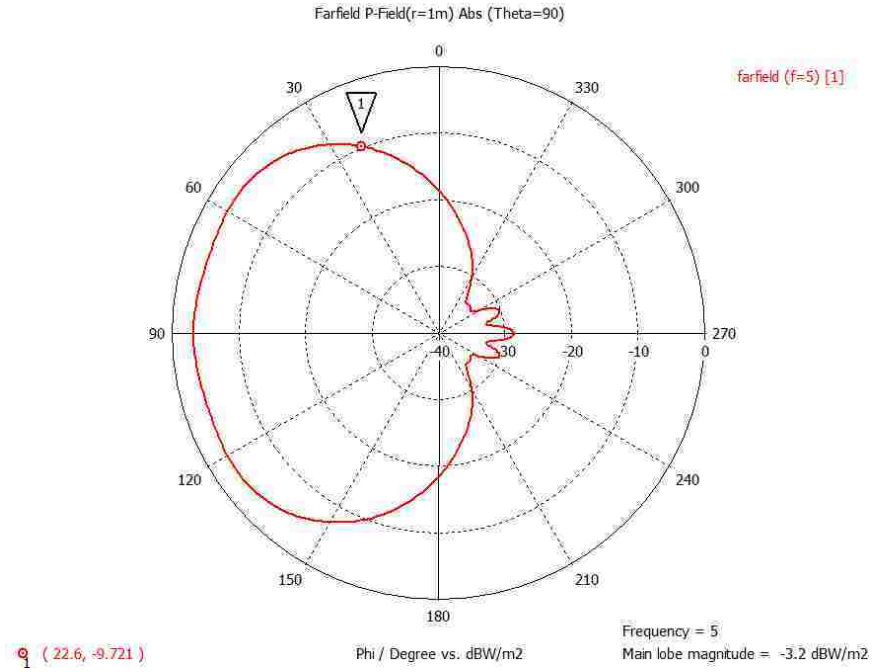

Figure 173: Power pattern of 4.995 GHz RSTN dipole in phi

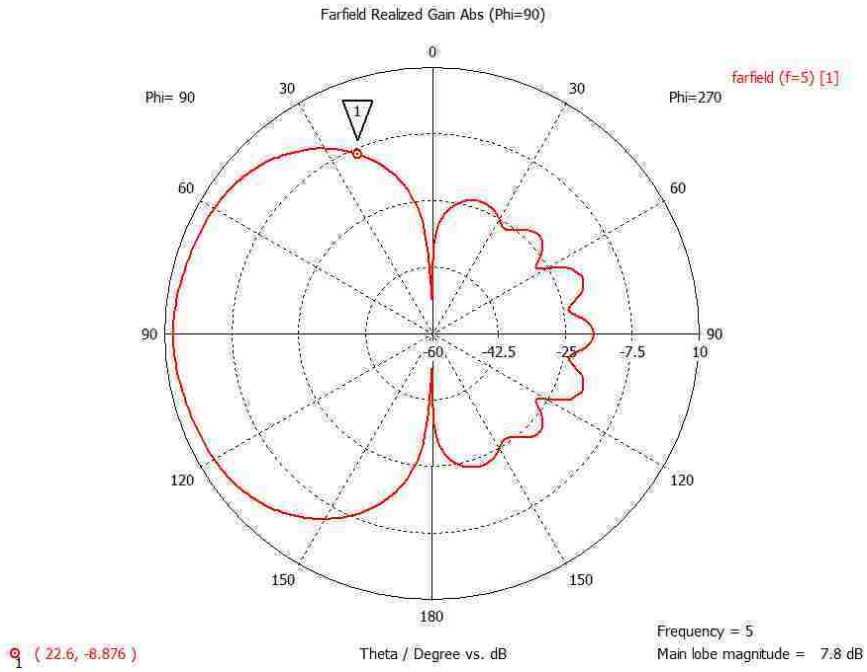

Figure 174: Realized gain pattern of 4.995 GHz RSTN dipole in theta

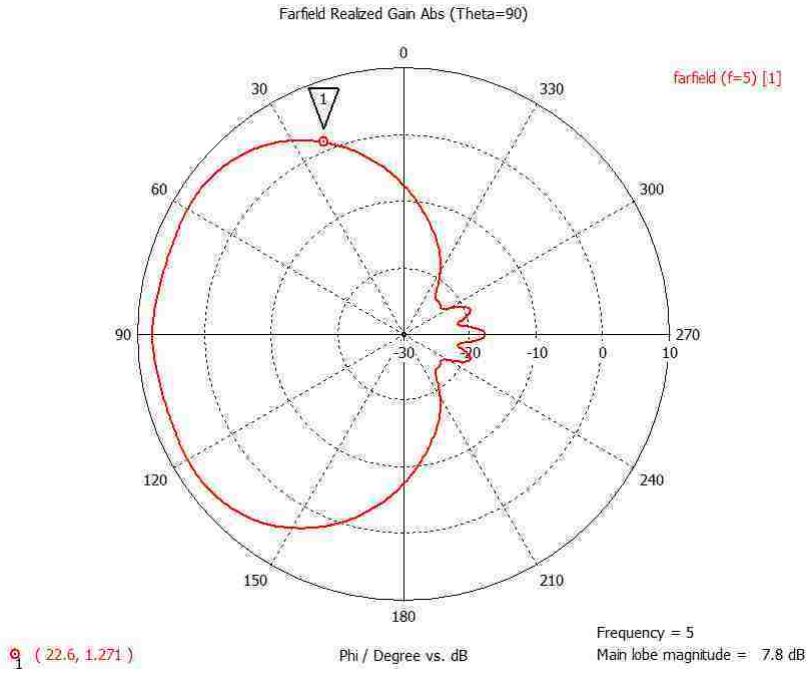

Figure 175: Realized gain pattern of 4.995 GHz RSTN dipole in phi

A 3D plot of realized gain was created for the 4.995 GHz RSTN dipole. As before the pattern as seen by the dish is not circular and displays a broader pattern in phi as compared to theta.

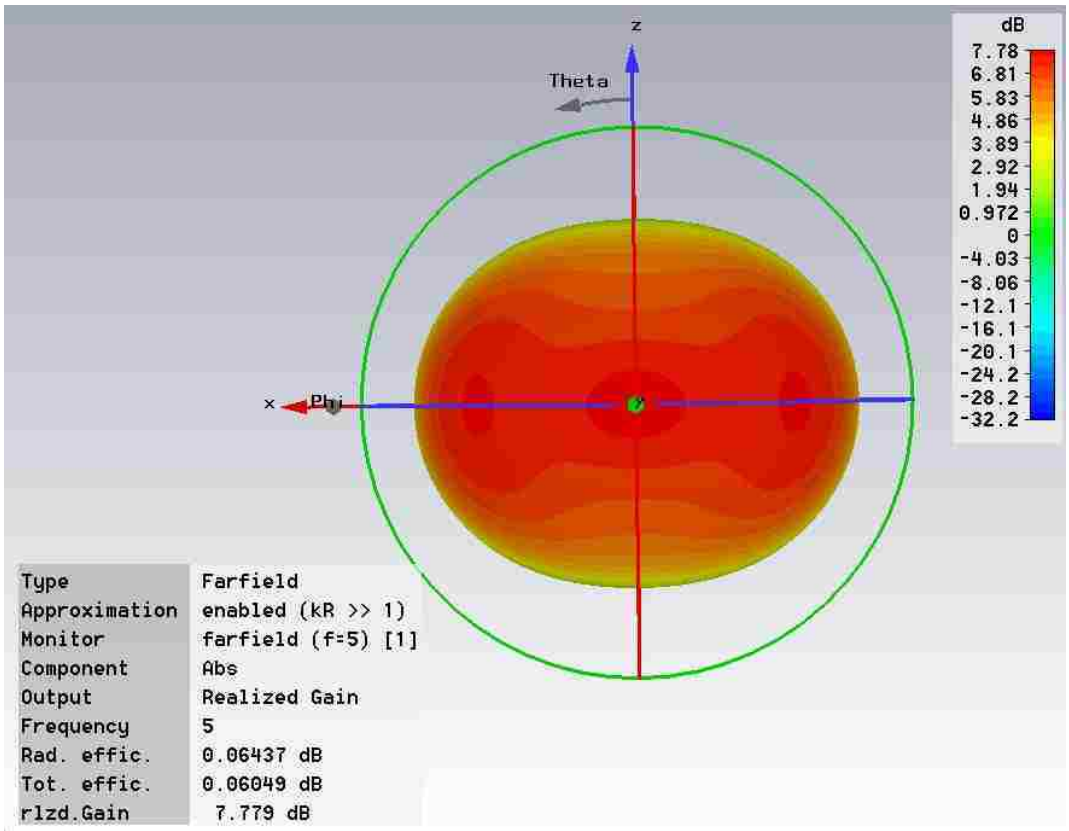

Figure 176: Boresight view of 4.995 GHz RSTN dipole pattern

In summary, simulations show the following feed tapers for the feed currently used in RSTN:

θ ranges from 14.3 to 16.7 dB

φ ranged from 6.3 to 6.5 dB

An improved feed would have a taper in phi that is greater than 6.5 dB, and a taper value that is closer to the simulated range for theta.

Owens Valley Solar Array Feed

The Owens Valley Solar Array (OVSA), now a legacy system, was one of the few ultrawideband solar observatories in existence. It was an interferometric imaging array using five 2.1m, f/D=0.35 dishes. These dishes subtend an angle of 142.2°, about 7.4° greater than the RSTN dishes. The beam squint observed from the feed used in the OVSA, the 1-18GHz TECOM Model 201302 log-periodic dipole array, will be discussed in the next section.

Typical radiation patterns for the 201302 [66] were provided by TECOM and measured to determine the beam width as shown in Figure 177 through Figure 179. The E-plane patterns are notated in red with the 134.8° dish edge limit for a RSTN dish. At 1GHz the main lobe at dish edge is 13.5dB less than its maximum value, 12.5dB at 5GHz and 19dB at 10GHz. It is likely that these patterns are for the theta direction, as the phi patterns would more resemble those of a dipole in phi.

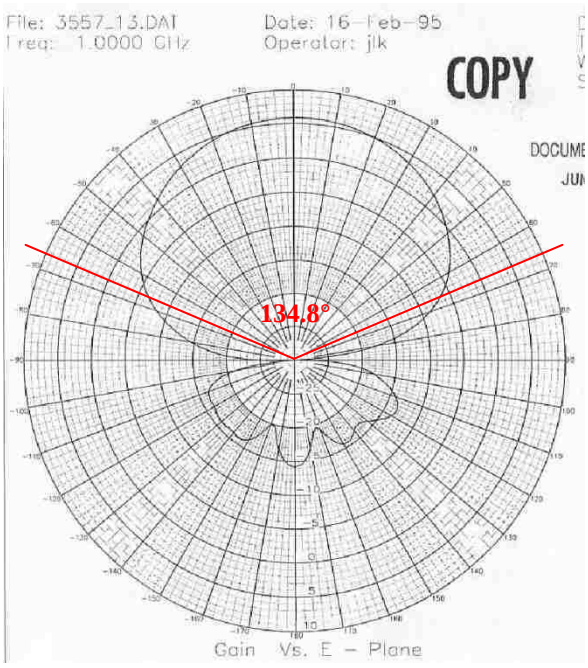

Figure 177: TECOM E-Plane Radiation Pattern at 1GHz
[66] Page 1.

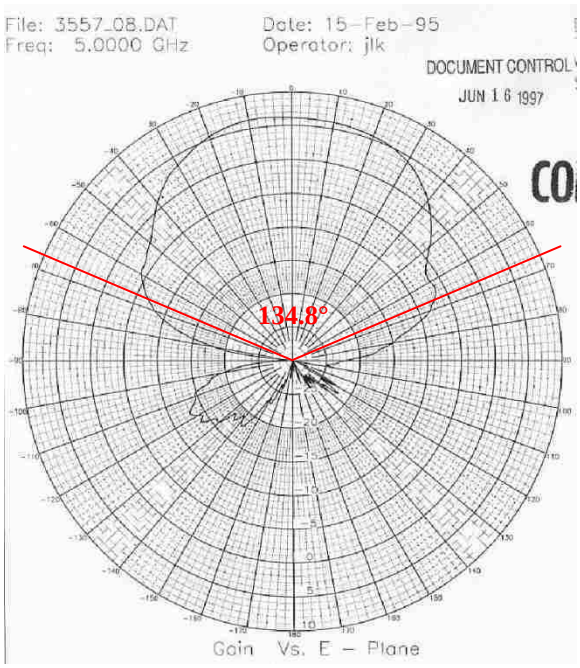

Figure 178: TECOM E-Plane Radiation Pattern at 5GHz
Page 5. [66]

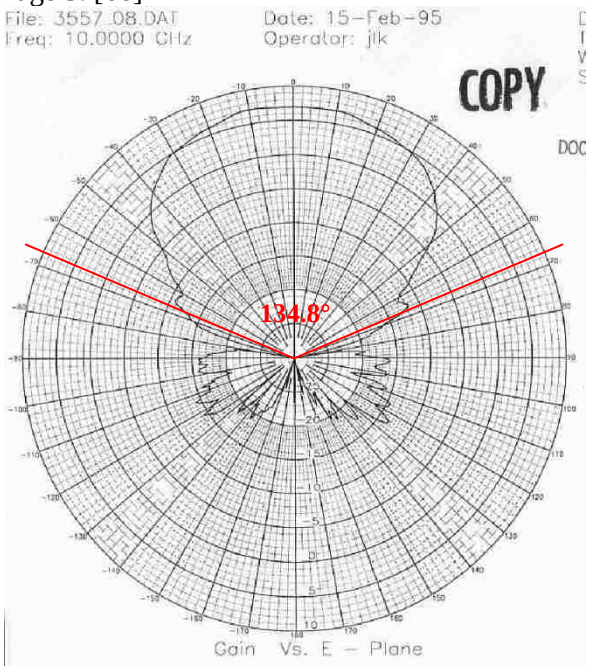

Figure 179: TECOM E-Plane Radiation Pattern at 10GHz
Page 10 [66]

The front to back ratio (FBR) was also measured from these patterns, as 20dB, 19dB, and 21dB at 1GHz, 5GHz, and 10GHz, respectively. A comparison to the diamond feed simulations is summarized in Table 12.

Table 12: Comparison of E-field tapers

Frequency, GHz	TECOM Feed Taper, dB	Simulated Diamond Feed Taper, dB
1	13.5	7.59
5	12.5	11.42
10	19	15.51

As shown in Table 12, the diamond feed has from 1 to 6 dB less E-field feed taper. Feed taper should be expressed in terms of power as was previously discussed, so without conversion such comparison is not complete. However, if it is assumed that the TECOM patterns are in the theta direction and that the phi patterns are broader due to it being a dipole array, then the diamond feed may be a candidate to be used in an OVSA system.

The Extended OVSA array is designed to use thirteen 2.1m dishes in an interferometric imaging array with a maximum baseline of about 1.5km and an expected resolution of about 60”/υ_{GHz} [34]. A further-refined diamond feed might be able to be characterized in one of the thirteen dishes without degrading observations.

Appendix B: The Finite Integration Technique (FIT)

It is assumed that the structure to be simulated has been captured by an appropriate grid.

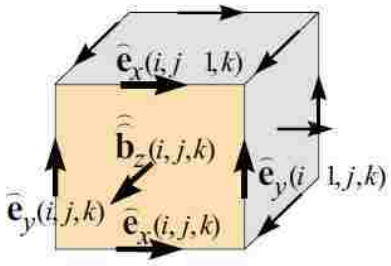

Figure 180: Cell depicting electric grid voltages.
Figure 1, p. 68. [67]

For each single cell volume, the integral form of Faraday's law may be written

$$\oint_{\partial A} \bar{E}(\bar{r},t) \bullet d\bar{s} = -\int\int_{A} \frac{\partial}{\partial t} \bar{B}(\bar{r},t) \bullet d\bar{A} \tag{B-1}$$

and can then be rewritten for a facet $A_z(i,j,k)$ as

$$\hat{e}_x(i,j,k) + \hat{e}_y(i+1,j,k) - \hat{e}_x(i,j+1,k) - \hat{e}_y(i,j,k) + = -\frac{d}{dt}\hat{\hat{b}}_z(i,j,k) \tag{B-2}$$

as shown in Figure 180 above. The scalar value

$$\hat{e}_x(i,j,k) = \int_{(x_i, y_j, z_k)}^{(x_{i+1}, y_j, z_k)} \bar{E} \bullet d\bar{s} \tag{B-3}$$

is the electric voltage alone the surface $A_z(i,j,k)$ on one edge, and is the integral over the electric field. The scalar value

$$\hat{\hat{b}}_z(i,j,k) = \int_{A_z(i,j,k)} \bar{B} \bullet d\bar{A} \tag{B-4}$$

is the magnetic flux through the cell facet $A_z(i,j,k)$.

The electric voltages $\hat{e}(i,j,k)$ and magnetic facet fluxes $\hat{\hat{b}}(i,j,k)$ are then composed into column vectors ordered in x, y, z such that

$$\hat{e} \ := \left(\hat{e}_{x,n} \mid \hat{e}_{y,n} \mid \hat{e}_{z,n}\right)^T_{n=1\ldots N_p} \tag{B-5}$$

and

$$\hat{\bar{b}} := \left(\hat{\bar{b}}_{x,n} \,|\, \hat{\bar{b}}_{y,n} \,|\, \hat{\bar{b}}_{z,n} \right)^{T}_{n=1\ldots N_p} \tag{B-6}$$

These can then be entered in matrix form:

$$\underbrace{\begin{pmatrix} & \cdots & \cdots & \cdots & & \\ 1 & \cdots & 1 & \cdots & -1 & \cdots & -1 \\ & \cdots & \cdots & \cdots & & \end{pmatrix}}_{\mathbf{C} :=} \underbrace{\begin{pmatrix} \hat{e}_{n_1} \\ \vdots \\ \hat{e}_{n_2} \\ \vdots \\ \hat{e}_{n_3} \\ \vdots \\ \hat{e}_{n_4} \end{pmatrix}}_{\hat{\mathbf{e}}} = -\frac{d}{dt} \underbrace{\begin{pmatrix} \vdots \\ \hat{\bar{b}}_n \\ \vdots \end{pmatrix}}_{\hat{\bar{\mathbf{b}}}}$$

where C is a discrete curl operator.

A second discrete differential operator is that of divergence, originating from Maxwell's equation,

$$\iint_{\partial V} \bar{B}(\bar{r},t) \bullet d\bar{A} = 0 \tag{B-7}$$

which is applied to a cell as shown in Figure 181 below.

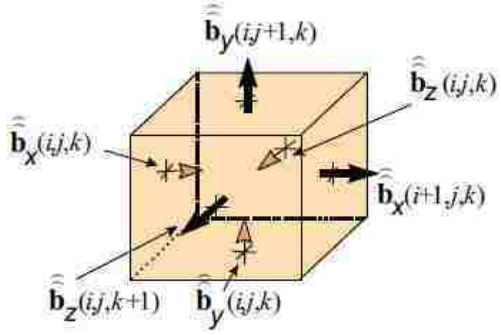

Figure 181: Cell showing six magnetic facet fluxes.
Figure 2, p. 69. [67]

Evaluation of the surface integral in the previous equation for this cell produces

$$-\hat{b}_x(i,j,k) + \hat{b}_x(i+1,j,k) - \hat{b}_y(i,j,k) + \hat{b}_y(i,j+1,k) - \hat{b}_z(i,j,k) + \hat{b}_z(i,j,k+1) = 0 \tag{B-8}$$

As before, this can be expressed in matrix form where S is a discrete divergence

$$\underbrace{\begin{pmatrix} . & -1 & 1 & \begin{matrix}\cdots\\ -1\\ \cdots\end{matrix} & \begin{matrix}\cdots\\ 1\\ \cdots\end{matrix} & -1 & 1 & . \end{pmatrix}}_{\mathbf{S}:=} \underbrace{\begin{pmatrix} \vdots \\ \hat{\hat{b}}_{m_1} \\ \hat{\hat{b}}_{m_2} \\ \hat{\hat{b}}_{m_3} \\ \hat{\hat{b}}_{m_4} \\ \hat{\hat{b}}_{m_5} \\ \hat{\hat{b}}_{m_6} \\ \vdots \end{pmatrix}}_{\hat{\hat{\mathbf{b}}}} = 0$$

A second cell complex is necessary to discretize the remaining two Maxwell's equations. In doing so there is a one-to-one correspondence between the cell edges cutting through cell surfaces. This is shown in Figure 182 below.

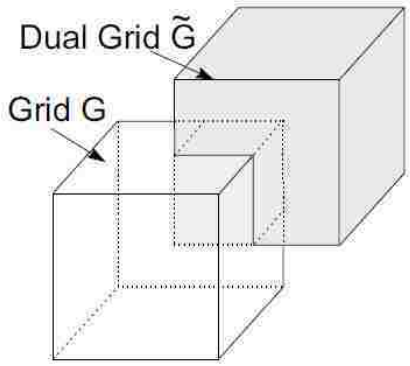

Figure 182: Dual grid system.
Figure 3, p. 71. [67]

The Maxwell-Grid-Equations (MGE) along with their familiar equivalents are

$$C\hat{e} = -\frac{d}{dt}\hat{\hat{b}} \quad \longleftrightarrow \quad \nabla \times \overline{E} = -\frac{d\overline{B}}{dt} \tag{B-9}$$

$$\tilde{C}\hat{h} = \frac{d}{dt}\hat{\hat{d}} + \hat{\hat{j}} \quad \longleftrightarrow \quad \nabla \times \overline{H} = \frac{d\overline{D}}{dt} + \overline{J} \tag{B-10}$$

$$S\hat{\hat{b}} = 0 \quad \longleftrightarrow \quad \nabla \bullet \overline{B} = 0 \tag{B-11}$$

$$\tilde{S}\hat{\hat{d}} = q \quad \longleftrightarrow \quad \nabla \bullet \overline{D} = q \tag{B-12}$$

where $\hat{e}$ and $\hat{h}$ are the electric and magnetic voltages respectively along both primary and dual edges. $\hat{\hat{d}}$, $\hat{\hat{b}}$ and $\hat{\hat{j}}$ are electric, magnetic, and current density fluxes respectively, across both primary and dual grid faces. The C and S matrices are the discrete equivalents of the curl and div operators on the primary grid. The $\tilde{C}$ and $\tilde{S}$ matrices are the same but for the dual grid. These grid structures are shown in Figure 182.

The time harmonic case in a loss free material with no source currents may be used as an example,

$$M_{\mu^{-1}} C\hat{e} = -j\omega\hat{h} \quad \longleftrightarrow \quad \nabla \times \bar{E} = -j\omega\mu\bar{H} \tag{B-13}$$

$$\tilde{C}\hat{h} = j\omega M_{\varepsilon}\hat{e} \quad \longleftrightarrow \quad \nabla \times \bar{H} = j\omega\varepsilon\bar{E} \tag{B-14}$$

and substitution yields

$$\tilde{C}M_{\mu^{-1}} C\hat{e} = \omega^2 M_{\varepsilon}\hat{e} \quad \longleftrightarrow \quad \nabla^2\bar{E} = \omega^2\mu\varepsilon\bar{E} \tag{B-15}$$

which is the discrete form of the wave equation.

To represent electric grid voltages along cell edges as differences in nodal potential values, discrete potential values *Φ(i,j,k)* are applied to intersecting grid mesh points of G so that

$$-\Phi(i+1, j, k) + \Phi(i, j, k) = \hat{e}_x(i, j, k) \tag{B-16}$$

and over the entire cell complex G,

$$\hat{e} = -G(\Phi) \tag{B-17}$$

where the discrete gradient matrix

$$G = -\tilde{S}^T \tag{B-18}$$

is the negative transpose of the dual grid discrete divergence operator. Similarly the magnetic potentials on dual cell $\tilde{G}$ are used for the discrete gradient matrix $-\tilde{S}^T$ with

$$\hat{h} = -\tilde{G}\Psi = S^T\Psi \tag{B-19}$$

where Ψ is a magnetic scalar nodal potential vector.

Discrete relationships exist for the material properties via the material matrices M_{ε}, $M_{\mu^{-1}}$ and M_{σ} as

$$\hat{\tilde{d}} = M_{\varepsilon}\hat{e} \quad \longleftrightarrow \quad \boldsymbol{D}=\varepsilon\boldsymbol{E} \tag{B-20}$$

$$\hat{h} = M_{\mu^{-1}}\hat{\tilde{b}} \quad \longleftrightarrow \quad \boldsymbol{B}=\mu\boldsymbol{H} \tag{B-21}$$

$$\hat{\tilde{j}} = M_{\sigma}\hat{e} + \hat{\tilde{j}}_A \quad \longleftrightarrow \quad \boldsymbol{J}=\sigma\boldsymbol{E}+\boldsymbol{J_A} \tag{B-22}$$

The matrix operators described so far have analogs to conventional vector analysis. Given that div(curl)=0,

$$SC = 0 \tag{B-23}$$

$$\tilde{S}\tilde{C} = 0 \tag{B-24}$$

and that curl(grad)=0,

$$\tilde{C}S^T = 0 \tag{B-25}$$

$$C\tilde{S}^T = 0 \tag{B-26}$$

The Finite Integration Technique also incorporates the continuity equation,

$$\nabla \bullet \left(\frac{\partial}{\partial t}\overline{D} + \overline{J} \right) = 0 \quad \longleftrightarrow \quad \tilde{S}\left(\tilde{C}\hat{h}\right) = \tilde{S}\left(\frac{d}{dt}\hat{\tilde{d}} + \hat{\tilde{j}} \right) \tag{B-27}$$

to ensure that no spurious charges are introduced.

For time domain analyses in MWS, time discrete energy conservation has been shown for the explicit FDTD leapfrog scheme [68] and for certain second order Newmark-type time marching schemes [69], [70]. The implicit two-step Crank-Nicolson scheme [71] and the one-step Averaged-Acceleration-scheme [72] are FDiTD (Finite Difference implicit Time Domain) methods, where the time discrete values for both magnetic and electric grid voltages $\hat{h}$ and $\hat{e}$ are evaluated at the same time. Methods such as the explicit Leapfrog implement a dual-staggered grid for the time axis.

FIT has the advantage of being able to accommodate any given mesh, whether 2D or 3D. Microwave Studio (MWS) offers the choice of tetrahedral or hexahedral meshes for both Transient Frequency Domain solvers. Simulations performed for this research were done with the default hexahedral mesh. Developments in sub gridding techniques permit local refinement of a Cartesian grid, such as in regions with either fine geometries or large variations in field, and this technique was used in MWS where needed.

MWS calculates and applies the Courant condition for stability where the maximum time step Δt is determined as

$$\Delta t \le \left(c\sqrt{\left[\frac{1}{\Delta x^2} + \frac{1}{\Delta y^2} + \frac{1}{\Delta z^2} \right]} \right)^{-1} \tag{B-28}$$

where Δx, Δy, Δz are the cell sizes in Cartesian coordinates [73].

Once the structure is meshed a frequency range for Time Domain analysis must be specified which then directs MWS to create an excitation pulse. If the lowest frequency is zero then the pulse will be a Gaussian waveform, and if the lowest frequency is greater than zero the pulse will be a differentiated Gaussian with no DC component.

A port must then be applied to the structure to provide the excitation. There are two choices of port, discrete and waveguide. Discrete ports are used to drive electrically small areas such as the input terminals of a bow tie antenna, whereas waveguide ports are used for larger structures. Discrete ports were used for all simulations.

For radiating structures such as antennas the boundary conditions must be chosen. The most appropriate boundary in this instance is a Perfectly Matched Layer (PML) with distance from the structure determined by the lowest frequency. A PML absorbs waves in the computational domain and minimizes reflections at the PML boundary.

In the general sense, for waves propagating in the x direction, the wave equation is altered such that wherever $\frac{\partial}{\partial x}$ occurs it is replaced as follows:

$$\frac{\partial}{\partial x} \to \frac{1}{1 + \frac{j\sigma(x)}{\varpi}} \frac{\partial}{\partial x} \tag{B-29}$$

where σ is a function of x, such that wherever σ is positive, propagating waves will be attenuated. Consider the equivalence of

$$x \to x + \frac{j}{\omega} \int^{x} \sigma(x')dx' \quad \text{to} \quad dx \to dx\left(1 + \frac{j\sigma}{\varpi}\right) \tag{B-30}$$

so that when a wave is propagating in the +x direction and σ is positive,

$$e^{j(kx-\varpi t)} \to e^{j(kx-\varpi t) - \frac{k}{\varpi}\int^{x} \sigma(x')dx'} \tag{B-31}$$

which will cause exponential attenuation [73].

MWS uses a multi-layer PML to account for discretization effects. All simulations performed for this research used the default setting of four layers.

Appendix C: ECCOSORB RF Absorbent Material

ECCOSORB MF-117 manufactured by Emerson & Cuming Microwave Products is a semi-rigid, magnetically loaded epoxide sheet that is absorbent in the 1-18 GHz range.

The manufacturer [74] provides specifications as listed in Table 13.

Table 13: MF-117 Specifications

	1MHz	**10MHz**	**100MHz**	**1GHz**	**3GHz**	**8.6GHz**	**10GHz**
K'	62	48	38	28	22.9	21.4	21
tan δ_d	0.22	0.18	0.12	0.09	0.06	0.02	0.02
K''	14	8.6	4.6	2.5	1.4	0.42	0.42
M'	5	5	4.8	4.1	3.4	1.2	1.1
tan δ_m	<0.01	<0.01	0.1	0.2	0.39	1.36	1.5
M''	<0.01	<0.01	0.48	0.82	1.33	1.63	1.7
dB/cm	<0.01	0.3	0.27	2.8	11	46	56
$\lvert Z\rvert/Z_o$	0.28	0.32	0.36	0.39	0.4	0.3	0.31

K' = real part of the permittivity (dielectric constant) = ε'

tan δ_d = dielectric loss tangent = $\tan\delta_d = \dfrac{\omega\varepsilon'' + \sigma}{\omega\varepsilon'}$

K" = imaginary part of the permittivity (loss) = ε''

M' = real part of the magnetic permeability = μ'

tan δ_m = magnetic loss tangent = $\tan\delta_m = \dfrac{\mu''}{\mu'}$

M" = imaginary part of the magnetic permeability (loss) = μ''

dB/cm = attenuation per unit distance

$|Z|/Z_o$ = normalized impedance magnitude ratio

Given the definition of complex permittivity as

$$\varepsilon = \varepsilon' - j\varepsilon'' \qquad \text{(C-1)}$$

and assuming the time harmonic form of Ampere's law,

$$\nabla \times \overline{H} = j\omega\overline{D} + \bar{J} \tag{C-2}$$

then substitution yields

$$\nabla \times \overline{H} = j\omega\left(\varepsilon' - j\varepsilon''\right)\overline{E} + \sigma\overline{E} \tag{C--3a}$$

$$\nabla \times \overline{H} = j\omega\varepsilon'\overline{E} + \left(\omega\varepsilon'' + \sigma\right)\overline{E} \tag{C--3b}$$

where it can be seen that both the complex component of the permittivity, and the ohmic resistance, give rise to losses.

It is typical to express the dielectric loss factor as a loss tangent, as

$$\tan\delta_d = \frac{\omega\varepsilon'' + \sigma}{\omega\varepsilon'} \tag{C-4}$$

A similar analysis may be applied to incorporate magnetic permeability, by considering the time harmonic form of Faraday's law,

$$\nabla \times \overline{E} = -j\omega\mu\overline{H} \tag{C-5}$$

and the definition of complex permeability,

$$\mu = \mu' - j\mu'' \tag{C-6}$$

Substituting [75],

$$\nabla \times \overline{E} = -j\omega\mu\overline{H} = -j\omega\left(\mu' - j\mu''\right)\overline{H} \tag{C-7a}$$

$$\nabla \times \overline{E} = -j\omega\mu'\overline{H} - \omega\mu''\overline{H} \tag{C-7b}$$

where, as before, the complex component magnetic permeability gives rise to a loss.

Like the dielectric permittivity the magnetic permeability loss is also expressed as a loss tangent,

$$\tan\delta_m = \frac{\mu''}{\mu'} \tag{C-8}$$

The complex magnetic permeability may also be a function of frequency, as in the ECCOSORB material, where

$$\dot{\mu} = \mu'\omega - j\mu''(\omega) \tag{C-9}$$

One way to view attenuation due to such loss is by the wave equation for source-free, lossy material, where

$$\nabla^2 \overline{H} - \gamma^2 \overline{H} = 0 \tag{C-10}$$

and

$$\gamma = \pm(\alpha + j\beta) \tag{C-11}$$

where γ is the propagation constant, α is the attenuation constant in Nepers/meter, and β is the wave number in radians/meter. β is also referred to as *k* where

$$k = \omega\sqrt{\mu\varepsilon'} = \frac{2\pi}{\lambda} \tag{C-12}$$

For a traveling wave in the z-direction in source-free and lossy media in rectangular coordinates, a solution to the wave equation may take on the form of,

$$h(z) = Ae^{-j\gamma z} \tag{C-13}$$

where

$$e^{-\gamma z} = e^{-\alpha z} e^{-j\beta z} \tag{C-14}$$

In this example it can be seen that the magnitude of the wave will be attenuated as z increases due to the attenuation constant. Considering the definition of the instantaneous Poynting vector

$$\overline{P} = \overline{E} \times \overline{H} \tag{C-15}$$

where solution to the electric field wave equation is of the form

$$e^{-jkz} \tag{C-16}$$

and a solution to the magnetic field wave equation due to losses is of the form

$$e^{-\gamma z} = e^{-\alpha z} e^{-jkz} \tag{C-17}$$

Then it can be seen that

$$P \propto e^{-\alpha z} \tag{C-18}$$

such that power will be attenuated over distance.

Appendix D: Perfect Symmetry Log-Periodic Dipole Array

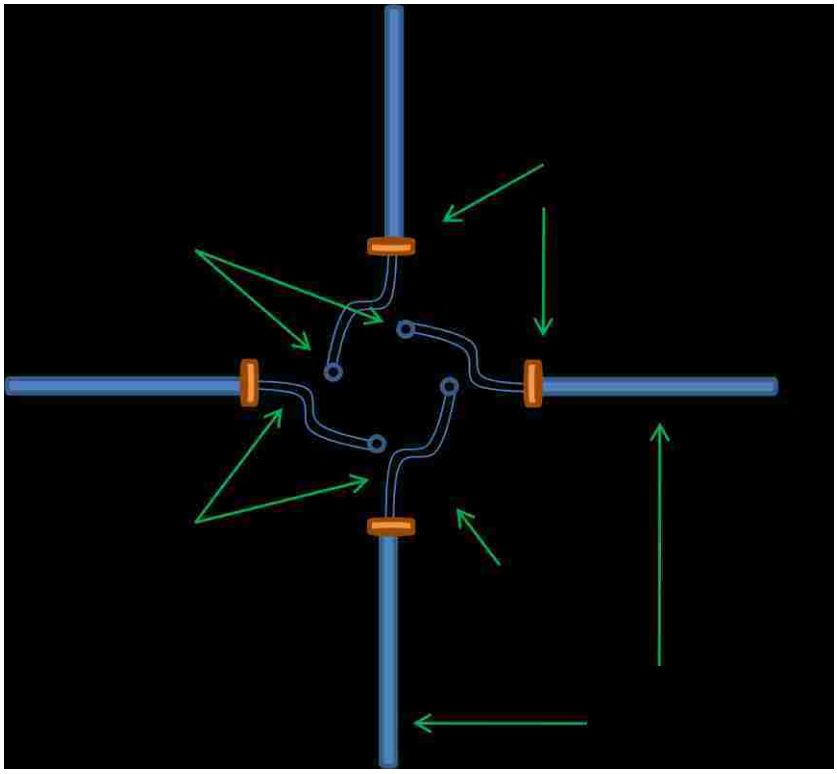

Figure 183: Concept Drawing of Perfect Symmetry LPDA.

Figure 183 depicts the concept of a perfect symmetry LPDA as proposed by Dr. Jerald Buchenauer. Unlike a conventional LPDA where the feed booms are exposed and may interact with the dipole elements, the feed booms are contained within a hollow cylindrical shield. Striplines, i.e., transmission lines buried between a top and bottom conducting plane, connect the dipole elements to the feed booms. Insulating gaskets prevent the dipole elements from shorting to the shield structure.

To prevent interactions within the shield structure more isolation must be implemented. The striplines must be shielded from each other. The feed booms must also be shielded from each other while at the same time possessing the desired characteristic impedance. This may be accomplished by fabricating the feed booms so that their structure resembles triaxial cable along with suitable internal shielding.

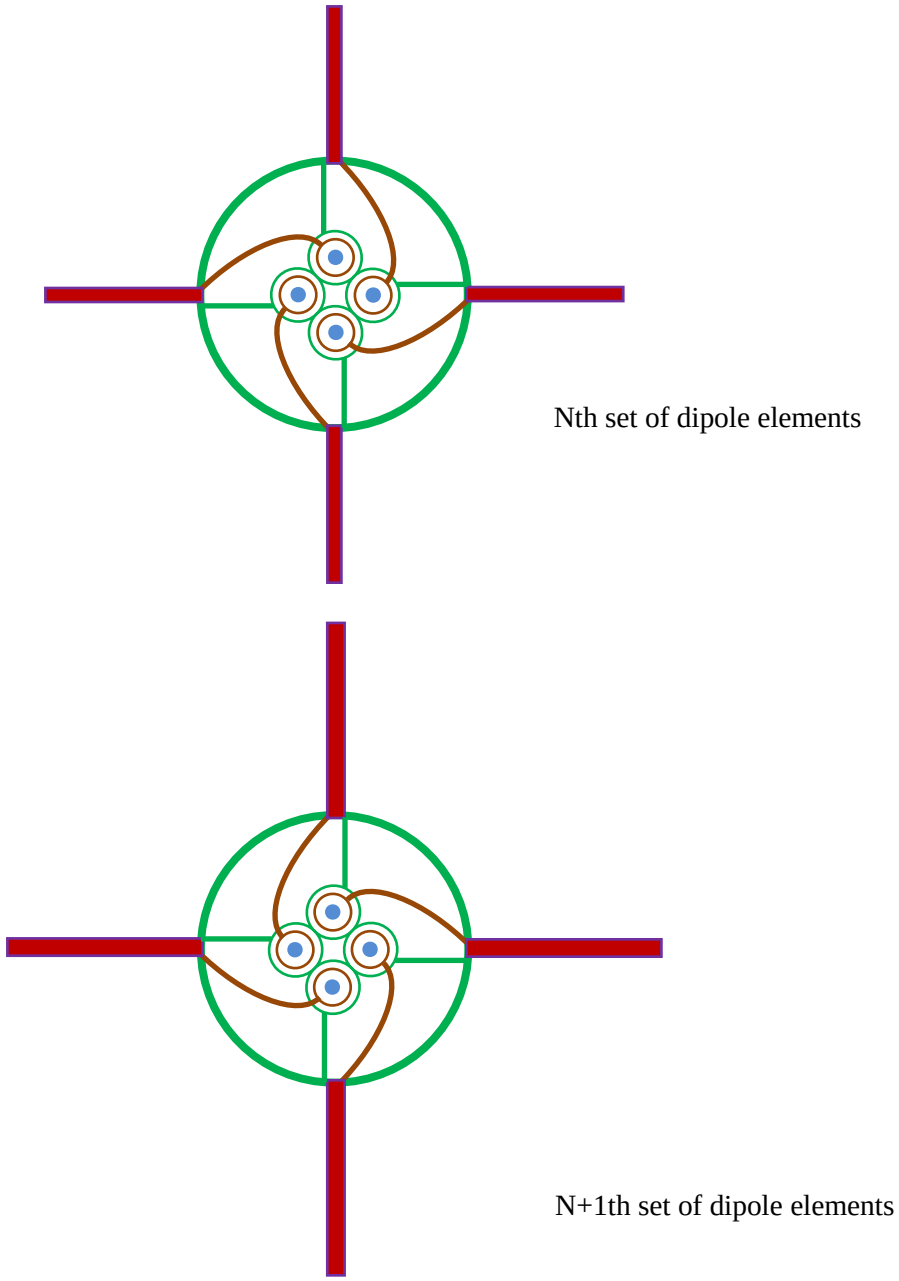

Figure 184: LPDA with High Degree of Symmetry.

Figure 184 depicts a possible implementation of a highly symmetrical dual-polarization LPDA. The drawing is not to scale. Triaxial structures in the center serve as the four feed booms for the dipole pairs and is customary with an LPDA, dipoles are fed from opposite booms. Striplines, shown in brown, feed the dipole elements from the

inner shield of the feed booms. Since these structures are striplines they are buried between conductive planes on top and bottom thus there should be very little interaction from one set of striplines to the next set farther along the boom. In this manner the Nth set of striplines should interact very little with the N+1th set. Metal shields shown in green connect the outer shields of the triaxial booms to the outer metallic cylinder which is also shown in green. These shields isolate striplines in the Nth set of dipoles from each other.

As the structure is examined along the apex the layout is seen to alternate as shown in Figure 184. This layout ensures that each dipole element is fed symmetrically and with the proper phasing.

It was shown by simulation in a previous section that physical offsets on the order of 100μm or 1° were sufficient to introduce a an amount of beam squint that could be undesirable in a high-gain system such as a RSTN dish. The interactions between elements, feed booms, and other structural elements was not modeled or analyzed but may be suspect when trying to minimize or eliminate squint. The physical implementation of an LPDA as shown in Figure 185 through Figure 191 may mitigate such concerns. Two concerns still remain:

1. Manufacturing tolerances will still remain a concern, and
2. Currently there exists no way to fabricate such a structure.

At some future date it is likely that 3D printing technology will advance to the point where such a structure could be fabricated using suitable microwave substrate and metallization and with the desired precision. Such a 3D printer would possess the capability of being able to deposit either microwave substrate material or metallization and with a precision on the order of 10μm or better.

At present such technology does not exist so this design was not pursued further. However, a representative three-dimensional model shown on the following pages was captured in MWS to illustrate a possible implementation.

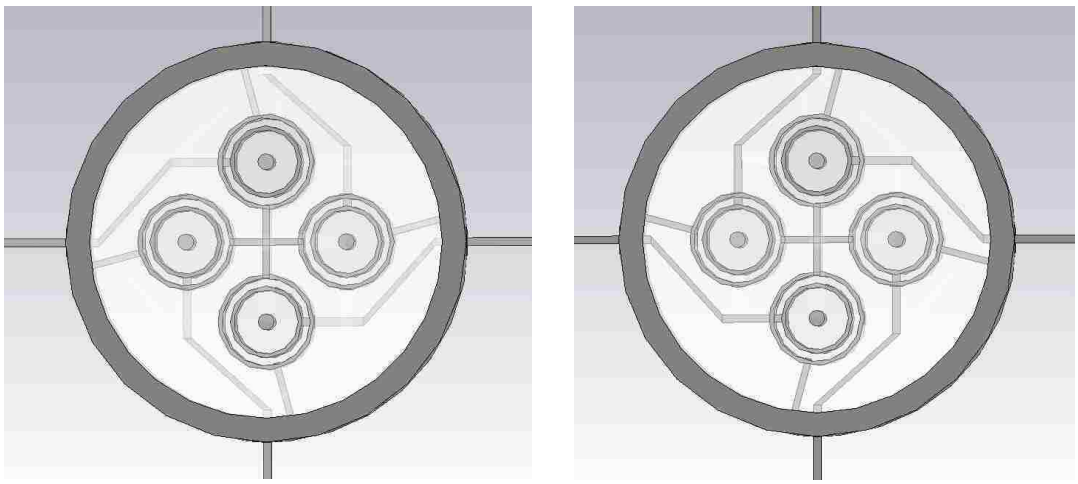

(a) (b)

Figure 185: Nth (a) and N+1th layer (b) of highly symmetric LPDA.

Figure 185(a) shows the Nth layer of the highly symmetric LPDA while Figure 185(b) depicts the N+1th layer. Metal is depicted in light or dark gray and everything else in the structure is comprised of a suitable microwave dielectric.

Four triaxial structures - two for each polarization - serve as feed lines. The outer conductor is a shield, and all four outer conductors are connected together by the '+' shaped structure in the center. Each outer conductor also connects to the outer tube so that each stripline is shielded from each other. It can be seen that the four regions in which each stripline is enclosed are identical.

Each stripline is fed by the middle conductor its corresponding triaxial structure. A gap exists in the outer conductor to allow passage of the stripline.

Each layer alternates direction regarding which dipole element is fed from a given feed line. For example, the top center triaxial structure feeds the left element in the Nth layer (a), but feeds the right element in the N+1th layer (b). As before, each region containing a stripline is identical to any other such region.

This layout would alternate throughout the length of the LPDA.

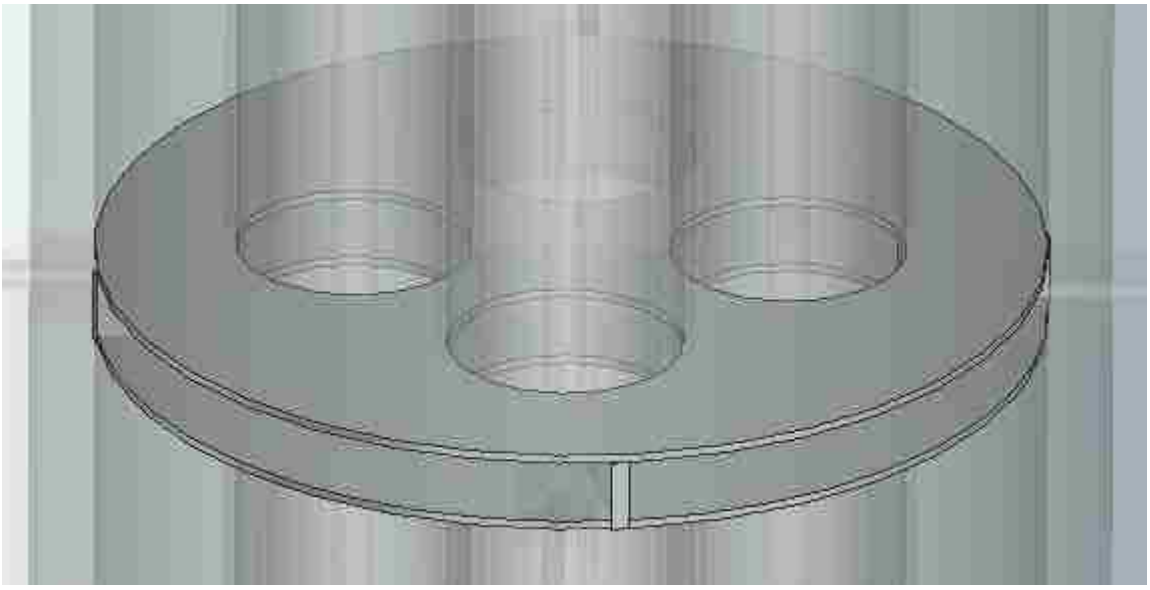

Figure 186: Ground planes for striplines.

A stripline is defined by a conductor between two ground planes. In Figure 186 the ground planes are depicted. while the triaxial structures are translucent. Except for shields and the stripline itself the region between ground planes is filled with dielectric.

Each layer (Nth, N+1th, etc) would have two such disk-shaped ground planes with circular cutouts for passage of the triaxial feed structures. Shields are placed each 90° around the structure to shield one stripline from another. One of these shields is visible in the center bottom of Figure 187.

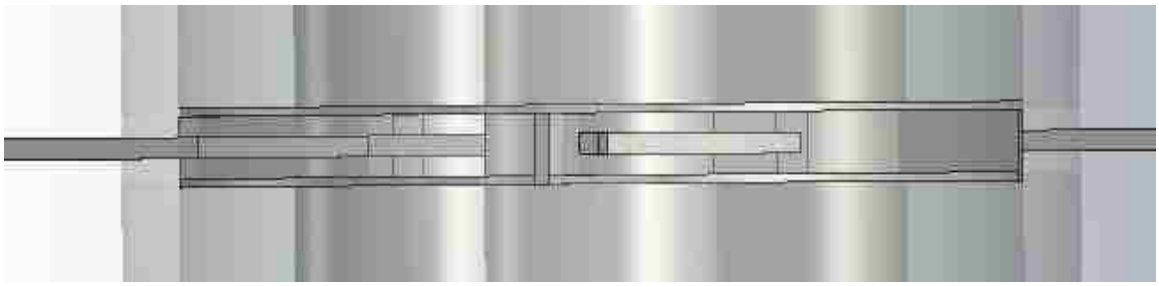

(a)

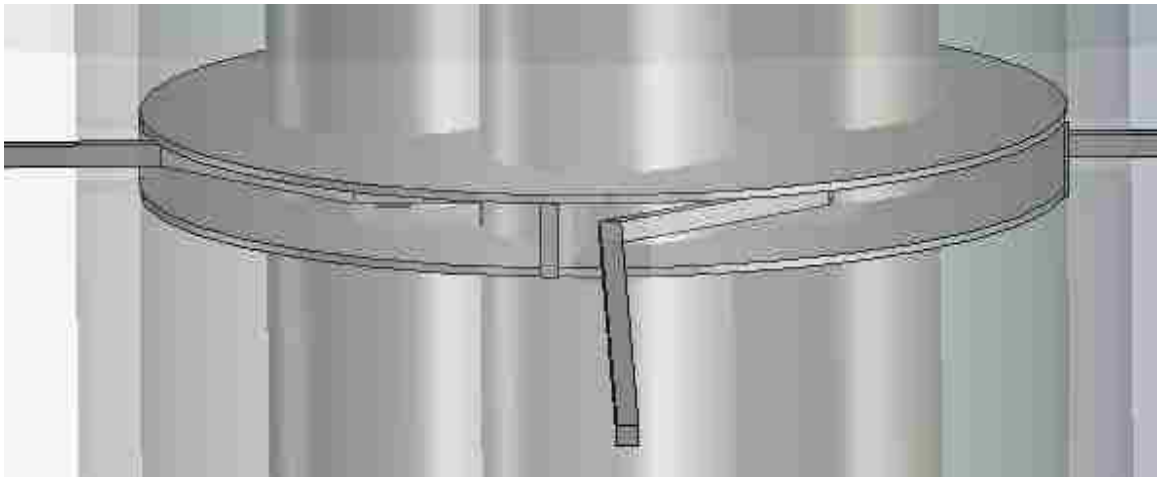

(b)

Figure 187: Stripline layout.

Figure 187(a) and Figure 187(b) depict the regions in which the striplines reside and how the striplines feed a given dipole element. As before these regions are filled with a suitable dielectric material. In this example each stripline has the same cross-sectional dimensions as the dipole element. This is not a necessary condition but was drawn in this fashion to simplify the drawing. If this structure becomes feasible to fabricate then a careful study of the stripline and triaxial feed impedances and dimensions should be performed.

Metal is shown in gray, everything else is dielectric material.

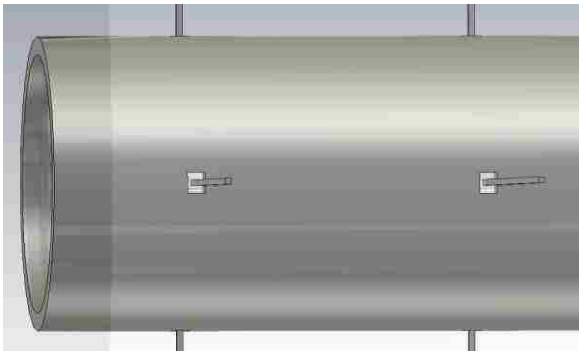

(a)

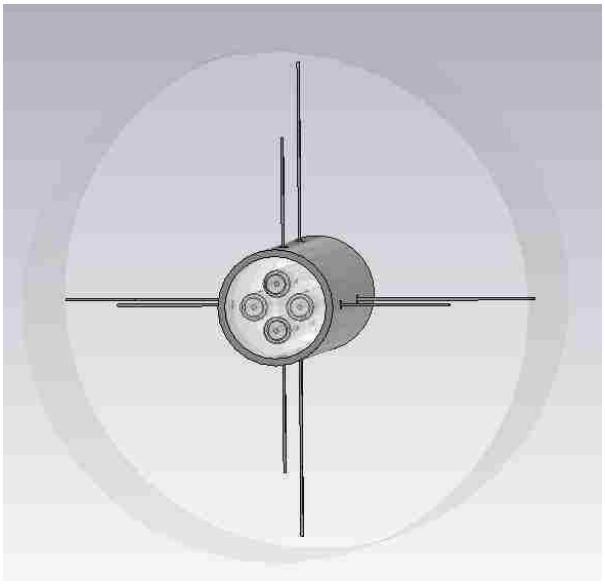

(b)

Figure 188: View of outer shield tube.

Figure 188(a) depicts the outer shield tube and the openings through which the striplines feed the dipole elements. Metal is shown in gray and everything else is dielectric. As the dipole elements increase in cross-sectional area logarithmically, the openings in the shield tube should increase proportionately.

Figure 188(b) shows a truncated version of the LPDA with two sets of dual-linear polarization dipole elements. The end cap is not shown so that the central longitudinal triaxial structures may be seen.

For strict LPDA implementation the feed tube would be a tapered cylinder. This feature is not shown in this example drawing.

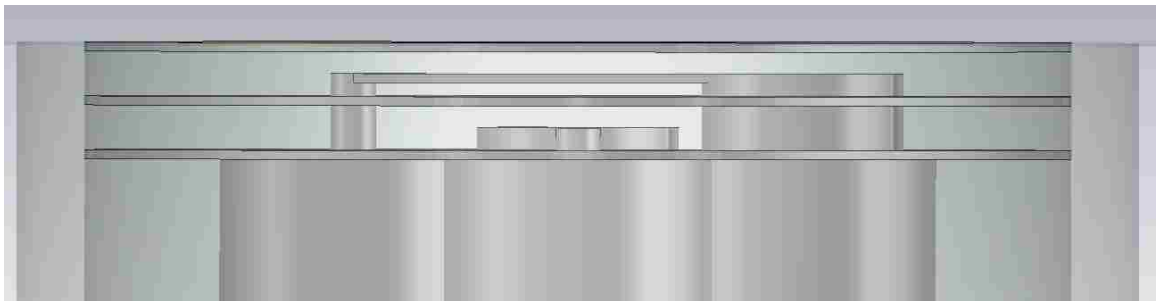

(a)

(b)

Figure 189: Balun implementation for dual-polarization.

A balun is typically implemented in an LPDA by running coaxial cable down the length of the LPDA towards the vertex. Here the same scheme is implemented except that the middle conductor of the triaxial structure is substituted for the outer conductor of a coaxial conductor, and the outer conductor of the triax becomes a shield. Such an implementation requires the central conductor to cross over and connect to the middle conductor of the triax and for each of the two linear polarizations.

Figure 189 depicts a possible manner in which this may be accomplished. In Figure 189(a), one of the pairs of triaxial structures is connected in such a manner. On the left the center conductor may be seen protruding in such a manner as to facilitate crossover to the complementary triaxial middle conductor via stripline. The upper two layers in the drawing form the ground planes for the crossover stripline.

Figure 189(b) shows the entire structure rotated 90° about its longitudinal axis to depict the stripline that effects the balun of the orthogonal polarization to (a).

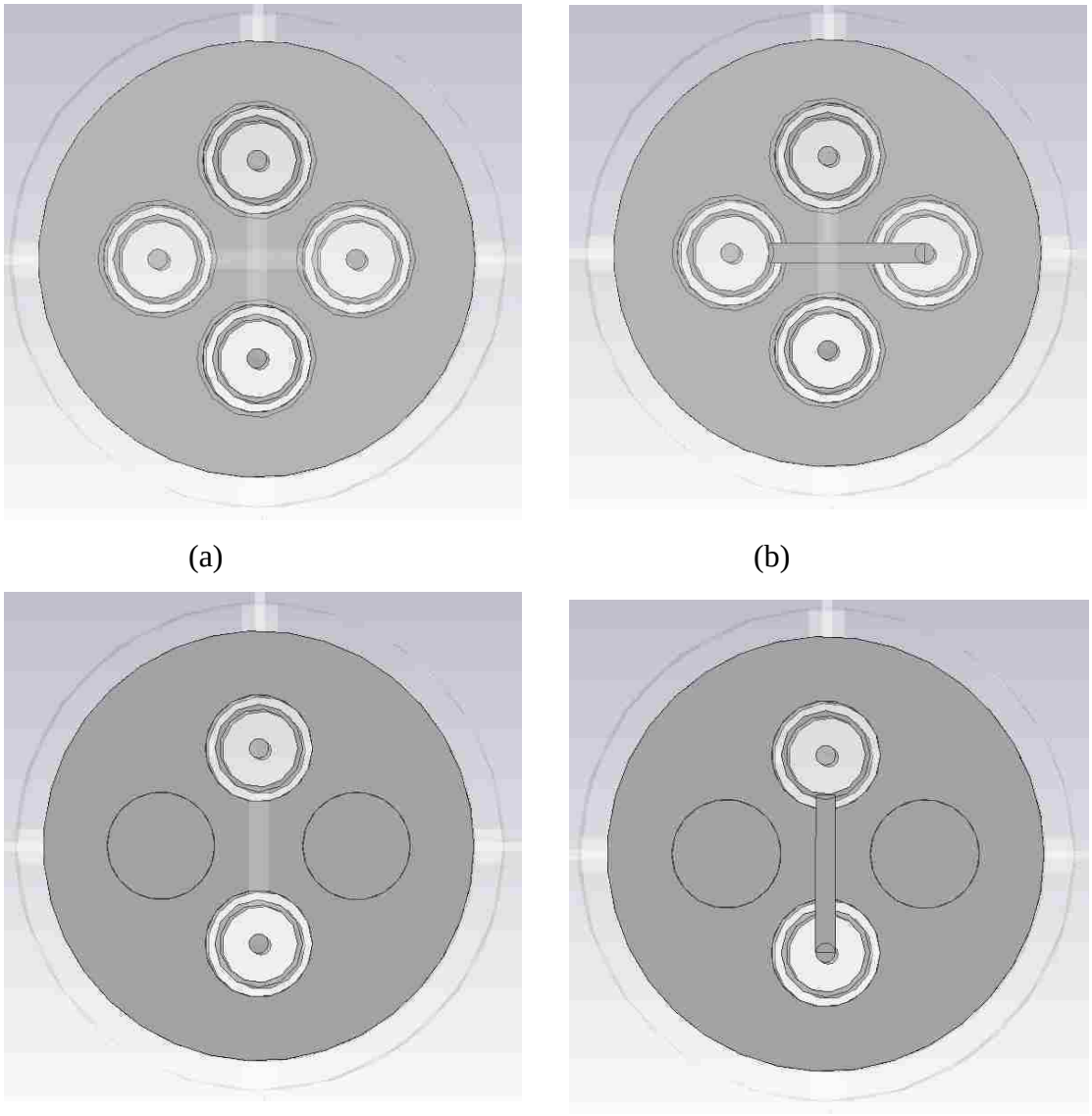

Figure 190: Ground planes and crossovers for balun.

Figure 190 depicts the buildup of metallization and dielectric to implement the dual-polarization balun structure described in Figure 189. Figure 190(a) shows the bottom most ground plane of Figure 189, and it can be seen that all four triaxial structures feed through this disk. The outer conductor of each triaxial structure merges with the ground plane. In (b), a stripline is implemented to connect the left triaxial middle conductor with the right triaxial central conductor. In (c) the middle of the three ground plane disks is seen as having the left and right holes filled in with metal. This serves to shield the lower balun crossover from the upper. In drawing (d) the stripline crossover

connecting the lower triaxial structure's center conductor to the top triax middle conductor is shown.

A third, top ground plane disk is added to complete the shielding of the structure. This is depicted in Figure 191(a). As previously stated the entire structure is embedded in dielectric to maintain mechanical tolerances on the order of 10μm and this is shown in (b), where the metal is gray and the dielectric is colored green. The outer dielectric fill need not be disk-shaped as depicted in Figure 191(b), and it may be desirable to implement a cone or other structure on the front face.

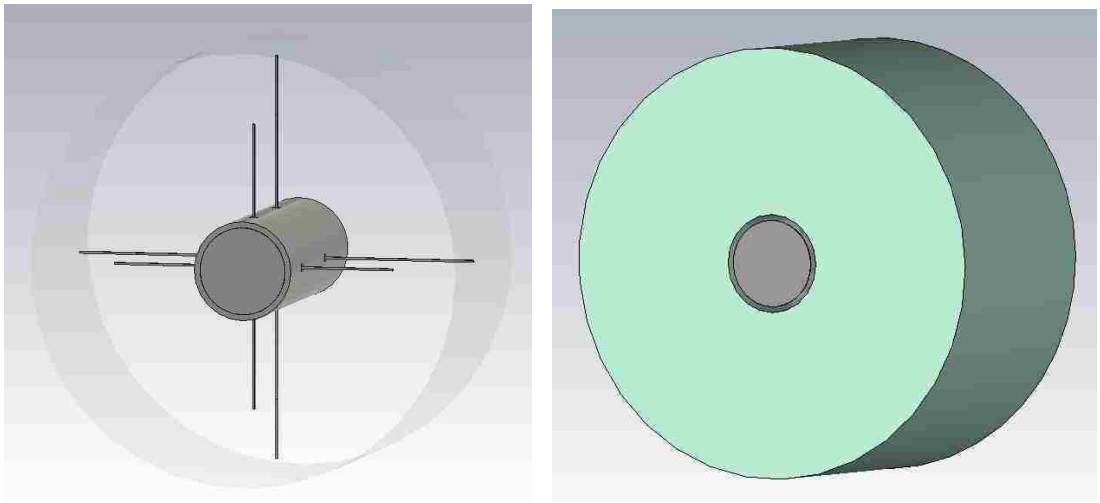

(a) (b)

Figure 191: Front view of LPDA.

Appendix E: Dr. Carl Baum's Design Suggestion

Dr. Carl Baum suggested a design approach using a planar bow tie antenna attached to a damped cavity. His design was simulated in Microwave Studio and then adapted based upon knowledge acquired from the folded diamond design.

It is highly likely that Dr. Baum's design approach would have worked given further insight and guidance from him.

While Dr. Baum's design approach was simulated it was not fabricated for purposes of this dissertation.

Figure 192depicts Dr. Baum's design suggestion. It consists of a cylindrical copper can of the dimensions to fit a SRBL mountain cavity, 175mm in diameter and 100mm deep. The bottom 25mm of the cavity was 25mm thick of ferrite with $\varepsilon_r = \sim 10$, and is shown in green. The bow tie antenna elements are on a suitable microwave substrate and connect to the cylinder. Only one polarization is shown in Figure 192. The red cone is the discrete excitation source used in MWS.

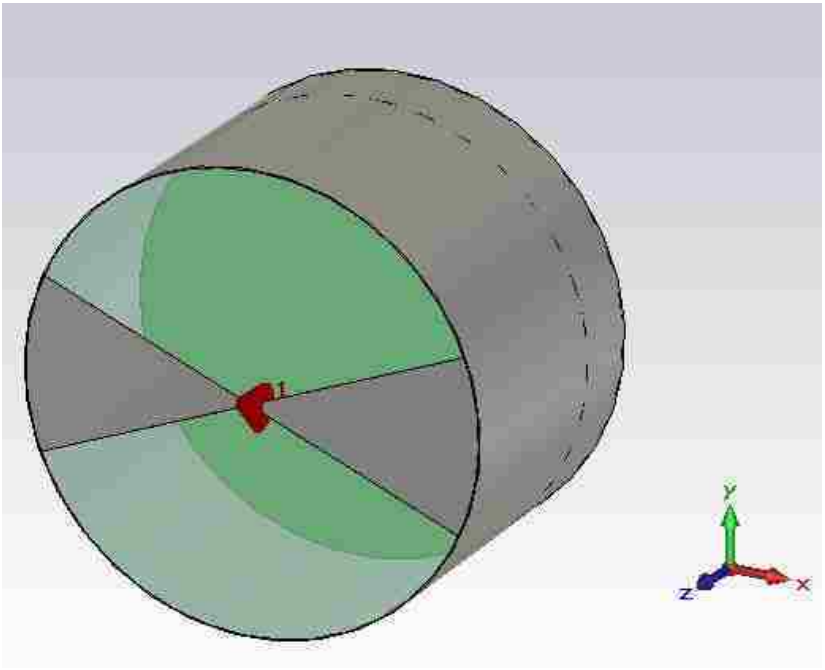

Figure 192: Dr. Baum's design suggestion.

Simulations were performed in Microwave Studio on the structure as initially described by Dr. Baum. A screenshot of the simulated dimensions of the structure as

shown in Figure 193. Simulated radiation patterns for 1, 5 and 10 GHz are shown in Figure 194 where it can be seen that at 5 and 10 GHz the side lobes point away from the dish, as the z-axis is directed towards the dish center. The simulated magnitude of impedance vs. frequency plot is presented in Figure 195 where it can be seen that the impedance varies greatly from 1-10 GHz.

Name	Value
add_space_bot	2
add_space_side	5
antenna_angle	45
antenna_l	antenna_r*cosD(antenna_angle/2)
antenna_r	75
antenna_w1	tanD(antenna_angle/2)*launch_gap/2+antenna_w1_add
antenna_w1_add	0.05
antenna_w2	sinD(antenna_angle)*antenna_r/(sinD((180-antenna_angle)/2))
can_h	100
can_t	0.5
ferrite_h	25
ferrite_mr	10
launch_gap	4
launch_w	0.5
mesh_step_antenna	0
mesh_step_ferrite	0
mesh_step_launch	launch_gap/4
port_z	50
sub_h	0.5
t	0.035

Figure 193: Dimensions of Dr. Baum's structure.

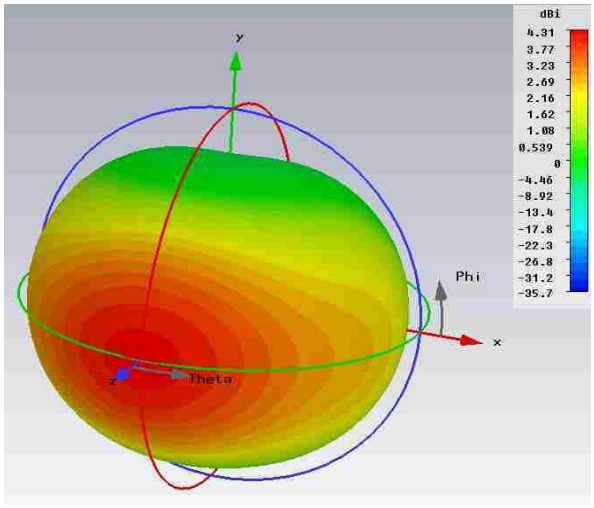

f = 1 GHz

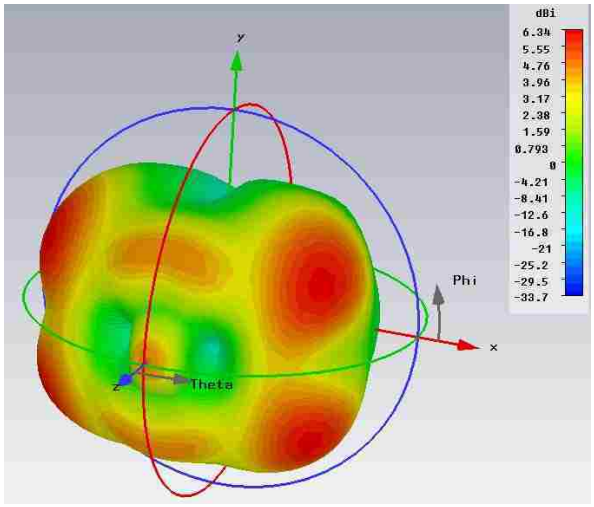

f = 5 GHz

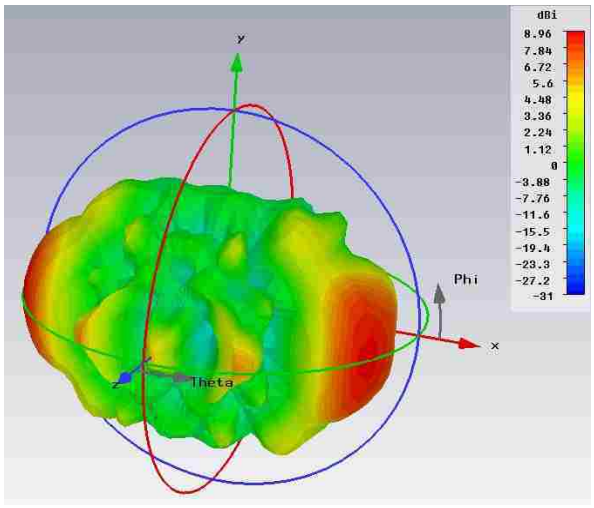

f = 10 GHz

Figure 194: Simulated radiation patterns for Dr. Baum's suggestion.

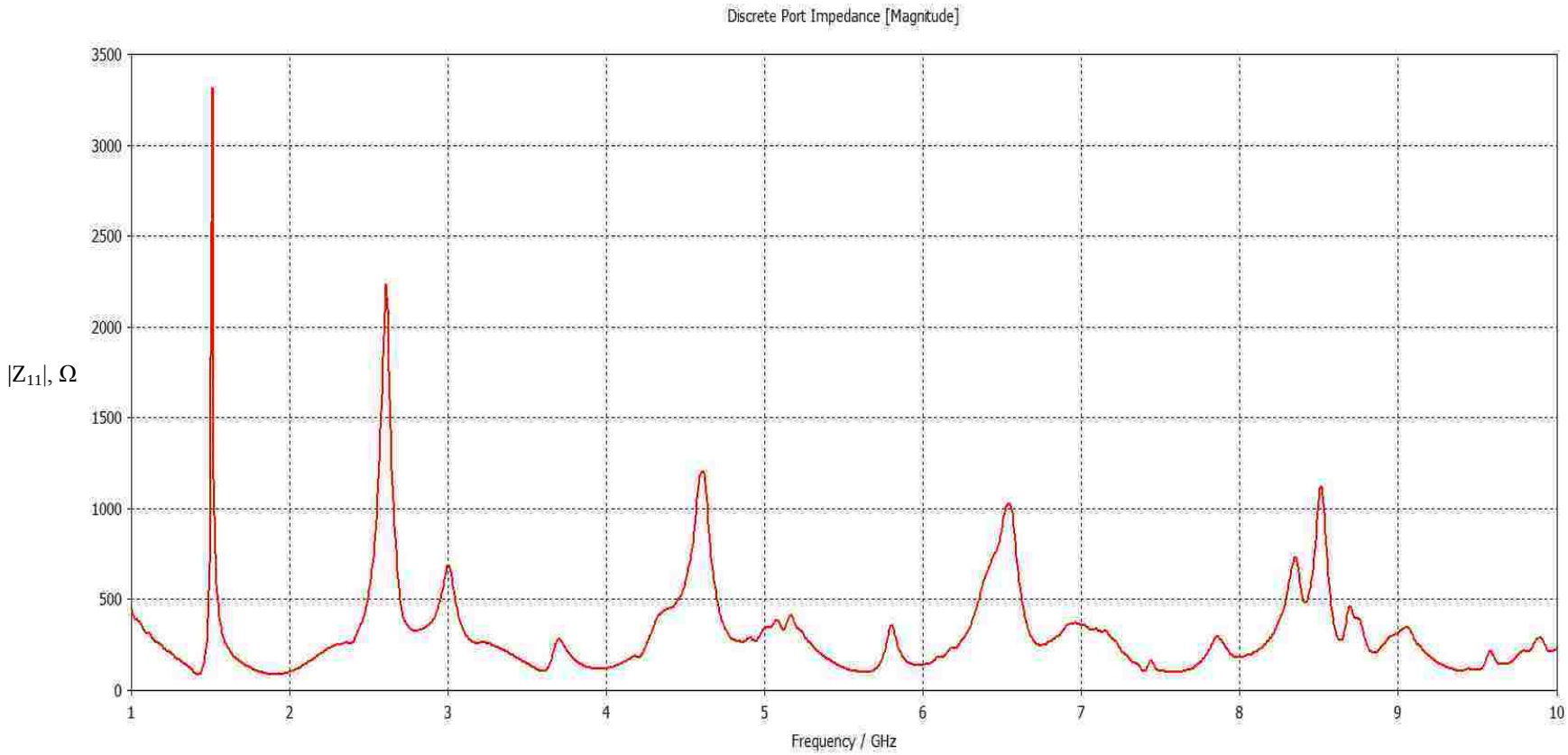

Figure 195: Simulated magnitude of impedance for Dr. Baum's suggestion.

In lieu of such insight, the approach was further worked and simulated in MWS. The first step was to remove the ferrite layer and examine the effects. The simulated radiation patterns without the ferrite layer are shown in Figure 196 and corresponding impedance plot in Figure 197.

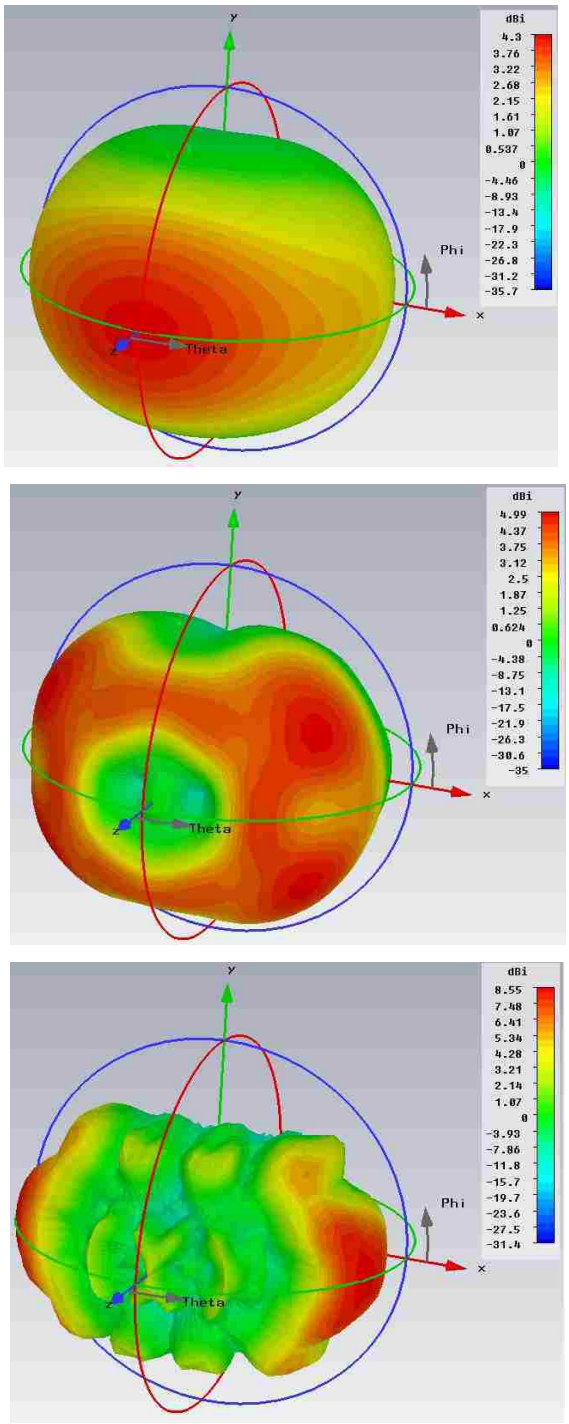

f = 1 GHz

f = 5 GHz

f = 10 GHz

Figure 196: Simulated radiation patterns without ferrite layer.

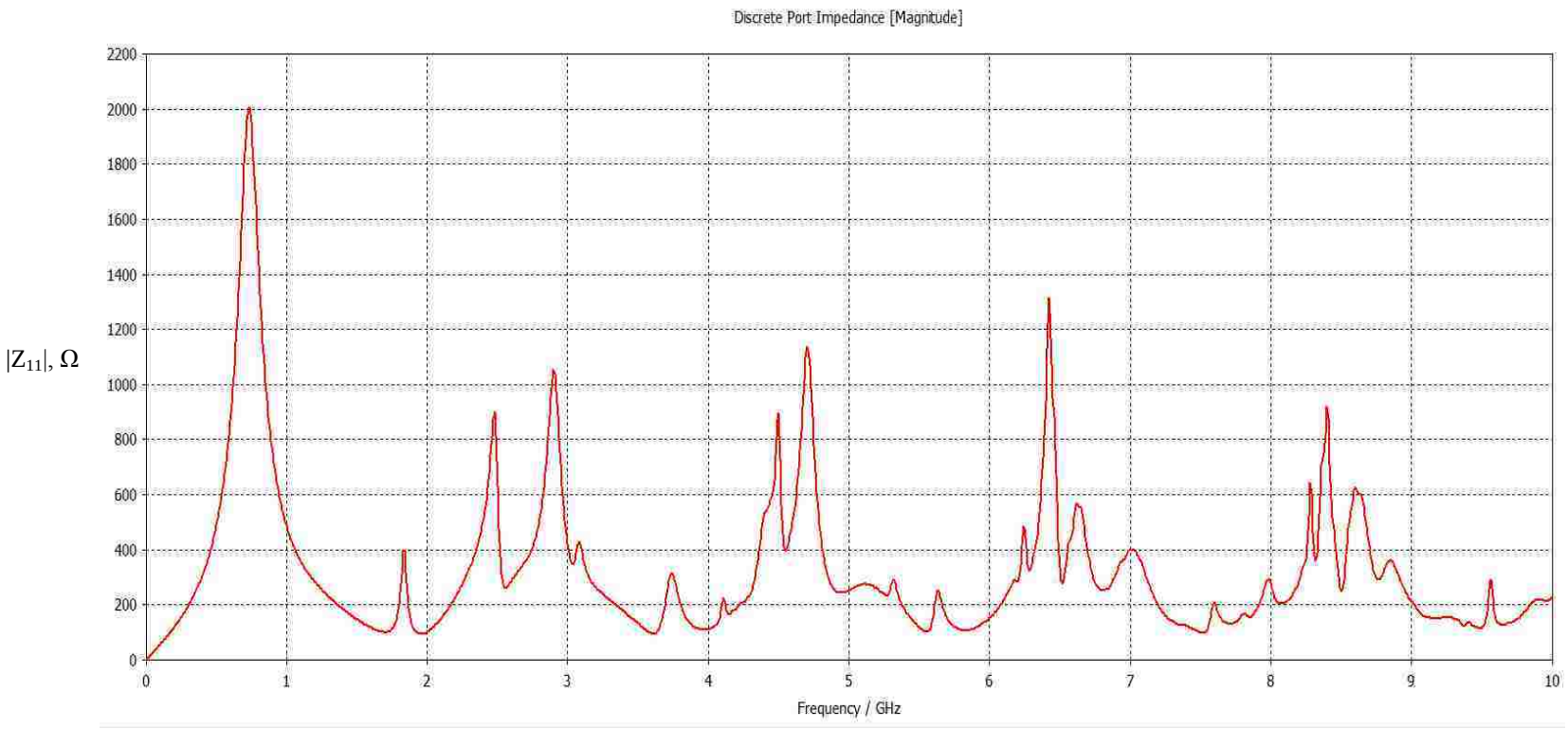

Figure 197: Simulated impedance plot without ferrite.

The simulated performance displays issues similar to the folded diamond structure before damping material was applied. Techniques borrowed from the folded diamond structure were applied with improved simulation results.

Figure 198 depicts the simulated structure, where gray represents copper and blue denotes ECCOSORB MF-117 and Figure 199 is a screenshot of the dimensions used for MWS simulations.

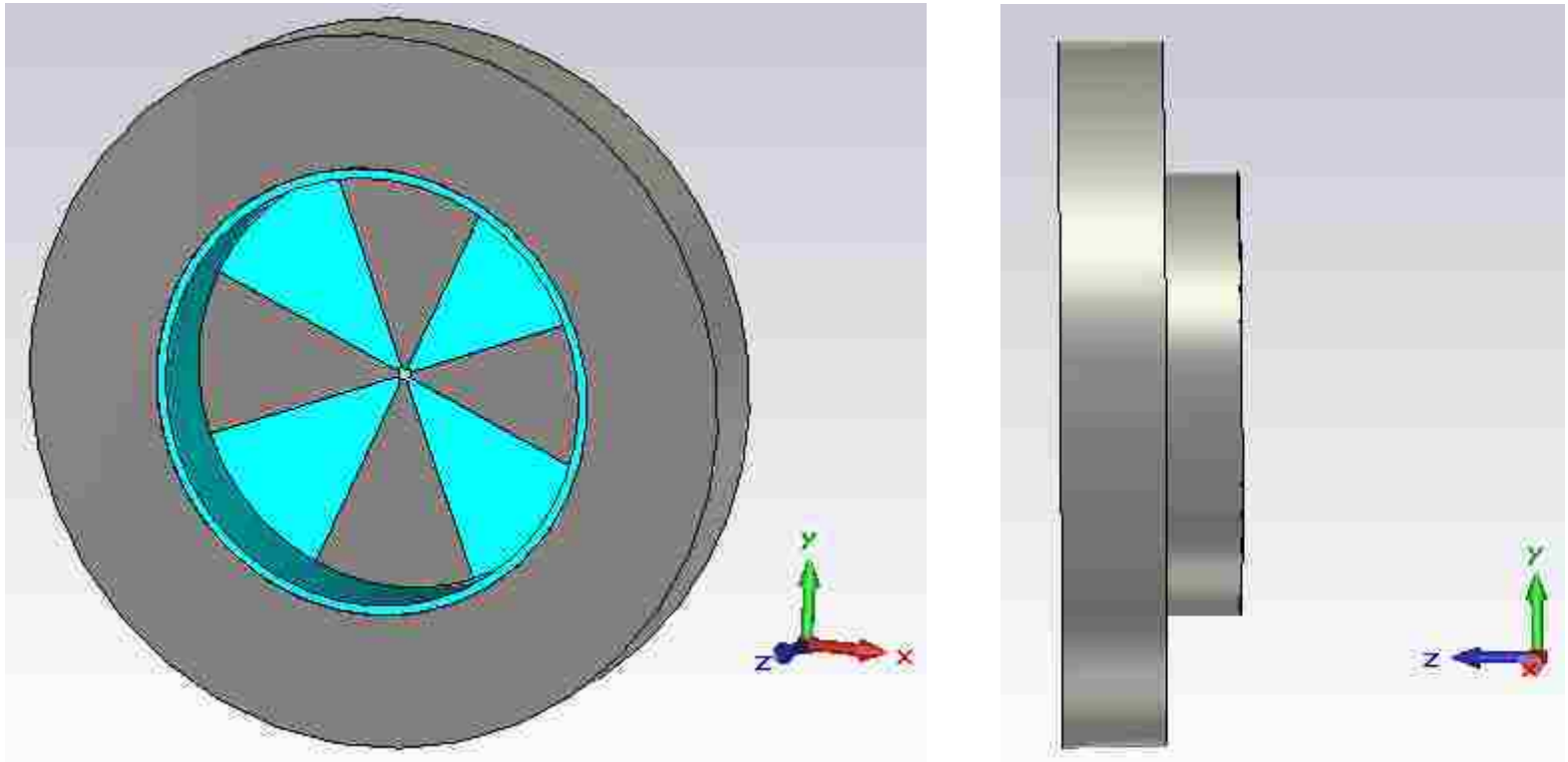

Figure 198: Front and side views of structure with damping.

Name	Value
add_space_bot	2
add_space_side	5
antenna_angle	45
antenna_l	antenna_r*cosD(antenna_angle/2)
antenna_r	75
antenna_w1	tanD(antenna_angle/2)*launch_gap/2+antenna_w1_add
antenna_w1_add	0.05
antenna_w2	sinD(antenna_angle)*antenna_r/(sinD((180-antenna_angle)/2))
can_h	25
can_t	0.5
ferrite_h	10
ferrite_mr	5
launch_gap	4
launch_w	0.5
lip_thick	35
lip_width	45
mesh_step_antenna	0
mesh_step_ferrite	0
mesh_step_launch	launch_gap/4
port_z	100
sub_h	3.2
t	0.035
wall_damp	3.2

Figure 199: Dimensions of structure with damping.

The magnitude of input impedance vs. frequency was simulated along with far field radiation patterns at 1, 2.5, 5 and 10 GHz. These results are displayed in Figure 200, Figure 201, and Figure 202.

The simulated impedance plot indicates a VSWR ≤ 2.3 over the 1-10GHz range. The radiation patterns still require some optimization as a higher directivity may be desired along with minimization of the back lobes and especially at mid-band. Since it was decided to not fabricate this structure, such optimization is left for future research.

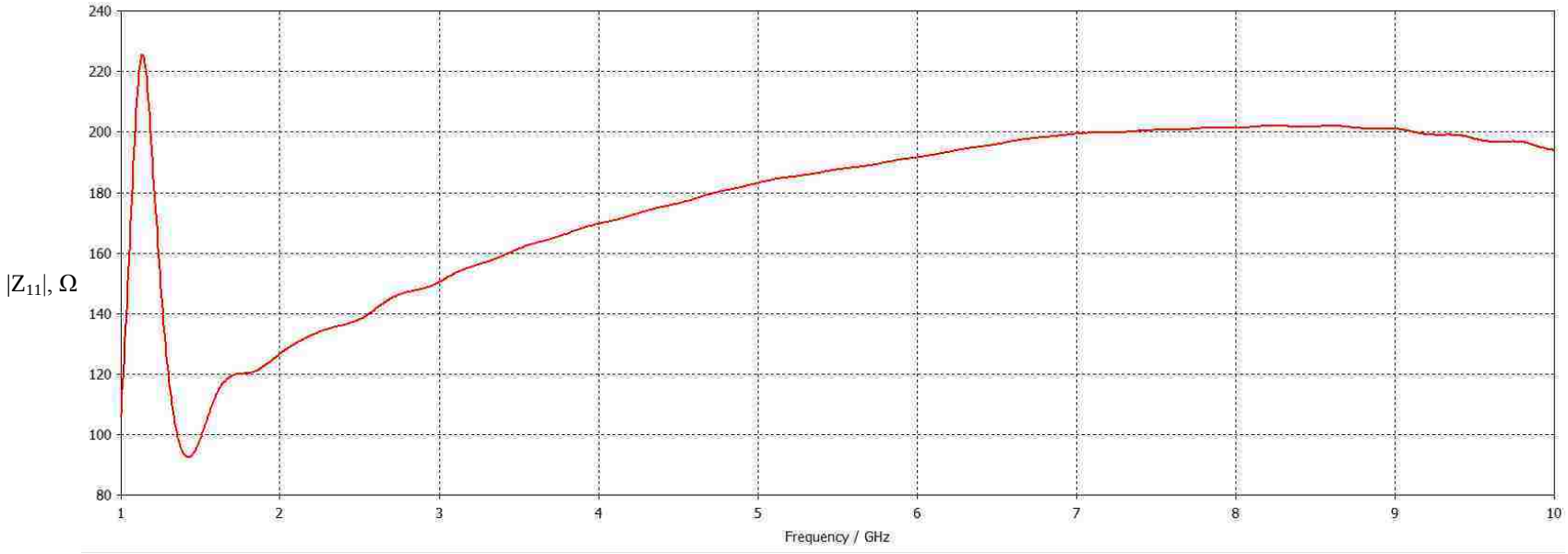

Figure 200: Impedance plot for damped structure.

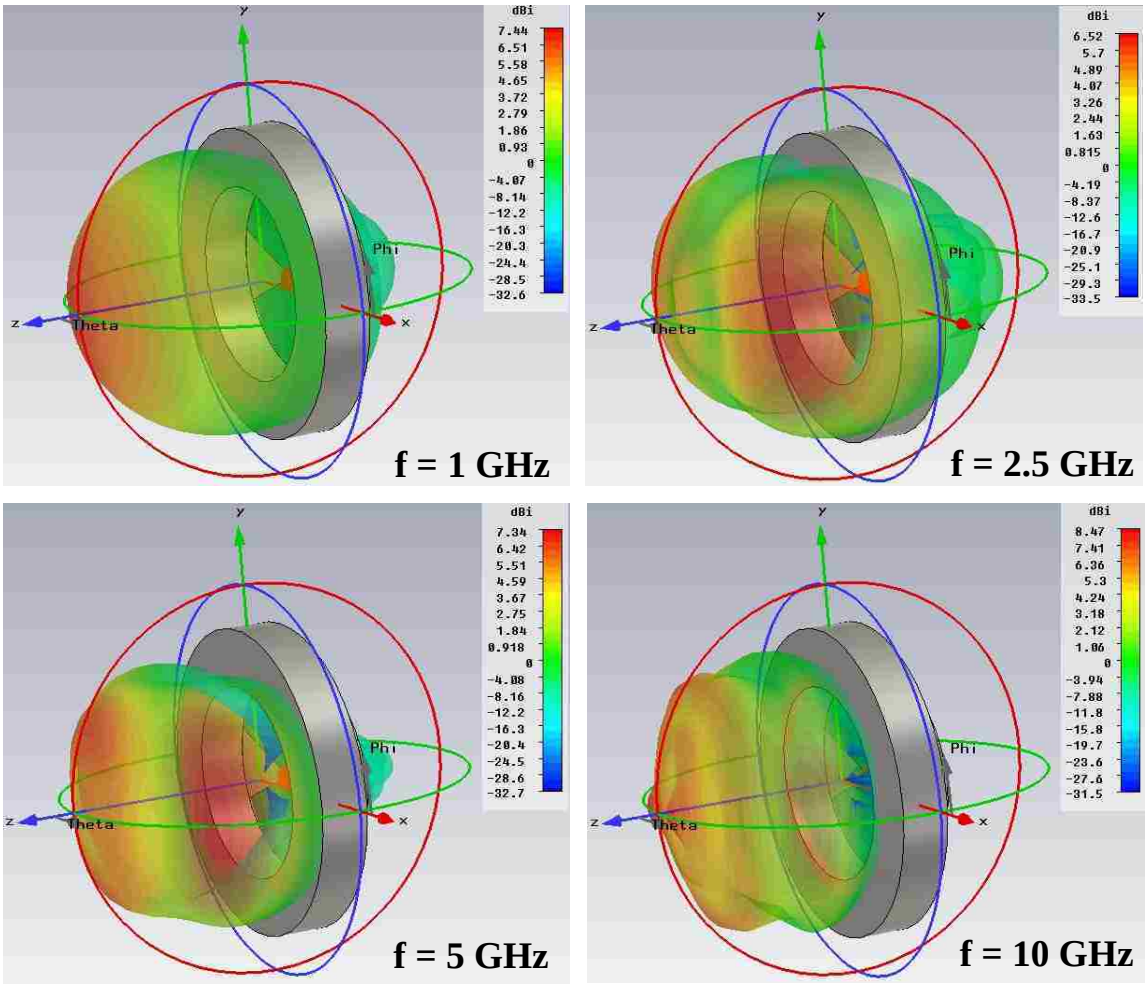

Figure 201: Radiation patterns of damped structure.

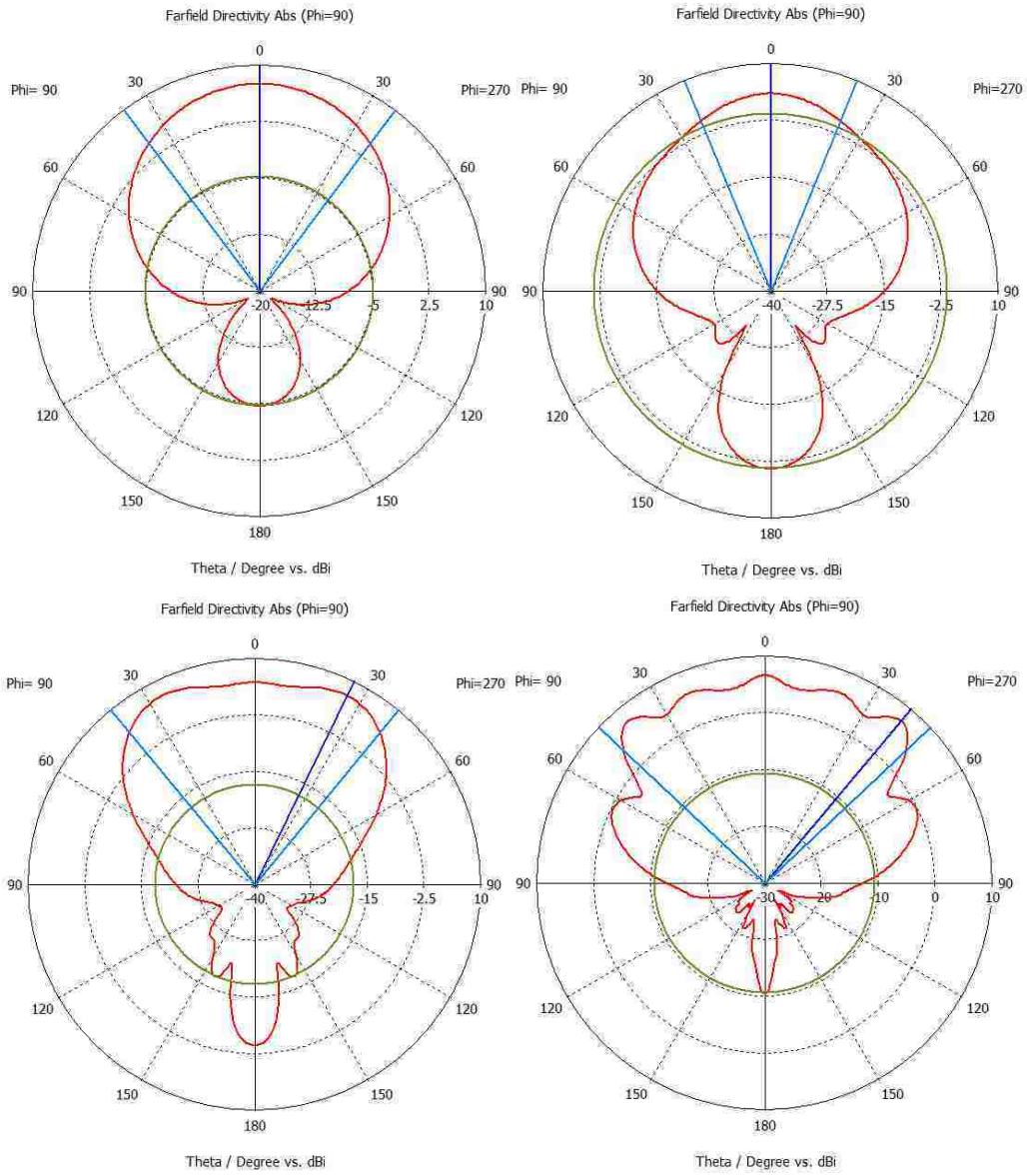

Figure 202: Polar radiation patterns of damped structure

Appendix F: Diamond Feed Simulation Results

Detailed simulation results for the diamond feed are documented in this appendix in Figure 203 through Figure 269.

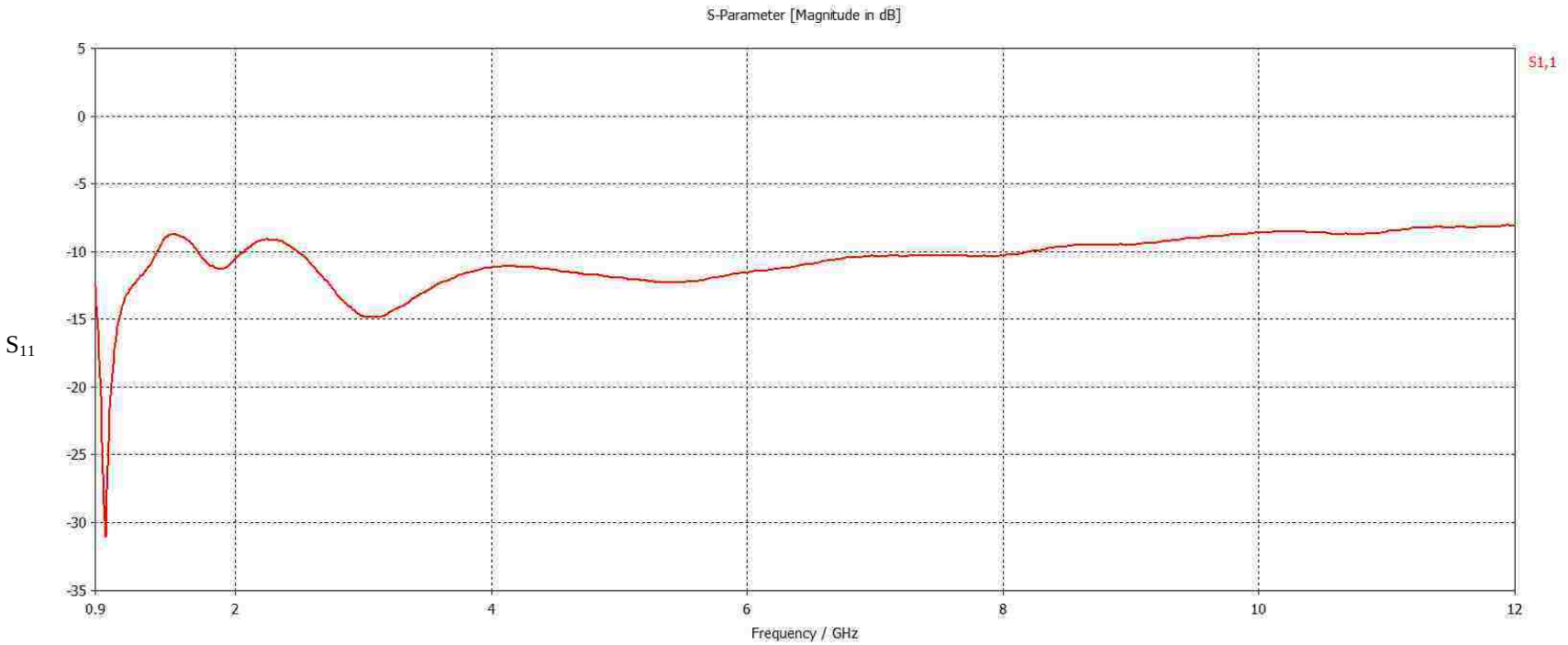

S_{11}

Figure 203: Simulated S1,1 for the diamond feed

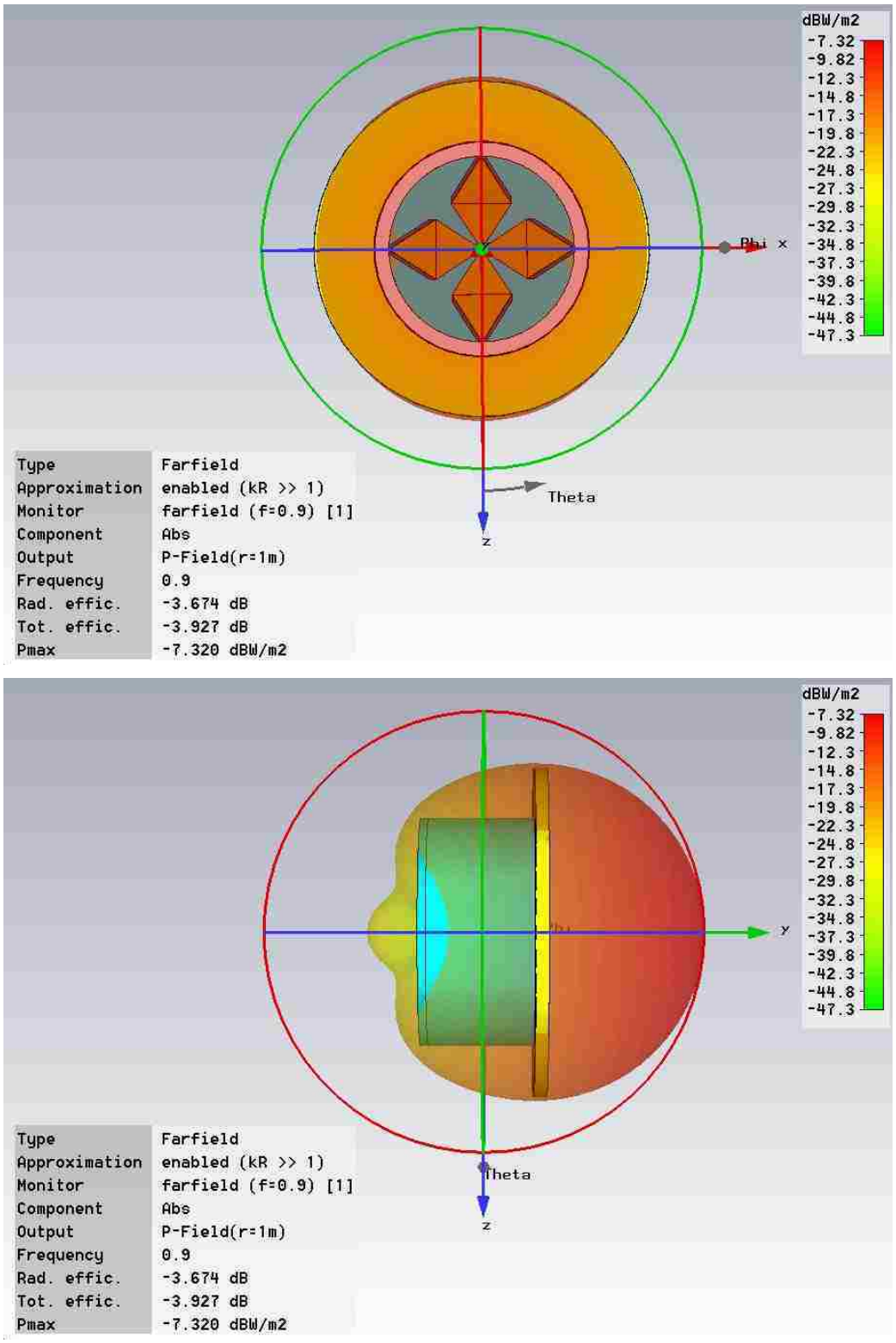

Figure 204: 900 MHz 3D power patterns

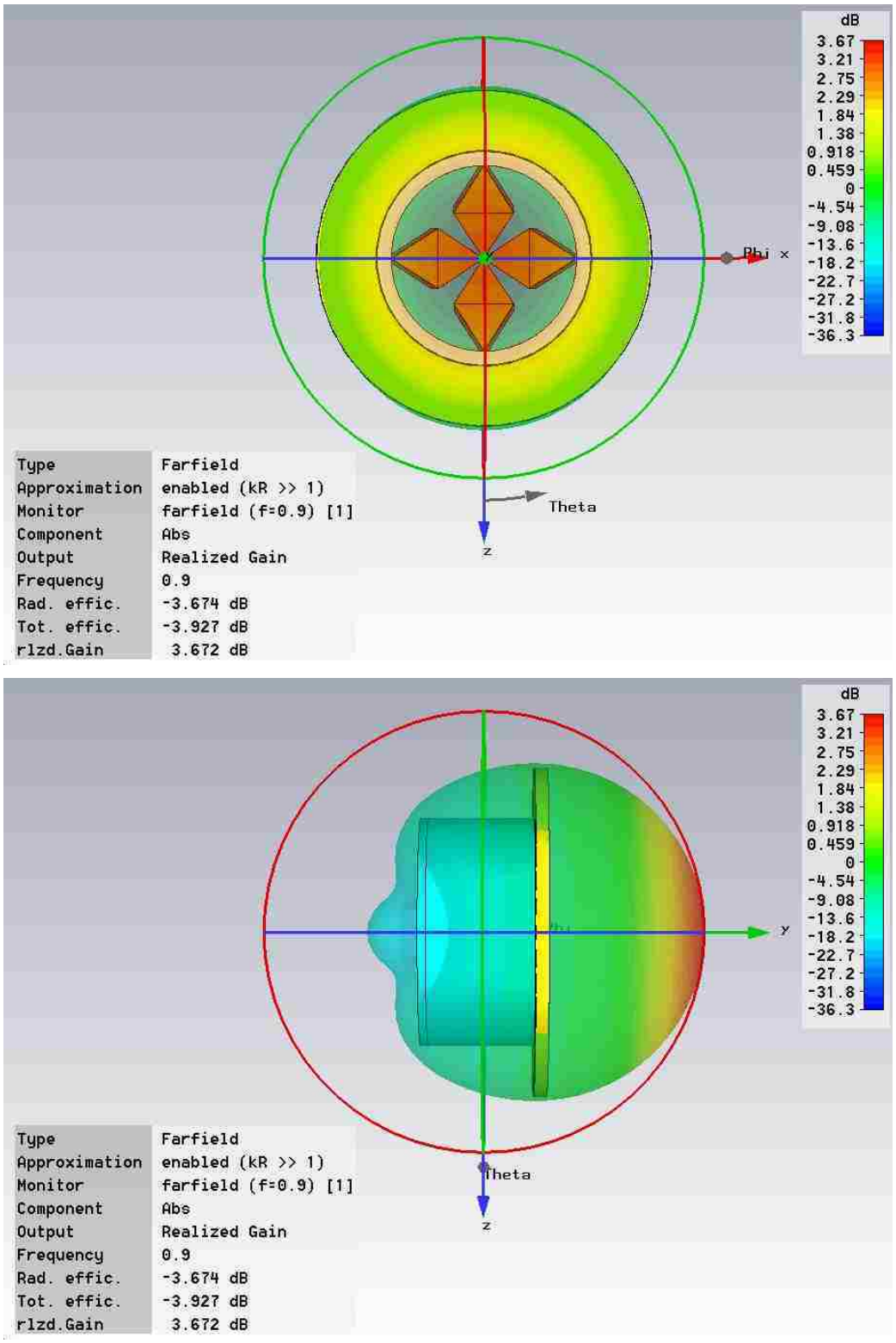

Figure 205: 900 MHz realized gain patterns

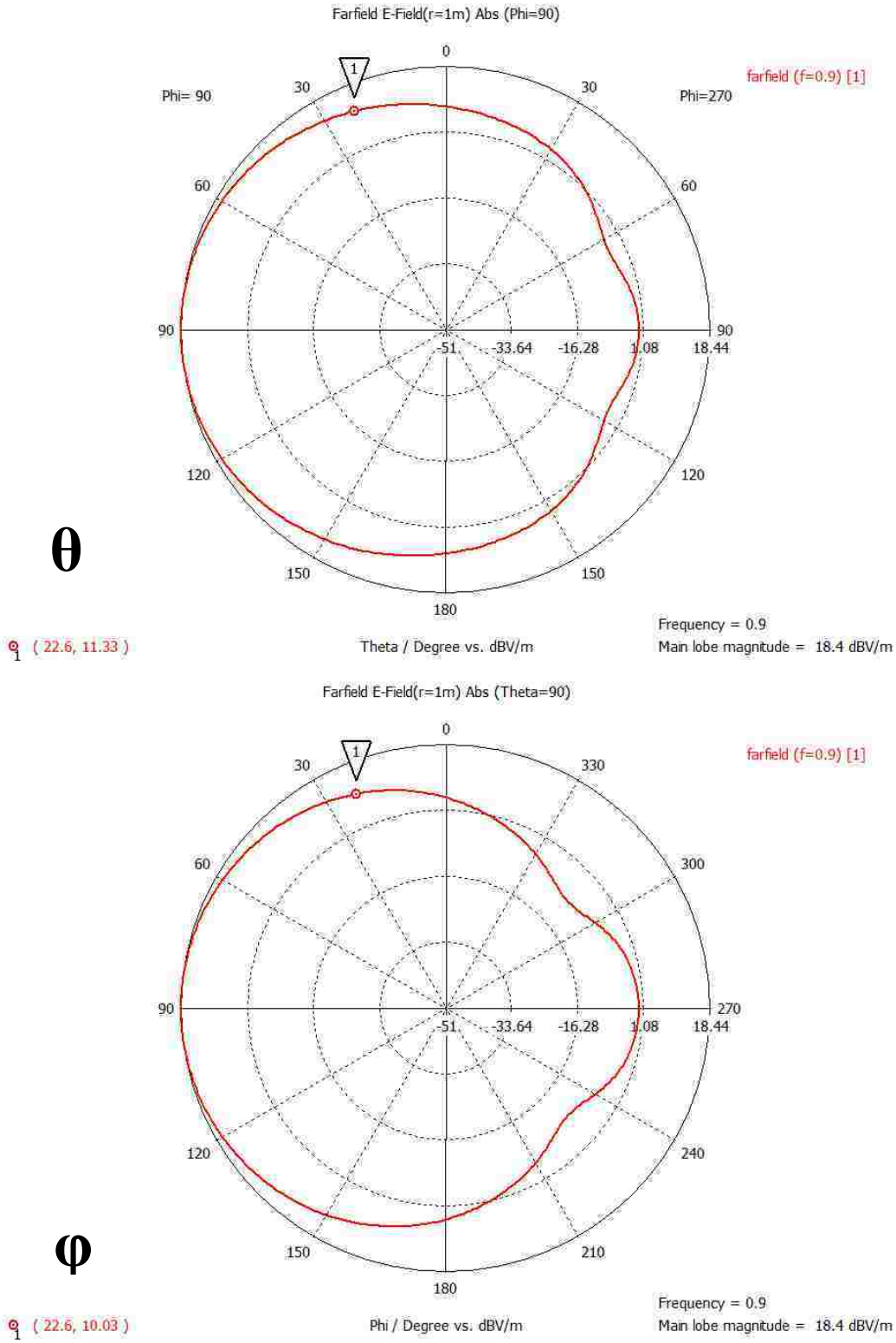

Figure 206: 900 MHz E-field patterns for theta and phi

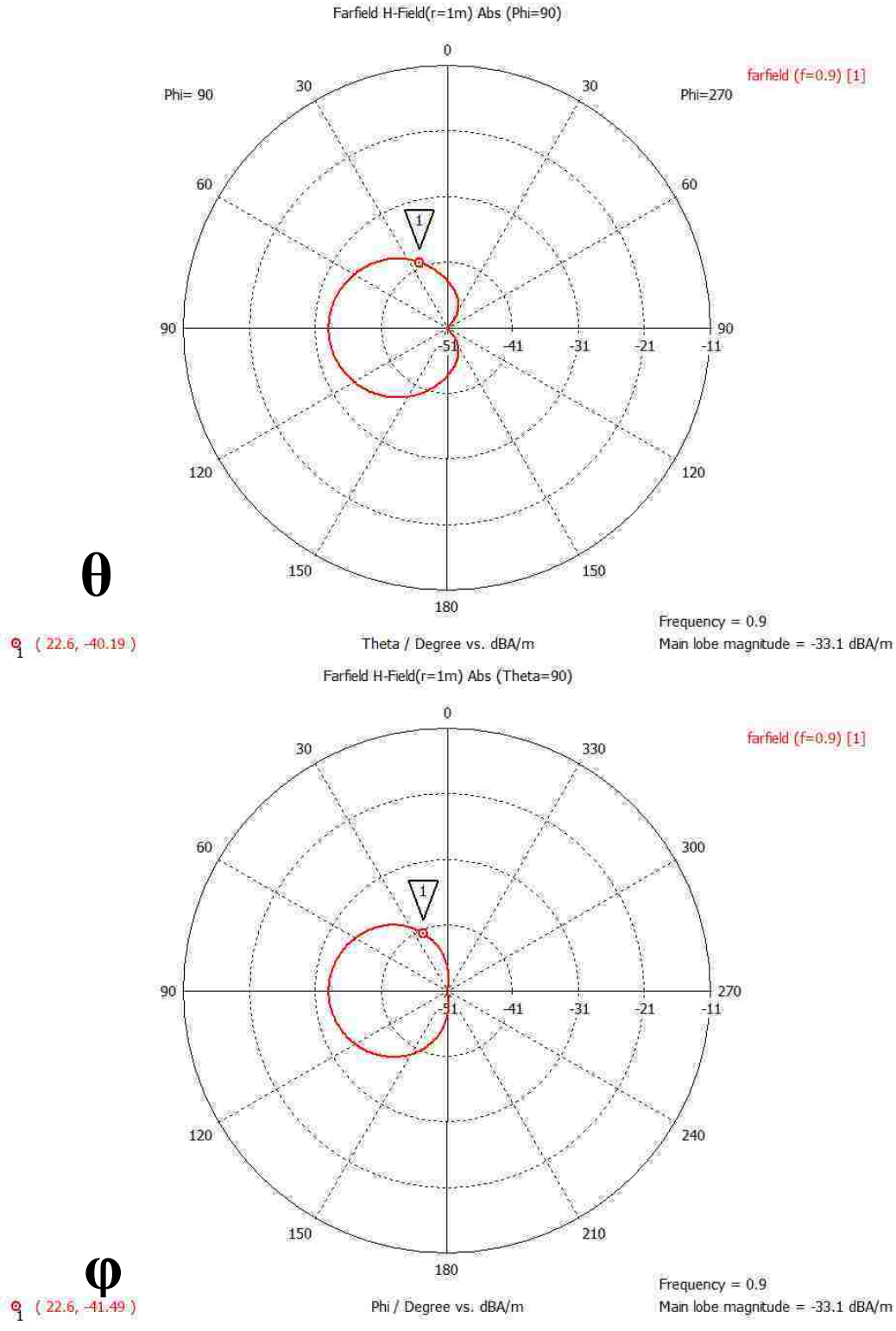

Figure 207: 900 MHz H-field patterns for theta and phi

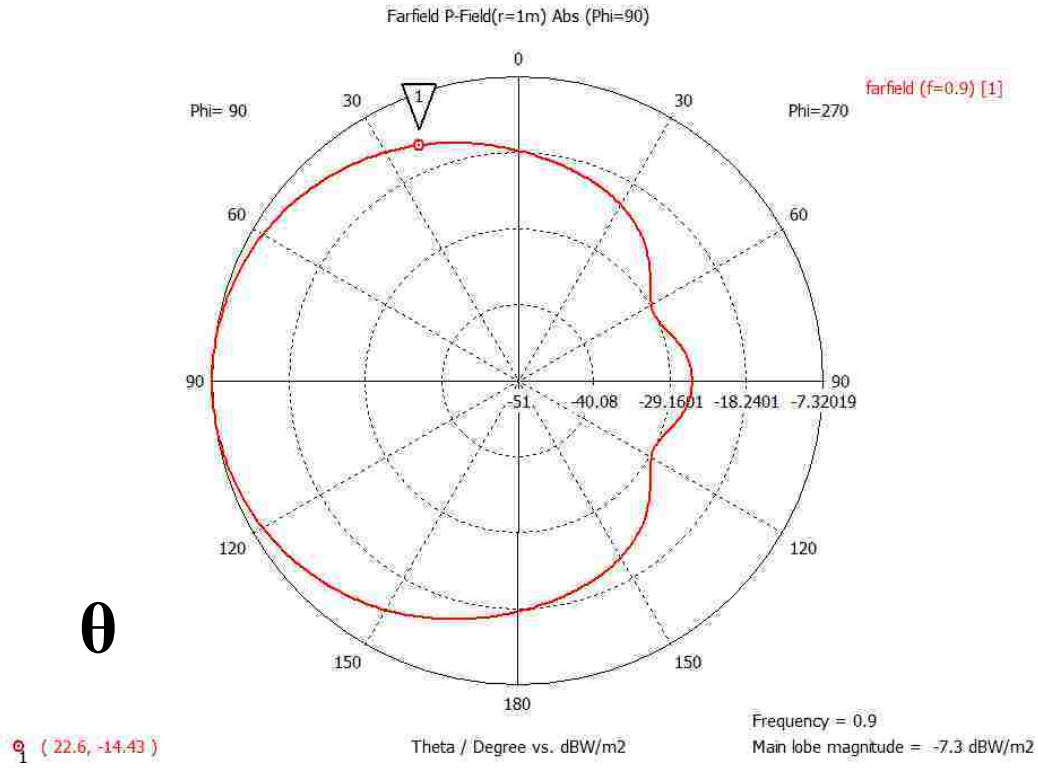

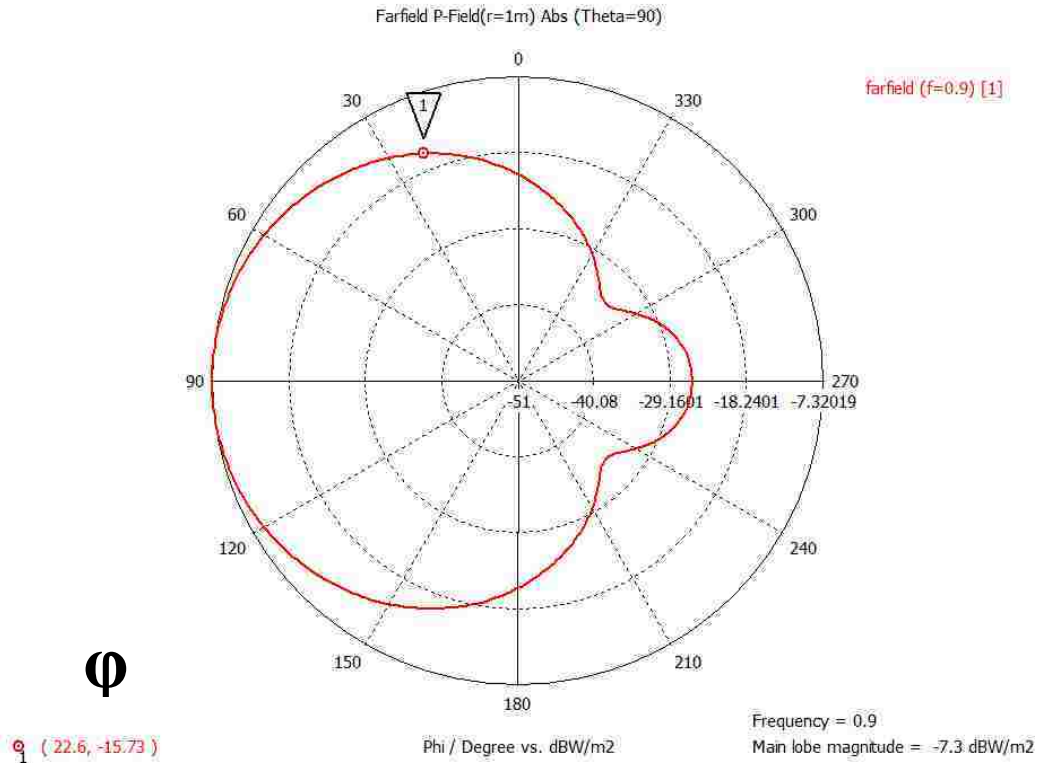

Figure 208: 900 MHz power patterns for theta and phi

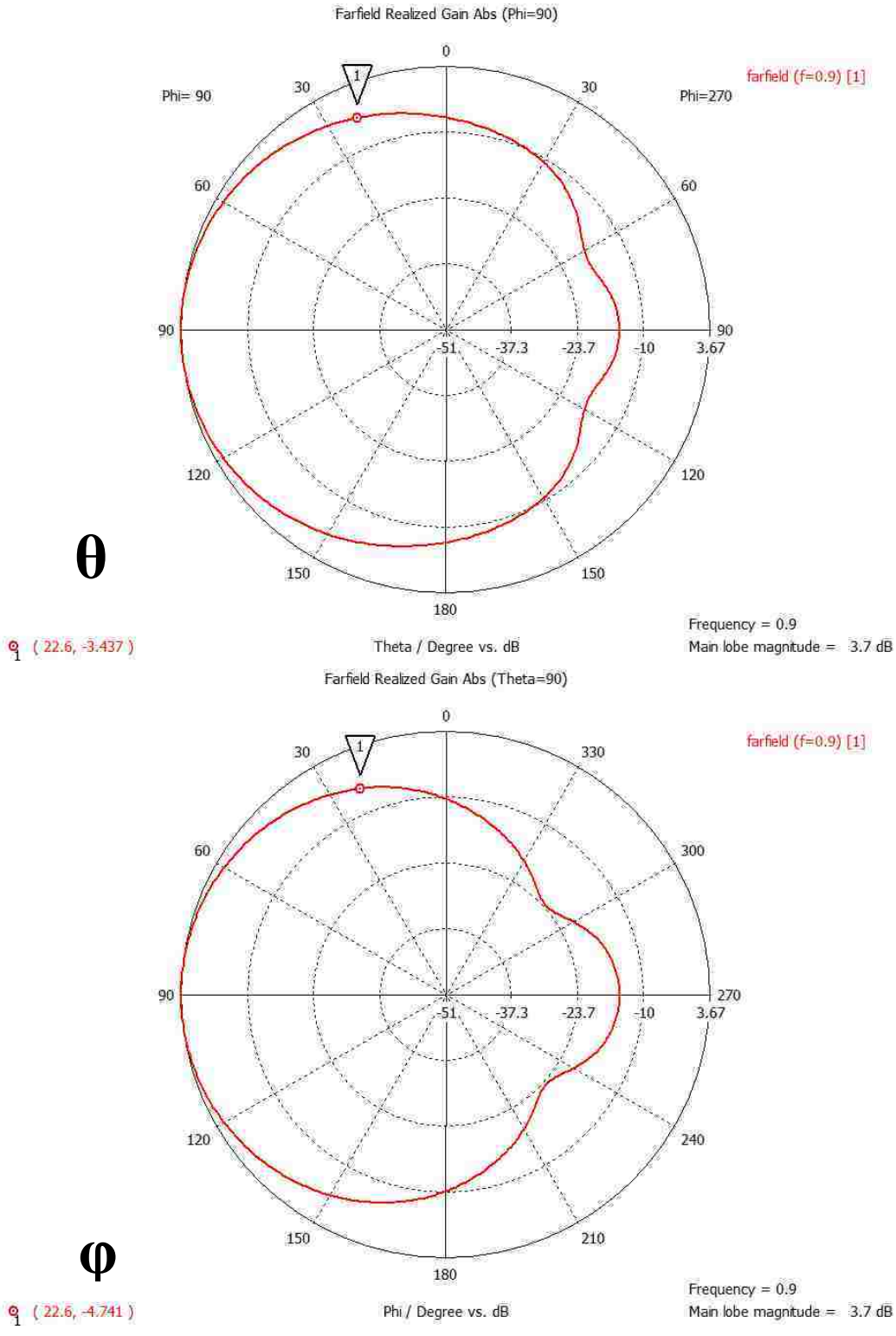

Figure 209: 900 MHz realized gain patterns for theta and phi

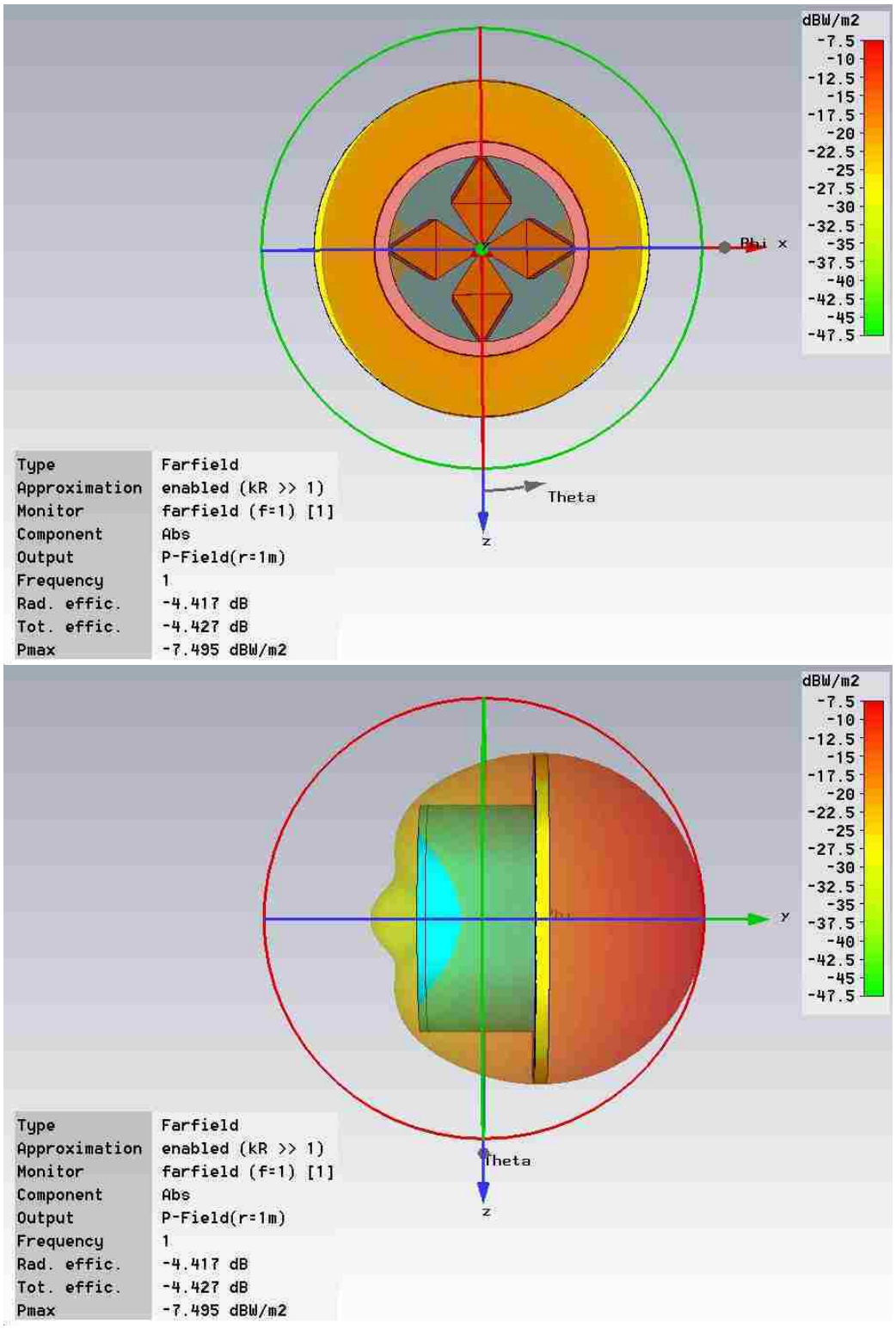

Figure 210: 1 GHz 3D power patterns

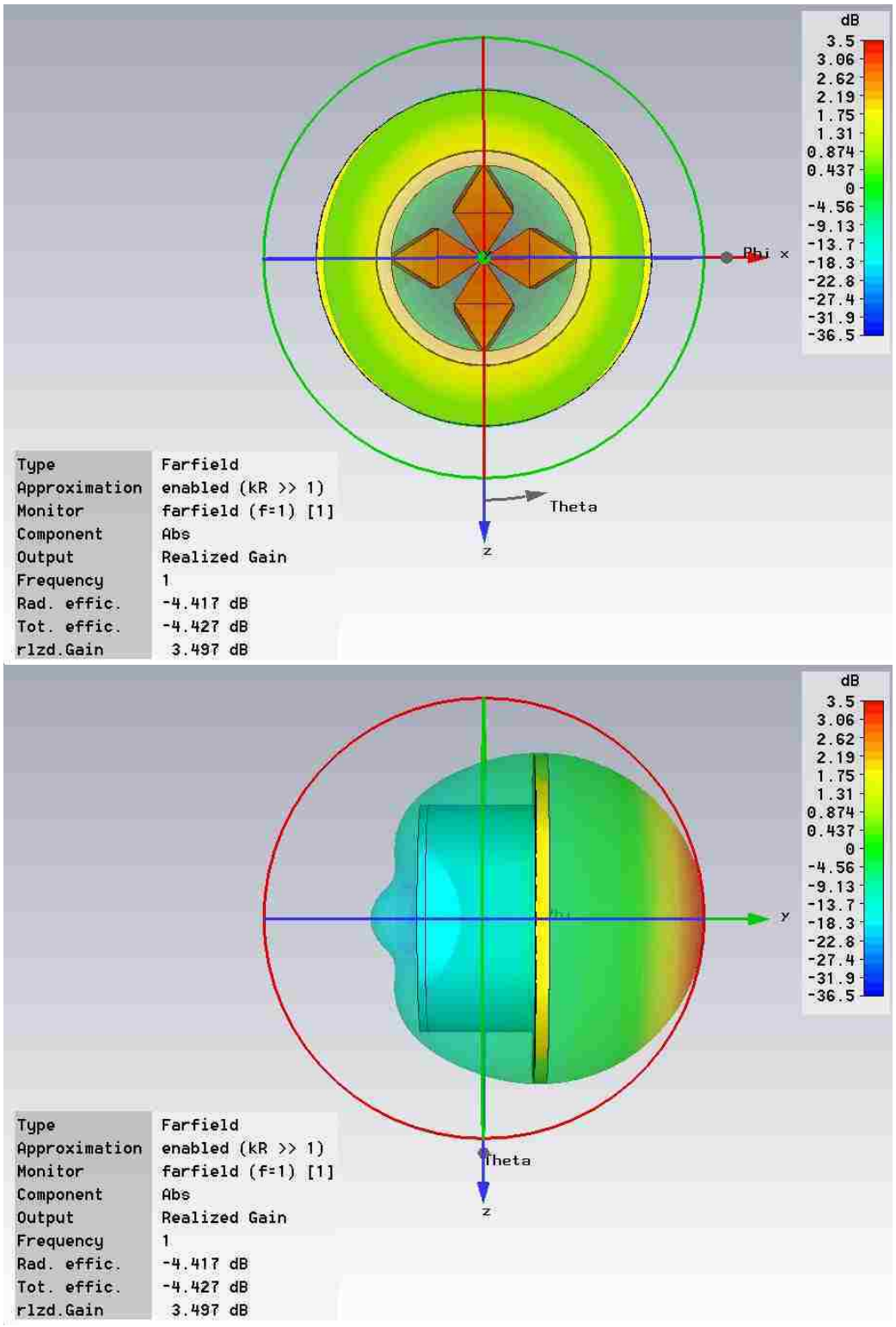

Figure 211: 1 GHz 3D realized gain patterns

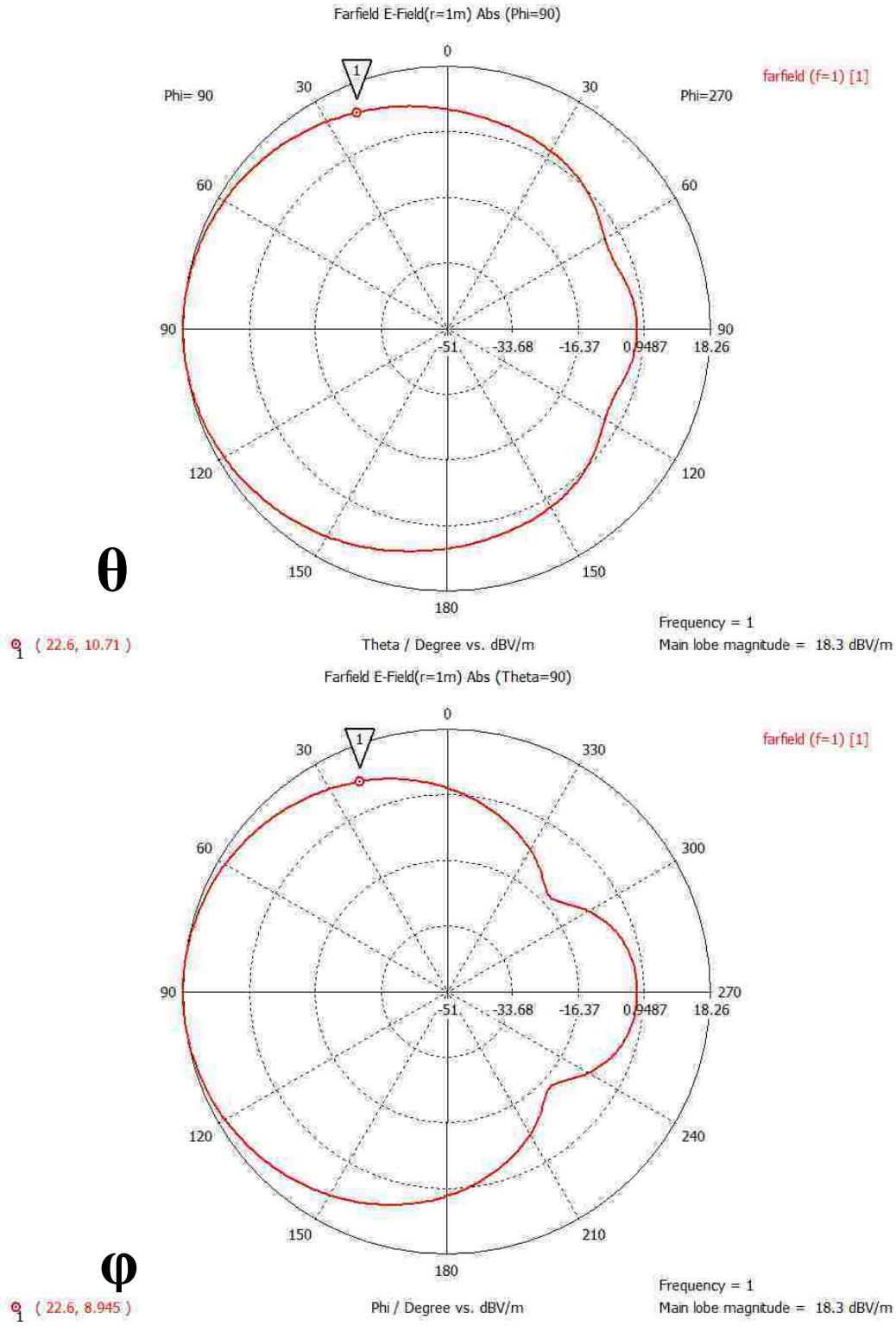

Figure 212: 1 GHz E-field patterns for theta and phi

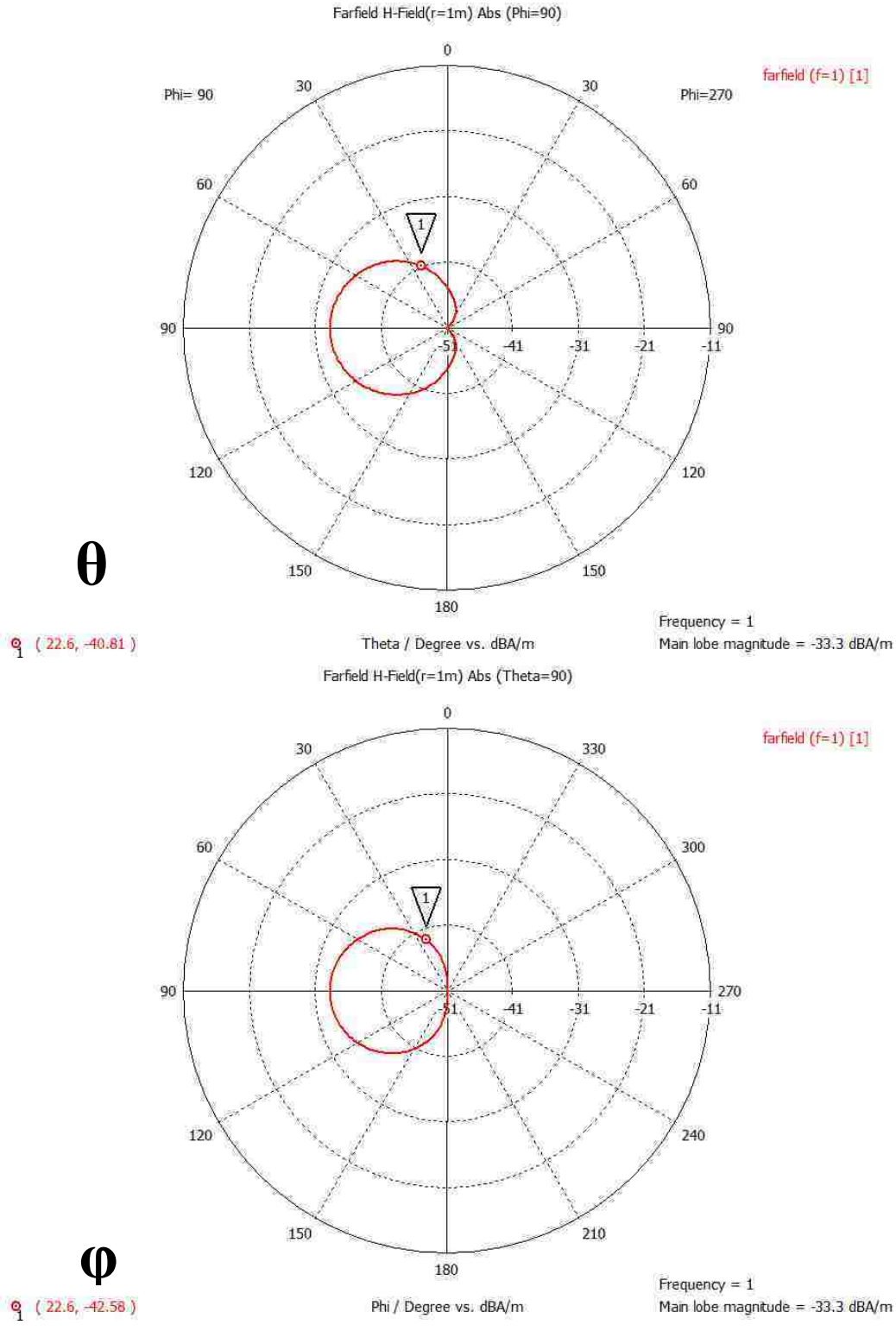

Figure 213: 1 GHz H-field patterns for theta and phi

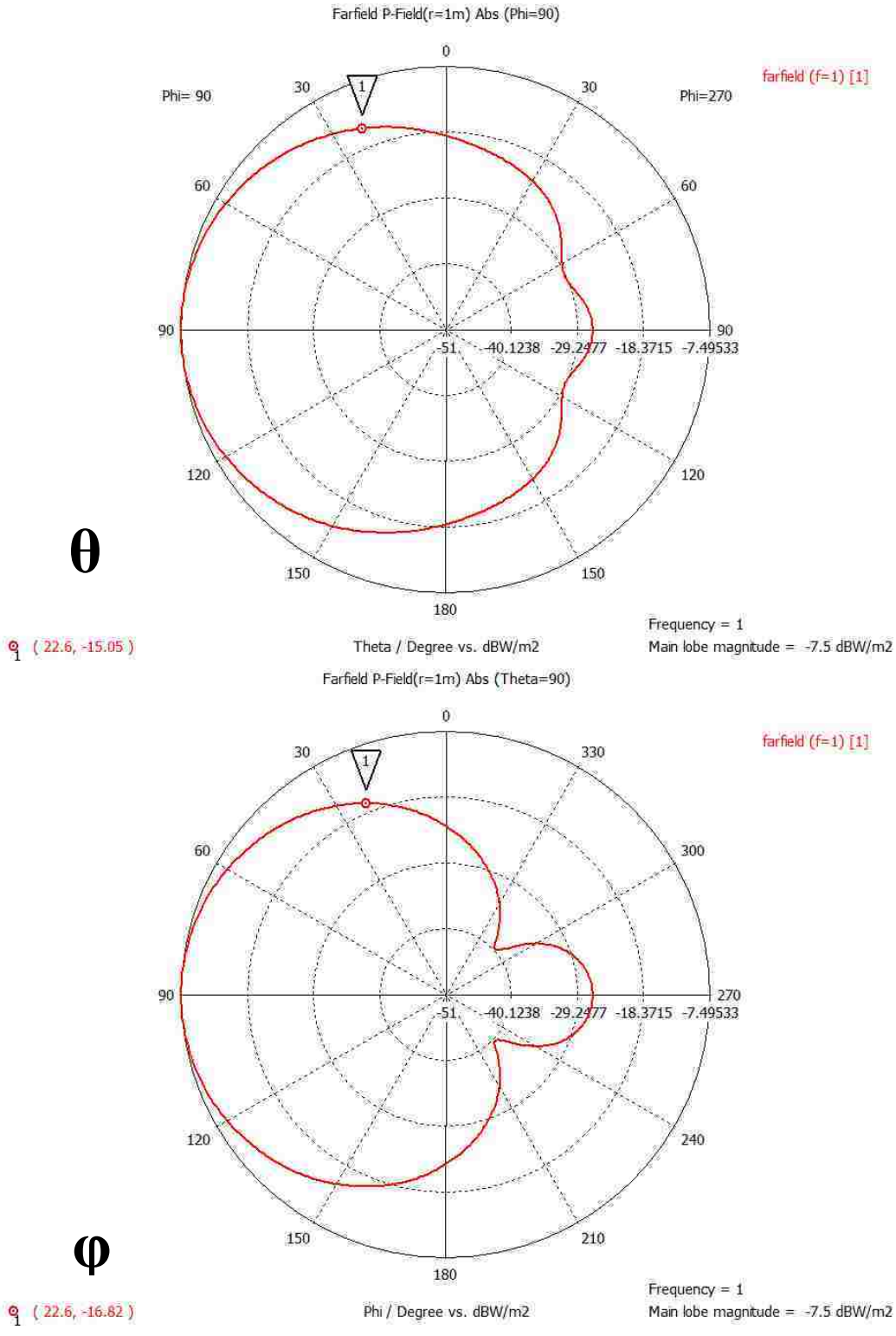

Figure 214: 1 GHz power patterns for theta and phi

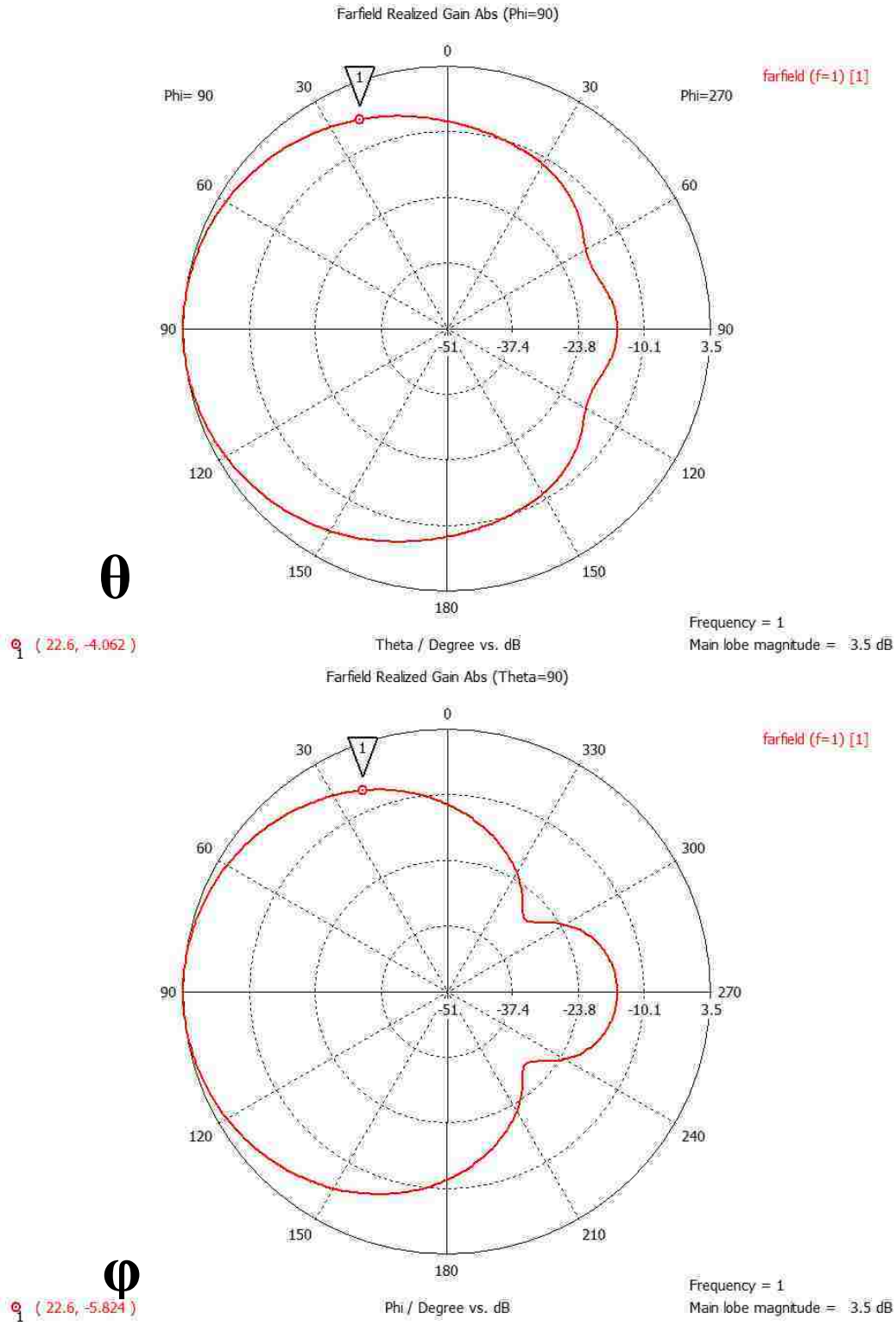

Figure 215: 1 GHz realized gain patterns for theta and phi

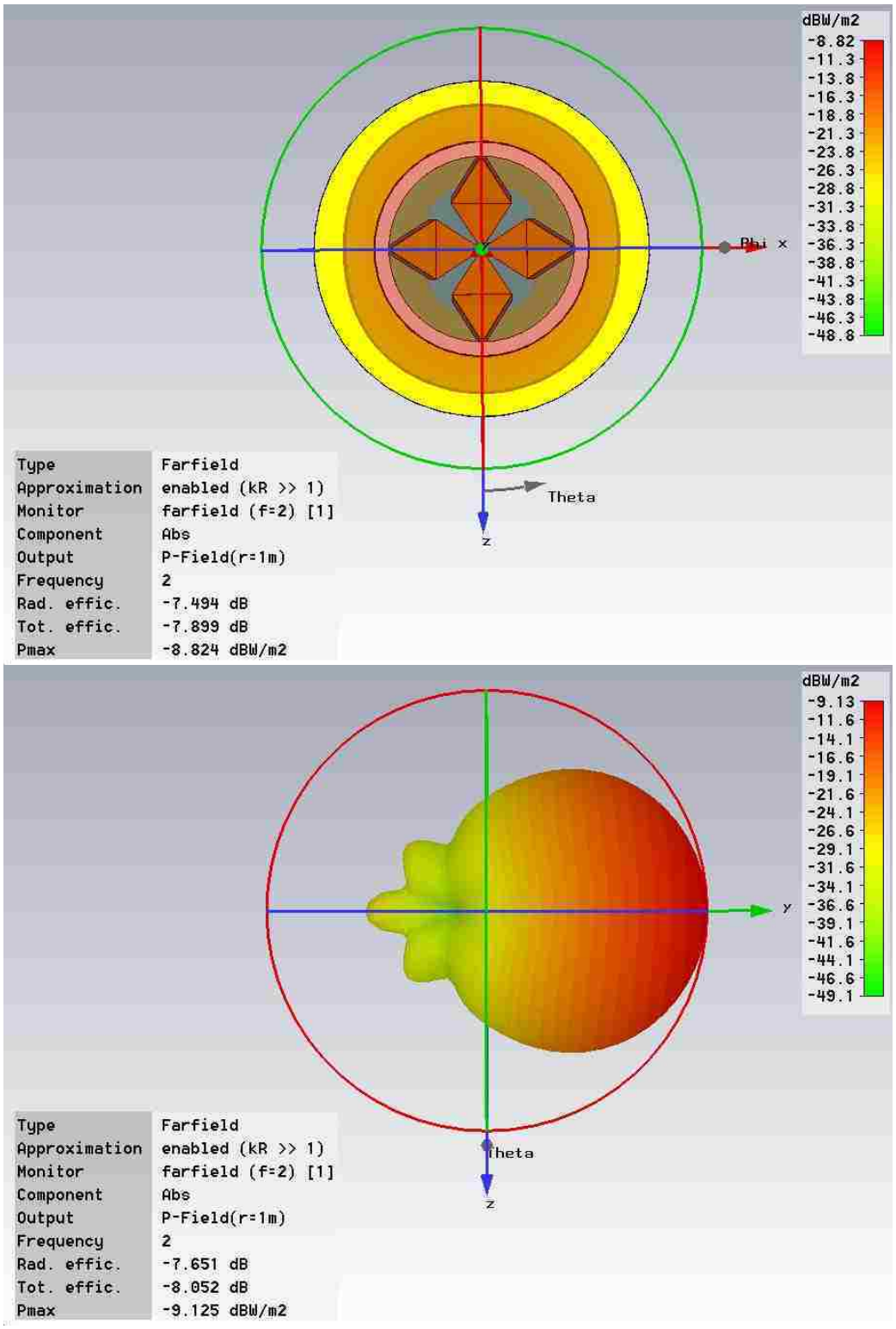

Figure 216: 2 GHz 3D power patterns

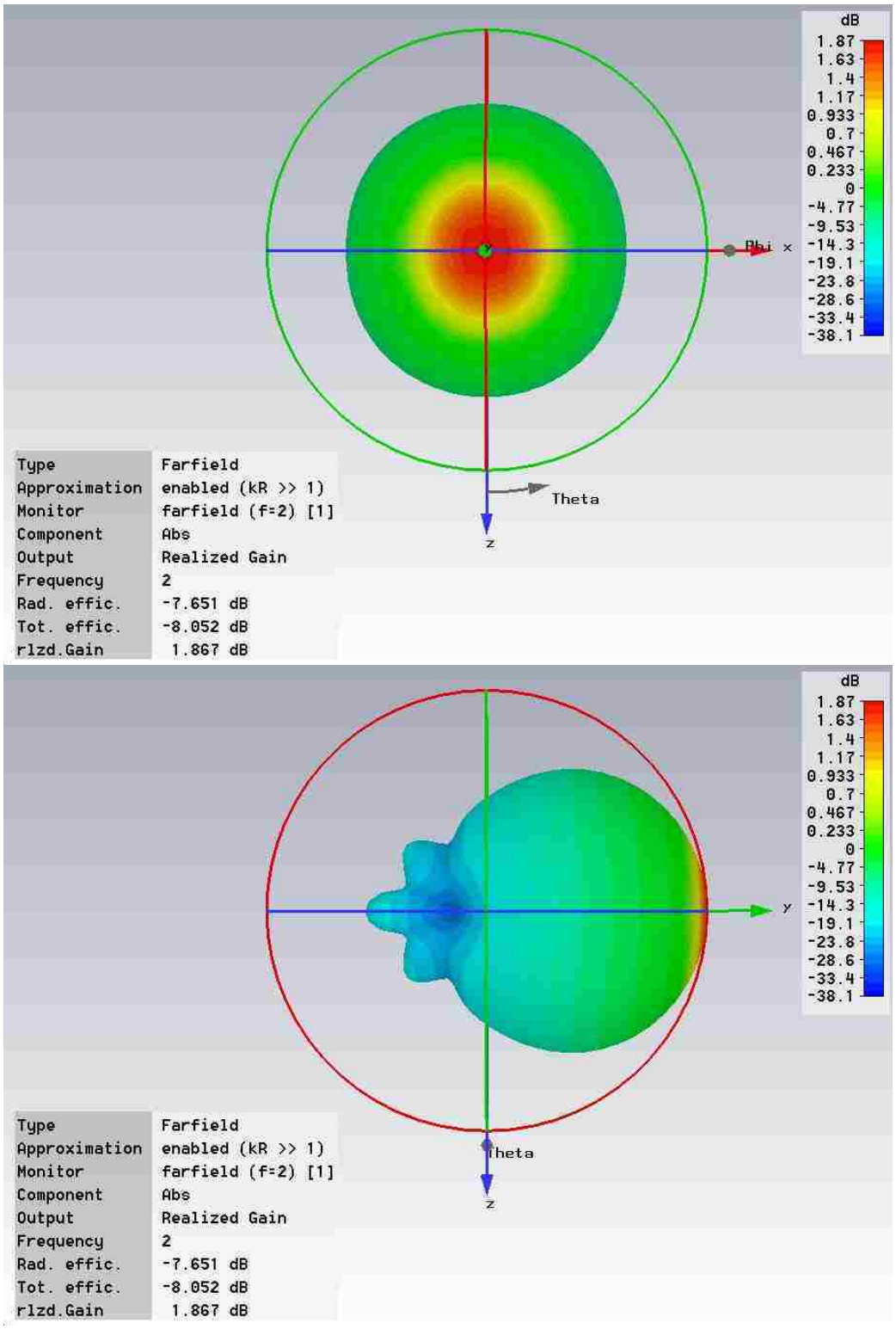

Figure 217: 2 GHz 3D realized gain patterns

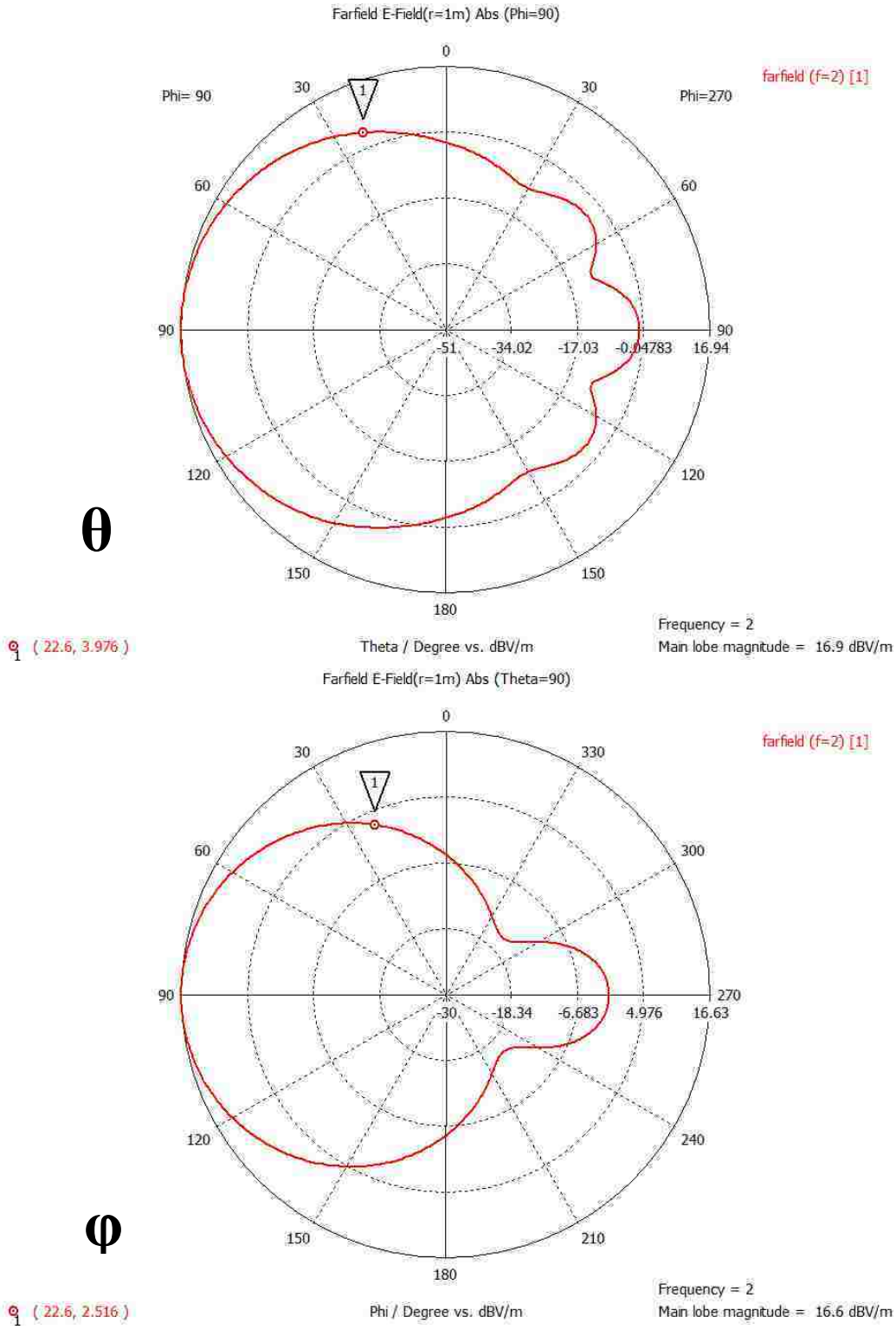

Figure 218: 2 GHz E-field patterns for theta and phi

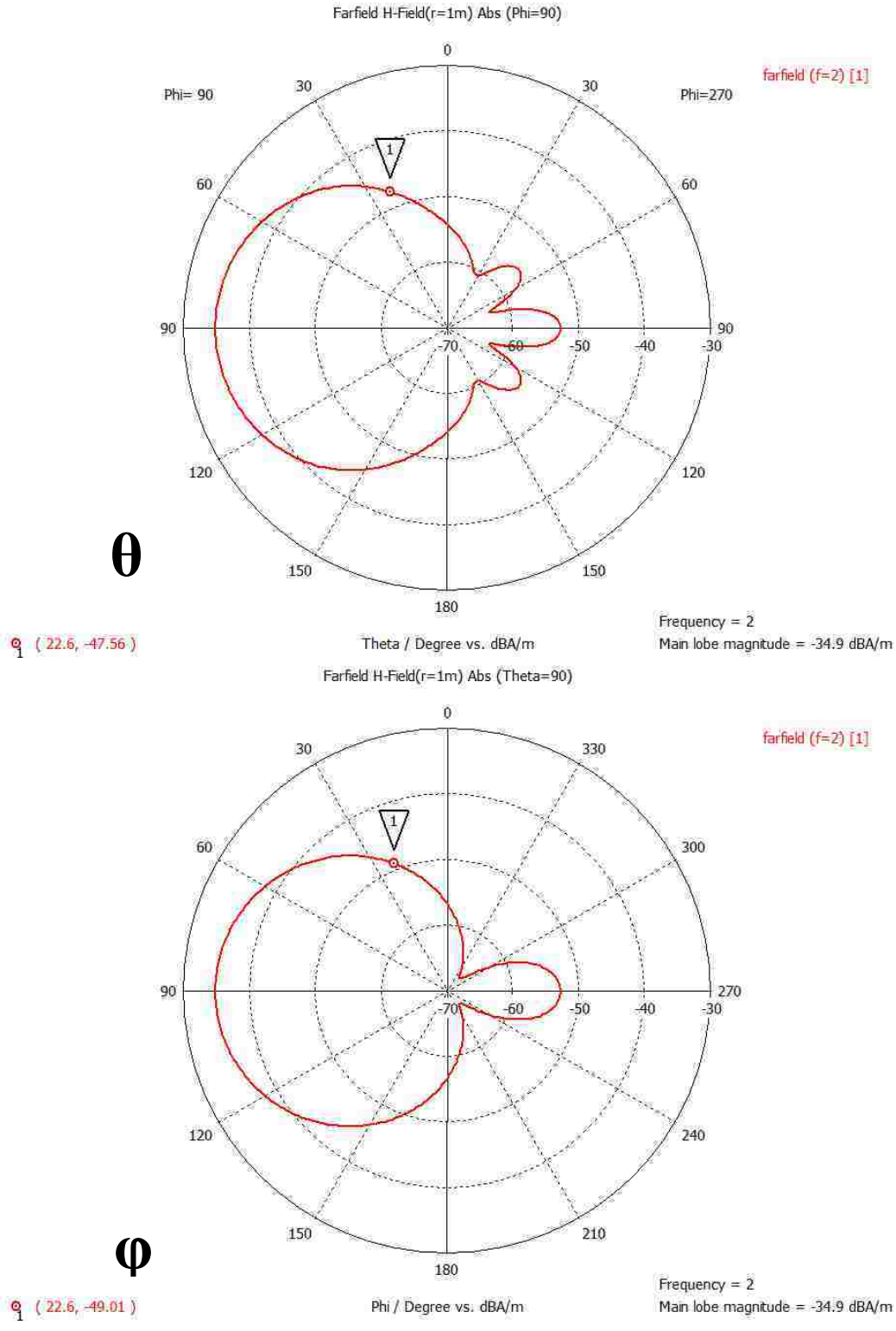

Figure 219: 2 GHz H-field patterns for theta and phi

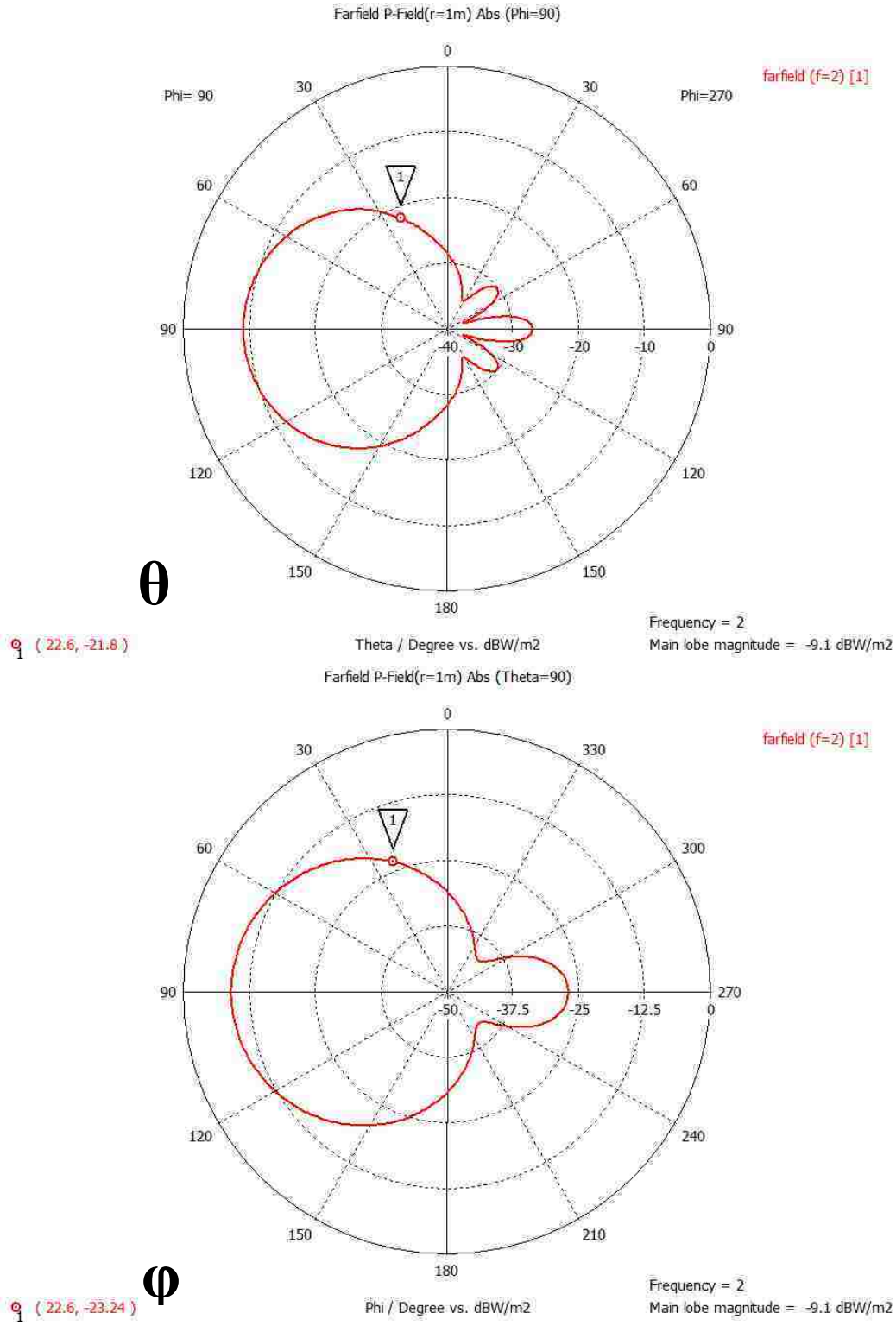

Figure 220: 2 GHz power patterns for theta and phi

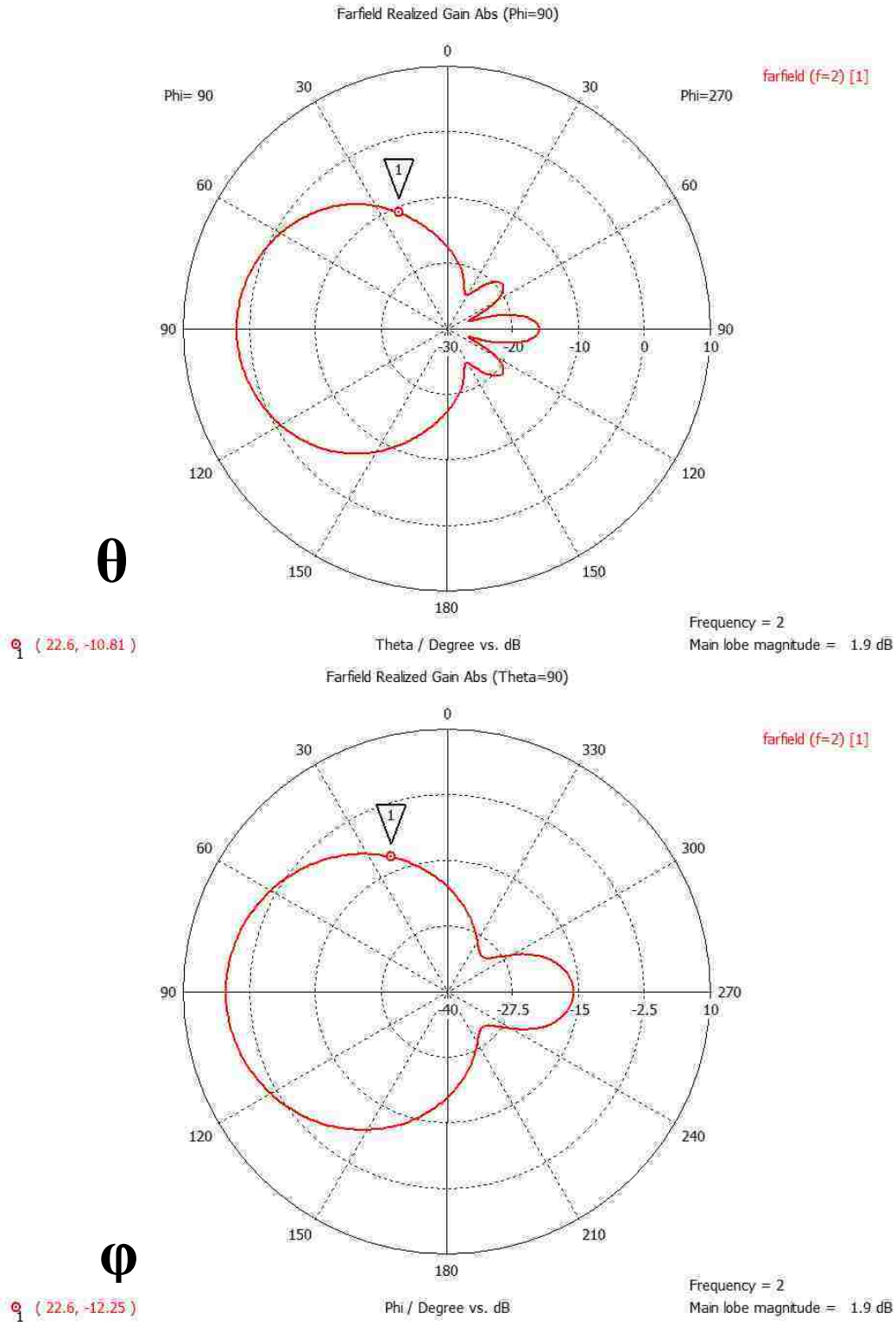

Figure 221: 2 GHz realized gain patterns for theta and phi

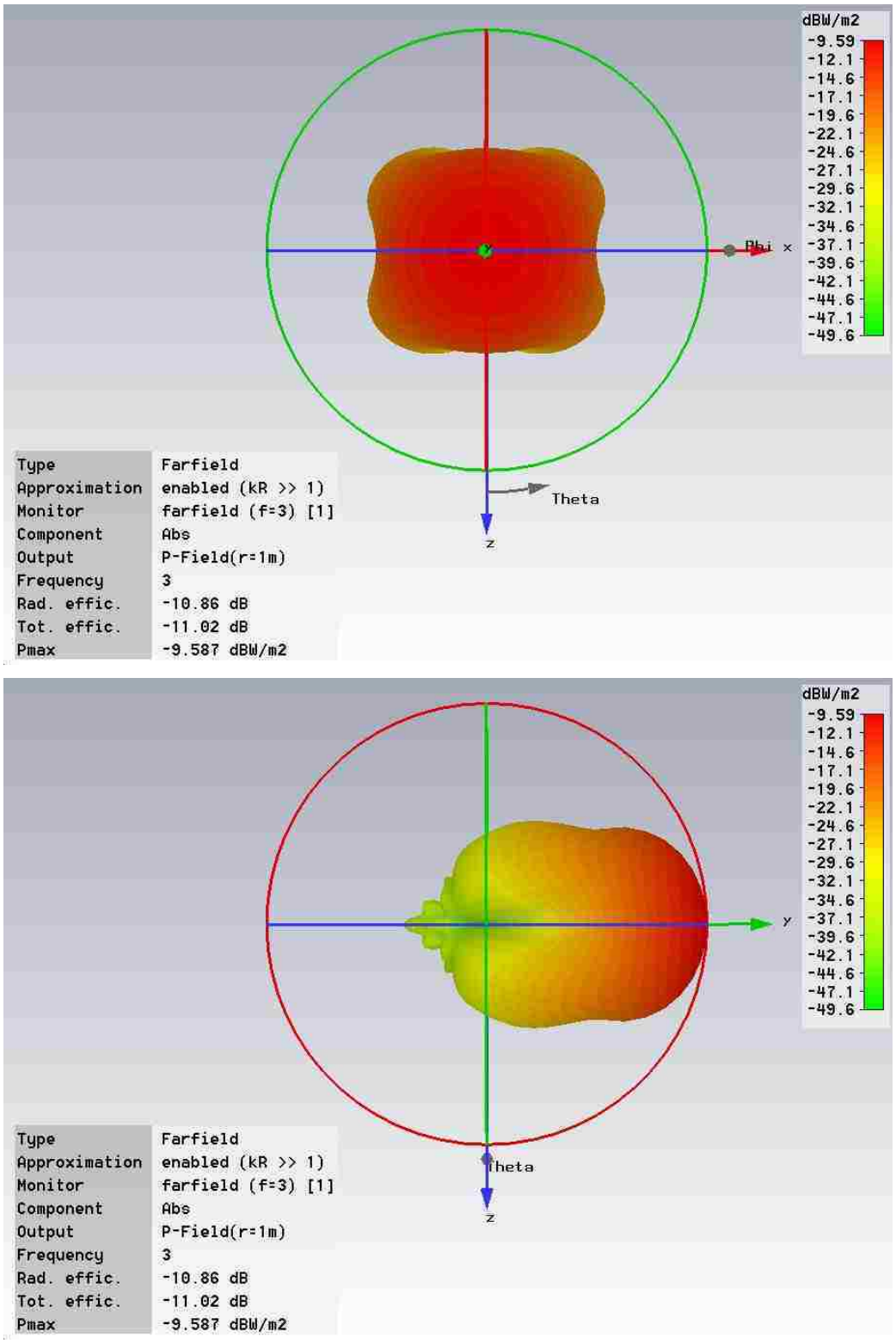

Figure 222: 3 GHz 3D power patterns

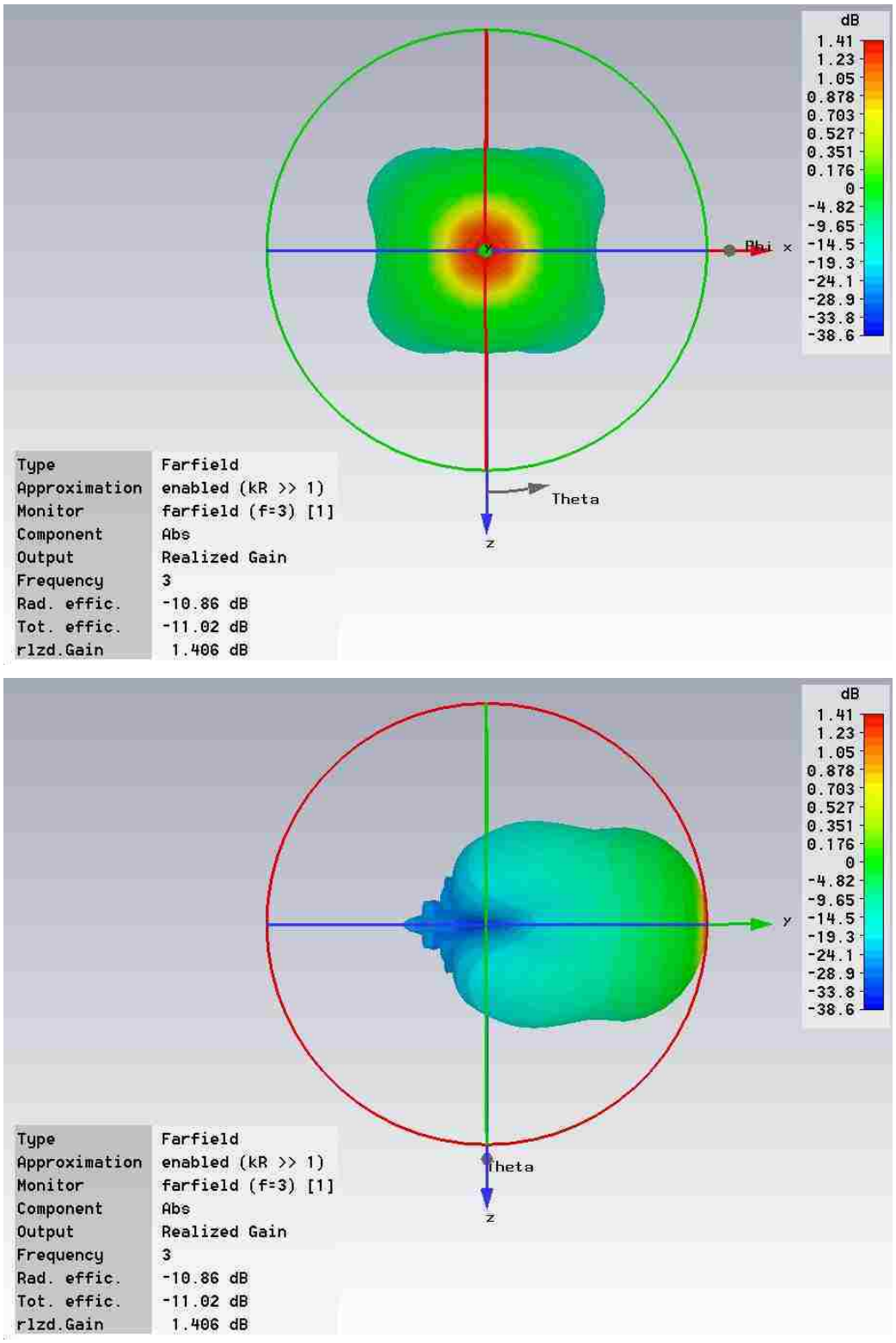

Figure 223: 3 GHz 3D realized gain patterns

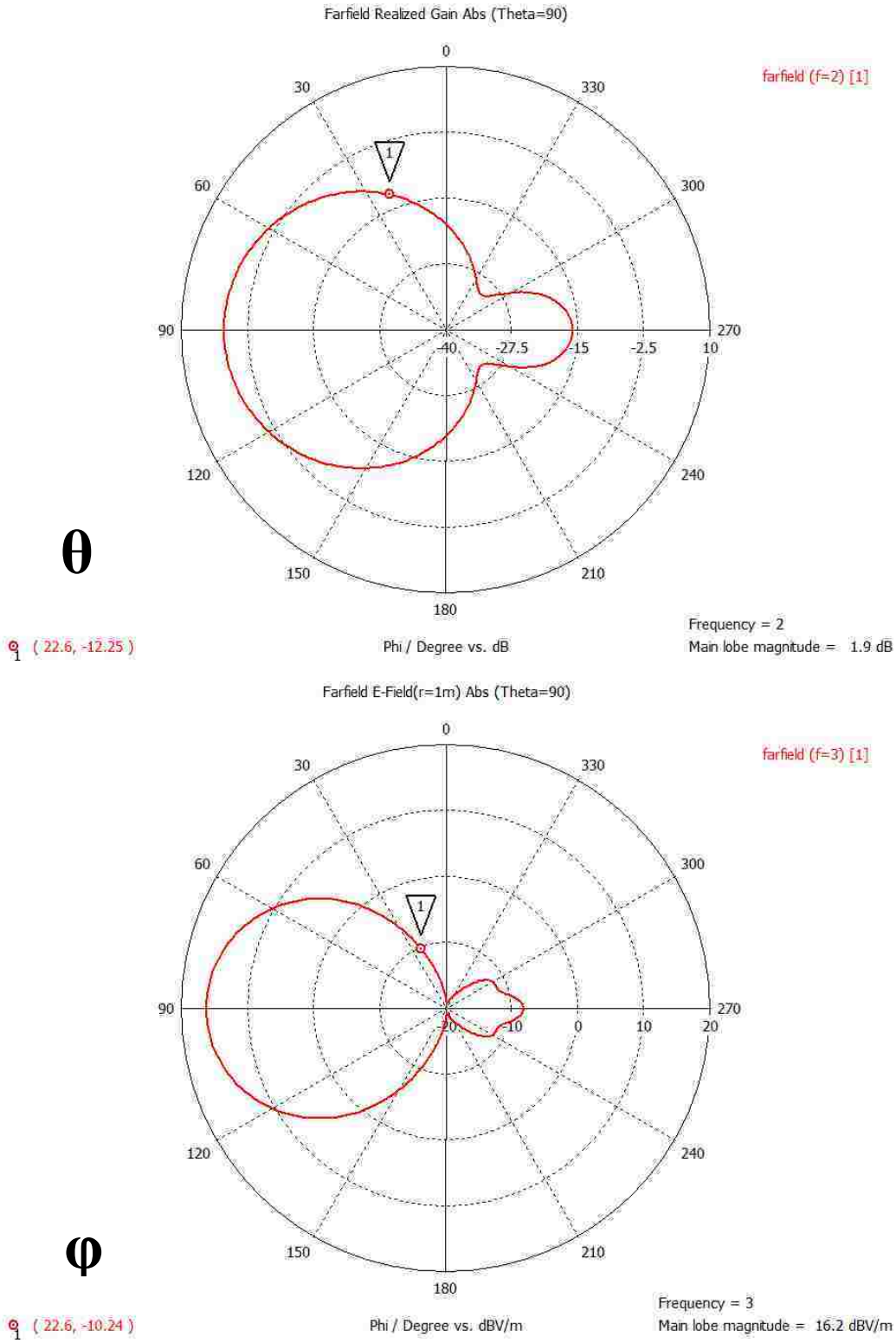

Figure 224: 3 GHz E-field patterns for theta and phi

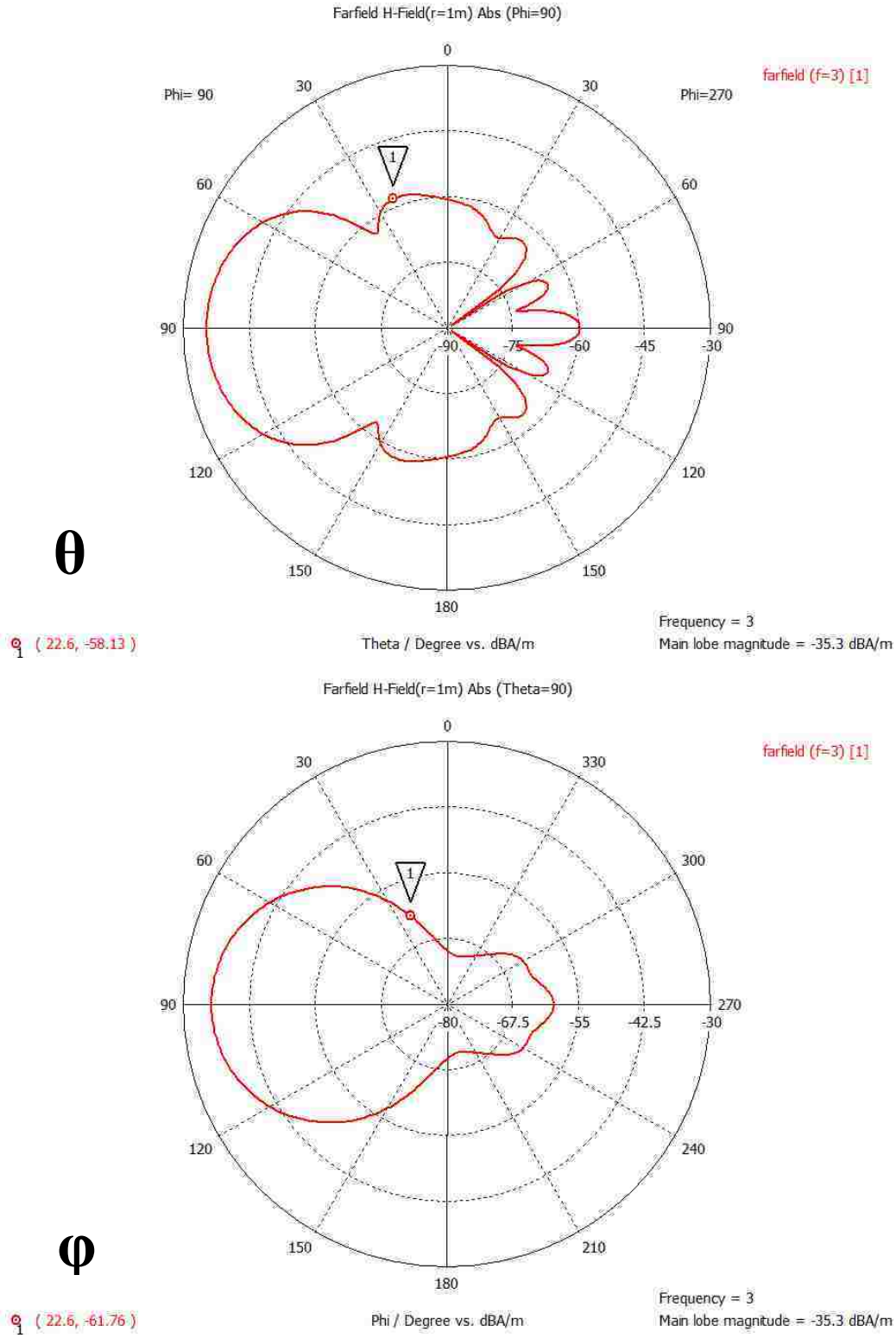

Figure 225: 3 GHz H-field patterns for theta and phi

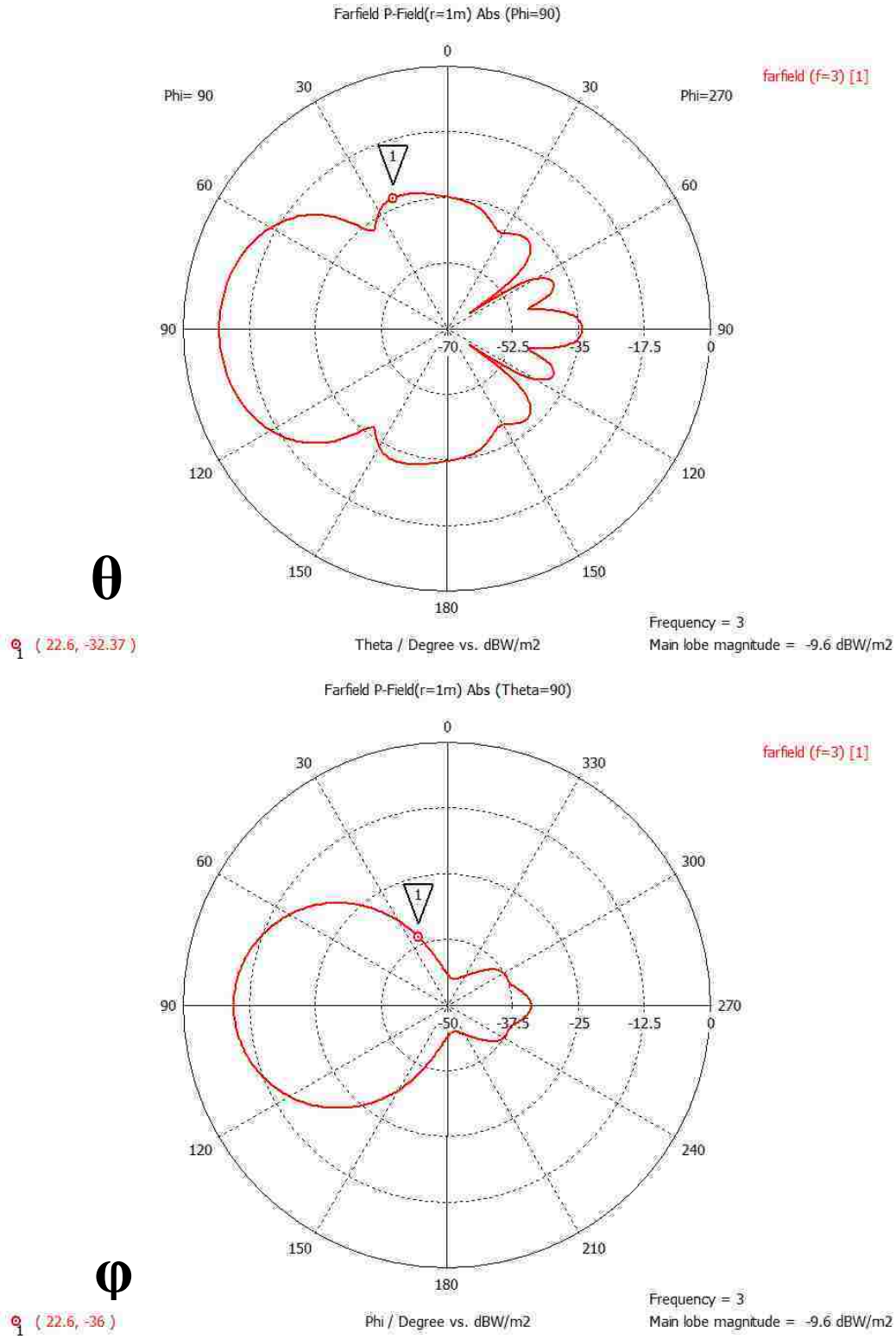

Figure 226: 3 GHz power patterns for theta and phi

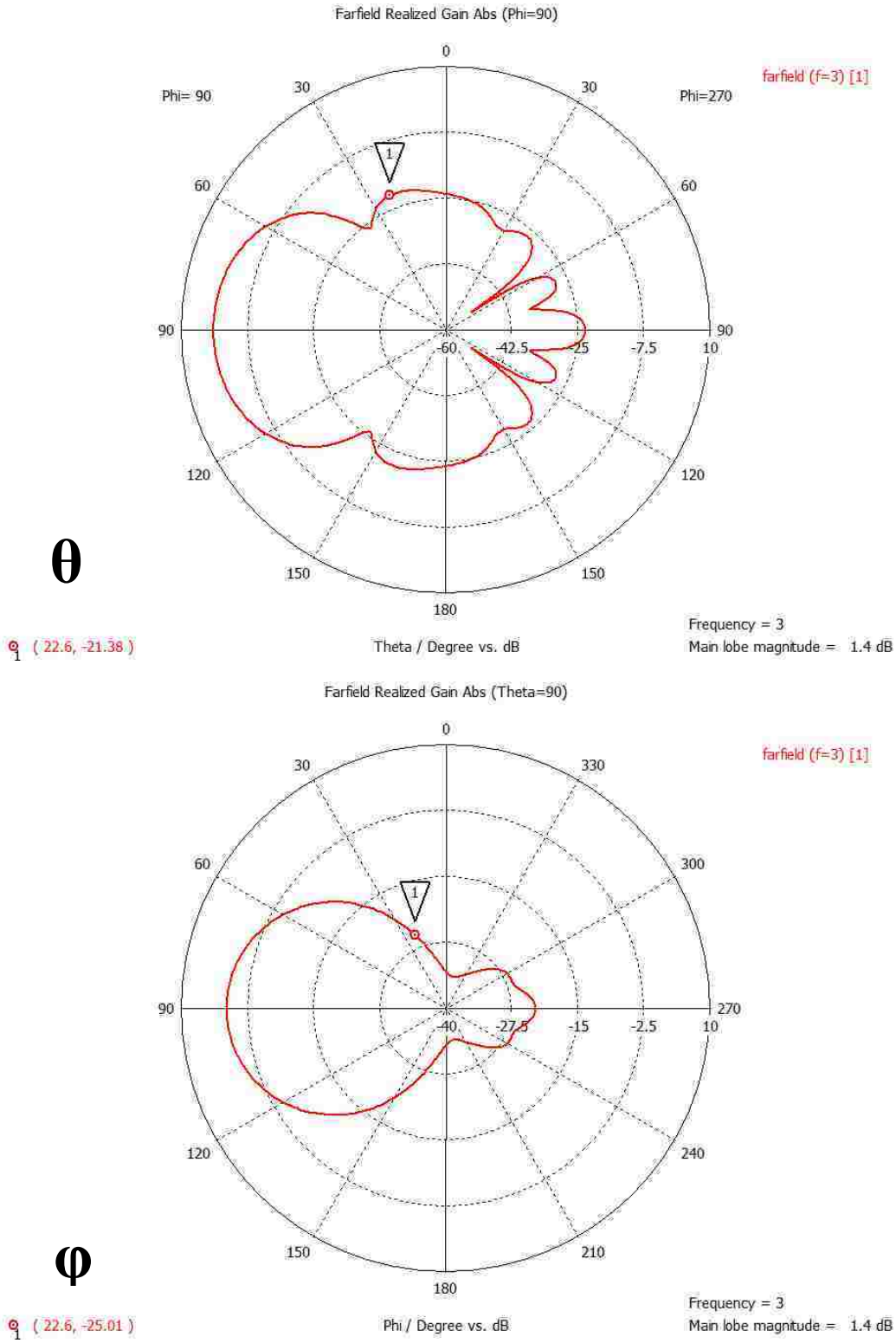

Figure 227: 3 GHz realized gain patterns for theta and phi

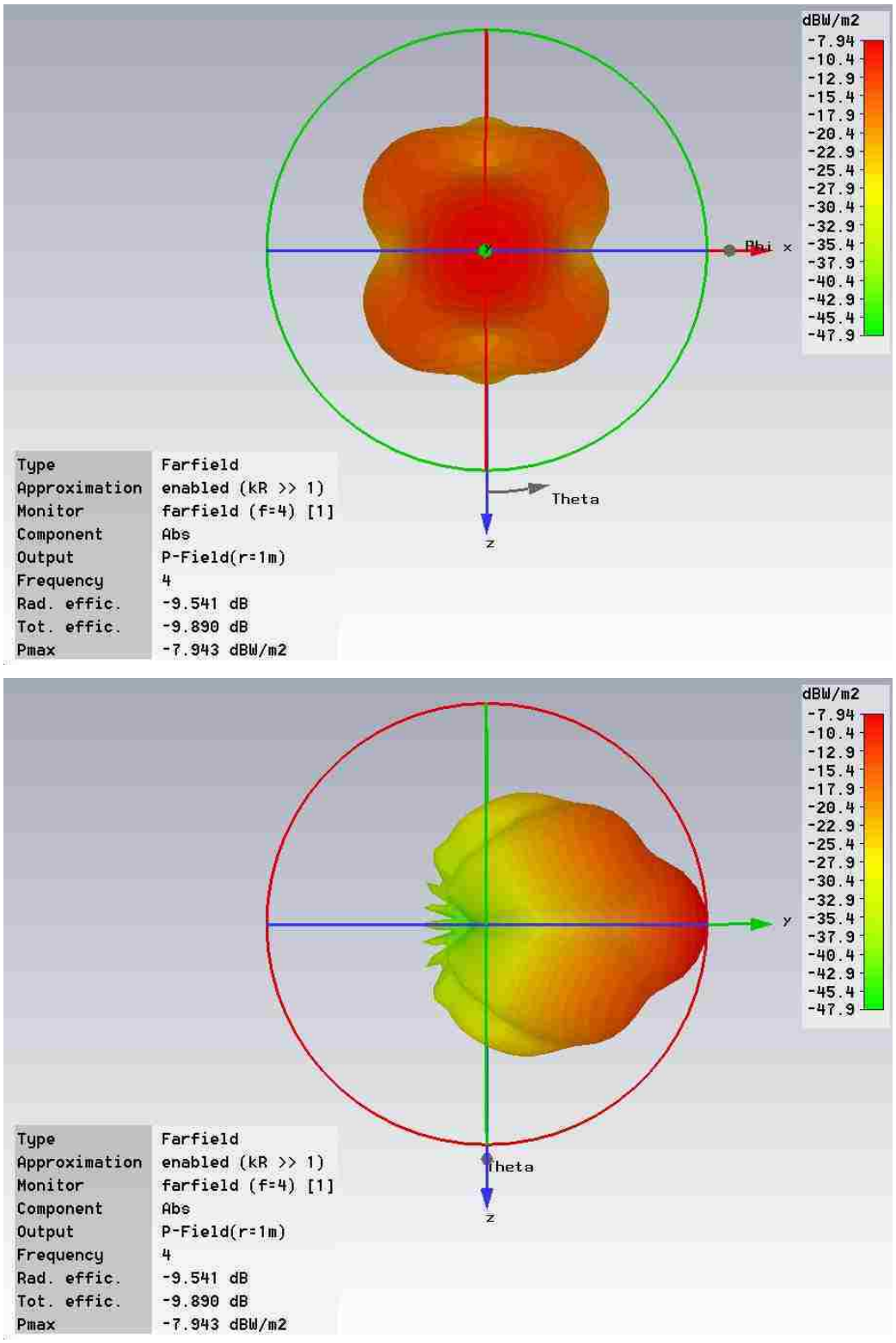

Figure 228: 4 GHz 3D power patterns

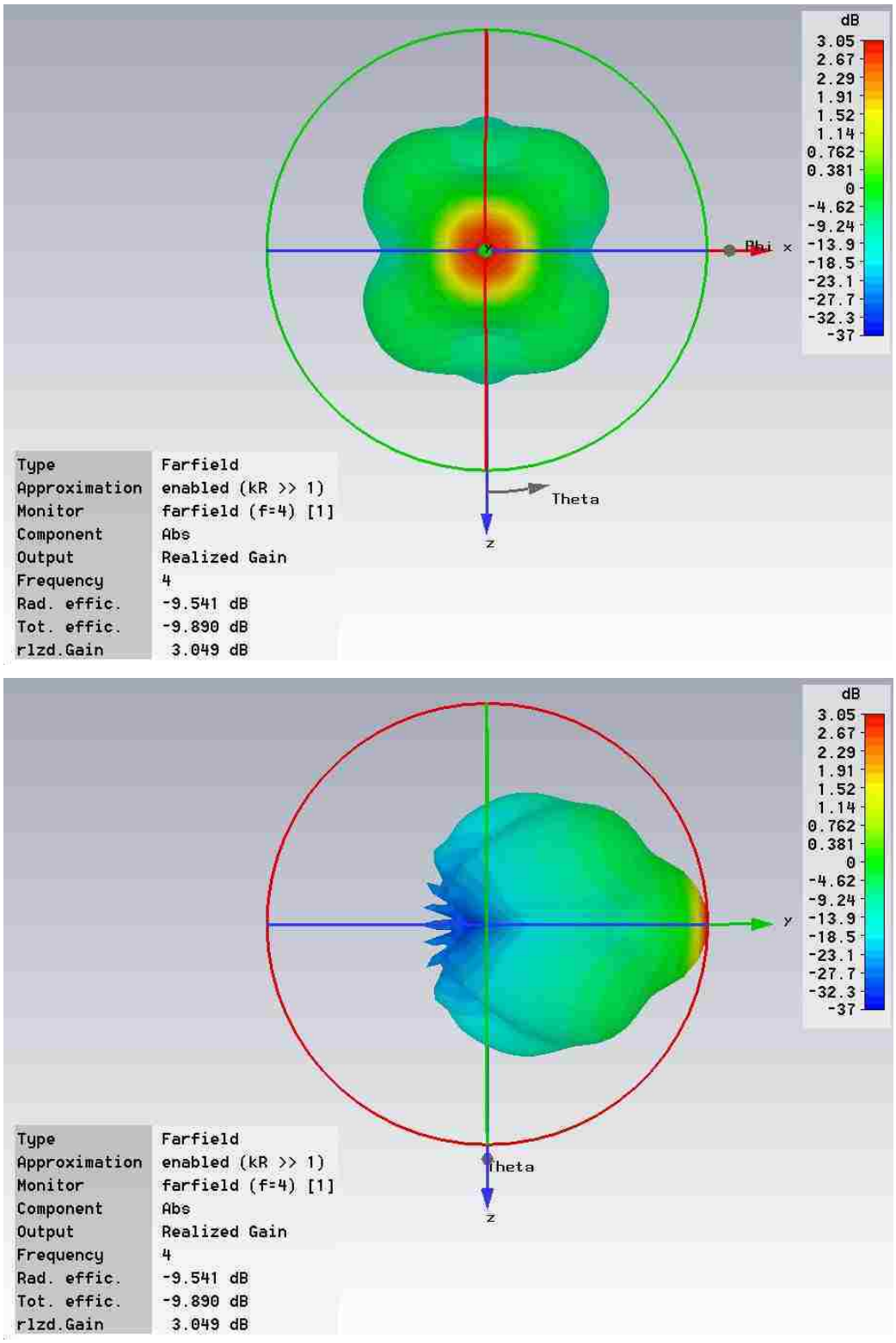

Figure 229: 4 GHz 3D realized gain patterns

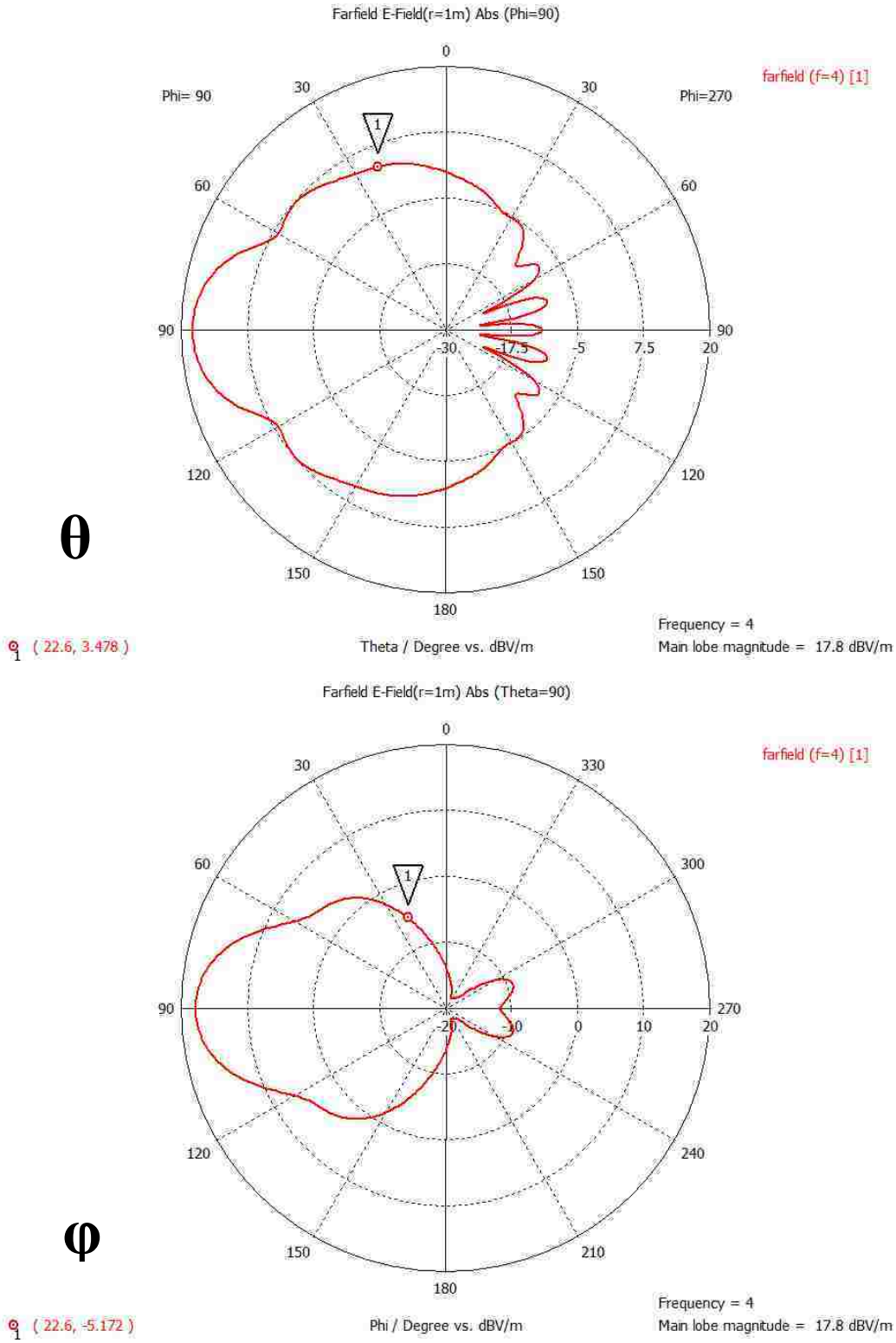

Figure 230: 4 GHz E-field patterns for theta and phi

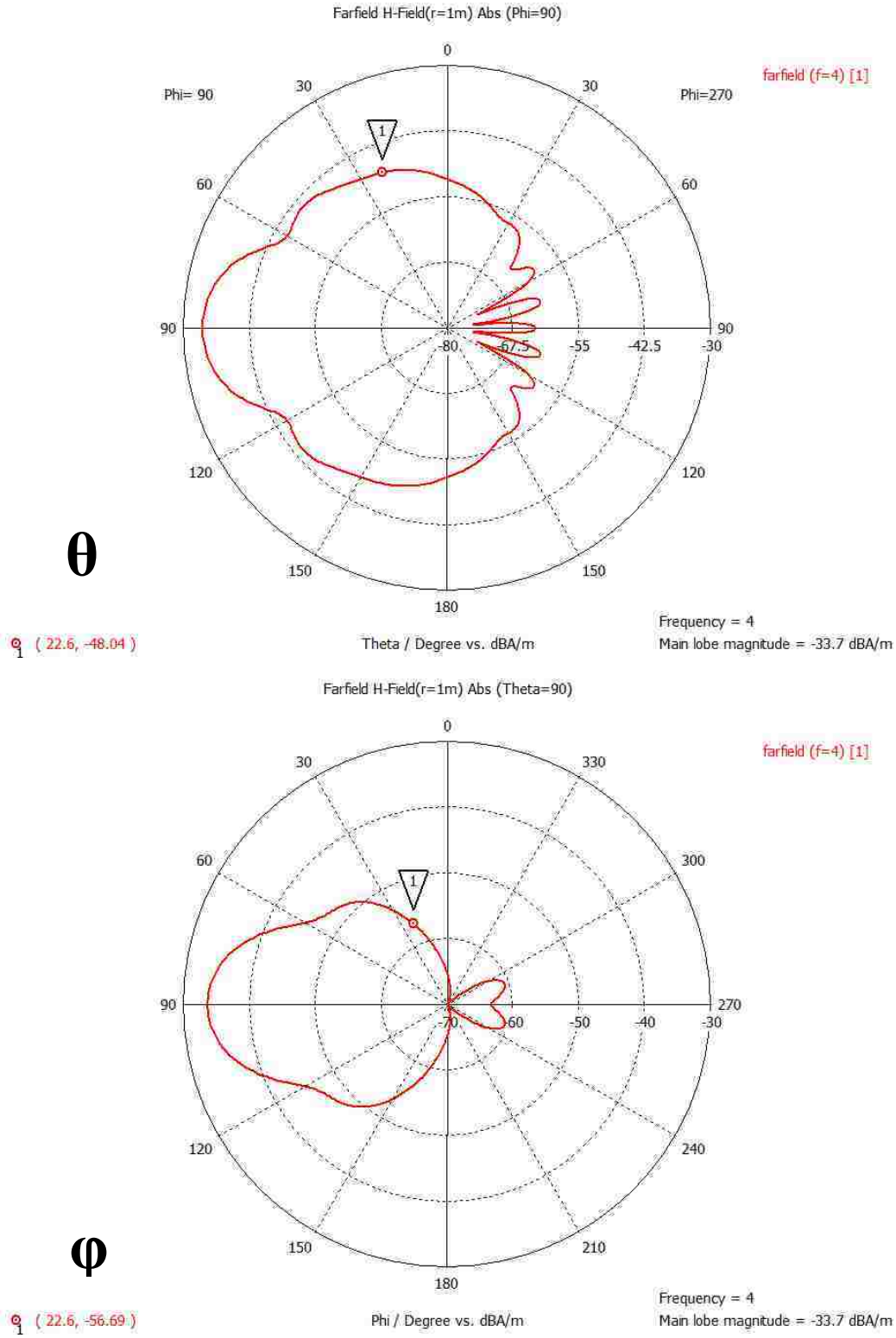

Figure 231: 4 GHz H-field patterns for theta and phi

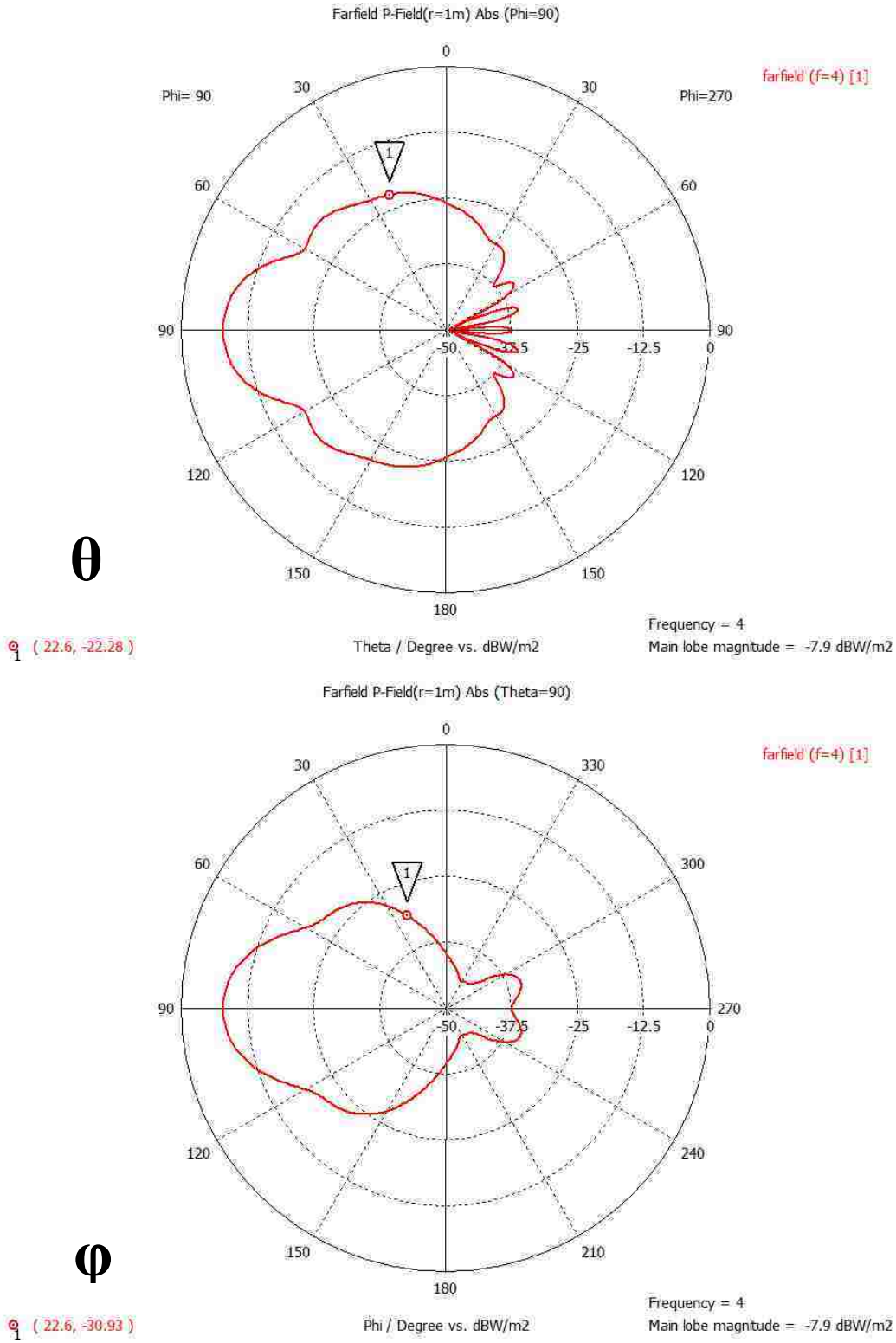

Figure 232: 4 GHz power patterns for theta and phi

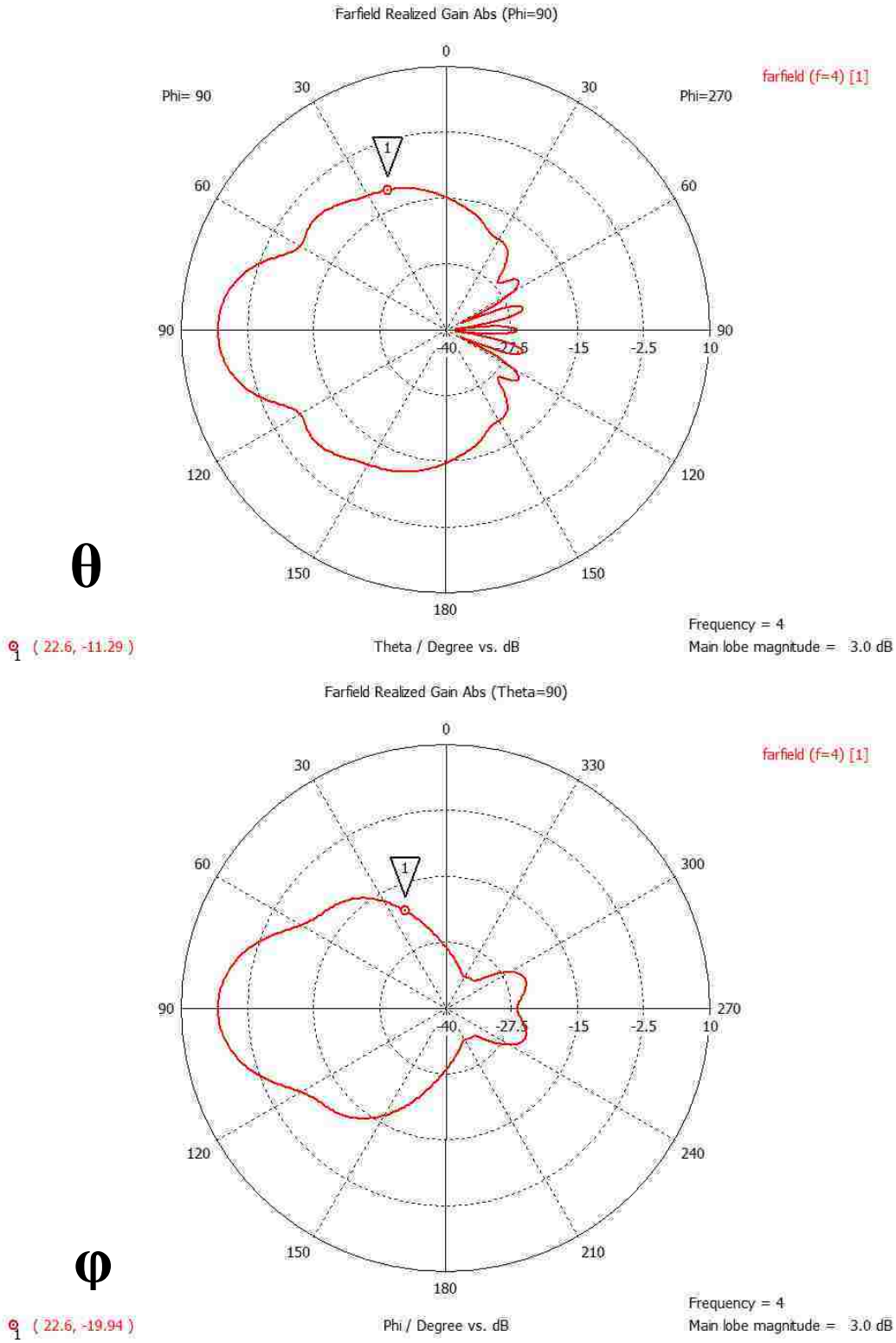

Figure 233: 4 GHz realized gain patterns for theta and phi

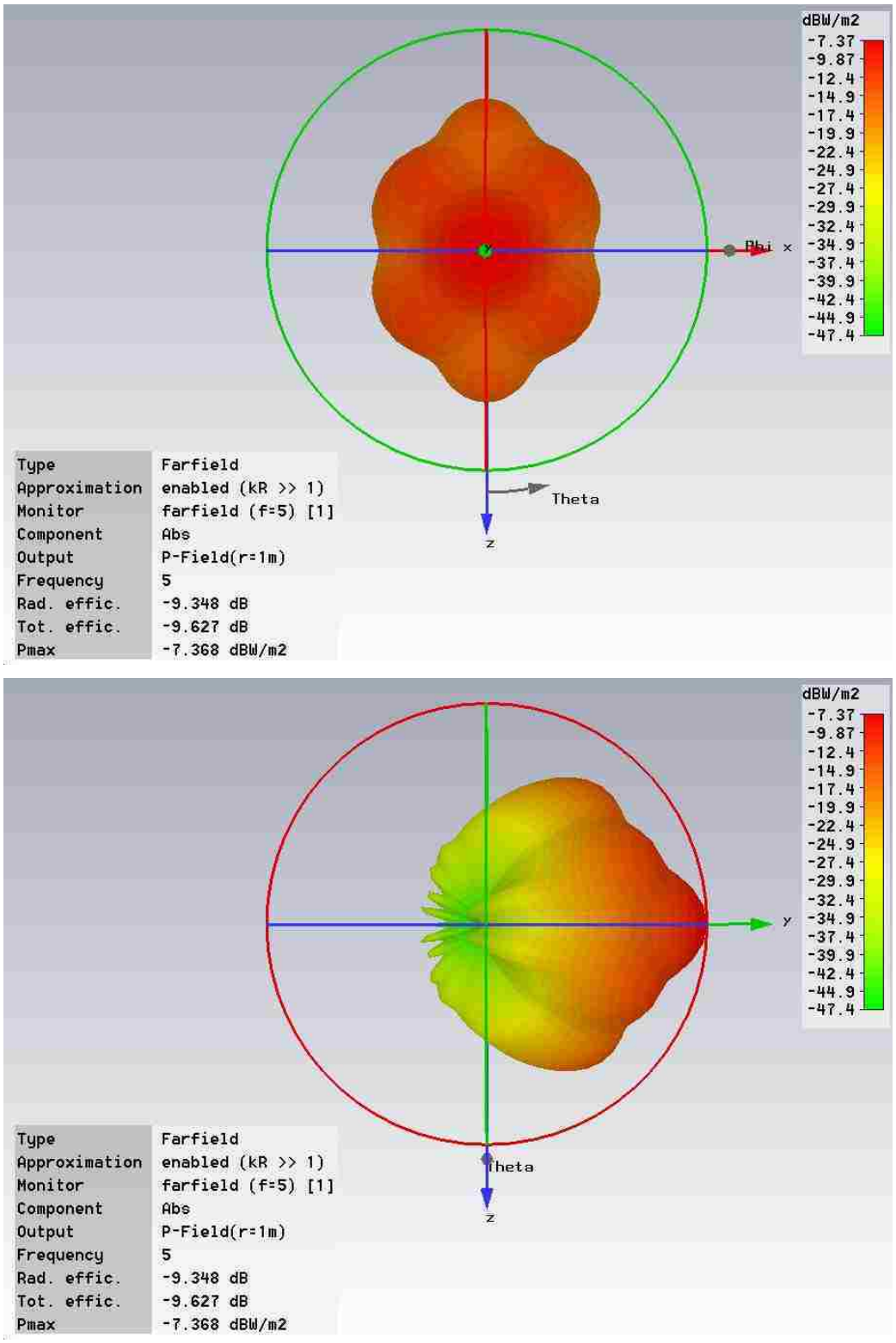

Figure 234: 5 GHz 3D power patterns

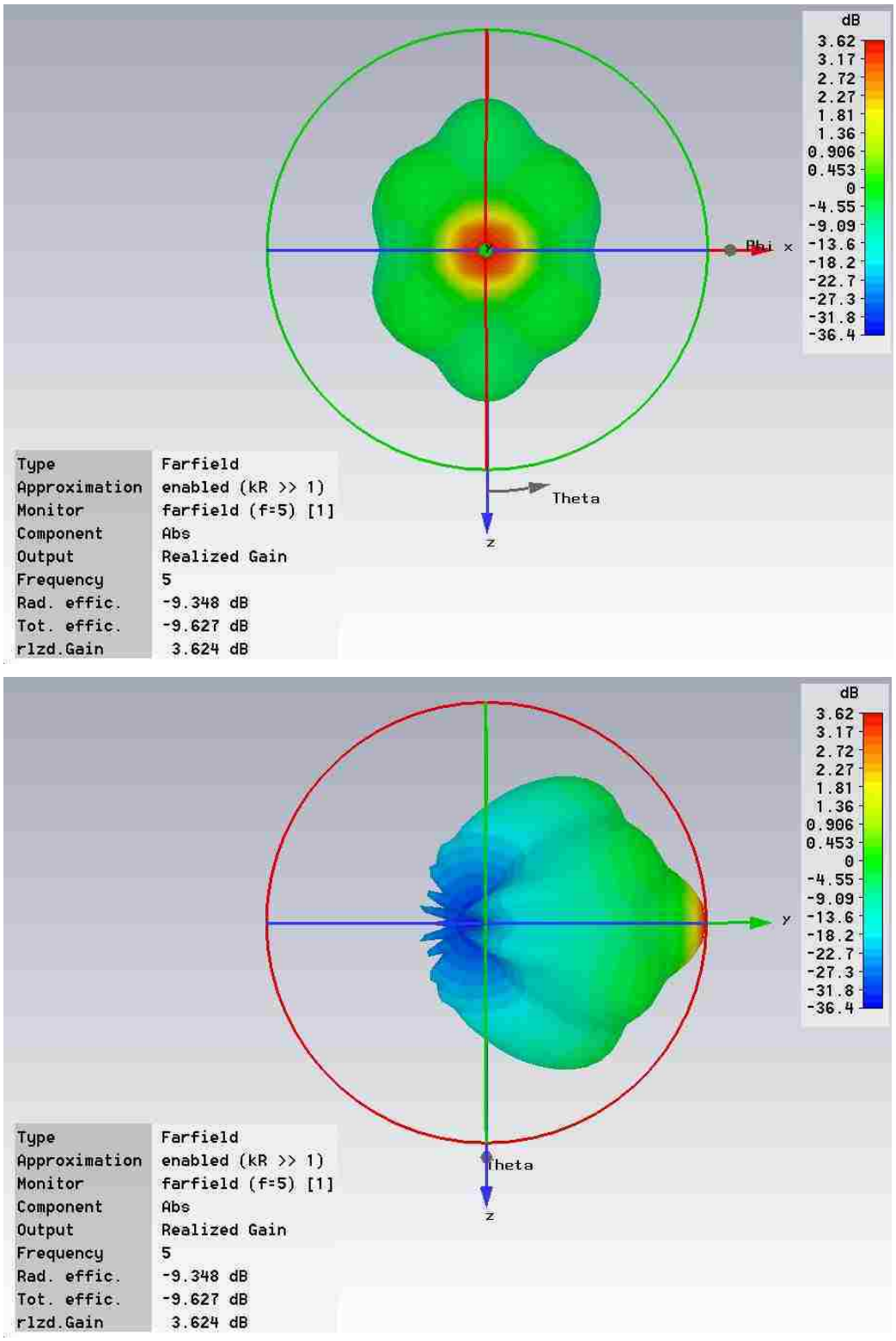

Figure 235: 5 GHz 3D realized gain patterns

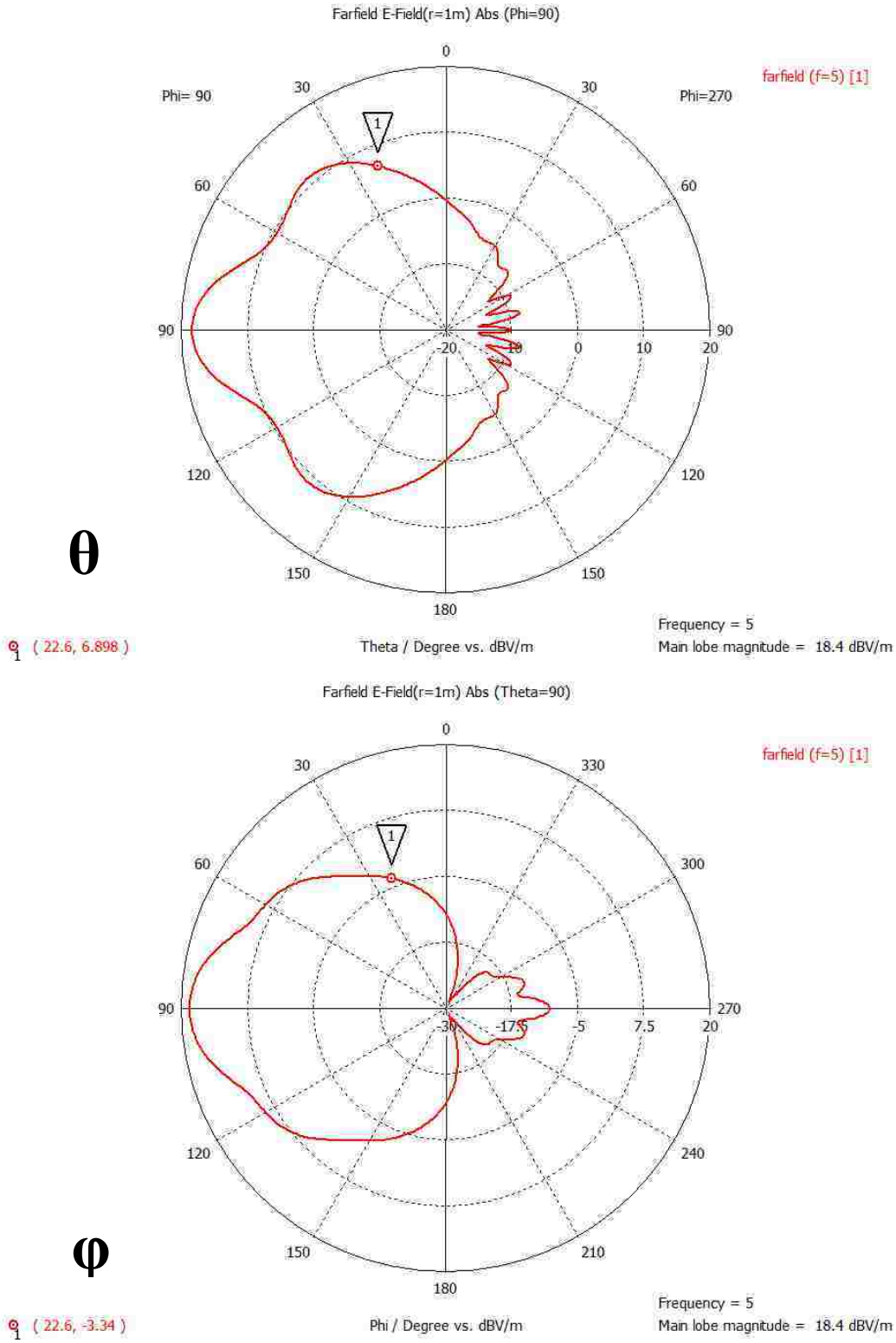

Figure 236: 5 GHz E-field patterns for theta and phi

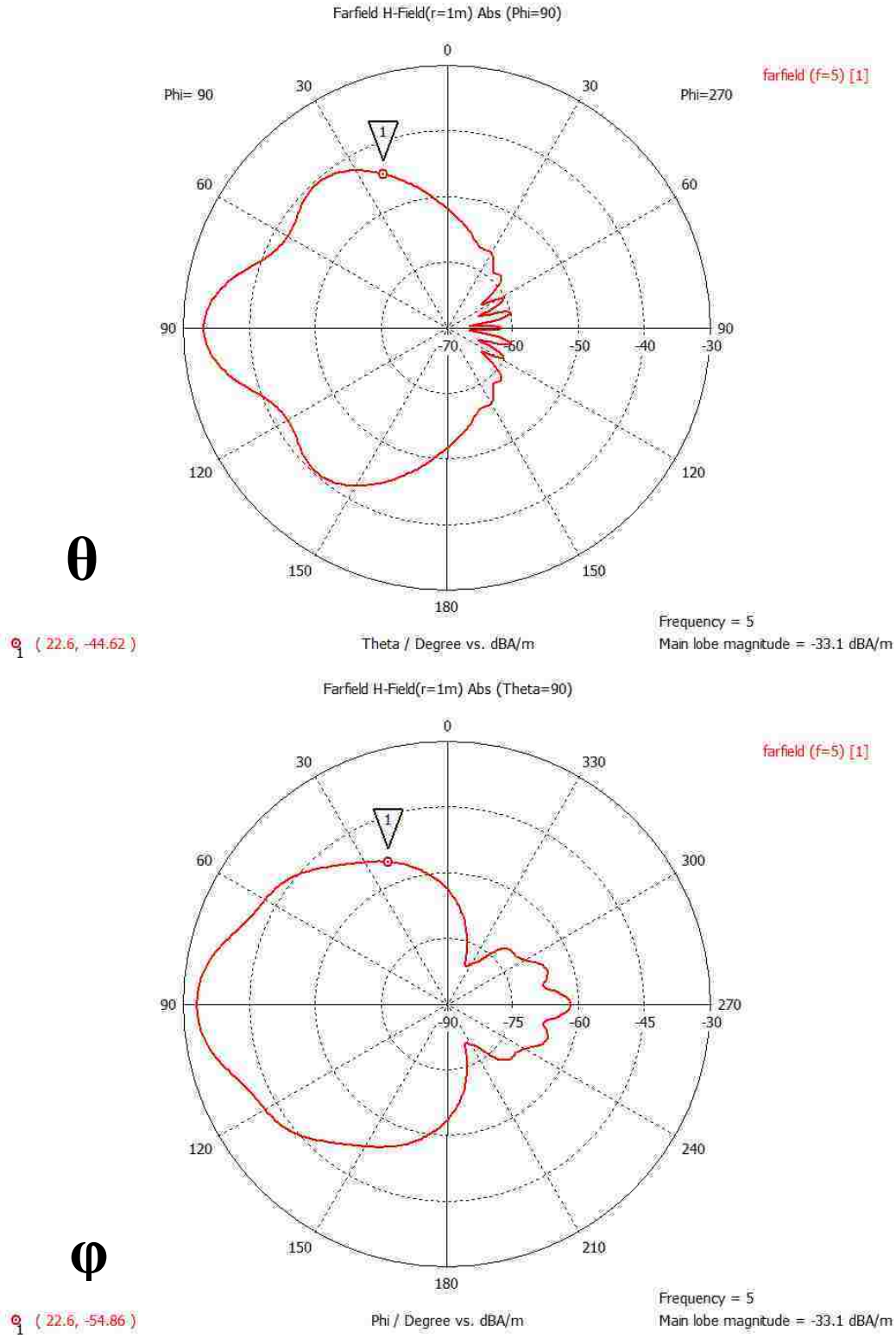

Figure 237: 5 GHz H-field patterns for theta and phi

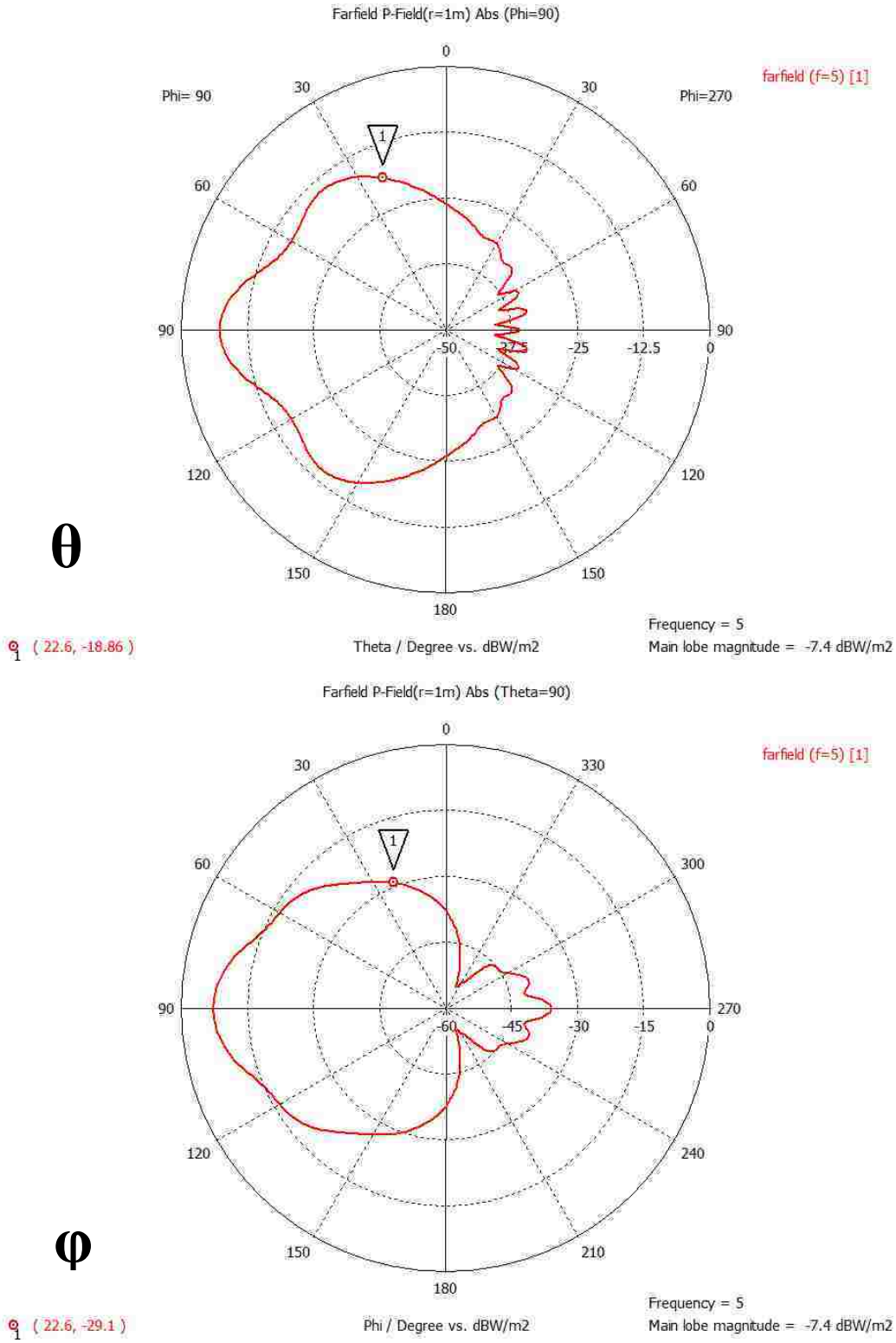

Figure 238: 5 GHz power patterns for theta and phi

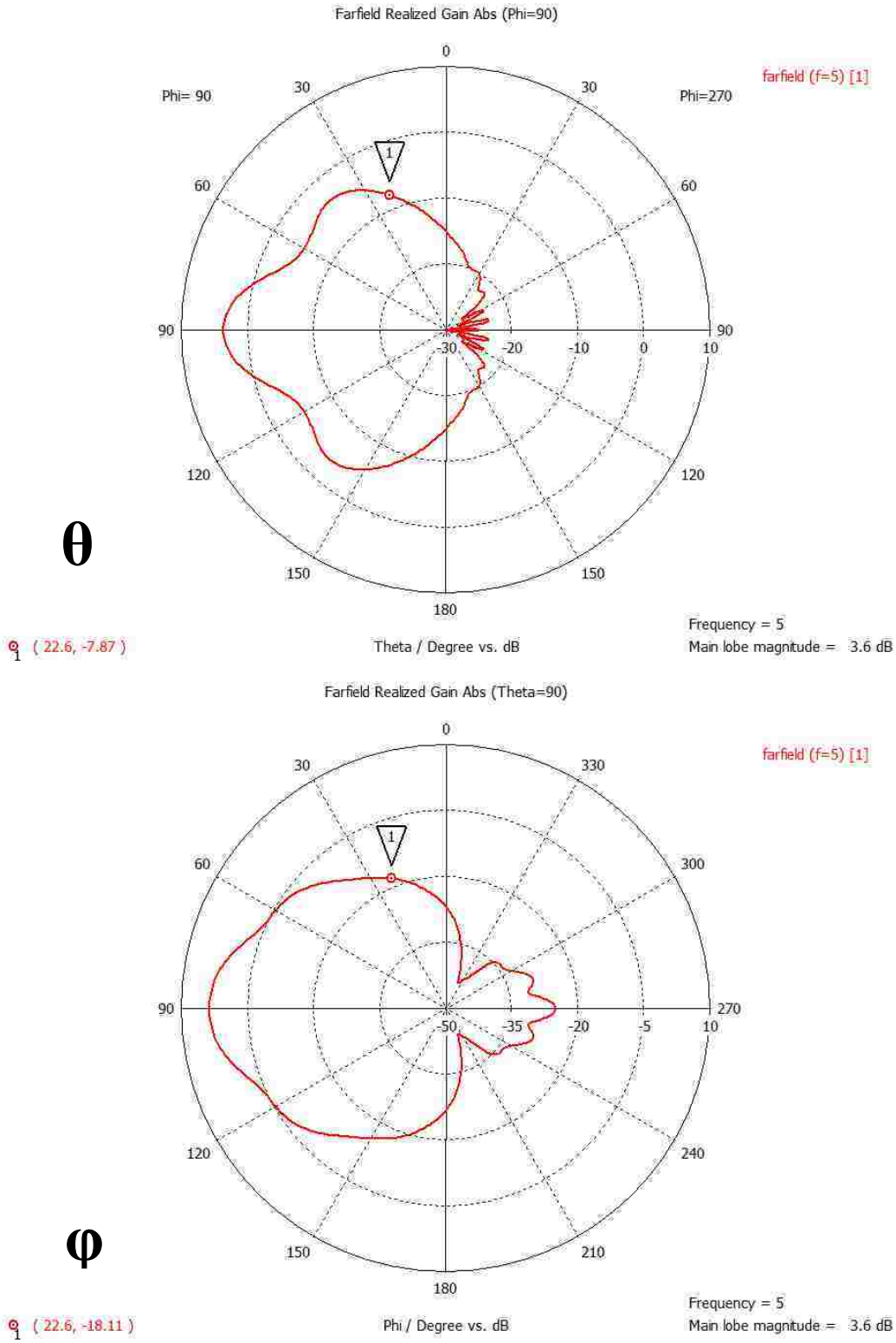

Figure 239: 5 GHz realized gain patterns for theta and phi

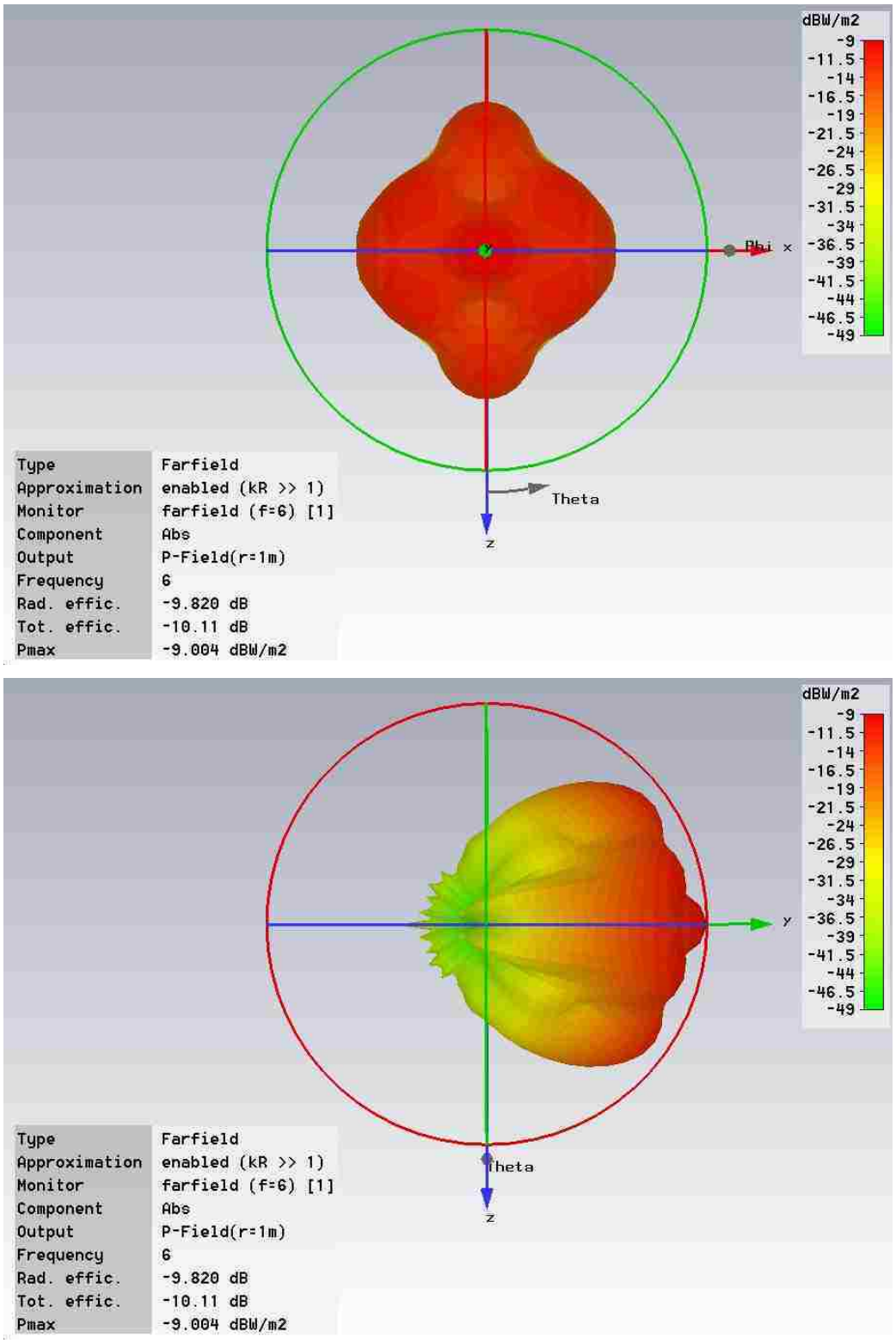

Figure 240: 6 GHz 3D power patterns

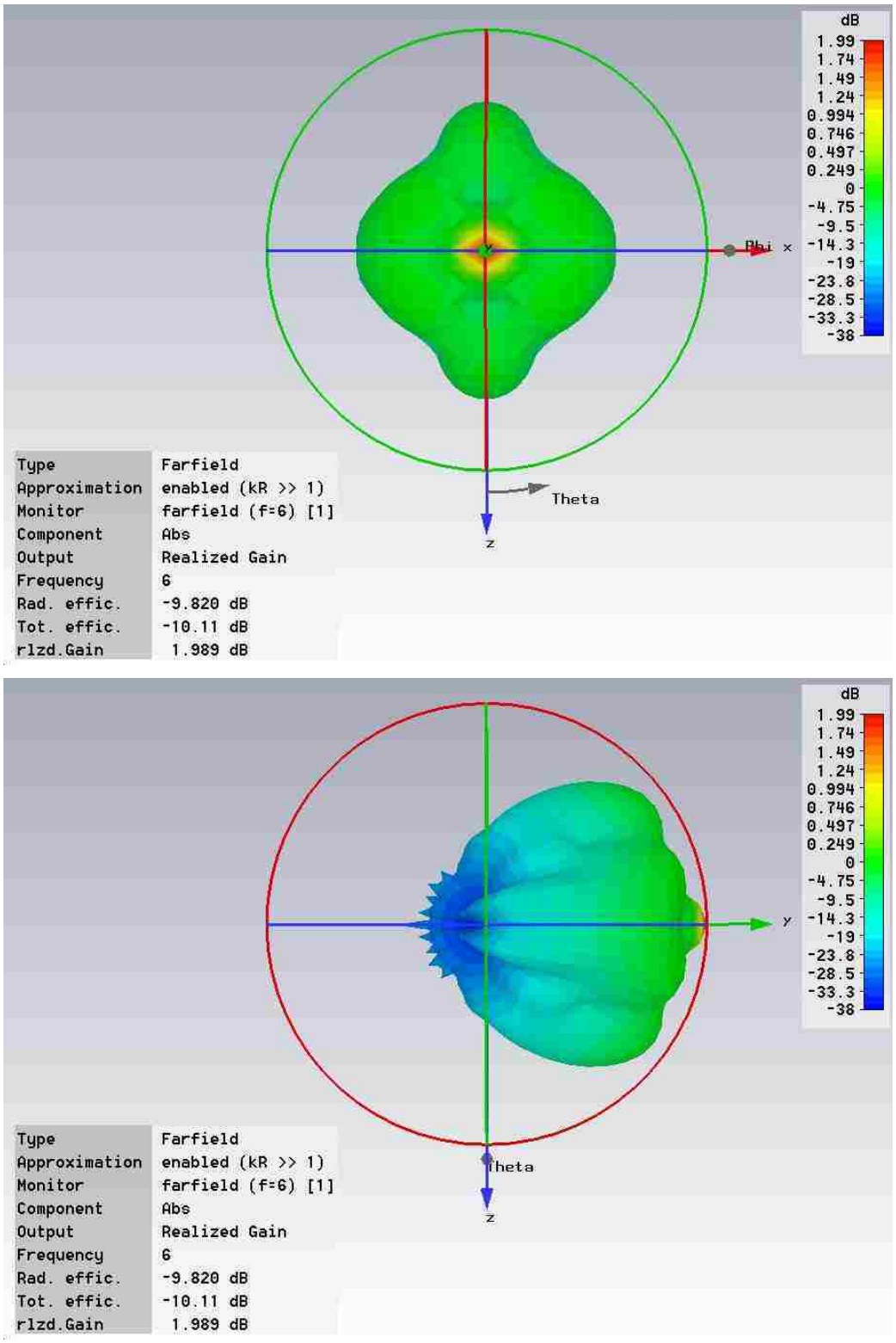

Figure 241: 6 GHz 3D realized gain patterns

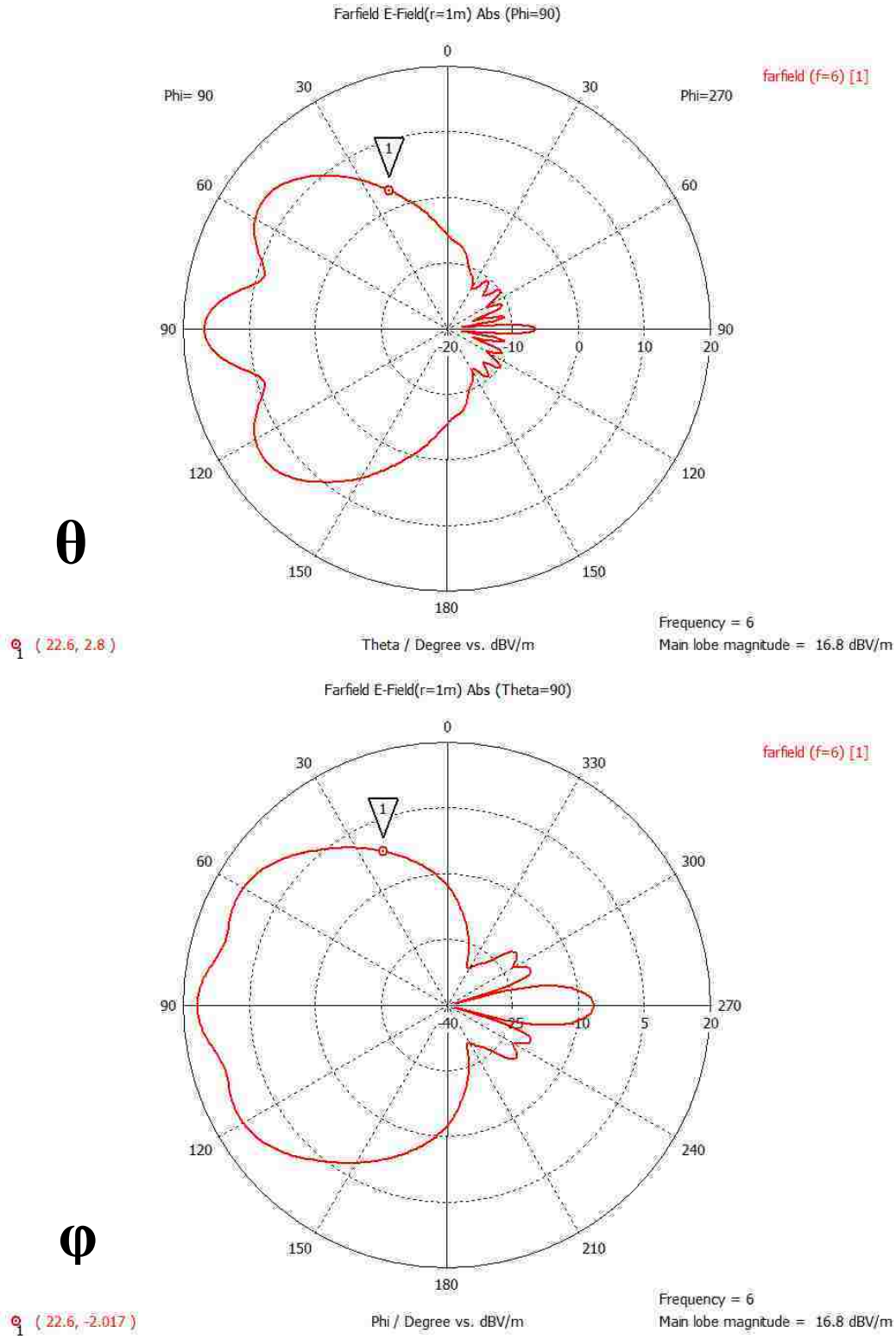

Figure 242: 6 GHz E-field patterns for theta and phi

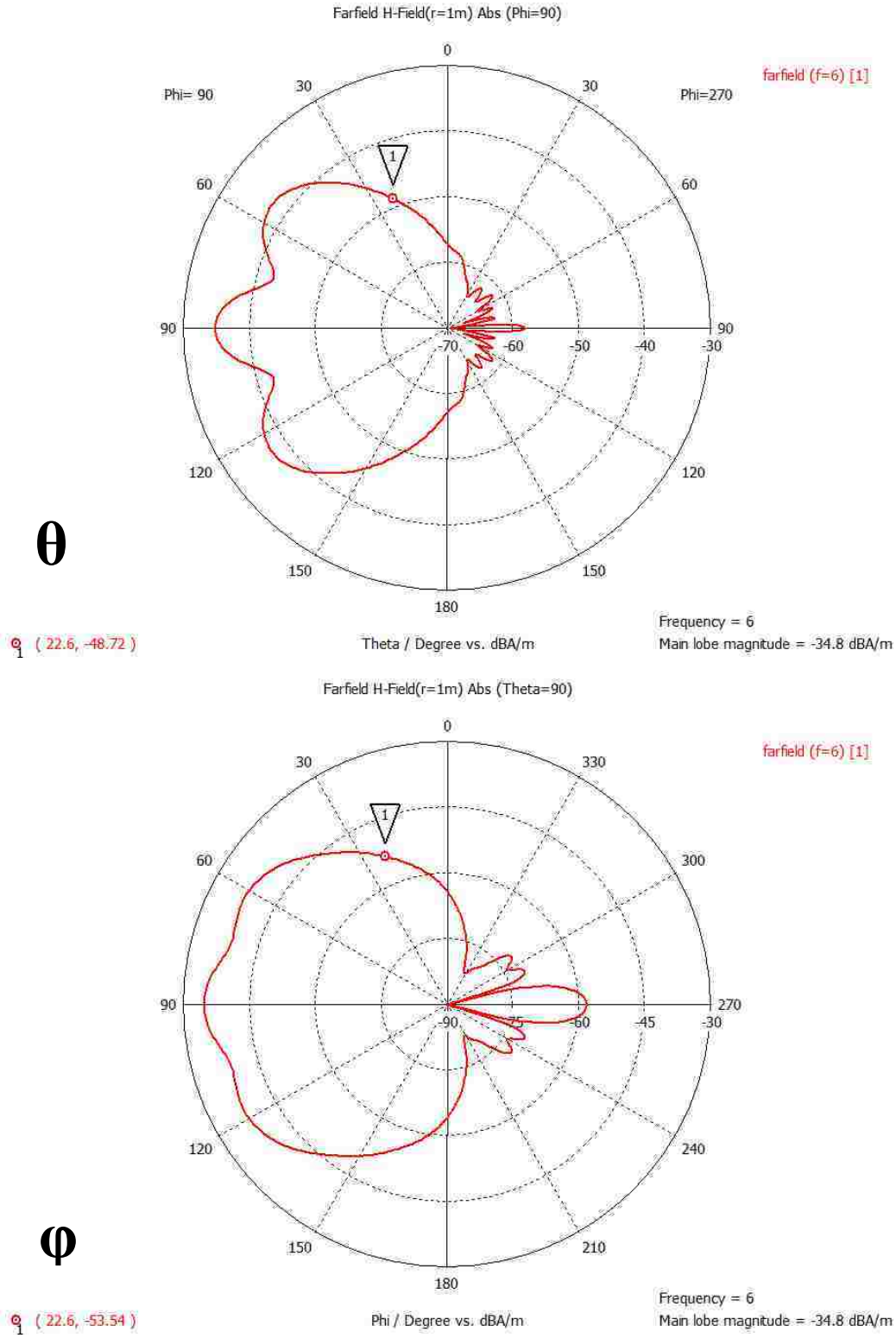

Figure 243: 6 GHz H-field patterns for theta and phi

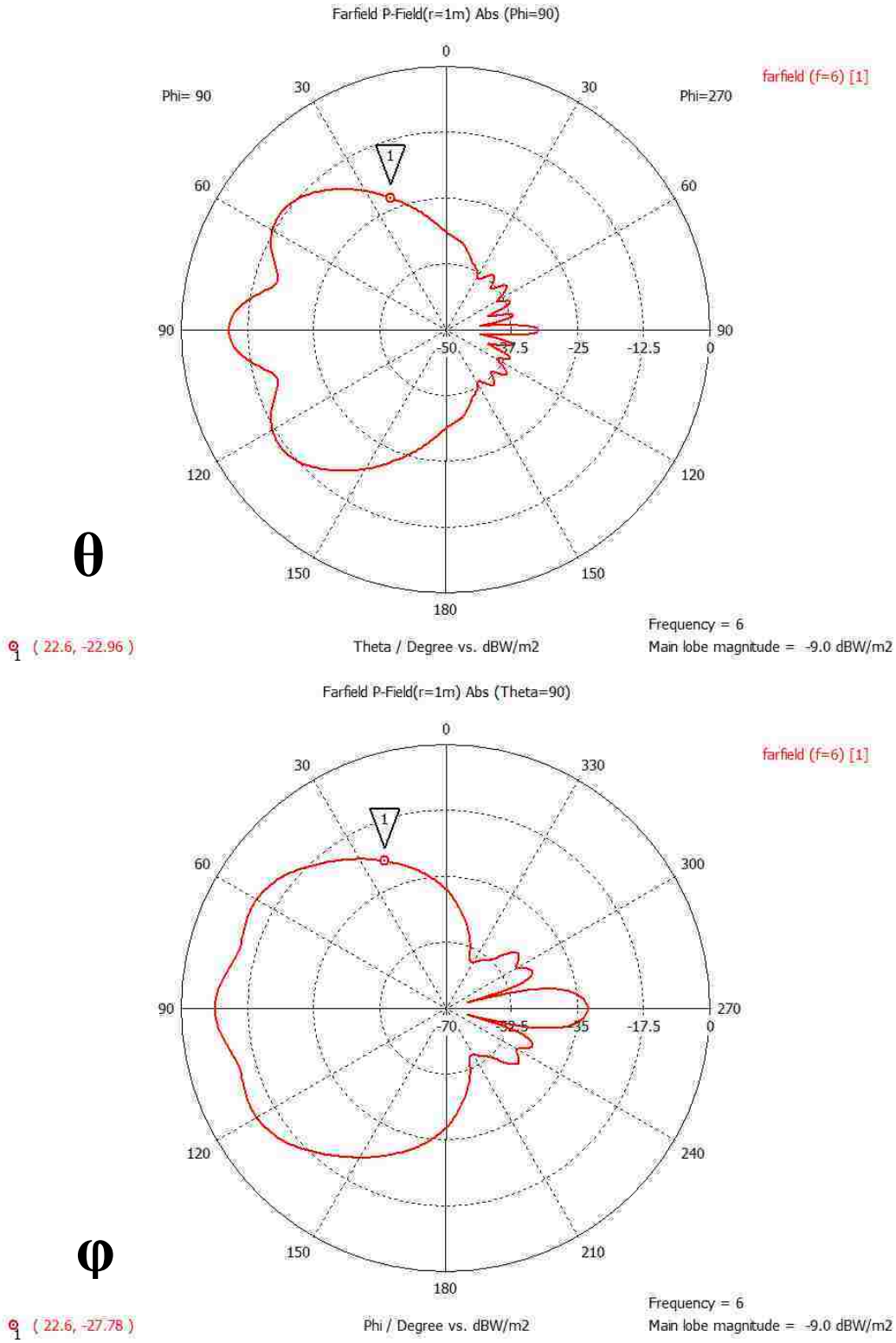

Figure 244: 6 GHz power patterns for theta and phi

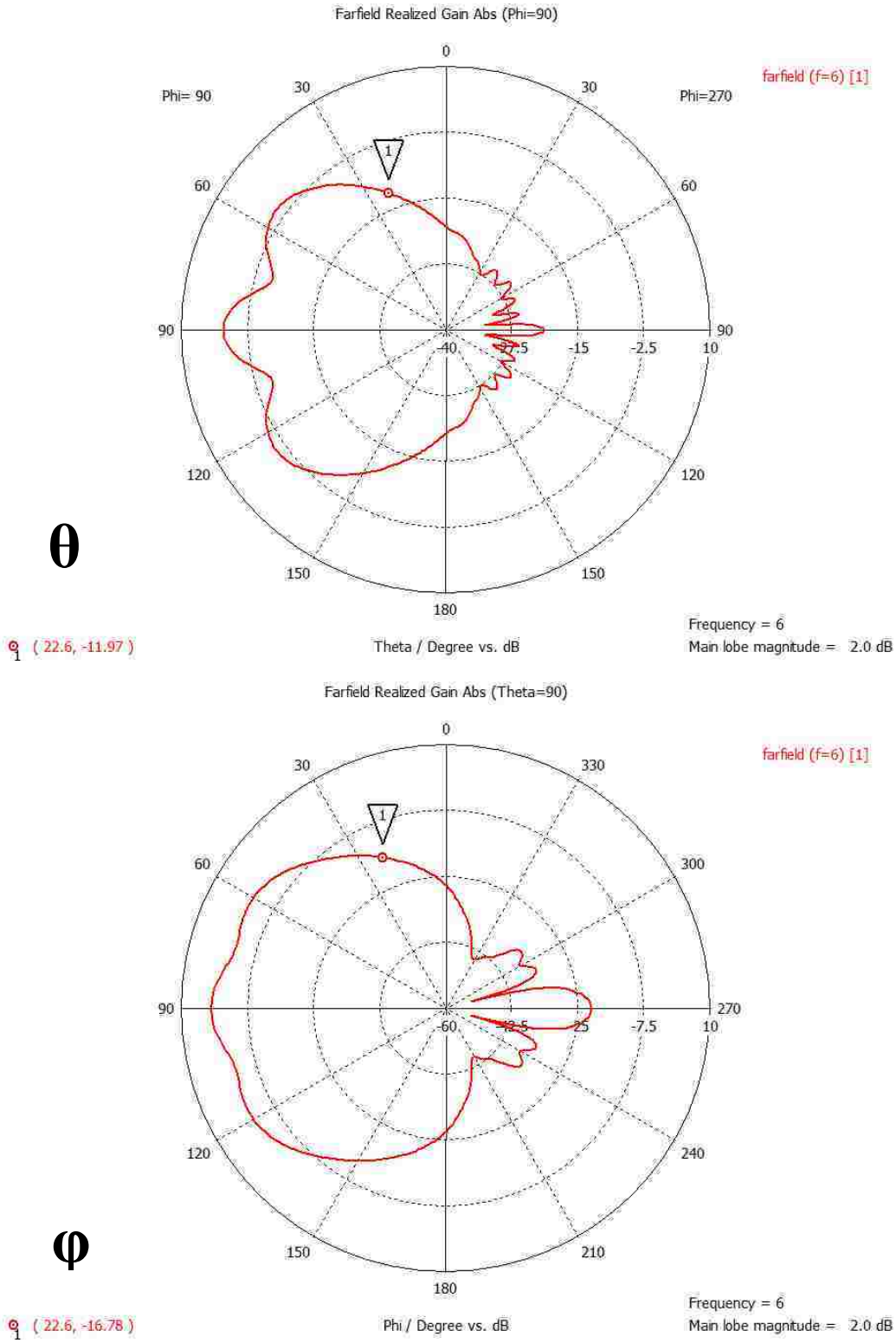

Figure 245: 6 GHz realized gain patterns for theta and phi

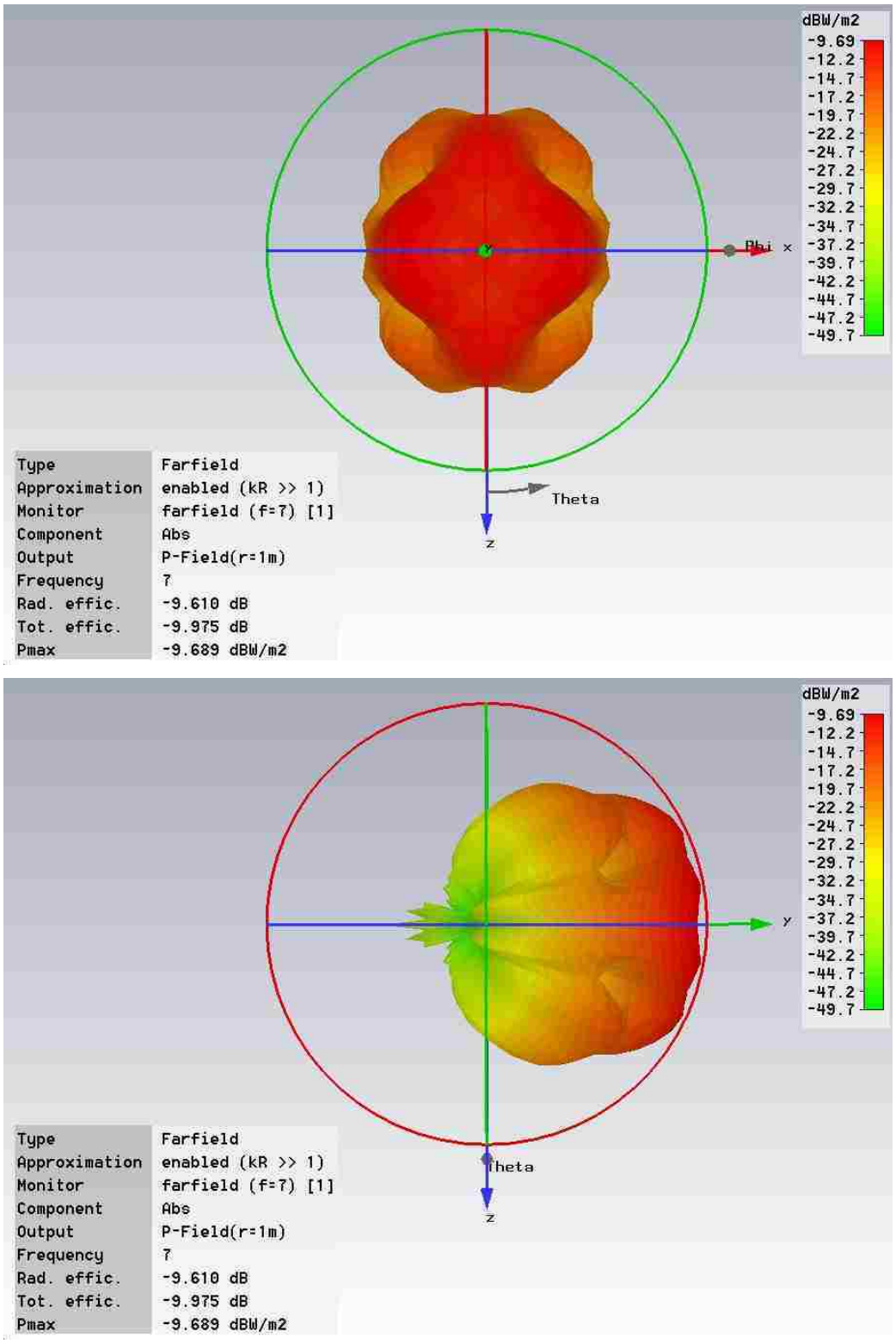

Figure 246: 7 GHz 3D power patterns

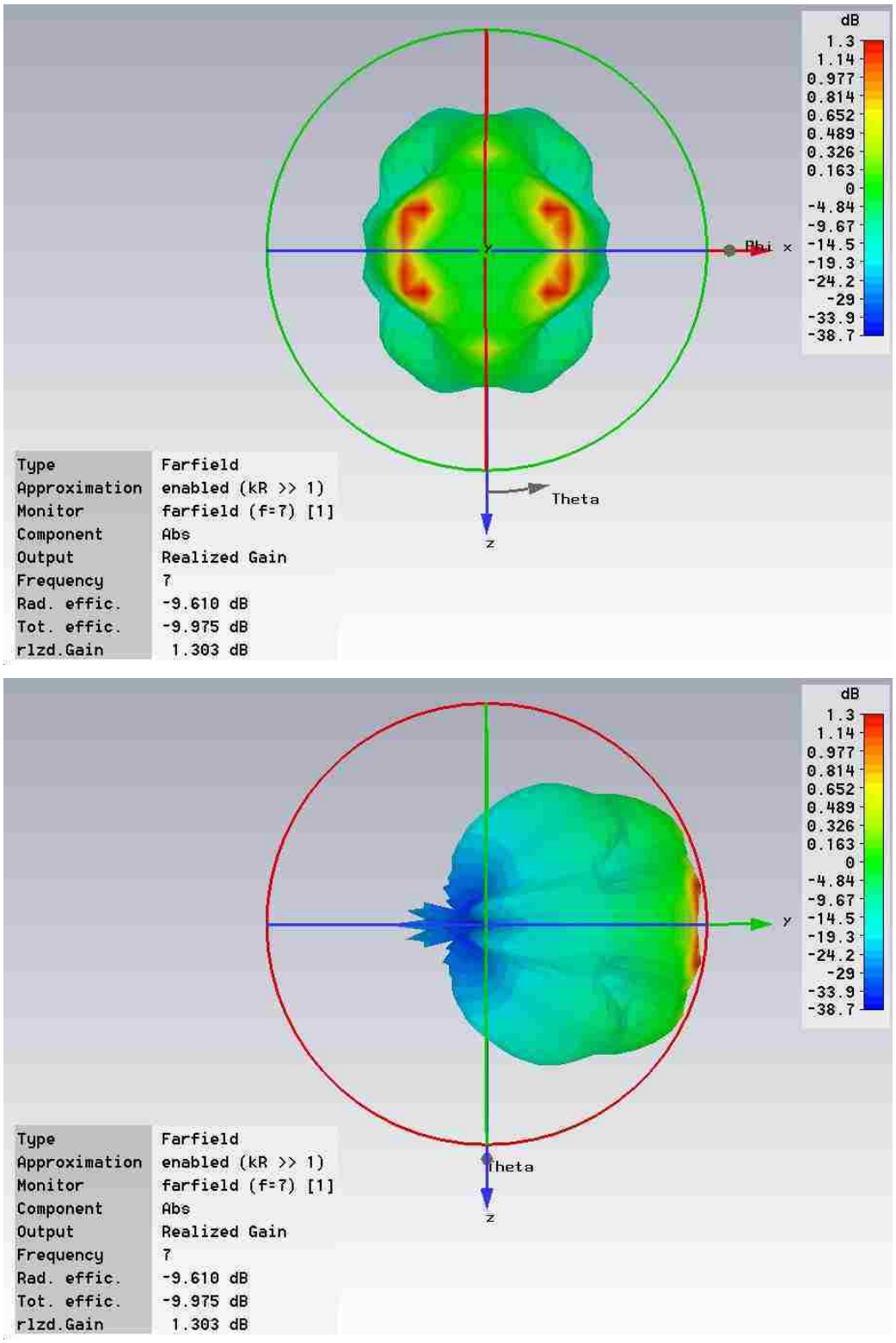

Figure 247: 6 GHz 3D realized gain patterns

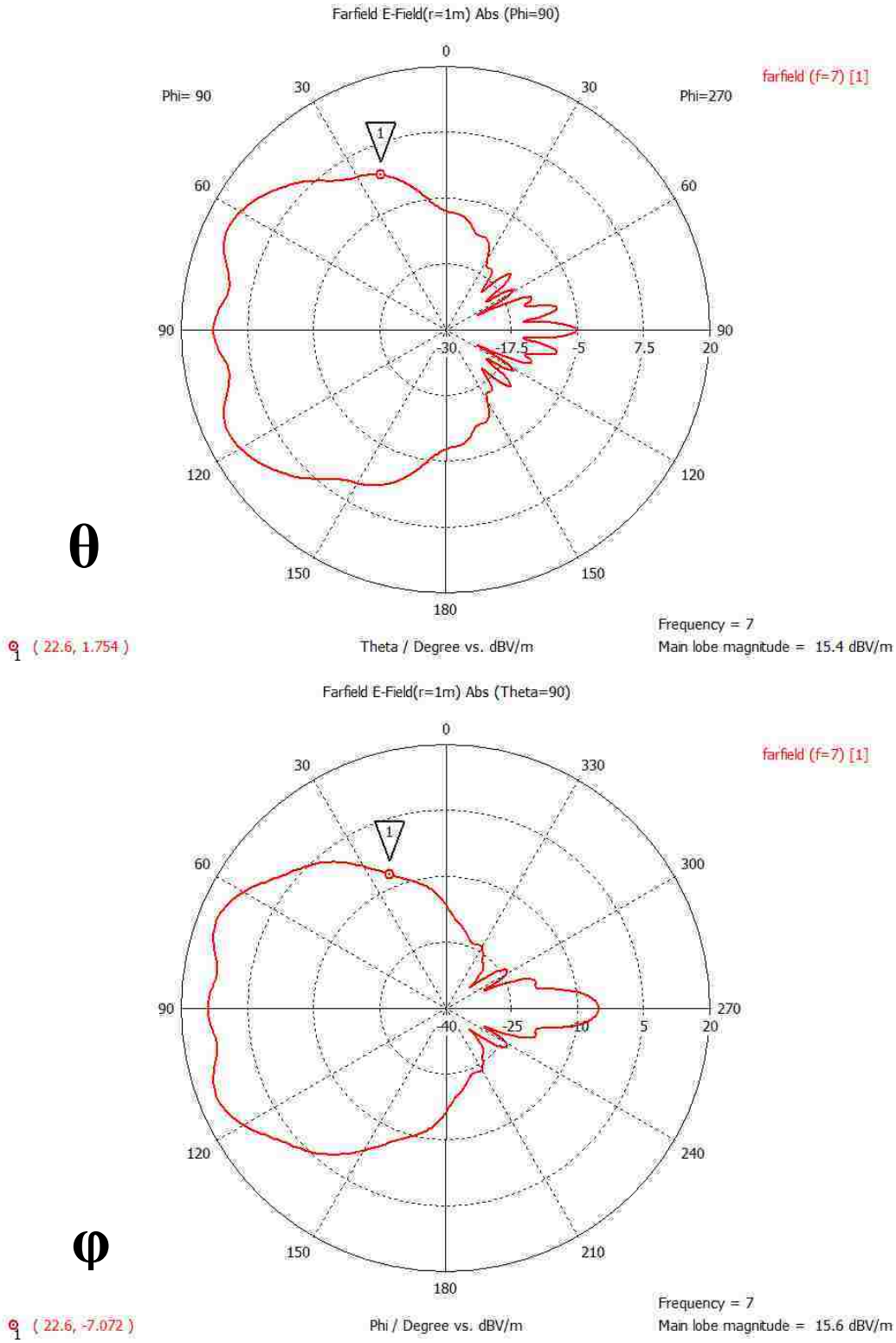

Figure 248: 7 GHz E-field patterns for theta and phi

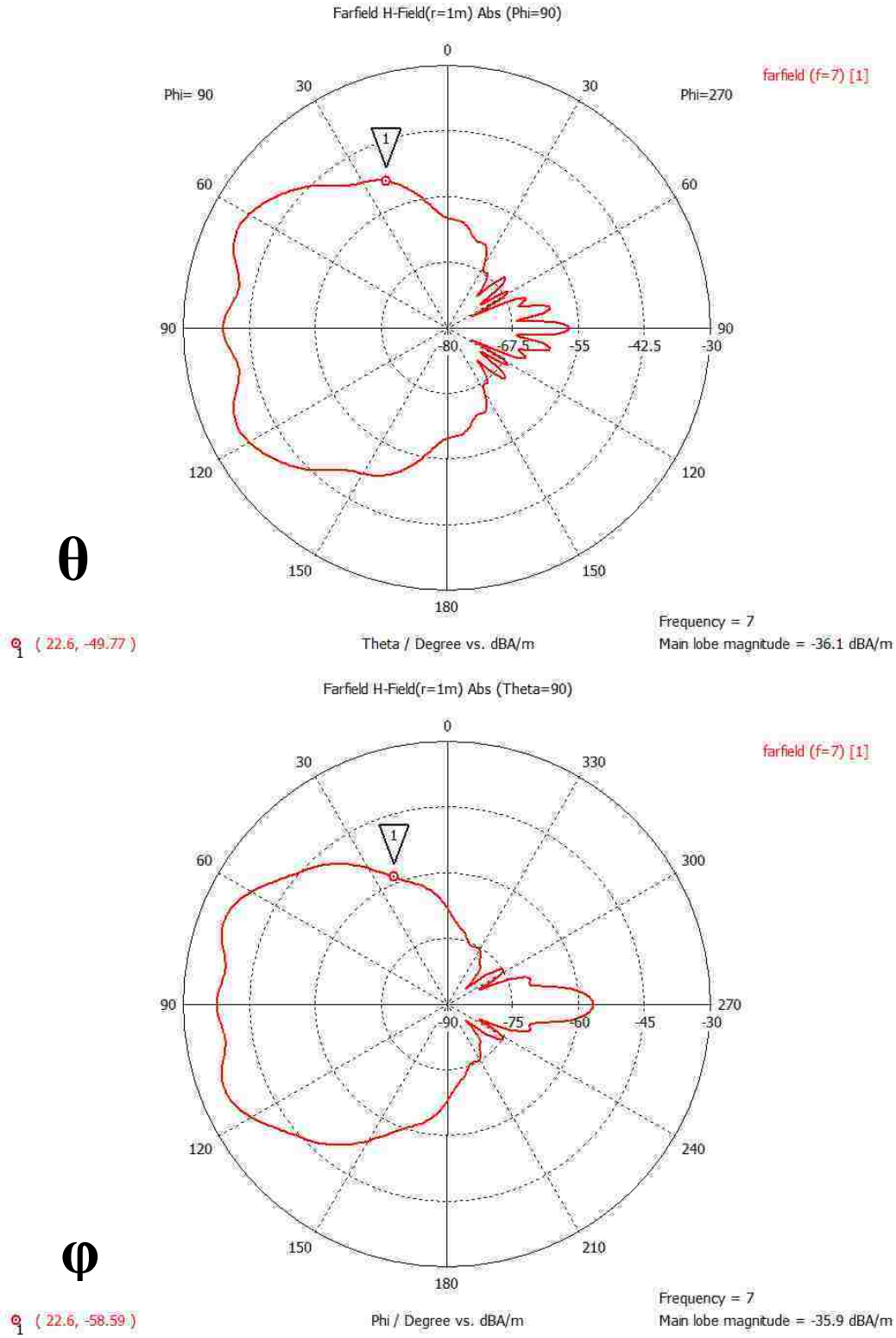

Figure 249: 7 GHz H-field patterns for theta and phi

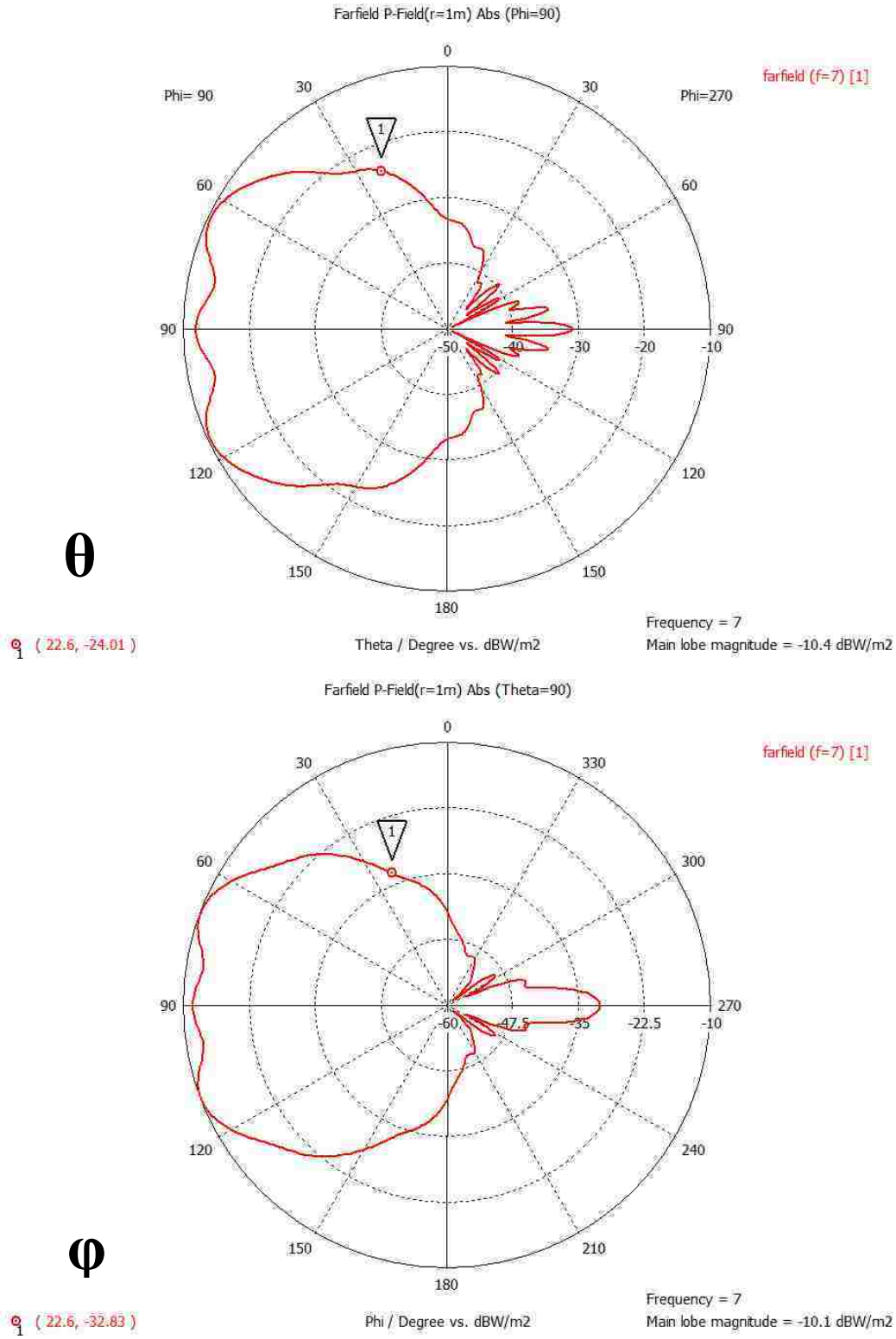

Figure 250: 7 GHz power patterns for theta and phi

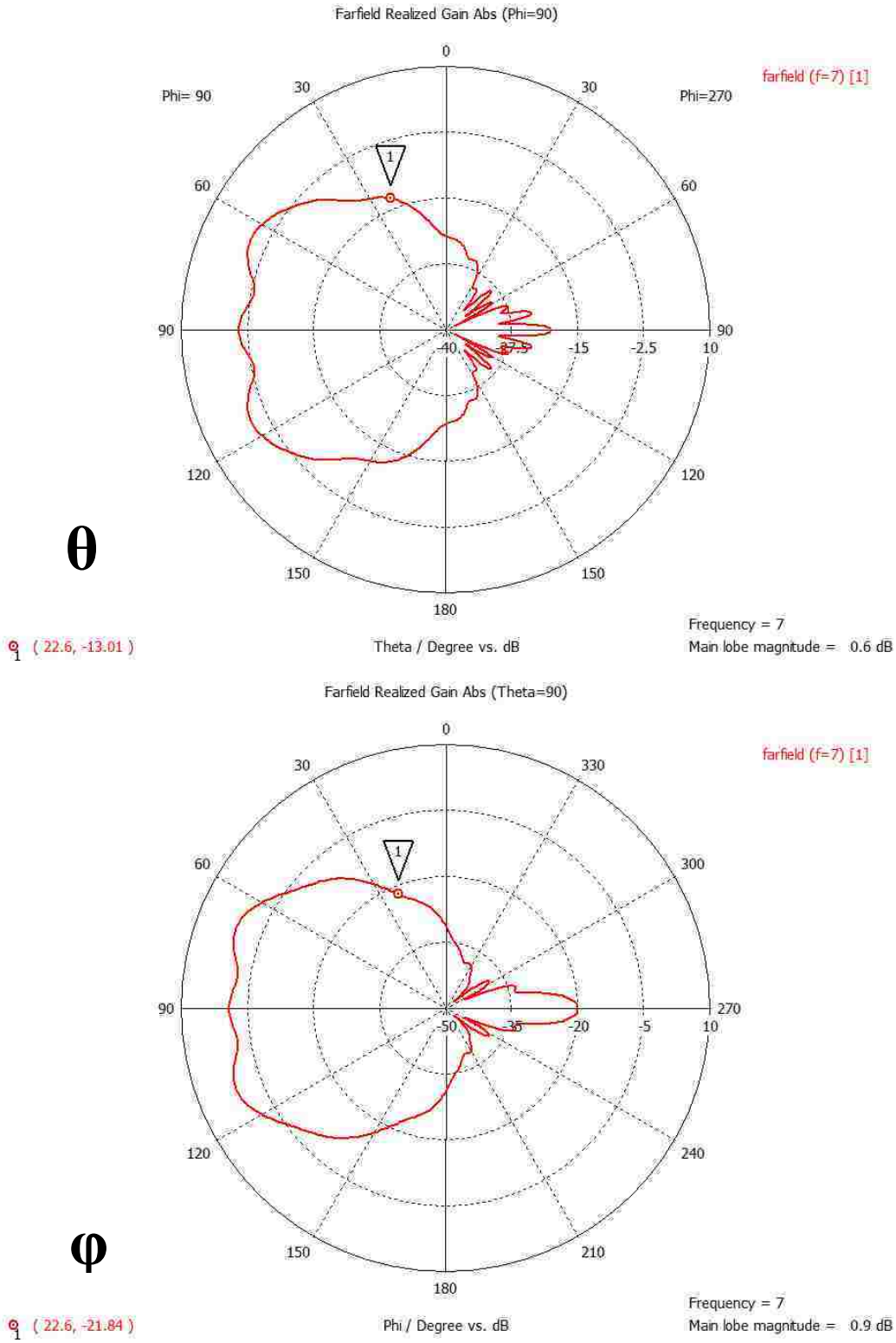

Figure 251: 7 GHz realized gain patterns for theta and phi

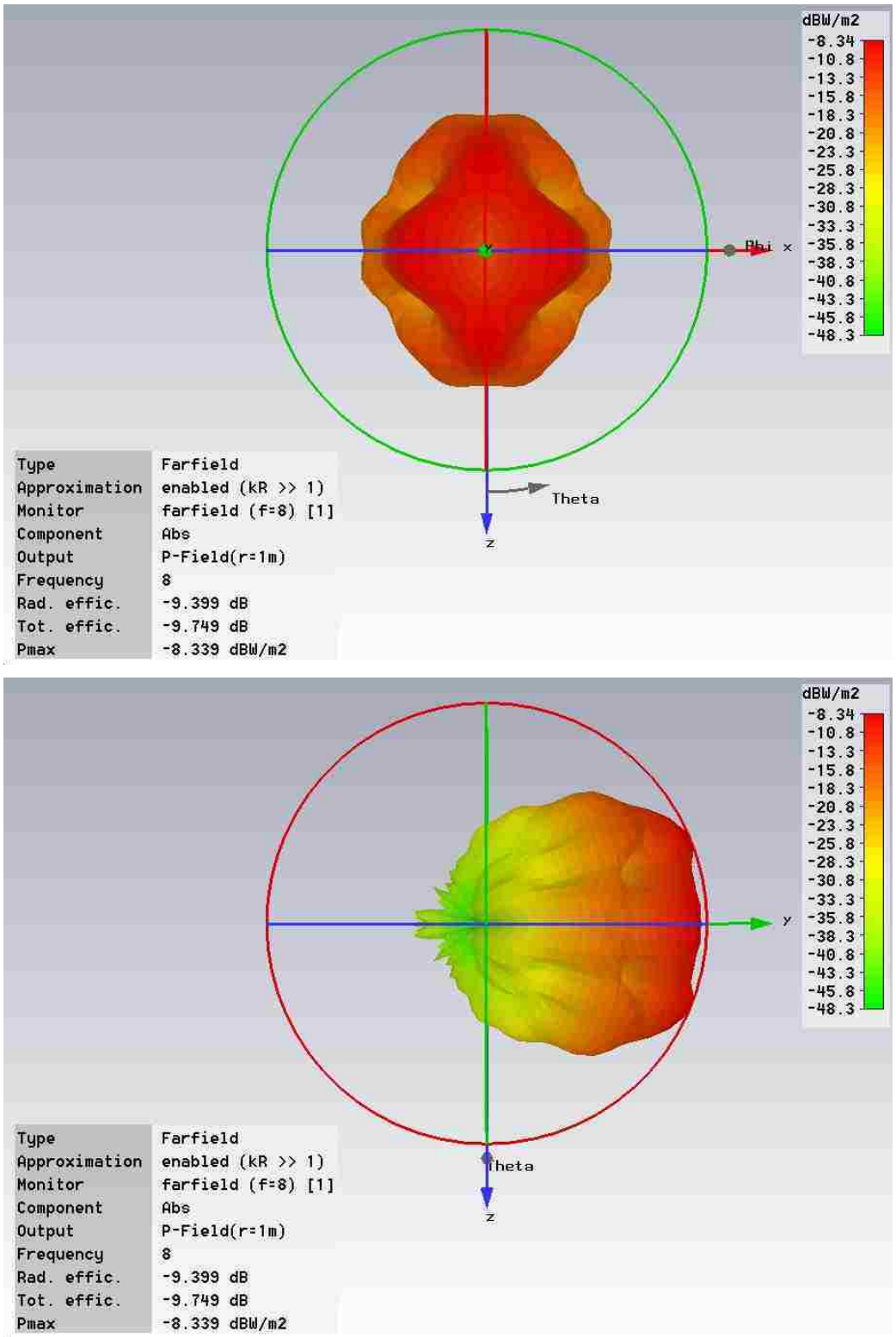

Figure 252: 8 GHz 3D power patterns

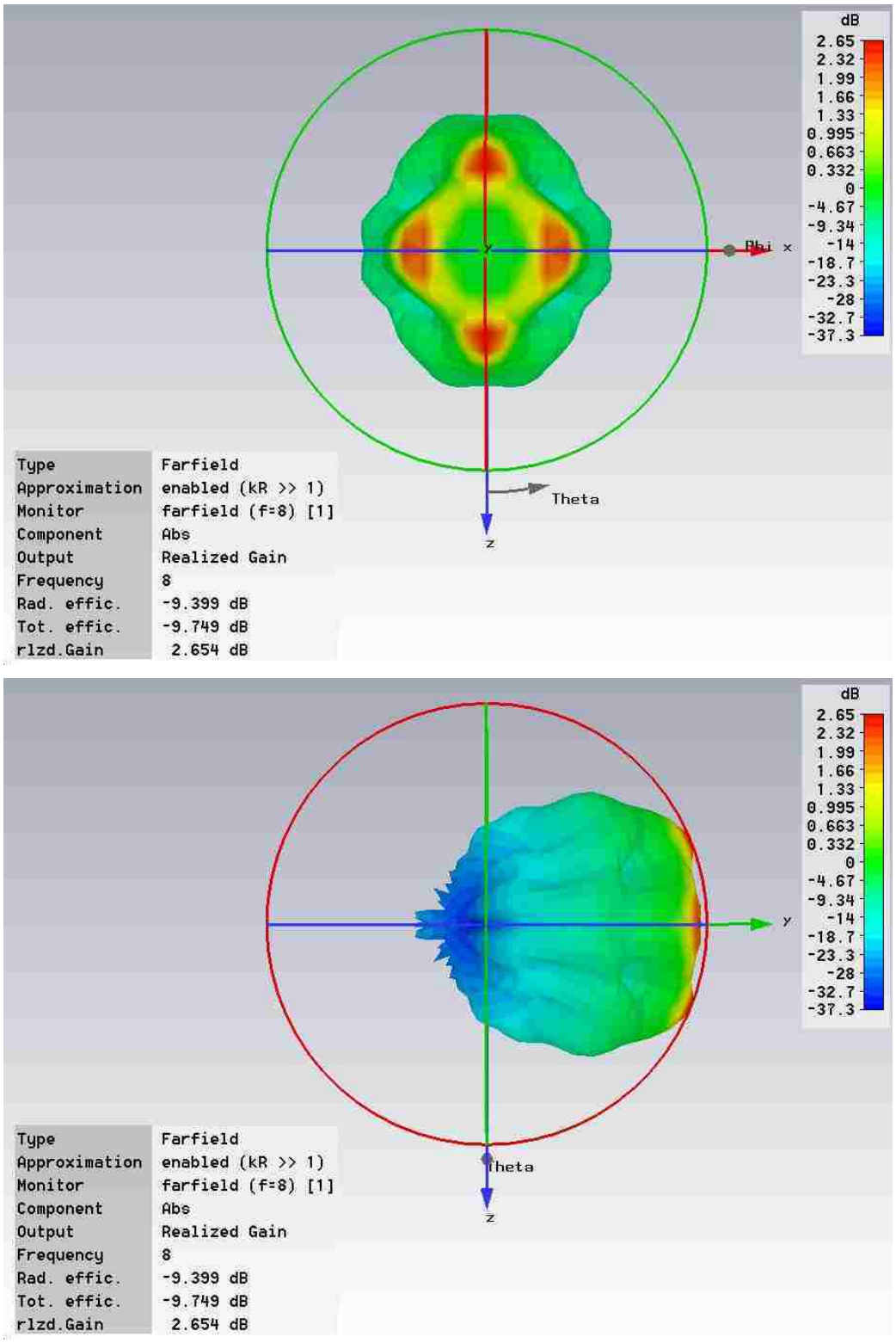

Figure 253: 8 GHz 3D realized gain patterns

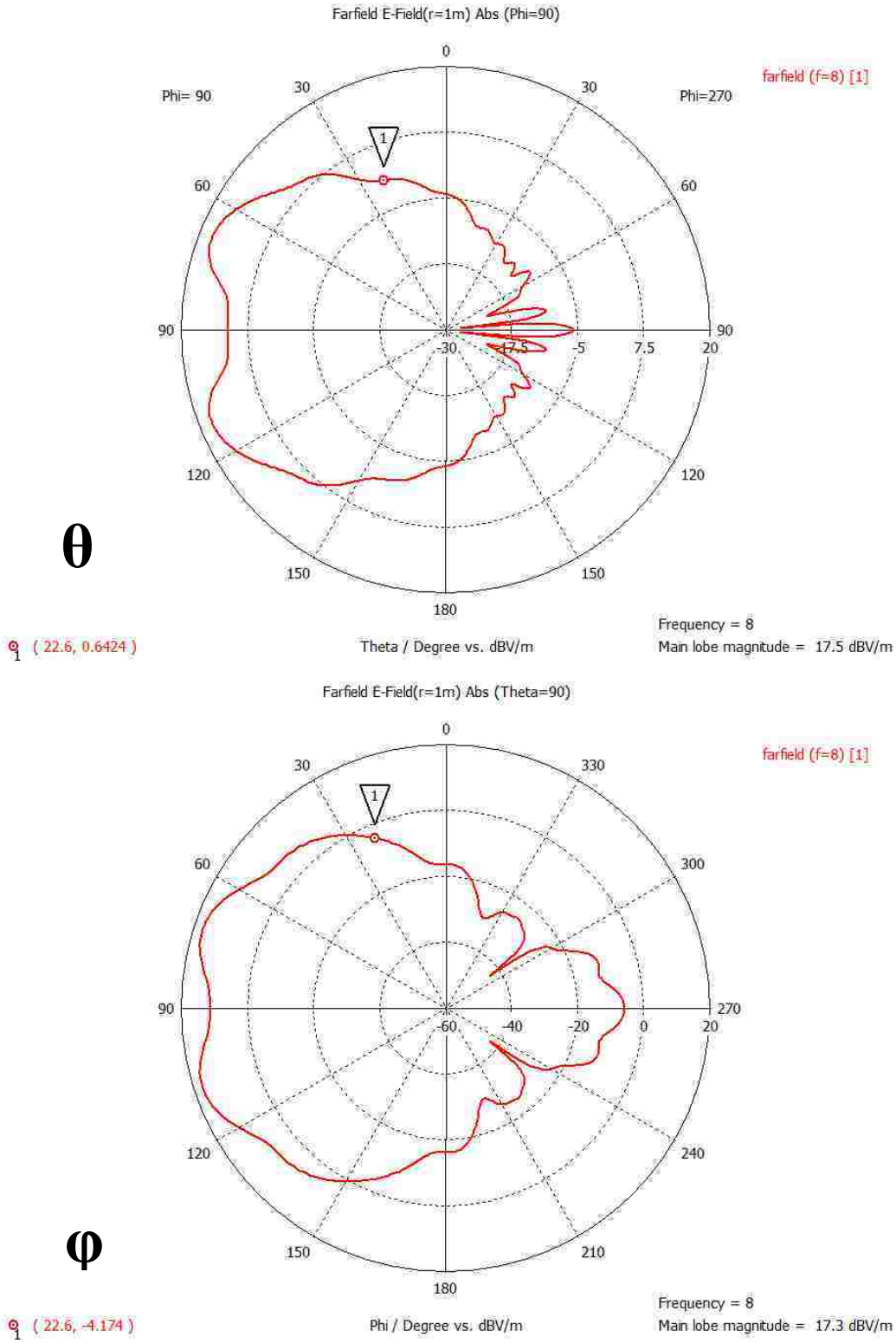

Figure 254: 8 GHz E-field patterns for theta and phi

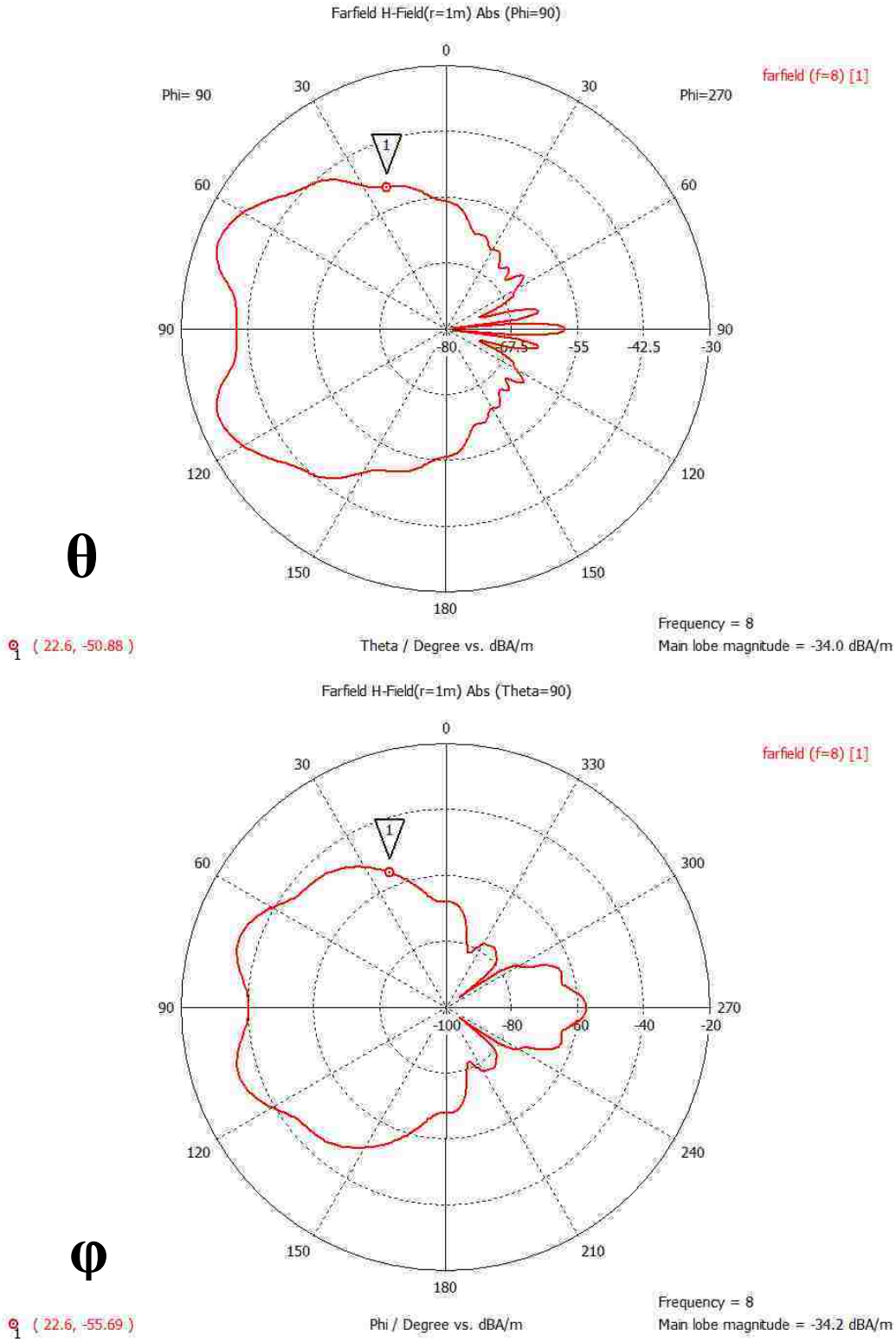

Figure 255: 8 GHz H-field patterns for theta and phi

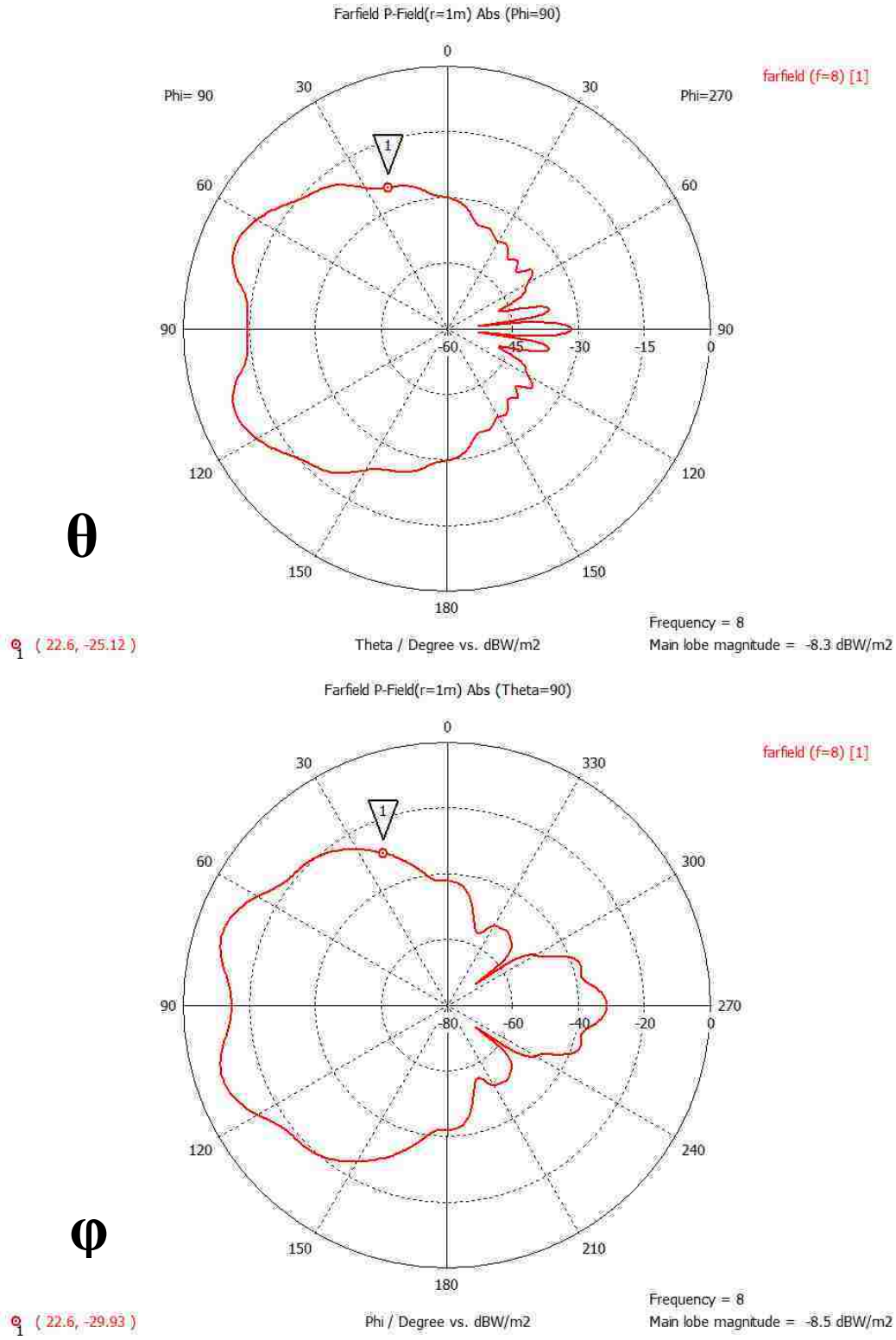

Figure 256: 8 GHz power patterns for theta and phi

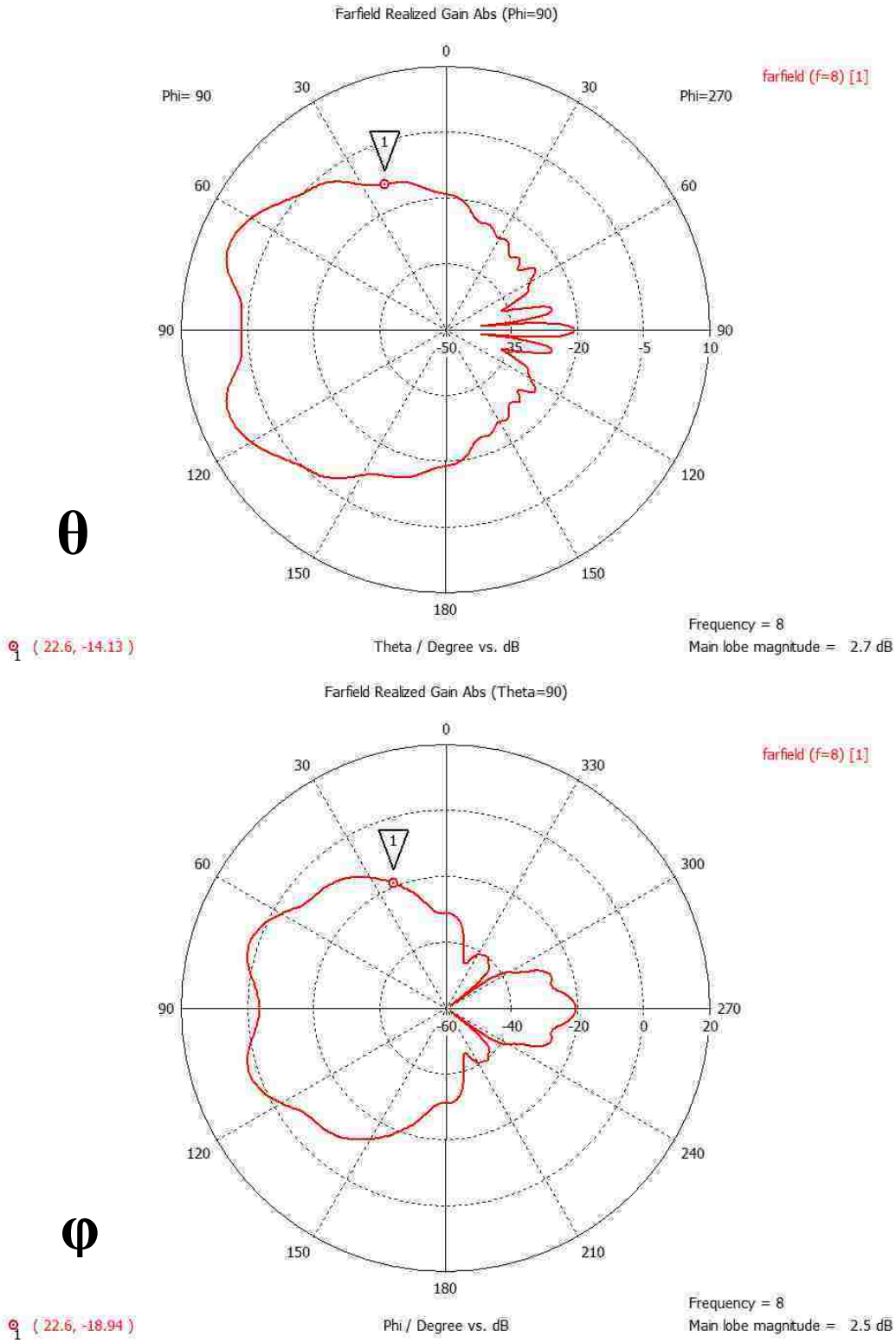

Figure 257: 8 GHz realized gain patterns for theta and phi

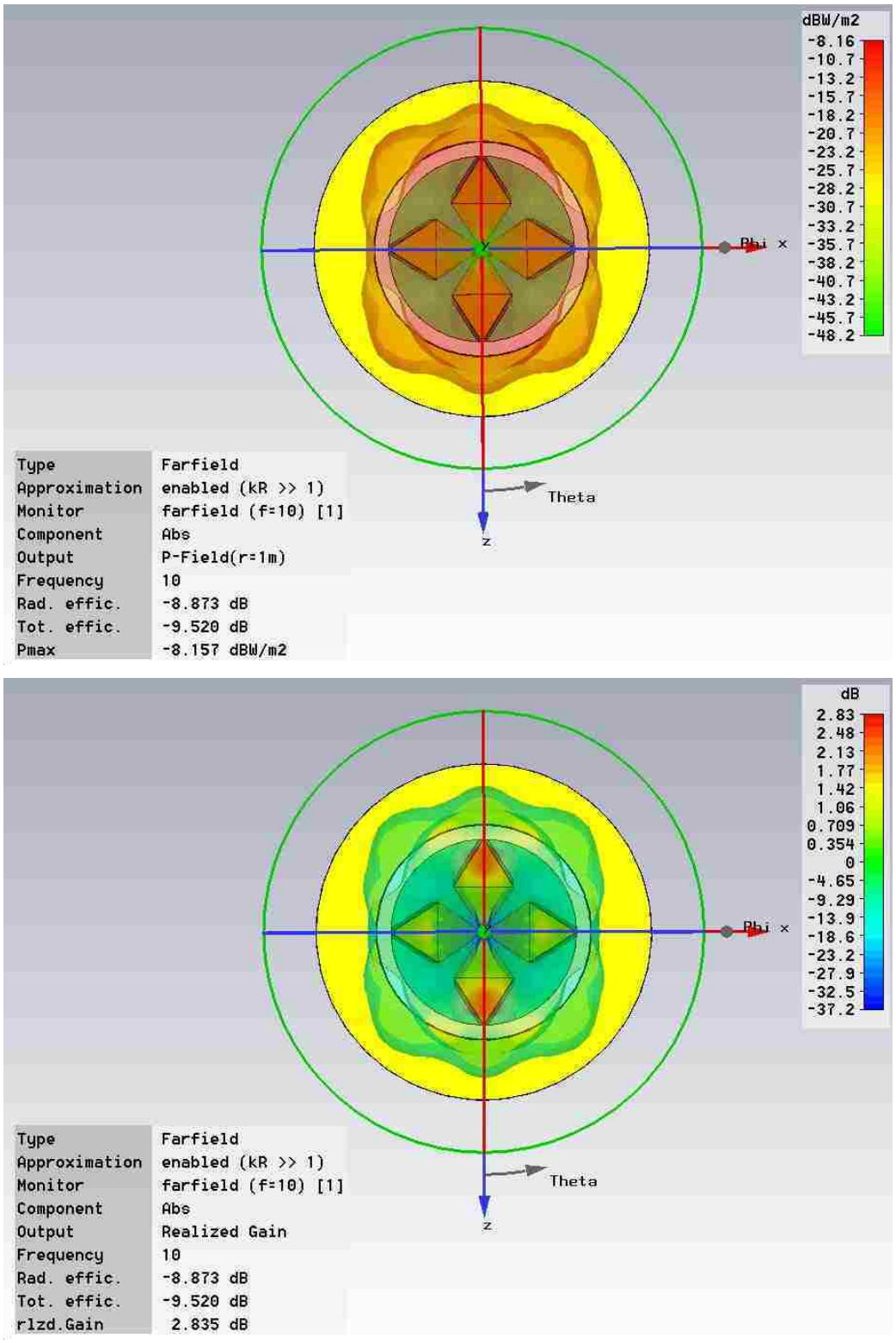

Figure 258: 10 GHz 3D power patterns

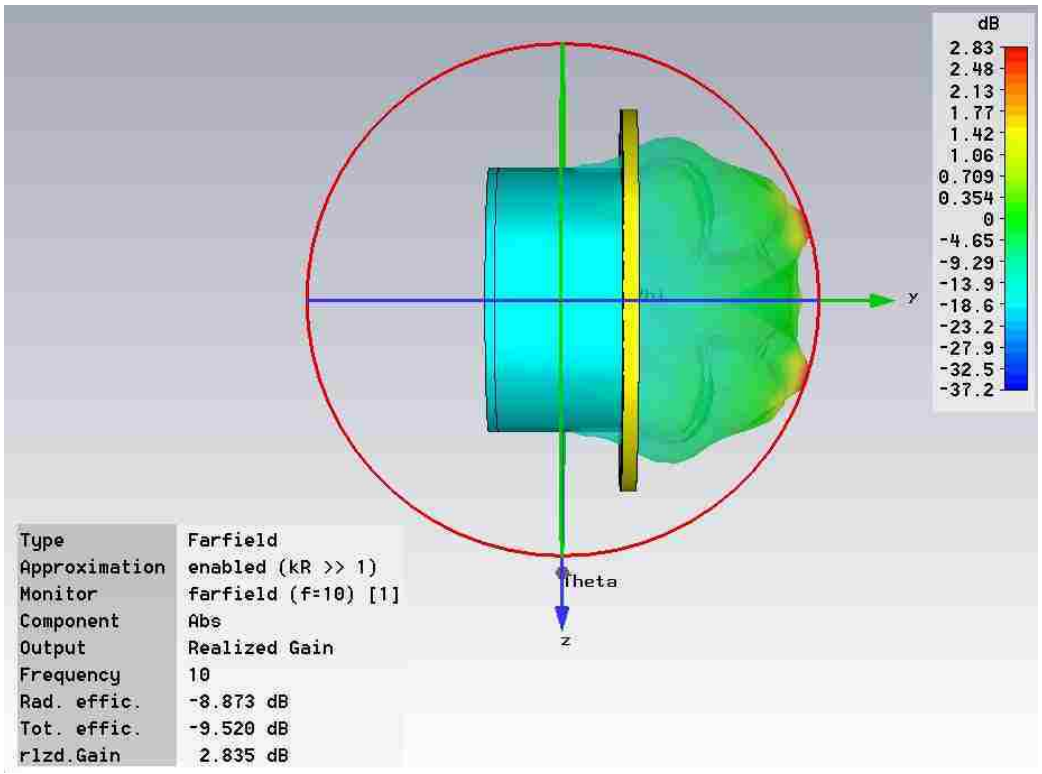

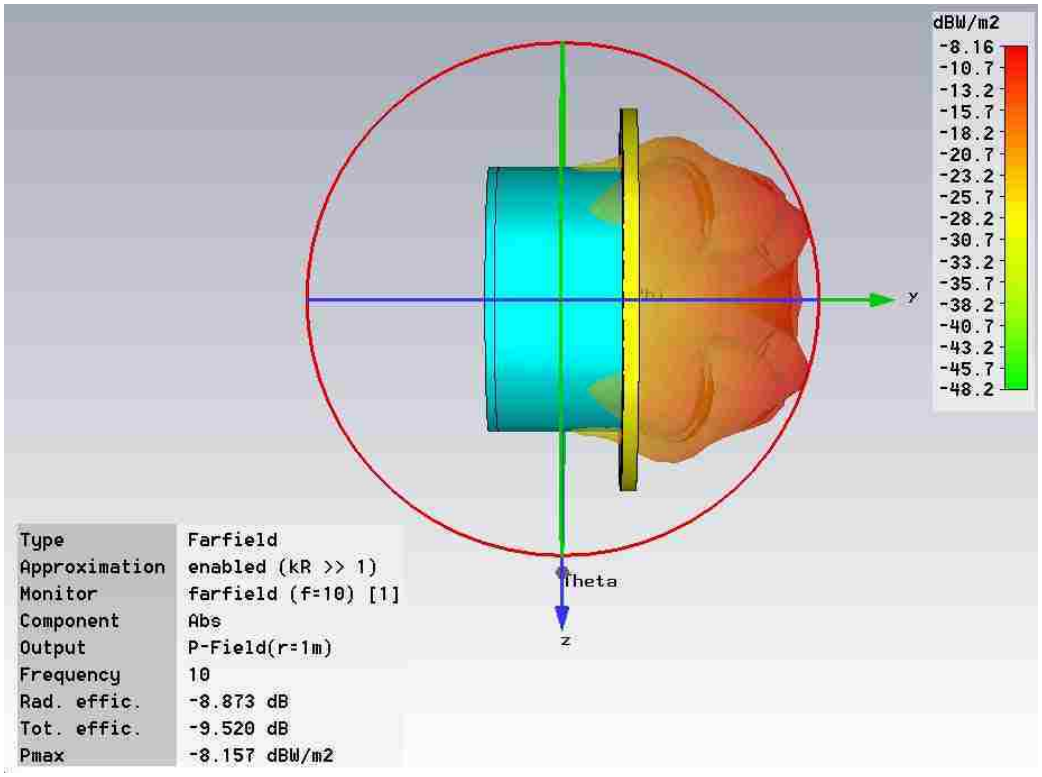

Figure 259: 10 GHz 3D realized gain patterns

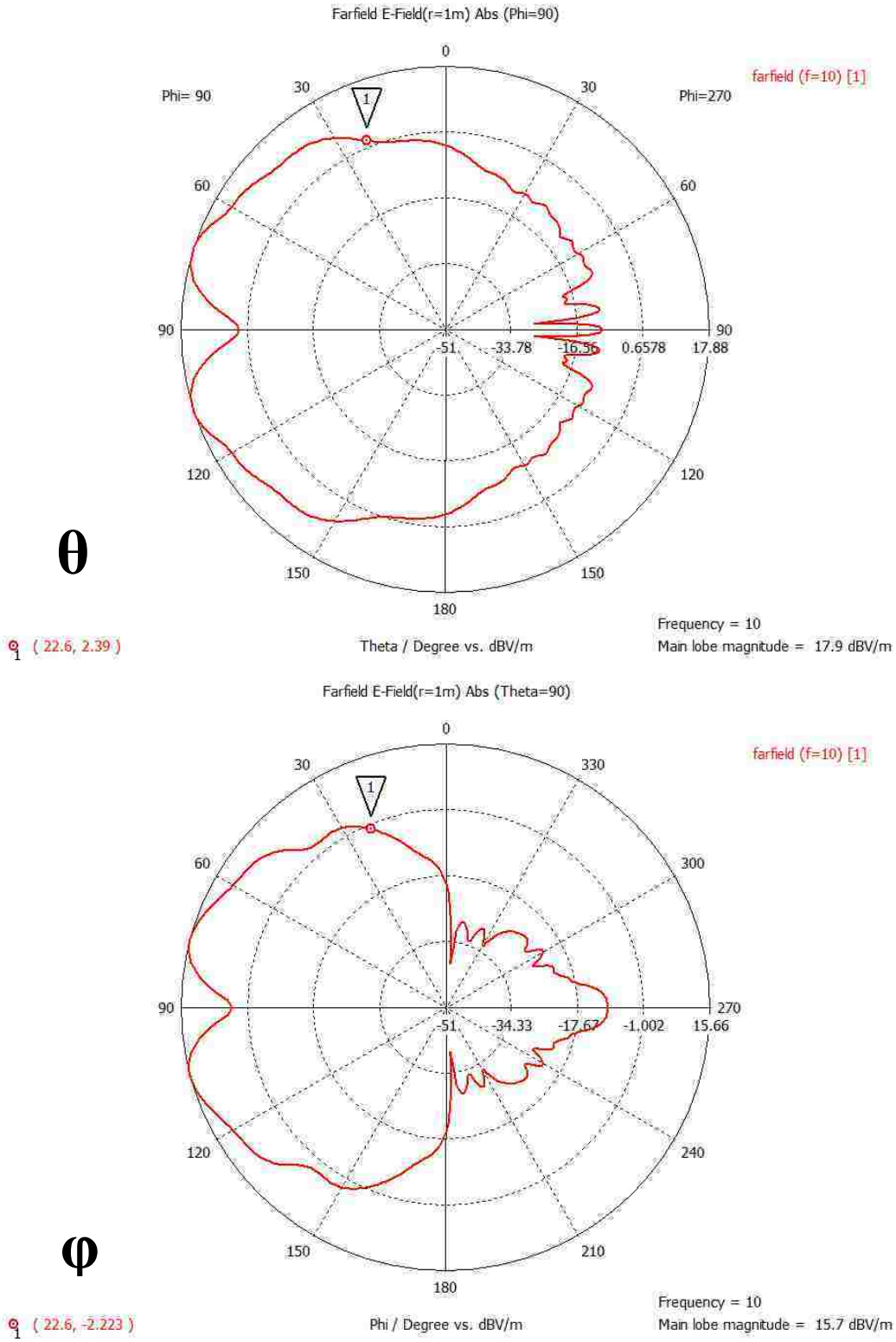

Figure 260: 10 GHz E-field patterns for theta and phi

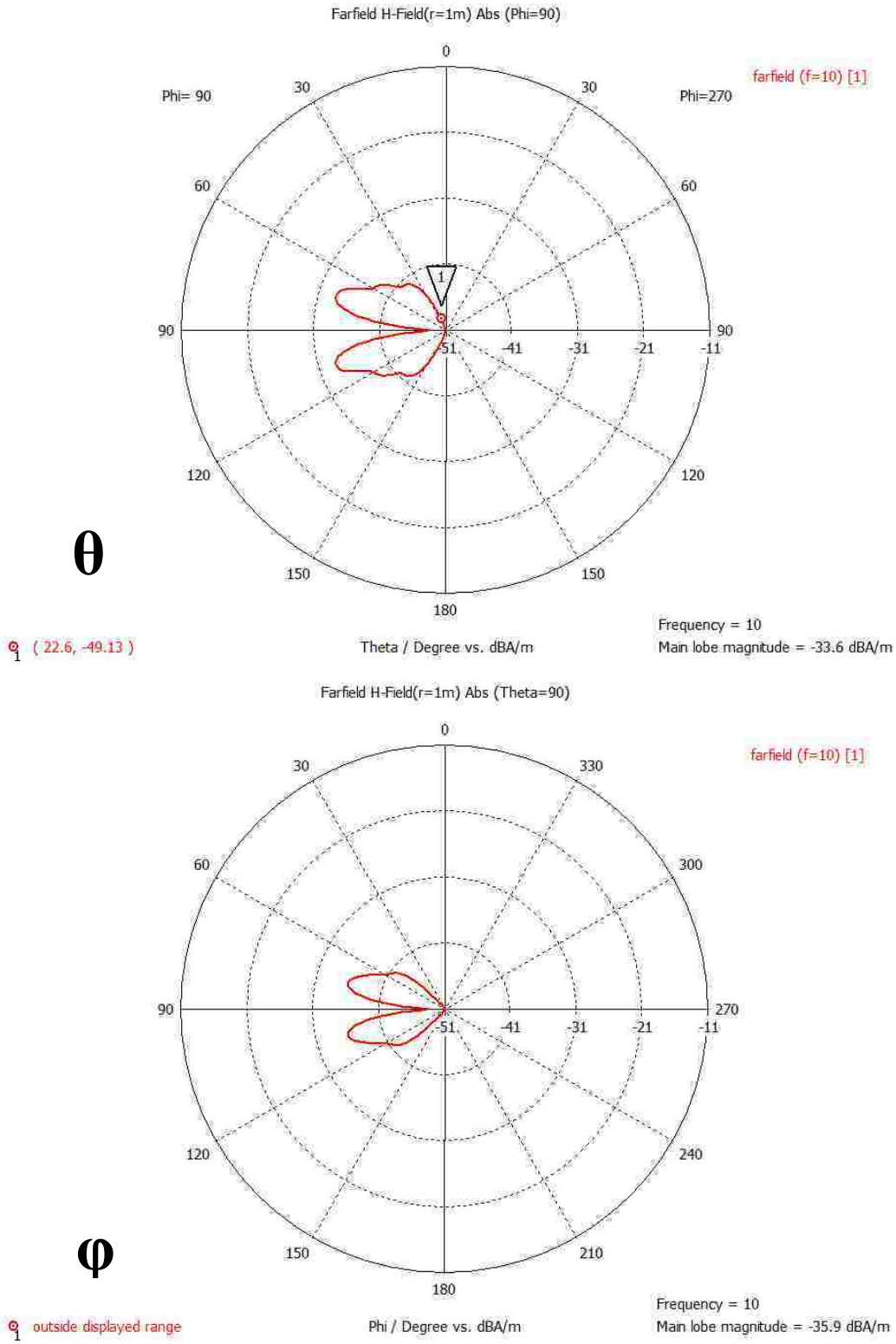

Figure 261: 10 GHz H-field patterns for theta and phi

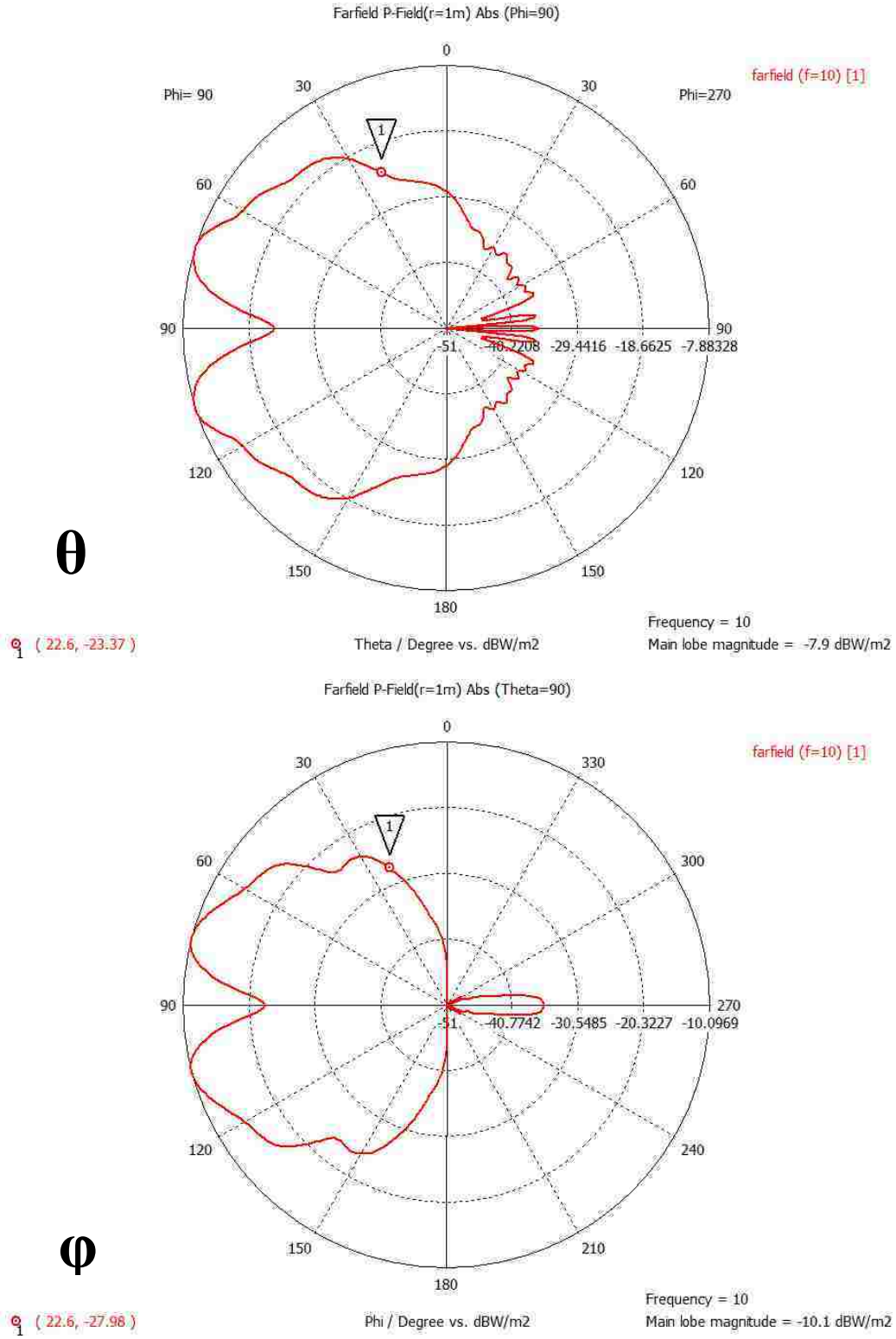

Figure 262: 10 GHz power patterns for theta and phi

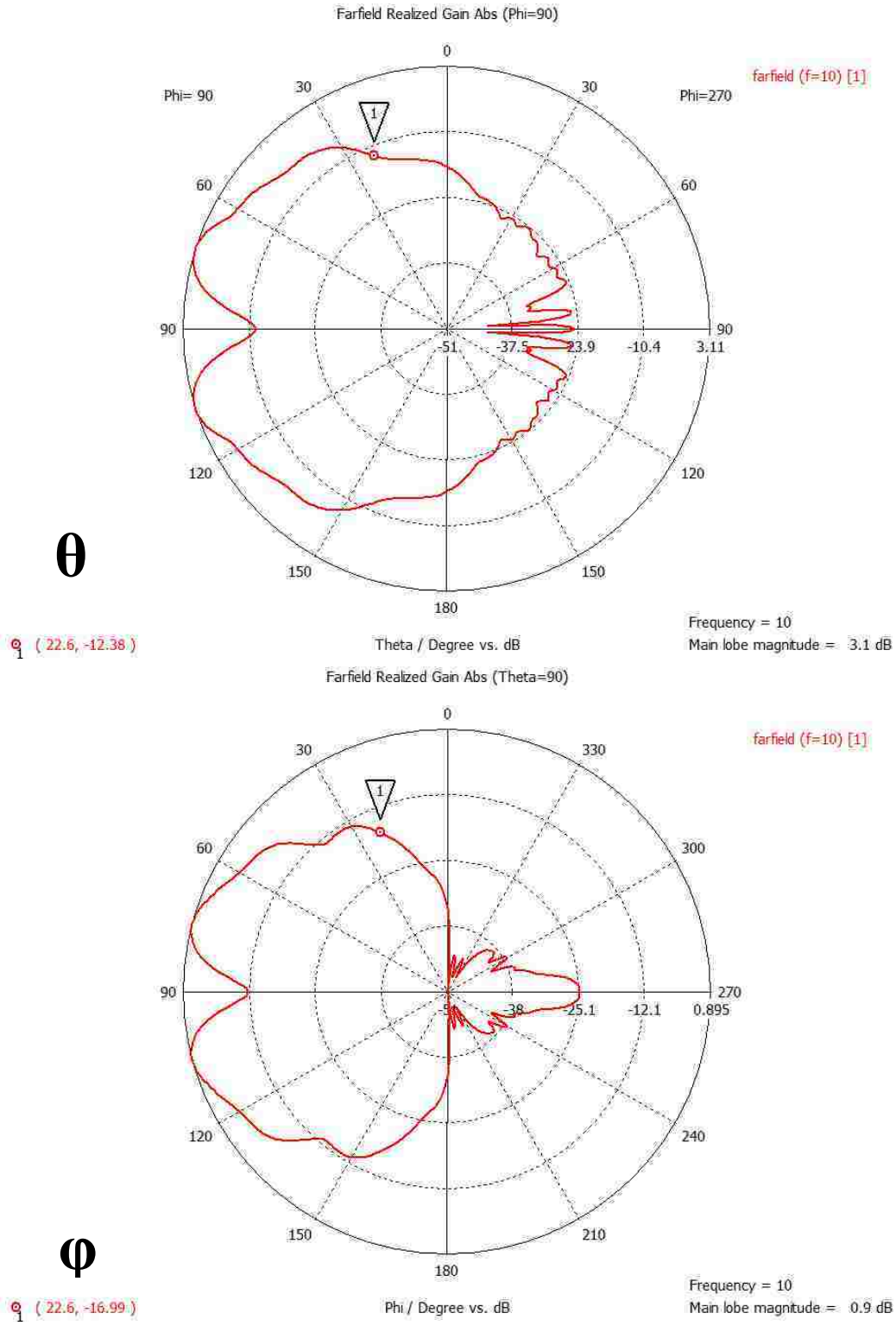

Figure 263: 10 GHz realized gain patterns for theta and phi

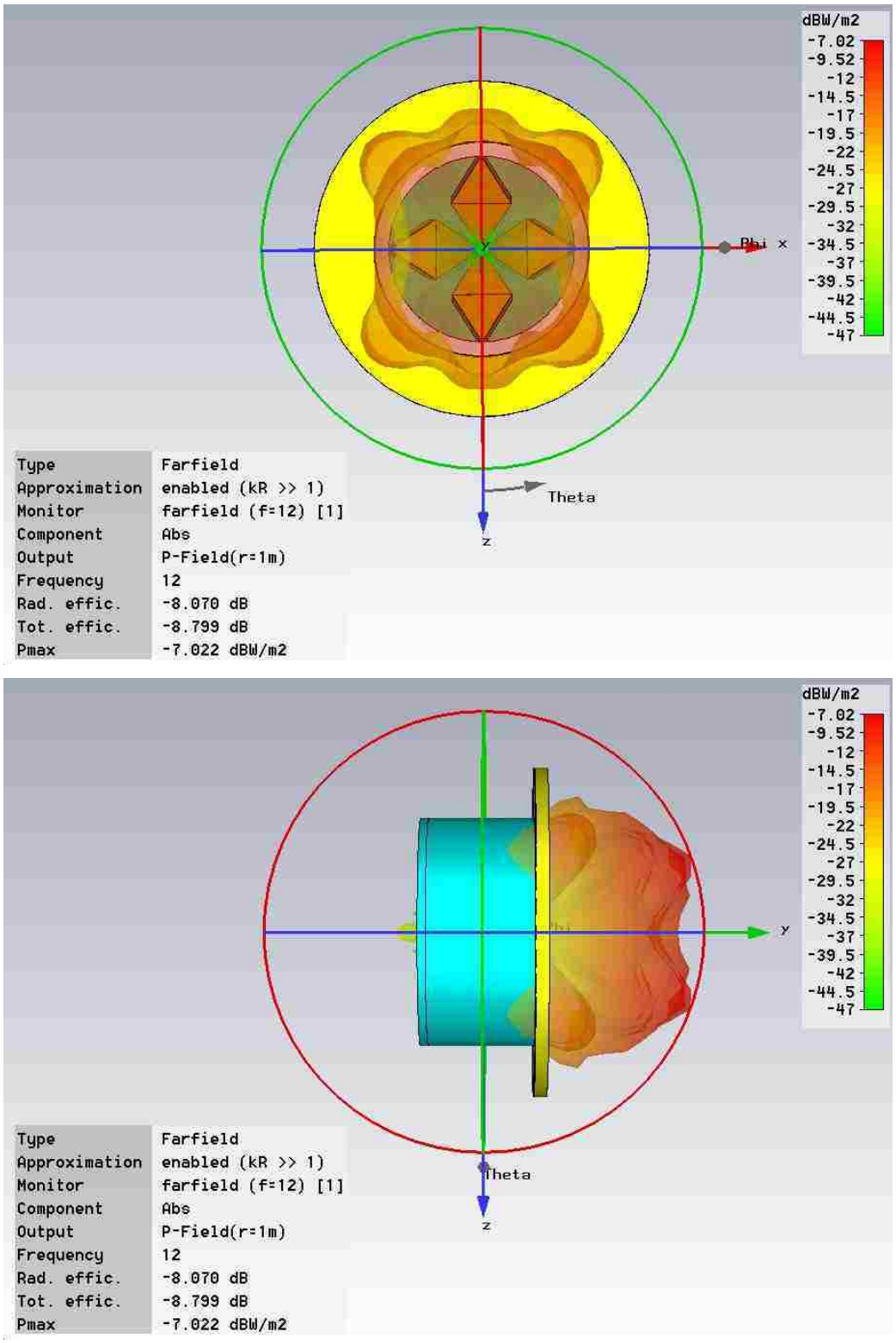

Figure 264: 12 GHz 3D power patterns

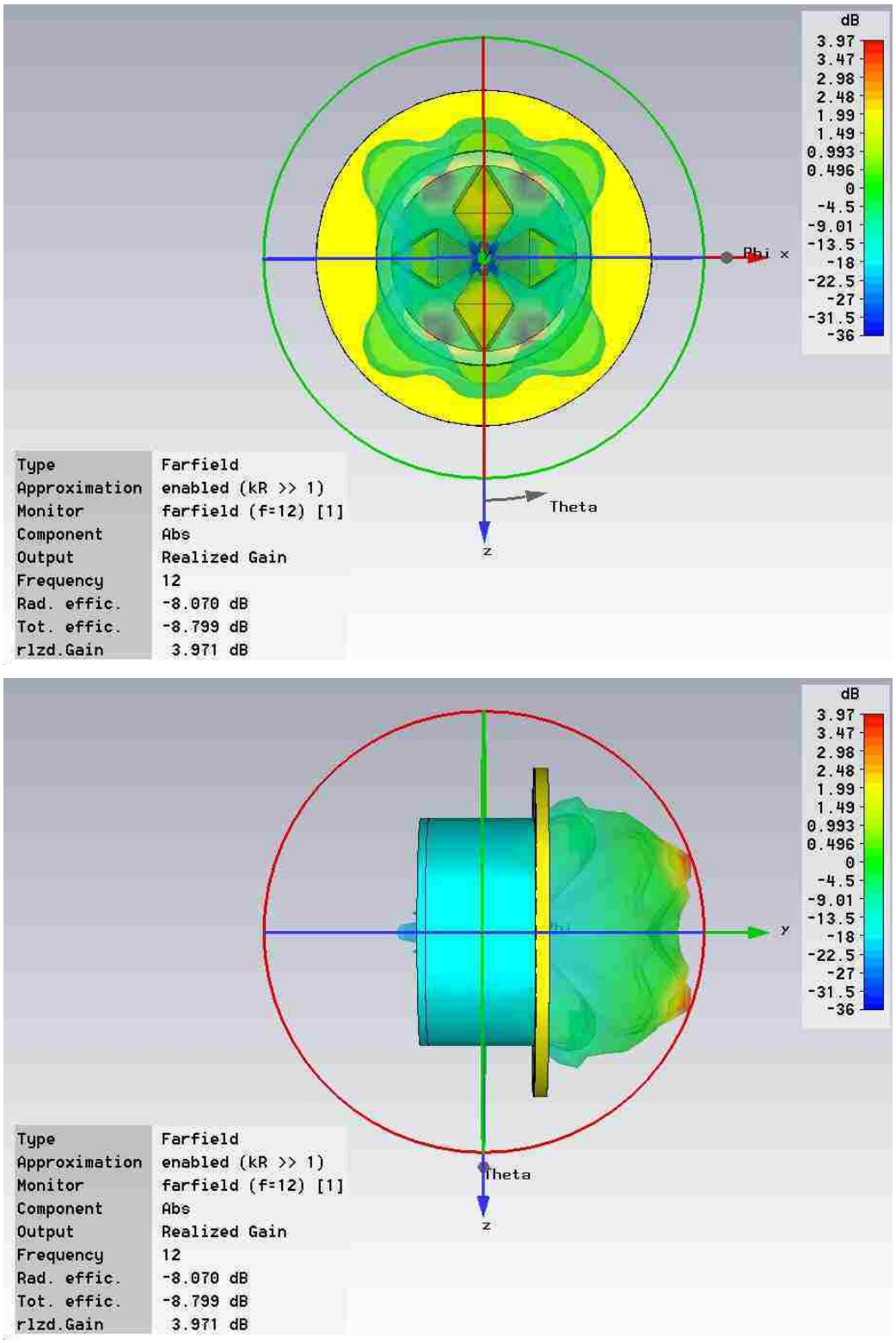

Figure 265: 12 GHz 3D realized gain patterns

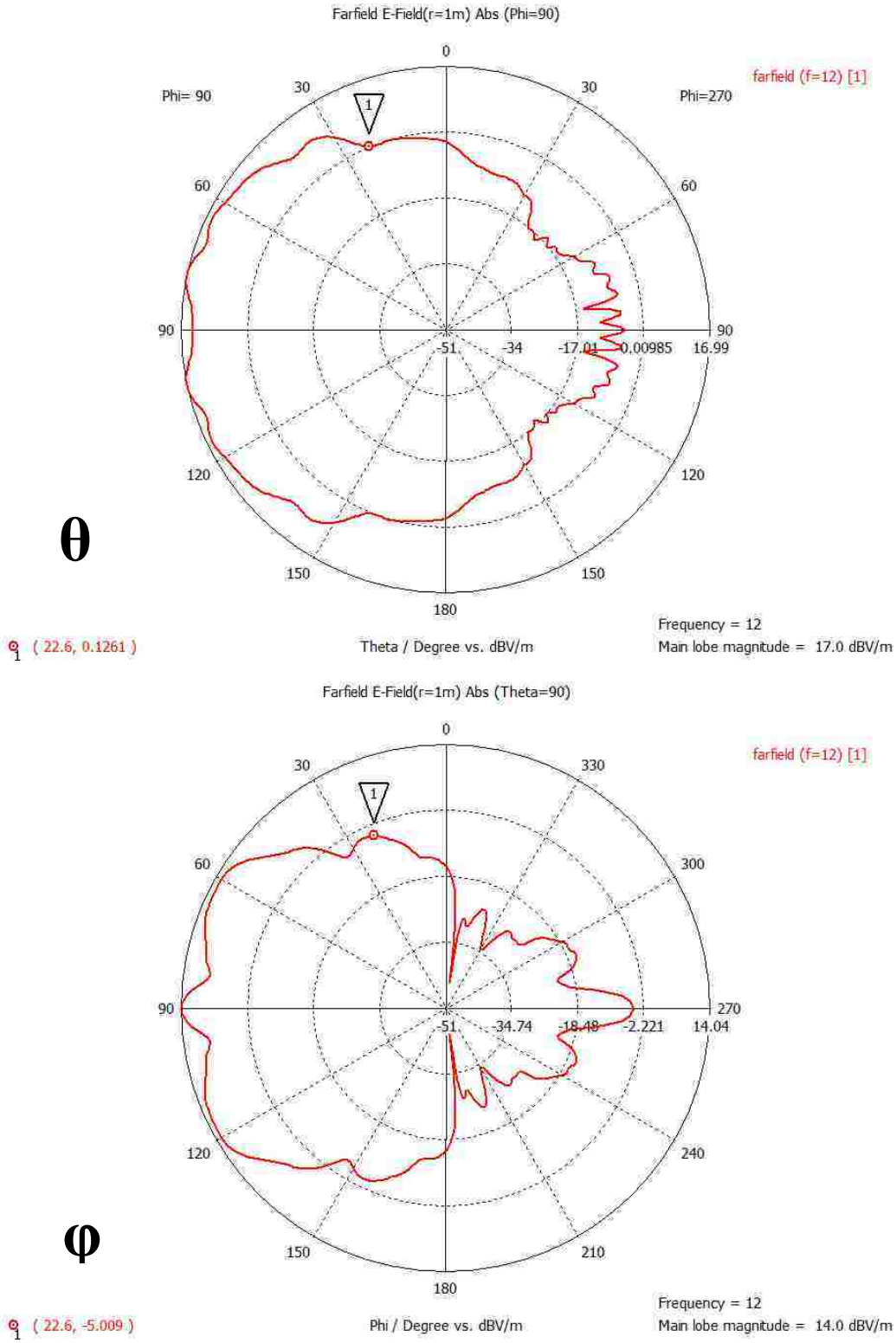

Figure 266: 12 GHz E-field patterns for theta and phi

θ

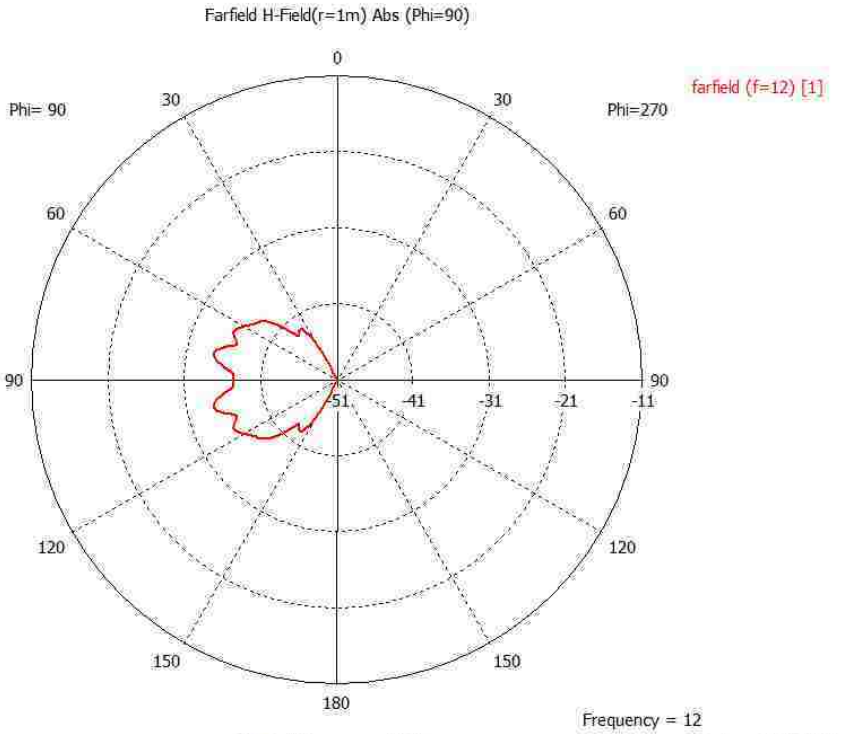

φ

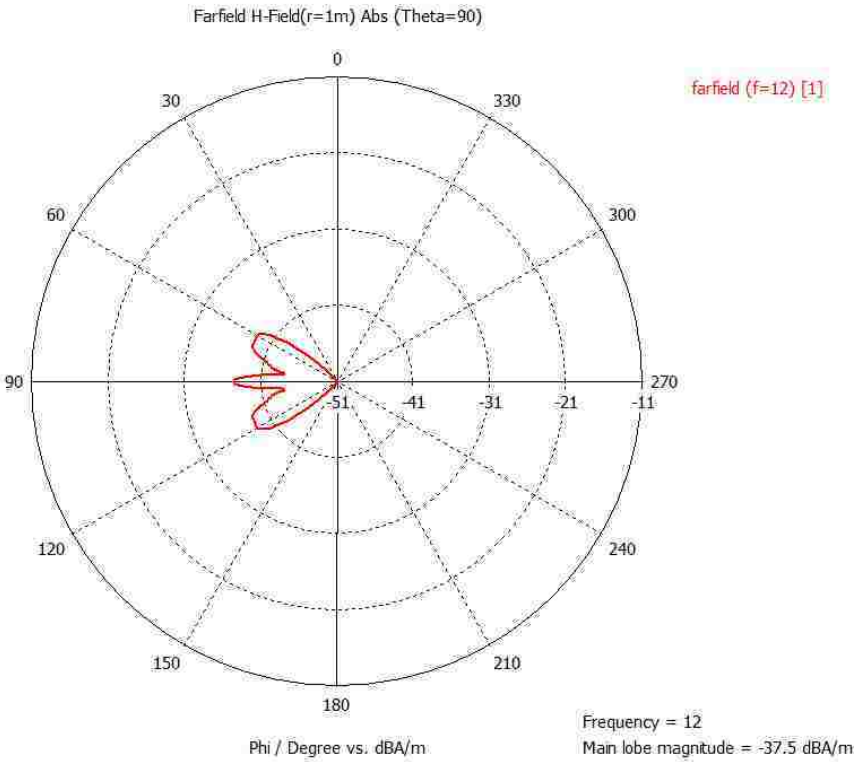

Figure 267: 12 GHz H-field patterns for theta and phi

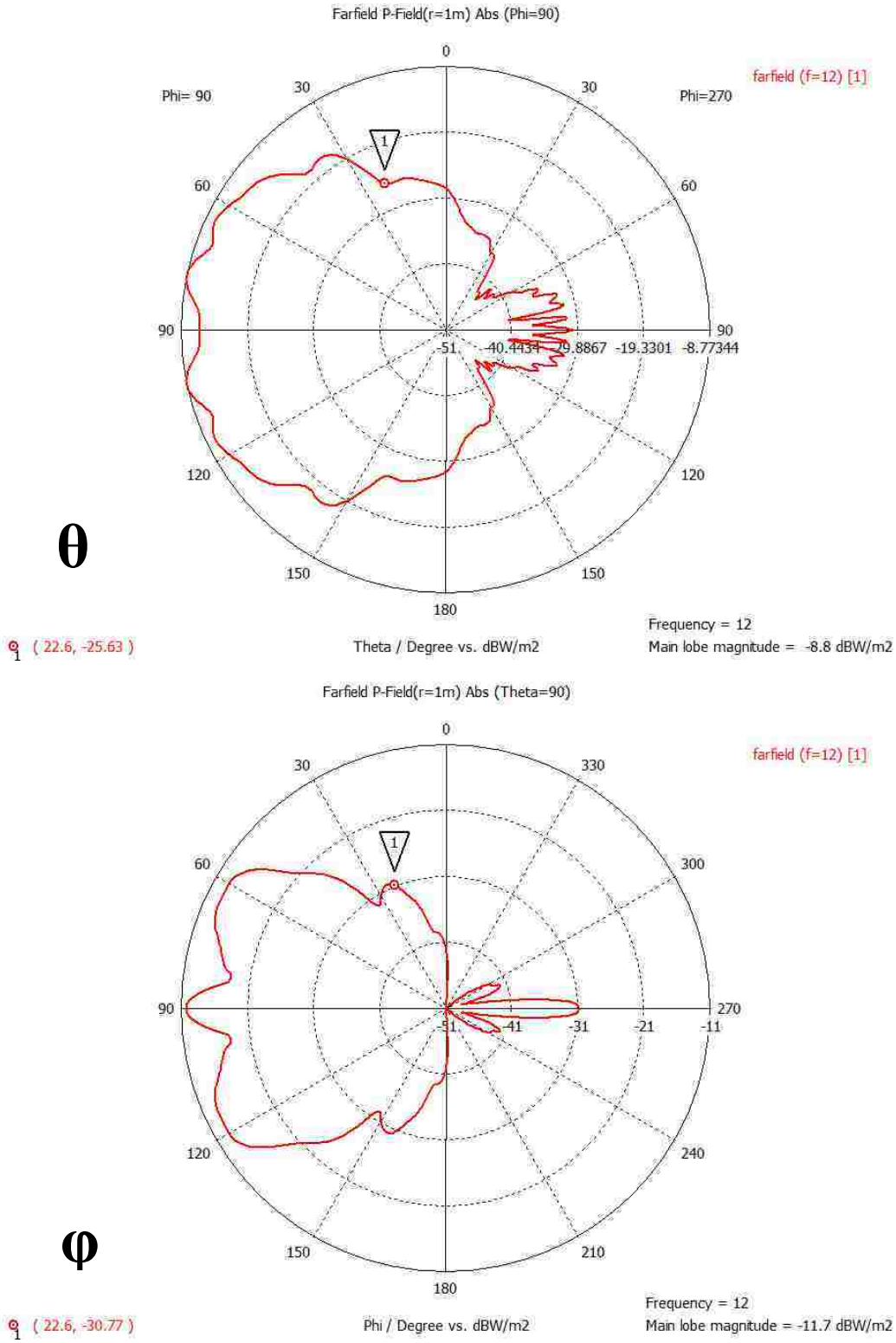

Figure 268: 12 GHz power patterns for theta and phi

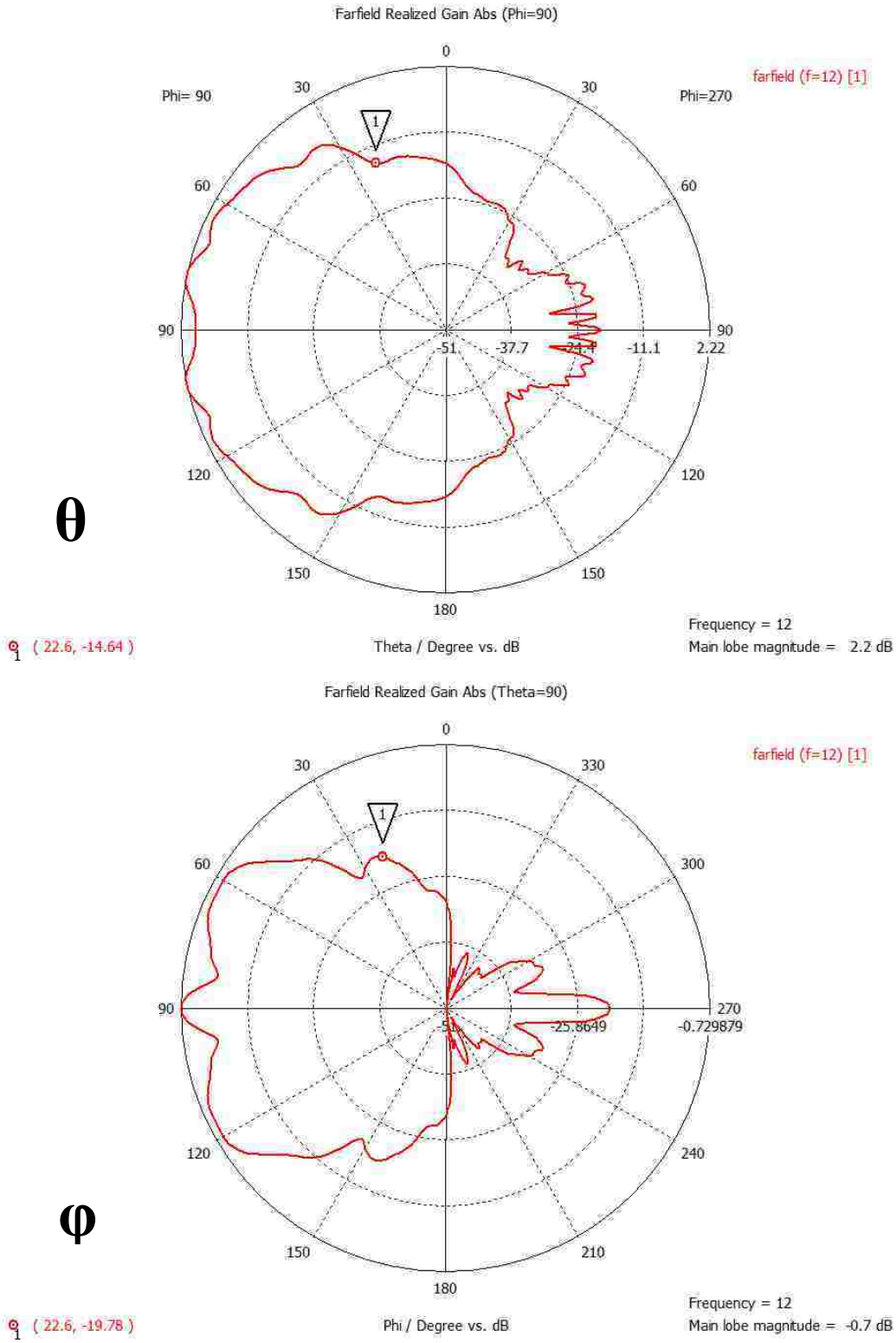

Figure 269: 12 GHz realized gain patterns for theta and phi

Appendix G: Diamond Feed Build Dimensions

This appendix contains detailed physical drawings with dimensions of the diamond feed. These drawings were provided to Electrodynamic Co. of Albuquerque, NM, for fabrication of the feed. Electrodynamic possessed the CNC machines and precision fabrication tools and techniques necessary to construct this feed.

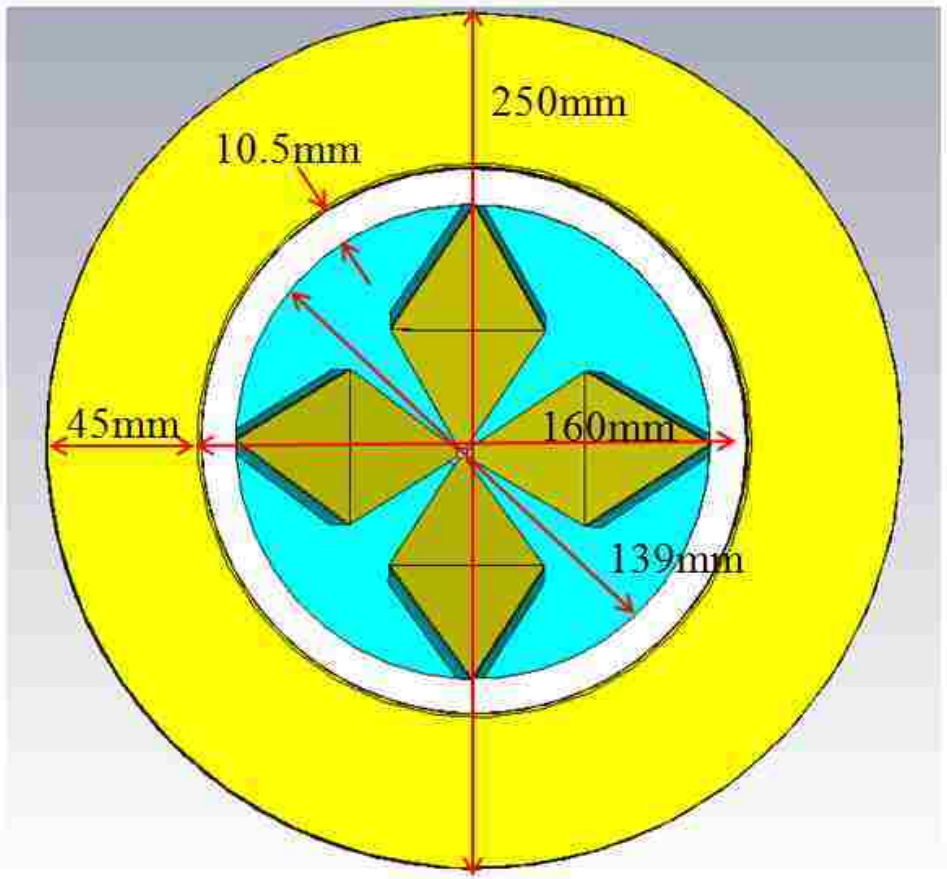

Figure 270: Front view of diamond feed

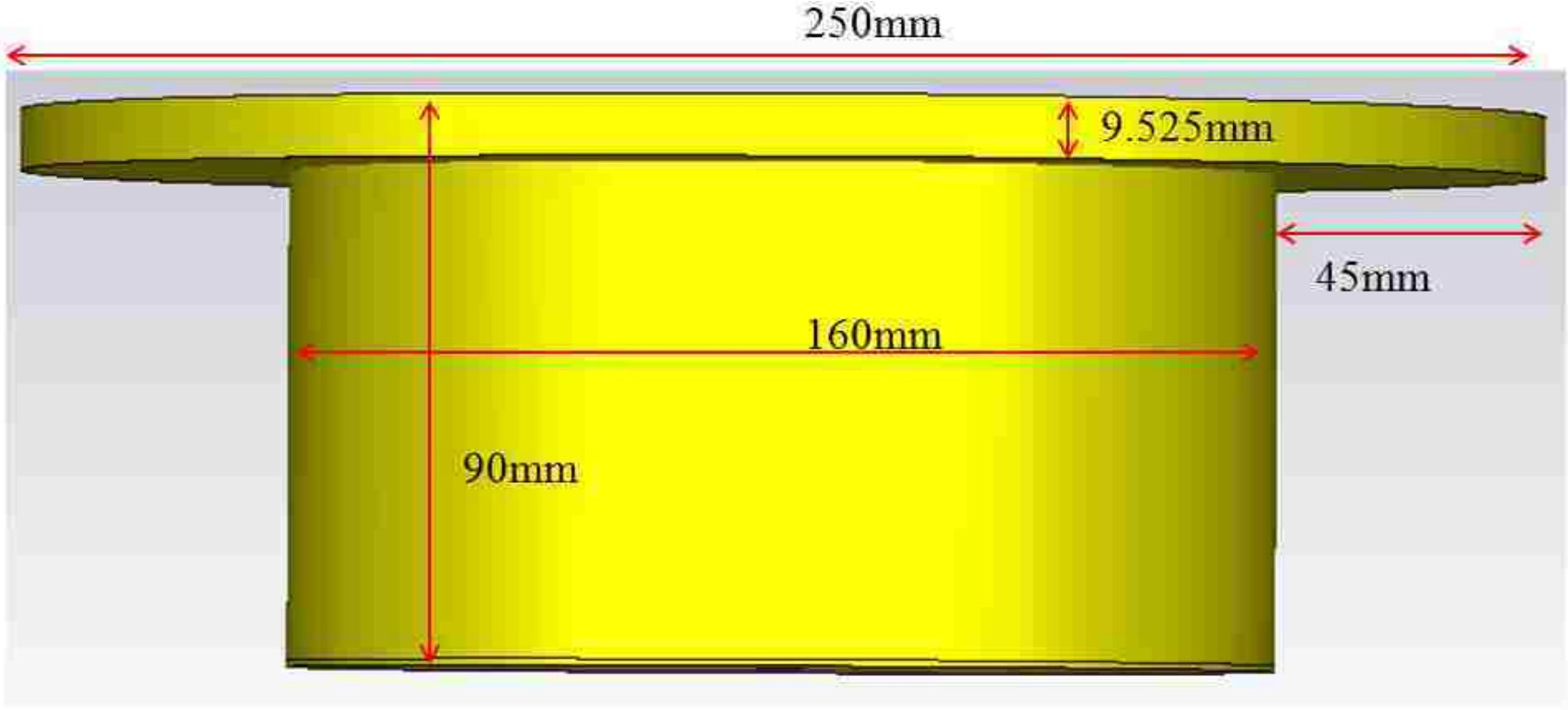

Figure 271: Side view of diamond feed

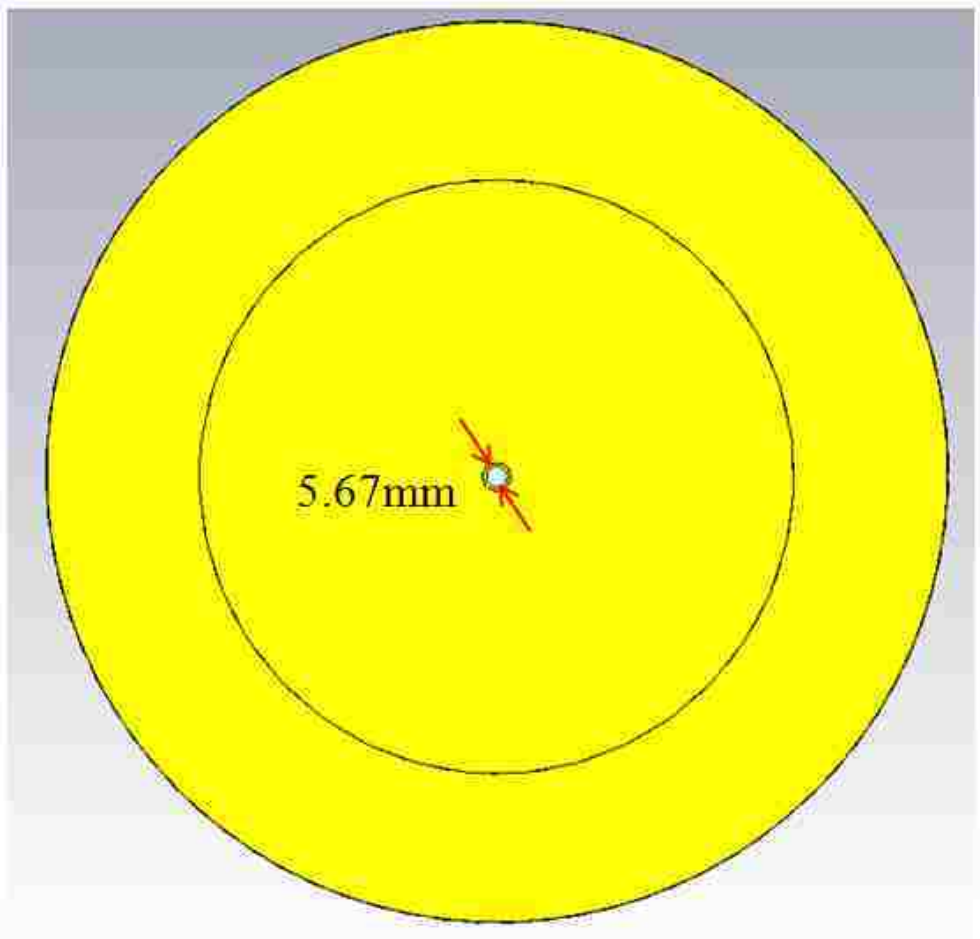

Figure 272: Rear view of diamond feed

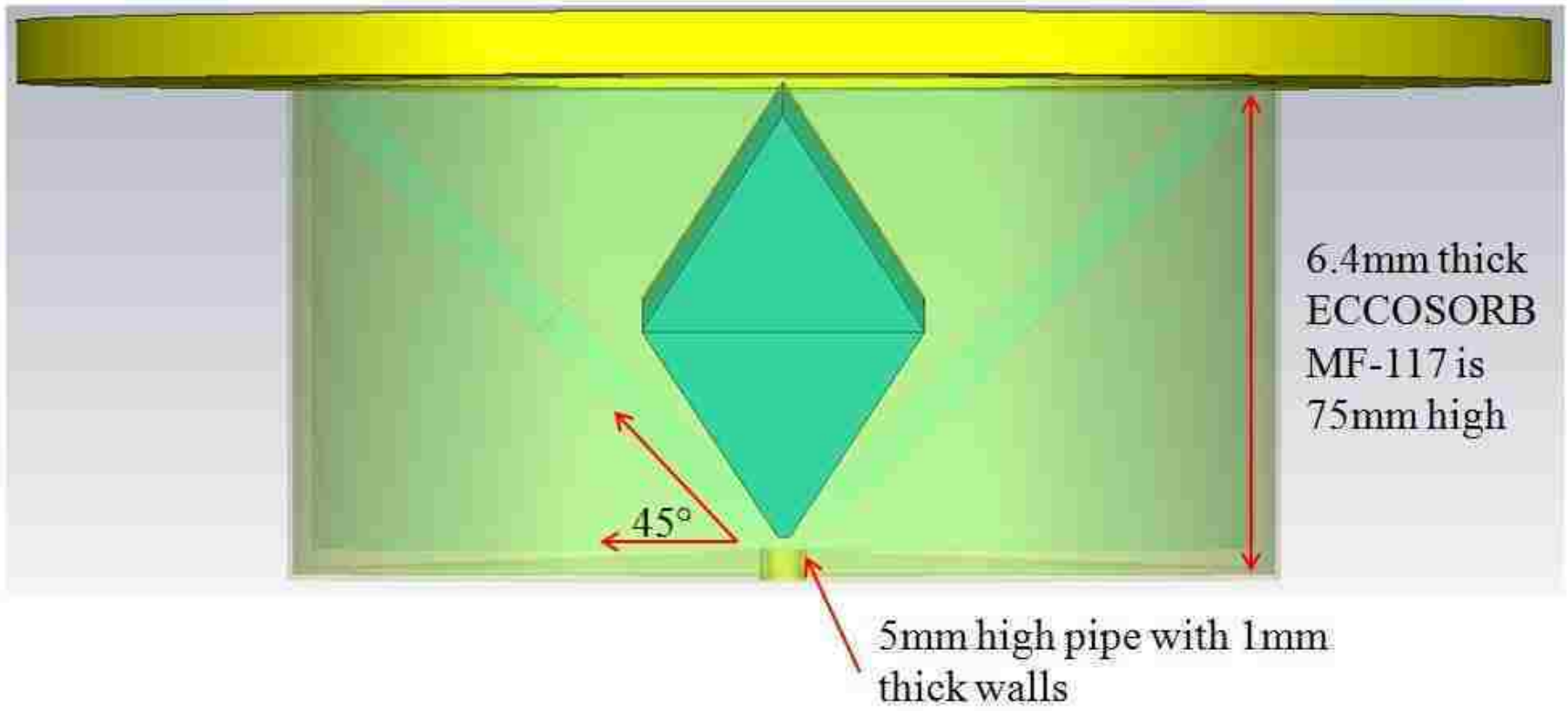

Figure 273: Side view with detail

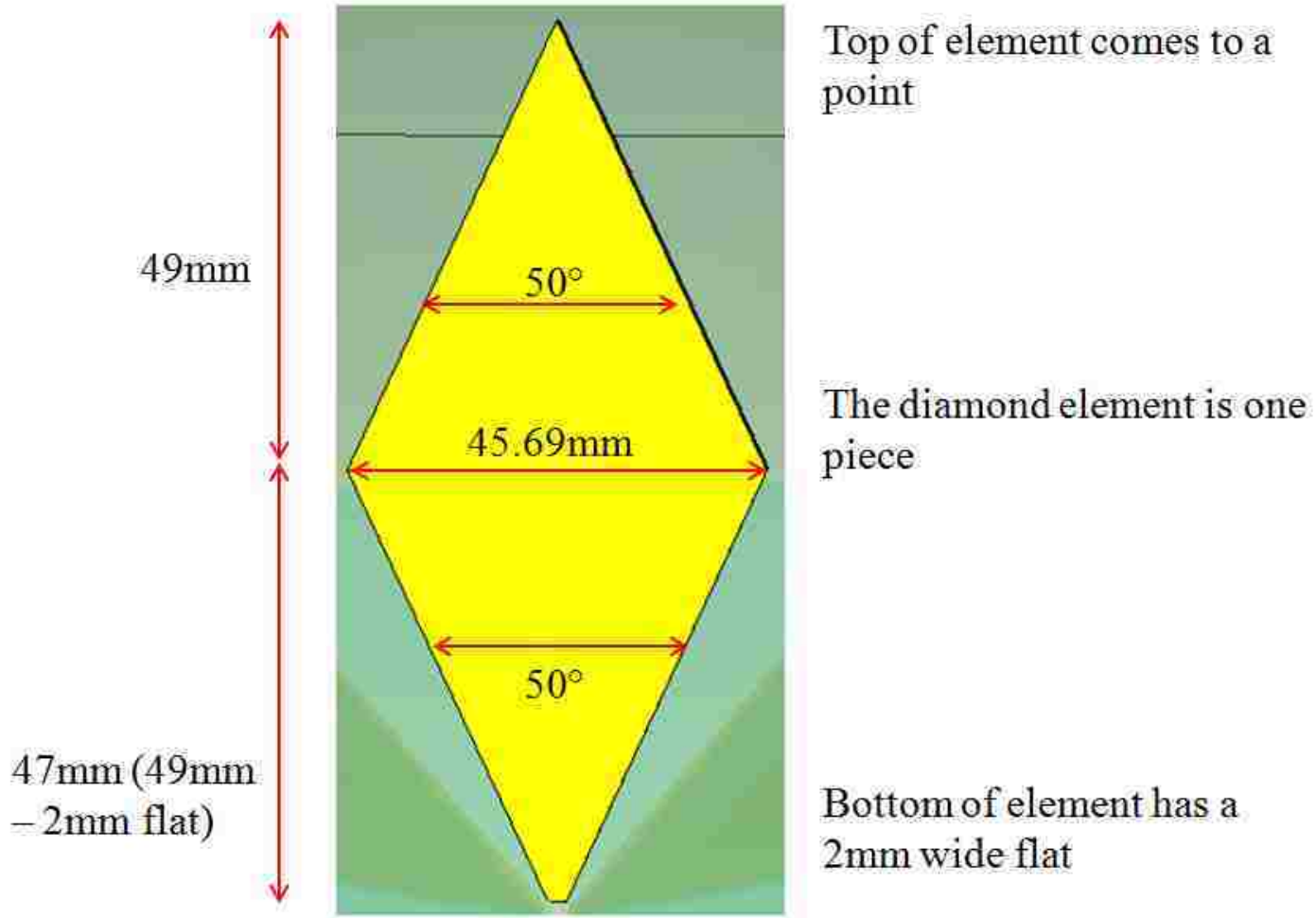

Figure 274: Top view of radiating element

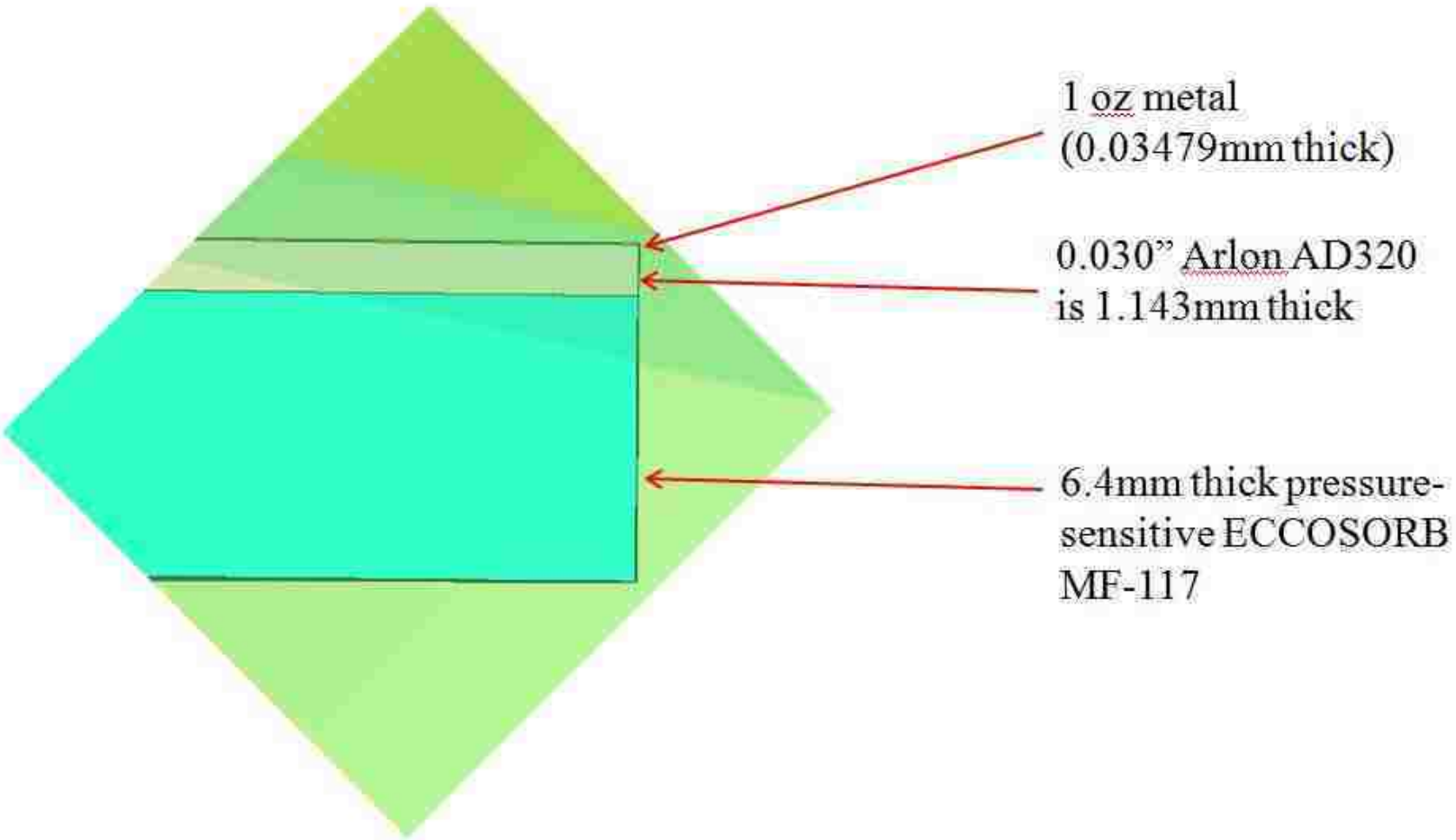

Figure 275: Side view of radiating element

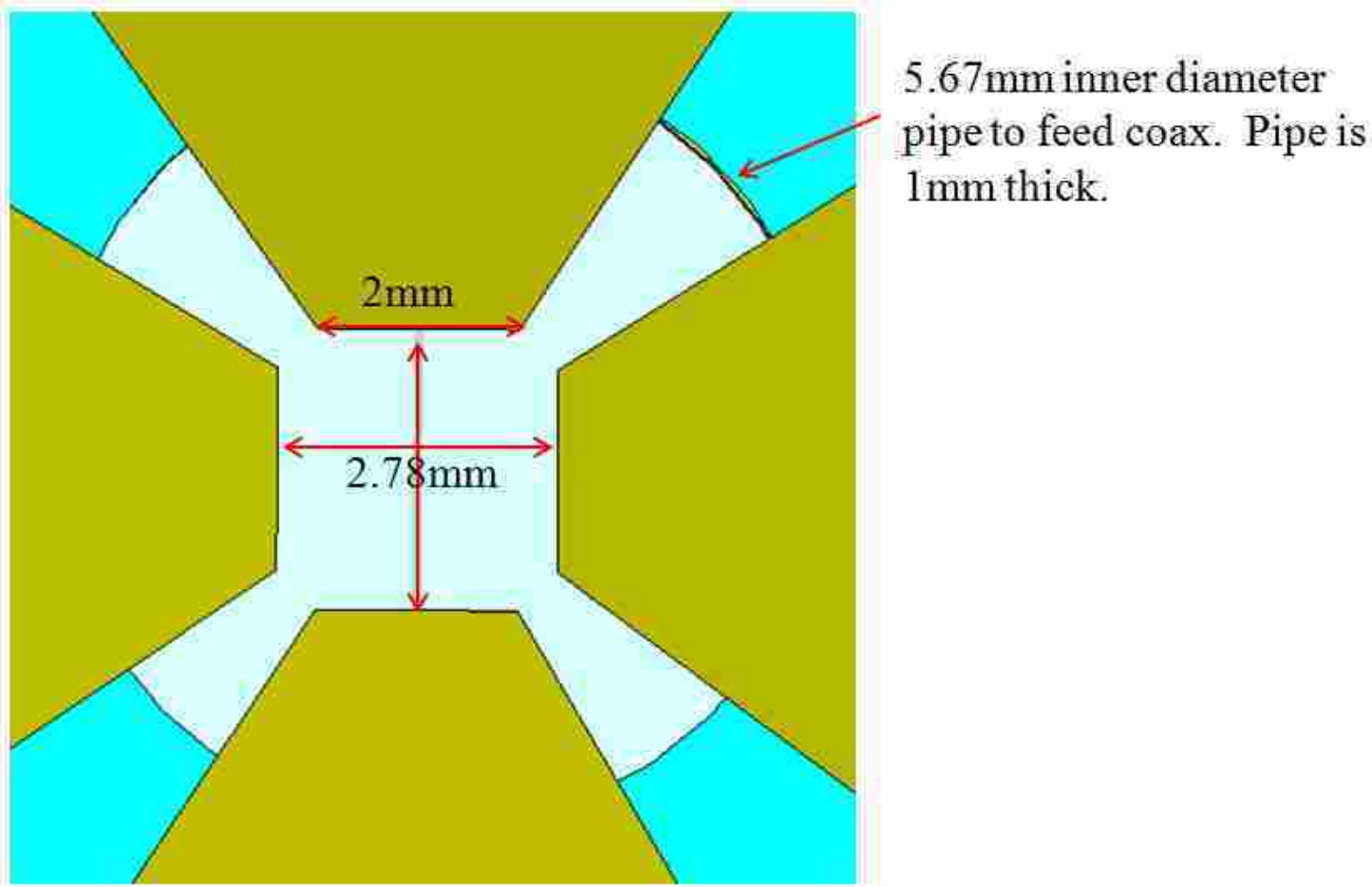

Figure 276: Feed gap region

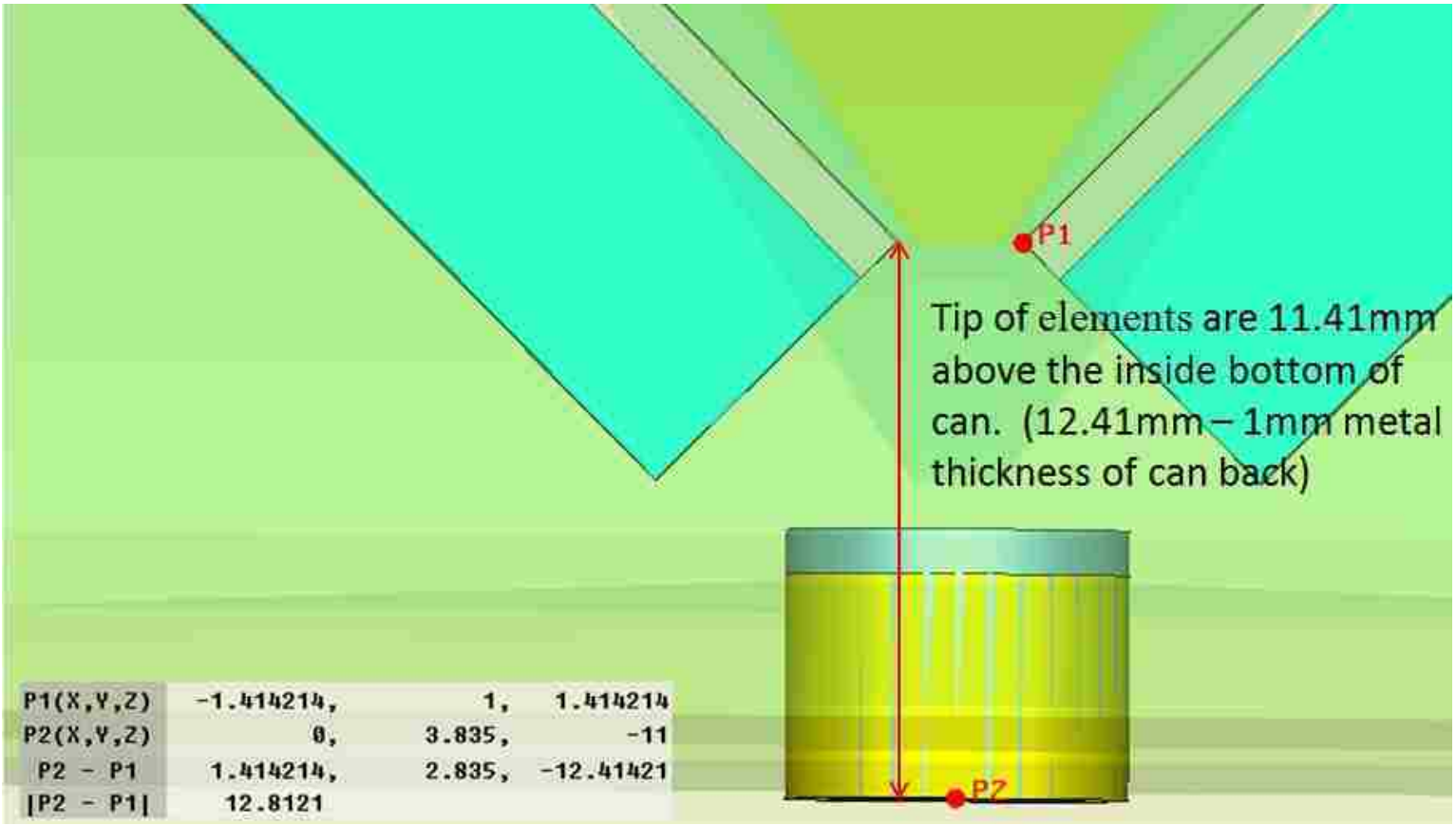

Figure 277: Location of radiating elements

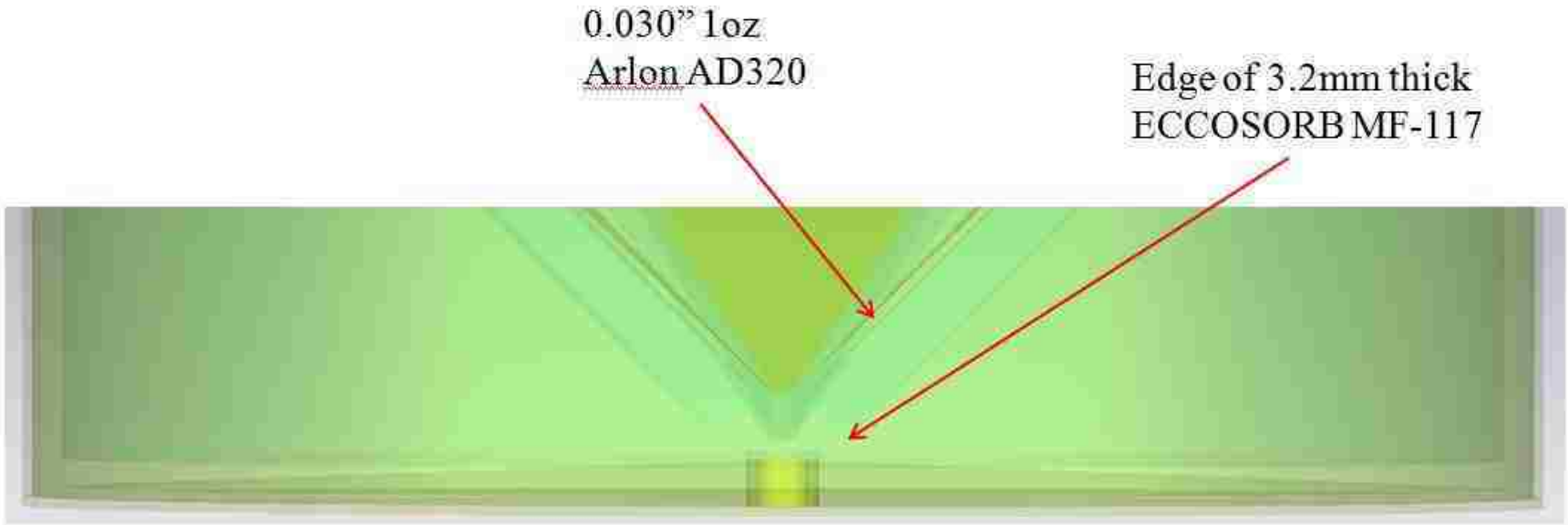

Figure 278: Side view at bottom of cavity

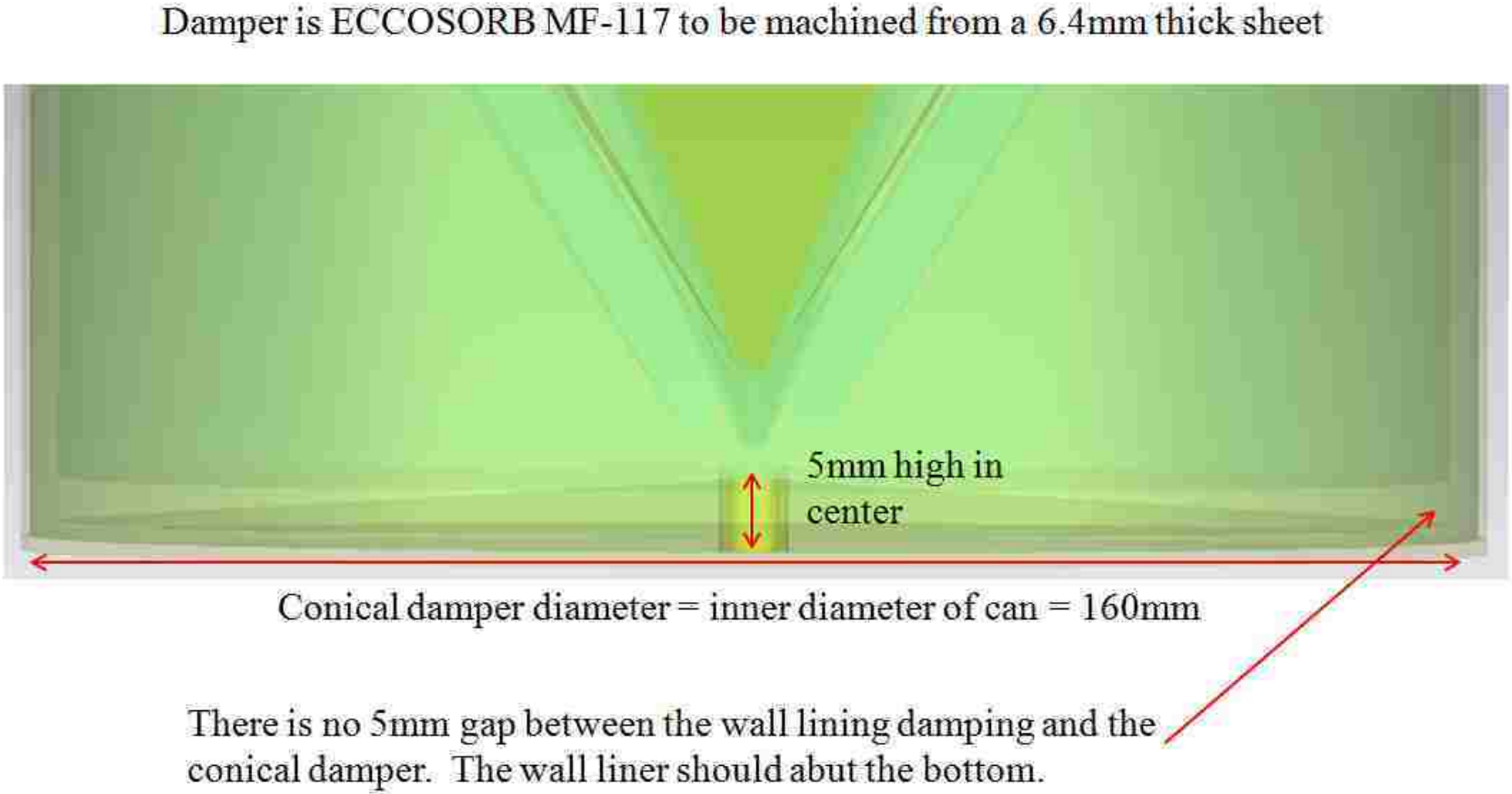

Figure 279: Conical damper at bottom of cavity

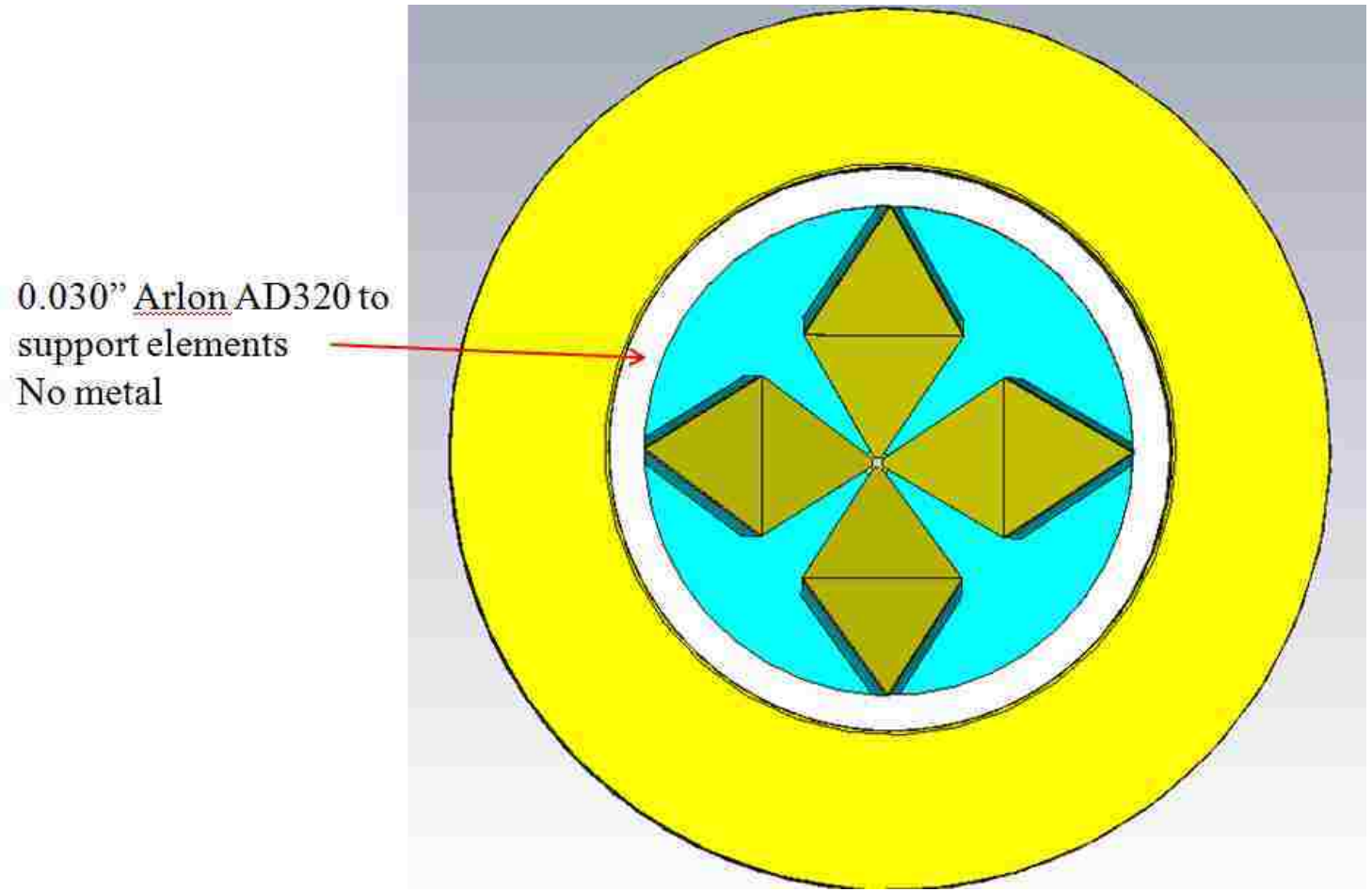

Figure 280: Top support ring for radiating elements

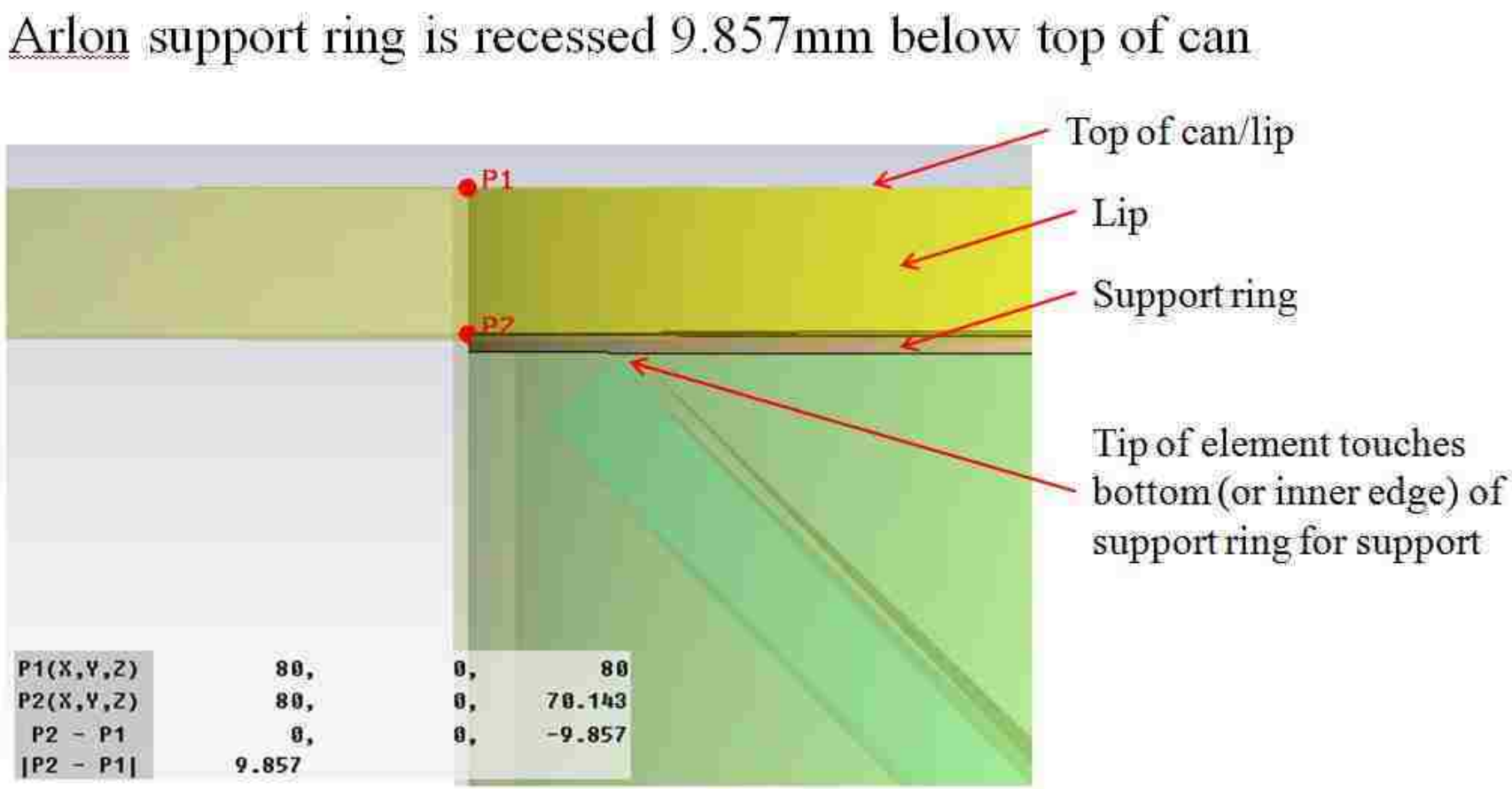

Figure 281: Recessed support ring

Bibliography

[1] M. L. Kodachenko et al, "Microwave diagnostics of dynamic processes and oscillations in groups of solar coronal magnetic loops," in *World Space Environment Forum 2005,* Austria, May 2-6, 2005.

[2] D. E. Gary, "Beam Squint with Broadband Feeds," Unpublished communication, Feb. 8, 2011.

[3] A-INFO, "A-INFO Antenna Products," [Online]. Available: http://www.ainfoinc.com/en/pro_pdf/antenna.pdf. [Accessed 7 August 2013].

[4] TECOM, "Broadband Dual Polarized Log Periodic Antennas," [Online]. Available: http://www.tecom-ind.com/files/1/4c9b84a6df021-DA0205001.pdf. [Accessed 7 August 2013].

[5] R. Dybdal, "Defocusing loss for a log-periodic fed reflector," *IEEE Transactions on Antennas and Propagation,* 33, 7:809, 1985.

[6] D. F. Martyn, "Temperature radiation from the quiet sun in the radio spectrum," *Nature,* 158 : 632, 1946.

[7] A. E. Covington, "Some Characteristics of 10.7-Centimetre Solar Noise, I," *Proc. Inst. Radio Eng.,* 36 : 454, 1948.

[8] A. E. Covington, "Some Characteristics of 10.7-Centimetre Solar Noise, II," *Royal Astronomical Society of Canada,* 45, 2: 389, 1951.

[9] K. Akabane, "Solar radio emission at 9500 Mc/s pt1; a polarimeter in the microwave region," *Annals of the Tokyo Astronomical Observatory,* 6, 2 : 55, 1958.

[10] H. Tanaka and T. Kakinuma, "Polarization of Bursts of Solar Radio Emission at Microwave Frequencies," *Proc. Res. Inst. Atm. Nagoya U.,* 5, 77, 1958.

[11] K.-A. Kawabata, "A Thermal Origin of the Postburst Increases of Solar Microwave Radiation," *Intl. Astron. Union,* 16 : 143, 1963.

[12] P. Kaufmann, O. T. Matsuura and P. Marques dos Santos, "On the possible emission of polarized microwave radiation from the solar hemispheres," *ApJ.,* 156 :

43, 1969.

[13] A. Magun and C. H. Matzler, "On the observation of linear polarization of solar microwave bursts," *Solar Physics*, 30 : 489, 1973.

[14] G. A. Dulk, "Radio emission from the sun and stars," *Ann. Rev. Astron. Astrophys.*, 23 : 169, 1985.

[15] S. M. White, "Coronal Magnetic Field Measurements Through Gyroresonance Emission," *Solar and Space Weather Radiophysics*, 89, 2004.

[16] V. V. Zaitsev, A. V. Stepanov and G. P. Chernov, "Pulations of Type IV radio bursts as an indicator of protonability of solar flares," *Solar Physics*, 93 : 363, 1984.

[17] I. P. Service. [Online]. Available: http://www.ips.gov.au/Category/World%20Data%20Centre/Data%20Display%20and%20Download/Spectrograph/Solar%20Radio%20Burst%20Classifications.pdf. [Accessed 7 August 2013].

[18] V. V. Zheleznyakov and E. Y. Zlotnik, "Cyclotron lines in the spectra of solar flares and solar active regions," *Solar Physics*, 121 : 449, 1989.

[19] H. Isliker and A. O. Benz, "On the reliability of peak-flux distributions, with an applilcation to solar flares," *Astron. Astrophys.*, 375 : 1040, 2001.

[20] A. P. Cerruti et al, "Effect of intense December 2006 solar radio bursts on GPS receivers," *Space Weather*, 6 : S10D07, 2008.

[21] T. S. Bastian, D. E. Gary, S. M. White and G. J. Hurford, "Broad-band microwave imaging spectroscopy with a solar-dedicated array," in *SPIE Conference on Advanced Technology MMW, Radio and Terahertz Telescopes*, Kona, Hawaii, SPIE 3357 : 609, 1998.

[22] T. S. Bastian, "The frequency agile solar radiotelescope," *Solar and Space Weather Radiophysics*, 47, 2004.

[23] J. A. Kennewell, "RSTN Solar Radio Telescopes (Discrete Frequency) and Data," [Online]. Available: http://www.ningalooskies.com/LSO/RSTN.pdf. [Accessed 7 August 2013].

[24] 5. W. P. Affairs, "2nd Weather Squadron, Radio Solar Telescope Network,"

[Online]. Available: http://www.afweather.af.mil/library/factsheets/factsheet_print.asp?fsID=16521&page=1. [Accessed 7 August 2013].

[25] H. Lehpamer, in *Microwave transmission networks: Planning, Design, and Deployment*, McGraw Hill Professional, 2010, pp. 268-272.

[26] "Global Positioning System Standard Positioning Service Signal Specification," 2 June 1995. [Online]. Available: http://www.gps.gov/technical/ps/1995-SPS-signal-specification.pdf. [Accessed 7 August 2013].

[27] E. Collett, Field Guide to Polarization, SPIE Field Guides, vol. FG05, 2005.

[28] "The Science Behind CAPMAP," Princeton University, 2003. [Online]. Available: http://wwwphy.princeton.edu/cosmology/capmap/polscience.html. [Accessed 7 August 2013].

[29] S. M. White, Interviewee, *Senior Research Astrophysicist.* [Interview]. 2010.

[30] C. A. Balanis, Antenna Theory: Analysis and Design, 3rd Edition, Hoboken, NJ: John Wiley & Sons, 2005.

[31] B. L. Dougherty, "Technical Review of the Solar Radio Burst Locator," California Institute of Technology, July 2001.

[32] D. E. Gary and B. L. Dougherty, "Evaluation of solar radio burst locator (SRBL) data from OVRO," [Online]. Available: http://sos.kasi.re.kr/common/publications/domesticpresentations/2005%20Evolution%20of%20Solar%20Radio%20Burst%20Locator%20(SRBL)%20at%20OVRO.ppt. [Accessed 7 August 2013].

[33] Y. Dou et al, "The Korean Solar Radio Burst Locator KSRBL," *Pubs. of the Astro. Society of the Pacific,* Vol. 121, No. 879, May 2009.

[34] N. J. I. o. Technology, "OVSA Expansion Project," [Online]. Available: http://www.ovsa.njit.edu/. [Accessed 7 August 2013].

[35] "LPDA: Logarithmic Periodic Dipole Antenna Calculator," Changpuak, 2006-2013. [Online]. Available: http://www.changpuak.ch/electronics/lpda.php. [Accessed 7 August 2013].

[36] V. H. Rumsey, "Frequency Independent Antennas," in *IRE National Convention Record, Pt. 1, pp. 114-118,* 1957.

[37] R. S. Elliott, "A View of Frequency Independent Antennas," *Microwave J.,* pp. 61-68, December 1962.

[38] R. H. DuHamel and D. E. Isbell, "Broadband logarithmically periodic antenna structures," in *IRE Nat. Conv. Record 5, Pt. 1, 119-128,* 1957.

[39] H. G. Booker, "Slot Aerials and Their Relation to Complementary Wire Aerials," *J. Inst. Elect. Eng. Part III A,* pp. 620-626, 1946.

[40] S. D. S. o. M. &. Technology, "Log-Periodic Dipole Array (LPDA)," 12 April 2005. [Online]. Available: http://montoya.sdsmt.edu/ee382/handouts/LPDA1.pdf. [Accessed 7 August 2013].

[41] O. Raisanen, "Impedance of a lambda/2 dipole antenna," 5 August 2007. [Online]. Available: https://plus.google.com/116317362025285673698/posts. [Accessed 7 August 2013].

[42] R. L. Carrel, "Analysis and Design of the Log-Periodic Dipole Antenna," University of Illinois, University Microfilms, Inc., Ann Arbor, MI, 1961.

[43] S. A. Schelkunoff, Electromagnetic Waves, New York: Van Nostrand, Chapter 11, p. 441, 1943.

[44] R. Chatterjee, Antenna Theory and Practice, 2nd Ed., New Age International, 1996, pp. 83-84.

[45] A. H. Systems, "SAS-542 Folding Biconical Antenna," 1996-2013. [Online]. Available: http://ahsystems.com/catalog/SAS-542.php. [Accessed 7 August 2013].

[46] F. J. Gonzalez and G. D. Boreman, "Comparison of dipole, bowtie, spiral and log-periodic IR antennas," *Infrared Physics & Technology,* pp. 418-428, 46, 2005.

[47] R. C. Compton et al, "Bow-Tie Antennas on a Dielectric Half-Space: Theory and Experiment," *IEEE Transactions on Antennas and Propagation,* Vol. Ap-35, No. 6, June 1987.

[48] T. Weiland, "A discretization method for the solution of Maxwell's equations for six-component fields," *Electronics and Communication AEUE,* pp. 116-120, Vol.

31, No. 3, 1977.

[49] "SG 64," Satimo , [Online]. Available: http://www.satimo.com/content/products/sg-64. [Accessed 1 November 2013].

[50] "IEEE Standard Test Procedures for Antennas," *IEEE Standard 149-2005*, p. Chapter 7.3, 2005.

[51] A. D. Yaghjian, "An Overview of Near-Field Antenna Measurements," *IEEE Transactions on Antennas and Propagation*, Vols. AP-34 (1), pp. 30-45, January 1986.

[52] RF-Lambda, "50W 2.0-8 GHz 180 Degree Hybrid Coupler," [Online]. Available: http://www.rflambda.com/pdf/hybrid/RFHB02G08GPI.pdf. [Accessed 1 November 2013].

[53] Wellshow, ".085 Semi-Flexible Coaxial Cable," [Online]. Available: http://www.wellshow.com/spec/cable/D08501C5ST.pdf. [Accessed 1 November 2013].

[54] J. E. Hwangbo et al, "An Evaluation of the Solar Radio Burst Locator (SRBL) at OVRO," *Journal of the Korean Astronomical Society*, vol. 38, pp. 447-443, 2005.

[55] Hyperlabs, "HL9402 Broadband Amplitude- and Phase-matched Balun," 2013. [Online]. Available: http://www.hyperlabsinc.com/datasheets/HL9402.pdf. [Accessed 1 November 2013].

[56] B. Doxey, Interviewee, *VP Sales and Marketing.* [Interview]. 26 August 2013.

[57] K. Takamizawa, Interviewee, *Technical Manager, Research and Technology.* [Interview]. 18 November 2013.

[58] P. Wade, "Parabolic Dish Antennas," 1994, 1998. [Online]. Available: http://www.qsl.net/n1bwt/chap4.pdf. [Accessed 7 August 2013].

[59] J. T. Saetre, "Prime Focus Satellite Antenna reflector calculation," 2004. [Online]. Available: http://www.satellite-calculations.com/Satellite/reflector.htm. [Accessed 7 August 2013].

[60] R. H. DuHamel and F. R. Ore, "Log Periodic Feeds for Lens and Reflectors," in *IRE Nat. Conv. Record*, Pt. 1, 128-137, 1959.

[61] H. Reasoner, "Microwave Feeds for Parabolic Dishes," in *Proceedings of Microwave Update '89*, 75-84, 1989.

[62] Y. Rahmat-Samii, Antenna Handbook: theory, applications, and design, Y. T. L. a. S. W. Lee, Ed., Van Nostrand Reinhold, 1988, pp. 15-42.

[63] B. W. Malowanchuk, "Selection of an Optimum Dish Feed," in *Proceedings of the 23rd Conference of the Central States VHF Society, ARRL*, 35-43, 1989.

[64] J. A. Kennewell, Interviewee, [Interview]. 2 September 2013.

[65] S. M. White, Interviewee, *Senior Research Astrophysicist.* [Interview]. 23 August 2013.

[66] TECOM, "Dual L.P. Antenna Assy," Chatsworth, CA, 1995.

[67] M. Clemens and T. Weiland, "Discrete Electromagnetism with the Finite Integration Technique," *Progress In Electromagnetics Research*, pp. 65-86, PIER 32, 2001.

[68] R. Schuhmann and T. Weiland, "Conservation of discrete energy and related laws in the finite integration technique," *Progress In Electromagnetics Research*, PIER 32, 2001.

[69] O. C. Zienkiewicz, "A new look at the Newmark, Houbolt and other time stepping formulas, a weighted residual approach," *Earthquake Engineering and Structural Dynamics*, pp. 413-418, No. 5, 1977.

[70] O. C. Zienkiewicz, W. L. Wood, N. H. Hine and R. L. Taylor, "A unified set of single step algorithms; part 1," *Int. J. for Num. Meth. in Eng.*, pp. 1529-1552, Vol. 20, 1984.

[71] P. Monk, "A mixed method for approximating Maxwell's equations," *SIAM J. Numer. Anal.*, pp. 1610-1634, December Vol. 28, 1991.

[72] M. Clemens, "Zur numerischen Berechnung zeitlich langsamver anderlicher elektromagnetischer Felder mit der Finiten-Integrations-Methode," Technische Universitat Darmstadt, Ph.D. Dissertation, 1998.

[73] A. Taflove and S. C. Hagness, Computational Electrodynamics The Finite-Difference Time-Domain Method, Norwood, MA: Artech House, 2005.

[74] E. &. Cuming, "ECCOSORB MF," 8 October 2008. [Online]. Available: http://www.eccosorb.com/Collateral/Documents/English-US/MF.pdf. [Accessed 7 August 2013].

[75] C. Bishop, "The Relationship Between Loss, Conductivity, and Dielectric Constant," 13 November 2001. [Online]. Available: http://www.electromagnetics.biz/The%20Relationship%20Between%20Loss.pdf. [Accessed 7 August 2013].